Role of substrate on formation process and properties of plasma electrolytic oxidation coatings

Dissertation
zur Erlangung des akademischen Grades
Doktorin der Ingenieurwissenschaften
(Dr.-Ing.)
der Technischen Fakultät
der Christian-Albrechts-Universität zu Kiel

vorgelegt von

Ting Wu

aus
Sichuan, VR China

Kiel 2022

Gutachtern der Dissertation

1. Gutachter: Prof. Dr. Mikhail Zheludkevich

2. Gutachter: Prof. Dr. Rastko Vasilic

3. Gutachter: Prof. Dr.-Ing. Jeffrey McCord

4. Gutachter: Prof. Dr. Stephan Wulfinghoff

Vorsitzender des Promotionsausschusses:

Prof. Dr.-Ing. Jeffrey McCord

Tag der mündlichen Prüfung:

8th September 2022

Eidesstattliche Erklärung

Hiermit erkläre ich, dass die beigefügte Dissertation, abgesehen von der Beratung durch die Betreuerin, nach Inhalt und Form meine eigene Arbeit ist.

Die Arbeit, ganz oder zum Teil, wurde nie schon einer anderen Stelle im Rahmen eines Prüfungsverfahrens vorgelegt und ist abgesehen, von den im Anhang angegebenen Veröffentlichungen, nicht anderweitig zur Veröffentlichung vorgelegt worden.

Außerdem ist die Arbeit unter Einhaltung der Regeln guter wissenschaftlicher Praxis der Deutschen Forschungsgemeinschaft entstanden.

Unterschrift 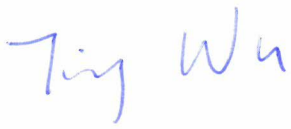

Geesthacht, den 05. 04. 2022

Abstract

Plasma electrolytic oxidation (PEO) is a promising surface treatment technology for commercial applications in order to improve the corrosion and wear resistance of light and valve metal substrates. Moreover, the potential to produce multifunctional coatings including biocompatibility, biodegradation, antifouling, electrical conductivity, magnetism as well as photocatalytic activity attracts further attention for a wide range of applications. However, often the lack of insight into the PEO mechanism restricts the optimization process of the coating performance. Furthermore, alloys and composite materials with addition of alloying elements and reinforcement phases even make the process more complex with respect to the pure metals. The understanding of the evolution of multi-phase materials in PEO processing and their influence on the PEO coating formation and properties could lay a solid foundation for an effective optimization strategy.

This thesis is a comprehensive study of PEO, covering a wide range of substrates from light metals such as Al and Mg alloys, to composite materials. It is aimed at revealing the influence of substrate microstructure/properties on PEO coating formation process, morphology, microstructure, composition and properties, as well as the evolution behavior of the coatings in presence of additional phases and intermetallics. The results have shown that, the presence of additional phases and intermetallics (caused by alloying elements), eg. Al_2O_3 fibers in Mg composite, and $MgLi_2Al$ (Li) in MgLi alloy, can be responsible for fluctuation of the voltage response and modified characteristics of the discharges during the processing. Moreover, the coatings are not uniform especially for short treatment duration due to the local morphology and microstructure of coatings on the intermetallics, such as $Mg_{17}Al_{12}$, Al-Nd, Al-Mn-Nd in AZ91Nd alloy, and Al_2Cu and Al_5FeSi in AlSi9Cu3 alloy. This heterogeneity of the coating can be fully eliminated by either increasing the current density or prolonging the processing time. However, it could be detrimental to the quality of the resultant coating.

New phases eg. $MgAl_2O_4$ in the coating on Mg composite are found due to the incorporation of the phases/alloying elements reacting with other coating forming species. The new phases can potentially endow the coating with improved performance and/or additional functions. Before the breakdown phenomena of the process, the oxidation of the substrate is controlled by the electrochemical stability of different phases in the substrate, for instance, $Mg_{17}Al_{12}$/α-Mg and Al_2Cu/α-Al. When the discharges are generated, the reaction of the substrate/coating is controlled by the electrochemical property together with the chemical stability and melting point of the additional phases and intermetallics, regarding their reactive and/or inert incorporation into the coatings. Besides, the distribution of these phases and intermetallics in the substrate can influence the evolution behavior, eg. the large size of Al_2O_3 fibers can delay the process and the incorporation will be postponed.

In addition, the in-situ PEO study of Ti alloy demonstrated a different oxidation behavior of Ti in comparison to Al and Mg, featured by the lattice expansion due to the oxygen penetration. Attractive combination of corrosion and photocatalytic properties were obtained on Ti and high melting

temperature Nb substrate. The introduction of species from the electrolyte is also a way to introduce new phases in the coatings, which can enable the coatings with improved performance and even other useful properties.

Zusammenfassung

Die plasmaelektrolytische Oxidation (PEO) ist eine vielversprechende Oberflächenbehandlungstechnologie für kommerzielle Anwendungen, um die Korrosions- und Verschleißfestigkeit von Leicht- und Ventilmetallsubstraten zu verbessern. Darüber hinaus weckt das Potenzial zur Herstellung multifunktionaler Beschichtungen inklusive Biokompatibilität, biologischem Abbau, Antifouling, elektrischer Leitfähigkeit, Magnetismus und photokatalytischer Aktivität weiteres Interesse für ein breites Spektrum von Anwendungen. Allerdings schränkt der fehlende Einblick in die Mechanismen der PEO oft den Optimierungsprozess der Leistungsfähigkeit der Beschichtung ein. Außerdem machen Legierungen und Verbundwerkstoffe mit zusätzlichen Legierungselementen und Verstärkungsphasen den Prozess im Vergleich zu reinen Metallen noch komplexer. Das Verständnis der Auswirkungen von Mehrphasenwerkstoffen auf den PEO-Prozess und deren Einfluss auf die Bildung und die Eigenschaften von PEO-Schichten könnte eine solide Grundlage für eine effektive Optimierungsstrategie bilden.

Diese Arbeit ist eine umfassende Studie über PEO, die ein breites Spektrum von Substraten abdeckt, von Leichtmetallen wie Al- und Mg-Legierungen bis hin zu Verbundwerkstoffen. Sie zielt darauf ab, den Einfluss der Mikrostruktur/Eigenschaften des Substrats auf den Prozess der PEO-Beschichtung, die Morphologie, die Mikrostruktur, die Zusammensetzung und die Eigenschaften sowie das Entwicklungsverhalten der Beschichtungen bei Vorhandensein zusätzlicher Phasen und intermetallischer Verbindungen aufzuzeigen. Die Ergebnisse haben gezeigt, dass das Vorhandensein zusätzlicher Phasen und intermetallischer Verbindungen (verursacht durch Legierungselemente), z. B. Al_2O_3-Fasern in Mg-Verbundwerkstoffen und $MgLi_2Al$ (Li) in MgLi-Legierungen, für Schwankungen der Prozessspannung und veränderte Eigenschaften der Entladungen während der Behandlung verantwortlich sein kann. Darüber hinaus sind die Beschichtungen insbesondere bei kurzer Behandlungsdauer aufgrund der lokalen Morphologie und Mikrostruktur der Beschichtungen auf den intermetallischen Werkstoffen wie $Mg_{17}Al_{12}$, Al-Nd, Al-Mn-Nd in der Legierung AZ91Nd sowie Al_2Cu und Al_5FeSi in der Legierung AlSi9Cu3 nicht gleichmäßig. Diese Heterogenität der Beschichtung kann entweder durch eine Erhöhung der Stromdichte oder eine Verlängerung der Bearbeitungszeit vollständig beseitigt werden. Dies kann sich jedoch nachteilig auf die Qualität der entstehenden Beschichtung auswirken.

Neue Phasen, z. B. $MgAl_2O_4$, in der Beschichtung auf dem Mg-Verbundwerkstoff sind auf die Einlagerung der Phasen/Legierungselemente zurückzuführen, die mit anderen beschichtungsbildenden Spezies reagieren. Die neuen Phasen können der Beschichtung möglicherweise eine verbesserte Leistung und/oder zusätzliche Funktionen verleihen. Vor Erreichen des Durchbruchspotentials wird die Oxidation des Substrats durch die elektrochemische Stabilität der verschiedenen Phasen im Substrat gesteuert, z. B. $Mg_{17}Al_{12}$/α-Mg und Al_2Cu/α-Al. Wenn die Entladungen auftreten, wird die Reaktion des Substrats/der Beschichtung durch die elektrochemischen Eigenschaften zusammen mit der

chemischen Stabilität und dem Schmelzpunkt der zusätzlichen Phasen und Intermetalle hinsichtlich ihrer reaktiven und/oder inerten Einbindung in die Beschichtungen gesteuert. Außerdem kann die Verteilung der Phasen und intermetallischen Verbindungen im Substrat das Evolutionsverhalten beeinflussen, z. B. kann das große Volumen der Al_2O_3-Fasern den Prozess verzögern und die Einlagerung wird hinausgezögert.

Darüber hinaus zeigte die In-situ-PEO-Studie der Ti-Legierung ein anderes Oxidationsverhalten von Ti im Vergleich zu Al und Mg, das zunächst durch eine Gitterexpansion aufgrund des Sauerstoffeinbaus gekennzeichnet ist. Eine attraktive Kombination von Korrosions- und photokatalytischen Eigenschaften wurde sowohl auf Ti- und Nb-Substraten mit hoher Schmelztemperatur erzielt. Der Einbau von Spezies aus dem Elektrolyten ist auch eine Möglichkeit, neue Phasen in die Beschichtungen einzubringen, die den Beschichtungen verbesserte Leistungen und weitere nützliche Eigenschaften verleihen können.

Table of contents

1. Introduction

Plasma electrolytic oxidation (PEO) is a surface treatment process developed from conventional anodization to produce ceramic-like coatings on different metallic substrates, eg. Al, Mg, Ti, Nb and Zr and their alloys [1-5]. The process is typically performed in environmentally friendly electrolytes, involving high voltage up to few hundred volts and accompanied by numerous short-living micro-discharges on the surface of the work pieces [6-8]. The PEO process is complex and involves electrochemical, chemical, plasma-chemical, thermal and pressure stimulated processes, which are decisive to the microstructure, morphology and composition of the coating and hence to the properties [9, 10]. The PEO coatings are attractive to provide high corrosion and wear resistance, as well as other advantages, such as biocompatibility and photocatalytic activity relying on the composition of electrolyte and substrate [11-16].

Optimizations and predictions of properties are limited since the formation process is influenced by many factors, including the substrate materials, the electrolyte, the power source and the electrical parameters. As a result, the properties of the PEO coatings are alterable and could not always meet the requirements. Many efforts have been taken to improve the performance, especially the corrosion and wear resistance of the coatings [17-19]. Some improvements have been achieved mainly through optimizing the electrical parameters, adjusting the constituent of the electrolytes and using combinations of PEO with various pre- and/or post-treatments [20-24]. However, some of the optimizations are designed for a specific material and if the substrate materials are changing, the optimizations may not work. Since the coating formation involves the oxidation of the substrate the coating is mainly composed of species from the substrate. The clear understanding of how the microstructure/composition of the substrate materials and the properties of oxides influence the PEO coatings formation could be the key for more effective optimization strategies.

Therefore, in present PhD thesis, a comprehensive study is focused on the influence of various substrates, including a wide range of Al, Mg, Ti and Nb based metals, alloys, and composites on the PEO process, and the characteristics of the coatings (morphology, microstructure and composition), as well as their effect on the final properties of the coatings.

2. State of the art

Material mix on micro- and macro scales: Impact on PEO processing – A review (Review paper submitted for publication)

Ting Wu [a], Carsten Blawert [a], Maria Serdechnova[a], Mikhail Zheludkevich [a, b]

[a] Institute of Surface Science, Helmholtz-Zentrum Hereon, Max-Planck Strasse 1, 21502 Geesthacht, Germany

[b] Institute for Materials Science, Faculty of Engineering, Kiel University, Kaiserstrasse 2, 24143 Kiel, Germany

Corresponding author. Tel +49 4152872590; fax: +49 4152871960; E-mail address: ting.wu@hereon.de

Abstract

Plasma electrolytic oxidation (PEO) processing of light metals has been established for decades and is in increasing industrial use sometimes even as an alternative surface treatment to produce multifunctional coatings with environmental-friendly processing concept. Significant efforts based on different substrate materials have been devoted to optimize the PEO process for endowing the coating with a combination of properties. However, the systematic process optimization focusing on the adjustment of electrical parameters and electrolytes are restricted due to the lack of understanding about the role of substrate materials, especially alloys or composites with a complex multiphase microstructure in the PEO process. Material mix is present on the micro-scale in almost every alloy or composite, but can reach macro-scale in the case of weldments of different light metals. The investigation of the oxidation behavior of the substrate materials during PEO is essential for optimal processing strategies, and further can be extended to the joint light metals/alloys in industrial applications. The properties of the additional phases, secondary phases, intermetallics, and reinforcement phases with different alloy content, microstructure and stability influence the current distribution and alter the discharging behavior. Additionally, the incorporation of additional phases into the coatings can modify the coating composition, and enable the coating with multifunctionalities. This paper present a critical review of the different aspects of PEO processing of material mixes (Mg, Al, Ti alloys/composites and joint metals/alloys) including the influence on the PEO process, on the coating formation as well as structure and properties of the coatings. The evolution of different substrate materials during PEO treatment is reviewed. Similarities and differences are highlighted. Based on the discussion, the ideas that could potentially optimize the properties and performance of PEO coatings are stated.

Keywords: plasma electrolytic oxidation, secondary phases, light metals, joint metals

1 Introduction

Plasma electrolytic oxidation (PEO) is a promising anodizing technique utilizing high-energy electric discharges to produce in-situ ceramic-like coatings mainly on the light metals [1-3]. Over the past fifteen years, there is an outburst of publications on the topic of plasma electrolytic oxidation due to the great concern for environmental protection, energy conservation and life extension. The main application of PEO is for Al, Mg and Ti alloys; however, other substrates such as Zr, Nb, Hf and Mo are also rising attention due to their potential applications. It is worth noting that PEO treatment of common metals, such as Fe, Cu and Ni, was also reported. However, the processes are more likely relying on the decomposition of species from the electrolyte and will not be discussed further here.

The process is commonly performed in dilute alkaline electrolytes containing components, such as F^-, SiO_3^{2-}, PO_4^{3-}, AlO_2^-, $B_4O_7^{2-}$, to promote strong passivation of the metallic substrates under a high electrical field [4-7]. The employment of high voltages also creates short-living plasma discharges at the interface of the work-piece and the electrolyte [8-10], involving chemical-, electrochemical-, plasma-chemical and thermal processes [11-13]. In spite of the complexity of the involved processes, a coating with different combination of properties, including hardness, corrosion resistance, wear resistance, biocompatibility, biodegradation, thermal stability, photocatalysis and dielectric properties can be obtained [14-19]. Therefore, PEO technique is very attractive for a wide range of applications requiring multifunctional properties [20-22]. It can be expected that the properties of PEO coatings are influenced by different factors, concisely ranging from the substrate composition to the power sources, electrical parameters, and electrolytes [23-26]. Due to the intrinsic porosity, frequent micro-cracks, and ceramic-like brittleness, further approaches are required to seal the coating to improve the performance, and thus expand their applications. In addition to sealing post treatments (eg. polymer coating, sol-gel, and LDH), the optimal combination of electrical and electrolyte parameters are commonly applied to achieve a certain optimization of the PEO coatings and/or fulfil the requirements of the intended applications.

Most of the recent developments of PEO treatment are focused on alloys aiming to address the galvanic corrosion between the matrix and alloying components, enhancing their surface mechanical, electrochemical and chemical stabilities, and further enable the coatings with new functionalities. However, strong differences can be still observed on the coating of different substrates. The performance is in fact a synergy of the substrate and coating properties, different types of base metal, alloying components and metallurgical states of the substrate materials result in different properties of the coating. Their different responses to the applied voltage/current influence the PEO process, including the breakdown threshold, discharge intensity and density, which could change the coating microstructure and properties. Moreover, it is certainly clear that the composition of PEO coatings is originated from the oxidation of the substrate and the decomposition of electrolyte components. The oxidation behavior of additional phases in the substrates is different from the base metals during the

PEO. These additional phases could dissolve into electrolyte directly and/or be incorporated into the coating reactively or inertly, which can correspondingly modify the coating composition, and endow the resultant coating with new functionalities. This means that the performance of PEO coatings greatly depends on the conditions of substrate materials [27-30].

The main galvanic corrosion issues at the phase interface of a multi material mix based on light metals, such as the dissimilar weldments of Mg and Al also exist. PEO treatment is nowadays expanded to such joint materials [31, 32], showing the possibility to coat the material mixes successfully. However, optimization of the process is still required, the same as for the alloys, which are regarded as material mixes however in micro scale. The successful optimization of PEO treatment on such material mix can bring in the desirable replacements for steel materials, boosting significant weight savings and energy consumption reduction. In this sense, the insight into evolution behavior of the substrate materials can be the fundamental for a clearer direction to optimize the coating microstructure and properties systematically.

The objective of this review is to give a critical state-of-the-art overview about the influence of material mixes, ranging from different phases in an alloy to multi-material components, on the PEO process. It starts with an overview of the aspects of additional phases in alloys and composites and their effect on the PEO process and the evolutions of the secondary phases during the processing. A summary of PEO treatment on Mg, Al and Ti alloys in the presence of different phases and the corresponding morphology, thickness, micro-hardness and the corrosion performance of the resultant PEO coatings are outlined next. Furthermore, the review is extending from the microscale to macroscale discussing the problems and possibility of PEO processing of multi material mix. Finally, the similarities and differences are critically addressed.

2 Influence of multi-phase substrates on PEO processing stages

2.1 Microstructure of substrates used for PEO treatment

In the majority of PEO studies, alloys are more widely selected as substrates rather than pure metals, since multi-phase alloys have more desirable mechanical performance and their applications are more widespread. Depending on the processing routes, the alloys which are suitable for PEO treatment usually consist of various primary (eg. primary Si in Al alloys [33, 34]) and secondary phases (eg. eutectics, intermetallics and precipitates), and polymorphs (eg. α- and β-Ti in Ti alloys [35, 36], α- and β-Mg in MgLi alloys [9, 37]). In addition to “pure” alloys, additional reinforcement phases (eg. AZ91/SiC [38], 2024/SiC [39]) can be incorporated for further strengthening forming metal matrix composites (MMCs). The reinforcement phases are often ceramics and may not be suitable for PEO. As a consequence of the multiphase microstructure, the compositional heterogeneity of these substrates is inevitable, and the physical, chemical and electrochemical properties of the substrate surfaces are influenced correspondingly. For instance, in AZ91/SiC_p MMC, the secondary phase β-$Mg_{17}Al_{12}$ and

reinforcement SiC particles display relatively higher Volta potentials compared to α-Mg matrix in Fig. 1 [40], potentially indicating their higher electrochemical stability with respect to α-Mg. A challenge is to obtain uniform PEO coatings in the presence of additional phases, especially for those showing significantly different oxidation behavior in comparison to the metal matrixes during PEO processing.

2.2 Process before "breakdown"

It is well known that in a PEO process several stages can be typically distinguished. There is the anodizing stage before the breakdown discharges start, and afterwards few stages can be distinguished by different characteristics of the discharges [8, 10, 41]. Thus, the different influence of additional phases that exhibit discernable oxidation behavior during the PEO coating formation can be derived before and after the occurrence of discharges.

Before the onset of discharges, the process is an electrochemically-driven dissolution and deposition process, normally considered similar to conventional anodization [42, 43]. At this stage, the local dielectric properties of the initial conversion products on the different phases depend on the composition of the forming layers, which further has an influence on the start of breakdown of those dielectric layers [44, 45].

The electrochemical stability is an important parameter at that time influencing the dissolution, emission and conversion processes at the surface. It was found that the conversion of Al_2Cu and β-Al_5FeSi intermetallics developed more slowly in comparison to α-Al in Al alloys [46-49]. The conversion products were preferentially accumulated at the periphery of the intermetallics, however, the boundary of the intermetallics remained visible. In contrast, the electrochemically anodic $MgLi_2Al$ particles in comparison to the surrounding Mg matrix are more likely to experience a faster dissolution and redeposition processes due to the local pH increase, resulting in the scattered protuberances on the surface of MgLi alloy [50]. If no adherent conversion products are formed, the dissolution of intermetallic phases without deposition is also commonly observed [3, 51]. However, the non-conductive nature of commonly used reinforcement phases may change the distribution of currents, especially at the initial stage of the process, which causes a non-uniform deposition on the substrates. For instance, SiC particles and Al_2O_3 fibers in Mg alloys appear with no change at the beginning of PEO treatment [52, 53].

In addition, the distribution of secondary phases shows an effect on the anodic conversion. Although β-$Mg_{17}Al_{12}$ (-0.9 V, NHE) and Al-Mn intermetallics (-0.42 V, NHE) are both nobler than α-Mg (-1.3 V, NHE) in Mg-Al alloys, the initial conversion products were observed to form only around the Al-Mn intermetallics during PEO processing [13, 54]. A possible explanation is that the presence of eutectic phases (α-Mg + β-$Mg_{17}Al_{12}$) can alleviate the electrochemical potential drop between α-Mg and β-$Mg_{17}Al_{12}$ since the eutectic distributed as a transition between the two different phases [54].

2.3 Process after breakdown

Once the strength of the electrical field across the dielectric layer reaches the dielectric breakdown level, the initial discharges will be generated on the surface of the oxide film. At this period, the discharges are the driving force for the coating growth. The discharge events induce the formation of high temperature phases and reconstruct the coatings via melting of coating materials, enabling the coatings with attractive properties (eg. hardness, wear resistance, and thermal stability) that cannot be achieved through traditional conventional anodizing [55]. Normally the plasmas contain species originating from the substrate and the electrolyte, and the characteristics of the discharges, eg., intensity, density and distribution, are different due to the participation of different species [8, 9, 56]. In this sense, the additional phases could influence the coating formation from participating in the plasma reactions and further modifying the discharging behavior.

For Al, Mg and Ti substrates, many studies have reported the presence of substrate species in the optical emission spectra of discharges [8, 50, 57-59]. Due to the relatively low amount of alloying elements, it is difficult to detect their emission in the discharges considering the detection limit, however, there are still exceptions, eg., Cu in 2024 Al alloy [60]. Furthermore, the spectral lines of Al were observed, originated from an AZ31 alloy when the electrolyte did not contain any Al additives [57]. For Mg-Li system, the alloying element Li was reported to participate in the plasma reactions, and the emission intensity of discharges declined compared to pure Mg during the processing [9, 50]. Additionally, after reinforced with SiC particles and Al_2O_3-SiO_2 short fibers, Si and C were detected in the emission spectra for SiC_p/AZ31 MMC, and Al and Si were also disclosed for Al_2O_3-SiO_2/AZ31 alloy, respectively [57]. Since the species can be only originated from the reinforcement phases, it confirms that the SiC and Al_2O_3-SiO_2 reinforcement take part in the plasma process during the treatment.

Alternatively, for Nb, the optical emission line was not detected during PEO treatment, which disclosed the absence of Nb in the plasma reaction [61]. It can be assigned to the high melting temperature of Nb, which is around 2477 ℃. Nevertheless, the large quantities of heat released from the discharges will stimulate thermal processes [7, 55], such as sintering and crystalline transformation reactions. The reinforcement phases with high melting point can not be reactively incorporated into the coating unless an efficient temperature of the discharges is reached. For AZ91Nd/Al_2O_3 MMC, the formation of $MgAl_2O_4$ spinel only happened from reactive sintering process between alumina fiber and MgO once the applied voltage exceeded 280 V, at which the effective temperature could be achieved [53].

The PEO process is also influenced by the size and amount of the additional phases in the substrates. It was observed that large sized Zn-rich intermetallics at the interface of coating/ZC71 Mg alloy were mostly embedded in the coating, which hindered the coating growth [2]. Only a lateral dispersion of alloying elements in the coating around the intermetallics demonstrated the slow stepwise degradation of the intermetallics. Furthermore, Rakoch et al. [62] have observed three types of discharges occurring at the vertical, spherical and inner layer horizontal pores near the substrate (Fig. 2). The larger amount

of big sized $Mg_{17}Al_{12}$ in AZ91 alloy in comparison to AZ31 alloy resulted in the formation of vertical pores in the coating, which were less curved.

Tabs. 1-3 summarize various secondary phases in Mg, Al and Ti alloys and their influence on the PEO process of substrate, as well as on PEO coating structure and properties.

In combination with the electrolytes, power sources and electrical parameters, the formation process of the PEO coatings is finally determined by a synergistic effect, not a separate or single factor.

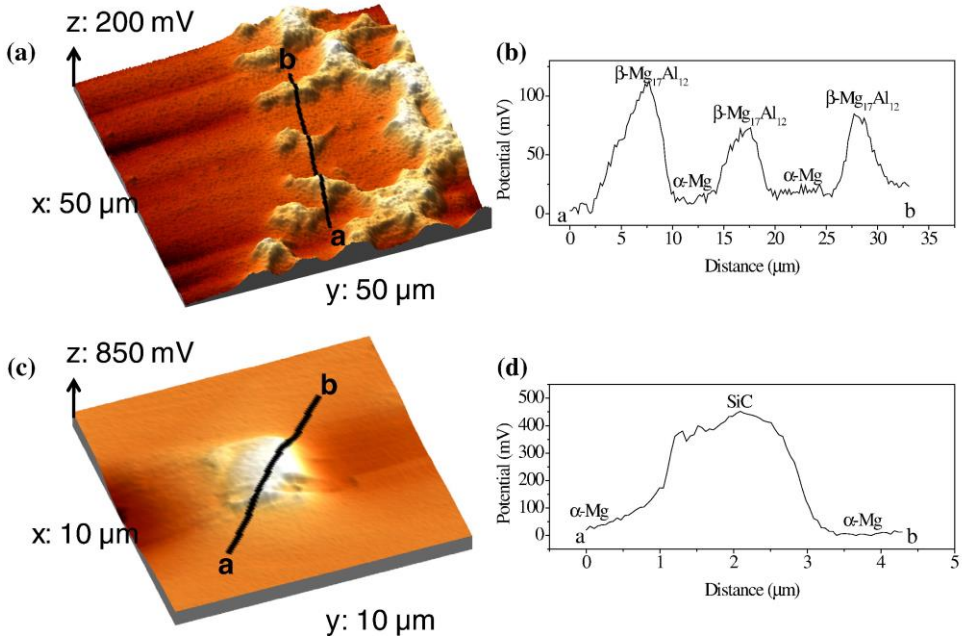

Figure 1 Surface potential maps and potential profiles in selected areas of (a, b) AZ91 and (c, d) AZ91/SiC/5p. [40]

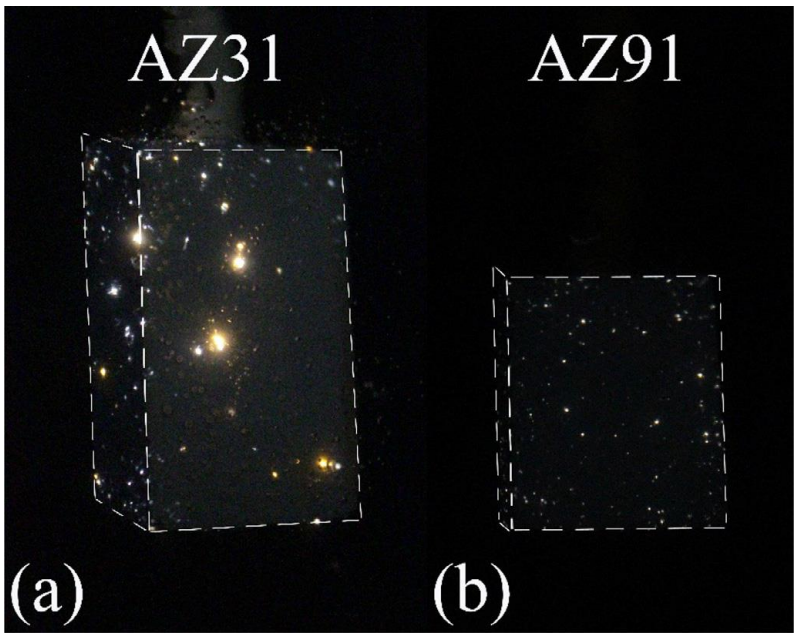

Figure 2 A typical change in the type of microdischarges during the PEO treatment of AZ31 (a) and AZ91 (b) alloys in alkaline-silicate electrolyte. [62]

2.4 Influence of additional phases on electrical response

Since the presence of additional phases shows different influence on the coating formation process, the electrical response usually presented as the voltage/current-time profiles can elucidate the evolution of PEO process. Generally, different electrical responses were demonstrated for various substrates. It was reported that additional phases could delay the voltage ramp-up during PEO processing in comparison with pure metals [21, 47, 88, 112]. Martin et al. observed that the voltage increase for the heat treated Mg-Gd-Y alloy (as-extruded + T6) was delayed due to the presence of $Mg_{24}Y_5$ and $Mg_5(GdY)$ intermetallics in comparison with as-extruded alloy (Fig. 3). Veys-Renaux et al. [88] reported that the voltage rise to the breakdown voltage and the initial discharges start more slowly in the presence of Cu-rich intermetallic particles in AA2214 Al alloy with respect to AA1050 Al alloy. Moreover, compared to pure AZ91 Mg alloy, Wang et al. [21] found that the voltage ramp rate of AZ91 Mg alloys after being reinforced with SiC particles was generally slower during PEO treatment. However, also more rapid increase of voltage was claimed in the presence of additional phases. It was found that the voltage of pure Zr substrate increased by 3 - 4 times slower compared with Zr-1% Nb alloy at the initial stage, but finally reached a similar value of 230 V [113].

The presence of different additional phases in the same metal matrix can result in different voltage responses [28, 66, 114]. Some studies [28, 78] have reported a more rapid voltage development and a higher final voltage for WE43-T6 Mg alloy compared to AZ91D Mg alloy. The two alloys have different intermetallics: WE43-T6 Mg alloy contains $Mg_{12}Nd$ particles, Nd-enriched phases, Y-rich particles and β-$Mg_{14}Nd_2Y$ in addition to α-matrix, however, AZ91D Mg alloy is composed of single β-$Mg_{17}Al_{12}$ and eutectic (α + β) phases. Nevertheless, there might be an influence of the main alloying elements Al and Nd, Y in the matrix (solid-solution) as well. The effect of alloying elements on PEO process of Mg, Al and Ti alloys is briefly summarized in Tabs. 4-6. For AZ31B alloy, the voltage is lower than that of RE containing alloy (E21 abd WE43) [66].

The distribution of additional phases, including alloying elements even in solid solution have an influence on the dielectric (passive) layer formation, the size and number of the phases in the substrates also has an effect on the electrical responses [29, 80, 115]. The voltage curve of peak aged T6 GW103K Mg alloy showed some fluctuations as sudden drop and jump at the beginning of the treatment, which is however not present in the solution T4 treated GW103K Mg alloy nor in the as-extruded alloy [29]. Compared with A319 Al-Si alloy (~7% Si), the higher content and larger size of highly stable primary Si in A390 Al-Si alloy (~17% Si) retarded the rapid increase of voltage during PEO treatment [80]. With the increase of Cu additives from 1 % to 4.5 % to an Al matrix, the voltage is slightly higher than that of pure Al at first, but then the voltage ramp slows down particularly at the initial stage of the PEO processing [115].

For metal matrix composites (MMCs) , such as 2024/SiC [39], SiC_p/AZ91 [21, 40], AZ92/SiC [38], ZC71/SiC [104], SiC_p/AZ31 [57, 101], TiB_2/A201 [108], the reinforcement phases are always nobler than the alloy matrix and have significant effect on the electrical response of PEO treatment. It was reported that the voltage slope decreased with the increasing volume of SiC particles in an AZ91 Mg matrix [40]. This is probably related to the presence of reinforcement phases disrupting the continuity of the initial conversion layer and hence changed the barrier property of the dielectric layer [38, 116].

In summary, it could be stated that the presence of additional phases in the substrates has significant influences on the electrical response. This is associated with their composition and distribution resulting, in different chemical-, electrochemical- and thermal stabilities and electrical conductivity of the alloys. The electrochemical stability and conductivity of the additional phases influence the formation of barrier layer and thus the duration of the first stage before breakdown. Reduction of this period by reaching the breakdown voltage promptly is beneficial for the more rapid start of discharge events and for coating production. This can be achieved by the selection of electrolyte composition/concentration, promoting strong and quick metal passivation. Thus, phosphate, silicate, aluminate, fluoride and their mixtures [117] have been widely used for PEO. The electrolytes also allows the modifications of the composition and properties of the barrier layers and thus changes the progress of the initial stage. Meanwhile, increasing the energy input (current/voltage) can also accelerate the growth of barrier layer and faster evolve into discharging stage.

When the discharging stage is established, a combined influence of melting point, conductivity, chemical and electrochemical stability of additional phases, as well as their size and amount in the substrates show a sophisticated influence on the properties of the discharges. This is correlated with the composition of substrate since changes of oxidation behavior of the substrate occurs in the presence of additional phases during PEO processing. In principal, the uniform and steady discharges are good to produce defect-less coatings because of the lower tendency to generate thermal-stress caused cracks and large micro-pores. Therefore, at this stage, a reasonable combination of electrical parameters, including current density, voltage, frequency, duty ratio could balance the requirement of efficient coating growth and good properties of the coating. In comparison to the oxidation of the substrate, some electrolytes containing additives such as aluminate and silicate [118, 119] can be decomposed and redeposited on the surface of the work-pieces more efficiently. In such cases, the coating is mainly composed of the species from the electrolytes and mixed with little oxides from the substrate only appearing near the substrate. This can be another option to form a relative homogeneous coating, which can at least eliminate the surface heterogeneity of the coatings in local areas enriched by secondary phases of the substrate.

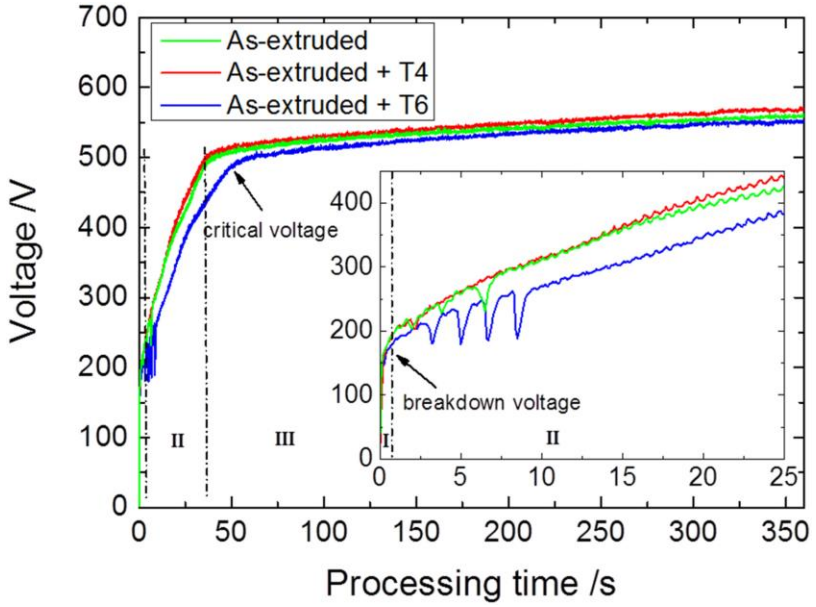

Figure 1 Voltage-time responses of PEO process conducted for (6 min) on the as- extruded substrate, on the solution (T4) substrate and on the peak-aged (T6) substrate. [29]

3 Mechanisms of conversion of additional phases during PEO treatment

During PEO processing, the alloying elements from the substrate can be incorporated in the coating or some of them can also be dissolved into the electrolyte [56, 57, 120-122]. The incorporation processes of additional phases into the PEO coatings involve interfacial reactions, including the electrochemical-driving dissolution, plasma-assisted and thermal-stimulated reactions under the high voltage [2].

For PEO coatings, the interface of coating between substrate is often found irregular due to the different oxidation rate at different locations [42, 70, 76, 84, 123-125]. Wu et al. [49] have shown a sequential oxidation of different phases in AlSi9Cu3 alloy. At the very beginning of the processing, the conversion products were primarily accumulated on α-Al adjacent to Al_2Cu and β-Al_5FeSi intermetallics. With increasing treatment time, the discharges mainly start on this layer surrounding Al_2Cu and β-Al_5FeSi. Later, even the stable eutectic Si was incorporated in the coating in form of mullite ($Al_2O_3{\cdot}SiO_2$ and finally the surface heterogeneity of the coating disappeared with extension of treatment time. It was also reported that the Mg_7Zn_3 intermetallic phases in Mg alloys interrupted the continuity of the PEO coating near the substrate and are simply embedded by the growing coating [2, 75]. The reason for the mitigation of oxidation may result from the higher electrochemical stability of Mg_7Zn_3 intermetallic phases relative to the Mg matrix, which caused a rapid passivation and further delay of their oxidation. However, the precipitate was disappearing towards the outer layer, which was associated with the effect of discharges.

The melting point of additional phases is an important factor, especially for metal matrix composites, which influences the incorporation process as well as the conversion products [39, 126]. Reinforcement phases have rather high melting points so that the reactive incorporation is influenced by the effective

temperature of discharges. A wide temperature range of discharges for PEO processes has been reported, due to the use of different processing conditions. However, the effective temperatures in the discharge affected zone is much lower than the temperature of electrons in the plasmas. There are studies that use particles with known melting temperatures to estimate the real temperature reached by the discharges. Lee et at. [127] have reported an estimation of the effective temperature in the range of 2116 - 2643 K, which is between the melting point of TiO_2 and ZrO_2 particles. A temperature gradient across the PEO coatings was also proposed, suggesting that the temperature at the surface raises faster than at the interface [128]. As a result, a clear crystallization and grain growth of the coating towards the coating surface. This observation could explain the decomposition and recrystallization of HNTs (halloysite nanotubes) near the coating surface during PEO processing of AM50 Mg alloy. In fact, oxide mixtures have often much lower melting points than single oxides and reactive incorporation can be achieved [129]. Liu et al. [57] have found that the reinforcement phases of Al_2O_3-SiO_2/AZ91 composite reacted with MgO (2852 ℃) and were incorporated in the coating by the formation of $MgAl_2O_4$ (2135 ℃) and $MgSiO_3$ (1890 ℃) during PEO processing. The larger size/volume of additional phases can also delay the reactive incorporation into the coatings, due to not enough time in the short discharges to melt the larger volume. Especially, for phases of higher thermal stability this process largely depends on the discharges and regions with repetitive discharges [89, 101].

Overall, how the additional phases in the substrate are incorporated into PEO coatings is influenced by their properties (mainly thermal-, chemical- and electrochemical properties), their sizes and distribution as well as the parameters of PEO processing, the electrical parameters and the electrolytes. The evolution of a micro scale material mix during PEO processing can be summarized in Fig. 4, illustrating the different coating formation processes in the presence of polymorph, intermetallic and reinforcement phases in the substrates, respectively.

Fig. 4(a) displays the growth behavior of the layer on a polymorph matrix. The more rapid conversion of one phase indicates the faster oxidation compared to another phase. Different oxidation behavior is originated from the compositional and structural heterogeneity of the different phases, causing the change of stabilities. It also depends on the solubility of oxygen in the lattice and how oxygen is influencing the stability of the polymorph phases. Such as the lattice transformation from β-Ti to α-Ti due to the penetration of oxygen [130]. In the presence of secondary phases (Fig. 4(b)), their stabilities relative to the matrix largely determine the sequence of oxidation and the evolution of coating formation process. Fig. 4(b (1-3)) illustrates the faster degradation of a more active secondary phase at different stages. It should be noted that the discharges are preferred to form on the layer adjacent to the secondary phases, as lattice and phase changes are disturbing the forming (oxide) layer. Thus, the barrier properties are reduced offering preferential sides for the discharges. However, Fig. 4(b (4-6)) shows the behavior when the secondary phase is nobler than the matrix and/or has larger size, resulting in a postponed conversion of those phases. The remaining additional phases stabilizes at the interface of coating/substrate due to different reasons (eg., size, melting temperature), and can be even embedded

in the coating. Similarly, the reinforcement phases in composite materials show two different incorporation modes in the PEO coating (Fig. 4(c)). The highly stable reinforcement phases, normally having quite high melting points, tend to incorporate in the coating inertly, as seen in Fig. 4(c(1-3)). They are just embedded by the growing coating. Sometimes, an interfacial conversion will occur at the boundary of the phase with the coating, leading to partial reactive incorporation. As indicated in Tab. 7, the majority of the reinforcement phases (preferentially oxides) can be still reactively incorporated in the coating, however the degradation is sometimes quite slow (Fig. 4(c(4-6))). Nanoparticles normally react faster with the coating phases than micro-sized particles. With increasing treatment time (number of discharges) and increasing energy of discharges, the reinforcement phases are disappearing gradually. In general, new phases are produced from the reaction between the reinforcement phases and the matrix oxides.

Thus, different electrical parameters of PEO treatment have an effect on the incorporation process of secondary phases. The energy of the discharges, for instance, intensive discharges can accelerate the process if they increase the melt volume, which can stimulate the reactive incorporation [131, 132]. In addition to different additives and particles added directly in the electrolytes, the formation of new components in the coatings from the reactive incorporation of additional substrate phases offers an alternative to modify the coating composition and properties. For example, mullite as a mixture of alumina and silica is an important ceramic materials due to its high thermal and corrosion stability, high creep resistance, low thermal expansion and conductivity. It was produced in PEO coatings on SiC_p/A356 Al composites because of the reactive incorporation of SiC particles from the composites [109]. Although the substrate preparation process is not as flexible as the adjustment of the electrolytes. The alloying elements, reinforcement particles and fibers on the one hand can significantly enhance the mechanical performance of the substrates, on the other hand, they also bring in the possibility to produce new phases in the coatings providing better performance and/or new functionalities.

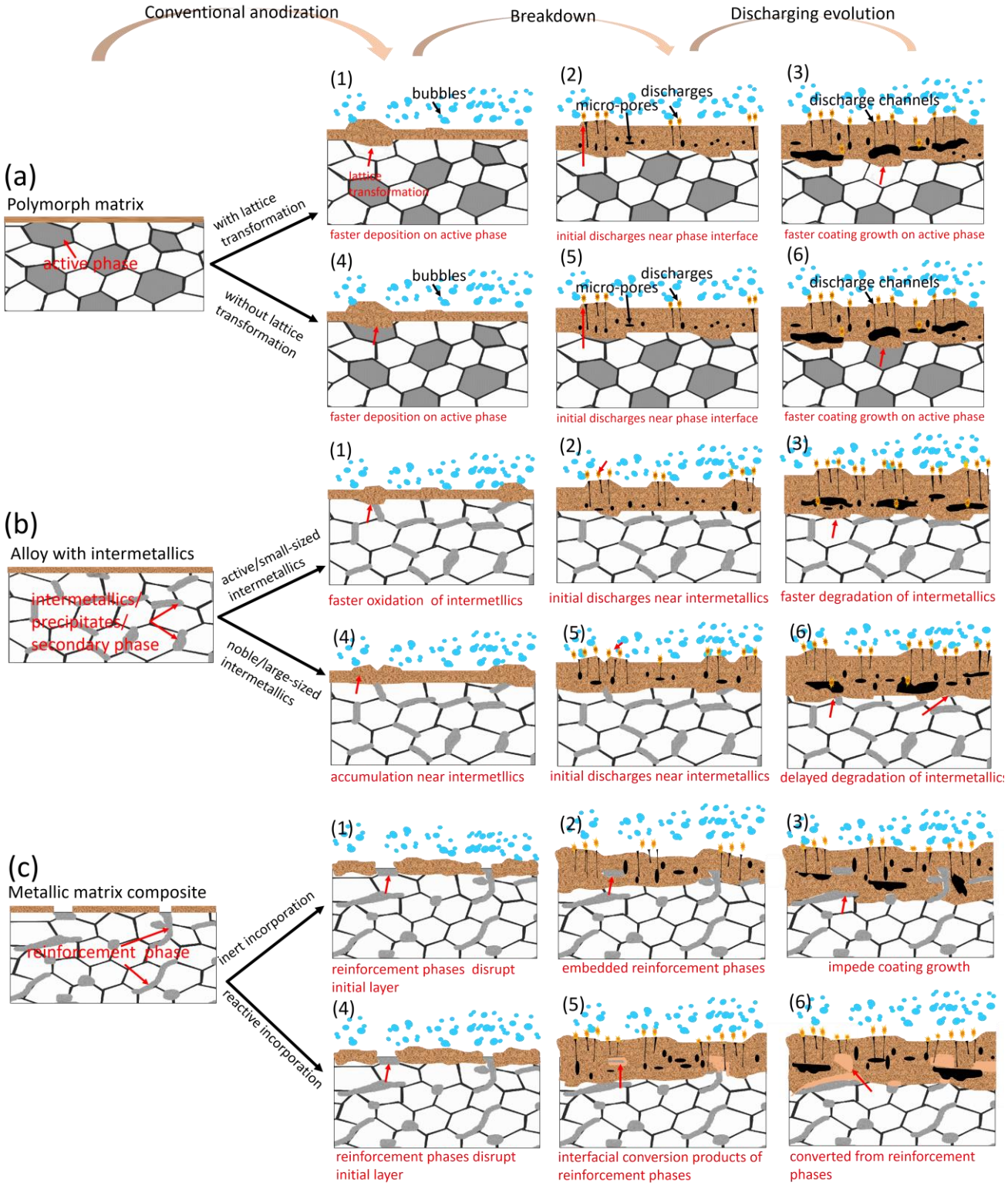

Figure 4 Schematic for the evolution process of (a) polymorph matrix, (b) secondary phase (precipitates and intermetallics) in alloys and (c) reinforcement phases in metallic matrix composite during PEO treatment.

4 Influence of multi-phase substrate materials on PEO coatings (formation, structure and properties)

A wide range of applications from transport, constructions, environmental protection to biomedical application require enhancement of the durability of PEO coatings and a reduction of costs [133-138]. In addition to the role of the electrolyte in coating formation, the composition and microstructure of the substrate materials are the key factors that determine the compositions, microstructures/morphologies and properties of PEO coatings. Different primary/secondary phases and/or reinforcement phases in the alloys can introduce a broad range of compositions and phases to the PEO coatings, which can be used to achieve a better performance of the coatings. A good example is the increase of corrosion resistance due to the formation of $MgAl_2O_4$ spinel in PEO coatings on AZ based Mg alloys [139-141].

In the present work, PEO coatings formed on Mg, Al, Ti alloys containing different intermetallics and reinforcement phases are summarized concerning coating thickness, morphology, and corrosion performance in Tab. 1-3, 7. The influence of the common alloying elements in Mg and Al alloys on the formation, properties and structures of PEO coatings is briefly stated in Tab. 4 and 5. The influence of additional phases and solid solution alloying elements can overlap and needs to be considered in the coating formation mechanisms. Further detailed discussions are provided as follows.

4.1 Mg alloys

PEO coatings have been mainly used to improve the corrosion performance of Mg and Mg alloys in respect to the high corrosion susceptibility of Mg. An improved corrosion resistance is primarily correlated with more uniform/compact coating morphology and the formation of more stable coating phases. The coating composition also has an effect on the wear protection ability, which is largely dependent on the electrolytes, electrical parameters and the substrate materials. Furthermore, the high surface roughness of PEO coatings on Mg alloys due to the intrinsic porosity is detrimental to the corrosion and tribological properties. Some publications have demonstrated photocatalytic properties of PEO coatings on Mg alloys [18, 142, 143]. However, it was originated from the incorporation of active photocatalytic species, such as TiO_2 and ZnO, in the electrolytes. The Mg alloy substrates do not show obvious influence on the photocatalytic ability of PEO coatings [144].

4.1.1 Intermetallic phases

Various intermetallic phases present in Mg alloys have been reported to participate in the PEO process and show significant effects on the coating morphology, eg., porosity, compactness, thickness, and the coating composition, hence resulting in changes of the corrosion performance of the formed coating [2, 14, 28, 30, 63, 65, 66, 70, 74, 77, 145-147]. In general, the intermetallic phases that have higher chemical-, electrochemical- and thermal stabilities in comparison to α-Mg matrix show retarded oxidation behavior, thus resulting in a non-uniform growth of the coating during PEO treatment.

Through the reactive participation of intermetallics, eg., $Mg_{17}Al_{12}$, Mg_7Zn_3, $MgZn_2$, $Mg_{12}Nd$, Mg_2Ca and $Mg_{17}Sr_2$ in the coating formation, the alloying elements can be incorporated in the coating in the form of $MgAl_2O_4$, ZnO, ZnF_2, Nd_2O_3, $CaSiO_3$ and $SrSiO_3$, respectively [63, 77, 148-152]. In contrast, some studies demonstrated that the effect of intermetallic phases can be ignored regarding the composition of PEO coatings, due to the relatively low content of alloying elements and/or their rapid dissolution into the electrolyte [153-155]. The alloy composition is diluted by the incorporation of electrolyte in the coating and concentration gradients are removed by subsequent discharges, eg., Li of MgLi alloy only participated in the early coating formation stages via enrichment in the conversion products close to the coating/substrate interface (Fig. 5). The bulk of the coating towards the coating surface does not show any noticeable Li enrichment or content.

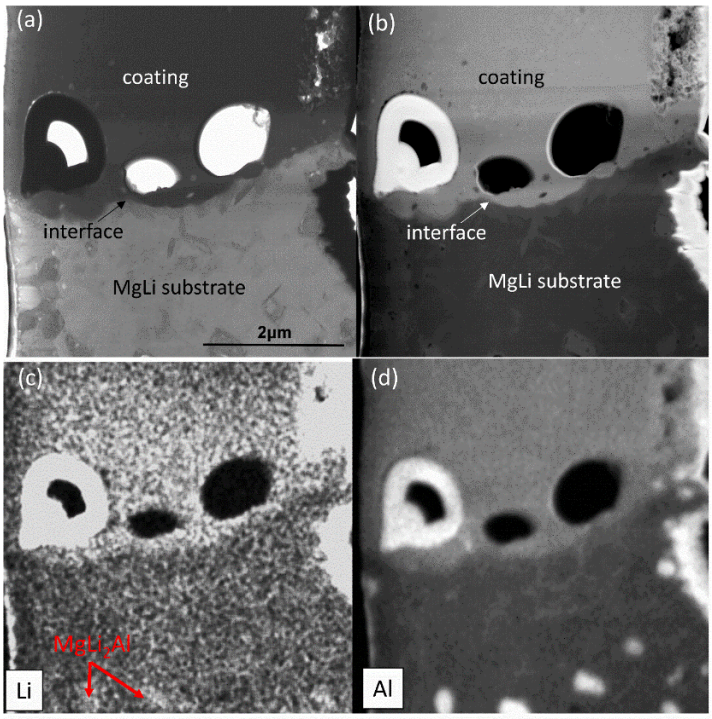

Figure 5 STEM micro images of interface of coating/ MgLi substrate after 3 min PEO treatment (a) bright field, (b) dark field, (c) the distribution of Li and (d) the distribution of Al. [50]

In Mg-Al systems, the initial oxidation process developed more slowly on β-$Mg_{17}Al_{12}$ phases with higher electrochemical stability (-0.9 V, NHE) compared with α-Mg (-1.3 V, NHE) [156, 157]. The coatings showed distinct local surface morphologies at the locations where the secondary phases were present. It was shown that the layer formed on β-$Mg_{17}Al_{12}$ phases had larger micro-pores than that of α-Mg due to stronger discharges in presence of higher Al content [78]. The non-uniformity of coating surface in the presence of β-phase can be eradicated by extension of processing time [67], however, the retarded oxidation process of secondary phases could be still recognized at the rough interface of the substrate and the coating (Fig. 4(b(4-6))).

Some studies [14, 75] revealed that the coating thickness was reduced by increasing the amount of β-$Mg_{17}Al_{12}$ phases in binary Mg-Al alloys. Nonetheless, after solution treatment of AZ91 Mg alloy, β-$Mg_{17}Al_{12}$ phases disappeared since Al is dissolving in the substrate completely. Afterwards, the PEO coating showed a more inhomogeneous microstructure [54]. It was explained by a more significant influence of cathodic AlMn intermetallics in localized oxidation behavior due to the absence of β-$Mg_{17}Al_{12}$ phase in the substrate. Note that AlMn intermetallics were not affected by the solution treatment and remained as the only dominating intermetallics in the matrix after heat treatment. Moreover, Al_8Mn_5 intermetallics (T_m=1321 K) in AZ31B Mg alloy were more difficult to be melted by the plasma discharges with respect to α-Mg (T_m=923 K) and were consequently entrapped in the PEO coating [74]. However, the melting temperature of β-$Mg_{17}Al_{12}$ phase is the lowest (710 K), thus they are melting and redistribute with Mg quite quickly.

The refinement of β-$Mg_{17}Al_{12}$ by addition of Zn [145] and Nd [63] in Mg-Al-Zn ternary system can effectively restrain the formation of destructive discharges, as a result, the PEO coating had fewer micro-pores and more compact outer layer. After Nd addition in AZ91 Mg alloy, the β phase in the substrate was refined and consequently the number and size of the open micro-pores were declined. It has been found that PEO coated AZ91Nd Mg alloy (with ca. 1 wt.% Nd addition to AZ91 alloy) has an improved resistance against galvanic corrosion due to the formation of denser coating in comparison to bare AZ91 Mg alloy [63]. The corrosion current density of the coating became 1.75 mA/cm^2, compared to 2.75 mA/cm^2 of the coating on pure AZ91 Mg alloy.

Electrochemical impedance spectra demonstrated that the aluminum containing compounds in a PEO coating of AZ91 alloy provided better passivation properties than $Mg(OH)_2$ and MgO. As a result, the PEO coating on AZ91 alloy has revealed better corrosion performance than that of WE43-T6 Mg alloy (Fig. 6) [28]. PEO coatings with relative high thickness on AM60B, AJ62 and AZ91D Mg alloys have demonstrated better corrosion performance in comparison to pure Mg [30]. Cakmak et al. [145] has reported that PEO coatings on AZ series alloys exhibited greater adhesion strength than AM series alloys. It was probably associated with the higher uniformity and lower porosity of the coatings. In addition, with increasing Al content from 3 wt.% to 9 wt.%, the micro-hardness of PEO coatings was demonstrated to increase from 380 HV to 775 HV (Fig. 7) [14]. The increasing formation of $MgAl_2O_4$ as a hard phase was related to the increasing Al content in AZ alloy series and to the elevated micro-hardness.

In the Mg-Zn system, it was reported that Mg_7Zn_3/$MgZn_2$ precipitates were embedded in the coating at the interface of coating and substrate with only lateral dispersion of alloying elements [2, 75, 104]. It has been claimed that the increasing amount of Mg_7Zn_3 in binary Mg-Zn alloys was detrimental to coating thickness[75] but overall reduced the porosity of the coating [14].

The high reactivity of alloying elements Y and Nd in WE43 alloy was found to increase the coating thickness in comparison to Al in AZ91 alloy [78]. It was also reported that the presence of Ca in AZ61

alloy tended to increase the coating thickness [158]. With increasing amount of Ca from 0 to 2 wt.%, the higher volume of Al_2Ca and Mg_2Ca phases in AM60 Mg alloy accelerated the coating thickening [158, 159]. Large sized micro-pores in the coating were observed near Al_2Ca intermetallics in AMX602 Mg alloy [74], possibly related to the altering of the discharging behavior during PEO treatment.
Additionally, the microstructure and morphology of PEO coating are also strongly correlated with the electrical PEO parameters and the electrolytes applied in PEO processing but this is not in the scope of this review.

4.1.2 Reinforcement phases

Studies of PEO treatment of Mg MMCs are relatively scarce. The presence of reinforcement particles/fibers, e.g., SiC [21, 40, 52, 101, 104], Al_2O_3, Al_2O_3-SiO_2 [57], generally hindered the coating growth and resulted in a relatively rough coating surface as well as non-uniform interfaces of coating and substrate. It has been reported that alumina fibers of an AZ91Nd/Al_2O_3 MMC were reactively incorporated in the coating and a $MgAl_2O_4$-rich layer was formed near the coating surface (Fig. 8). The incorporation mode of the reinforcement particle/fibers can be greatly influenced by their amount, size and melting point. For instance, reactive incorporation of SiC particles into PEO coating was reported for SiCp/AZ31 Mg MMC (6 vol.% SiC particles, 10 μm in diameter), resulting in the formation of $MgSiO_4$ [101]. However, partly reactive incorporation of SiC particles of ZC71/SiC/12p-T6 (2 - 20 μm in diameter) was demonstrated and only a thin layer of SiO_2 formed at the interface between coating/SiC particles [104]. In contrast, an inert incorporation of SiC whiskers (20 vol.%, 0.1 - 1.0 μm in diameter and 30 - 100 μm in length) was claimed by Wang et al [52], which can be referred to the mechanism diagram in Fig. 4(c(1-3)). PEO coatings on Mg MMCs reinforced with YAl_2 intermetallic particles [103], HA (hydroxyapatite) [107] and MWCNTs (multiwalled carbon nanotubes) [105, 106] were also reported, unfortunately, whether and how these reinforcement phases were incorporated in the coating was not discussed.

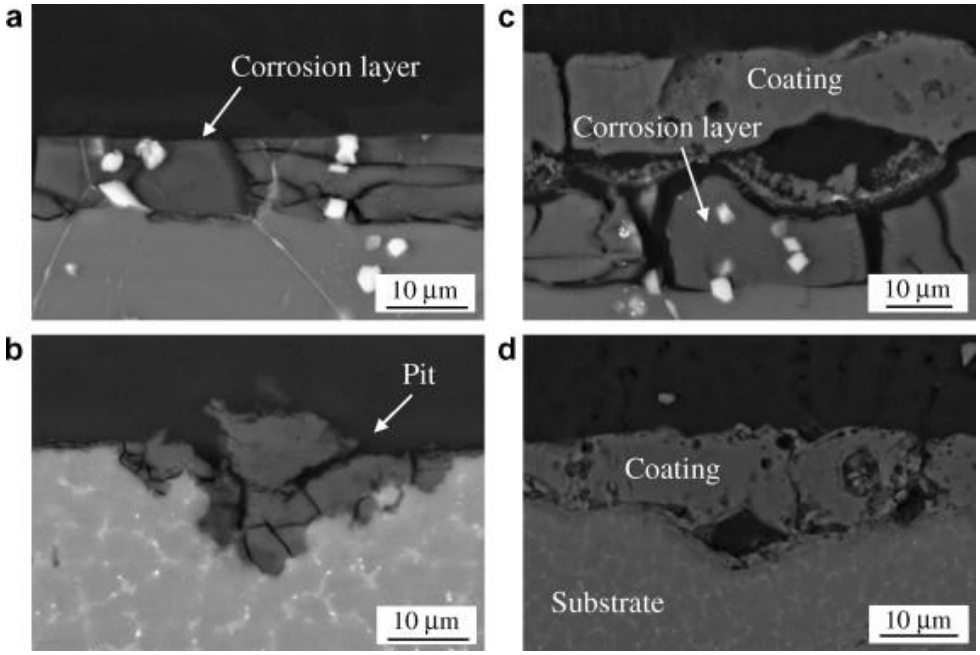

Figure 6 Back-scattered electron micrographs of the cross-sections of WE43-T6 and AZ91D alloys after 5 days of immersion in 3.5 wt.% NaCl. (a) Untreated WE43-T6, (b) untreated AZ91D, (c) WE43-T6 with PEO treatment and (d) AZ91D with PEO treatment. [28]

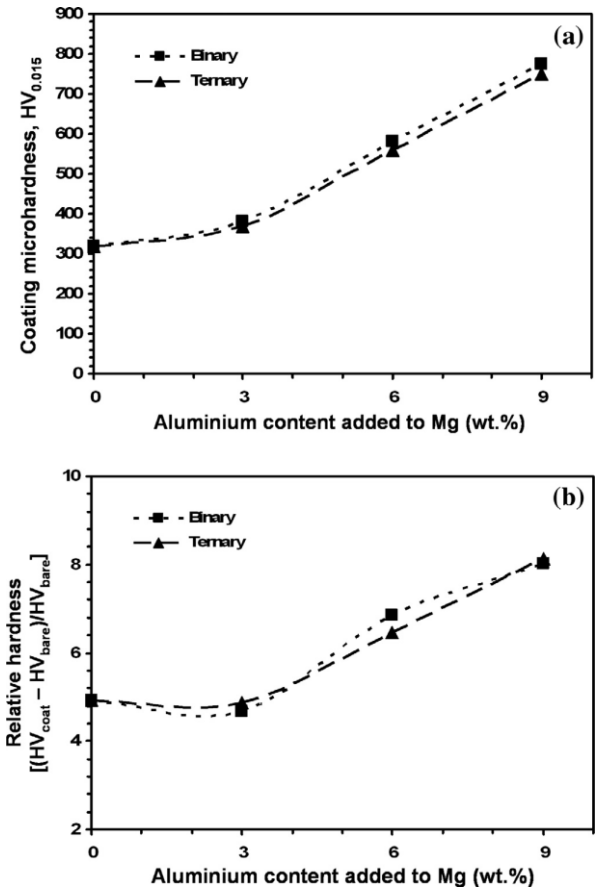

Figure 7 Influence of Al content added to Mg substrate on (a) MAO coating microhardness and (b) relative hardness of Mg-Al binary and Mg-Al-Zn ternary alloys. [14]

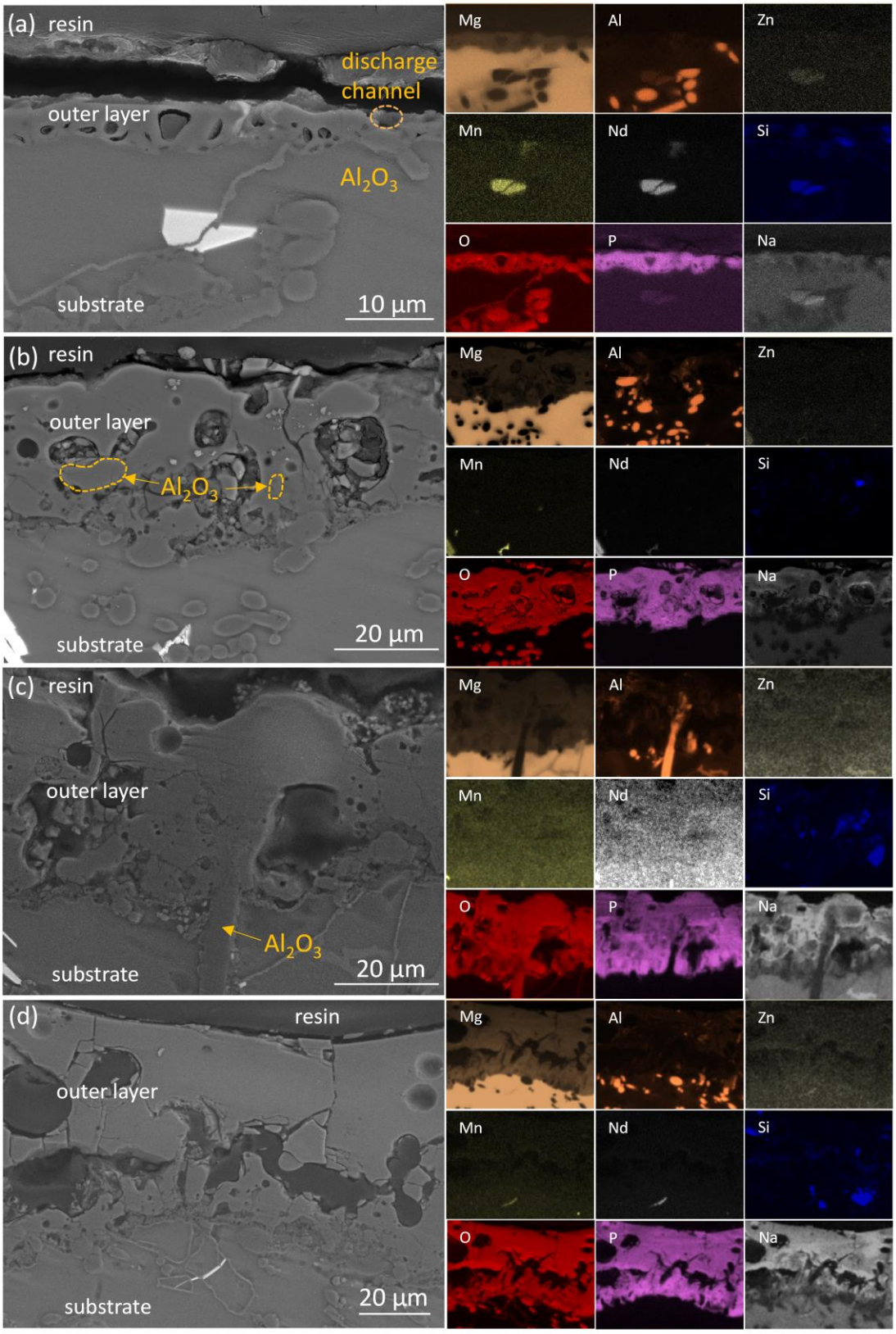

Figure 8 Cross-section morphology (BSE) and elemental distribution (EDS) of PEO coatings on AZ91Nd/Al_2O_3 MMC in sodium phosphate-based electrolyte after different processing time: (a) 60 s, (b) 300 s, (c) 600 s and (d) 1200 s. [53].

4.2 Al alloys

Different series of Al alloys, such as 2xxx (Al-Cu based), 3xxx (Al-Mn based), 4xxx (Al-Si based), 5xxx (Al-Mg based), 6xxx (Al-Mg based) and 7xxx (Al-Zn based) have been used for most of the PEO studies [49, 160-163]. The effect of individual alloying elements (Cu, Mn, Si, Mg and Zn) on PEO coating microstructures was studied on binary Al-X alloys (Tab. 5) [84, 87, 95-97, 112, 115]. Similar to the coating on Mg alloys, the primary/secondary phases in Al alloys can be involved in the plasma reactions and influence the coating compositions, microstructures and morphologies. The presence of primary/secondary phases in Al alloys also has an influence on the corrosion properties of PEO coatings [88, 89, 112, 115, 164].

4.2.1 Primary/secondary phases

In an Al9Si3Cu alloy, it has been claimed that larger micro-pores were distributed near Al_2Cu and β-Al_5FeSi intermetallics in comparison to α-Al as seen in Fig. 9 [49]. However, the layer on eutectic Si exhibited the most tiny micro-pores in the coating on Al9Si3Cu alloy. It was reported that the oxidation of noble and low electrically conductive primary/eutectic Si (T_m=1410 °C) in Al alloys in PEO treatment is difficult, while the reactive incorporation of Si in the coating is still possible with extension of treatment duration and proper PEO parameter adjustment [46, 49, 84, 112, 165]. Without addition of Si in the electrolyte, the incorporation of Si phases into the coating experienced different stages, which finally resulted in the formation $Al_2O_3{\cdot}SiO_2$ (mullite) at the outer region of the coating in addition to the main aluminum oxide phases (Fig. 10) [48, 80, 84, 112, 166]. Moreover, the high electrical resistivity of Si could retard the rapid growth of the coating and result in a decrease of coating thickness [84, 165]. The coating surface became smoother with lower surface roughness as the amount of Si phase increased, although a higher porosity was demonstrated [84]. In addition, refined Si phases can effectively improve the uniformity and compactness of the coating, which also impeded the inward growth of the coating [112]. Li et al [112] have introduced 0.1 wt% Sr into Al-Si alloy for grain refinement. The corrosion potential of the PEO coating on the refined Al-Si alloys was -0.58 V, around 15% higher than that of the unmodified alloy. The corrosion current density of the coatings in 3.5 % NaCl solution decreased from 1.52 μA/cm^2 to 0.29 μA/cm^2 after Sr modification.

The formation of Cu_2O and CuO, visible by a color change to brownish and blackish, has been claimed in the PEO processing of Al-Cu-Li alloy due to the oxidation of Al_2Cu intermetallics [167, 168]. Veys-Renaux et al [88] studied the effect of Cu intermetallics on the corrosion resistance of PEO coated AA2214 alloy in comparison with PEO coated AA1050 alloy in 0.1 mol/L Na_2SO_4 solution. The results showed that the presence of Cu particles inside of the aluminum oxide led to a decrease of electrochemical resistance by one order of magnitude (from 10^9 Ω to 10^8 Ω), compared with the coating without Cu. A similar result was demonstrated in the work of [115] showing that Cu additions in Al alloys impaired the corrosion performance of the PEO coatings. It was reported that PEO coating on

friction stirred welded 6061 Al alloy has shown better corrosion properties in the NZ (nugget zone) compared to the TMAZ (thermomechanical affected zone) and HAZ (heat affected zone) (Fig. 11) [89]. This is correlated with the presence of Al-Fe-Si particles in TMAZ and HAZ and a denser inner layer at NZ.

Aluminum oxides (α-, γ- and θ-Al_2O_3) are the main coating forming phases in PEO coatings on Al alloys. The micro-hardness of PEO coatings on Al alloys is proportional to the content of α-Al_2O_3, as seen in Fig 12. The addition of Mg, Mn, Zn and Sn in Al alloy is reported to be detrimental to the formation of α-Al_2O_3 in PEO coating and thus results in a decrease of micro-hardness of the coatings [87, 95-97, 169]. With increasing Mg content (0 -15 wt.%), the micro-hardness values of PEO coatings on Al-Mg binary alloys decreased from 2200 HV to 400 HV due to the reduced amount of α-Al_2O_3 and even the presence of α-Al_2O_3 was not noticeable in the coating with 15 wt.% Mg addition in the alloy [95]. It is also revealed in [169], that a lower Mg content in Al-Mg alloy causes a higher α- to γ-Al_2O_3 ratio and thus results in higher hardness. By a comparison of PEO coated 2024 (Cu-containing), 6061 (Mg-containing) and 7075 (Zn-containing) Al alloys [169], α-Al_2O_3 was found to be more compact in the coatings on 2024 and 7075 alloys. However, the highest wear rate was revealed for the coating on 7075 Al alloy, which could be expected from the largest network of micro-cracks in the coating on 7075 alloy. Similar to Mg alloys, Mn as alloying element in Al alloy also suppress the formation of α-Al_2O_3 and a high content of Mn tends to produce more porous and loose coatings. As a result, the coatings on Al-Mn alloys with higher Mn content showed a lower micro-hardness [87]. For Al-Zn alloys, α-Al_2O_3 was only produced in the coatings with up to 10 wt.% Zn addition. The micro-hardness of the coatings reduced with increasing amount of Zn (1 - 33 wt.%) [96]. For Al-Sn system, the highest micro-hardness of PEO coating was 1957 HV with 1 at.% Sn addition, then a further increase of Sn content to 6 at.% resulted in lower micro-hardness values [97]. It was also found that the presence of $Al_{11}Ce_3$ precipitates increased the size and amount of porosity of PEO coatings and reduced the formation of α-Al_2O_3 [98].

4.2.2 Reinforcement phases

There are only few studies focusing on PEO of Al matrix composites, reinforced with TiB_2 [108], CuO [110] and SiC [39, 109, 111] respectively. TiB_2 particles as a reinforcement phase in TiB_2/A201 Al MMC was reported to be converted into TiO_2 and then dissolved in the coating uniformly with increasing processing time [108]. Reinforced with CuO particles [110], the reaction of CuO with Al substrate has already occurred before the PEO processing, since the metallic copper in the original composite has been detected. After the PEO processing, an adherent Al_2O_3 coating was produced, without delamination or cracking. Additionally, the coating showed an effective protection during dry sliding wear tests, in comparison to the original composite.

There is no agreement on the incorporation mode of SiC in Al composites. Cui et al. [109] have reported the presence of mullite phase in the coating, however, the formation of mullite was assigned to the decomposition of the electrolyte. Nevertheless, Xue et al. [39] have demonstrated that most of SiC

reinforcement particles in 2024/SiC MMC have been molten and silicon oxide was produced. But still a few small SiC particles remained at the interface of coating/substrate, interrupting the continuity of the coating. Du et al. [111] have compared the influence of SiC particles in Al alloy with two different sizes of 40 and 60 μm, respectively, on the PEO process. Since SiC is a semiconducting ceramic phase, and does not have valve metal characteristic, a smaller current density was presented for the specimens having larger sized SiC particles. Furthermore, discharges seemed more likely occur in the area without SiC and the large-sized SiC particles resulted in an unstable process and even hindered the rapid formation of barrier layer. Moreover, mullite phase was also revealed and the content of mullite in the coating was affected by the SiC particles. The coating formed on the substrate consisting of larger SiC particles has higher amount of mullite compared to 40 μm SiC reinforced Al composite.

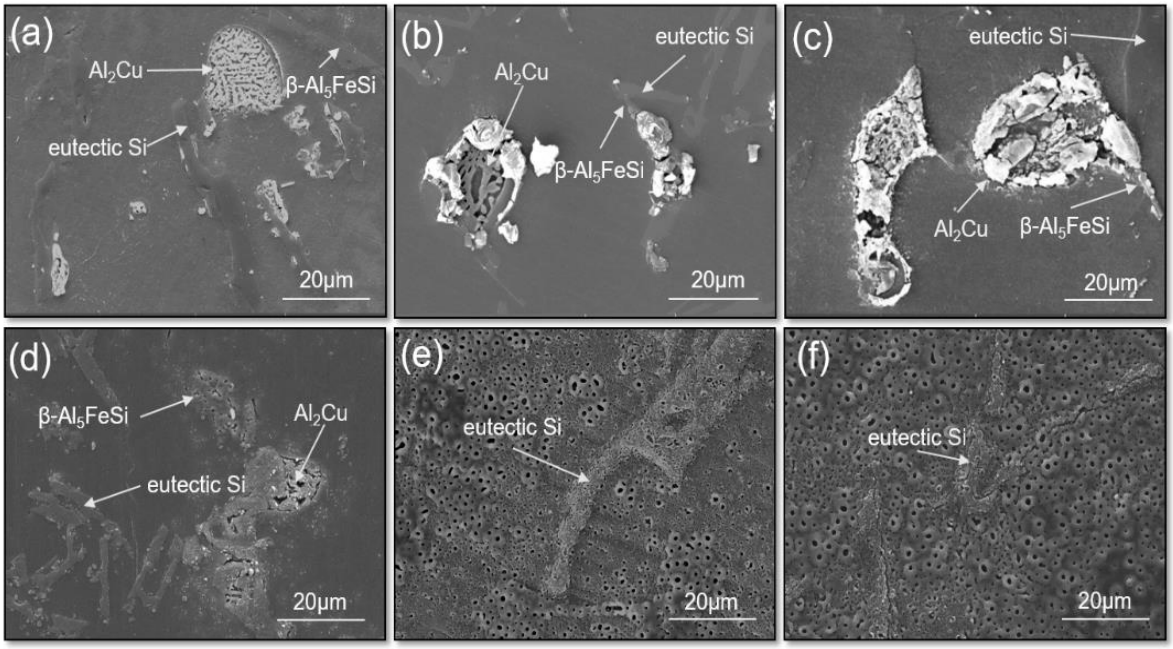

Figure 9 Surface micro-morphologies on specimens after PEO treatment: (a) 15 s; (b) 30 s; (c) 60 s; (d) 120 s; (e) 240 s; (f) 480 s. [49]

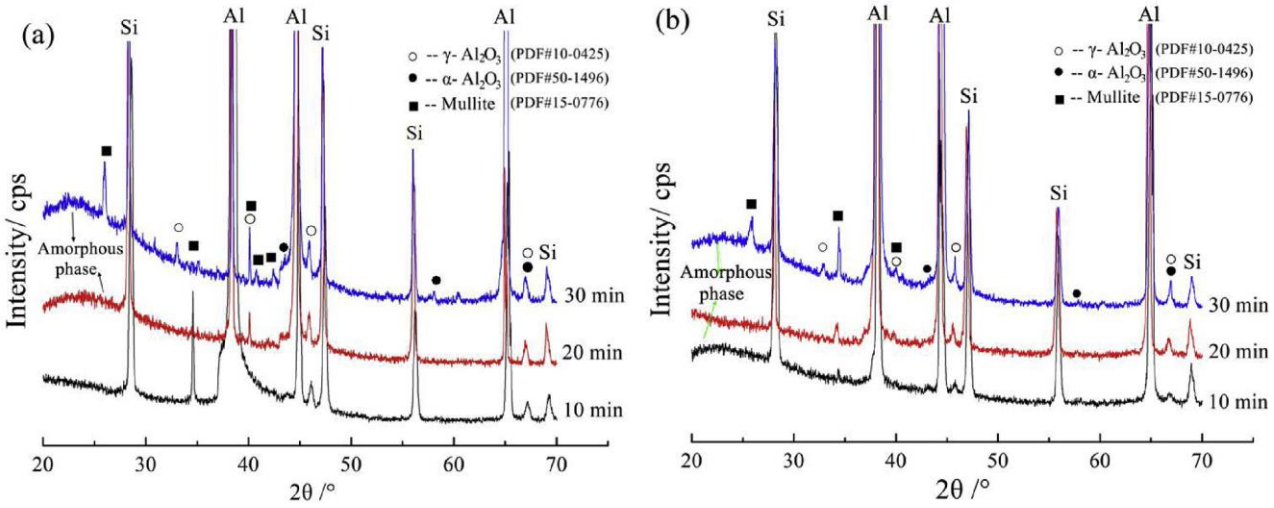

Figure 10 XRD of PEO coatings on (a) un-modified alloy, (b) 0.1 wt% Sr modified alloy. [112]

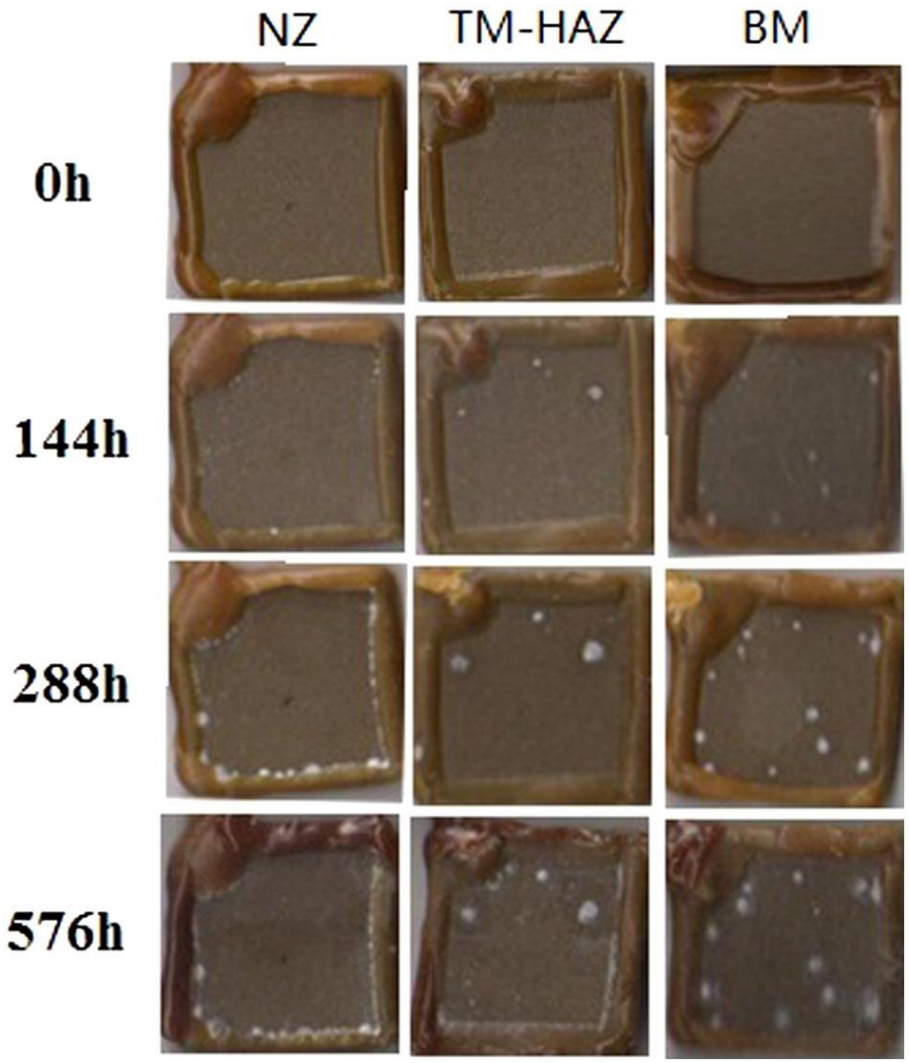

Figure 2 Effect of friction stirred Al-Fe-Si particles in 6061 aluminum alloy on structure and corrosion performance of MAO coating: NZ (nugget zone), TM-HAZ (thermomechanical affected zone and heat affected zone) and BM (base metal). [89]

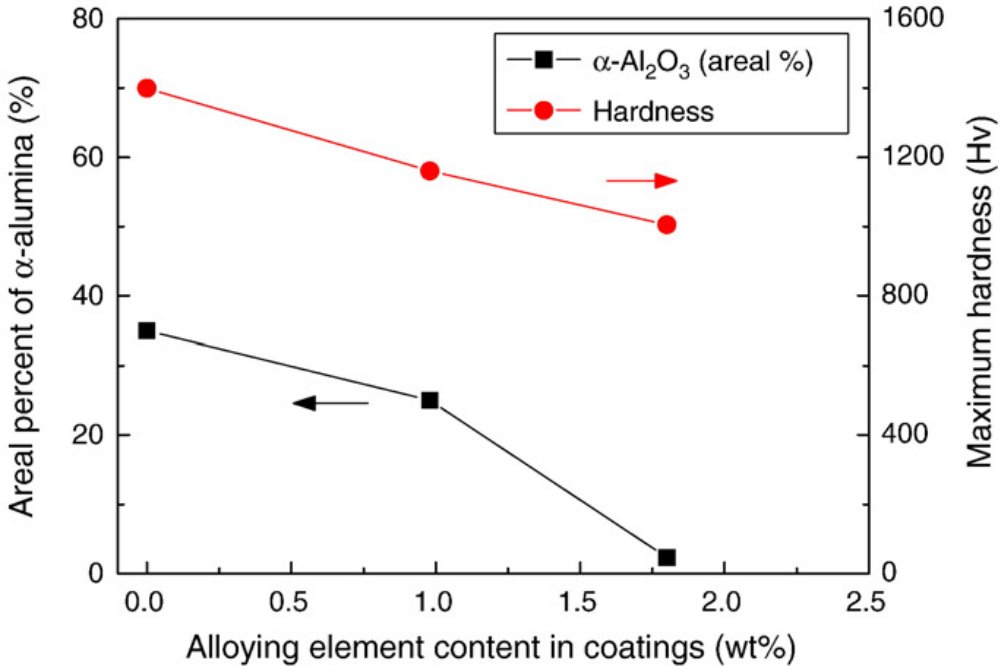

Figure 3 Correlation between the total residual alloying elements (Mg, Cu and Zn) and the percent of α-Al_2O_3 measured on the cross-sections of the coating layer, and maximum Vickers coating hardness metrics. [169]

4.3 Ti alloys

4.3.1 Polymorph microstructure

Ti alloys mostly consist either of α-Ti, biphasic (α + β)-Ti or metastable β-Ti. Ti6Al4V alloy as the most prevalent Ti alloy for PEO treatment is composed of mainly α and β phases [10, 51, 118, 170]. An PEO treatment in combination with in-situ high-energy synchrotron XRD has demonstrated an initial lattice expansion of α-Ti phases near the surface region of Ti6Al4V (Fig. 13) [130]. The lattice expansion was assigned to the high solubility of oxygen in α-Ti lattices before the formation of titanium oxide. However, β-Ti was not detected for the entire processing. The possible rapid up-take of oxygen could have already stimulated a fast transformation of β-Ti to α-Ti [130]. Furthermore, the discharges were observed firstly on β phases with higher content of vanadium in comparison with α phases [130]. This can be related to that vanadium oxides are not stable in alkaline electrolyte due to the high solubility, and the initial oxide layer on β phases was characterized with nodular surface morphology during the PEO processing of Ti-6Al-4V alloy [171, 172]. During the processing, the formation of crystalline TiO_2 can be hardly observed. Only after switching off the high voltage, the crystalline TiO_2 starts to precipitate from the amorphous phase or nanocrystalline TiO_2 (Fig. 14).

Normally the coating thicknesses on Ti alloys are in the range of 5 - 40 µm [3, 51, 105, 173]. There is a grain side effect on the coating thickness. The PEO coating on ultrafine grained Ti (grain size ~25 nm) revealed an average thickness of 36.5 µm, compared to 24.4 µm of original Ti (grain size ~100 nm- 150 nm) [173]. Wu et al. [170] have shown that after SLM (selective laser melting) processing TC4 alloy

contained smaller grain sized single α′ martensite grains and a faster coating growth rate was revealed in comparison to α + β structured TC4 alloy (Fig. 15) [170]. In addition, a uniform micro-pore distribution and relatively small micro-pores were observed on the coating surface in the presence of α' phase. In contrast, the phase transformation from single α' to multiphase α'+ α''+ β and complete β transformation of Ti-xNb alloys (x = 10, 30 and 50) did not have significant influence on coating thickness. However, the micro-pores size was increased with increasing Nb concentration [92]. Furthermore, larger micro-pores were also found on the coating in the presence of sub-micro scaled grains (Fig. 16) [174]. This could be explained by the increasing high-energy grain boundaries and structural defects, leading to less stability and more active dissolution. In comparison to CP Ti, PEO coating on Ti-6Al-7Nb alloy had a lower thickness and surface roughness [90].

The formation of different titanium oxides including anatase, rutile and brookite in the PEO coatings on Ti alloys is greatly depending on the processing conditions, e.g. applied voltage, substrates and electrolytes [10, 91, 92, 100, 170, 175]. Nevertheless, it was claimed that the content of rutile increased in the coating after the microstructure transformation of TC4 from biphasic α + β to needle α' phase [170]. Kaseem et al. [92] have reported that only anatase was formed in the coating on α' phase structured Ti-10Nb alloys. The formation of rutile in PEO coatings on (α + β)/β-Ti alloys could be controlled by the selected treatment parameters [91, 175]. At lower discharge energy, anatase can be formed and at higher energies, the rutile phase becomes more dominant.

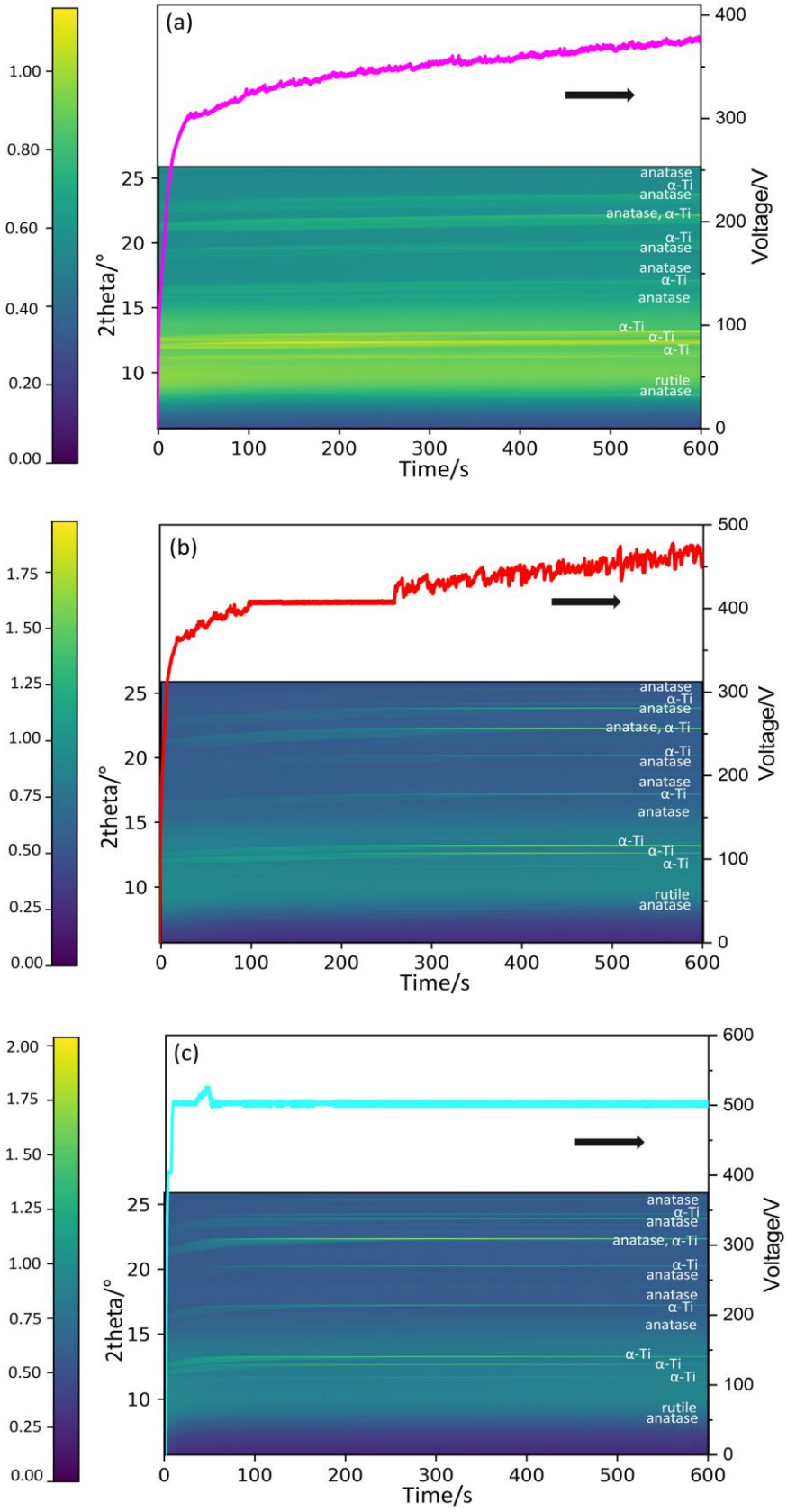

Figure 13 In-situ characterization of phase (wavelength 0.0496 nm)/voltage evolution on Ti6Al4V surface as a function of time at different current density: (a) 3 A/dm^2, (b) 5 A/dm^2 and (c) 10 A/dm^2. [130]

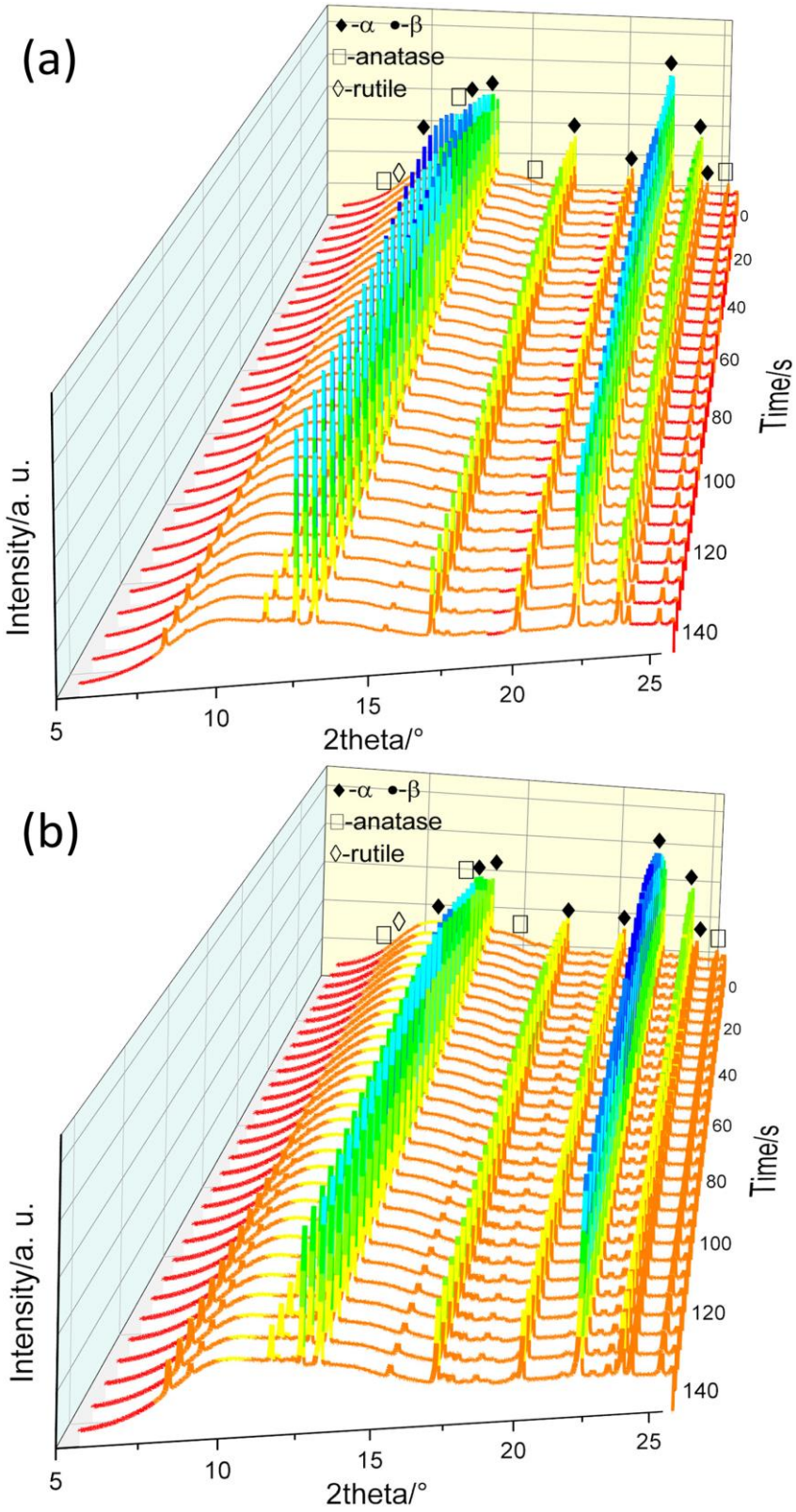

Figure 14 Changes of phase composition (wavelength 0.0496 nm) on the surface of in-situ treated specimens with time when PEO treatment is off: (a) 5 A/dm^2 and (b) 10 A/dm^2.. [130]

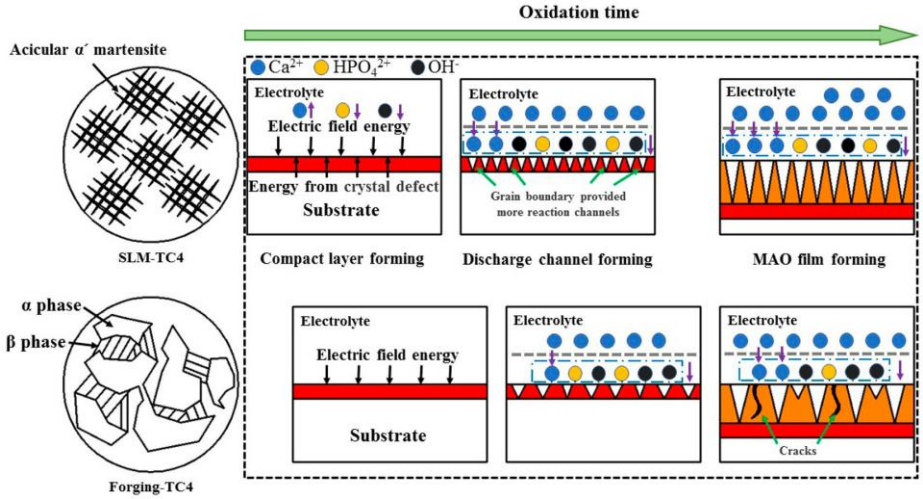

Figure 15 Schematic diagram of the growth behavior of the MAO coatings on SLM-TC4 and forging-TC4. [170]

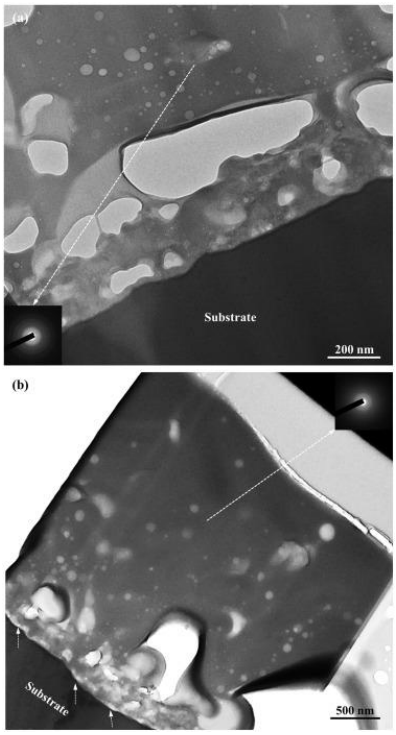

Figure 16 Cross-sectional TEM micrograph of the micro-arc oxidized film of (a) TiNiMo-120V and (b) TiNiMo-150V. [174]

Fazel et al [100] have compared the corrosion and tribocorrosion properties of PEO coated CP Ti and Ti6Al4V alloy. The PEO coating on CP Ti has revealed a lower capacitance of the inner barrier layer, leading to a higher corrosion resistance than that of the coating on Ti6Al4V alloy in a 0.9 wt.% NaCl solution. However, a better tribocorrosion resistance was demonstrated for the coatings on Ti6Al4V alloy. The tribocorrosion test showed a longer delay before a decrease in corrosion potential of the coating on Ti6Al4V was realized. Matykina et al. [51] reported a higher stability of PEO coatings on cp Ti in SBF (simulated body fluid) conditions with respect to Ti^{4+} release, compared to PEO coated

Ti6Al4V alloy. Furthermore, the release of Al^{3+} and V^{5+} through the coating on Ti6Al4V in SBF solution should be taken into consideration in respect to biocompatibility. Gu et al. [176] has claimed that PEO coating on a surface grain refined Ti6Al4V via UCFT (ultrasonic cold forging technology) has a higher micro-hardness of 568 HV relative to 501 HV of a coating for a non-modified Ti6Al4V alloy. Subsequently, a lower corrosion current density of 1.5 μA/cm^2 was revealed on the modified Ti6Al4V alloy, in comparison to 2.01 μA/cm^2 on the PEO coated non-modified Ti6Al4V alloy in 3.5 wt.% NaCl solution.

4.3.2 Alloying elements

The alloying elements in the Ti substrate can be incorporated in the PEO coatings, such as Nb and Zr, in the form of Nb_2O_5 (Fig. 17) [177] and Ti_2ZrO_6 [175]. It was reported that the incorporation of Nb in a Ti-35Ta alloy increased the size of HA particle grown on the surface during PEO processing (Fig. 18) [91]. In general, Nb as in the case of alloying element (30 wt.%) in a Ti substrate can accelerate the growth of HA on a PEO coating, which is related to a better bioactivity. A lower corrosion current density, 6.00×10^{-9} A/cm^2, of PEO coated Ti-30 wt% Nb alloy was revealed and related to the formation of a more compact coating, compared with that of Ti-10 wt% Nb (6.95×10^{-6} A/cm^2) and Ti-50 wt% Nb alloys (2.53×10^{-7} A/cm^2) [92]. It was also observed that the fatigue behavior of the alloy was not changed by the PEO processing, and different fatigue property of a PEO coated CP Ti and Ti-6Al-7Nb alloy was determined by the substrate materials only [90].

With addition of Mo to a Ti alloy, Hsieh et al. [174] have found a higher adhesive strength of the PEO coating on $Ti_{50}Ni_{48.5}Mo_{1.5}$ alloy compared to $Ti_{50}Ni_{50}$ alloy. The metallurgical state of the substrate can also influence the corrosion resistance of the PEO coating. It was demonstrated that a grain refinement of CP Ti could enhance the corrosion resistance of the PEO coating due to a highly stable oxide layer easily produced with the higher grain boundary fraction [173].

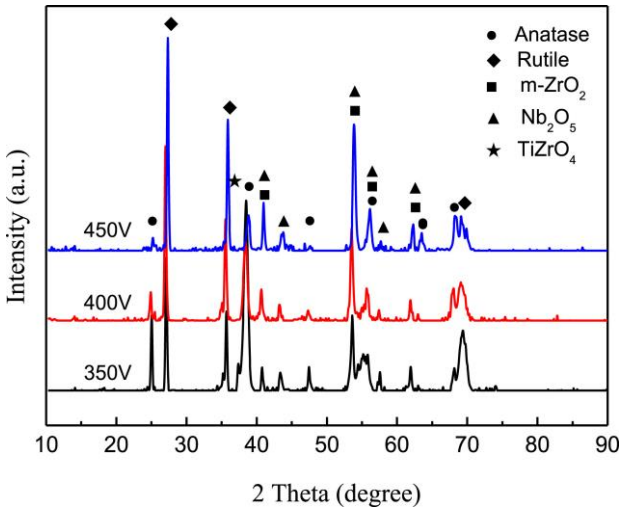

Figure 17 XRD patterns of the MAO films on Ti-39Nb-6Zr alloy after treatment with different positive voltages. [177]

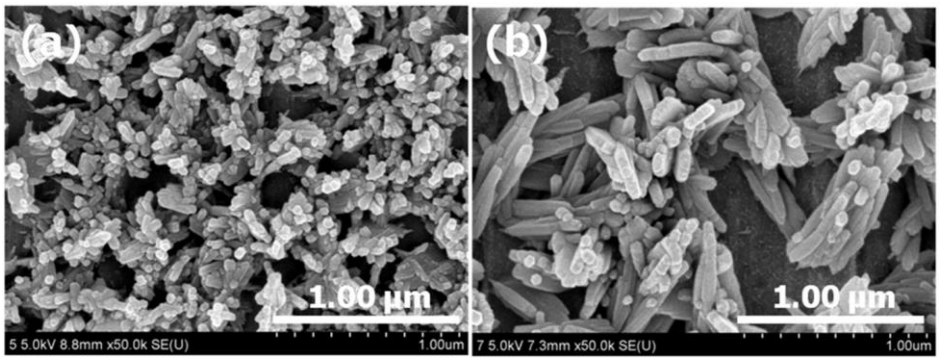

Figure 18 FE-SEM images of non-NaOH treated Ti-35Ta alloy in 2.5 mM $Ca(NO_3)_2 \cdot 4H_2O$ + 1.5 mM $NH_4H_2PO_4$ solutions after PEO processing: (a) Ti-35Ta alloy and (b) Ti-35Ta-10Nb alloy. [91]

4.4 Impact of micro-scale material mix and consequences for PEO processing

There is a triple-fold impact of micro-scale material mix: First on the formation of the dielectric layer and thus on the early stage voltage-time response, second on the later-stage coating growth and finally on the coating composition and properties.

The PEO process in the presence of different phases in different alloys and composites changes the coating composition, mainly due to different conversion oxides developing from the additional metal phases or the limit reactive incorporation of inorganic/ceramic compounds in the coating. PEO treatment improves often the surface corrosion and wear resistance through increasing the surface homogeneity and decreasing the surface free energy. However, the non-uniform growth of the coating on local areas is quite common for such micro-scaled material mixes, characterized by the locally larger micro-pores/cracks and thinner layers. For the micro-scale material mix, the most important solutions to obtain coating uniformity are

-Use of "depositing" electrolytes. Forming mainly coatings with electrolyte components/compounds.

-Stimulating/retarding dissolution in a controlled way for the different phases.

-Use of longer treatment times and higher discharge energies to force coating uniformity by reactive incorporation.

-Multi-stage PEO processing of base materials and use of different coating growth behavior.

For instance, these weak and/or non-uniform areas of the coating could be healed through using "repair" electrical mode [7], e.g. combining current-controlled mode with voltage controlled mode. At first, using a relatively high current accelerates the coating thickening; afterwards, switching to an appropriate constant voltage at higher frequencies maintains high-energy discharges to remelt the coating/substrate and release thermal stress.

In other cases with a more complex microstructure, such as metallic matrix composites, the adjustment of the PEO conditions can only achieve a very limited optimization. Moreover, the energy consumption is significant during the processing if longer treatment times or higher energy discharges are required. As a result, flash-PEO [178-180], which is proposed to achieve energy conservation using shorter

treatment time and lower energy input, could not be a good solution for such complex substrates. The surface differences/heterogeneity of the substrates cannot be easily removed with a coating thickness of only about 1 - 5 µm. To some certain degree, such a flash-PEO produced coating can remove the surface contamination, partly impede the potential galvanic corrosion between the metal matrixes and additional phases, expand the surface area and modify the surface chemistry. In that way it can still form conversion layer where other processes fail. In those cases a combination with other surface treatments (polymer coatings, sol-gel, LDH etc.) is regarded to optimize the surface properties more efficiently.

5 PEO processing of macro-scaled joint materials

Joining of different metals or alloys as a design improvement is applied to offer specific properties, weight reduction and performance enhancement in structural applications [181-184]. However, surface treatment strategies for the joint materials are necessary due to galvanic protective differences. In this sense, PEO could be a potential coating candidate, however, there are only a few studies [164, 185-195] focusing on the PEO processing of joint mixed different materials, including joining of dissimilar Mg alloys [187], Al alloys [164, 186], Mg/Al alloys [185, 186, 195] and Mg/Ti alloys [188].

5.1 Coupled Mg alloys

Savguira et al. [187] have evaluated the feasibility of PEO processing of AZ31/AZ80 FSW (friction stir welded) joints for the purpose of corrosion mitigation. At different current densities, the coating roughness did not show significant difference across the interface of two substrates. However, a dramatic change in PEO coating thickness was observed when a current density of 10 mA/cm^2 was applied. The coating thickness on AZ80 was about three times higher compared to the AZ31, which was likely related to the different electrochemical activities of AZ31 and AZ80 Mg alloys. In contrast, the coating became more uniform in thickness across all regions of the joints while using a current density of 20 mA/cm^2. As a result, the corrosion rate of PEO coated dissimilar joints has been reduced by around 63% at higher current density (Fig. 19), due to the obvious difference in coating thickness at the interface region of the substrates. It is possible that the corrosion resistance could be further improved by an appropriate selection of current density during PEO processing.

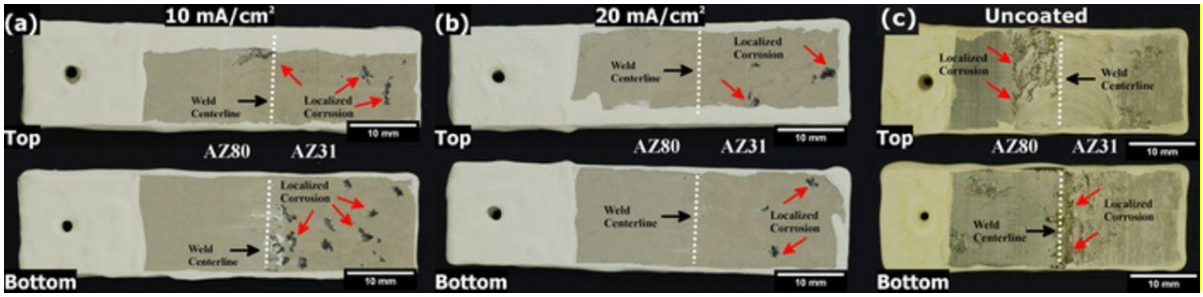

Figure 19 Corrosion morphology after a 5 day exposure to 0.086 M NaCl of a PEO processed FSW weldment coated at: (a) 10 mA/cm^2 and (b) 20 mA/cm^2. For comparison purposes (c) images showing the corrosion morphology of uncoated specimens were included as well. [187]

5.2 Coupled Al alloys

An attempt to apply PEO on coupled Al/AA7075 alloy has been made by Baron-Wiechec et al [186], since AA7075 alloy was generally considered more difficult to be anodized compared to pure Al. The transition of discharging mode from "hard" to "soft" did not show any time difference on both components of the coupled Al/AA7075 alloy. However, there were different currents passing through the different parts at different stages when a current density of 525 mA/cm^2 was applied (Fig. 20), such that the rate of coating growth was different from the separate oxidation of the alloys. The current density was firstly higher for AA7075 Al alloy, then dropping down to a lower value and finally ramped back to a higher value compared to pure Al. However, no more than 15% of difference in the charge passing through each of the two separate metals was observed, as a result, it is not sufficient to give rise to major differences in the coating thickness of the two parts.

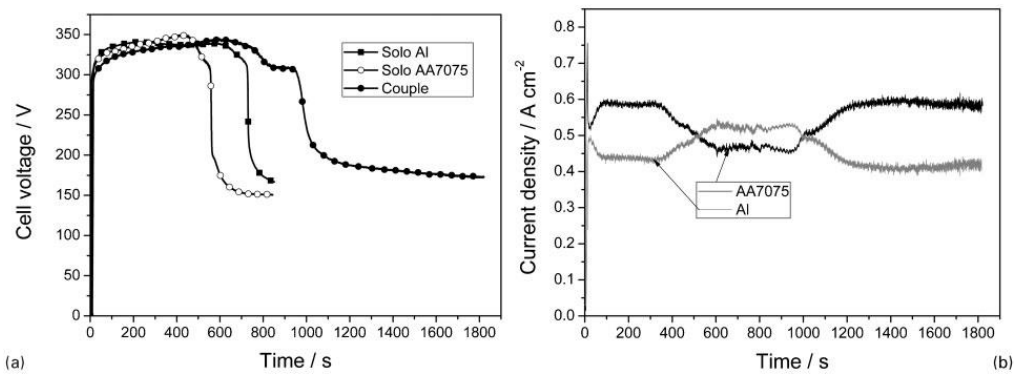

Figure 20 (a) voltage–time responses of Al/AA7075 alloy couple and separately oxidized specimens in sodium silicate electrolyte at 525 mA/cm^2 and (b) current densities for each component of couple. [186]

In order to overcome the galvanic corrosion of friction stir welded 6061/7075 alloys, a PEO treatment was performed [164] . The coating on 6061 and 7075 surfaces was much more similar and flat with micro-pores about 0.5-2 μm in diameter. However, different surface morphologies of the PEO coating on the welding area of 6061-7075 alloys was observed [164], with some island-shaped and volcano-like objects. Additionally, the content of Si (silicate-containing electrolyte) of the island-shaped porous

layer was higher compared to the coating on the alloys. Nevertheless, the coating on the welding area was integrated firmly to the substrate material. The average coating thickness was 5, 4, and 3.5 µm on 6061, 7075 and welding area, respectively, indicating different coating growth rate of different areas in the coupled welding part. The phase composition of the coating was also not uniform at different areas. In addition to α- and γ-Al_2O_3, there was also mullite ($3Al_2O_3$-$2SiO_2$) in the coating. In comparison to uncoated welded part, the PEO coating reduced the corrosion potential between the different areas, and thus decreased the galvanic corrosion susceptibility between the two alloys.

5.3 Coupled Mg/Al alloys

For the PEO treatment of AZ31/AA5754 (AlMg3) friction stir welding joints, the results have demonstrated that the coatings have been produced successfully on AZ31/AA5754 (AlMg3) FSW joints using a hydroxide, phosphate and silicate containing electrolyte. Furthermore, the optimized PEO processing resulted in the coating without any separation of the joints after being exposed to three days salt spray (5% NaCl) as seen in Fig. 21. Blawert et al. [195] have stated that the different breakdown potential for Mg and Al alloys could result in the different starting time of the discharges. The rapid formation of thicker initial barrier layer on Mg alloy can guarantee the achievement of breakdown voltage for Al, which is generally higher compared to Mg alloy. As a consequence, a constant voltage treatment mode in combination with the high current densities can be a solution. Additionally, the different coating growth rate on Mg and Al sides, respectively will lead to the non-uniform coating thickness. To address this issue, the selection of electrolyte could minimize the difference in coating growing rate for the two different substrates. However, the difference in coating composition and properties cannot be erased since the coating species are originated from the substrates and electrolytes. But the fine-tuning of the electrical parameters could at least produce coatings with the similar structure, which is help to minimize the difference of the thermal resistance.

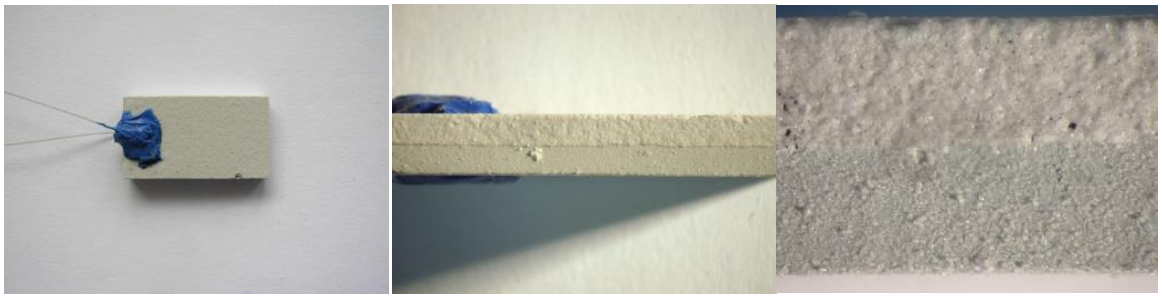

Figure 21 Optimised processing of a Mg/Al-FSW lap joint resulting in no separation of the two sheets after being exposed to three days salt spray (5% NaCl). [195]

In the sense of corrosion mitigation, PEO can not only be a useful method to protect Mg alloys, but also can be extended to Mg dissimilar metal joints to prevent galvanic corrosion. Baron-Wiechec et al [186] have demonstrated that PEO is feasible to produce protective coating on joined AA7075/ZE41 alloy using an AC PEO process. A difference in charge passing of 22-38 % was revealed for the AA7075/ZE41 alloy couple during the processing. In spite of the different composition in the substrates,

the transition of discharges to “soft” sparking appeared simultaneously for the coupled alloys. The current flow was briefly favored to the ZE41 alloy at first, but a stronger current switched to the AA7075 alloy after the start of “soft” sparking. Furthermore, the coating on the Mg alloy part was thicker compared to the Al alloy part.

Bai et al [185] has studied the corrosion behavior of a PEO coated AZ31 Mg coupled with 2024/7075 Al alloys, in order to effectively block the corrosive medium and improved the resistance against galvanic corrosion. It was reported that the life span of the coated Mg alloy coupled to Al alloy was extended by more than 7 times longer in comparison to uncoated AZ31 alloy coupled to Al alloy.

5.4 Coupled Mg/Ti alloys

Aliasghari et al. [188] have studied PEO processing of FSW AZ31B alloy-titanium joints under a voltage ramp from 0 to 500 V in 1 min at first, and then a fixed current density of 200 mA/cm^2. At a voltage above 20 V, the film growth was accompanied by the evolution of oxygen, explaining the increase of current density. The sparks were firstly commenced on the Ti part and later on the AZ31B alloy. The current density and the coating thickness are lower on the Mg alloy part than on the Ti part, in agreement with the current-voltage behaviors for the joints. The surface appearance on the Ti part is much coarser than on the AZ31B alloy part. There was no gradient region of intermediate morphology observed only a sharp interface boundary between the AZ31B alloy and titanium (Fig. 22). The processing produced a PEO coating with thickness between 4 - 12 μm on the AZ31B alloy and 5 - 18 μm on the titanium. In regard to the corrosion behavior, a severely corroded AZ31B alloy was revealed without PEO coating, but limited corrosion with only a few dark localized corrosion sites were found after PEO treatment. The PEO coating on the weld can block the access of the solution to the more stable Ti and thus there is no chance to form a circuit, to a certain degree, reducing the galvanic influence of the Ti on corrosion of the coated AZ31B alloy.

5.5 Impact of macro-scale material mix and consequence for PEO processing

Macro-scale material mix is of great importance for engineering solution but suffers from galvanic corrosion. PEO treatment can be an option to treat joint metals/alloys with the flexibility to inhibit galvanic corrosion but studies are still limited compared to other aspects of PEO processing. Overall the potential of PEO seems to be largely underestimated to offer solutions for material mix, the related research is still limited and industrial scale solutions are missing. This review is addressing PEO processing on the micro-scale material mix, which can be a base for comparison with PEO on the macro-scale. Overall problems are similar, but the treatment on micro-scale material mix has the advantage, that a secondary phase in the matrix can be embedded by the growing coating on the matrix surrounding the secondary phase. This is not possible on the macro-scale material mix. However, still a number of problems are similar, and can give good suggestions (as seen in 4.4) for solving or at least improving the PEO processing for macro-scale material mix.

Different requirements for the application in the future should be taken into consideration. Although a wide range of electrolytes and electrical parameters can be used for PEO treatment of separate alloys, they may not work for coupled materials. For the joining of dissimilar metals/alloys, the different sensitivities/responses of either parts to the PEO processing is a challenge to produce a uniform coating with high quality. For example, in bio application, intensive galvanic corrosion of Mg side for the bare coupled Mg/Ti is an essential issue. Surface protection measures at least on Mg side are required. Regarding the different coating growth rate on dissimilar materials, the exploration of suitable electrolytes and optimal electrical parameters can be a solution. For instance, a lower duty cycle can achieve the best coating performance for the Mg side when Mg/Al couples are treated together. Similar to the complexed micro-scale material mix, the employment of constant high voltage maintained by an initial high current density can also decrease the difference of coating growth rate, as it helps to ramp quickly through the anodizing stage. One electrolyte containing 12.72 g/L $Na_2SiO_3 \cdot 5H_2O$ has been developed and claimed as universal to ensure the formation of a PEO coating on separate Al and Mg alloys around 30 - 40 µm thick and with the micro-hardness of 800 - 1000 HV_{10} [196]. However, the formation of discharges on Ti6Al4V in the silicate-based electrolyte is demonstrated to not as easy as in the phosphate- and aluminate-based electrolytes [197]. More attempts are still required for the further development of PEO treatment on joint materials.

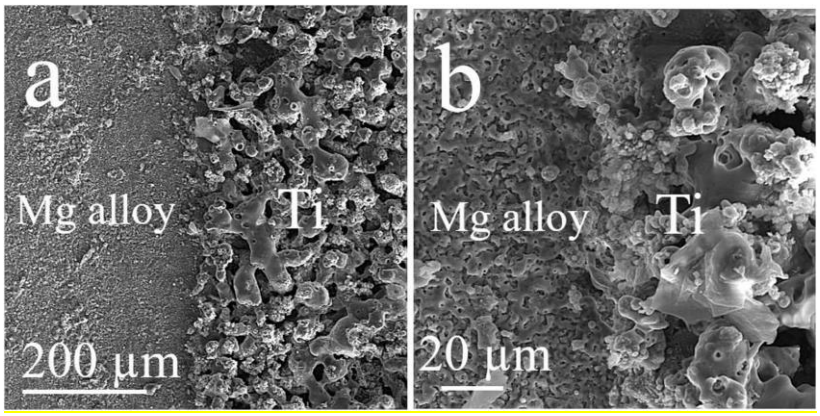

Figure 22 (a) Scanning electron micrograph (secondary electrons) of the surface of an FSW AZ31B alloy-titanium joint following DC PEO at 200 $mA \cdot cm^{-2}$ for 10 min in an alkaline silicate-based electrolyte. (b) At increased magnification. [188]

6 Summary and outlook

The presence of different phases in alloys has shown a significant effect on the PEO processes and the composition, morphologies, microstructures and properties of PEO coatings. The start of discharges shows a sequence on different stages, such as starting on β-Ti and then extending to α-Ti in Ti6Al4V. The sequential discharges result in a different local surface morphology; however the differences cannot be noticed after longer period of treatment. The properties of phases including the composition, stability, melting point, amount, size and distribution can influence the PEO process and the PEO coatings. These

aspects are mainly related to the participation of the phases in the coating formation process and also the discharges. Therefore, the phases with more active chemical- and/or electrochemical properties and/or lower thermal stabilities in the alloys can be involved in the coating formation more efficiently, eg., $MgLi_2Al$ in MgLi alloy, and Al matrix in comparison to Al_2Cu and Al_5FeSi intermetallics. Thus, more homogeneous PEO coatings can be produced compared to more noble or thermal stable phases, such as reinforcement phases of metallic matrix composites. The distribution of secondary phases concerning their amount and size controlled by the type/concentration of alloying elements and the metallurgical processing of the alloys also shows an influence on the PEO process and the microstructure of resultant coatings. Normally, uniformly distributed fine secondary phases are more likely to stimulate the formation of uniform and compact coatings rather than interrupt the continuity of the layers. The properties of the PEO coatings such as corrosion, wear, biocompatibility, photocatalytic activity is affected by a combination of factors including the coating compositions, microstructures and morphologies, in which the substrate microstructure has an considerable effect. Nevertheless, it is certain that the PEO process and coatings are also determined by the electrical parameters and the electrolytes.

In summary, it can be stated that the current driving force to study the influence of substrate microstructure on the PEO coatings comes from the incomplete understanding of the fundamental knowledge about the PEO process. It is clear that the PEO process is considerably controlled by a wide range of parameters. The desired formation of multi-functional PEO coatings in controlled and reproducible manner can be hardly achieved without the understanding of the role of substrate materials in PEO processes and their effect on PEO coatings. Delay in the coating formation by secondary phases, such as Si phase in Al alloys, has direct consequences for new trends in PEO processing such as flash PEO, which utilizes short treatment times of only a few minutes. The careful selection of alloys for desirable applications and the insight into the role of substrate microstructure are both necessary to expand the application of PEO technique.

From a practical perspective, coupled materials in engineering are of great interests for weight reduction, energy conservation, bio-implants, environmental protection and other functionality combination. The joining of dissimilar light metals especially at the joint region may need a surface treatment to protect against galvanic corrosion. In this sense, PEO huge potential due to the designable coating properties and performance through parameter adjustment ranging from electrolyte to the electrical processing options. The mechanisms on the small scale in an alloy with different phases are similar to what happens on a large scale in a PEO treatment of a material mix. The studies of the evolution of multiphase materials during PEO processing are profound to lay the foundation of its application in large-scaled multi-components materials, because solving the problems in the small scale can solve the problems in the large scale.

However, a universal electrolyte working for all materials in the same manner is not existing up to now. The problems in the PEO processing of dual or multiphase alloys, such as different coating growth rates on different materials and distinct properties of the coating on dissimilar materials, are also the challenges for the material mixes on a large scale. Although there are challenging issues in respect to the complexity of PEO process, modelling approaches could be included to construct a database that covers different substrate microstructures and process parameters to obtain a full picture of their interactions and influence on the treatment result. Thus, to conduct more systematic studies on the behavior of multiphase materials in PEO processing contributes to broaden PEO applications to dissimilar materials joints at a larger scale.

Appendix

List of symbols and abbreviations

2D	Two dimension
AC	Alternating current
Al	Aluminum
BM	Base metal
BSE	Backscattered electron
Ca	Calcium
Ce	Cerium
CP	Commercial purity
Cu	Copper
DC	Direct current
ECAP	Equal-channel angular pressed
Fe	Iron
FSW	Friction stir welding
HA	Hydroxyapatite
HAZ	Heat affected zone
Hf	Hafnium
HNT	Halloysite nanotubes
HV	Vickers hardness
I_{corr}	Corrosion current density
Li	Lithium
MAO	Micro arc oxidation
Mg	Magnesium
Mn	Manganese

MMC	Metal matrix composite
Nb	Niobium
NHE	Normal hydrogen electrode
Ni	Nickel
NZ	Nugget zone
OCP	Open circuit potential
P	Phosphorous
PEO	Plasma electrolytic oxidation
R_a	Arithmetical mean roughness
R_z	Arithmetic mean value of the single roughness depths
R_p	Polarization resistance
SBF	Simulated body fluid
SE	Secondary electron
SEM	Scanning electron microscopy
SiC	Silicon carbide
SLM	Selective laser melting
Sn	Tin
Sr	Strontium
STEM	Scanning transmission electron microscopy
SZ	Sensitized zone
T6	Solution heat treated then artificially aged
TEM	Transmission electron microscopy
Ti	Titanium
TiB_2	Titanium diboride
T_m	Melting point
TMAZ	Thermomechanical affected zone
UCFT	Ultrasonic cold forging technology
V	Vanadium
V_{rms}	Root mean square voltage
XRD	X-ray diffraction
Y	Yttrium
ZC71	Mg-7 wt.% Zn-1 wt% Cu
Zr	Zirconium

Acknowledgement

T. Wu would like to thank the China Scholarship Council (NO.201708510113) for fellowship and funding.

Reference

[1] A.L. Yerokhin, A.A. Voevodin, V.V. Lyubimov, J. Zabinski, M. Donley, Plasma electrolytic fabrication of oxide ceramic surface layers for tribotechnical purposes on aluminium alloys, Surface and Coatings Technology (1998) 7.

[2] R. Arrabal, E. Matykina, T. Hashimoto, P. Skeldon, G.E. Thompson, Characterization of AC PEO coatings on magnesium alloys, Surface and Coatings Technology, 203 (2009) 2207-2220.

[3] A.L. Yerokhin, X. Nie, A. Leyland, A. Matthews, Characterisation of oxide films produced by plasma electrolytic oxidation of a Ti–6Al–4V alloy, Surface and Coatings Technology, 130 (2000) 12.

[4] A. Němcová, P. Skeldon, G.E. Thompson, B. Pacal, Effect of fluoride on plasma electrolytic oxidation of AZ61 magnesium alloy, Surface and Coatings Technology, 232 (2013) 827-838.

[5] Y. Mori, A. Koshi, J. Liao, H. Asoh, S. Ono, Characteristics and corrosion resistance of plasma electrolytic oxidation coatings on AZ31B Mg alloy formed in phosphate – Silicate mixture electrolytes, Corrosion Science, 88 (2014) 254-262.

[6] H. Duan, C. Yan, F. Wang, Growth process of plasma electrolytic oxidation films formed on magnesium alloy AZ91D in silicate solution, Electrochimica Acta, 52 (2007) 5002-5009.

[7] C. Blawert, S.A. Karpushenkov, M. Serdechnova, L.S. Karpushenkava, M.L. Zheludkevich, Plasma electrolytic oxidation of zinc alloy in a phosphate-aluminate electrolyte, Applied Surface Science, 505 (2020) 144552.

[8] R.O. Hussein, X. Nie, D.O. Northwood, A. Yerokhin, A. Matthews, Spectroscopic study of electrolytic plasma and discharging behaviour during the plasma electrolytic oxidation (PEO) process, Journal of Physics D: Applied Physics, 43 (2010) 105203.

[9] Z. Yao, Q. Xia, H. Wei, D. Li, Q. Sun, Z. Jiang, Study on coating growth characteristics during the electrolytic oxidation of a magnesium-lithium alloy by optical emission spectroscopy analysis, RSC Advances, 5 (2015) 68806-68814.

[10] R.O. Hussein, X. Nie, D.O. Northwood, A spectroscopic and microstructural study of oxide coatings produced on a Ti-6Al-4V alloy by plasma electrolytic oxidation, Materials Chemistry and Physics, 134 (2012) 484-492.

[11] E. Matykina, R. Arrabal, D.J. Scurr, A. Baron, P. Skeldon, G.E. Thompson, Investigation of the mechanism of plasma electrolytic oxidation of aluminium using ^{18}O tracer, Corrosion Science, 52 (2010) 1070-1076.

[12] M.M.S. Al Bosta, K. Ma, Suggested mechanism for the MAO ceramic coating on aluminium substrates using bipolar current mode in the alkaline silicate electrolytes, Applied Surface Science, 308

(2014) 121-138.

[13] X. Lu, C. Blawert, K.U. Kainer, M.L. Zheludkevich, Investigation of the formation mechanisms of plasma electrolytic oxidation coatings on Mg alloy AM50 using particles, Electrochimica Acta, 196 (2016) 680-691.

[14] L.R. Krishna, G. Poshal, A. Jyothirmayi, G. Sundararajan, Relative hardness and corrosion behavior of micro arc oxidation coatings deposited on binary and ternary magnesium alloys, Materials & Design, 77 (2015) 6-14.

[15] M. Shokouhfar, S.R. Allahkaram, Effect of incorporation of nanoparticles with different composition on wear and corrosion behavior of ceramic coatings developed on pure titanium by micro arc oxidation, Surface and Coatings Technology, 309 (2017) 767-778.

[16] M. Sandhyarani, T. Prasadrao, N. Rameshbabu, Role of electrolyte composition on structural, morphological and in-vitro biological properties of plasma electrolytic oxidation films formed on zirconium, Applied Surface Science, 317 (2014) 198-209.

[17] D. Kim, D. Sung, J. Lee, Y. Kim, W. Chung, Composite plasma electrolytic oxidation to improve the thermal radiation performance and corrosion resistance on an Al substrate, Applied Surface Science, 357 (2015) 1396-1402.

[18] S. Stojadinović, N. Tadić, N. Radić, B. Grbić, R. Vasilić, MgO/ZnO coatings formed on magnesium alloy AZ31 by plasma electrolytic oxidation: Structural, photoluminescence and photocatalytic investigation, Surface and Coatings Technology, 310 (2017) 98-105.

[19] R.J. Sengwa, S. Choudhary, Dielectric and electrical properties of PEO–Al_2O_3 nanocomposites, Journal of Alloys and Compounds, 701 (2017) 652-659.

[20] S. Ono, S. Moronuki, Y. Mori, A. Koshi, J. Liao, H. Asoh, Effect of electrolyte concentration on the structure and corrosion resistance of anodic films formed on magnesium through plasma electrolytic oxidation, Electrochimica Acta, 240 (2017) 415-423.

[21] Y.Q. Wang, X.J. Wang, W.X. Gong, K. Wu, F.H. Wang, Effect of SiC particles on microarc oxidation process of magnesium matrix composites, Applied Surface Science, 283 (2013) 906-913.

[22] A.R. Fatkullin, E.V. Parfenov, A. Yerokhin, D.M. Lazarev, A. Matthews, Effect of positive and negative pulse voltages on surface properties and equivalent circuit of the plasma electrolytic oxidation process, Surface and Coatings Technology, 284 (2015) 427-437.

[23] Q. Li, J. Liang, B. Liu, Z. Peng, Q. Wang, Effects of cathodic voltages on structure and wear resistance of plasma electrolytic oxidation coatings formed on aluminium alloy, Applied Surface Science, 297 (2014) 176-181.

[24] G. Rapheal, S. Kumar, N. Scharnagl, C. Blawert, Effect of current density on the microstructure and corrosion properties of plasma electrolytic oxidation (PEO) coatings on AM50 Mg alloy produced in an electrolyte containing clay additives, Surface and Coatings Technology, 289 (2016) 150-164.

[25] J. Karbowniczek, F. Muhaffel, G. Cempura, H. Cimenoglu, A. Czyrska-Filemonowicz, Influence

of electrolyte composition on microstructure, adhesion and bioactivity of micro-arc oxidation coatings produced on biomedical Ti6Al7Nb alloy, Surface and Coatings Technology, 321 (2017) 97-107.

[26] X. Wang, Z. Zhu, Y. Li, H. Chen, Characterization of micro-arc oxidation coatings on 6N01 aluminum alloy under different electrolyte temperature control modes, Journal of Materials Engineering and Performance, 27 (2018) 1890-1897.

[27] E. Matykina, R. Arrabal, P. Skeldon, G.E. Thompson, P. Wang, P. Wood, Plasma electrolytic oxidation of a zirconium alloy under AC conditions, Surface and Coatings Technology, 204 (2010) 2142-2151.

[28] R. Arrabal, E. Matykina, F. Viejo, P. Skeldon, G.E. Thompson, Corrosion resistance of WE43 and AZ91D magnesium alloys with phosphate PEO coatings, Corrosion Science, 50 (2008) 1744-1752.

[29] J. Martin, A.V. Nominé, J. Stef, A. Nominé, J.X. Zou, G. Henrion, T. Grosdidier, The influence of metallurgical state of substrate on the efficiency of plasma electrolytic oxidation (PEO) process on magnesium alloy, Materials & Design, 178 (2019).

[30] R.O. Hussein, D.O. Northwood, X. Nie, The effect of processing parameters and substrate composition on the corrosion resistance of plasma electrolytic oxidation (PEO) coated magnesium alloys, Surface and Coatings Technology, 237 (2013) 357-368.

[31] T.Y. Kuo, H.C. Lin, Effects of pulse level of Nd-YAG laser on tensile properties and formability of laser weldments in automotive aluminum alloys, Materials Science and Engineering: A, 416 (2006) 281-289.

[32] R. Manti, D.K. Dwivedi, A. Agarwal, Microstructure and hardness of Al-Mg-Si weldments produced by pulse GTA welding, The International Journal of Advanced Manufacturing Technology, 36 (2006) 263-269.

[33] P. Wang, J. Li, Y. Guo, J. Wang, Z. Yang, M. Liang, The formation mechanism of the composited ceramic coating with thermal protection feature on an Al12Si piston alloy via a modified PEO process, Journal of Alloys and Compounds, 682 (2016) 357-365.

[34] A.B. Rogov, H. Lyu, A. Matthews, A. Yerokhin, AC plasma electrolytic oxidation of additively manufactured and cast AlSi12 alloys, Surface and Coatings Technology, 399 (2020).

[35] T.A. Soares, H. Mozaffari, H. Reinecke, Generation of microstructures on a Ti-6Al-4V substrate through anodization, Surface and Coatings Technology, 278 (2015) 64-70.

[36] A. Kazek-Kęsik, G. Dercz, K. Suchanek, I. Kalemba-Rec, J. Piotrowski, W. Simka, Biofunctionalization of Ti–13Nb–13Zr alloy surface by plasma electrolytic oxidation. Part I, Surface and Coatings Technology, 276 (2015) 59-69.

[37] S.-J. Lee, L.H.T. Do, Effects of copper additive on micro-arc oxidation coating of LZ91 magnesium-lithium alloy, Surface and Coatings Technology, 307 (2016) 781-789.

[38] R. Arrabal, A. Pardo, M.C. Merino, M. Mohedano, P. Casajús, E. Matykina, P. Skeldon, G.E. Thompson, Corrosion behaviour of a magnesium matrix composite with a silicate plasma electrolytic oxidation coating, Corrosion Science, 52 (2010) 3738-3749.

[39] W. Xue, X. Wu, X. Li, H. Tian, Anti-corrosion film on 2024/SiC aluminum matrix composite fabricated by microarc oxidation in silicate electrolyte, Journal of Alloys and Compounds, 425 (2006) 302-306.

[40] B. Mingo, R. Arrabal, M. Mohedano, A. Pardo, E. Matykina, Corrosion and wear of PEO coated AZ91/SiC composites, Surface and Coatings Technology, 309 (2017) 1023-1032.

[41] A.L. Yerokhin, X. Nie, A. Leyland, A. Matthews, S.J. Dowey, Plasma electrolysis for surface engineering, Surface and Coatings Technology, 122 (1999) 73-93.

[42] Y. Ma, X. Zhou, G.E. Thompson, M. Curioni, P. Skeldon, X. Zhang, Z. Sun, C. Luo, Z. Tang, F. Lu, Anodic film growth on Al–Li–Cu alloy AA2099-T8, Electrochimica Acta, 80 (2012) 148-159.

[43] F. Monfort, A. Berkani, E. Matykina, P. Skeldon, G.E. Thompson, H. Habazaki, K. Shimizu, Development of anodic coatings on aluminium under sparking conditions in silicate electrolyte, Corrosion Science, 49 (2007) 672-693.

[44] X. Zhou, G.E. Thompson, P. Skeldon, Effect of grain orientation on the morphology, dielectric breakdown and optical behaviour of anodic film formed on Al–2wt%Cu binary alloy, Electrochimica Acta, 53 (2008) 5684-5691.

[45] H. Birey, Thickness dependence of the dielectric constant and resistance of Al2O3films, Journal of Applied Physics, 48 (1977) 5209-5212.

[46] F. Xu, Y. Xia, G. Li, The mechanism of PEO process on Al–Si alloys with the bulk primary silicon, Applied Surface Science, 255 (2009) 9531-9538.

[47] L.E. Fratila-Apachitei, H. Terryn, P. Skeldon, G.E. Thompson, J. Duszczyk, L. Katgerman, Influence of substrate microstructure on the growth of anodic oxide layers, Electrochimica Acta, 49 (2004) 1127-1140.

[48] J. He, Q.Z. Cai, H.H. Luo, L. Yu, B.K. Wei, Influence of silicon on growth process of plasma electrolytic oxidation coating on Al–Si alloy, Journal of Alloys and Compounds, 471 (2009) 395-399.

[49] T. Wu, C. Blawert, M.L. Zheludkevich, Influence of secondary phases of AlSi9Cu3 alloy on the plasma electrolytic oxidation coating formation process, Journal of Materials Science & Technology, 50 (2020) 75-85.

[50] T. Wu, C. Blawert, X. Lu, M. Serdechnova, M.L. Zheludkevich, Difference in formation of plasma electrolytic oxidation coatings on MgLi alloy in comparison with pure Mg, Journal of Magnesium and Alloys, (2021).

[51] E. Matykina, R. Arrabal, B. Mingo, M. Mohedano, A. Pardo, M.C. Merino, In vitro corrosion performance of PEO coated Ti and Ti6Al4V used for dental and orthopaedic implants, Surface and Coatings Technology, 307 (2016) 1255-1264.

[52] Y.Q. Wang, M.Y. Zheng, K. Wu, Microarc oxidation coating formed on SiCw/AZ91 magnesium matrix composite and its corrosion resistance, Materials Letters, 59 (2005) 1727-1731.

[53] T. Wu, C. Blawert, M. Serdechnova, P. Karlova, G. Dovzhenko, D.C.F. Wieland, M.L.

Zheludkevich, PEO processing of AZ91Nd/Al2O3 MMC-the role of alumina fibers, Journal of Magnesium and Alloys, (2021).

[54] Y. Chen, Y. Yang, W. Zhang, T. Zhang, F. Wang, Influence of second phase on corrosion performance and formation mechanism of PEO coating on AZ91 Mg alloy, Journal of Alloys and Compounds, 718 (2017) 92-103.

[55] T.W. Clyne, S.C. Troughton, A review of recent work on discharge characteristics during plasma electrolytic oxidation of various metals, International Materials Reviews, 64 (2018) 127-162.

[56] X. Yang, L. Chen, Y. Qu, R. Liu, K. Wei, W. Xue, Optical emission spectroscopy of plasma electrolytic oxidation process on 7075 aluminum alloy, Surface and Coatings Technology, 324 (2017) 18-25.

[57] R. Liu, N. Weng, W. Xue, M. Hua, G. Liu, W. Li, Analyses of reinforcement phases during plasma electrolytic oxidation on magnesium matrix composites, Surface and Coatings Technology, 269 (2015) 212-219.

[58] R.O. Hussein, X. Nie, D.O. Northwood, An investigation of ceramic coating growth mechanisms in plasma electrolytic oxidation (PEO) processing, Electrochimica Acta, 112 (2013) 111-119.

[59] R.O. Hussein, D.O. Northwood, X. Nie, Coating growth behavior during the plasma electrolytic oxidation process, Journal of Vacuum Science & Technology A: Vacuum, Surfaces, and Films, 28 (2010) 766-773.

[60] R. Liu, J. Wu, W. Xue, Y. Qu, C. Yang, B. Wang, X. Wu, Discharge behaviors during plasma electrolytic oxidation on aluminum alloy, Materials Chemistry and Physics, 148 (2014) 284-292.

[61] S. Stojadinović, N. Tadić, N. Radić, P. Stefanov, B. Grbić, R. Vasilić, Anodic luminescence, structural, photoluminescent, and photocatalytic properties of anodic oxide films grown on niobium in phosphoric acid, Applied Surface Science, 355 (2015) 912-920.

[62] A.G. Rakoch, E.P. Monakhova, Z.V. Khabibullina, M. Serdechnova, C. Blawert, M.L. Zheludkevich, A.A. Gladkova, Plasma electrolytic oxidation of AZ31 and AZ91 magnesium alloys: Comparison of coatings formation mechanism, Journal of Magnesium and Alloys, 8 (2020) 587-600.

[63] Y.L. Song, Y.H. Liu, S.R. Yu, X.Y. Zhu, Q. Wang, Plasma electrolytic oxidation coating on AZ91 magnesium alloy modified by neodymium and its corrosion resistance, Applied Surface Science, 254 (2008) 3014-3020.

[64] S.F. Zhang, R.F. Zhang, W.K. Li, M.S. Li, G.L. Yang, Effects of tannic acid on properties of anodic coatings obtained by micro arc oxidation on AZ91 magnesium alloy, Surface and Coatings Technology, 207 (2012) 170-176.

[65] J. Jiang, Q. Zhou, J. Yu, A. Ma, D. Song, F. Lu, L. Zhang, D. Yang, J. Chen, Comparative analysis for corrosion resistance of micro-arc oxidation coatings on coarse-grained and ultra-fine grained AZ91D Mg alloy, Surface and Coatings Technology, 216 (2013) 259-266.

[66] K.C. Tekin, U. Malayoğlu, S. Shrestha, Electrochemical behavior of plasma electrolytic oxide coatings on rare earth element containing Mg alloys, Surface and Coatings Technology, 236 (2013)

540-549.
[67] Y. Wang, X. Wang, T. Zhang, K. Wu, F. Wang, Role of β Phase during Microarc Oxidation of Mg Alloy AZ91D and Corrosion Resistance of the Oxidation Coating, Journal of Materials Science & Technology, 29 (2013) 1129-1133.
[68] T. Chen, W. Xue, Y. Li, X. Liu, J. Du, Corrosion behavior of friction stir welded AZ31B magnesium alloy with plasma electrolytic oxidation coating formed in silicate electrolyte, Materials Chemistry and Physics, 144 (2014) 462-469.
[69] A. Němcová, P. Skeldon, G.E. Thompson, S. Morse, J. Čížek, B. Pacal, Influence of plasma electrolytic oxidation on fatigue performance of AZ61 magnesium alloy, Corrosion Science, 82 (2014) 58-66.
[70] F. Muhaffel, F. Mert, H. Cimenoglu, D. Höche, M. L. Zheludkevich, C. Blawert, Characterisation and corrosion behaviour of plasma electrolytic oxidation coatings on high pressure die cast Mg–5Al–0.4Mn–xCe (x=0, 0.5, 1) alloys, Surface and Coatings Technology, 269 (2015) 200-211.
[71] C. Liu, J. Liang, J. Zhou, Q. Li, Z. Peng, L. Wang, Characterization and corrosion behavior of plasma electrolytic oxidation coated AZ91-T6 magnesium alloy, Surface and Coatings Technology, 304 (2016) 179-187.
[72] A. Ma, F. Lu, Q. Zhou, J. Jiang, D. Song, J. Chen, Y. Zheng, Formation and Corrosion Resistance of Micro-Arc Oxidation Coating on Equal-Channel Angular Pressed AZ91D Mg Alloy, Metals, 6 (2016) 308.
[73] E. Matykina, I. Garcia, R. Arrabal, M. Mohedano, B. Mingo, J. Sancho, M.C. Merino, A. Pardo, Role of PEO coatings in long-term biodegradation of a Mg alloy, Applied Surface Science, 389 (2016) 810-823.
[74] Y. Mori, A. Koshi, J. Liao, Corrosion resistance of plasma electrolytic oxidation layer of a non-ignitable Mg–Al–Mn–Ca magnesium alloy, Corrosion Science, 104 (2016) 207-216.
[75] K.O. Gunduz, Z.C. Oter, M. Tarakci, Y. Gencer, Plasma electrolytic oxidation of binary Mg-Al and Mg-Zn alloys, Surface and Coatings Technology, 323 (2017) 72-81.
[76] M. Mohedano, B.J.C. Luthringer, B. Mingo, F. Feyerabend, R. Arrabal, P.J. Sanchez-Egido, C. Blawert, R. Willumeit-Römer, M.L. Zheludkevich, E. Matykina, Bioactive plasma electrolytic oxidation coatings on Mg-Ca alloy to control degradation behaviour, Surface and Coatings Technology, 315 (2017) 454-467.
[77] F. Wei, W. Zhang, T. Zhang, F. Wang, Effect of variations of Al content on microstructure and corrosion resistance of PEO coatings on Mg-Al alloys, Journal of Alloys and Compounds, 690 (2017) 195-205.
[78] C. Liu, T. Xu, Q. Shao, S. Huang, B. Jiang, J. Liang, H. Li, Effects of beta phase on the growth behavior of plasma electrolytic oxidation coating formed on magnesium alloys, Journal of Alloys and Compounds, 784 (2019) 414-421.

[79] D.T. Asquith, A.L. Yerokhin, J.R. Yates, A. Matthews, Effect of combined shot-peening and PEO treatment on fatigue life of 2024 Al alloy, Thin Solid Films, 515 (2006) 1187-1191.
[80] L. Wang, X. Nie, Silicon effects on formation of EPO oxide coatings on aluminum alloys, Thin Solid Films, 494 (2006) 211-218.
[81] D.T. Asquith, A.L. Yerokhin, J.R. Yates, A. Matthews, The effect of combined shot-peening and PEO treatment on the corrosion performance of 2024 Al alloy, Thin Solid Films, 516 (2007) 417-421.
[82] I.J. Hwang, D.Y. Hwang, Y.M. Kim, B. Yoo, D.H. Shin, Formation of uniform passive oxide layers on high Si content Al alloy by plasma electrolytic oxidation, Journal of Alloys and Compounds, 504 (2010) S527-S530.
[83] Y. Cheng, M. Mao, J. Cao, Z. Peng, Plasma electrolytic oxidation of an Al-Cu-Li alloy in alkaline aluminate electrolytes: A competition between growth and dissolution for the initial ultra-thin films, Electrochimica Acta, 138 (2014) 417-429.
[84] A.E. Gulec, Y. Gencer, M. Tarakci, The characterization of oxide based ceramic coating synthesized on Al–Si binary alloys by microarc oxidation, Surface and Coatings Technology, 269 (2015) 100-107.
[85] M. Mohedano, E. Matykina, R. Arrabal, B. Mingo, A. Pardo, PEO of pre-anodized Al–Si alloys: Corrosion properties and influence of sealings, Applied Surface Science, 346 (2015) 57-67.
[86] M. Mohedano, E. Matykina, R. Arrabal, B. Mingo, M.L. Zheludkevich, PEO of rheocast A356 Al alloy: energy efficiency and corrosion properties, Surface and Interface Analysis, 48 (2016) 953-959.
[87] Z.C. Oter, Y. Gencer, M. Tarakci, The characterization of the coating formed by Microarc oxidation on binary Al–Mn alloys, Journal of Alloys and Compounds, 650 (2015) 185-192.
[88] D. Veys-Renaux, E. Rocca, Initial stages of multi-phased aluminium alloys anodizing by MAO: micro-arc conditions and electrochemical behaviour, Journal of Solid State Electrochemistry, 19 (2015) 3121-3129.
[89] M. Chen, Y. Ou, Y. Fu, Z. Li, J. Li, S. Liu, Effect of friction stirred Al-Fe-Si particles in 6061 aluminum alloy on structure and corrosion performance of MAO coating, Surface and Coatings Technology, 304 (2016) 85-97.
[90] L.C. Campanelli, L.T. Duarte, P.S.C.P. da Silva, C. Bolfarini, Fatigue behavior of modified surface of Ti-6Al-7Nb and CP-Ti by micro-arc oxidation, Materials & Design, 64 (2014) 393-399.
[91] S. Park, C. Jo, H. Choe, W.A. Brantley, Hydroxyapatite deposition on micropore-formed Ti-Ta-Nb alloys by plasma electrolytic oxidation for dental applications, Surface and Coatings Technology, 294 (2016) 15-20.
[92] M. Kaseem, H.-C. Choe, Electrochemical and bioactive characteristics of the porous surface formed on Ti-xNb alloys via plasma electrolytic oxidation, Surface and Coatings Technology, 378 (2019).
[93] O.L. Li, M. Tsunakawa, Y. Shimada, K. Nakamura, K. Nishinaka, T. Ishizaki, Corrosion resistance of composite oxide film prepared on Ca-added flame-resistant magnesium alloy AZCa612 by micro-

arc oxidation, Corrosion Science, 125 (2017) 99-105.
[94] R. Arrabal, E. Matykina, P. Skeldon, G. E. Thompson, A. Pardob, Transport of species during plasma electrolytic oxidation of WE43-T6 magnesium alloy.
[95] M. Tarakci, Plasma electrolytic oxidation coating of synthetic Al-Mg binary alloys, Materials Characterization, 62 (2011) 1214-1221.
[96] Y. Gencer, A.E. Gulec, The effect of Zn on the microarc oxidation coating behavior of synthetic Al–Zn binary alloys, Journal of Alloys and Compounds, 525 (2012) 159-165.
[97] Y. Gencer, M. Tarakci, A.E. Gulec, Z. Cagatay Oter, Plasma Electrolytic Oxidation of Binary Al-Sn Alloys, Acta Physica Polonica A, 125 (2014) 659-663.
[98] S. Cengiz, Synthesis of eutectic Al–18Ce alloy and effect of cerium on the PEO coating growth, Materials Chemistry and Physics, 247 (2020).
[99] W. Simka, A. Krząkała, D.M. Korotin, I.S. Zhidkov, E.Z. Kurmaev, S.O. Cholakh, K. Kuna, G. Dercz, J. Michalska, K. Suchanek, T. Gorewoda, Modification of a Ti–Mo alloy surface via plasma electrolytic oxidation in a solution containing calcium and phosphorus, Electrochimica Acta, 96 (2013) 180-190.
[100] M. Fazel, H.R. Salimijazi, M.A. Golozar, M.R. Garsivaz jazi, A comparison of corrosion, tribocorrosion and electrochemical impedance properties of pure Ti and Ti6Al4V alloy treated by micro-arc oxidation process, Applied Surface Science, 324 (2015) 751-756.
[101] W. Xue, Q. Jin, Q. Zhu, M. Hua, Y. Ma, Anti-corrosion microarc oxidation coatings on SiCP/AZ31 magnesium matrix composite, Journal of Alloys and Compounds, 482 (2009) 208-212.
[102] T. Wu, C. Blawert, M. Serdechnova, P. Karlova, G. Dovzhenko, D.C.F. Wieland, M.L. Zheludkevich, PEO processing of AZ91Nd/Al_2O_3 MMC – The role of alumina fibers, Submitted, (2021).
[103] Z. Chen, C. Bao, Y. Jian, Q. Wang, F. Chen, Microstructure and corrosion resistance of SiC nanoparticles reinforced ceramic composite coating on Mg-Li based composite by micro-arc oxidation, Journal of The Electrochemical Society, 166 (2019) C571-C579.
[104] R. Arrabal, E. Matykina, P. Skeldon, G.E. Thompson, Coating formation by plasma electrolytic oxidation on ZC71/SiC/12p-T6 magnesium metal matrix composite, Applied Surface Science, 255 (2009) 5071-5078.
[105] F. Aydin, A. Ayday, M.E. Turan, H. Zengin, Role of graphene additive on wear and electrochemical corrosion behaviour of plasma electrolytic oxidation (PEO) coatings on Mg–MWCNT nanocomposite, Surface Engineering, 36 (2019) 791-799.
[106] C.A. Isaza M, B. Zuluaga D, J.S. Rudas, H.A. Estupiñán D, J.M. Herrera R, J.M. Meza, Mechanical and Corrosion Behavior of Plasma Electrolytic Oxidation Coatings on AZ31B Mg Alloy Reinforced with Multiwalled Carbon Nanotubes, Journal of Materials Engineering and Performance, 29 (2020) 1135-1145.

[107] R. Viswanathan, N. Rameshbabu, S. Kennedy, D. Sreekanth, K. Venkateswarlu, M. Sandhya Rani, V. Muthupandi, Plasma Electrolytic Oxidation and Characterization of Spark Plasma Sintered Magnesium/Hydroxyapatite Composites, Materials Science Forum, 765 (2013) 827-831.

[108] H. Zhang, J. Geng, X. Li, Z. Chen, M. Wang, N. Ma, H. Wang, The micro-arc oxidation (MAO) behaviors of in-situ TiB_2/A201 composite, Applied Surface Science, 422 (2017) 359-371.

[109] S. Cui, J. Han, Y. Du, W. Li, Corrosion resistance and wear resistance of plasma electrolytic oxidation coatings on metal matrix composites, Surface and Coatings Technology, 201 (2007) 5306-5309.

[110] Y. Erarslan, Wear performance of in-situ aluminum matrix composite after micro-arc oxidation, Transactions of Nonferrous Metals Society of China, 23 (2013) 347-352.

[111] C. Du, S. Huang, X. Yu, Q. Wang, H. Zhao, Microstructure and properties of plasma electrolytic oxidation coating on 55% SiCp/Al matrix composites, Surface and Coatings Technology, 420 (2021).

[112] K. Li, W. Li, G. Zhang, W. Zhu, F. Zheng, D. Zhang, M. Wang, Effects of Si phase refinement on the plasma electrolytic oxidation of eutectic Al-Si alloy, Journal of Alloys and Compounds, 790 (2019) 650-656.

[113] A.V. Apelfeld, A.M. Borisov, B.L. Krit, V.B. Ludin, M.N. Polyansky, E.A. Romanovsky, S.V. Savushkina, I.V. Suminov, N.V. Tkachenko, A.V. Vinogradov, V.G. Vostrikov, The study of plasma electrolytic oxidation coatings on Zr and Zr-1% Nb alloy at thermal cycling, Surface and Coatings Technology, 269 (2015) 279-285.

[114] H. Soliman, A.S. Hamdy, Comparative study of micro-arc oxidation treatment for AM, AZ and MZ magnesium alloys, Protection of Metals and Physical Chemistry of Surfaces, 51 (2015) 620-629.

[115] L. Agureev, S. Savushkina, A. Ashmarin, A. Borisov, A. Apelfeld, K. Anikin, N. Tkachenko, M. Gerasimov, A. Shcherbakov, V. Ignatenko, N. Bogdashkina, Study of Plasma Electrolytic Oxidation Coatings on Aluminum Composites, Metals, 8 (2018).

[116] Z. Li, Y. Yuan, X. Jing, Composite coatings prepared by combined plasma electrolytic oxidation and chemical conversion routes on magnesium-lithium alloy, Journal of Alloys and Compounds, 706 (2017) 419-429.

[117] F. Liu, D. Shan, Y. Song, E.-H. Han, Effect of additives on the properties of plasma electrolytic oxidation coatings formed on AM50 magnesium alloy in electrolytes containing K_2ZrF_6, Surface and Coatings Technology, 206 (2011) 455-463.

[118] J. Han, Y. Cheng, W. Tu, T. Zhan, Y. Cheng, The black and white coatings on Ti-6Al-4V alloy or pure titanium by plasma electrolytic oxidation in concentrated silicate electrolyte, Applied Surface Science, 428 (2018) 684-697.

[119] T. Wu, C. Blawert, M. Serdechnova, P. Karlova, G. Dovzhenko, D.C. Florian Wieland, S. Stojadinovic, R. Vasilic, K. Mojsilovic, M.L. Zheludkevich, Formation of plasma electrolytic oxidation coatings on pure niobium in different electrolytes, Applied Surface Science, 573 (2022).

[120] L.O. Snizhko, A.L. Yerokhin, A. Pilkington, N.L. Gurevina, D.O. Misnyankin, A. Leyland, A.

Matthews, Anodic processes in plasma electrolytic oxidation of aluminium in alkaline solutions, Electrochimica Acta, 49 (2004) 2085-2095.

[121] B. Kasalica, J. Radić-Perić, M. Perić, M. Petković-Benazzouz, I. Belča, M. Sarvan, The mechanism of evolution of microdischarges at the beginning of the PEO process on aluminum, Surface and Coatings Technology, 298 (2016) 24-32.

[122] J. Martin, P. Leone, A. Nominé, D. Veys-Renaux, G. Henrion, T. Belmonte, Influence of electrolyte ageing on the plasma electrolytic oxidation of aluminium, Surface and Coatings Technology, 269 (2015) 36-46.

[123] R. Arrabal, J.M. Mota, A. Criado, A. Pardo, M. Mohedano, E. Matykina, Assessment of duplex coating combining plasma electrolytic oxidation and polymer layer on AZ31 magnesium alloy, Surface and Coatings Technology, 206 (2012) 4692-4703.

[124] M. Mohedano, C. Blawert, M.L. Zheludkevich, Cerium-based sealing of PEO coated AM50 magnesium alloy, Surface and Coatings Technology, 269 (2015) 145-154.

[125] C. Liu, P. Liu, Z. Huang, Q. Yan, R. Guo, D. Li, G. Jiang, D. Shen, The correlation between the coating structure and the corrosion behavior of the plasma electrolytic oxidation coating on aluminum, Surface and Coatings Technology, 286 (2016) 223-230.

[126] W. Xue, X. Shi, M. Hua, Y. Li, Preparation of anti-corrosion films by microarc oxidation on an Al–Si alloy, Applied Surface Science, 253 (2007) 6118-6124.

[127] K.M. Lee, B.U. Lee, S.I. Yoon, E.S. Lee, B. Yoo, D.H. Shin, Evaluation of plasma temperature during plasma oxidation processing of AZ91 Mg alloy through analysis of the melting behavior of incorporated particles, Electrochimica Acta, 67 (2012) 6-11.

[128] B. Mingo, Y. Guo, A. Němcová, A. Gholinia, M. Mohedano, M. Sun, A. Matthews, A. Yerokhin, Incorporation of halloysite nanotubes into forsterite surface layer during plasma electrolytic oxidation of AM50 Mg alloy, Electrochimica Acta, 299 (2019) 772-788.

[129] M. Mohedano, C. Blawert, M.L. Zheludkevich, Silicate-based Plasma Electrolytic Oxidation (PEO) coatings with incorporated CeO_2 particles on AM50 magnesium alloy, Materials & Design, 86 (2015) 735-744.

[130] T. Wu, C. Blawert, M. Serdechnova, P. Karlova, G. Dovzhenko, D.C.F. Wieland, M.L. Zheludkevich, Role of polymorph microstructure of Ti6Al4V alloy on PEO coating formation in phosphate electrolyte, Surface and Coatings Technology, 428 (2021).

[131] A. Němcová, I. Kuběna, M. Šmíd, H. Habazaki, P. Skeldon, G.E. Thompson, Effect of current density and behaviour of second phases in anodizing of a Mg-Zn-RE alloy in a fluoride/glycerol/water electrolyte, Journal of Solid State Electrochemistry, 20 (2015) 1155-1165.

[132] J. Martin, A. Melhem, I. Shchedrina, T. Duchanoy, A. Nominé, G. Henrion, T. Czerwiec, T. Belmonte, Effects of electrical parameters on plasma electrolytic oxidation of aluminium, Surface and Coatings Technology, 221 (2013) 70-76.

[133] A.L. Yerokhin, X. Nie, A. Leyland, A. Matthews, S.J. Dowey, Plasma electrolysis for surface engineering, Surface and Coatings Technology, (1999) 21.

[134] X. Nie, A. Leyland, H.W. Song, A.L. Yerokhin, S.J. Dowey, A. Matthews, Thickness effects on the mechanical properties of micro-arc discharge oxide coatings on aluminium alloys, Surface and Coatings Technology, 116-119 (1999) 1055-1060.

[135] X. Wang, X. Lu, P. Ju, Y. Chen, T. Zhang, F. Wang, Thermal control property and corrosion resistance of PEO coatings on AZ91 Mg alloy, Surface and Coatings Technology, 393 (2020).

[136] Z. Shahri, S.R. Allahkaram, R. Soltani, H. Jafari, Optimization of plasma electrolyte oxidation process parameters for corrosion resistance of Mg alloy, Journal of Magnesium and Alloys, 8 (2020) 431-440.

[137] J. Joseph, S.C. Gallo, R. Catubig, K. Wang, A. Somers, P. Howlett, D. Fabijanic, Formation of a corrosion-resistant coating on zinc by a duplex plasma electrolytic oxidation and conversion surface treatment, Surface and Coatings Technology, 395 (2020).

[138] M. Sowa, M. Piotrowska, M. Widziolek, G. Dercz, G. Tylko, T. Gorewoda, A.M. Osyczka, W. Simka, Bioactivity of coatings formed on Ti-13Nb-13Zr alloy using plasma electrolytic oxidation, Mater Sci Eng C Mater Biol Appl, 49 (2015) 159-173.

[139] O. Tazegul, F. Muhaffel, O. Meydanoglu, M. Baydogan, E.S. Kayali, H. Cimenoglu, Wear and corrosion characteristics of novel alumina coatings produced by micro arc oxidation on AZ91D magnesium alloy, Surface and Coatings Technology, 258 (2014) 168-173.

[140] L. Pezzato, K. Brunelli, S. Gross, M. Magrini, M. Dabalà, Effect of process parameters of plasma electrolytic oxidation on microstructure and corrosion properties of magnesium alloys, Journal of Applied Electrochemistry, 44 (2014) 867-879.

[141] D. Veys-Renaux, E. Rocca, G. Henrion, Micro-arc oxidation of AZ91 Mg alloy: An in-situ electrochemical study, Electrochemistry Communications, 31 (2013) 42-45.

[142] B. Mingo, Y. Guo, R. Leiva-Garcia, B.J. Connolly, A. Matthews, A. Yerokhin, Smart Functionalization of Ceramic-Coated AZ31 Magnesium Alloy, ACS Appl Mater Interfaces, 12 (2020) 30833-30846.

[143] X. Lu, M. Schieda, C. Blawert, K.U. Kainer, M.L. Zheludkevich, Formation of photocatalytic plasma electrolytic oxidation coatings on magnesium alloy by incorporation of TiO 2 particles, Surface and Coatings Technology, 307 (2016) 287-291.

[144] W. Li, M. Tang, L. Zhu, H. Liu, Formation of microarc oxidation coatings on magnesium alloy with photocatalytic performance, Applied Surface Science, 258 (2012) 10017-10021.

[145] E. Cakmak, K.C. Tekin, U. Malayoglu, S. Shrestha, The effect of substrate composition on the electrochemical and mechanical properties of PEO coatings on Mg alloys, Surface and Coatings Technology, 204 (2010) 1305-1313.

[146] Y. Jang, Z. Tan, C. Jurey, Z. Xu, Z. Dong, B. Collins, Y. Yun, J. Sankar, Understanding corrosion behavior of Mg-Zn-Ca alloys from subcutaneous mouse model: effect of Zn element concentration and

plasma electrolytic oxidation, Mater Sci Eng C Mater Biol Appl, 48 (2015) 28-40.
[147] Q. Xia, D. Zhang, D. Li, Z. Jiang, Z. Yao, Preparation of the plasma electrolytic oxidation coating on Mg Li alloy and its thermal control performance, Surface and Coatings Technology, 369 (2019) 252-256.
[148] Z. Ding, L. Cui, X. Chen, R. Zeng, S. Guan, S. Li, F. Zhang, Y. Zou, Q. Liu, In vitro corrosion of micro-arc oxidation coating on Mg-1Li-1Ca alloy - The influence of intermetallic compound Mg_2Ca, Journal of Alloys and Compounds, 764 (2018) 250-260.
[149] Y.K. Pan, D.G. Wang, C.Z. Chen, Effect of negative voltage on the microstructure, degradability and in vitro bioactivity of microarc oxidized coatings on ZK60 magnesium alloy, Materials Letters, 119 (2014) 127-130.
[150] Y.K. Pan, C.Z. Chen, D.G. Wang, T.G. Zhao, Effects of phosphates on microstructure and bioactivity of micro-arc oxidized calcium phosphate coatings on Mg-Zn-Zr magnesium alloy, Colloids Surf B Biointerfaces, 109 (2013) 1-9.
[151] W. Chen, Z. Wang, L. Sun, S. Lu, Research of growth mechanism of ceramic coatings fabricated by micro-arc oxidation on magnesium alloys at high current mode, Journal of Magnesium and Alloys, 3 (2015) 253-257.
[152] D. Gao, J. Dou, C. Hu, H. Yu, C. Chen, Corrosion behaviour of micro-arc oxidation coatings on Mg–2Sr prepared in poly(ethylene glycol)-incorporated electrolytes, RSC Advances, 8 (2018) 3846-3857.
[153] B. Mingo, R. Arrabal, M. Mohedano, Y. Llamazares, E. Matykina, A. Yerokhin, A. Pardo, Influence of sealing post-treatments on the corrosion resistance of PEO coated AZ91 magnesium alloy, Applied Surface Science, 433 (2018) 653-667.
[154] Z. Li, Y. Yuan, P. Sun, X. Jing, Ceramic coatings of LA141 alloy formed by plasma electrolytic oxidation for corrosion protection, ACS Appl Mater Interfaces, 3 (2011) 3682-3690.
[155] C. Ma, Y. Lu, P. Sun, Y. Yuan, X. Jing, M. Zhang, Characterization of plasma electrolytic oxidation coatings formed on Mg-Li alloy in an alkaline polyphosphate electrolyte, Surface and Coatings Technology, 206 (2011) 287-294.
[156] G. Song, A.L. Bowles, D.H. StJohn, Corrosion resistance of aged die cast magnesium alloy AZ91D, Materials Science and Engineering: A, 366 (2004) 74-86.
[157] M. Esmaily, J.E. Svensson, S. Fajardo, N. Birbilis, G.S. Frankel, S. Virtanen, R. Arrabal, S. Thomas, L.G. Johansson, Fundamentals and advances in magnesium alloy corrosion, Progress in Materials Science, 89 (2017) 92-193.
[158] A. Anawati, H. Asoh, S. Ono, Degradation behavior of coatings formed by the plasma electrolytic oxidation technique on AZ61 magnesium alloys containing 0, 1 and 2 wt% Ca, International Journal of Technology, 9 (2018).
[159] A. Anawati, H. Asoh, S. Ono, Effects of alloying element Ca on the corrosion behavior and

bioactivity of anodic films formed on AM60 Mg alloys, Materials (Basel), 10 (2016).
[160] A.L. Yerokhin, A. Shatrov, V. Samsonov, P. Shashkov, A. Pilkington, A. Leyland, A. Matthews, Oxide ceramic coatings on aluminium alloys produced by a pulsed bipolar plasma electrolytic oxidation process, Surface and Coatings Technology, 199 (2005) 150-157.
[161] M. Kaseem, M.P. Kamil, J.H. Kwon, Y.G. Ko, Effect of sodium benzoate on corrosion behavior of 6061 Al alloy processed by plasma electrolytic oxidation, Surface and Coatings Technology, 283 (2015) 268-273.
[162] S. Aliasghari, M. Ghorbani, P. Skeldon, H. Karami, M. Movahedi, Effect of plasma electrolytic oxidation on joining of AA 5052 aluminium alloy to polypropylene using friction stir spot welding, Surface and Coatings Technology, 313 (2017) 274-281.
[163] A. T, R.K. L, A. S, U.R. R, R. N, Fabrication of multifunctional black PEO coatings on AA7075 for spacecraft applications, Surface and Coatings Technology, 307 (2016) 735-746.
[164] Y. Chen, X. Song, J. Zhou, H. Liu, Y. Yang, The study on the overall plasma electrolytic oxidation for 6061-7075 dissimilar aluminum alloy welded parts based on the dielectric breakdown theory, Materials, 11 (2018).
[165] M.M. Krishtal, Effect of structure of aluminum-silicon alloys on the process of formation and characteristics of oxide layer on microarc oxidizing, Metal Science and Heat Treatment, 46 (2014) 8.
[166] H. Yu, Q. Dong, Y. Chen, C. Chen, Influence of silicon on growth mechanism of micro-arc oxidation coating on cast Al-Si alloy, R Soc Open Sci, 5 (2018) 172428.
[167] Y. Cheng, J. Cao, M. Mao, H. Xie, P. Skeldon, Key factors determining the development of two morphologies of plasma electrolytic coatings on an Al–Cu–Li alloy in aluminate electrolytes, Surface and Coatings Technology, 291 (2016) 239-249.
[168] Y. Cheng, Z. Xue, Q. Wang, X. Wu, E. Matykina, P. Skeldon, G.E. Thompson, New findings on properties of plasma electrolytic oxidation coatings from study of an Al–Cu–Li alloy, Electrochimica Acta, 107 (2013) 358-378.
[169] Y.-J. Oh, J.-I. Mun, J.-H. Kim, Effects of alloying elements on microstructure and protective properties of Al_2O_3 coatings formed on aluminum alloy substrates by plasma electrolysis, Surface and Coatings Technology, 204 (2009) 141-148.
[170] G. Wu, Y. Wang, M. Sun, Q. Zhang, J. Yao, Influence of microstructure of TC4 substrate on the MAO coating, Surface Engineering, 36 (2019) 827-836.
[171] E. Matykina, J.M. Hernandez-López, A. Conde, C. Domingo, J.J. de Damborenea, M.A. Arenas, Morphologies of nanostructured TiO_2 doped with F on Ti-6Al-4V alloy, Electrochimica Acta, 56 (2011) 2221-2229.
[172] E. Matykina, A. Conde, J. de Damborenea, D.M.y. Marero, M.A. Arenas, Growth of TiO_2-based nanotubes on Ti–6Al–4V alloy, Electrochimica Acta, 56 (2011) 9209-9218.
[173] F. Reshadi, G. Faraji, M. Baniassadi, M. Tajeddini, Surface modification of severe plastically deformed ultrafine grained pure titanium by plasma electrolytic oxidation, Surface and Coatings

Technology, 316 (2017) 113-121.
[174] S.-F. Hsieh, S.-F. Ou, C.-K. Chou, The influence of the substrate on the adhesive strength of the micro-arc oxidation coating developed on TiNi shape memory alloy, Applied Surface Science, 392 (2017) 581-589.
[175] S.A. Yavari, B.S. Necula, L.E. Fratila-Apachitei, J. Duszczyk, I. Apachitei, Biofunctional surfaces by plasma electrolytic oxidation on titanium biomedical alloys, Surface Engineering, 32 (2016) 411-417.
[176] Y. Gu, L. Chen, W. Yue, P. Chen, F. Chen, C. Ning, Corrosion behavior and mechanism of MAO coated Ti6Al4V with a grain-fined surface layer, Journal of Alloys and Compounds, 664 (2016) 770-776.
[177] L. Chen, Y. Qu, K. Wei, X. Jin, B. Liao, W. Xue, Fabrication and characterization of microarc oxidation films on Ti-39Nb-6Zr alloy at different voltages in KOH electrolyte, Journal of Alloys and Compounds, 725 (2017) 1158-1165.
[178] E. Wierzbicka, B. Vaghefinazari, S.V. Lamaka, M.L. Zheludkevich, M. Mohedano, L. Moreno, P. Visser, A. Rodriguez, J. Velasco, R. Arrabal, E. Matykina, Flash-PEO as an alternative to chromate conversion coatings for corrosion protection of Mg alloy, Corrosion Science, 180 (2021).
[179] R. del Olmo, M. Mohedano, B. Mingo, R. Arrabal, E. Matykina, LDH Post-Treatment of Flash PEO Coatings, Coatings, 9 (2019).
[180] R. del Olmo, M. Mohedano, P. Visser, E. Matykina, R. Arrabal, Flash-PEO coatings loaded with corrosion inhibitors on AA2024, Surface and Coatings Technology, 402 (2020).
[181] M. Aonuma, K. Nakata, Effect of alloying elements on interface microstructure of Mg–Al–Zn magnesium alloys and titanium joint by friction stir welding, Materials Science and Engineering: B, 161 (2009) 46-49.
[182] Y.C. Kim, A. Fuji, Factors dominating joint characteristics in Ti – Al friction welds, Science and Technology of Welding and Joining, 7 (2013) 149-154.
[183] J. Shang, K. Wang, Q. Zhou, D. Zhang, J. Huang, G. Li, Microstructure characteristics and mechanical properties of cold metal transfer welding Mg/Al dissimilar metals, Materials & Design, 34 (2012) 559-565.
[184] L.M. Liu, H.Y. Wang, Z.D. Zhang, The analysis of laser weld bonding of Al alloy to Mg alloy, Scripta Materialia, 56 (2007) 473-476.
[185] L. Bai, G. Kou, K. Zhao, G. Chen, F. Yan, Effect of in-situ micro-arc oxidation coating on the galvanic corrosion of AZ31Mg coupled to aluminum alloys, Journal of Alloys and Compounds, 775 (2019) 1077-1085.
[186] A. Baron-Wiecheć, M. Curioni, R. Arrabal, E. Matykina, P. Skeldon, G.E. Thompson, Plasma electrolytic oxidation of coupled light metals, Transactions of the IMF, 91 (2013) 107-112.
[187] Y. Savguira, T.H. North, S.J. Thorpe, Plasma electrolytic oxidation coating of dissimilar

AZ31/AZ80 friction stir welds, Journal of The Electrochemical Society, 165 (2018) C11-C18.
[188] S. Aliasghari, A. Rogov, P. Skeldon, X. Zhou, A. Yerokhin, A. Aliabadi, M. Ghorbani, Plasma electrolytic oxidation and corrosion protection of friction stir welded AZ31B magnesium alloy-titanium joints, Surface and Coatings Technology, 393 (2020).
[189] Y. Chen, J. Zhou, H. Liu, X. Song, Y. Yang, Overall micro-arc oxidation treatment for AZ31B–6061 magnesium–aluminium dissimilar metal connecting parts, Corrosion Engineering, Science and Technology, 52 (2017) 470-475.
[190] Q. Chen, W. Li, K. Ling, R. Yang, Investigation of growth mechanism of plasma electrolytic oxidation coating on Al-Ti double-layer composite plate, Materials, 12 (2019).
[191] R. Gecu, Y. Yurekturk, E. Tekoglu, F. Muhaffel, A. Karaaslan, Improving wear resistance of 304 stainless steel reinforced AA7075 aluminum matrix composite by micro-arc oxidation, Surface and Coatings Technology, 368 (2019) 15-24.
[192] J. Liu, W. Pan, Y. Liu, Y. Wang, Effect of graphene on corrosion resistance of micro-arc oxidation coatings on 6061/7075 dissimilar laser-MIG hybrid welded joint, Materials Research Express, 6 (2019).
[193] A. Aliabadi, M. Ghorbani, G. Barati Darband, Plasma electrolytic oxidation of Mg–Ti couple metals fabricated by friction stir welding: characterization and corrosion studies, Materials Research Express, 6 (2019).
[194] V.M. Garamus, W. Limberg, M. Serdechnova, D. Mei, S.V. Lamaka, T. Ebel, R. Willumeit-Römer, Degradation of Titanium Sintered with Magnesium: Effect of Hydrogen Uptake, Metals, 11 (2021).
[195] Carsten Blawert, Hyunju Jeong, Jaehoon Oh, Y.S. Shin, Treatment of Dissimilar Weld Joints (Mg/Al) by Plasma Electrolytic Oxidation, in: Proceedings of 10th International Conference on Magnesium Alloys and Their Applications, Mg 2015, 2015, pp. 10.
[196] A. Kossenko, M. Zinigrad, A universal electrolyte for the plasma electrolytic oxidation of aluminum and magnesium alloys, Materials & Design, 88 (2015) 302-309.
[197] T. Wu, C. Blawert, M. Serdechnova, P. Karlova, G. Dovzhenko, D.C. Florian Wieland, S. Stojadinovic, R. Vasilic, L. Wang, C. Wang, K. Mojsilovic, M.L. Zheludkevich, Role of phosphate, silicate and aluminate in the electrolytes on PEO coating formation and properties of coated Ti6Al4V alloy, Applied Surface Science, 595 (2022).

3. Motivation and Objectives

PEO has developed into an attractive surface modification technology to improve the surface performance of different metals and their alloys. In general, the coating formation process involves the oxidation of substrate and the incorporation of electrolyte species [25-27]. Thus, many attempts have been carried out through changing the processing parameters to further improve the coating performance [21, 28, 29]. However, because of the insufficient understanding of the role of substrate in the PEO coating formation process and properties, the optimization of the processing parameters are often relying on trial error approaches lacking clear strategies. In comparison to pure metals, the PEO optimizations for alloys are more complex since the microstructure of alloys is controlled and modified by the addition of alloying elements. The presence of primary and secondary phases and intermetallics leads to a local heterogeneity of the coating, which has been reported in different studies [30-35]. However, a systematic investigation is still required to construct a roadmap for future PEO optimizing strategies. The objectives of this work are focused on:

1. Understanding the role of substrate properties, eg. chemical stability (Mg/MgLi), solubility of oxygen (Mg, Al and Ti), and melting temperature (Mg, Al, Ti and Nb) in PEO coating formation.
2. Studying the influence of additional phases and intermetallics in localized micro-scale material mixes (Al, Mg and Ti substrates) on PEO process.
3. Understanding the influence of the properties (electrochemical, chemical stability, melting point and distribution) of these phases and intermetallics on their evolution and incorporation behavior during PEO processing.
4. Role of hydroxide and oxide properties on coating growth.
5. Evaluating the morphology, microstructure, and composition of PEO coatings in presence of different phases and intermetallics in the substrate.
6. Attempting to produce multifunctional PEO coatings and exploring the possibility to improve the performance of the coating via changing the composition of electrolyte, adjusting the current density and altering the processing duration.
7. Understanding the differences and similarities between micro-scale material mixes and macro-scale multi-metal joints (eg. α-Ti/β-Ti.).

4. Methodology

4.1 Coating preparation

4.1.1 Substrate materials

A set of relevant metals (Al, Mg, Ti and Nb) and their alloys was used in this work. The detailed information of the substrates can be found in Tab. 4-1. The chemical composition of the substrate materials was analyzed using Arc Spark OES (Spark analyser M9, Spectro Ametek, Germany) or Energy Dispersive Spectrometer system (EDS, eumeX IXRF systems). The selected substrates have many different secondary phases and intermetallics, which allows to study their evolution during PEO processing. The specimens were grinded using emery sheets up to 2500 grits and then polished with polishing suspension diamond 1 μm. It should be noted that the polishing process performed is intended to clearly expose the metallurgical morphology of the substrates, which is necessary to observe the evolution of the phases during PEO processing.

The microstructure of the substrates were firstly studied by using an optical microscope (OLYMPUS BX53M) and a scanning electron microscope (SEM, TESCAN Vega3 SB). Fig. 4-1 shows the microstructure of all the used substrates. The main phases in the substrate have been indexed. The selection of substrates can be divided into three groups regarding the phase composition/microstructure and melting temperature.

The first group includes MgLi (pure Mg, paper *1*) and Ti6Al4V (paper *2* and *3*) alloys. With only lattice transformation, they are the simplest material mixes. This is resulted from the completely dissolution of the alloy elements in the matrix. Since there is no significant precipitation of additional phases, the substrates do not show significant heterogeneity in the phase composition. For MgLi alloy, with excess of Li addition, there exists a lattice transformation that α-Mg (hexagonal) grains have been transformed into β-Mg (cubic) grains completely, accompanied by the precipitation of $MgLi_2Al$ particles. For Ti6Al4V alloy, it has a polymorph microstructure, composed of both α-Ti and β-Ti.

The second group is characterized by the presence of various additional phases in the micro-scaled material mixes, which has more complex microstructure compared to the first group. AlSi9Cu3 alloy (paper *4*) and AZ91Nd/Al_2O_3 MMC (pure AZ91Nd, paper *5*) are included in this group. They have primary and secondary phases, intermetallics, as well as reinforcement phases, which are apparently different from the matrix concerning the composition and properties. AlSi9Cu3 alloy is a typical Al-Si alloy, which can be regarded as an Al alloy (Al_2Cu and Al_5FeSi interetallics are contained) mixed with Si phases. It is known that Si phase is not suitable for PEO. For Mg composite, in addition to β-$Mg_{17}Al_{12}$, Al-Nd, and Al-Mn-Nd intermetallics, the reinforcement phase Al_2O_3 fiber is incorporated and it is already in a stable phase that is not ideal for PEO.

The last group is devoted to the investigation of the PEO coating formation on pure Nb with high melting temperature (paper *6*). Nb has a very high melting point around 2447 ℃, obviously higher in comparison to the commonly used Mg (650 ℃), Al (660 ℃) and Ti (1668 ℃) substrates. It is important

to study the oxidation behavior of Nb substrate and the corresponding coating formation behavior during PEO processing.

Table 4-1 The selected substrate materials and parameters for PEO processing

Substrates	Composition	Size	Processing parameters	Electrolytes	Paper
pure Mg	0.022 wt.% Mn, 0.017 wt.% Si, 0.014 wt.% Al, 0018 wt.% Zn, 0.0017 wt.% Fe, 0.0002 wt.% Cu , <0.0002 wt.% Ni and Mg balance	15 × 15 × 4 mm	constant current density 3 A/dm^2, duty ratio 10 %, frequency 100 Hz, 10 ± 2 ℃, processing time 15, 30, 60, 180, 600 and 1200 s, respectively	20 g/L Na_3PO_4 and 1 g/L KOH	1
MgLi	11.36 wt.% Li, 2.39 wt.% Al, 0.0093 wt.% Mn, 0.0072 wt.% Zn, 0.0032 wt.% Fe, 0.0012 wt.% Ni, 0.0009 wt.% Sn and Mg balance				
Ti6Al4V	7.564 wt.%Al, 2.809 wt.% V, 0.097 wt.% Mn, 0.182 wt.% Fe, 0.102 wt.% Ge, 0.104 wt.% Nb, 0.108 wt.% Sn, 0.574 wt.% Ta, Ti balance	20 × 16 × 4 mm	constant current density 3 (only in-situ PEO), 5 and 10 A/dm^2, duty ratio 10 %, frequency 100 Hz, 20 ± 2 ℃ (only for ex-situ PEO), processing time 15, 30, 60, 300 and 600 s, respectively	20 g/L Na_3PO_4 and 1 g/L KOH	2
			constant current density 10 A/dm^2, duty ratio 10 %, frequency 100 Hz, 20 ± 2 ℃, processing time 600 s	Electrolyte 1: 20 g/L Na_3PO_4 and 1 g/L KOH	3
				Electrolyte 2: 20 g/L $NaAlO_2$ and 1 g/L KOH	
				Electrolyte 3 : 20 g/L Na_2SiO_3 and 1 g/L KOH	
Al9Si3Cu	9.57 wt.% Si, 2.56 wt.% Cu, 0.93 wt.% Sn, 0.83 wt.% Mg, 0.38 wt.% Zn, 0.35 wt.% Fe, 0.14 wt.% Mn and Al balance	15 × 15 × 4 mm	constant current density 3 A/dm^2, duty ratio 10 %, frequency 100 Hz, 20 ± 1 ℃, processing time 15, 30, 60, 120, 240 and 480 s, respectively	20 g/L Na_3PO_4 and 1 g/L KOH	4

AZ91Nd	7.16 wt.% Al, 0.57 wt.% Zn, 1.14 wt.% Nd, 0.21 wt. % Mn, 0.0049 wt.% Fe, 0.0044 wt.% Cu, 0.0006 wt.% Ni and Mg balance	15 × 15 × 4 mm	constant current density 6 A/dm^2, duty ratio 10 %, frequency 100 Hz, 10 ± 2 ℃, processing time 15, 30, 60, 180, 600 and 1200 s, respectively	Electrolyte 1: 20 g/L Na_3PO_4 and 1 g/L KOH	5
				Electrolyte 2 : 10 g/L Na_3PO_4, 15 g/L $NaAlO_2$ and 1 g/L KOH	
AZ91Nd/Al_2O_3	7.16 wt.% Al, 0.57 wt.% Zn, 1.14 wt.% Nd, 0.21 wt. % Mn, 0.0049 wt.% Fe, 0.0044 wt.% Cu, 0.0006 wt.% Ni and Mg balance + 20 vol.% Saffil δ-Al_2O_3			20 g/L Na_3PO_4 and 1 g/L KOH	
pure Nb	0.483 wt.% Ta, 0.3573 wt.% Sn, 0.315 wt.% Ge, 0.26833 wt.% La, 0.044 wt.% Mn, 0.0353 wt.% Fe, Nb balance	15 × 15 × 4 mm	constant current density 10 A/dm^2, duty ratio 10 %, frequency 100 Hz, 20 ± 2 ℃, processing time 600 s	Electrolyte 1: 20 g/L Na_3PO_4 and 1 g/L KOH	6
				Electrolyte 2: 20 g/L $NaAlO_2$ and 1 g/L KOH	
				Electrolyte 3 : 20 g/L Na_2SiO_3 and 1 g/L KOH	

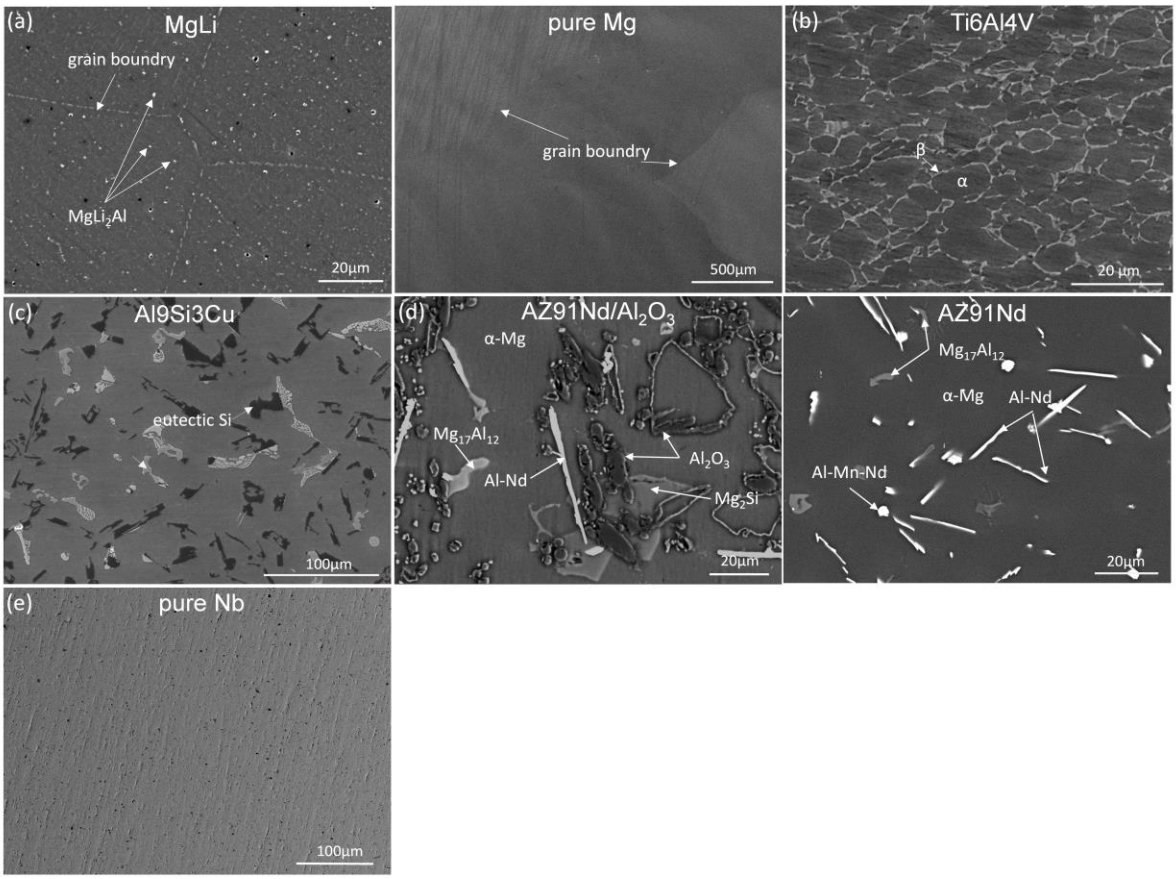

Figure 4-1 Micrographs of different substrate materials: (a) MgLi alloy and pure Mg, (b) Ti6Al4V alloy, (c) Al9Si3Cu, (d) AZ91Nd/Al_2O_3 composite and AZ91Nd alloy, and (e) pure Nb.

4.1.2 PEO set-up

Lab PEO set-up

The PEO process was carried out as a function of treatment time, of which the intention is to understand the transformation process for the phases present in the substrate into the coatings during the treatment. In the present study, PEO processing was carried out using a lab-made DC pulsed power source as shown in Fig. 4-2(a). A constant current mode was adopted and the selection of the current density is based on the different responses of substrate materials to the current in PEO processing. For instance, the MgLi alloy containing 11.36 wt.% of Li is a highly active substrate and shows a high sensitivity to the current density. After the comparison of two current densities (3 and 5 A/dm^2), it is decided to follow the evolution of the surface under the lower current density of 3 A/dm^2. The respective processing parameters, including electrical parameters (current density, duty ratio and frequency), electrolyte composition, temperature of electrolyte and the processing durations are presented in Tab. 4-1. As shown in Fig. 4-2(b), the specimen was connected as anode and a stainless steel tube was used as the cathode (surface area ca. 5 dm^2), integrated into the cooling system to keep the temperature of the electrolyte at 10 ± 2 ℃ or 20 ± 2 ℃ (also based on the stability of the substrate materials). A magnetic stirrer was used for agitation the electrolyte in order to maintain a homogeneous electrolyte

and prevent temperature and concentration gradients. The voltage response as a function of treatment time was recorded using Q-gate data acquisition system and SignaSoft 6000 software package (Gantner, Germany). Due to the interests in the role of Li in MgLi alloy and the evolution of pure Nb substrate during PEO processing, optical emission spectroscopy (OES, PLASUS, Germany) was also applied during PEO processing to monitor the optical emission of the discharges. The analysis of the species incorporated in the plasmas was conducted using PLASUS SpecLine software (PLASUS, Germany).

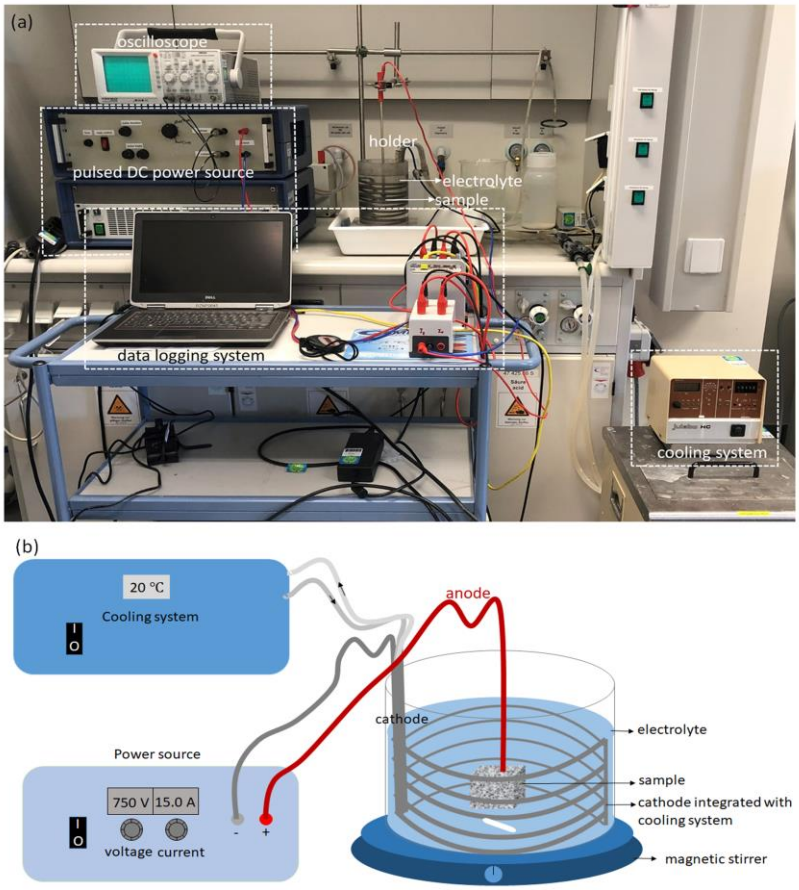

Figure 4-2 Schematic of lab PEO set-up.

In-situ PEO-XRD set-up

Additional in-situ PEO-XRD treatment of Ti6Al4V alloy was performed at the beamline P23 at PETRAIII storage ring (DESY, Deutsches Elektronen-Synchrotron), in order to track the coating formation process and unveil the phase evolution in time-resolution during PEO processing. Fig. 4-3(a) illustrates the schema of the in-situ PEO set-up, while Fig. 4-3(b) shows an actual in-situ PEO treatment. During the PEO processing, the X-ray diffraction data acquisition was performed simultaneously with a beam energy of 25 KeV and a beam size of 0.4 × 0.4 mm. To minimize signal from the substrate, measurements were performed in grazing incidence geometry with an incidence angle of 0.5°. The diffraction pattern were continuously acquired throughout the PEO process by a Lambda detector with a pixel size 55 × 55 µm and a measurement time of 100 ms (10 frames per second). After the HV (high voltage) was turned-off (at 10 min), the acquisition of the diffraction patterns continued for around 5

minutes more. Data reduction was attained employing an in-house developed Matlab® code and the PyFAI [61] routine.

The cell set-up was changed in comparison to the standard set-up (Fig. 4-2(b)) in a way that only a thin film of electrolyte was continuously running over the specimen surface, in order to minimize background scattering and achieve a good diffraction signal. Although the same power supply and nominally the same processing parameters were used, a different voltage response was still observed (see Fig. 3 and 15 in paper *2*), due to the different arrangement and size of the counter electrode. In combination with the different geometry of the cells and no cooling integrated in the DESY cell set-up, thus, even under the identical electrical PEO parameters, the behavior of the PEO process in the in-situ DESY cell and standard lab cell are not fully the same. The voltage ramp in the DESY set-up is much faster and therefore a voltage limit of 500 V was preset and the temperature of the electrolyte was recorded at the end of the treatment, because there was no additional cooling system added. The only cooling was obtained by pumping continuously new electrolyte from a 1-liter reservoir to the specimen. In the DESY cell set-up, the 10 A/dm^2 treatment was almost an ideal constant voltage treatment at 500 V while the 5 A/dm^2 treatment was similar to the 10 A/dm^2 standard cell treatment. To have a comparison with the 5 A/dm^2 standard cell treatment, an additional current density of 3 A/dm^2 was adopted for the DESY cell set-up. Furthermore, it can slow down the efficiency of the coating formation process by delaying the voltage increase and thus the PEO process. The lower current density is beneficial to track the progress with more details by the diffraction experiments.

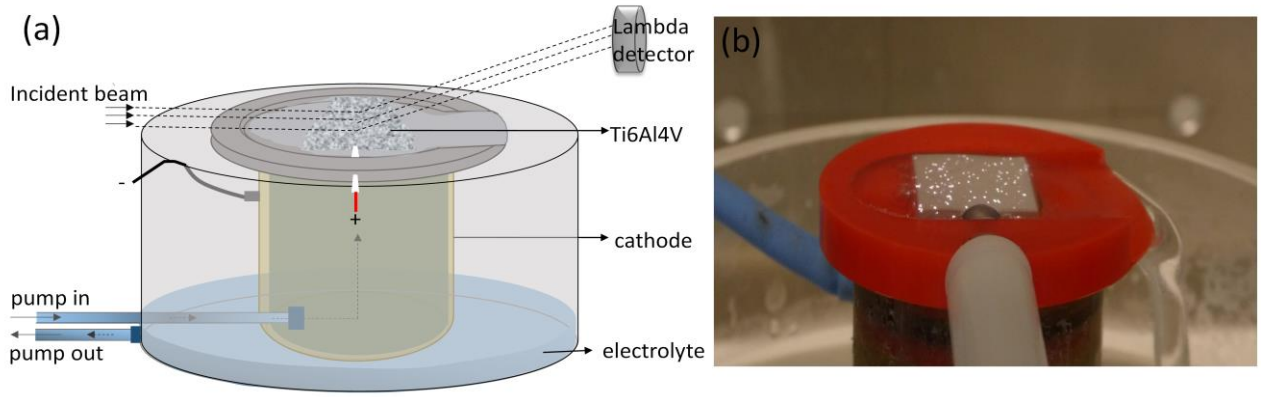

Figure 4-3 (a) schematic representation of in-situ PEO-XRD set-up used at P23, DESY, and (b) actual in-situ PEO treatment of a specimen.

4.1.3 Preparation of electrolytes

The phosphate-based electrolyte (pH 12.72, conductivity 529 µS/cm), prepared via dissolution of 20 g/L Na_3PO_4 and 1 g/L KOH in deionized water, was mainly used to study the oxidation of the substrate as a function of processing time. Nevertheless, different electrolytes were also prepared to study the influence of the electrolyte compositions on the PEO coating formation on AZ91Nd, Ti6Al4V and pure Nb respectively (Tab. 4-1). The specific chemical compositions of the electrolytes can be seen in Fig.

4-4.

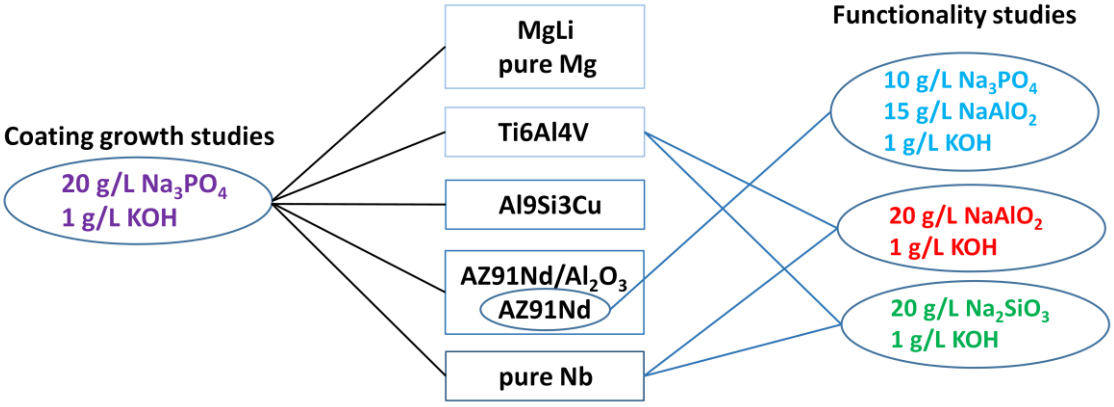

Figure 4-4 Electrolytes and substrates used for PEO processing

4.2 Coating characterization

4.2.1 Thickness measurement

Two different methods were used to evaluate and further validate the thickness of the PEO coatings. The first measurement was performed using an eddy-current gauge (MiniTest 2100, ElektroPhysik), with a resolution of 0.1 μm and measurement ability in the range of 1-200 μm. The average coating thickness was calculated from ten times measurements. Furthermore scanning electron microscope (SEM) observations from the cross-sections of the coatings was adopted to verify the coating thickness and further confirm the results evaluated by the eddy-current gauge. The cross-sectional observations will be introduced further in 4.2.2 section.

4.2.2 Surface and cross-sectional morphologies

A laser scanning confocal microscope (LSM 800, ZEISS) was applied with 20× lens exclusively used in air to characterize the surface morphology and the surface roughness of the coatings. The arithmetical mean roughness Ra as seen in Fig. 4-5 (a) and the mean width of the profile elements RSm (Gaussian filter, 0.8 mm) were adopted to indicate the waviness profile and the average value of the length of the profile element along the sampling length of the coatings [36]:

$$Ra=\frac{1}{l}\int_0^l |Z(x)|\,dx \quad (4\text{-}1)$$

$$RSm=\frac{1}{m}\sum_{i=1}^{m} X_{s_i} \quad (4\text{-}2)$$

The surface and cross-sectional micro-morphologies of the PEO coatings were examined by a scanning electron microscope (SEM, TESCAN Vega3 SB) in secondary electron (SE) and backscattered electron (BSE) modes. An energy dispersive spectrometer system (EDS, eumeX IXRFsystems) was performed to analyzed the near surface and cross-sectional elemental composition and distribution of the coatings, using point, line (paper *6*) and area scans respectively. An acceleration voltage was applied at 15 - 20 kV for the operations of SEM and EDS. Prior to the operations, a thin Au layer was sputtered on the specimens in order to eliminate surface charges due to the non-/low conductive PEO coatings. The

evaluation of the surface porosity of the PEO coatings was based on SEM micrographs using ImageJ 1.53e software. Before the cross-sectional observation, the PEO coated specimens embedded in resin for the preparation of cross-sections, by grinding successively using 500, 800, 1200, 2500 and 4000 grit emery sheets and then polishing with colloidal silica suspension.

A closer investigation of the cross-sections of the PEO coatings on MgLi alloy was also carried out using a windowless Oxford Ultim Extreme EDS detector (OXFORD ULTIM EXTREME), which is capable to detect Li. The preparation of a lamella, milled from the bulk PEO coated specimen, was attained using focus ion beam cutting in a field-emission-scanning electron microscopy (FIB-SEM, TESCAN Lyra3).

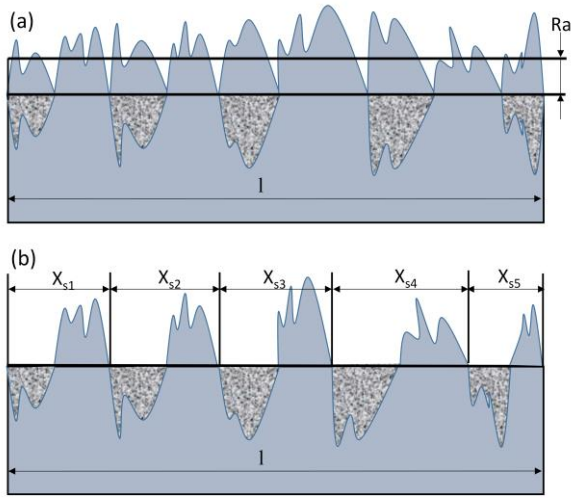

Figure 4-5 Schematic of surface roughness measurement: (a) arithmetical mean roughness, (b) mean width.

4.2.3 Phase composition and distribution

The phase composition of bare substrates and the PEO coated specimens were determined by X-ray diffractions (XRD) measurement (XRD, D8 Advance, Bruker AXS) with Cu Kα radiation (1.5406 Å). The measurements were performed at a voltage of 40 kV and a current of 40 mA. The following diffraction settings were selected: diffraction angle 2θ between 20 °and 80 °, step size of 0.02 °/s, dwell time of 1 s and grazing angle of 3 °. A continuous change of incident angles from 0.5 to 13° was also adopted for PEO coated Ti6Al4V in order to characterize the variation of coating formation phases along the coating thickness. Additionally, the in-situ treated Ti6Al4V specimens were also measured using the laboratory X-ray diffraction at the same settings as the ex-situ processed specimens however with a grazing angle of 10 °.

Synchrotron X-ray diffractions phase mappings were performed at Deutsches Elektronen-Synchrotron (DESY, Hamburg, Germany) using the nano-focus end station of the beamline P03 at PETRAIII storage ring [37]. Fig. 4-6 illustrates the schematic of the scanning and positions of the single diffraction acquisitions. An Eiger 9 M detector was used with a pixel size of 75 µm by 75 µm. The X-ray beam had an energy of 19.7 keV and was focused to a beam size of 1.5 µm by 1.5 µm. A mapping of the specimen was performed with a step size of 2 µm in the vertical direction (from air, across the coating

thickness and towards the interface of coating and substrate materials), and a step size of 4 µm in the horizontal direction parallel to the interface of coating and substrate materials. Overall, an area of 80 × 80 µm was mapped in each measurement. We have chosen this setting because a better resolution parallel to the interface was not necessary and would have doubled the acquisition time. At each point, a diffraction pattern was acquired with the dwell time of 0.5 s. Data reduction was done by employing in-house developed MAtlab® code and the PyFAI [38] routine. The scattering angles of the diffraction patterns were transformed to Cu K-alpha radiation for simplicity and comparison with the XRD results measured by the regular X-ray diffractometer (D8 Advance, Bruker AXS). To study the phase distribution across the coating thickness, a lab-made script in Python programming language, operated in the "Spyder" package software environment included with Anaconda Navigator, was used for analyzing and generating two-dimensional phase mapping graphics.

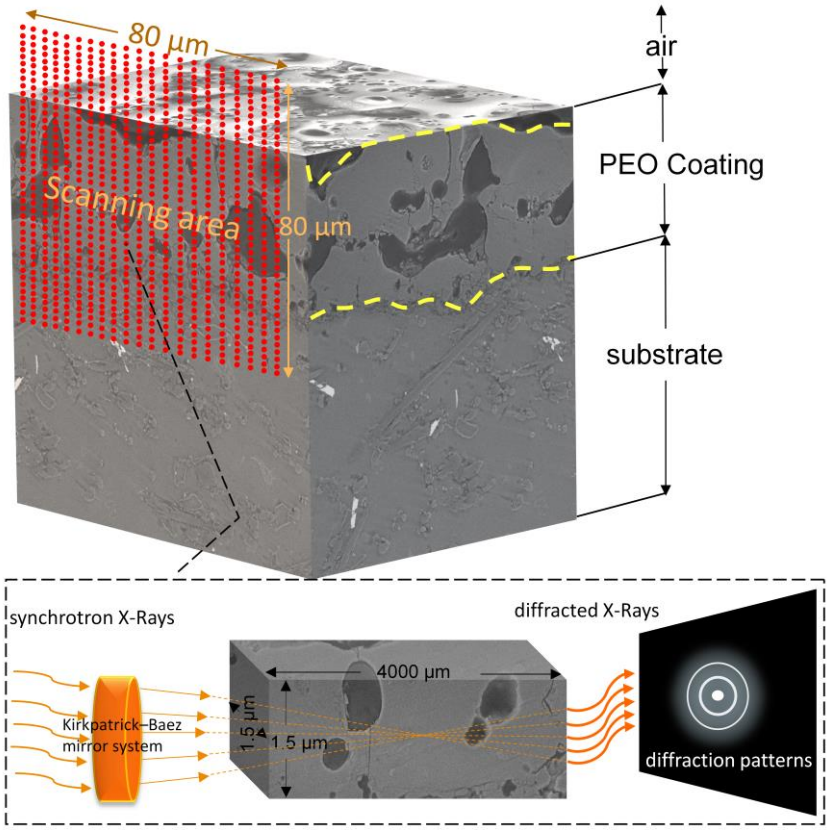

Figure 4-6 Schematic scanning diagram of each point of analysis (1.5 µm × 1.5 µm, 0.5 s) via synchrotron X-ray diffraction giving a total scanning area of 80 µm × 80 µm across three-phase of air/PEO coating/substrate.

4.3 Coating properties

4.3.1 Corrosion resistance

The electrochemical tests were performed using a Gamry Potentiostat (Gamry, United States) in order to evaluate the corrosion performance of the PEO coated specimens, and detailed parameters can be found in Tab. 4-2. A 0.5 wt.% NaCl solution was prepared to evaluate the corrosion resistance of PEO coated pure Mg and MgLi alloy. The electrochemical impedance spectroscopy (EIS) tests were carried

out in conjunction with a classical three-electrode cell system. The coated specimens were adopted as working electrode with an exposed surface area of 0.5 cm^2. The counter and the reference electrode were a platinum wire and a saturated Ag/AgCl electrode, respectively. The tests were performed at ambient temperature, covering a frequency range from 100 kHz to 0.1 Hz at open circuit potential (OCP), with 10 mV RMS sinusoidal potential perturbations on specimens exposed to the solution for different durations: 5 min, 1 h, 3 h, 6 h, 12 h, 24 h and 48 h respectively. Electrochemical impedance spectroscopy studies for PEO coatings on Ti6Al4V alloy and pure Nb and the bare substrates were also carried out, however, in Ringer's solution (8.6 g/L NaCl, 0.3 g/L KCl and 0.56 g/L $CaCl_2 \cdot 6H_2O$) to preliminary study the biodegradation of the PEO coatings. The same cell set up was selected, nevertheless, the frequency range was from 100 kHz - 0.01 Hz at open circuit potential (OCP) and the immersion time started from 5 min, 1 h, 3 h, 6 h, 12 h, 24 h, 48 h and 72 h respectively. The measurement was reproduced on three samples of each PEO processing.

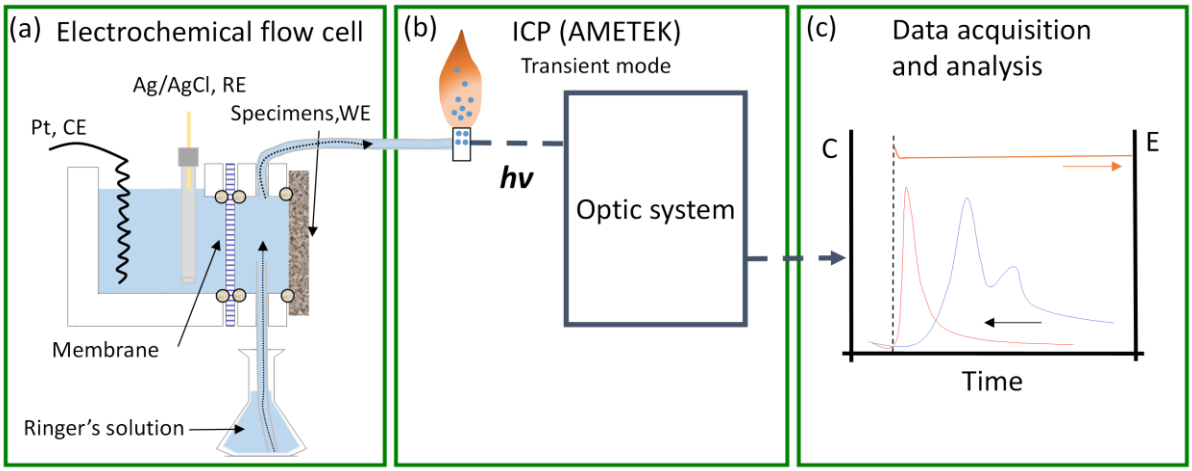

Figure 4-7 Diagram of atomic emission spectroelectrochemistry (AESEC) system

Atomic emission spectroelectrochemistry (AESEC) measurements (coupled atomic emission spectroscopy measurements with electrochemical investigations) [39-41] were used to provide a direct analysis of elemental dissolution rates of the PEO coated specimens and bare Ti6Al4V alloy during electrochemical testing. The selected AESEC set-up is illustrated in Fig. 4-7.

A three-electrode electrochemical flow cell (flow rate ca. 2 mL/min) was connected to an ICP-OES (Inductively Coupled Plasma-Optical Emission Spectrometry) from Spectro Ametek (Acros II FHX22), in radial plasma observation mode. Following sets-up were used during the measurements: generator power of 1300 watts, 12 L/min cooling gas, 1.2 L/min auxiliary flow, 0.8 L/min nebulizer flow, measured with a water cross flow nebulizer chamber (SCOTT AD36/DURAN) with 2 mL/min sample flow. The specimens were acting as a working electrode with an exposed surface area of 0.5 cm^2 to Ringer's solution and connected to a computer controlled Gamry potentiostat Interface 1010E. The counter and the reference electrode were a Pt wire and a saturated Ag/AgCl electrode, respectively. After 1000 s immersion at open circuit potential, potentiodynamic polarization (PDP) scan started from -1.0 V vs reference electrode at a scan rate of 0.5 mV/s and terminated at 10 V.

Table 4-2 Corrosion, wear and photocatalytic measurements of bare and PEO coated specimens

Measurements		Substrate	Parameters
Corrosion test	Electrochemical impedance	MgLi (Pure Mg)	0.5 wt.% NaCl solution, frequency range of 100 kHz - 0.1 Hz at OCP, 10 mV RMS sinusoidal potential perturbations, immersion time 5 min, 1 h, 3 h, 6 h, 12 h, 24 h and 48 h, respectively
		Ti6Al4V	Ringer's solution, frequency range from 100 kHz - 0.01 Hz at OCP, 10 mV RMS sinusoidal potential perturbations, immersion time 5 min, 1 h, 3 h, 6 h, 12 h, 24 h, 48 h and 72 h, respectively
		Nb	
	Potentiodynamic polarization	Ti6Al4V	Ringer's solution, scan from 1.0 to 10 V vs. reference electrode, 0.5 mV/s scan rate
		Nb	
Wear test		MgLi (Pure Mg)	2 N load, 10 mm oscillating amplitude, 5 mm/s sliding velocity and 12 m total sliding distance
Photocatalytic test		Ti6Al4V	8 mg/L MO solution, simulated solar radiation of 16,000 lux intensity, total 6 h irradiation duration
		Nb	

4.3.2 Wear resistance

In paper *1*, the dry sliding wear behavior of the PEO coatings on pure Mg and MgLi alloy were evaluated using a ball-on-disk oscillating tribotester (TRIBOtechnic). The static friction partner was a steel ball (AISI 52,100) with a diameter of 6 mm. All of the tests were performed under ambient conditions of 25 ± 2 °C and 30% r. H. Following parameters were applied for all wear tests (Tab. 4-2): load of 2 N, oscillating amplitude of 10 mm, sliding velocity of 5 mm/s and a total sliding distance of 12 m. The width and depth of the wear tracks on the specimens were measured using a laser scanning confocal microscopy (LSM 800, ZEISS) and the wear tracks were observed by means of the scanning electron microscope (SEM, TESCAN Vega3 SB). The wear rate was calculated using the wear depth. Each measurement was performed for three times in order to check reproducibility.

4.3.3 Photocatalytic activity

In paper *3* and *6*, the photocatalytic properties of PEO coated Ti6Al4V alloy and pure Nb were evaluated via photodegradation measurements of methyl orange (MO) (Tab. 4-2). The temperature in the photoreactor was kept at room temperature by a water recirculation system. The specimen surface was placed on a perforated holder and then immersed in a 10 mL aqueous solution containing 8 mg/L of MO under constant stirring (300 rpm) and exposed to the irradiation source. Prior to the measurement, MO solution was firstly tested for photocatalysis in the absence of the photocatalyst to confirm its stability. Then, the solution were stirred in the dark for 30 minutes with the presence of specimen to achieve adsorption-desorption equilibrium before initiating the irradiation. A lamp (Osram Vitalux 300 W) was used to simulate the solar radiation providing 16000 lux intensity and it was fixed at 25 cm above the surface of the solution. Six hours of irradiation duration in total was selected. A Agilent Cary 60 UV-Vis spectrophotometer was applied to measure the MO concentration at the maximum of the absorption spectra ($\lambda = 464$ nm) for every hour by taking a fixed quantity of 1 ml MO solution from the photocatalytic reactor. The tested solution was returned to the photocatalytic reactor after each

measurement. The absorption was converted to concentration based on a standard curve exhibiting a linear dependence between MO concentration and absorption at 464 nm wavelength. A change of MO concentration was absent after 6 h of irradiation without PEO treated specimen indicating its stability and the observed degradation should result only from the presence of a photocatalyst under the applied condition. The degradation rate of MO was given as $((C_0-C)/C_0)$, where C_0 was the initial MO concentration and C was the tested MO concentration after increasing exposure duration.

5. Results (Published)

The work in frame of this PhD thesis has the aim to study the evolution behavior of PEO coatings on different materials during PEO processing. The obtained results are mainly presented and discussed in form of six papers in scientific journals. The different substrates in present work include Al, Mg, Ti and Nb based metals, alloys and composites. The results (papers) are arranged in three sections, based on the microstructure and the melting temperature of the substrates, as divided in 4.1.1 regarding the selection of the substrates. The first two sections start from the comparison of the simplest one-phase structured substrates, to the polymorph-structured alloy, and then extend to the more complex composite materials with various additional phases. Finally, the results are reviewed under general aspects like role of melting temperature of substrate and oxide phases, oxygen solubility in the substrate, substrate ion solubility in the electrolytes, oxide stability and mixed oxide formation.

The influence of lattice structure of substrate on PEO coating formation is the first section, including paper *1* (MgLi alloy and pure Mg), and paper *2* and *3* (Ti6Al4V alloy). In paper *1*, the effect of the lattice structure of Mg (hexagonal (hcp) and body-centered (bcc)) was studied, however, the influence turned out to be not dominant. The alloying element Li and its influence on the chemical stability of the substrate have more significant influence on the PEO coating formation process, by comparing the PEO of pure Mg (hcp) and MgLi alloy (bcc).

In paper *2*, an in-situ PEO treatment combined with high-energy XRD diffraction was conducted using Ti6Al4V alloy. As an essential innovative approach, the in-situ experiments revealed the time-resolved coating formation process. The absence of β-Ti signal could be assigned to the rapid transformation from β-Ti to α-Ti due to the penetration of oxygen. Interestingly, a lattice expansion of α-Ti phases before the formation of the oxide layer has been revealed due to the high solubility of oxygen. In ex-situ experiments, the PEO process showed a more rapid coating evolution on β-Ti and the initially discharges were preferred to start on β-Ti.

Afterwards, a further study on producing functional PEO coatings on Ti6Al4V was also performed in paper *3*. Good corrosion property and photocatalytic activity of the PEO coatings on Ti6Al4V alloy were obtained.

Moving forward to the second section, it is focusing on the influence of additional phases in material mixes (macro-scaled) on the coating formation, including paper *4* (AlSi9Cu3 alloy) and paper *5* (AZ91Nd/Al_2O_3 MMC and AZ91Nd alloy). Al9Si3Cu alloy was selected as the substrate since it is a typical cast Al-Si-Cu alloy containing four different phases/intermetallics. The oxidation of the intermetallics in Al9Si3Cu alloy and the evolution of coating on the different phases during the PEO processing were studied in paper *4*, and a sequential oxidation of the phases in the Al alloy was proposed, starting on α-Al, then extending to Al_2Cu and β-Al_5FeSi, and finally to Si phase.

In paper *5*, the oxidation behavior of intermetallics in a typical Mg-Al-Zn alloy (AZ91Nd alloy) was studied and the evolution of the reinforcement phase (alumina fiber) in the same AZ91Nd alloy was

tracked. The response of the alloy and MMC reinforced with Saffil alumina fiber (AZ91Nd/Al_2O_3 MMC) to a PEO treatment was investigated. A reactive incorporation of alumina fiber into the coating forming $MgAl_2O_4$ was demonstrated. The source of Al_2O_3 either from matrix or electrolyte does not matter during PEO processing.

Finally, the last section is concentrating on the PEO coating formation on Nb with a high melting temperature, in paper *6*. PEO of Nb is less studied, thus, a preliminary study of the PEO process on pure Nb in different electrolytes was carried out in this work and multifunctional PEO coatings were obtained.

The brief overview of the arrangement of the work is presented in Fig. 5-1. It is worth noting that the main results and discussion of each study are separately summarized in the publications.

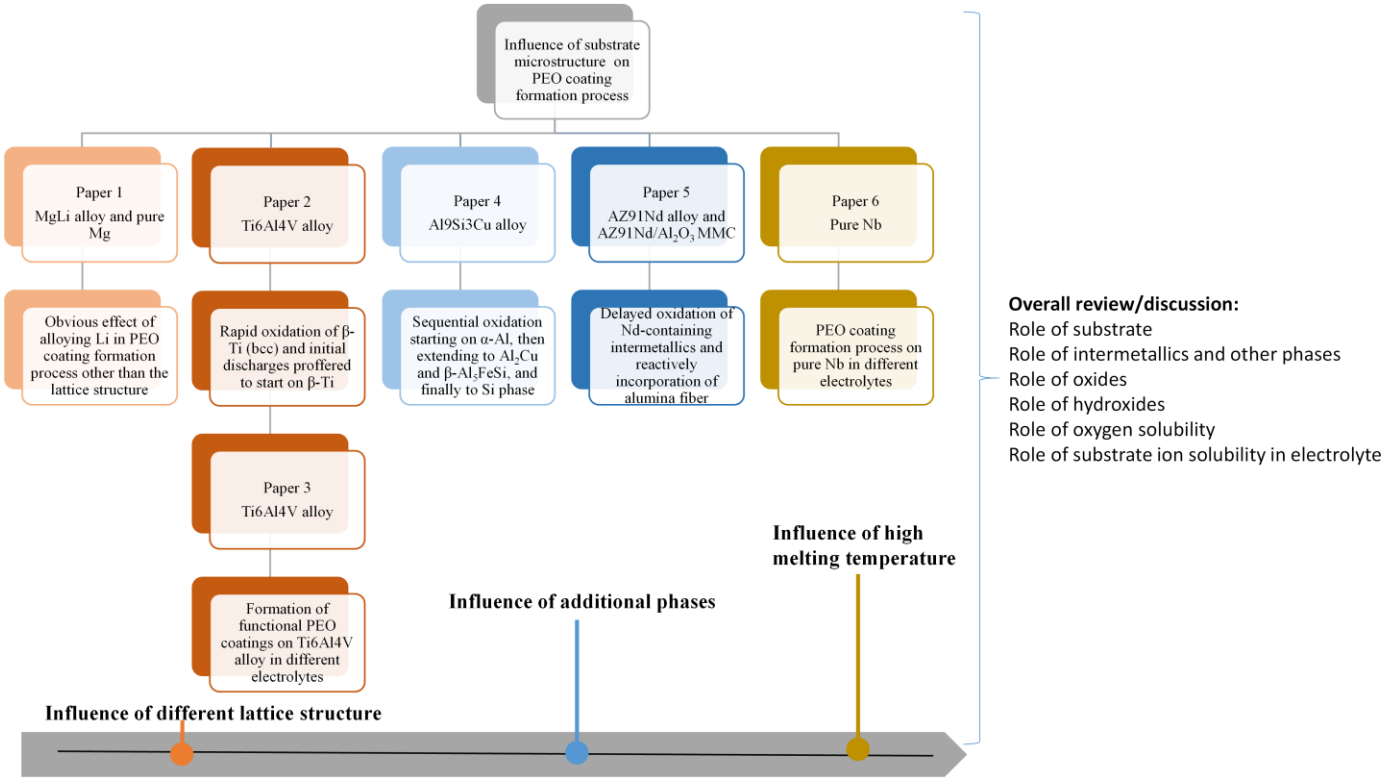

Figure 5-1 Schematic illustration of the structure of the thesis

5.1 Influence of lattice structure of substrate

5.1.1 PEO of one-phase structured MgLi alloy

Paper 1: Ting Wu, Carsten Blawert, Xiaopeng Lu et al., Difference in formation of plasma electrolytic oxidation coatings on MgLi alloy in comparison with pure Mg, Journal of Magnesium and Alloys 9(2021). https:// doi.org/ 10.1016/ j.jma.2021.03.017

Graphical abstract

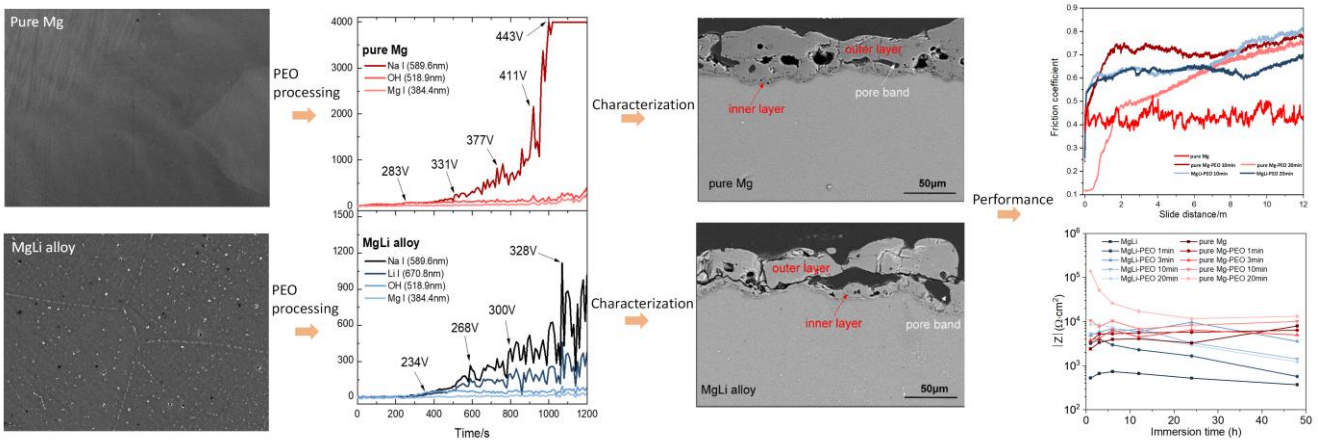

The motivation of this work was to study the effect of two different lattice structures of Mg based materials, hexagonal pure Mg and body-centered MgLi alloy (11.36 wt.% Li), on the PEO coating formation and the properties of resultant coatings, including corrosion and wear resistance. Compared to the different original lattice structures, the presence of Li in the MgLi alloy showed a more essential influence on the PEO coatings. The initial conversion products were accumulated on the $MgLi_2Al$ particles, which were distributed in the grains and grain boundaries. Li was only incorporated in the initial conversion layer at the interface of the coating/MgLi substrate and then dissolved from the coating. Li participated in discharges but possibly there is no direct correlation with the intensities. It is more the compactness of the layer that allows higher voltage for Mg, which resulted in the different microstructure of PEO coatings. PEO coatings enabled a better corrosion and wear resistance than the bare substrates; however, the much more active MgLi substrate always has lower resistance against corrosion and abrasion than pure Mg, either before or after PEO treatment.

Available online at www.sciencedirect.com

ScienceDirect

Journal of Magnesium and Alloys 9 (2021) 1725–1740

www.elsevier.com/locate/jma

Full Length Article

Difference in formation of plasma electrolytic oxidation coatings on MgLi alloy in comparison with pure Mg

Ting Wu[a,*], Carsten Blawert[a], Xiaopeng Lu[b], Maria Serdechnova[a], Mikhail L. Zheludkevich[a,c]

[a] Institute of Surface Science, Helmholtz-Zentrum Hereon, 21502 Geesthacht, Germany
[b] Shenyang National Laboratory for Materials Science, Northeastern University, 110819 Shenyang, China
[c] Institute for Materials Science, Faculty of Engineering, Kiel University, Kaiserstrasse 2, 24143 Kiel, Germany

Received 22 October 2020; received in revised form 22 February 2021; accepted 30 March 2021
Available online 15 May 2021

Abstract

In order to study the substrate lattice structure (Li addition) on the growth of plasma electrolytic oxidation (PEO) coatings, MgLi alloy (11.36 wt.% of Li, cubic) and pure Mg (hexagonal) were treated under a pulsed direct PEO mode in a phosphate electrolyte for different periods of time. The results revealed that the presence of Li and Li-rich phases in the cubic Mg alloy seems to be essential for the treatment result rather than the original lattice structure. A modified discharge behavior of MgLi alloy finally led to a different microstructure of the coating. The unstable coatings of MgLi alloy tended to dissolve rapidly though shared the similar composition to that of pure Mg. Li was incorporated only in the primary conversion products at the interface of coating/MgLi. In spite of the advanced efficiency of energy input during processing, the more porous and thinner PEO coatings on the MgLi alloy were less resistant to abrasion and corrosion.

Keywords: Plasma electrolytic oxidation; Magnesium lithium alloy; Pure magnesium; Microstructure.

1. Introduction

Plasma electrolytic oxidation (PEO) is a plasma-assisted anodizing process for the surface modification of lightweight metals [1–8], such as Al, Mg and Ti alloys [9–12], in order to improve their surface hardness, wear and corrosion resistance. The process is characterized by numerous short-lived micro-discharges under high voltage [13–15], which forces the formation of PEO coatings with intrinsic cavities and cracks [16–18].

In the framework of understanding the growth behavior of PEO coating, some researches [19–26] were focused on the migration of species, originated from the electrolyte during PEO processing. Alloying elements, such as Ti, Nb and Zr from the substrates used as tracers, were also reported and provided a solid evidence of the dielectric breakdown of the oxide layer [25,26]. PEO processing of AZ magnesium alloys (eg., AZ31, AZ61 and AZ91) showed a sequential oxidation at the initial stage starting with α-Mg and then extending to the β-phase ($Mg_{17}Al_{12}$). A higher rate of coating formation was observed on α-Mg, deriving from the higher reactivity of Mg compared to Al [3,27–29]. Also, the discharges were more intensive in the presence of Al in Mg alloys, resulting in the more porous coatings [3]. Nevertheless, the PEO processing of WE43 magnesium alloy developed more rapidly and presented a reverse oxidation order compared to AZ91. The growth of the initial conversion film started on the β-phase ($Mg_{14}Nd_2Y$), possibly stemming from the higher reactivity of Y and Nd than that of Al [30,31]. In binary Mg-Zn alloys the presence of Mg_7Zn_3 phase was found to reduce the thickness, however, smoothen the surface morphology of the PEO coatings, ascribed to the hardship in passivating the Mg_7Zn_3 intermetallics [31,32]. That is to say, from manipulating the composition and microstructure of Mg alloys, the alloying elements have a significant influence on the PEO process and hence on the properties of the PEO coatings.

* Corresponding author.
E-mail address: ting.wu@hereon.de (T. Wu).

https://doi.org/10.1016/j.jma.2021.03.017

Magnesium lithium (MgLi) alloys have recently been developed as potential engineering materials [33–39] due to the desirable low temperature ductility and cold formability from the body-centered cubic β-Mg containing more slip systems [40]. PEO treatment has been adopted to improve the surface stability of the vulnerable substrate materials considering the chemically active nature and ionization tendency of Li [20,41–47]. Researchers have claimed that the PEO coatings of MgLi alloy doped with salt additives, such as tungstate [41] , molybdate [48], cerium salts [49], or sol additives, for instance, silica [20] and titania sols [43], revealed a significant enhancement in wear and corrosion resistance [41]. In fact, it is not surprising that the cooperation of different additives in the electrolytes can improve the coating performance on MgLi alloys, since it has been established already for many other magnesium alloys [2,50]. However, the effect of Li in the Mg matrix during PEO processing is less taken into consideration, regarding its active nature and the difficulty to trace the light element with standard techniques used for characterization of PEO coatings. Particular for high Li containing Mg alloys (> 10.3 wt% Li), the mechanical strength declines considerably thus the surface protection is more necessary [51,52]. Optical emission spectra of plasma discharges during the treatment of MgLi alloy evidenced the participation of Li in the plasma reactions due to the high temperature-forced excitation of Li, although the absence of Li containing phase in the PEO coating [53].

Despite the progresses, the characteristics (thickness and microstructure) and performance (wear and corrosion resistance) of PEO coatings on MgLi alloys with high Li contents remain unclear. The role of Li during PEO process still requires further elucidation since the intrinsic chemical reactivity of MgLi alloy is more susceptible in aggressive environment. Thus, the aim of this work is to study the evolution of the coating growth of MgLi alloy and to understand if the different lattice structure has an effect on the coating formation and growth. Furthermore, the role of Li in the phase formation of the PEO coatings should be studied in more details. To do this, PEO coatings on a selected MgLi alloy (11.36 wt.% Li), were compared at different stages of the PEO process with coatings formed on pure Mg under the same conditions.

2. Experimental

2.1. Materials and PEO treatment

Rectangular specimens of size 15 mm × 15 mm × 4 mm made of MgLi alloy with the chemical composition of 11.36 wt.% Li, 2.39 wt.% Al, 0.0093 wt.% Mn, 0.0072 wt.% Zn, 0.0032 wt.% Fe, 0.0012 wt.% Ni, 0.0009 wt.% Sn and Mg balance as measured by an Arc Spark OES (Spark analyze M9, Spectro Ametek, Germany) were selected. Pure Mg specimens with the same dimensions (15 mm × 15 mm × 4 mm) and a purity of 99.94 wt.% (0.022 wt.% Mn, 0.017 wt.% Si, 0.014 wt.% Al, 0018 wt.% Zn, 0.0017 wt.% Fe, 0.0002 wt.% Cu , <0.0002 wt.% Ni and Mg balance) were adopted as references. All of the specimens were mechanically ground up to 2500 grit, cleaned in water and ethanol and dried with compressed air at ambient temperature. A phosphate-based aqueous electrolyte was prepared by the dissolution of trisodium phosphate (Na_3PO_4, ≥ 98%, Carl Roth, Germany, 20 g/L) and potassium hydroxide (KOH, ≥ 85%, Th. Geyer, Germany, 1 g/L) in deionized water. The pH and conductivity of the electrolyte were 12.4 and 23.2 mS/cm respectively. The temperature of the electrolyte was kept at 10 ± 2 °C by a cooling system. The specimens were screwed to a holder acting as the anode. A stainless steel tube was integrated as the cathode and part of the water-cooling system. During the PEO process, continuous stirring of the electrolyte was applied to prevent concentration and temperature gradients as much as possible. PEO treatment was carried out for six different treatment durations (15 s, 30 s, 1 min, 3 min 10 min and 20 min) using a pulsed DC power supply at a constant current density of 3 A/dm^2 with a duty cycle of 10% (1ms:9 ms) and a frequency of 100 Hz. The voltage-time response was recorded using a data acquisition system (SignaSoft 6000 software package, Gantner, Germany). The optical emission spectra of the discharges during the processing was recorded using Emicon system (PLASUS, Germany) with a spectral resolution of ∼ 1.5 nm in the range of 180 - 880 nm, in combination with PLASUS SpecLine software (PLASUS, Germany). The species (Na, Mg, Li and OH) involved in the plasma reactions and the variation of emission intensity of these species as function of treatment time were monitored.

2.2. Coating characterization

Scanning electron microscopy (SEM, TESCAN Vega3 SB) combined with an energy dispersive spectrometer system (EDS, eumeX IXRFsystems) were used to characterize the surface and the cross sections of the PEO coatings in association with SE (secondary electron) and BSE (back scattering electron) modes. A lamella milled from the bulk sample of MgLi alloy after 3 min of PEO treatment was obtained using focus ion beam cutting in a field-emission-scanning electron microscopy (FIB-SEM, TESCAN Lyra3). Further information about the presence of Li in the coating was obtained using a windowless Oxford Ultim Extreme EDS detector (OXFORD ULTIM EXTREME), which is capable to Li detection. The coating thickness measured by a microprocessor coating thickness gage (MiniTest 2100, ElektroPhysik) was validated and integrated with the observation of the coating cross sections. Phase composition studies were performed by X-ray diffraction (XRD, D8 Advance, Bruker AXS) with Cu Kα radiation. The following diffraction settings were selected: diffraction angle 2θ between 20° and 80°, step size of 0.02°/s, dwell time of 1 s and grazing angle of 1° Laser scanning confocal microscope (LSM 800, ZEISS) was employed to monitor the roughness profile of the coating surface.

2.3. Wear test

The dry sliding wear behavior of the thicker PEO coatings (10 min and 20 min) were evaluated using a ball-on-disk oscil-

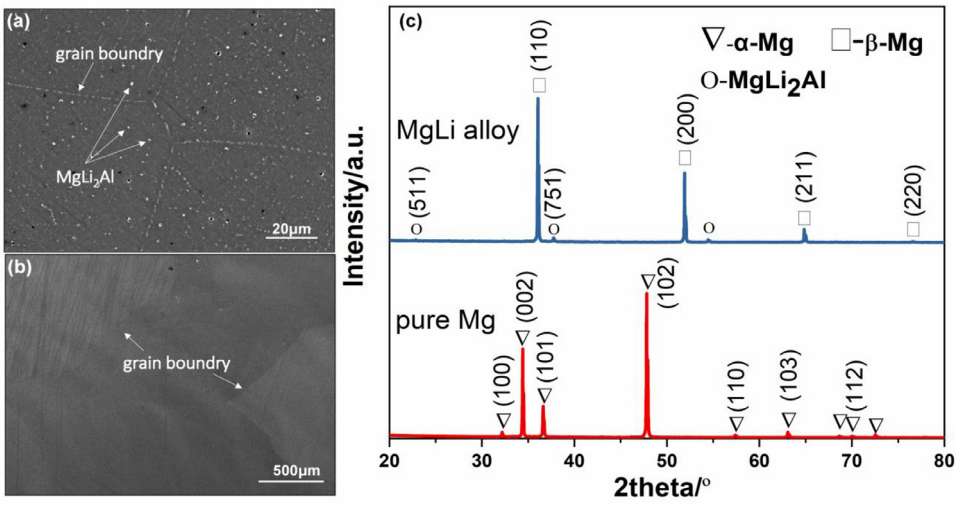

Fig 1. (a) back scattered electron (BSE) micrograph of MgLi alloy, (b) secondary electron (SE) micrograph of pure Mg and (c) the XRD patterns of MgLi alloy and pure Mg.

lating tribotester (TRIBOtechnic). The static friction partner was a steel ball (AISI 52,100) with a diameter of 6 mm. All of the tests were performed under ambient conditions of 25 ± 2 °C and 30% r.H. Following parameters were applied for all wear tests: load of 2 N, oscillating amplitude of 10 mm, sliding velocity of 5 mm/s and a total sliding distance of 12 m. The width and depth of the wear tracks on the specimens were measured using a laser scanning confocal microscopy (LSM 800, ZEISS) and the wear tracks were observed by means of a scanning electron microscopy (SEM, TESCAN Vega3 SB). The wear rate was calculated using the wear depth. Each measurement was performed for three times in order to check reproducibility.

2.4. Electrochemical measurements

To evaluate the corrosion performance of the PEO coatings (1 min, 3 min, 10 min and 20 min) on MgLi alloy and pure Mg, electrochemical impedance spectroscopy (EIS) tests were carried out using a Gamry Potentiostat (Gamry, United States) in conjunction with a classical three-electrode cell system. The coated specimens were adopted as working electrode with an exposed surface area of 0.5 cm^2. The counter and the reference electrode were a platinum wire and a saturated Ag/AgCl electrode, respectively. Tests were performed in 0.5 wt.% NaCl solution at ambient temperature, over a frequency range from 100 kHz to 0.1 Hz at open circuit potential (OCP), with 10 mV RMS sinusoidal potential perturbations on specimens exposed to the solution for different durations: 5 min, 1 h, 3 h, 6 h, 12 h, 24 h and 48 h respectively. The measurement was reproduced on three samples of each PEO processing.

3. Results

3.1. Microstructure of the substrate materials

The grain boundaries of selected MgLi alloy with an average grain size of 230 μm are visible in the BSE mode, because they are decorated with small precipitates (Fig. 1(a)). The bright and fine particles scattered also within the grains are identified by X-ray diffraction (Fig. 1(c)) as $MgLi_2Al$ intermetallics, whereas the darker micro-pores seem to be the result of the mechanical removal of $MgLi_2Al$ intermetallics during the grinding preparation. Beside the fine $MgLi_2Al$ intermetallics, XRD pattern of MgLi alloy only presents intensive peak signals of cubic β-Mg phases in comparison to the hexagonal α-Mg of pure Mg. This is in accordance with the common knowledge of cubic structure of MgLi alloy when the content of Li exceeds 10.3 wt.% [54]. Without precipitation at the grain boundary, the microstructure of as-cast pure Mg can be only recognized under SE mode (Fig. 1(b)) displaying the irregular grain boundaries due to the different sizes of grains.

3.2. Characterization of PEO process

The voltage-time responses of the PEO process of MgLi alloy and of pure Mg exhibit the initial fast ramps of voltage (Fig. 2(a)), suggesting a rapid electrochemical formation of barrier layers of similar thickness (Fig. 2(b)) on both substrates. As soon as the voltage reaches 110 V for MgLi alloy and 150 V for pure Mg, the breakdown of the initial barrier layers occurs, being accompanied with visible sparks. This period of development is shorter than 30 s. The discrepancy in breakdown voltage can be explained via the electrical resistance of the initial layer, which seems to be lower for MgLi alloy and therefore needs a lower voltage to ignite the discharges. After 1 min of treatment, frequent fast moving white sparks cover the entire surface of both substrates; however, the voltage increase for MgLi specimen slows down earlier and more rapidly compared to pure Mg. From 3 min to 10 min of PEO processing, there is a sluggish increase of voltage in both cases, probably because of a competition between coating formation and dissolution at this stage. Nevertheless, for MgLi alloy this stage takes longer until the voltage continues

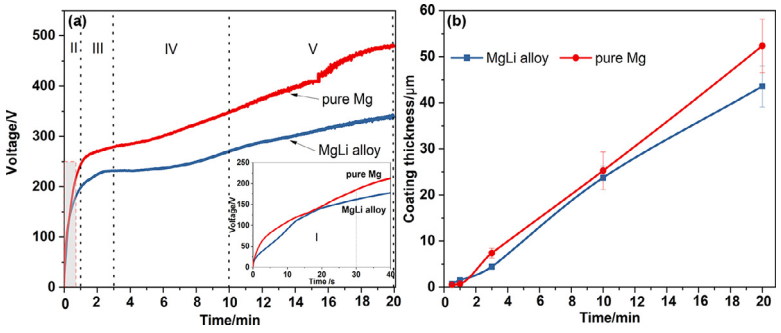

Fig 2. (a) Voltage-time curves of PEO processing on MgLi alloy and pure Mg and (b) PEO coating thickness of MgLi alloy and pure Mg at different treatment time.

to rise faster again. This stage is characterized by less numerous but larger and slowly moving orange discharges on the surface of both substrates. Voltage fluctuation are observed after 13 min and are associated with the evolution of the plasma discharges [55], which are also recognized from the sporadic long-lasting large sparks before the end of the processing. The final voltage of MgLi alloy and pure Mg is 340 V and 480 V respectively. It is obvious that the electrical resistance of the coating on the MgLi alloy is always lower than the one on pure Mg as the same current density requires less voltage to drive the current through the layer on the MgLi alloy.

The evolution of coating thickness with treatment time is shown in Fig. 2(b). At the final treatment time of 20 min the PEO coating on MgLi alloy reaches a thickness of $43.5 \pm 4.4\,\mu m$ and on pure Mg it is $52.3 \pm 5.8\,\mu m$ with a growth rate of 2.2 $\mu m \cdot min^{-1}$ and 2.6 $\mu m \cdot min^{-1}$, respectively. Obviously, under the same treatment conditions the response of the MgLi alloy to a PEO treatment in the sense of coating formation and resistance (lower process voltage necessary to let the predefined treatment current pass through the coating) is worse compared to pure Mg. Whether this difference is related to the different lattice structure, the lower corrosion resistance of the MgLi substrate, less stable coating phases or whether it is a combination of all possible influencing factors, still needs to be studied in more details. The optical emission spectra as depicted in Fig. 3(a) and (c) confirm the involvement of Na, Mg and OH in the discharges on both substrate materials after 20 min of the PEO treatment. Following lines are observed during the measurements: Na I, Mg I and OH. In the case of MgLi alloy, an additional emission line of Li (Li I line at 670.8 nm) is detected, indicating its participation in the plasma reactions. All the emission intensities of mentioned species, especially Na I (of pure Mg and of MgLi alloy) and Li I (of MgLi alloy) increase gradually with treatment time (Fig. 3(b) and (d)), which are however related to respective trends of voltage increase. The initial white luminescence during conventional anodic oxidation, resulting from the radiative recombination of electrons at flaws in the initial oxide film [56], shows the lowest emission intensity of all species because the voltage is not adequate to excite them. Afterwards, the emission of Na (Na I emission line) for both pure Mg and MgLi alloy and the emission of Li (Li I line) for MgLi alloy are distinguished from ca. 300 s (6 min) of treatment until the end of the process. The appearance of both lines takes place at initial voltages of 283 V and 234 V for pure Mg and MgLi alloy, respectively, latter, indicates an easier excitation of Na and Li for MgLi alloy. Nevertheless, the intensity of Na I emission line for pure Mg increases more rapidly in comparison with MgLi alloy. This can be correlated with the faster rising of the voltage in the case of pure Mg. Afterwards, the emission intensity of Na I line for pure Mg reaches the technical saturation limit of the detector once the voltage exceeds 443 V. For the MgLi alloy, the emission of Li I shows a similar pattern as Na I however at a lower intensity. In regard to the emission of Mg (Mg I emission line) and OH, they show a slight increase with moderate oscillation on both substrate materials and, once appears, does not depend much on the treatment time/applied voltage.

3.3. Coating characterization

3.3.1. Surface morphology

Figs. 4 and 5 exhibit the surface morphology and element distribution of the coatings on MgLi alloy and pure Mg after 15 s, 30 s, 1 min and 3 min of PEO processing respectively. The coverage of O over the entire surface of MgLi alloy indicates the formation of a barrier layer within 15 s (Fig. 4(a)). Bright fine protuberances scattered on the surface of the MgLi alloy are also observed at the earliest stage. The higher concentration of Al in these protuberances demonstrates the accumulation of initial conversion products on $MgLi_2Al$ intermetallics. The first conversion products appear to be Mg/Na based phosphates. In comparison, larger protuberances of conversion products are found spreading randomly on the surface of pure Mg (Fig. 5(a)). As the "footprints" of plasma discharges, sporadic micro-pores are distributed on the surface of MgLi alloy and more frequent on pure Mg substrates after 30 s of treatment (Figs. 4(b) and 5(b)), confirming that the breakdown of the barrier layers is triggered in the range between 15 and 30 s (120 to 180 V). The discharge channels are considered to be the pathways for transporting the species from the substrate outwards (Mg, Mg^{2+}, Li and Li^{+}) and from the electrolyte inwards (OH^{-}, H_2O and PO_4^{3-}) respectively. Regions of strong interactions and reactions between the different compounds refreshing the coating materials [57] can be

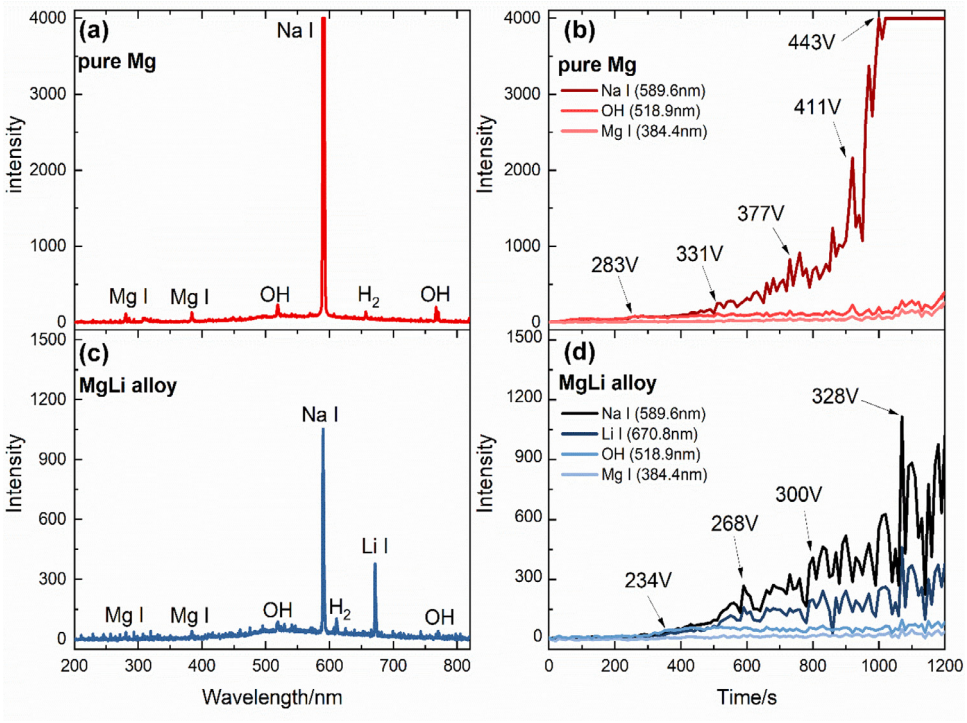

Fig 3. Optical emission spectra obtained after 20 min PEO treatment and evolution of the emission line intensity as a function of treatment times: (a) optical emission spectrum of pure Mg, (b) emission line intensity of Na I, Mg I and OH for pure Mg treatment, (c) optical emission spectrum of MgLi alloy, (d) emission line intensity of Na I, Li I, Mg I and OH for MgLi alloy treatment.

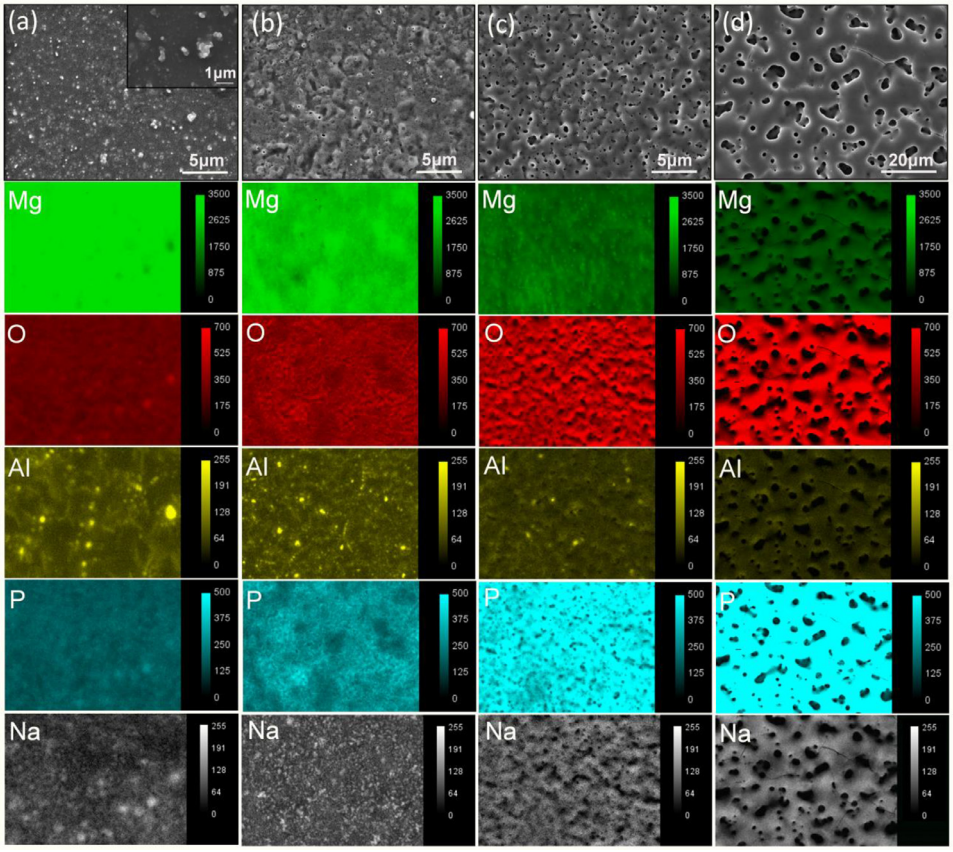

Fig 4. Surface morphologies and element distribution (Mg, O, Al, P and Na) of PEO coatings on MgLi alloy after the treatment time of (a) 15 s, (b) 30 s, (c) 1 min and (d) 3 min.

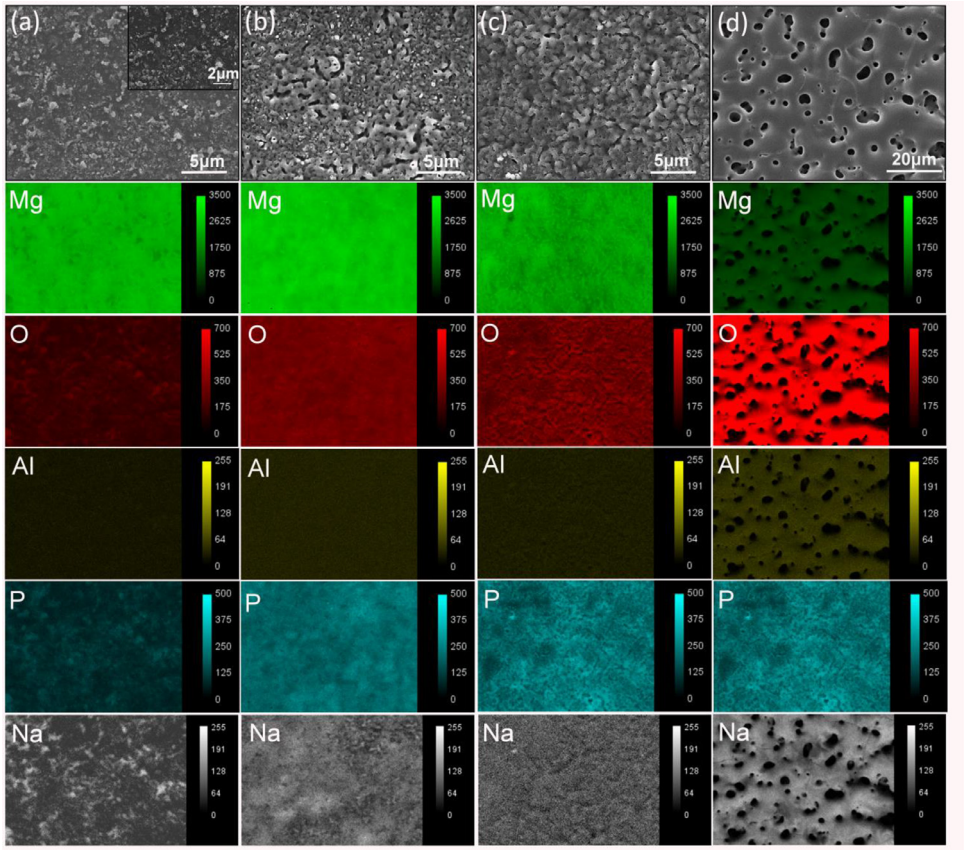

Fig 5. Surface morphologies and element distribution (Mg, O, Al, P and Na) of PEO coatings on pure Mg after the treatment time of (a) 15 s, (b) 30 s, (c) 1 min, and (d) 3 min.

distinguished in the figures as well. The larger micro-pores and volume of strongly melted regions on pure Mg reflect more intensive and frequent plasma discharges at a higher voltage. The higher intensity of Al on the surface of MgLi alloy after 30 s of processing is from the penetration of electrons into the substrate material underneath the thin surface film during the SEM examination. Hence, the intensity of Al from the MgLi alloy substrate is also indicative of the coating thickness. The signal of Al moderates gradually with further increase of the treatment time as the coating is thickening steadily. Hereafter, typical pancake features with centered micro-pores are observed on both coatings (Figs. 4(c) and 5(c)), which become larger and more dominant after 3 min treatment (Figs. 4(d) and 5(d)).

Fig. 6(a)-(d) display the typical surface morphology of PEO coatings with the open micro-pores (remains of discharge channels) on MgLi alloy and pure Mg after 10 min and 20 min of PEO treatment. The micro-pores cover about 21% and 11% of the surface area for the MgLi alloy and around 15% and 13% for pure Mg after 10 and 20 min of treatment, respectively. Considering also the less frequent surface micro-cracks after the longest treatment time (20 min), in particular of MgLi alloy, the coating seems to be healed to a certain degree since the discharge process always initiates in the weakest regions of the coating [58]. Interestingly, an accumulation of bright fine particulates adjacent to the micro-pores are noticed on the surface of PEO coatings on the MgLi alloy, as revealed in the insertions at higher magnification (Fig. 6(a) and (c)). It is reasonable to associate the formation of bright particulates with the presence of abundant Li since a modified voltage response and less intensive discharges are observed. XRD patterns suggest a similar PEO layer composition based on MgO and $Mg_3(PO_4)_2$ for both substrates after 10 min of treatment. Nevertheless, there is no Li containing phase detected after PEO processing of MgLi alloy. A bump in intensity between 2θ angles of 20° to 40° especially on the MgLi alloy indicates the formation of amorphous phosphate, most likely to the fact that the discharge energy is lower, causing less crystalline phases and more phases that are amorphous.

Chemical composition and contents of the fine particulates (A and D) and the regions without particulate (B, C, E and F) are listed in Table 1. Li of light weight is beyond the detectability of current main EDS and not available here. The bright particulates (A and D) contain higher ratios of elements from the electrolyte (P, O, Na) compared to the regions of B, C, E and F without particulates. This could stem from the less intensive A-type discharges [55,59,60] occurring near the interface of coating/electrolyte, thus involving the deposition of species mainly from the electrolyte. Another explanation might be related to the fact, that those regions are further away from the discharge channels, where the material is less mixed and sintered. The surface around the discharges looks

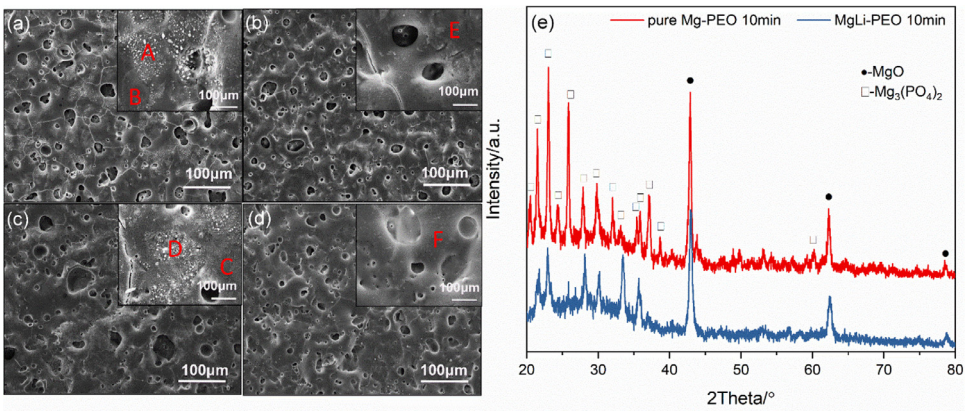

Fig 6. Surface morphologies of PEO coatings after 10 min and 20 min treatment on MgLi alloy (a) 10 min, (c) 20 min; on pure Mg (b) 10 min, (d) 20 min and (e) XRD patterns of PEO coatings after 10 min treatment.

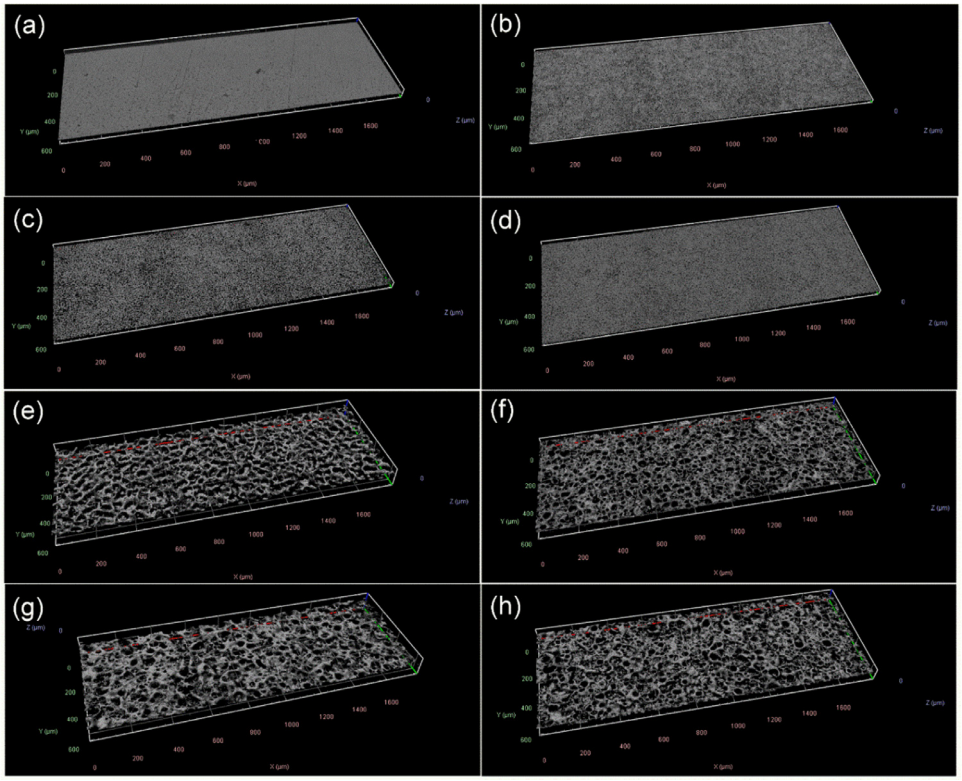

Fig 7. Surface roughness profile of PEO coatings on MgLi alloy: (a) 1 min, (c) 3 min, (e) 10 min and (g) 20 min; on pure Mg: (b) 1 min, (d) 3 min, (f) 10 min and (h) 20 min.

normally melted, uniform and smoother. Due to less sintering in those regions, they might be also prone to more attack from the electrolyte and those white particles are conversion products.

Fig. 7(a)-(d) exhibit similar surface morphologies of the coatings after shorter treatment durations (1 min and 3 min). Due to the limited thickness of the coatings, scratches produced during grinding still present on the surface of MgLi alloy after 1 min of treatment. The presence of Li or the different lattice structure of the substrate does not significantly change the surface roughness of the coatings at this stage and the respective Ra values are $0.58 \pm 0.07\,\mu m$ and $1.59 \pm 0.04\,\mu m$ for MgLi alloy and $0.45 \pm 0.03\,\mu m$ and $1.94 \pm 0.02\,\mu m$ for pure Mg after 1 min and 3 min treatments. However, the surface of the PEO coatings on MgLi alloy is rougher after 10 min and 20 min of treatment compared with pure Mg. The Ra values of the PEO coatings on MgLi alloy are $7.86 \pm 0.34\,\mu m$ and $5.59 \pm 1.12\,\mu m$ (Fig. 7(e) and (g)), while the Ra values of the PEO coating on pure Mg are $6.43 \pm 2.31\,\mu m$ and $4.31 \pm 0.42\,\mu m$ (Fig. 7(f) and (h)) respectively. The healing effect of the discharges is herein revealed at the later stage of PEO treatment. Since the PEO coatings after 10 min of treatment are thick enough to resist frequent destructive B type of discharges, relatively soft discharges of

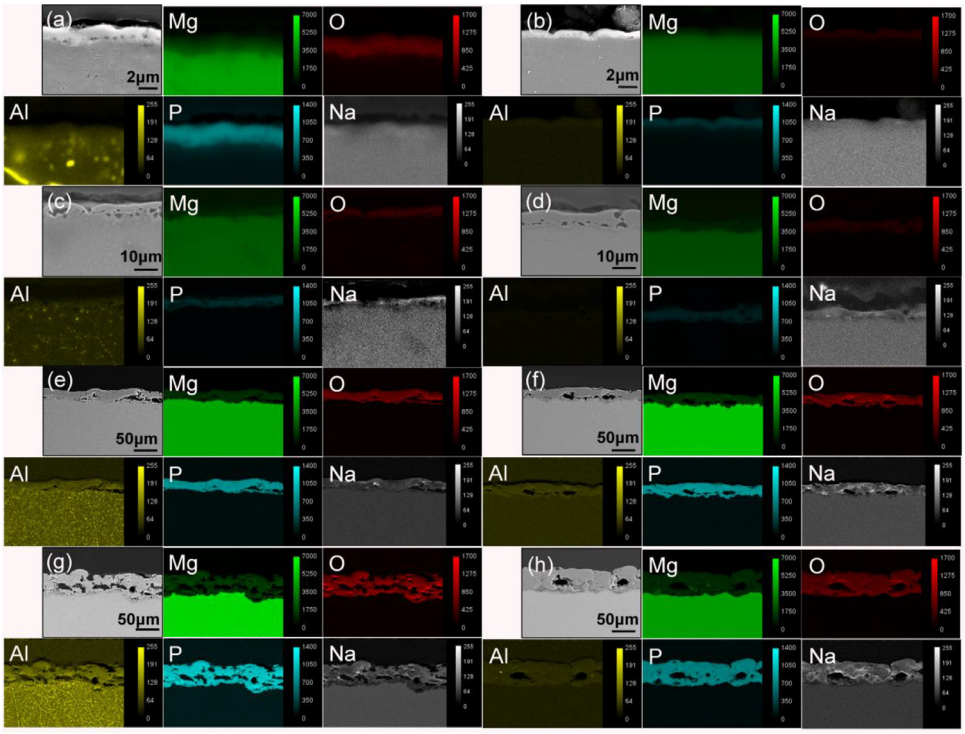

Fig 8. Cross-sectional morphologies and EDS mapping results of PEO coatings at different duration of PEO treatment on MgLi alloy: (a) 1 min, (c) 3 min, (e) 10 min and (g) 20 min; on pure Mg: (b) 1 min, (d) 3 min, (f) 10 min and (h) 20 min.

Table 1
Content of main elements (Mg, P, O, Na, Al) at the regions of A, B, C, D, E and F in Fig. 6.

Elements (at.%)	Mg	P	O	Na	Al	O/Mg
A	15.5	16.5	58.9	8.9	0.2	3.80
B	25.6	21.7	46.5	6	0.2	1.82
C	26.1	16.9	51.5	5.4	0.1	1.97
D	17	19.3	55.7	7.9	0.1	3.28
E	23.5	16.7	53.8	5.8	0.2	2.29
F	26.5	19.5	47.2	6.7	0.1	1.78

A and C types are more likely generate at the pores and fissures within the coatings. As a result, the sequential remelting and sintering process could explain the modification of the surface morphologies of the coatings with increasing treatment time.

3.3.2. Cross-sectional morphology

The cross-sectional morphology and element distribution of the PEO coatings on the two substrates after different treatment times are depicted in Fig. 8. The typically layered coatings are formed in both cases. A thin denser barrier layer can be differentiated from the main outer porous PEO layer by a pore bands (elongated horizontal cavity regions of agglomerated pores). The pore band starts to be formed already after 1 min treatment of both substrates and expands more in volume on both substrates with the increase of treatment time. More and larger cavities are always present in the coatings on MgLi alloy compared to pure Mg, corresponding to the rough microstructure of the coating on MgLi alloy [61]. Distributions of Mg, O, P and Al are quite homogeneous across the coatings regardless of the base materials and processing durations. Nevertheless, Na originating from the electrolyte concentrates around the edges of pores and large cavities and on the coating surface (Fig. 8(e)-(h)) due to the penetration of electrolyte.

The interface of the coating/MgLi substrate after 3 min treatment is studied additionally in higher resolution. STEM micrographs are shown in Fig. 9(a) and (b). By the different contrast a narrow inner layer not more than 0.5 μm thick presents, which contains sporadic micro-pores. The distribution of Li and Al shows relative high intensity of Li at the sites of $MgLi_2Al$ intermetallic and at the interface of coating/substrate (Fig. 9(c) and (d)). It seems as if Li is involved in the early coating formation via the formation of conversion products and remains enriched close to the coating/substrate interface throughout the process.

The cross-sectional morphologies of the thicker PEO coatings on MgLi alloy and on pure Mg after 10 min and 20 min treatments are shown in Fig. 10. Since the discharges are the driving force for the coating growth, the process is impeded by the thicker coatings with increasing treatment time, especially from blocking the transport of the reaction species. Nevertheless, beside the plasma discharge channels, frequent cracks and defects are visible in the thicker outer layer on both substrates. They are the additional pathways for the species from the substrate and the electrolyte [21]. Thus, the coating growth rate remains stable and constant with increase of treatment duration. In addition, next to the pore bands the

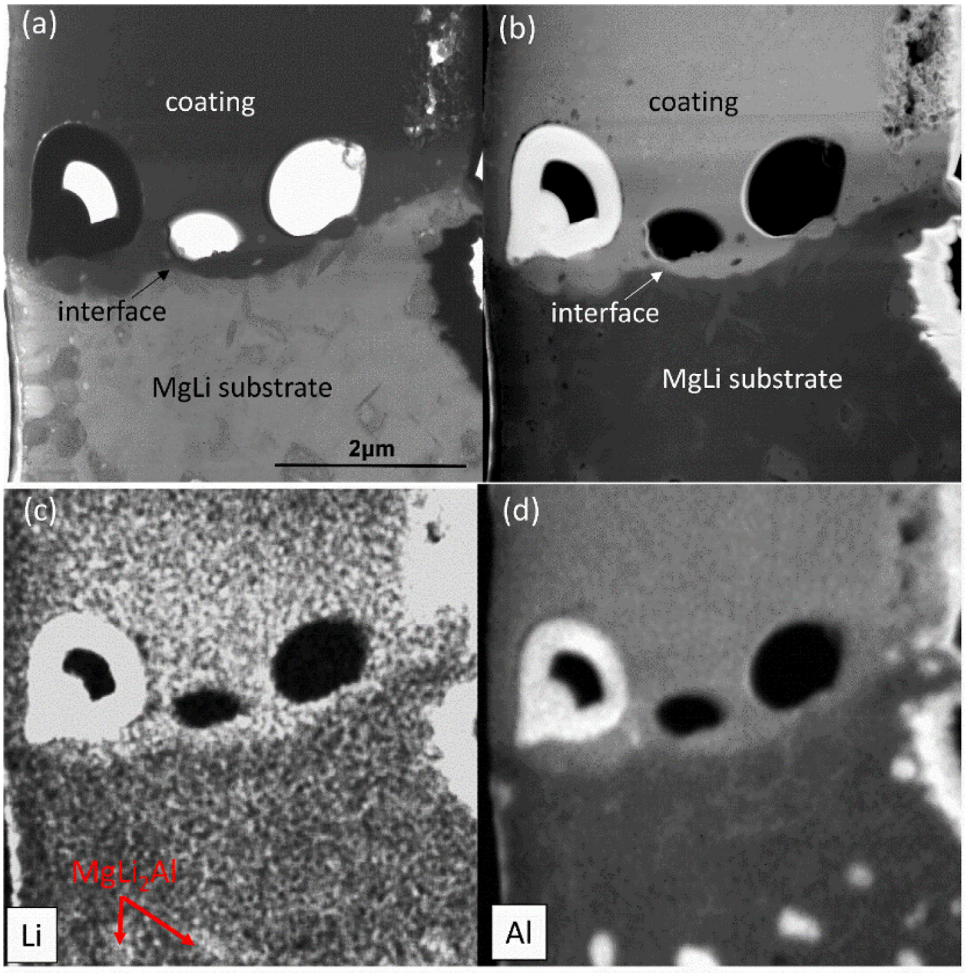

Fig 9. STEM micro images of interface of coating/ MgLi substrate after 3 min PEO treatment (a) bright field, (b) dark field, (c) the distribution of Li and (d) the distribution of Al.

inner layer allows a continuous growth due to electrolyte inward diffusion and the generation of discharges within the coating.

3.4. Wear resistance of PEO coatings

The friction coefficients as function of sliding distance of the substrate materials and the different coatings running against a steel ball under a load of 2 N without additional lubrication are displayed in Fig. 11. The friction coefficient of pure Mg oscillates slightly around a value of 0.42 ± 0.05 presenting an average wear rate of 4.51×10^{-3} mm^3/ (N·m). However, for the MgLi alloy the wear test is interrupted already after few cycles, because the friction force exceeds the safety setting of the wear tests. The high ductility of the cubic structured MgLi substrate has a higher friction coefficient compared to the hexagonal Mg. Already after the few cycles a clear wear track has formed in the soft MgLi substrate and the material that has been worn off remains in the track as shown in Fig. 12(a). PEO coatings can improve the wear performance drastically. For the PEO coatings on MgLi alloy at 10 min and 20 min, both friction coefficients increase to about 0.62 within the first 2 m of sliding remaining quite constant up to 7 m of sliding. Until the end of the test, the friction coefficient of the thicker coating (20 min) fluctuates around 0.65 showing an average wear rate of 2.26×10^{-3} mm^3/ (N·m). It implies that there is no coating failure as manifested by the remaining full coverage of PEO coating (Fig. 12(e)). However, the friction coefficient of the thinner coating (10 min treatment) rises to a value of 0.85 within the remaining sliding distance but the coating is not failing. The worn track of the sample in Fig. 12(c) unveils an average wear rate of 3.823×10^{-3} mm^3/ (N·m), which is related to the lower load bearing capacity and the coating being deeper pressed into the soft substrate.

The coating on pure Mg after 10 min treatment shows a rapid rise of the friction coefficient to 0.77 at the initial sliding and then some slight oscillations. Without coating failure (Fig. 12(d)), the average wear rate of the coating is 3.75×10^{-3} mm^3/ (N·m). For the thickest coating on pure Mg after 20 min of processing, the first increase of the friction coefficient reaches a relative low value of 0.5 at the first 2 m of sliding. After that, the friction coefficient ramps constantly to a final value of 0.72 after 10 m sliding distance. Compared

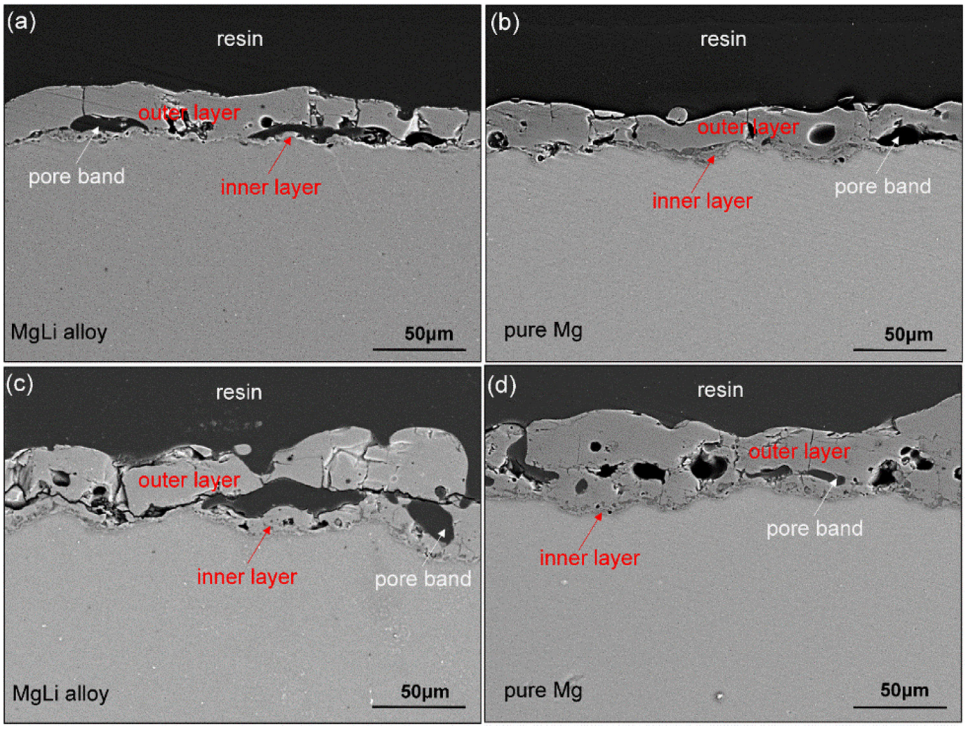

Fig 10. Cross-sectional morphology of PEO coatings on MgLi alloy: (a) 10 min and (c) 20 min; and on pure Mg: (b) 10 min and (d) 20 min.

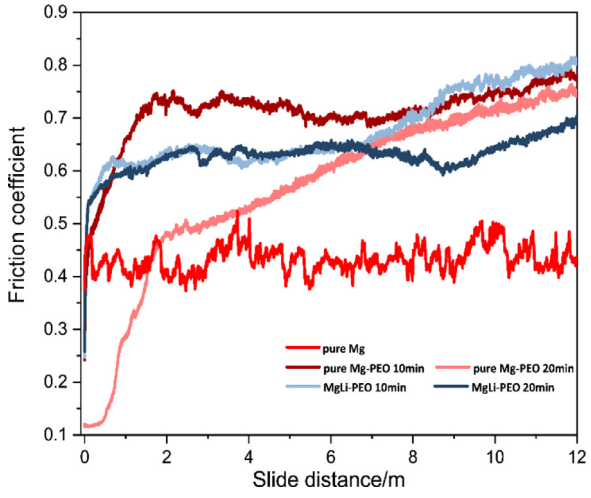

Fig 11. Variation of friction coefficients versus sliding distance for pure Mg substrate and the PEO coatings on MgLi alloy and pure Mg.

to the other coatings, the thicker coating on pure Mg has the lowest wear rate of 1.15×10^{-3}mm^3/(N·m).

3.5. Corrosion behavior of PEO coatings

The Nyquist and Bode plots in Figs. 13 and 14 compare the respective responses of substrate materials and PEO coatings (1 min, 3 min, 10 min and 20 min) on the MgLi alloy and the pure Mg in 0.5 wt% NaCl aqueous solution with continuous immersion up to 48 h. For the uncoated MgLi alloy (Fig. 13(a)), one well-defined time constant is detected in the medium frequency range (~10 Hz) after different immersion times, which could be ascribed to the response of the native oxide film. At low frequencies there is a relaxation process (~0.2 Hz) assigned to the double layer capacitance and charge transfer resistance. The shrink of capacitive loops and drop of the total impedance during 48 h immersion confirm the less protection of the oxide film and the active dissolution of MgLi alloy. The well-defined time constant corresponding to the native oxide film at medium frequencies is also found for uncoated pure Mg (Fig. 14(a)) as well as the low-frequencies relaxation process during 48 h of immersion. However, the expanding of the capacitive loops and the increased sum of impedance modulus evidence the increase of stability of the oxide film.

Fig. 13(b)-(e) clearly illustrate the degradation processes of PEO coatings on MgLi alloy. The coating after 1 min of PEO processing increases the total impedances slightly until 12 h of immersion. Although the layered structure of the coating has been revealed, there is only one well-defined time constant assigned to the inner layer. Afterwards, a relaxation process presented as scattering at the low frequencies reveals the failure of the coating as a result of the local breakdown of the coating. For the coating after 3 min of PEO treatment, a similar behavior with only one capacitive loop in the medium frequency range can be seen after 24 h of immersion. This explains the corrosion resistance of the coating, which however deteriorated after 48 h immersion (corrosion pits were observed). The initial test (5 min immersion) of the obvious two layered coating on MgLi alloy after 10 min PEO treat-

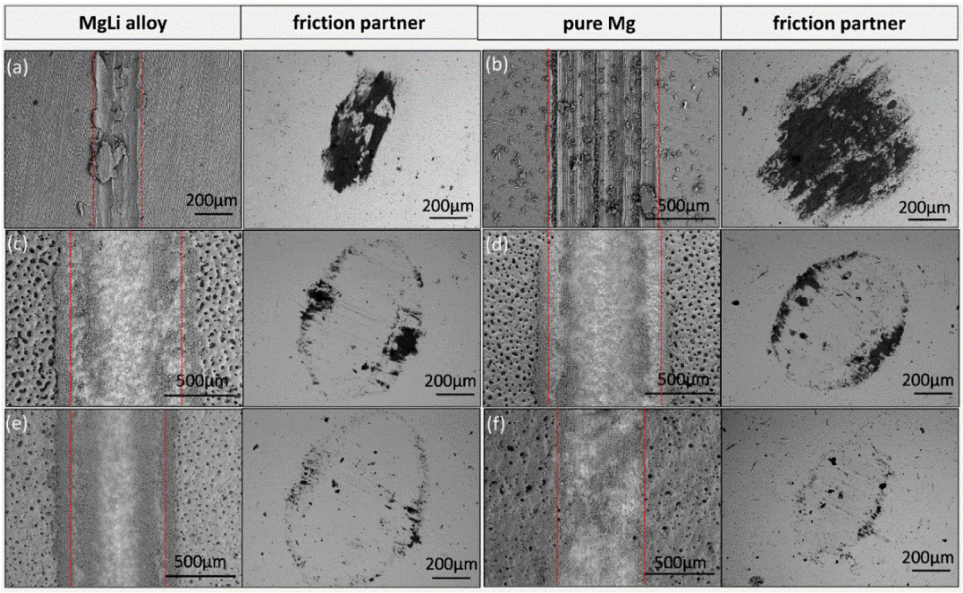

Fig 12. Worn tracks of substrate materials, PEO coatings and counter parts on MgLi alloy: (a) MgLi alloy (unfinished), (c) 10 min and (e) 20 min; and on pure Mg: (b) pure Mg, (d) 10 min and (f) 20 min.

ment demonstrates the efficient protection of the inner layer. However, the shrink of the capacitive loop at the medium frequency with increasing immersion time afterwards indicates the gradual degradation of the coating. As for the PEO coating on MgLi alloy after 20 min of PEO processing, the Bode plots at high frequencies ($\sim 6 \times 10^4$ Hz) demonstrates the relaxation process of the outer layer during the immersion due to the remarkable thickness hindering the penetration of the solution. The full penetration of corrosive solution through the outer layer is revealed after 12 h of immersion. Afterwards, the relaxation process at high frequencies is no longer differentiable and the outer layer contributes nearly nothing to the high frequency impedance. PEO coatings on MgLi alloy can effectively inhibit the penetration of corrosive solution and thus delay the corrosion process in comparison to the bare MgLi alloy. The higher total impedance |Z| of the coated MgLi specimens in Fig. 15 also claims that the PEO coating can significantly improve the corrosion resistance. Furthermore, the corrosion resistance of the coating increases with treatment time from 1 min to 3 min. However, after 10 min and 20 min of processing the |Z| values decrease rapidly and show a similar trend with immersion time, which could ascribed to the high porosity of the coating after longer treatment.

In Fig. 14(b) the initial measurement (after 5 min of immersion) of the coating on pure Mg after 1 min of PEO treatment validates the increase of the total impedance in respective to pure Mg. However, the shrink of the capacitive loop at medium frequencies ($\sim$10 Hz) correlated to the coating after 1 h of immersion demonstrates the immediate deterioration of the coating. The morphology of the exposed region also reveals scattered corrosion pits at the exposed coating. For the coating obtained after 3 min of PEO treatment after the immersion from 5 min to 1 h (Fig. 14(c)), the similar behavior as the coating after 1 min of PEO treatment reveals the degradation of the coating. The total impedance of PEO coatings on pure Mg after 10 min and 20 min of PEO treatments at initial immersion stage is two or three order of magnitude higher than that of the pure Mg substrate, ascribed to the dense inner layer. A capacitive impedance (Fig. 14(d) and (e)) observed at high frequencies ($\sim 10^5$ Hz) is associated with the evolution of the outer layers. The response of outer layer at high frequencies disappears gradually in course of immersion due to the penetration process through the thickness. The gradual degradation of the coatings can be inferred from the sharp shrink of the capacitive loop at medium frequency (inner layer) afterwards. PEO coatings on pure Mg show a slight improvement in corrosion resistance compared to bare Mg and the total impedance value increases with the treatment time from 1 min to 20 min. In summary, the evaluation of the PEO coatings on pure Mg demonstrates a better corrosion resistance in comparison to the coatings on MgLi alloy as revealed by the larger magnitude of total impedance at 0.1 Hz (Fig. 15).

4. Discussion

The alloying of Li (11.36 wt.%) to Mg transforms the hexagonal α-Mg to a cubic β-Mg. However, it is not possible to assign the observed changes in the PEO process directly to the lattice structure of the two materials since the presence of Li also changes the electrochemical stability of the alloy and of corresponding coatings further. Thus for the MgLi alloy a discrepancy in voltage-time response to the applied current density results in the different coating thicknesses under equal basic PEO processing conditions. The sluggish increase of the voltage for MgLi alloy does not delay the initiation of plasma discharges since the critical dielectric breakdown voltage is reached at the same treatment time around 15 to 30 s, although about 40 V lower than that of pure Mg. The reason

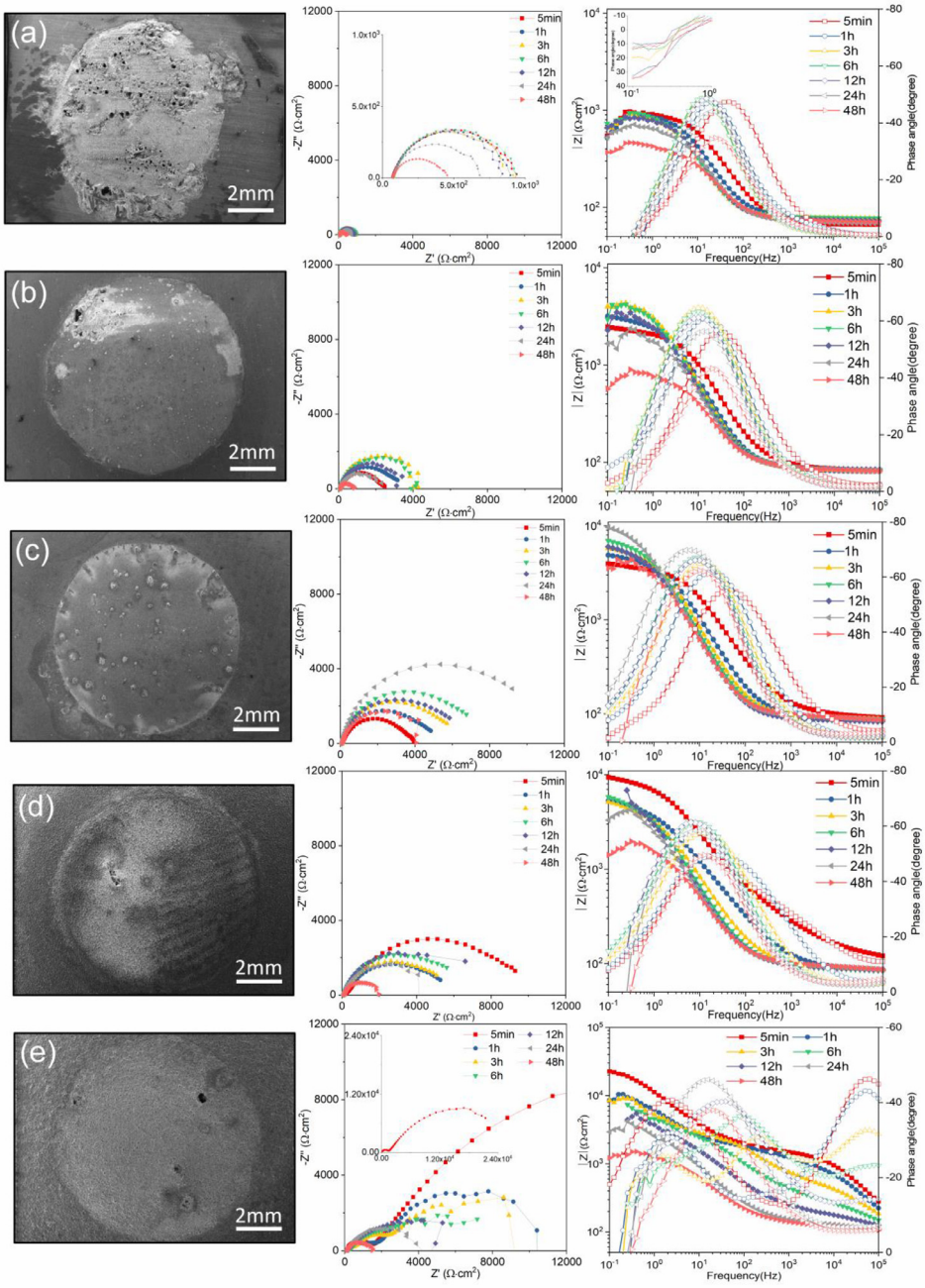

Fig 13. EIS results of PEO coatings on MgLi alloy: (a) bare substrate, (b) 1 min, (c) 3 min, (d) 10 min and (e) 20 min.

for the lower breakdown voltage might be a higher conductivity of the coating due to the incorporation of Li in the initial conversion layer. Since the PEO process is following Faraday's laws [62], a lower electrical resistivity of the barrier oxide layer is established on MgLi alloy against the flow of current compared to pure Mg. The lower voltage of MgLi alloy also implies less energy input for the coating growth thus a thinner PEO coating in the results [63] in terms of constant current-driven process. The efficiency of the energy input (voltage) on coating growth with the duration of PEO treatment could be evaluated by the coating growth rate relative to the voltage. Hence, after 20 min of PEO processing, the average efficiency of the energy input for MgLi alloy is 0.13 μm/(V·min), higher than 0.11 μm/(V·min) for pure Mg. There might be a positive role of Li for coating growth on MgLi alloy as well as energy conservation, since a lower voltage is sufficient to excite the species of MgLi alloy involving them in the plasma discharges during the process.

At the initial stage of PEO processing the conventional anodization is dominant for both substrates. The conversion products of MgLi alloy are preferentially accumulated on the $MgLi_2Al$ intermetallics, appearing mainly as fine protuberances due to aluminum oxide, which has better adherence to the substrate and higher Pilling-Bedworth ratio of 1.28 than

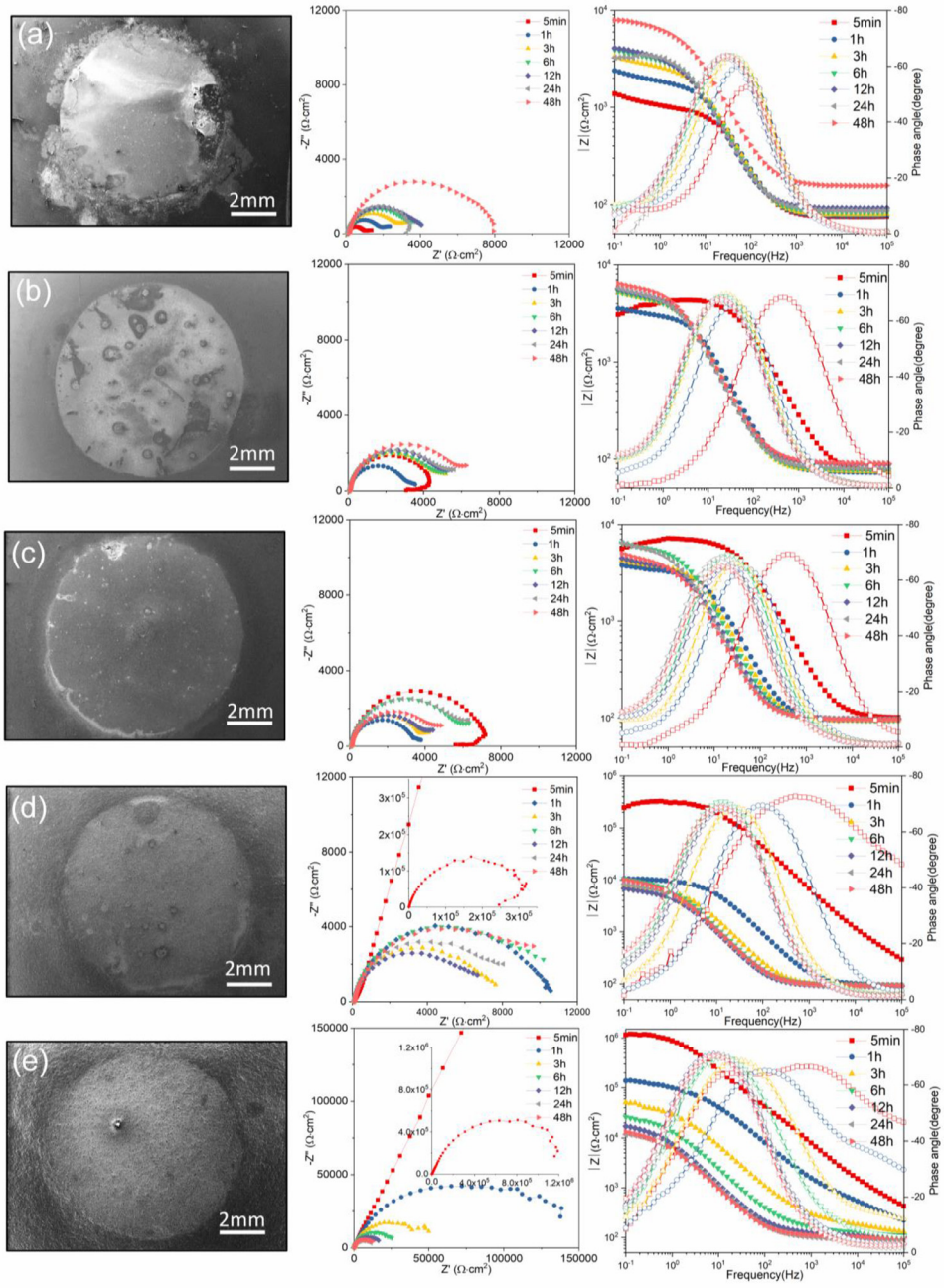

Fig 14. EIS results of PEO coatings on pure Mg: (a) bare substrate, (b) 1 min, (c) 3 min, (d) 10 min and (e) 20 min.

MgO (Pilling-Bedworth ratio 0.804). In spite of the participation of Li in the plasma reactions, it seems that Li only presents in the primary conversion products at the interface between coating/MgLi substrate, as the corresponding Li oxide/hydroxide is freely soluble in aqueous alkaline solutions. After longer PEO processing (10 min and 20 min), there are the large amount of bright particulates formed on the coating of MgLi alloy around the micro-pores. The main coating composition (MgO and $Mg_3(PO_4)_2$) have O/Mg atomic ratios of 1.00 and 2.67, respectively. The O/Mg atomic ratios of the areas without the particulates (B, C, E and F in Fig. 6) falls into the range of 1.00–2.67 exactly evidencing the main phase composition of MgO and $Mg_3(PO_4)_2$. Interestingly, the O/Mg atomic ratios of the particulates (A and D in Fig. 6) are far beyond the range of 1.00–2.67 and even reach the values of 3.80 and 3.28 respectively, indicating overwhelming O at the bright particulates of the PEO coating on MgLi alloy. Combined with the higher concentration of element P and Na in the particulates, the sintering of the electrolyte (Na_3PO_4) on the surface of the coatings is reasonable due to the local high temperature.

After equal processing time, PEO coating on MgLi alloy always exhibits higher inner porosity, which can be partly associated with the type of discharges since the plasma re-

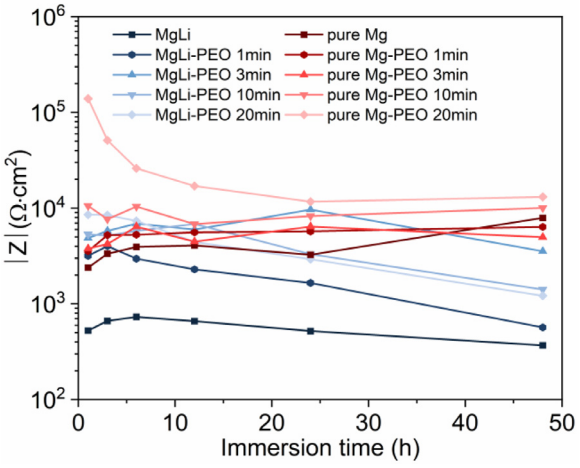

Fig 15. Total impedance of MgLi alloy and pure Mg before and after different time of PEO processing at 0.1 Hz.

actions involving Li in comparison to pure Mg. Further, the lower stability of the PEO coating on MgLi alloy could be also responsible for the more porous coating, considering the rapid dissolution of the coating under the elevated temperatures and alkaline conditions, which appear in the coating pores. Additionally, the gas generation could be also responsible for the high porosity. The excess formation of oxygen gas during PEO processing can be trapped within the coating and present as coating porosity due to the quick solidification of the melted coating.

After PEO treatment, the wear and corrosion resistance of the coating evolves, compared with the uncoated MgLi alloy and pure Mg. Nevertheless, they are mostly dependent on the microstructure of the coatings such as the coating thickness, uniformity, porosity and other defects. In our case, the higher porosity within the PEO coatings on MgLi alloy having lower thickness particularly after longer duration of PEO treatment (10 min and 20 min) results in the less resistance of the coatings in comparison to pure Mg.

5. Conclusion

(1) The presence of Li and the Li containing intermetallics modified the behavior of the PEO process on the MgLi alloy. A lower breakdown threshold of the initial dielectric layer on MgLi alloy maintains the progress as that of pure Mg in terms of the slower increase of the voltage for the MgLi alloy. The efficiency of energy input (voltage) for coating formation on MgLi alloy is higher than that of pure Mg.

(2) PEO coatings were mainly composed of MgO and $Mg_3(PO_4)_2$. Though the Li-containing phase was not found in the coatings of MgLi alloy, Li was probably incorporated in the primary conversion products at the interface of coating/MgLi substrate during the processing.

(3) Due to the less energy input (voltage), the sintered particulates from the insufficient recrystallization around the micro-pores on the surface of PEO coatings on MgLi alloy, is mainly originated from the electrolyte.

(4) The wear and corrosion resistance of the PEO coatings on MgLi alloy and pure Mg were improved compared with the uncoated substrates, but especially the corrosion resistance was quite poor for all coatings. The less stable coatings of MgLi alloy having the higher inner porosity even present the lower resistance to wear and corrosion.

Deceleration of Competing Interests

None.

Acknowledgement

Ting Wu would like to acknowledge China Scholarship Council for the award of fellowship and funding (NO.201708510113). The technical support of Mr. Volker Heitmann, Mr. Ulrich Burmester and Mr. Wiese Gert during this work is gratefully acknowledged. X. Lu would like to acknowledge the financial support from National Natural Science Foundation of China (NO. 52071067 and U1737102), Mobility Programme of the Sino-German Center (M-0056) and the Fundamental Research Funds for the Central Universities (N2002009).

References

[1] A.L. Yerokhin, X. Nie, A. Leyland, A. Matthews, S.J. Dowey, Plasma electrolysis for surface engineering, Surf Coatings Technol. (1999) 73, doi:10.1016/S0257-8972(99)00441-7.

[2] A. Jangde, S. Kumar, C. Blawert, Influence of glycerol on plasma electrolytic oxidation coatings evolution and on corrosion behaviour of coated AM50 magnesium alloy, Corros Sci (2019), doi:10.1016/j.corsci.2019.05.024.

[3] R. Arrabal, E. Matykina, T. Hashimoto, P. Skeldon, G.E. Thompson, Characterization of AC PEO coatings on magnesium alloys, Surf. Coatings Technol. 16 (2009) 2207 doi:10.1016/j.surfcoat.2009.02.011.

[4] S. Ono, S. Moronuki, Y. Mori, A. Koshi, J. Liao, H. Asoh, Effect of electrolyte concentration on the structure and corrosion resistance of anodic films formed on magnesium through plasma electrolytic oxidation, Electrochim. Acta (2017), doi:10.1016/j.electacta.2017.04.110.

[5] M. Sun, A. Yerokhin, M.Y. Bychkova, D.V. Shtansky, E.A. Levashov, A. Matthews, Self-healing plasma electrolytic oxidation coatings doped with benzotriazole loaded halloysite nanotubes on AM50 magnesium alloy, Corros Sci (2016), doi:10.1016/j.corsci.2016.06.016.

[6] X. Lu, C. Blawert, D. Tolnai, T. Subroto, K.U. Kainer, T. Zhang, F. Wang, M.L. Zheludkevich, 3D reconstruction of plasma electrolytic oxidation coatings on Mg alloy via synchrotron radiation tomography, Corros Sci (2018) 395 doi:10.1016/j.corsci.2018.05.019.

[7] T. Wu, C. Blawert, M.L. Zheludkevich, Influence of secondary phases of AlSi9Cu3 alloy on the plasma electrolytic oxidation coating formation process, J. Mater. Sci. Technol. (2020) 75 doi:10.1016/j.jmst.2019.12.031.

[8] S.C. Troughton, T.W. Clyne, Cathodic discharges during high frequency plasma electrolytic oxidation, Surf. Coatings Technol. (2018) 591 doi:10.1016/j.surfcoat.2018.08.049.

[9] B. Mingo, R. Arrabal, M. Mohedano, Y. Llamazares, E. Matykina, A. Yerokhin, A. Pardo, Influence of sealing post-treatments on the corrosion resistance of PEO coated AZ91 magnesium alloy, Appl Surf Sci (2018), doi:10.1016/j.apsusc.2017.10.083.

[10] M. Shbeh, A. Yerokhin, R. Goodall, Cyclic voltammetry study of PEO processing of porous Ti and resulting coatings, Appl Surf Sci (2018), doi:10.1016/j.apsusc.2017.12.236.
[11] S.A. Adeleke, S. Ramesh, A.R. Bushroa, Y.C. Ching, I. Sopyan, M.A. Maleque, S. Krishnasamy, H. Chandran, H. Misran, U. Sutharsini, The properties of hydroxyapatite ceramic coatings produced by plasma electrolytic oxidation, Ceram Int 2 (2018) doi:10.1016/j.ceramint.2017.10.114.
[12] T. Arunnellaiappan, S. Arun, S. Hariprasad, S. Gowtham, B. Ravisankar, L. Rama Krishna, N. Rameshbabu, Fabrication of corrosion resistant hydrophobic ceramic nanocomposite coatings on PEO treated AA7075, Ceram Int 1 (2018), doi:10.1016/j.ceramint.2017.10.014.
[13] F. Gao, L. Hao, G. Li, Y. Xia, The plasma electrolytic oxidation micro-discharge channel model and its microstructure characteristic based on Ti tracer, Appl Surf Sci (2018), doi:10.1016/j.apsusc.2017.07.281.
[14] J. Martin, A. Nominé, F. Brochard, J.L. Briançon, C. Noël, T. Belmonte, T. Czerwiec, G. Henrion, Delay in micro-discharges appearance during PEO of Al: evidence of a mechanism of charge accumulation at the electrolyte/oxide interface, Appl Surf Sci (2017), doi:10.1016/j.apsusc.2017.03.088.
[15] Y. Cheng, T. Wang, S. Li, Y. Cheng, J. Cao, H. Xie, The effects of anion deposition and negative pulse on the behaviours of plasma electrolytic oxidation (PEO)-A systematic study of the PEO of a Zirlo alloy in aluminate electrolytes, Electrochim. Acta (2017) doi:10.1016/j.electacta.2016.12.115.
[16] R.O. Hussein, D.O. Northwood, X. Nie, Coating growth behavior during the plasma electrolytic oxidation process, J. Vac. Sci. Technology A: Vac., Surf. Films 4 (2010) 766 doi:10.1116/1.3429583.
[17] Y. Cheng, Z. Peng, X. Wu, J. Cao, P. Skeldon, G.E. Thompson, A comparison of plasma electrolytic oxidation of Ti-6Al-4V and Zircaloy-2 alloys in a silicate-hexametaphosphate electrolyte, Electrochim. Acta (2015), doi:10.1016/j.electacta.2015.03.020.
[18] V. Dehnavi, D.W. Shoesmith, B.L. Luan, M. Yari, X.Y. Liu, S. Rohani, Corrosion properties of plasma electrolytic oxidation coatings on an aluminium alloy - The effect of the PEO process stage, Mater Chem Phys (2015), doi:10.1016/j.matchemphys.2015.04.058.
[19] L. Zhu, Z. Guo, Y. Zhang, Z. Li, M. Sui, A mechanism for the growth of a plasma electrolytic oxide coating on Al, Electrochim. Acta (2016), doi:10.1016/j.electacta.2016.04.186.
[20] J. Liu, Y. Lu, X. Jing, Y. Yuan, M. Zhang, Characterization of plasma electrolytic oxidation coatings formed on Mg-Li alloy in an alkaline silicate electrolyte containing silica sol, Materials and Corrosion 11 (2009), doi:10.1002/maco.200805204.
[21] E. Matykina, R. Arrabal, D.J. Scurr, A. Baron, P. Skeldon, G.E. Thompson, Investigation of the mechanism of plasma electrolytic oxidation of aluminium using 18O tracer, Corros Sci 3 (2010) 1070 doi:10.1016/j.corsci.2009.11.038.
[22] X. Lu, C. Blawert, M.L. Zheludkevich, K.U. Kainer, Insights into plasma electrolytic oxidation treatment with particle addition, Corros Sci (2015), doi:10.1016/j.corsci.2015.09.016.
[23] X. Lu, C. Blawert, K.U. Kainer, M.L. Zheludkevich, Investigation of the formation mechanisms of plasma electrolytic oxidation coatings on Mg alloy AM50 using particles, Electrochim. Acta (2016), doi:10.1016/j.electacta.2016.03.042.
[24] R. Arrabal, E. Matykina, P. Skeldon, G.E. Thompson, Incorporation of zirconia particles into coatings formed on magnesium by plasma electrolytic oxidation, J Mater Sci 5 (2008) 1532 doi:10.1007/s10853-007-2360-9.
[25] X. Liu, G. Li, Y. Xia, Investigation of the discharge mechanism of plasma electrolytic oxidation using Ti tracer, Surf. Coatings Technol. 21 (2012) 4462 doi:10.1016/j.surfcoat.2012.05.002.
[26] A. Kazek-Kęsik, M. Krok-Borkowicz, A. Jakóbik-Kolon, E. Pamuła, W. Simka, Biofunctionalization of Ti-13Nb-13Zr alloy surface by plasma electrolytic oxidation. Part II, Surf. Coatings Technol. (2015) 23 doi:10.1016/j.surfcoat.2015.06.035.
[27] H. Duan, C. Yan, F. Wang, Growth process of plasma electrolytic oxidation films formed on magnesium alloy AZ91D in silicate solution, Electrochim. Acta 15 (2007) 5002 doi:10.1016/j.electacta.2007.02.021.
[28] Y. Chen, Y. Yang, W. Zhang, T. Zhang, F. Wang, Influence of second phase on corrosion performance and formation mechanism of PEO coating on AZ91 Mg alloy, J Alloys Compd (2017), doi:10.1016/j.jallcom.2017.05.010.
[29] D. Veys-Renaux, E. Rocca, G. Henrion, Micro-arc oxidation of AZ91 Mg alloy: an in-situ electrochemical study, Electrochem commun (2013) 42 doi:10.1016/j.elecom.2013.02.023.
[30] C. Liu, T. Xu, Q. Shao, S. Huang, B. Jiang, J. Liang, H. Li, Effects of beta phase on the growth behavior of plasma electrolytic oxidation coating formed on magnesium alloys, J Alloys Compd (2019), doi:10.1016/j.jallcom.2019.01.095.
[31] R. Arrabal, E. Matykina, F. Viejo, P. Skeldon, G.E. Thompson, Corrosion resistance of WE43 and AZ91D magnesium alloys with phosphate PEO coatings, Corros Sci 6 (2008) 1744 doi:10.1016/j.corsci.2008.03.002.
[32] K.O. Gunduz, Z.C. Oter, M. Tarakci, Y. Gencer, Plasma electrolytic oxidation of binary Mg-Al and Mg-Zn alloys, Surf. Coatings Technol. (2017), doi:10.1016/j.surfcoat.2016.08.040.
[33] J.F. Li, Z.Q. Zheng, S.C. Li, W.D. Ren, Z. Zhang, Preparation and galvanic anodizing of a Mg-Li alloy, Mater. Sci. Eng. A (2006) 233 1-2 doi:10.1016/j.msea.2006.06.107.
[34] Y. Ma, N. Li, D. Li, M. Zhang, X. Huang, Performance of Mg-14Li-1Al-0.1Ce as anode for Mg-air battery, J Power Sources 4 (2011) 2346 doi:10.1016/j.jpowsour.2010.07.097.
[35] O. Pavlic, W. Ibarra-Hernandez, I. Valencia-Jaime, S. Singh, G. Avendaño-Franco, D. Raabe, A.H. Romero, Design of Mg alloys: the effects of Li concentration on the structure and elastic properties in the Mg-Li binary system by first principles calculations, J Alloys Compd (2017) 15, doi:10.1016/j.jallcom.2016.08.217.
[36] N. Wang, R. Wang, Y. Feng, W. Xiong, J. Zhang, M. Deng, Discharge and corrosion behaviour of Mg-Li-Al-Ce-Y-Zn alloy as the anode for Mg-air battery, Corros Sci (2016) 13 doi:10.1016/j.corsci.2016.07.002.
[37] Y. Zou, L. Zhang, H. Wang, X. Tong, M. Zhang, Z. Zhang, Texture evolution and their effects on the mechanical properties of duplex Mg-Li alloy, J Alloys Compd (2016) 72 doi:10.1016/j.jallcom.2016.01.174.
[38] Z. Drozd, Z. Trojanová, S. Kúdela, Deformation behaviour of Mg-Li-Al alloys, J Alloys Compd (2004) 192 1-2 doi:10.1016/j.jallcom.2004.01.040.
[39] A.A. Luo, R.K. Mishra, B.R. Powell, A.K. Sachdev, Magnesium alloy development for automotive applications, Mater. Sci. Forum (2012) 69, doi:10.4028/www.scientific.net/MSF.706-709.69.
[40] R. Wu, Y. Yan, G. Wang, L.E. Murr, W. Han, Z. Zhang, M. Zhang, Recent progress in magnesium-lithium alloys, Int. Mater. Rev. 2 (2014), doi:10.1179/1743280414y.0000000044.
[41] Z. Li, Y. Yuan, P. Sun, X. Jing, Ceramic coatings of LA141 alloy formed by plasma electrolytic oxidation for corrosion protection, ACS Appl. Mater. Interfaces 9 (2011), doi:10.1021/am200863s.
[42] C. Ma, M. Zhang, Y. Yuan, X. Jing, X. Bai, Tribological behavior of plasma electrolytic oxidation coatings on the surface of Mg-8Li-1Al alloy, Tribol. Int. (2012), doi:10.1016/j.triboint.2011.10.006.
[43] C. Ma, Y. Lu, P. Sun, Y. Yuan, X. Jing, M. Zhang, Characterization of plasma electrolytic oxidation coatings formed on Mg-Li alloy in an alkaline polyphosphate electrolyte, Surf. Coatings Technol. 2-3 (2011) 287 doi:10.1016/j.surfcoat.2011.07.019.
[44] Z. Yao, P. Ju, Q. Xia, J. Wang, P. Su, H. Wei, D. Li, Z. Jiang, Preparation of thermal control coatings on Mg-Li alloys by plasma electrolytic oxidation, Surf. Coatings Technol. (2016), doi:10.1016/j.surfcoat.2016.06.019.
[45] S.-J. Lee, L.H.T. Do, Effects of copper additive on micro-arc oxidation coating of LZ91 magnesium-lithium alloy, Surf. Coatings Technol. (2016), doi:10.1016/j.surfcoat.2016.10.008.
[46] Z. Li, X. Wang, X. Dong, F. Hu, S. Liu, M. Zhang, T. Yuan, Y. Yu, Q. Kuang, Q. Ren, J. Wang, X. Jing, Creating high-performance bi-functional composite coatings on magnesium−8lithium alloy through electrochemical surface engineering with highly enhanced corrosion and wear protection, J Alloys Compd (2020) 153341, doi:10.1016/j.jallcom.2019.153341.

[47] Z. Li, Q. Ren, X. Wang, Q. Kuang, D. Ji, R. Yuan, X. Jing, Effect of phosphate additive on the morphology and anti-corrosion performance of plasma electrolytic oxidation coatings on magnesium–lithium alloy, Corros Sci (2019) 295 doi:10.1016/j.corsci.2019.06.005.

[48] Z.J. Li, Y. Yuan, X.Y. Jing, Comparison of plasma electrolytic oxidation coatings on Mg-Li alloy formed in molybdate/silicate and aluminate/silicate composite electrolytes, Mater. Corrosion 5 (2014) 493 doi:10.1002/maco.201206652.

[49] Z. Li, Q. Kuang, X. Dong, T. Yuan, Q. Ren, X. Wang, J. Wang, X. Jing, Characteristics of high-performance anti-corrosion/anti-wear ceramic coatings on magnesium–lithium alloy by plasma electrolytic oxidation surface engineering, Surf. Coatings Technol. (2019) 600 doi:10.1016/j.surfcoat.2019.07.066.

[50] S. Stojadinović, R. Vasilić, J. Radić-Perić, M. Perić, Characterization of plasma electrolytic oxidation of magnesium alloy AZ31 in alkaline solution containing fluoride, Surf. Coatings Technol. (2015), doi:10.1016/j.surfcoat.2015.03.032.

[51] S.R. Agnew, H. Yoom, T.C.N., Application of texture simulation to understanding mechanical behavior of Mg and solid solution alloys containing Li or Y, Acta Mater. (2001).

[52] R.Z. Wu, Z.K. Qu, M.L. Zhang, Reviews on the influences of alloying elements on the microstructure and mechanical properties of Mg-Li base alloys, Rev. Adv. Mater. Sci. (2010).

[53] Z. Yao, Q. Xia, H. Wei, D. Li, Q. Sun, Z. Jiang, Study on coating growth characteristics during the electrolytic oxidation of a magnesium-lithium alloy by optical emission spectroscopy analysis, RSC Adv 84 (2015) 68806 doi:10.1039/c5ra09378c.

[54] W. Xu, N. Birbilis, G. Sha, Y. Wang, J.E. Daniels, Y. Xiao, M. Ferry, A high-specific-strength and corrosion-resistant magnesium alloy, Nat Mater 12 (2015), doi:10.1038/nmat4435.

[55] R.O. Hussein, X. Nie, D.O. Northwood, A. Yerokhin, A. Matthews, Spectroscopic study of electrolytic plasma and discharging behaviour during the plasma electrolytic oxidation (PEO) process, J Phys D Appl Phys 10 (2010) 105203 doi:10.1088/0022-3727/43/10/105203.

[56] S. Stojadinović, R. Vasilić, M. Petković, I. Belča, B. Kasalica, M. Perić, L. Zeković, Luminescence during anodization of magnesium alloy AZ31, Electrochim. Acta (2012) 354 doi:10.1016/j.electacta.2011.10.084.

[57] E. Matykina, R. Arrabal, P. Skeldon, G.E. Thompson, Investigation of the growth processes of coatings formed by AC plasma electrolytic oxidation of aluminium, Electrochim. Acta 27 (2009) 6767 doi:10.1016/j.electacta.2009.06.088.

[58] C. Blawert, S.A. Karpushenkov, M. Serdechnova, L.S. Karpushenkava, M.L. Zheludkevich, Plasma electrolytic oxidation of zinc alloy in a phosphate-aluminate electrolyte, Appl Surf Sci (2020) 144552 doi:10.1016/j.apsusc.2019.144552.

[59] R.O. Hussein, X. Nie, D.O. Northwood, An investigation of ceramic coating growth mechanisms in plasma electrolytic oxidation (PEO) processing, Electrochim. Acta (2013), doi:10.1016/j.electacta.2013.08.137.

[60] R.O. Hussein, X. Nie, D.O. Northwood, A spectroscopic and microstructural study of oxide coatings produced on a Ti-6Al-4 alloy by plasma electrolytic oxidation, Mater Chem Phys 1 (2012) 484 doi:10.1016/j.matchemphys.2012.03.020.

[61] R.O. Hussein, D.O. Northwood, X. Nie, The effect of processing parameters and substrate composition on the corrosion resistance of plasma electrolytic oxidation (PEO) coated magnesium alloys, Surf. Coatings Technol. (2013) 357 doi:10.1016/j.surfcoat.2013.09.021.

[62] T.W. Clyne, S.C. Troughton, A review of recent work on discharge characteristics during plasma electrolytic oxidation of various metals, Int. Mater. Rev. 3 (2018) 127 doi:10.1080/09506608.2018.1466492.

[63] A.R. Fatkullin, E.V. Parfenov, A. Yerokhin, D.M. Lazarev, A. Matthews, Effect of positive and negative pulse voltages on surface properties and equivalent circuit of the plasma electrolytic oxidation process, Surf. Coatings Technol. (2015), doi:10.1016/j.surfcoat.2015.07.075.

5.1.2 PEO of polymorph structured Ti6Al4V alloy

Paper 2: Ting Wu, Carsten Blawert, Maria Serdechnova et al., Role of polymorph microstructure of Ti6Al4V alloy on PEO coating formation in phosphate electrolyte, Surface & Coating Technology 428(2021). https://doi.org/10.1016/j.surfcoat.2021.127890

Graphical abstract

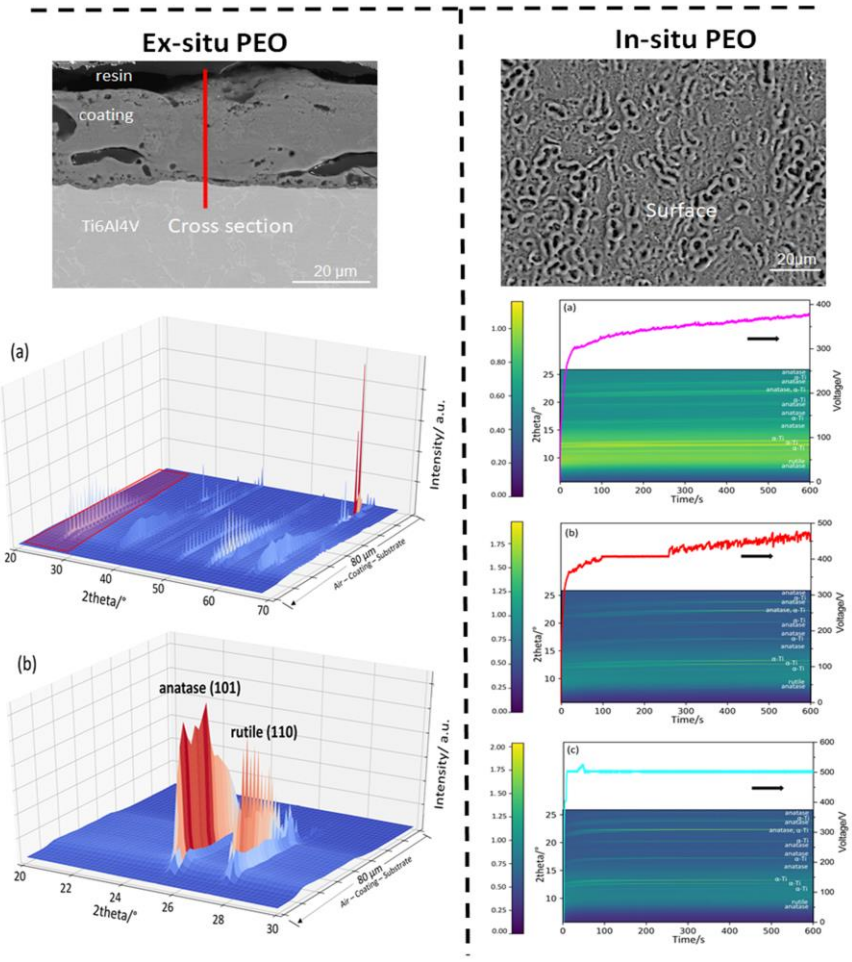

Since the comparison of PEO coating formation on the separate α-Mg and β-Mg did not show obvious difference, the work moved forward to a biphasic substrate, to have a closer observation of the lattice difference on the coating formation process.

In paper *2*, the work investigated the influence of polymorph microstructure of Ti6Al4V alloy on PEO coating formation under the control of constant current density (3, 5 and 10 A/dm^2). Ti6Al4V alloy contained typical hexagonal α-Ti with enrichment of Al and body-centered β-Ti phases enriched with V. In an in-situ PEO measurement, it has been elucidated that the high solubility of O in α-Ti lattice resulted in the lattice expansion before the formation of Ti oxides. The absence of β-Ti was correlated with its low amount in the substrate and possibly the fast transformation of β-Ti into α-Ti due to the rapid oxygen penetration. The transformation to crystalline Ti oxides was highly related to the temperature (voltage). With the treatment time, rutile and anatase were formed at certain voltage, however; they just disappeared at higher voltage and showed up again after switching-off HV. In the

ex-situ PEO treatment, the development of discharges started preferentially on β-Ti phases, mainly at the grain boundaries. Besides, the sintered morphology appear on the same locations where β-Ti phases were originated. With increasing of processing time, the surface morphology of PEO coatings became more uniform, but revealed still differences for a while as a consequence of the discharges starting earlier on the dielectric layer on β-Ti phases. In addition, the higher current density accelerated the formation of a more uniform coating. Hence, regarding the idea to produce a uniform coating on Ti6Al4V alloy, further investigation could pay attention to either extend the processing time or further increase the energy input.

Surface & Coatings Technology 428 (2021) 127890

Contents lists available at ScienceDirect

Surface & Coatings Technology

journal homepage: www.elsevier.com/locate/surfcoat

Role of polymorph microstructure of Ti6Al4V alloy on PEO coating formation in phosphate electrolyte

Ting Wu [a,*], Carsten Blawert [a], Maria Serdechnova [a], Polina Karlova [a], Gleb Dovzhenko [b], D. C. Florian Wieland [c], Mikhail L. Zheludkevich [a,d]

[a] Institute of Surface Science, Helmholtz-Zentrum Hereon, Max-Planck Strasse 1, 21502 Geesthacht, Germany
[b] Institute of Materials Physics, Helmholtz-Zentrum Hereon, Max-Planck Strasse 1, 21502 Geesthacht, Germany
[c] Institute of Metallic Biomaterials, Helmholtz-Zentrum Hereon, Max-Planck Strasse 1, 21502 Geesthacht, Germany
[d] Institute for Materials Science, Faculty of Engineering, Kiel University, Kaiserstrasse 2, 24143 Kiel, Germany

ARTICLE INFO

Keywords:
Plasma electrolytic oxidation
Titanium alloy
Microstructure

ABSTRACT

In this work, the formation behavior of PEO coatings on polymorph Ti6Al4V alloy with two different lattice structures (hexagonal close packed α-Ti and cubic body centered β-Ti phases) was studied, using two galvanostatically controlled processes. The phase formation as a function of treatment time was studied ex-situ locally on the two Ti phases by interrupting the treatment after certain time intervals and in-situ continuously in an integral manner by recording diffraction patterns from the changing surface during the PEO process. The initial discharges were preferred to start on β-Ti phases localized at the grain boundaries and then extends to the surrounding α-Ti grains. The presence of α- and β-Ti phases was also responsible for the different local coating surface morphology. A highly sintered morphology and larger-sized micro-pores developed firstly on the layer on β-Ti phases, with higher concentration of vanadium. These findings highlight the importance of microstructure of Ti6Al4V alloy on the formation of PEO coatings. Under the selected conditions of PEO processing, the higher current density promotes the growing of the coating and reduces the surface roughness of the resultant coating. The ex-situ characterization of the coatings after certain periods shows that the final coatings mainly consist of anatase, rutile and an amorphous phase containing phosphorous. The formation of rutile, transformed from anatase, is influenced by the effective temperature of the discharges, thus the ratio of anatase to rutile is decreasing with treatment time. The in-situ characterization of phase evolution showed the formation of an amorphous phase in parallel with an expanded α-Ti phase, which is a result of oxygen incorporation into solid solution into the titanium lattice. Interestingly, the main formation of crystalline phases occur only when the HV is turned off and the coating obviously cools down.

1. Introduction

Plasma electrolytic oxidation (PEO) is a surface modification technique derived from conventional anodization under a high applied voltage (up to a few hundred volts) [1–5]. It is also known as an efficient and environmentally friendly process to produce durable ceramic-like coatings on metallic substrates, such as Al [6,7], Mg [8,9], Ti [10,11], Zr [12,13] and Nb [14,15] and their alloys. The process is typically accompanied by the occurrence of numerous micro-discharges on the surface of specimens in addition to an electrochemical and chemical dissolution and deposition [8,16]. The coatings are generally composed of amorphous and crystalline phases synthesized from the species originated from substrate material and electrolyte [17–19]. As a result of the discharge channels and gas evolution, PEO coatings inherently contains noticeable porosity, thus a post sealing is necessary in severe application conditions [5,20–24].

The main advantages of PEO coatings are improved corrosion [25] and wear resistance [26,27] together with other additional properties such as bioactivity [19], photocatalysis [28], and thermal stability [29]. It is now well established that the substrate materials play a significant role in the coating formation process and have a serious effect on the coating properties [2,6,8,25,30–34]. The incorporation of alloying elements can modify the coating composition and microstructure [6,8], and further offer enhanced surface wear and corrosion resistance [32]. Such

* Corresponding author.
E-mail address: ting.wu@hereon.de (T. Wu).

https://doi.org/10.1016/j.surfcoat.2021.127890
Received 31 August 2021; Received in revised form 20 October 2021; Accepted 1 November 2021
Available online 5 November 2021

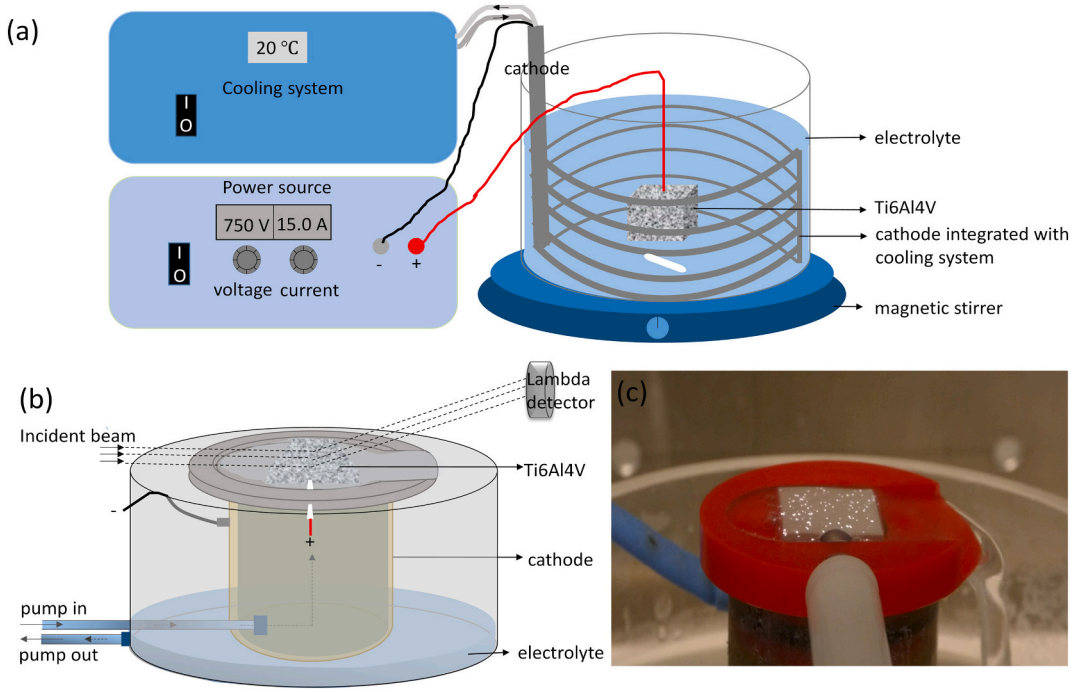

Fig. 1. Schematic representation of laboratory PEO set-up (a), and in-situ one used at P23, DESY (b) and actual in-situ PEO treatment of a specimen (c).

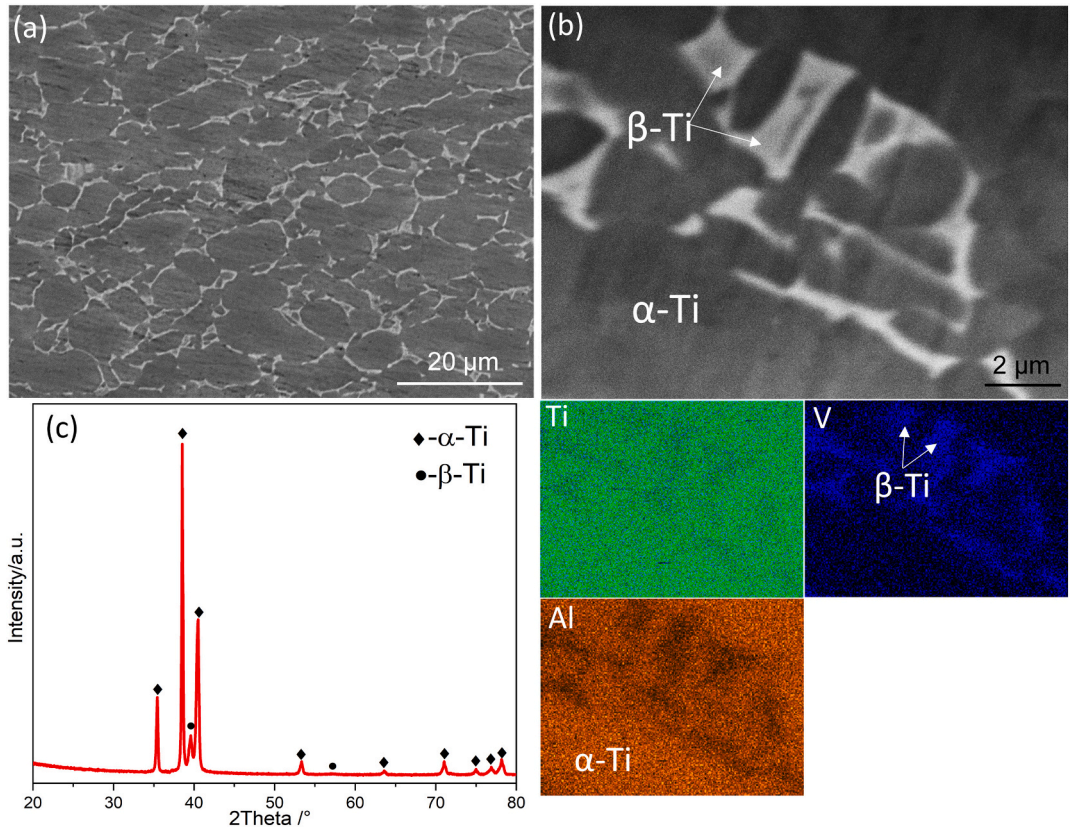

Fig. 2. (a) and (b) SEM (BSE, back scattered electron) images with elemental distribution, and (c) XRD pattern and of Ti6Al4V alloy.

an influence comes from the altered behavior of discharges with the alloying elements incorporated [35–38]. The discharges are recognized as the driving force for coating growth [4,39,40], stimulating various thermal-driven reactions, and facilitating the formation of high-temperature stable phases in the coating. The variation of substrate composition and microstructure makes it possible to change the nature and distribution of discharges in time, and subsequently influence the composition, microstructure and properties of PEO layers [8].

PEO processing of Al and Mg alloys have been extensively studied in respect to their different composition and microstructure

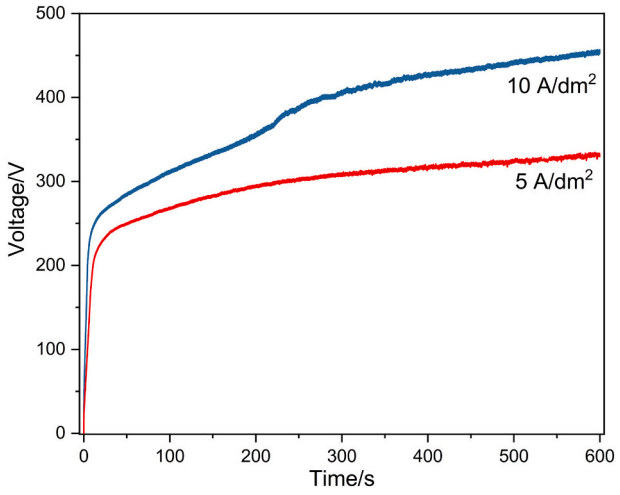

Fig. 3. Voltage-time curves of PEO process as a function of time for phosphate-base electrolyte.

[6,8,32,41–45]. At the initial stage of PEO processing, different evolution behavior was disclosed in local sites where secondary phases, intermetallics or precipitates are present in the matrix [6,8,46]. As a result, the initial conversion layer was not uniform and a distinguishable local morphology could be observed [32,33]. The fast-moving discharges then can mostly eliminate the heterogeneity through continuously restructuring the layer, and finally producing uniform coatings as far as suitable electrical parameters, electrolyte constituent and processing times are applied [2]. The electrochemical potential and chemical stability as well as the distribution of the phases in the alloys also show an influence on the coating growth and properties. For instance, electrochemically and chemically inert Saffil alumina fibers in Mg composite material interrupted the continuity of the coating, especially at the interface of the coating and substrate. Only partially and stepwise the fibers were incorporated into the coating through reaction with MgO near the coating surface.

In terms of titanium and its alloys, they have received increased attention for a number of applications in recent years [47,48]. Ti6Al4V alloy is one of the most commonly used titanium alloys and typically contains α- and β-Ti phases [49,50]. PEO coated Ti6Al4V alloy shows not only a good corrosion and wear resistance [51–53], but also potential in biomedical and photocatalytic applications in regard to TiO_2 as the main constituent in the coatings [54–56]. So far, there was not much attention paid to the effect of the polymorphous microstructure of Ti6Al4V alloy on the PEO coating formation [57–59], which can provide insight to the fundamental understanding of the PEO process on Ti alloys. In the present study, the respective coating evolution behavior on α- and β-Ti phases in Ti6Al4V alloy during PEO processing has been investigated in a phosphate electrolyte both ex-situ and in-situ. Phase composition and microstructure of the coating was analyzed as a function of processing time and current density applied, in order to understand the coating formation process on Ti6Al4V alloy and reveal the role of the substrate microstructure in PEO treatment.

2. Experimental

Specimens of Ti6Al4V alloy (7.564 wt%Al, 2.809 wt% V, 0.097 wt% Mn, 0.182 wt% Fe, 0.102 wt% Ge, 0.104 wt% Nb, 0.108 wt% Sn, 0.574 wt% Ta, Ti balance), with the respective sizes of 20 mm × 16 mm × 4 mm and 15 mm × 15 mm × 4 mm, were used as anode material subjected to the ex-situ and in-situ PEO treatment.

2.1. Ex-situ experiment

The standard PEO set-up (Fig. 1(a)) included a pulsed DC power source and a cathode stainless steel tube (surface area ca. 5 dm^2) integrated with the cooling system by circulating water through the tube, to keep the temperature of the electrolyte at 20 ± 2 °C. An electrolyte with the composition of 20 g/L Na_3PO_4 and 1 g/L KOH was used for PEO processing. Magnetic stirring was used to agitate the electrolyte keeping it homogeneous and to avoid temperature gradients. The specimens were treated for 15 s, 30 s, 60 s, 300 s and 600 s respectively, under two different current densities of 5 and 10 A/dm^2 at a duty cycle of 10% and a frequency of 100 Hz. The selection of the two current densities is based on the principle that, the lower one (5 A/dm^2) provides the better option to follow the PEO process especially at the early stage, while the higher current density (10 A/dm^2) speeds up the coating formation process and ensure a more uniform coating in the same time. The voltage response as a function of processing time during the treatment was record with a data acquisition system (SignaSoft 6000 software package, Gantner, Germany). Additionally, a model experiment according to a set-up suggested by ref. [60] was performed with a pure α-Ti (pure Ti) coupled with β-Ti (T-35Nb-6Ta) using the same parameters with the standard PEO set-up to further confirm the different discharging behavior on different Ti phases. The appearance of discharges and the current was recorded as a function of treatment time.

Surface morphology and surface roughness of the coatings were characterized with a laser scanning confocal microscope (LSM 800, ZEISS). A scanning electron microscope (SEM, TESCAN Vega3 SB) equipped with an energy dispersive spectrometer system (EDS, eumeX IXRFsystems) was used to observe the surface and cross-sectional morphology and evaluate the elemental composition of the coatings. A microprocessor coating thickness gauge (MiniTest 2100, ElektroPhysik) was adopted to measure the coating thickness. Additionally, the coating thickness was validated from the SEM cross-section observations. X-ray diffraction (XRD, D8 Advance, Bruker AXS) with Cu Kα radiation (wavelength 0.15406 nm) was applied to analyze the crystalline phase composition of the substrate and the coatings. The measurement was performed at the voltage of 40 kV and the current of 40 mA. The detailed parameters selected in the measurement included a diffraction angle 2θ range between 20° and 80°, a step size of 0.02° and a dwell time of 1 s, with a grazing angle of 3°. The evaluation and variation of phase composition across the thickness of the coating (10 A/dm^2, 600 s) was carried out using the nano focus end station of the beamline P03 at PETRAIII storage ring, at Deutsches Elektronen-Synchrotron (DESY, Hamburg, Germany) [61]. The X-ray beam energy of 19.7 keV (beam size 1.5 × 1.5 μm) was used. The sample was scanned across the surface by the beam in steps of 2 μm in vertical and 4 μm in horizontal direction finally covering an exposure area of 80 × 80 μm. Each XRD pattern was acquired by an Eiger 9 M detector with an acquisition time of 0.5 s and a pixel size 75 × 75 μm. Data reduction was attained employing an in-house developed Matlab® code and the PyFAI [62] routine. The diffraction patterns concerning scattering angle 2θ were converted to Cu K-alpha radiation (wavelength 1.5406 Å). A lab-made Python script was operated to analyze and construct two-dimensional phase map graphics, in order to reveal the phase distribution across the coating thickness.

2.2. In-situ experiment

In order to further track coating formation and unveil the phase evolution in time-resolution during PEO processing, additional in-situ characterization of PEO formation process was conducted at the beamline P23 at PETRAIII storage ring (DESY). Fig. 1(b) illustrate the schematic set-up of the in-situ measurement, while Fig. 1(c) shows a specimen during PEO processing. To minimize background scattering achieving a good diffraction signal the cell set-up was changed in comparison to the standard set-up (Fig. 1(a)) in a way that only a thin film of electrolyte was continuously running over the specimen surface.

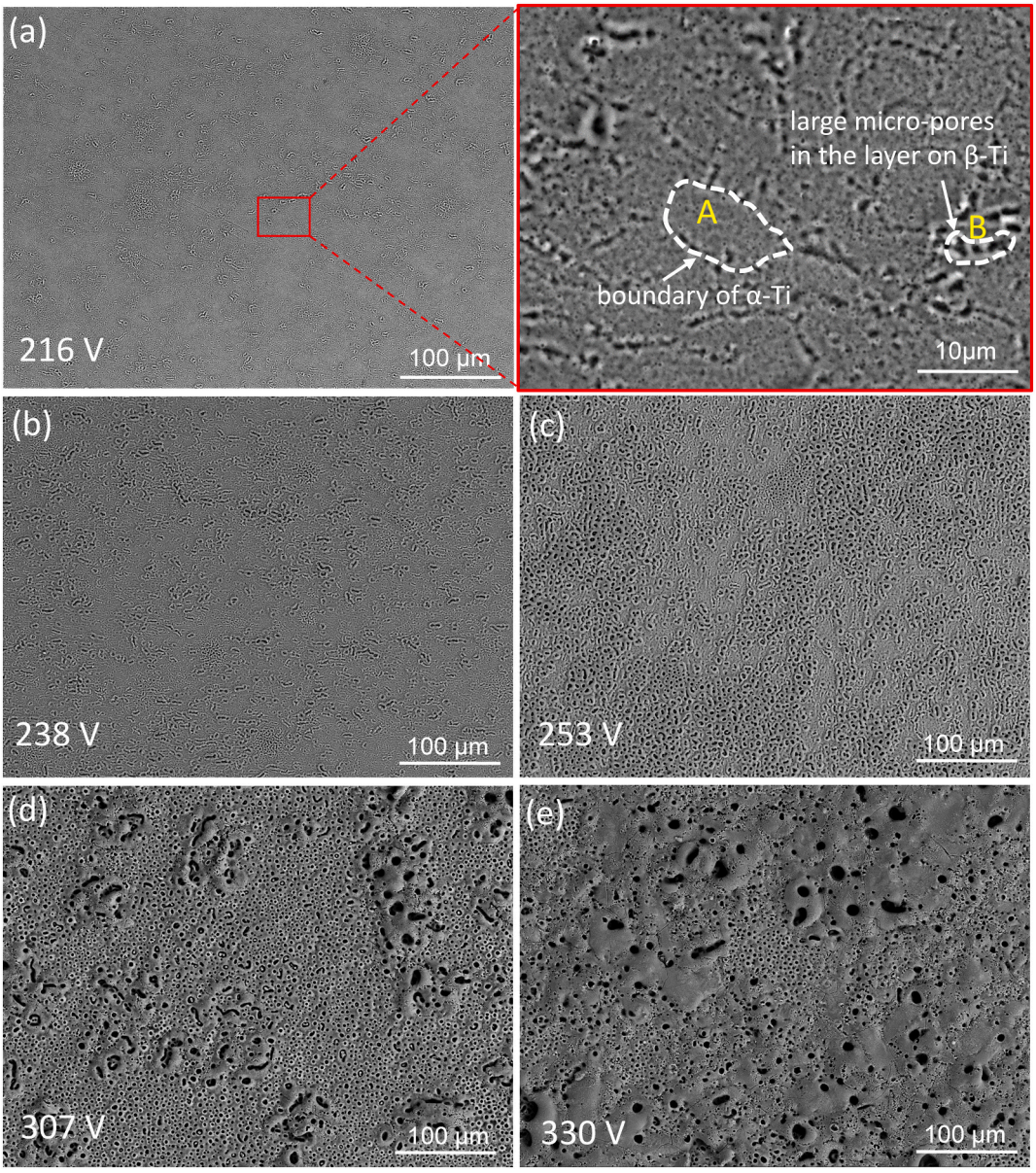

Fig. 4. Surface morphology of PEO coatings at 5 A/dm^2 after different treatment time: (a) 15 s, (b) 30 s, (c) 60 s, (d) 300 s and (e) 600 s in phosphate-based electrolyte.

In spite of using the same power supply and nominally the same processing parameters, the different arrangement and size of the counter electrode resulted in a different voltage response (see Figs. 3 and 15). Thus, even under identical electrical PEO parameters, the behavior of the PEO process in the in-situ DESY cell and standard lab cell are not the same due to the different geometry of the cells and no cooling integrated in the DESY cell set-up. The voltage ramp in the DESY set-up is much faster and therefore a voltage limit of 500 V was preset and the temperature of the electrolyte was recorded at the end of the treatment, because there was no additional cooling system added. The only cooling was obtained by pumping continuously new electrolyte from a 1 L reservoir to the specimen. In the DESY cell set-up, the 10 A/dm^2 treatment was almost an ideal constant voltage treatment at 500 V while the 5 A/dm^2 treatment was similar to the 10 A/dm^2 standard cell treatment. To have a comparison with the 5 A/dm^2 standard cell treatment, an additional current density of 3 A/dm^2 was adopted for the DESY cell set-up. Furthermore, it can slow down the coating formation process efficiency by delaying the voltage increase and thus the PEO process. The lower current density is beneficial to track the progress with more details by the diffraction experiments. During the PEO processing, the X-ray diffraction data acquisition was performed synchronously with a beam energy of 25 KeV and a beam size of 0.4 × 0.4 mm. To minimize signal from the substrate, measurements were performed in grazing incidence geometry with an incidence angle of 0.5°. Single diffraction pattern were continuously acquired throughout the PEO process by a Lambda detector with a pixel size 55 × 55 μm and a measurement time of 100 ms (10 frames per second). After the HV was turned-off (at 10 min), the acquisition of the diffraction pattern continued for around 5 min more. Data reduction was attained employing an in-house developed Matlab® code and the PyFAI [61] routine. Afterwards, the in-situ treated specimens were also measured using X-ray diffraction (XRD, D8 Advance, Bruker AXS) with Cu Kα radiation (wavelength 0.15406 nm) at the same settings as the ex-situ processed specimens however with a grazing angle of 10°.

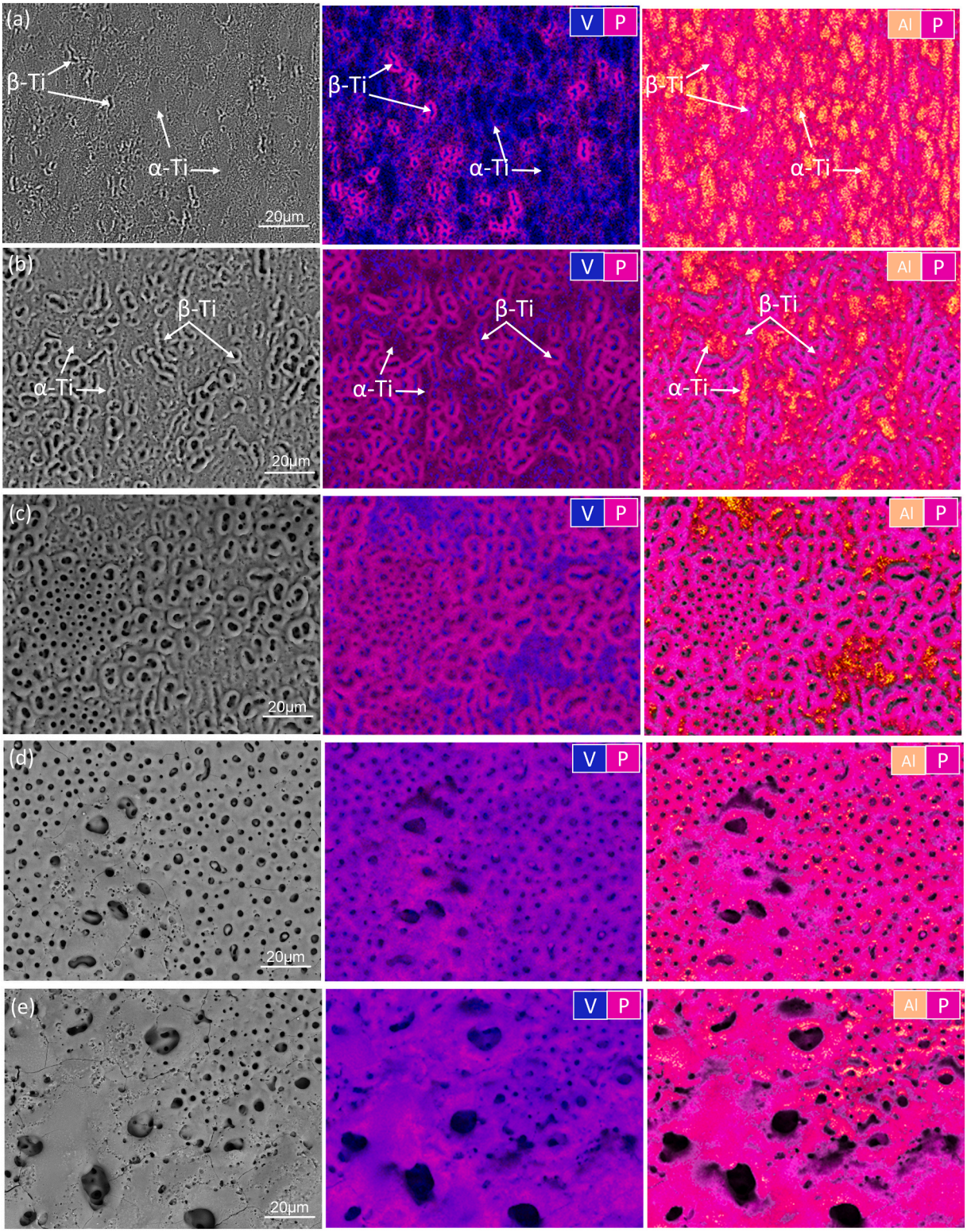

Fig. 5. Overlap elemental mapping of PEO coating on Ti6Al4V alloy at 5 A/dm^2: (a) 15 s, (b) 30 s, (c) 60 s, (d) 300 s and (e) 600 s in phosphate-based electrolyte.

3. Results

3.1. Microstructure of Ti6Al4V alloy

Fig. 2 illustrates that Ti6Al4V alloy contains α-Ti phase (hexagonal) stabilized by aluminum and β-Ti phase (cubic) stabilized by vanadium. Different from Al and Mg alloys, intermetallics are absent in Ti6Al4V alloy due to the high solid solution ability of the alloying elements in the Ti matrix. XRD pattern in Fig. 2 (c) validates the main signals of α-Ti phase and the presence of few β-Ti phase peaks with much lower intensity. Fig. 2 (a) shows the microstructure of the substrate including the equiaxed α-Ti grains with the distribution of β-Ti at the grain boundaries. The main elemental composition/distribution (titanium, aluminum and vanadium) in the substrate is revealed in Fig. 2(b), which

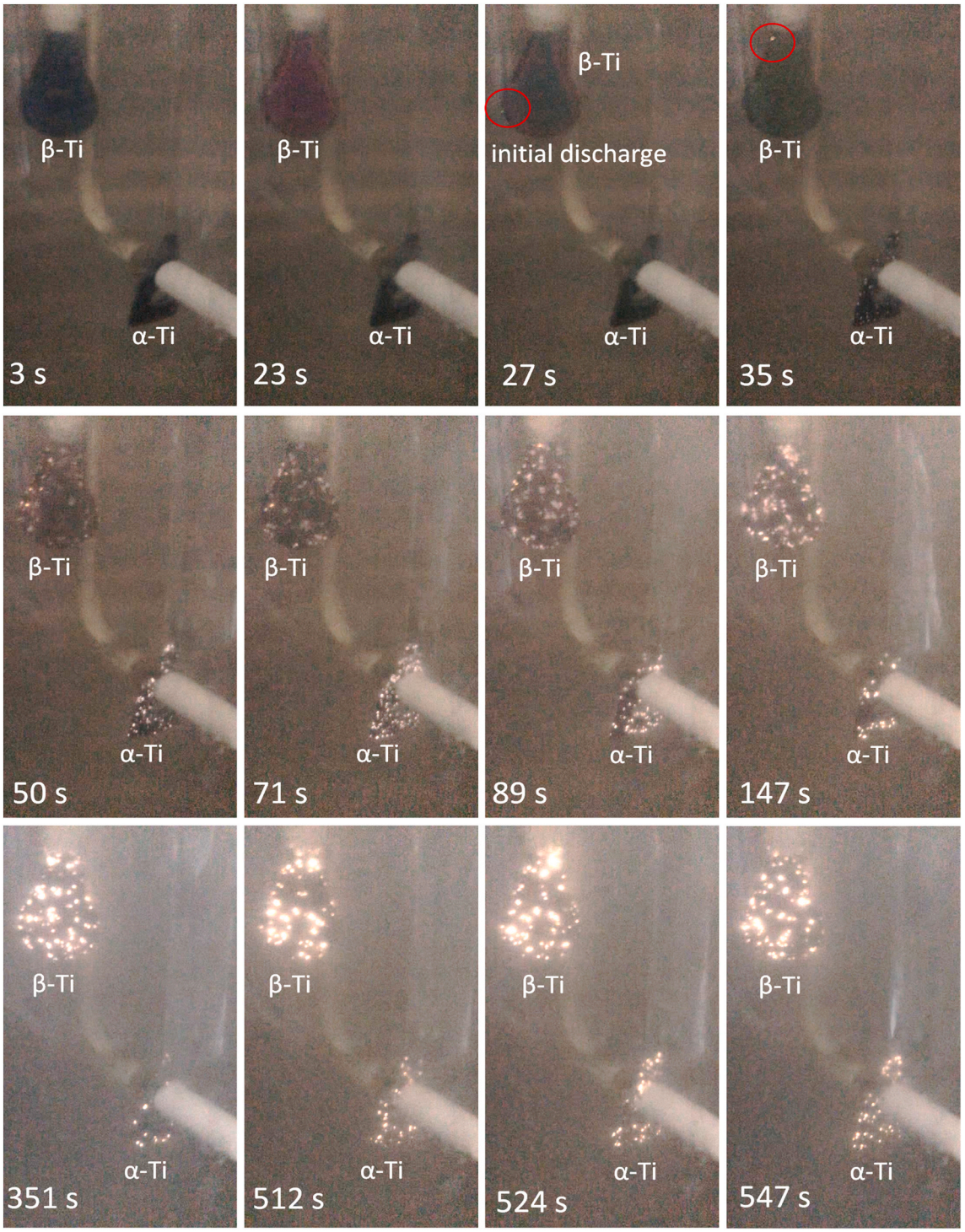

Fig. 6. Evolution of discharges on coupled α-Ti and β-Ti substrates.

obviously illustrates the distribution of the two phases. The α-Ti contains a higher aluminum content of 8.1 ± 0.3 wt% and only 1.1 ± 0.5 wt% of vanadium. However, the β-Ti consists of a higher vanadium content of 11.4 ± 0.6 wt% and 4.8 ± 0.1 wt% of aluminum.

3.2. Voltage - time response during PEO processing

The changes of voltage as a function of treatment time at two different current densities for PEO processing of Ti6Al4V alloy using the standard set-up and phosphate-based electrolyte are shown in Fig. 3. Regardless of applied current density, the voltage increases rapidly from the beginning of the processing and the first discharges appears at around 190 V. A steeper voltage ramp is revealed with increasing current density from 5 to 10 A/dm^2. The higher current density obviously facilitates the layer deposition/growth, and thus the electrical resistance of the layer raises faster and stimulates the more rapid increase of voltage to maintain the pre-selected current density. According to the change of voltage ramp, it is possible to divide the PEO process into four stages. At the initial stage prior to the occurrence of discharges, the voltage shows a linear dependence on treatment time, which is typical

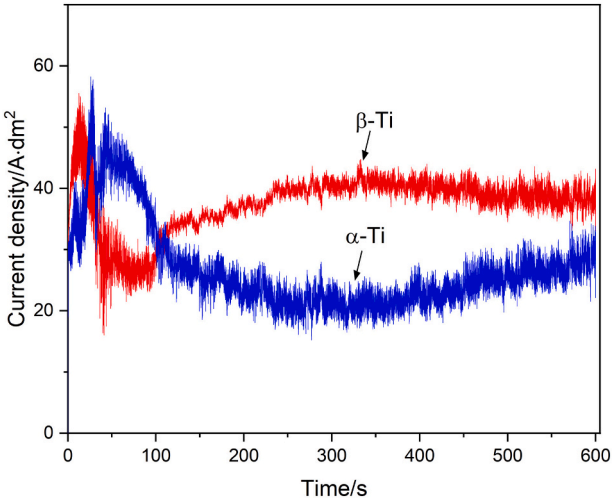

Fig. 7. Change of current density as a function of processing time for coupled α-Ti and β-Ti substrates.

Table 1
Atomic content of main coating forming elements at local areas of the PEO coating after 15 s of processing.

	Ti	Al	V	O	P	Na	K
A	42.338	7.23	0.072	46.429	3.46	0.444	0.026
B	35.299	4.831	1.58	44.462	13.358	0.435	0.035
C	52.07	10.832	0.316	26.267	6.687	2.536	1.302
D	33.952	5.599	2.437	40.722	14.079	2.149	1.061

for conventional anodization. Acoustic emission can be noticed at this stage when the voltage increases to 150–160 V after around 4 s. The discharges start at ca. 10 and 7 s (190 V) under the current density of 5 and 10 A/dm^2, respectively. After the occurrence of discharges, the voltage ramp declines significantly. The second stage is characterized by the fast migration of white micro-discharges. With slow increasing of voltage, the discharges grow in size, however, their population decreases in the third stage. The size and mobility change is also accompanied by a color evolution from white to yellow-orange. The fourth stage for 5 A/dm^2 does not really reach since the voltage change is not obvious and the final voltage for this condition is 330 V. Nevertheless, for the higher current density, the discharges become larger but their density decreases further with prolonged treatment time in the last stage. The voltage becomes more stable with lower increase rate and the final voltage is 450 V after 600 s of processing.

3.3. Surface morphology

Fig. 4 shows the evolution of surface morphology of the coatings with processing time under 5 A/dm^2 in the phosphate-based electrolyte. It is apparent that micro-pores have been formed on the coating surface already after 15 s of processing (Fig. 4(a)), and the obvious sintered morphology can be recognized in contrast to the uniform anodized surrounding. The first discharges are observed already at 10 s, and the formation of the micro-pores and the sintered surface around is a consequence of the discharges. With closer observation of local morphology in Fig. 4(a) on the right side, it is interesting to notice that the larger micro-pores with surrounding sintered morphology seem to start at the grain boundaries. Their presence even make the grain boundaries more visible. Fig. 5(a) discloses the respective overlap mappings of phosphorous/vanadium and phosphorous/aluminum on the surface after 15 s. In the center of the micro-pores, vanadium is detected, around which the segregation of phosphorous can be found on the sintered coating materials. However, the surface areas with accumulation of aluminum do not contain any micro-pores left by discharges. Tracking of the elemental distribution suggests that the discharges initially occurred on the β-Ti phase rather than on α-Ti phase. In order to validate this observation, a model experiment was designed with a different pure β —Ti alloy coupled to pure α-Ti. The PEO process of coupled α-Ti and β-Ti substrates under the same condition demonstrates the discharges are firstly appearing on the surface of β-Ti specimens and only after that on α-Ti (Figs. 6, 27 s). Since the voltage is the same, the change of current density as a function of processing time in Fig. 7 reveals a higher current passing through the layer formed on β-Ti at the very beginning stage. It further confirms the observation of initial discharges/micro-pores appearing on β-Ti. Then, tiny discharges rapidly envelope the surface of α-Ti specimen (Figs. 6, 35 s). At this stage, the discharges are found on both specimens, while the current density (Fig. 7) indicates actually that they are stronger on α-Ti specimen after the initiation of the breakdown. After around 100 s of treatment, stronger discharges (higher current density) are always noticed on β-Ti.

Table 1 illustrates the higher content of vanadium and phosphorous, and lower aluminum content in area B (sintered porous appearance) compared to the area A (uniform appearance). Thus, the original heterogeneity in the microstructure of Ti6Al4V alloy influences the early growth of PEO coating and is a consequence of the earlier breakdown of the dielectric layer on β-Ti phases.

With treatment time prolonging to 30 and 60 s, the sintered morphology becomes more pronounced (Fig. 4(b) and (c)) and is extending beyond the local areas related to β-Ti phases starting to cover more or less the entire coating surface (Fig. 5(b) and (c)). There are almost no discharges on the α-Ti phases firstly because the layer is denser and discharge energy is not high enough. Only with increasing time, the coating is growing thicker on the β-Ti phases and require even more energy to drive the discharges. At this point discharges also appear on α-Ti phases. The size of micro-pores also increases obviously, indicating that the intensity of discharges elevates due to the continuous increasing of layer resistance, stimulating further increase of voltage. Fig. 4(d) displays that the coating surface is fully covered with micro-pores after 300 s of PEO processing, which are mainly of similar size and shape compared to those in Fig. 4(c), but in addition, some larger micro-pores can be found on highly sintered islands. The island morphology is associated with the stronger discharges at the last stage of PEO processing and reduced discharge population. After 600 s of processing, Fig. 4(e) shows that the highly sintered islands developed further and started to interconnect each other. With increasing processing time, the vanadium distribution became more uniform, nonetheless, the accumulation of aluminum is still distinguishable in regions, where the micro-pores are still smaller and the coating is thinner (Fig. 5 (d) and (e)). Some micro-cracks can be observe on the sintered islands, which could be a result of thermal stresses [63,64] due to the large heat release from the discharges.

Fig. 8 presents the change of surface morphology of PEO coatings after the same treatment times, but under higher current density of 10 A/dm^2 in phosphate electrolyte. Although the higher current density accelerates the process and the increase of voltage is more rapid, a similar sintering morphology is still recognized in Fig. 8(a) after 15 s of processing. The elemental content of area C (less sintered) and D (highly sintered) in Table 1 indicates a higher vanadium content at D, also suggesting stronger sintering (arcing) is preferred to occur at the β-Ti phase. From 15 to 60 s (Fig. 8(a-c)), it is evident that the highly sintered morphology is gradually spreading to the entire surface, similar to the evolution under 5 A/dm^2 but much faster. However, with increasing processing time to 300 s, the coating surface as seen in Fig. 8(d) becomes more uniform in comparison to the surface morphology prepared under 5 A/dm^2, and the size of micro-pores seem to be decreased in general values. There are sintered islands showing hazy boundaries that can be only recognized by the slightly larger micro-pores in contrast to the surroundings. The sintered islands evolve and cover the entire surface with further processing. After 600 s of treatment, the coating shows

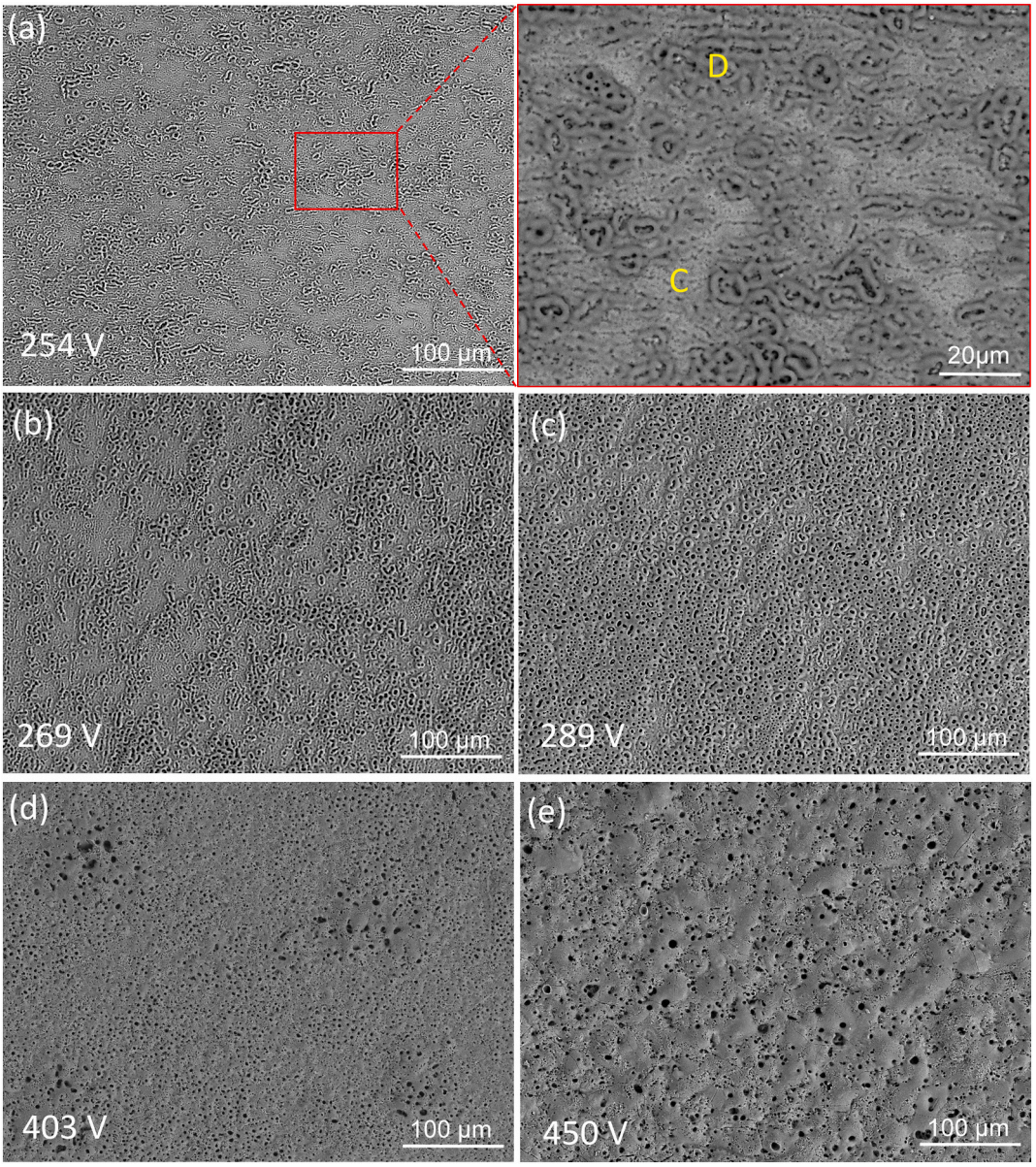

Fig. 8. Surface morphology of PEO coatings at 10 A/dm^2 after different treatment time: (a) 15 s, (b) 30 s, (c) 60 s, (d) 300 s and (e) 600 s in phosphate-based electrolyte.

almost uniform surface morphology with a wider distribution of micro-cracks Fig. 8(e).

Fig. 9 reveals that the surface roughness increases with processing time. The surface roughness Ra of the coatings under 5 A/dm^2 increases from 0.69 ± 0.18 to 1.45 ± 0.25 and finally to 3.11 ± 0.18 μm, and for 10 A/dm^2, it increases from 1.01 ± 0.07 to 1.91 ± 0.17 and 2.19 ± 0.28 μm. This correlates with the SEM observations (Fig. 4(c-d) and Fig. 8(c-d)) and demonstrates that finally with the higher current density a more uniform and flatter surface is obtained.

3.4. Cross-sectional morphology

The cross-sectional observations combined with elemental maps of the coatings prepared in phosphate-based electrolyte are shown in Fig. 10 and Fig. 11 in respect to different processing time (15, 30, 60, 300 and 600 s) and current density (5 and 10 A/dm^2). Many studies have reported a layered morphology of PEO coatings [28,64,65]. For the processing under 5 A/dm^2, the coating firstly shows a compact and thin layer consisting of only few micro-pores after 60 s of treatment (Fig. 10 (a) and (b)). With increasing processing time, a thicker outer porous layer and a thinner inner layer with smaller micro-pores can be found. A similar evolution can be observed for the coatings prepared under higher current density of 10 A/dm^2 in Fig. 11, however, it looks as if the final coating is less porous. According to the contrast in BSE images, one can find in Fig. 11(a) and (b) that some tiny micro-pores are primarily accumulated at the interface of coating and substrate, where β-Ti phase can be recognized. This further confirms that the initial discharges are preferred to start at the layer on the β-Ti phase, and agrees with the initial surface sintered morphology on β-Ti phase in Fig. 8. Gas is captured in the melted volume and entrapped after rapid cooling down when the discharges are turned off. It can be seen from the cross sections that the coating thickness is proportional to the processing time and current density. The elemental mappings indicate that all coatings contain titanium, aluminum, vanadium, oxygen, phosphorus, sodium and potassium, suggesting a contribution of substrate material and electrolyte species in the coating formation process. Closer analysis of the mapping results shows a contrast gradient of phosphorous across the coating thickness, which develops gradually with processing time. It

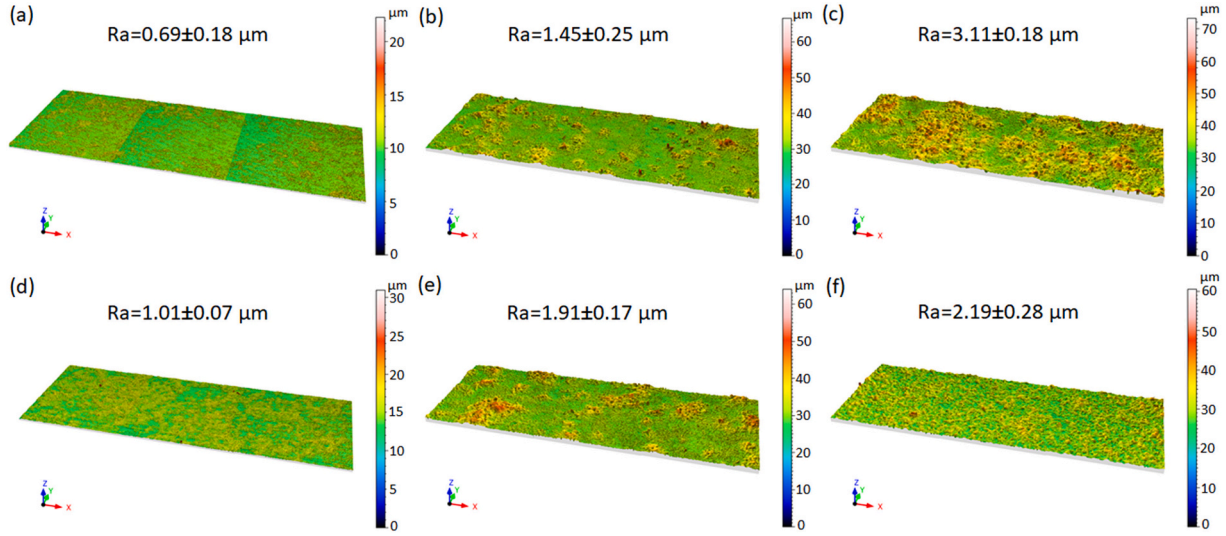

Fig. 9. Surface profiling of PEO coatings after (a) 60 s, (b) 300 s and (c) 600 s of processing under 5 A/dm^2, and after (d) 60 s, (e) 300 s and (f) 600 s of processing under 10 A/dm^2 in phosphate-based electrolyte.

might lead to a change of phase composition across the coating thickness and further discussion will follow in the coming sections.

The change of coating thickness as a function of processing and current density is presented in Fig. 12. The coating thickness increases with treatment time, and the coating grows more rapidly for the first 60 s of treatment and then slows down with further processing time. The average coating thickness at higher current density is always higher than at 5 A/dm^2, whereas, the difference is not that significant. Doubling the current density is by far not resulting in a twice-fold increase of coating thickness.

3.5. Phase composition

The XRD patterns of the PEO coated Ti6Al4V specimens formed under different current density and processing time are displayed in Fig. 13. It reveals two TiO_2 phases namely anatase and rutile in the coating, in combination with amorphous phases, which are visible by a broad halo in the diffraction patterns at two theta ranging from 20° to 30°. For both used current densities, anatase is revealed after only 15 s of processing. With prolonged treatment time until 60 s, the intensity of the scattering peaks for anatase increase further. The formation of rutile shows a dependence on the treatment time and voltage/current density. The peaks of rutile can be observed after 60 s of treatment for 5 A/dm^2 and maybe slightly earlier for higher current density. It is associated with the energy of discharges, as the formation of rutile requires a higher transition temperature (~600 °C) compared to anatase (~250 °C) [66]. Thus, the effective temperature of initial discharges might not be high enough for the formation process, while with the continuous increasing voltage, the intensity and energy of the discharges are increasing as observed during the PEO processing. This could also explain the high drop of faradic efficiency in coating growth (coating thickness) with increasing current density in Fig. 12. The fast phase transformation from anatase to rutile at higher current density results in the higher amount of rutile. The coatings composed of higher concentration of rutile may have lower electrical resistance, concerning a relatively lower band gap (3.0 eV) of rutile compared to anatase (3.2 eV) [67]. As a result, the voltage ramp at 10 A/dm^2 does not increase to the value twice of that at 5 A/dm^2 (Fig. 3) and the coating growth rate is dropping down accordingly. According to the elemental analysis, the coatings also contain significant amount of phosphorous, which is not included in the crystalline phase composition of the coatings. Nevertheless, the preferential synthesis of amorphous phosphate in PEO coatings prepared in phosphate-containing electrolyte was reported [5,68]. Therefore, the presence of the amorphous phase can be most likely assigned to the formation of amorphous phosphate. However, the in-situ experiments, which will be discussed later suggest that the amorphous phase may contain also titanium oxide in the form of TiO_x with x ranging from 0 to 2.

For a better understanding of the phase distribution within the coating, additional localized XRD measurements were performed at P03. Fig. 14(a) shows a spatial XRD scan across the coating thickness from the surface towards the substrate after 600 s of processing at 10 A/dm^2. Based on the appearance of the different phases, the coating can be distinguished from the air and the substrate. The strongest peaks of anatase and rutile are also demonstrated at the two theta range of 20–30°, which is shown in Fig. 14(b). It was of interest to understand if the original Ti structure has an influence on the formation of the oxide film. However, the oxide phases are all enriched near the coating surface, considering that the peak intensity visibly decreases from the outer layer towards the interface of coating/substrate. Since the phase transformation of titanium oxides may depend on the temperature stimulated by the discharges, it is reasonable to find crystalline TiO_2 phases accumulation near the interface of coating and electrolyte. Amorphous phases may remain closer to the interface of coating and substrate considering the EDS mapping results and the found distribution of phosphorous closer to the substrate.

Moreover, it is obvious that the concentration of rutile remains lower than that of anatase. Obviously, the efficient treatment temperature necessary for the transformation process from anatase to rutile was only locally reached. The coating thickness from the XRD depth profile is estimated to be ca. 35 µm, which is higher than the measured coating thickness from the cross sections in Fig. 12. The rough interfaces at the coating/air and the coating/substrate might be responsible for the overestimated coating thickness.

3.6. In-situ characterization of phase evolution

The in-situ results obtained by high energy synchrotron XRD at P23 suggest that there are amorphous phases existing during the whole treatment period (Fig. 15(a-c)), which are presented as halos with different intensity through the entire processing. The origin for this amorphous signal is the specimen, as observed in the ex-situ measurements, and as well from the water as a background signal. At the beginning of the treatment during the linear voltage ramp, the XRD patterns (Fig. 16) show broad peaks expanded from α-Ti (hcp) most likely due to solid solution incorporation of oxygen in the lattice. This expansion is reduced with time and discharge energy, most likely due to

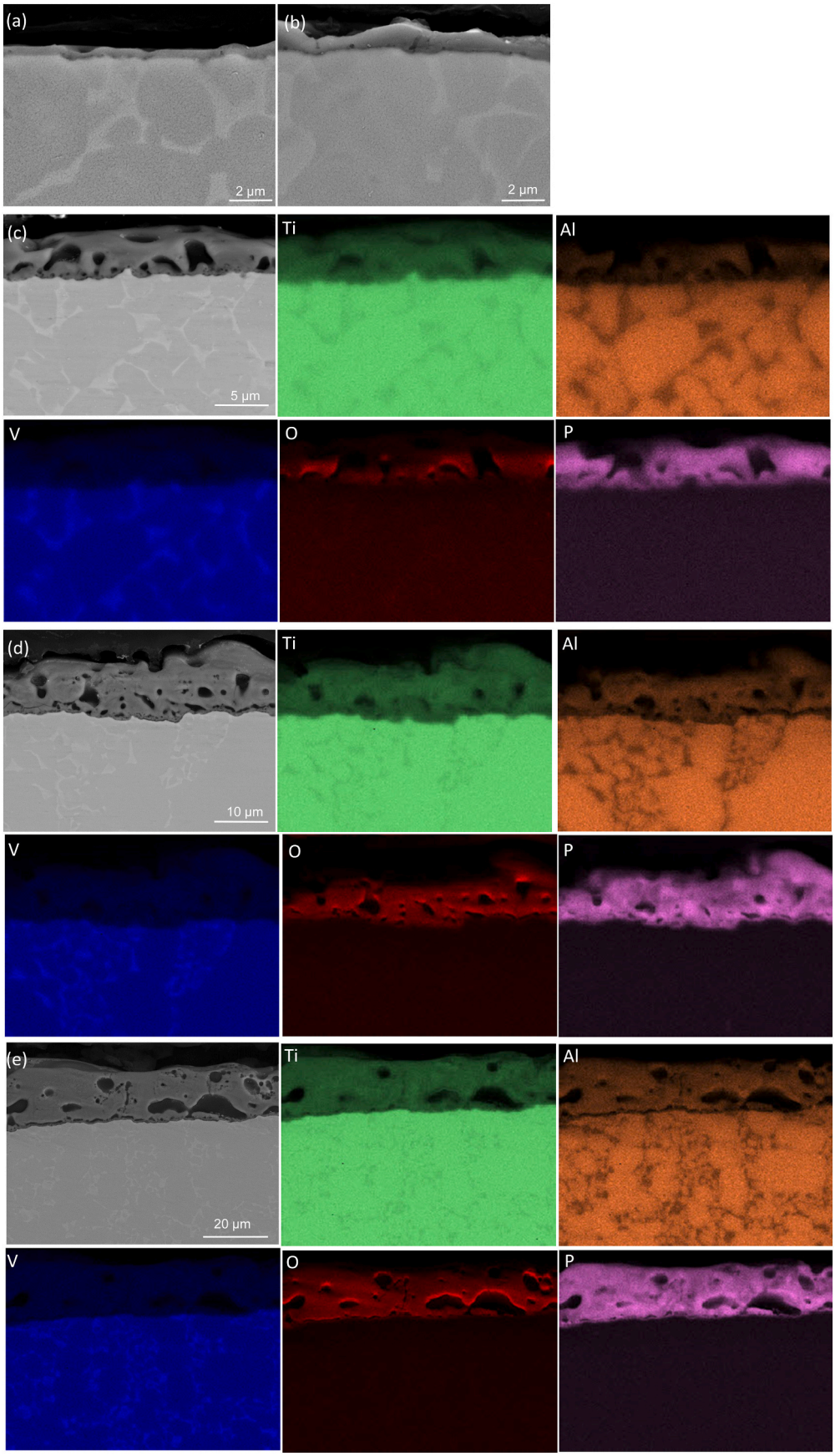

Fig. 10. Cross-sectional morphology and elemental mappings of PEO coatings at 5 A/dm^2 after different treatment time: (a) 15 s, (b) 30 s, (c) 60 s, (d) 300 s and (e) 600 s in phosphate-based electrolyte.

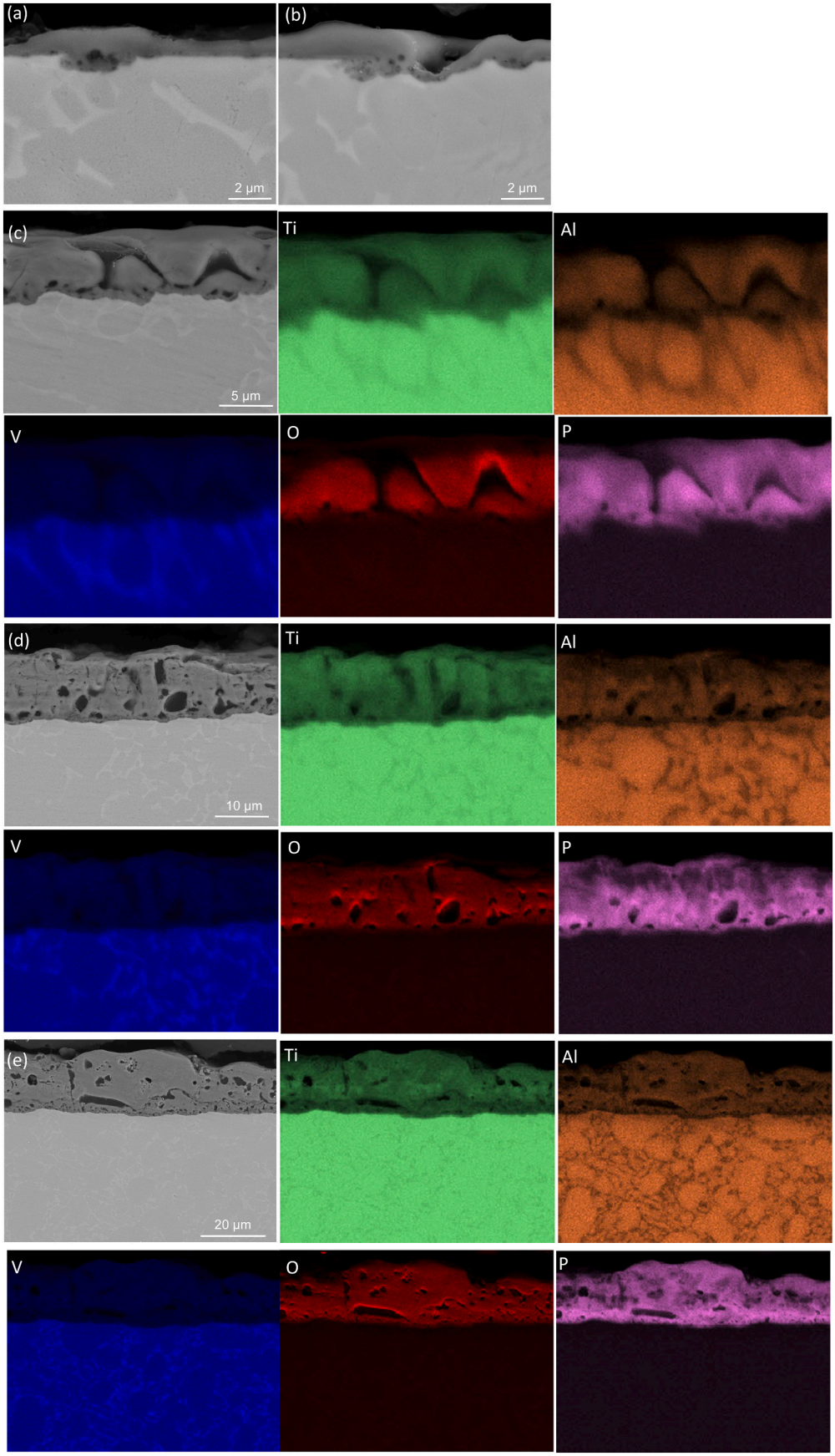

Fig. 11. Cross-sectional morphology and elemental mappings of PEO coatings at 10 A/dm^2 after different treatment time: (a) 15 s, (b) 30 s, (c) 60 s, (d) 300 s and (e) 600 s in phosphate-based electrolyte.

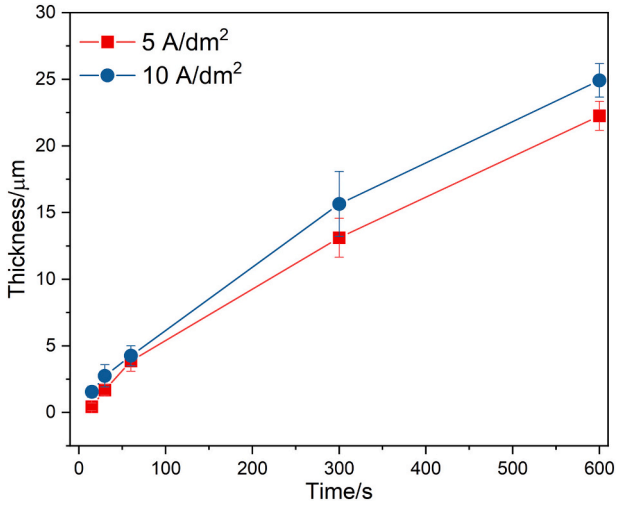

Fig. 12. Change of coating thickness with treatment time under the two different current densities.

a temperature increase during the treatment and further in- or outward diffusion of the oxygen.

Taking into account the incident angle of 0.5° and an energy of 25 KeV, the main information comes from a depth of 6 µm. At a penetration depth of 10 µm the intensity is dropped already to 1%. Thus, it is quite likely that an amorphous oxide layer and underneath an oxygen expanded α-Ti phase extending down to more than 10 µm is forming within milliseconds as soon as the voltage is applied. The calculation of the changes for α-Ti lattice parameters (Fig. 17) demonstrates the obvious lattice expansion, considering the typical lattice parameters of α-Ti as a = 0.295 nm and c = 4.683 nm [69]. However, the lattice expansion is going back again with processing time and reaches some equilibrium condition determined obviously by the current density driving the discharges responsible on the one hand for the oxygen formation and up-take and on the other hand in- and outward and diffusion via temperature increase. This could explain why the highest expansion is not found for the highest current density, but for the medium one and the longest lasting expansion for the lowest current density.

The diffraction peaks for α-Ti (not expanded), anatase and rutile become visible gradually during the progress of the treatment/oxidation while the signal of β-Ti is absent. The short acquisition time may not be sufficient to resolve the low amount of β-Ti or it is quickly transformed to α-Ti, as oxygen as alloying element is stabilizing the α-Ti phase. For the lowest current density (3 A/dm^2), the process shows a gradual intensity increasing of anatase and rutile until the end of PEO processing, and the voltage only reaches 390 V. However, at higher current densities, an interesting observation (Fig. 15(b) and (c)) is that both crystalline titanium oxides phases form, disappear and reappear with different texture suggesting that both lower temperature and higher discharge energy support the formation of amorphous oxide layer. When the temperature is increasing crystallization should occur, but the involved higher discharge energy (above 400 V) prevents the long lasting formation of crystalline oxides by continuous re-melting them in the discharge and subsequent solidification mainly as amorphous phase. Surprisingly, the diffraction peaks of anatase and rutile appear again (and much more pronounced) after switching off the HV (PEO treatment). After few seconds, it seems that a continuous ongoing process starts that parts of the amorphous oxide phase do transform into crystalline anatase and rutile, visible by increasing intensity of the respective peaks (Fig. 18). Unfortunately, it was not possible to observe this transformation for a longer time in the beam line experiments. However, a week after the beamline treatment the same specimen were remeasured with the lab-XRD (Fig. 19) confirming almost the full transformation of the amorphous phase into anatase and rutile in the final coating. Only small bumps around the main rutile and anatase peak positions are visible. Interestingly, stronger intensity of rutile is still observed at 10 A/dm^2, which we have always associated with the higher temperature/discharge energy causing the transformation of anatase to rutile during the PEO processing. Now it seems as if both phases are mainly forming simultaneously after the PEO processing from an amorphous oxide phase.

4. Discussion

Ti6Al4V alloy is a polymorph alloy consisting of α- and β-Ti phases, with hexagonal and cubic crystals respectively. The in-situ characterization of PEO coating formation process gives a time-resolved phase evolution, which somehow differs from the expectations obtained after the interrupted ex-situ characterization. During the initial periods of PEO processing, a fast broadening and shift of α-Ti peaks can be observed. The shift of peaks can be attributed to the oxygen diffusion into the α-Ti lattice, expanding it in the near surface region of the specimens (down to 10 µm). In terms of the high solubility of oxygen in the hcp lattice structure, the lattice expansion is a result from the continuous formation of interstitial solid solution before the formation of titanium oxide [69,70]. That finally the expanded α-Ti almost disappear at the end of the treatment can be explained by the formation of the oxide layer as well as by a faster diffusion of oxygen when an overall higher temperature level of the specimen is reached. The absence of β-Ti in the diffraction pattern can be firstly attributed to the low

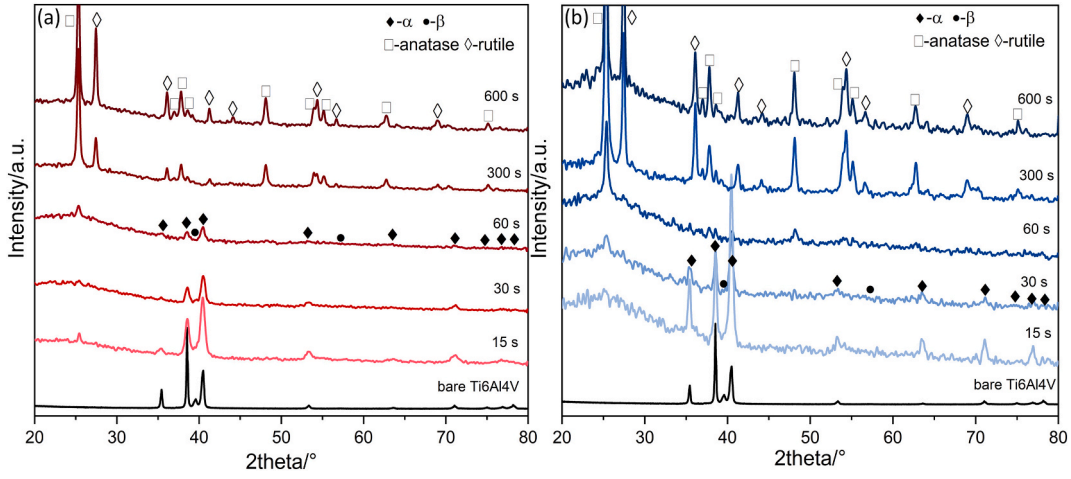

Fig. 13. XRD patterns (wavelength 0.15406 nm) of PEO coatings under (a) 5 A/dm^2 and (b) 10 A/dm^2 after different treatment time in phosphate-based electrolyte.

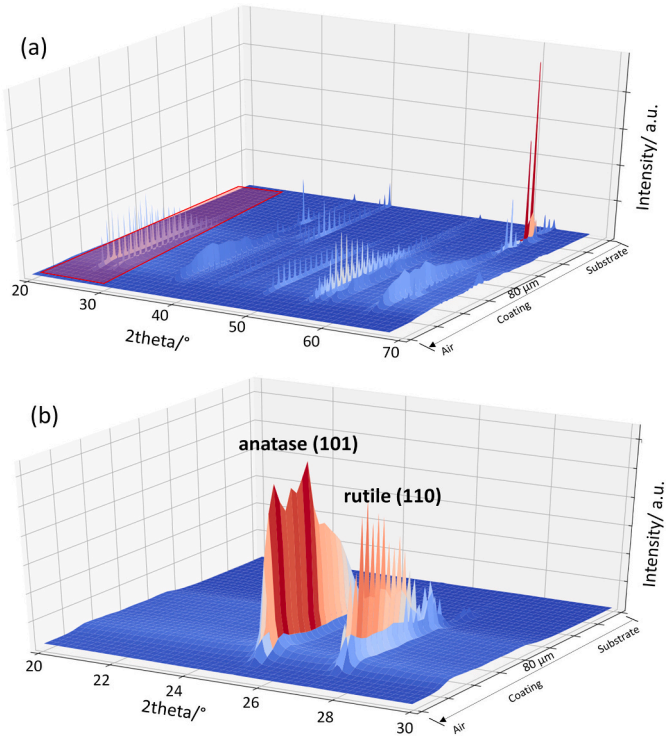

Fig. 14. (a) Spatial phase distribution across the PEO coating thickness formed at 10 A/dm^2 for 600 s and (b) rutile (110) and anatase (101) intensity distribution across coating thickness using the nano focus end station of the beamline P03 (wavelength 0.15406 nm).

content considering the cubic structure is stabilized only by nominal 4 wt% vanadium. Another alternative explanation is that the continuous penetration/diffusion of oxygen into the alloy surface broadens the α-Ti stability range, stimulating the transformation from bcc to hcp before the oxygen saturation in α-Ti ($TiO_{0.5}$) is reached [71]. As the ex-situ measurements show the existence of an amorphous phase we speculate that this phase will be also visible in the in-situ measurement. The observed halo has contributions from water and the specimens. However, there is a clear influence of the current density on the intensity of the halo visible as well as an absence of crystalline TiO_2 peaks, supporting the theory of mainly amorphous oxide formation during the early stages of PEO processing. The amorphous titanium oxide then transforms into the different crystalline TiO_{2-x} phases, including anatase and rutile [72]. The formation disappearing and reappearing of crystal TiO_2 under the current density of 5 and 10 A/dm^2 could be associated with the higher voltages and discharge energies changing the temperature regimes for melting and solidification. The high energy input (voltage) can induce rather high temperature and pressure in local areas on the surface of the specimens [36] and the still cold surrounding of the electrolyte bath (max. 43.5 °C after 10 min treatment at 10 A/dm^2) can provide fast quenching, and thus mainly amorphous titanium oxide exist in such severe condition. Interestingly, the lower current density results in a more stable crystalline TiO_2 formation already during the PEO processing, which is supposed to be related with less melt volume generated by the less intense discharges. For the higher current densities, the main formation of the anatase and rutile phases occurs after the HV is turned off, obviously by precipitation out of the amorphous oxide phase. At this time, the intensity of the halo is decreasing.

Coming back to the original question of the study, if there is an effect of the two Ti phases on the coating formation the in-situ study would suggest that it is quite limited because of the possible fast up-take of oxygen, which should stimulate the transformation of β-Ti to α-Ti. With regard to the different local morphology of the initial coating (Figs.4(a)

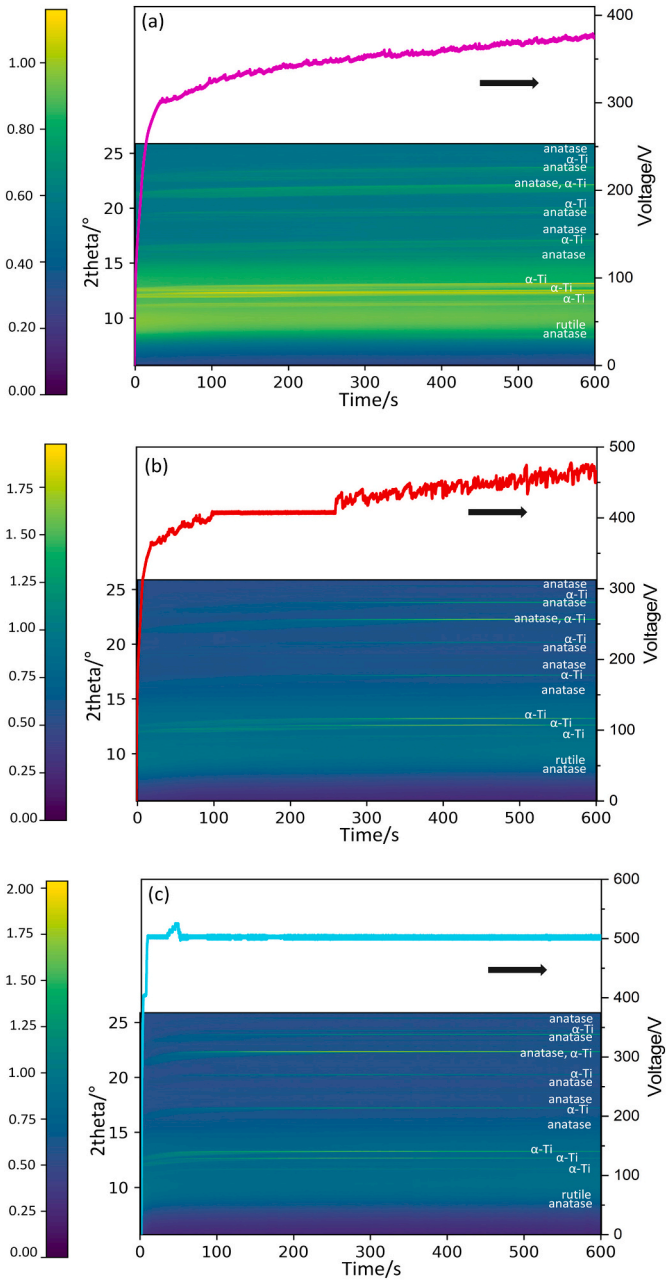

Fig. 15. In-situ characterization of phase (wavelength 0.0496 nm)/voltage evolution on Ti6Al4V surface as a function of time at different current density: (a) 3 A/dm^2, (b) 5 A/dm^2 and (c) 10 A/dm^2.

and 5(a)), it is obvious that the coating formation involves the oxidation of the two phases with different elemental composition. Thus, the initial coating material comprises a modified titanium oxide-dominant layer containing relatively different aluminum and vanadium contents on α and β phases respectively (Table 1). Galvanic effects between the α- and β-Ti phases have indicated their different electrochemical activity and a higher electrochemical stability of β-Ti phase was demonstrated [73,74]. This results in an initial layer showing different oxidation rates of the two different phases and influencing the local morphology. With continuous deposition of the coating, the increasing applied voltage stimulates the generation of discharges, preferentially at the weakest locations or "defects" [36]. It is clear that the local microstructural features of the layer have an effect on the discharges, which is correlated with the local electrical resistance [4]. Only if the initial dielectric layers are overall strong enough to let the voltage ramp to breakdown voltage

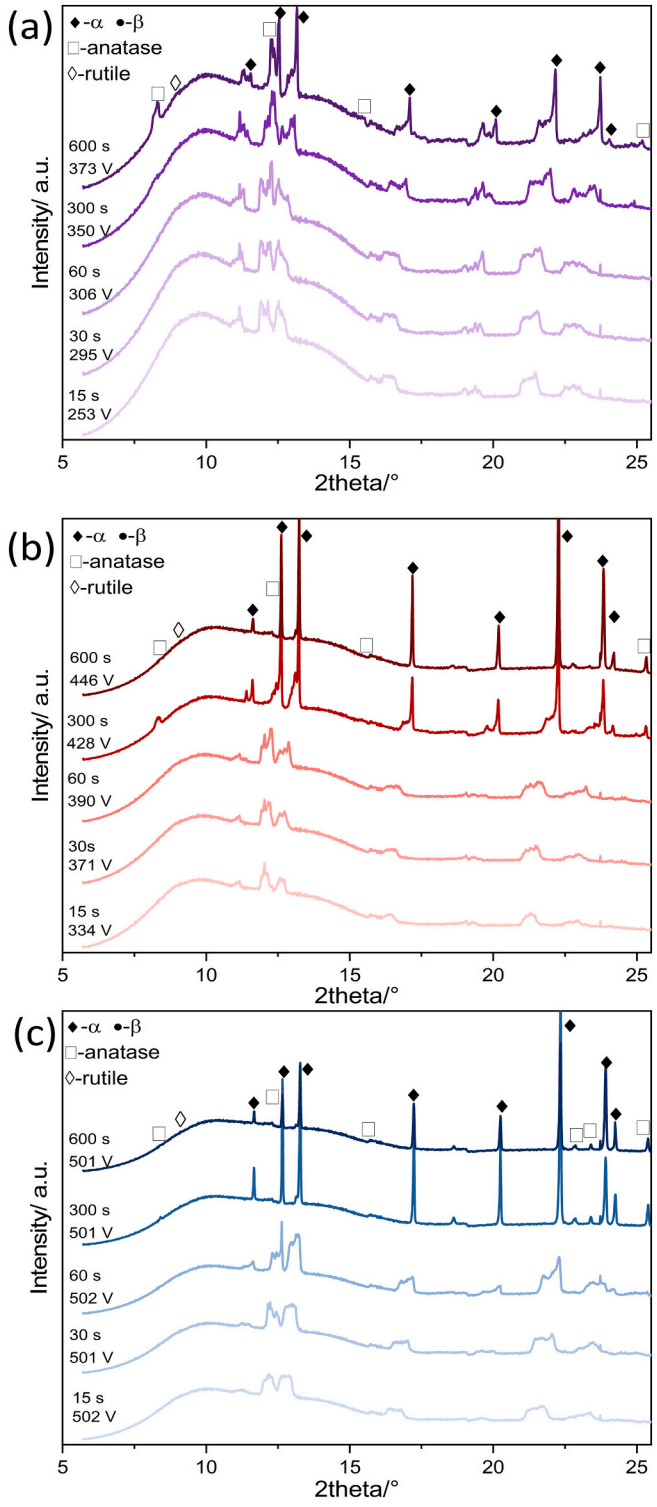

Fig. 16. In-situ XRD patterns (wavelength 0.0496 nm) of specimens treated at different current density: (a) 3 A/dm^2, (b) 5 A/dm^2 and (c) 10 A/dm^2.

discharges will form. If not, no discharge will occur at all. In the model experiment, where β-Ti was separated from α-Ti, the first breakdown appeared on the β-Ti. Afterwards, the conditions are changing and discharges appear on both samples, but with changing intensity, correlating with the amount of current through the samples. In the case of a polymorph Ti6Al4V alloy containing α-Ti and β-Ti, the voltage is the same but the current is different through the two phases in substrate and corresponding layers, similar to the model experiment (Fig. 7). Hence, the so-called "defects" could be associated with local areas of the coating with lower electrical resistance than others nearby. The sintered morphology resulted from the high temperature of discharges appears firstly on the coating surface on β-Ti phase. Therefore, the β-Ti most possibly forms the less resistant dielectric layer in comparison to that of α-Ti phase. The β-Ti phase is rich in vanadium and it has been demonstrated that vanadium oxides are not stable in alkaline electrolyte due to a high solubility [75]. The coating on β-Ti phase is possibly more porous due to the dissolving vanadium oxides or has more defects due to the oxygen driven transformation to α-Ti and thus might have more preferred locations for the discharges. Furthermore, it is known that the atomic packing of the body-centered cubic β-Ti phase is lower than close-packed α-Ti phase [74]; hence, the diffusion of oxygen is higher in β-Ti phase stimulating the transformation. Overall, the differences are getting smaller with increasing treatment time as the coating gets more uniform and thicker.

The discharges migrate to the surface of α-Ti phase after "healing" the layer on β-Ti phase. Consequently, the highly sintered morphology in combination with large micro-pores spreads on the entire coating surface, from the β-Ti phase to α-Ti phase with further increasing of voltage (Fig. 4(b-e)). With thickening of the coating, more energetic discharges are required, which could also cause the enlargement of the micro-pores [35]. Meanwhile, the discharges rebuilds the coating structure, and the high temperature and repetition of the discharges promote sufficient diffusion and mixing of coating compounds making the coating more homogeneous. As seen in Fig. 8(e), the coating formed under higher current density after 600 s is quite uniform distributed with highly sintered crater-centered islands. In summary, the different oxidation and coating formation behavior at local areas can be assigned to the microstructure of Ti6Al4V alloy due to the different composition and electrochemical stability of α-Ti and β-Ti phases and as consequence the chemical stability and electrical conductivity of the growing coating. The different lattice structure seems to be less important, considering its possible early transformation into one expanded α-Ti phase.

With the increasing of current density from 5 A/dm^2 to 10 A/dm^2, the initial local differences on the coatings can be also recognized, however, the higher current density indicates a higher energy input, which spontaneously accelerates the process for coating formation confirmed by the slight increase of coating thickness. Furthermore, the resultant coating (600 s) formed under 10 A/dm^2 exhibits more smooth coating surface morphology compared to that of 5 A/dm^2. As a consequence, increasing the current density can be a good idea to quickly erase the coating differences at local areas, which is caused by the polymorph structure of the substrate and to produce a higher quality coating for potential applications.

5. Conclusion

This study revealed that the microstructure of Ti6Al4V alloy has an effect on the formation process of PEO coating in phosphate-based electrolyte. Different coating formation behavior was disclosed on α-Ti and β-Ti phases due to their different composition and heterogeneous electrochemical and chemical properties rather their different lattice structure. At the initial stage of PEO process, the oxygen diffusion caused a lattice expansion in α-Ti and a lattice transformation from bcc (β-Ti) to hcp structure before the formation of amorphous titanium oxide. The earliest discharges commenced at the layers on β-Ti phases and forming micro-pores with a sintered ring-like morphology. With increasing voltage/processing time, the discharges also developed further to the entire coating surface, however, only small-sized micro-pores were generated on the coating of α-Ti phases. The highly sintered morphology was found to form at the coating regions with higher content of vanadium (β-Ti phases), and also gradually expanded to the surroundings. The local difference of the coating is still visible even for the higher current density and the longest treatment (600 s). To reach a uniform surface coverage on the polymorph alloy it seems to be necessary to

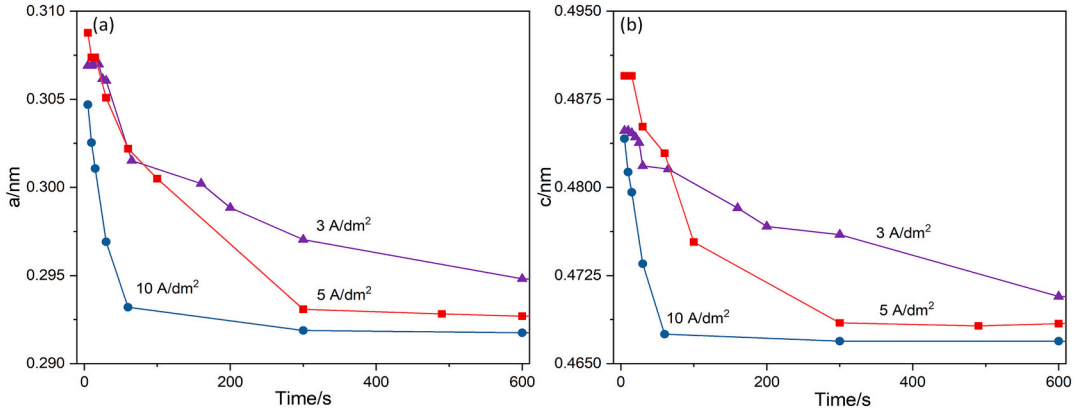

Fig. 17. α-Ti lattice expansion as the function of processing time.

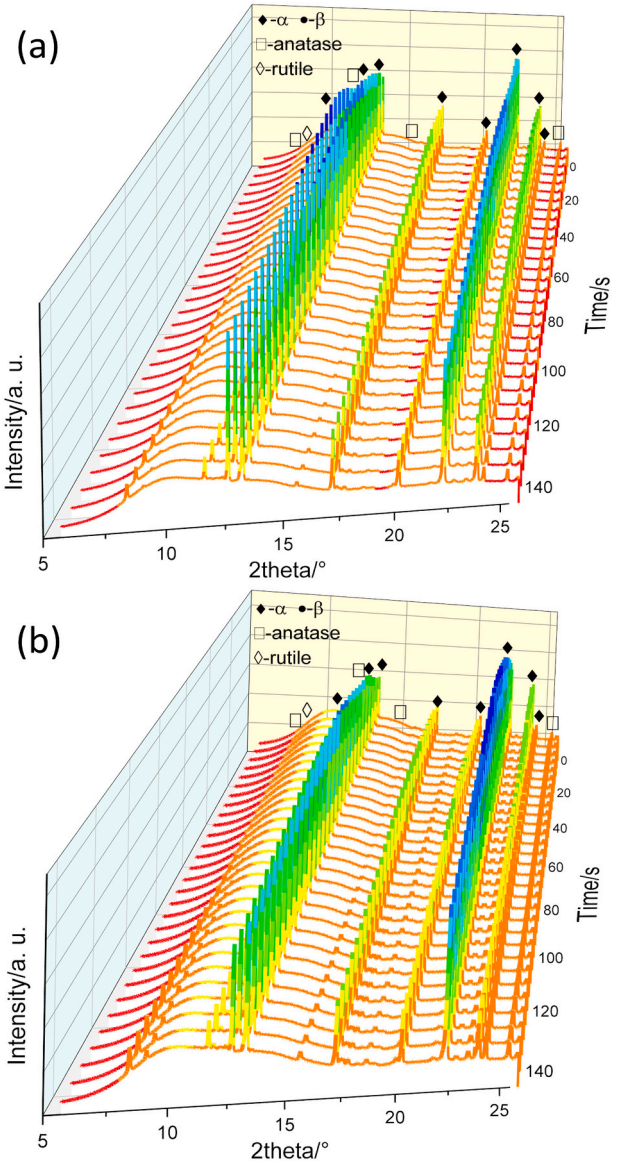

Fig. 18. Changes of phase composition (wavelength 0.0496 nm) on the surface of in-situ treated specimens with time when PEO treatment is off: (a) 5 A/dm^2 and (b) 10 A/dm^2.

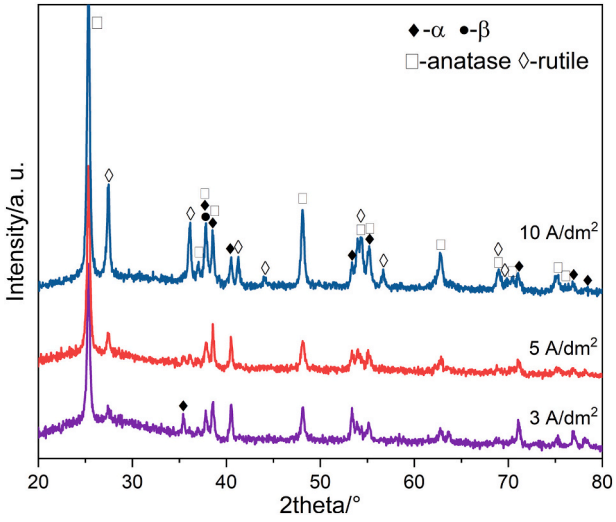

Fig. 19. Lab XRD patterns (wavelength 0.15406 nm) of specimens after in-situ treatment at 3, 5, and 10 A/dm^2.

either extent treatment time or further increase current density. Looking on the phase composition, in addition to amorphous phosphate/oxide, the PEO coating is mainly composed of anatase and rutile. At lower voltage, anatase is preferentially forming, but with increasing voltage and discharge energy, the ratio is shifting towards rutile. Interestingly the crystalline phase occurs mainly after the actual PEO processing by a precipitation from the amorphous oxide film formed during the PEO process.

CRediT authorship contribution statement

T. Wu – Visualization, Formal analysis, Investigation, Writing - Original Draft, Writing – review & editing.

C. Blawert – Conceptualization, Supervision, Writing – review & editing.

M. Serdechnova – Formal analysis, Visualization, Writing - Review & Editing.

P. Karlova – Investigation, Visualization, Writing - Review & Editing.

G. Dovzhenko – Investigation, Visualization, Writing - Review & Editing.

D. C. F. Wieland – Investigation, Writing - Review & Editing.

M. L. Zheludkevich – Supervision, Writing - Review & Editing.

Declaration of competing interest

The authors declare that they have no known competing financial interests or personal relationships that could have appeared to influence the work reported in this paper.

Acknowledgement

Ting Wu thanks China Scholarship Council for the award of fellowship and funding (NO. 201708510113). The technical support of Mr. Volker Heitmann, Mr. Ulrich Burmester during this work is gratefully acknowledged. We also thank PETRA III (Hamburg, Germany) for accepting and granting the proposals I-20191340 (P.03 end-station) and I-20210305 (P. 23 end-station) and Dr. Anton Davydok for technical support at the beamline for localized phase composition analysis of PEO layers.

References

[1] A.L. Yerokhin, X. Nie, A. Leyland, A. Matthews, S.J. Dowey, Surf. Coat. Technol. (1999) 21.
[2] R. Arrabal, E. Matykina, T. Hashimoto, P. Skeldon, G.E. Thompson, Surf. Coat. Technol. 203 (2009) 2207–2220.
[3] X. Lu, M. Mohedano, C. Blawert, E. Matykina, R. Arrabal, K.U. Kainer, M. L. Zheludkevich, Surf. Coat. Technol. 307 (2016) 1165–1182.
[4] T.W. Clyne, S.C. Troughton, Int. Mater. Rev. 64 (2018) 127–162.
[5] C. Blawert, W. Dietzel, E. Ghali, G. Song, Adv. Eng. Mater. 8 (2006) 511–533.
[6] T. Wu, C. Blawert, M.L. Zheludkevich, J. Mater. Sci. Technol. 50 (2020) 75–85.
[7] E. Matykina, R. Arrabal, P. Skeldon, G.E. Thompson, Electrochim. Acta 54 (2009) 6767–6778.
[8] T. Wu, C. Blawert, X. Lu, M. Serdechnova, M.L. Zheludkevich, J. Magnes. Alloys 9 (5) (2021) 1725–1740.
[9] X. Lu, C. Blawert, D. Tolnai, T. Subroto, K.U. Kainer, T. Zhang, F. Wang, M. L. Zheludkevich, Corros. Sci. 139 (2018) 395–402.
[10] S. Stojadinović, N. Radić, B. Grbić, S. Maletić, P. Stefanov, A. Pačevski, R. Vasilić, Appl. Surf. Sci. 370 (2016) 218–228.
[11] S. Stojadinović, R. Vasilić, M. Petković, B. Kasalica, I. Belča, A. Žekić, L. Zeković, Appl. Surf. Sci. 265 (2013) 226–233.
[12] A.V. Apelfeld, A.A. Ashmarin, A.M. Borisov, A.V. Vinogradov, S.V. Savushkina, E. A. Shmytkova, Surf. Coat. Technol. 328 (2017) 513–517.
[13] M. Sandhyarani, M. Ashfaq, T. Arunnellaiappan, M.P. Selvan, S. Subramanian, N. Rameshbabu, Surf. Coat. Technol. 269 (2015) 286–294.
[14] S. Stojadinović, N. Tadić, N. Radić, P. Stefanov, B. Grbić, R. Vasilić, Appl. Surf. Sci. 355 (2015) 912–920.
[15] S. Stojadinović, R. Vasilić, J. Alloys Compd. 685 (2016) 881–889.
[16] C. Blawert, S.A. Karpushenkov, M. Serdechnova, L.S. Karpushenkava, M. L. Zheludkevich, Appl. Surf. Sci. 505 (2020), 144552.
[17] A. Jangde, S. Kumar, C. Blawert, Corros. Sci. 157 (2019) 220–246.
[18] Q. Chen, Z. Jiang, S. Tang, W. Dong, Q. Tong, W. Li, Appl. Surf. Sci. 423 (2017) 939–950.
[19] I.-J. Hwang, H.-C. Choe, Appl. Surf. Sci. 432 (2018) 337–346.
[20] M. Mohedano, E. Matykina, R. Arrabal, B. Mingo, A. Pardo, Appl. Surf. Sci. 346 (2015) 57–67.
[21] G. Zhang, L. Wu, A. Tang, Y. Ma, G.-L. Song, D. Zheng, B. Jiang, A. Atrens, F. Pan, Corros. Sci. 139 (2018) 370–382.
[22] A. Castellanos, A. Altube, J.M. Vega, E. García-Lecina, J.A. Díez, H.J. Grande, Surf. Coat. Technol. 278 (2015) 99–107.
[23] T. Zehra, M. Kaseem, S. Hossain, Y.-G. Ko, Metals 11 (2021).
[24] D.V. Mashtalyar, K.V. Nadaraia, I.M. Imshinetskiy, S.L. Sinebryukhov, S. V. Gnedenkov, J. Magnes. Alloys (2021), https://doi.org/10.1016/j.jma.2021.07.020. In press.
[25] R. Arrabal, E. Matykina, F. Viejo, P. Skeldon, G.E. Thompson, Corros. Sci. 50 (2008) 1744–1752.
[26] D.V. Mashtalyar, I.M. Imshinetskiy, K.V. Nadaraia, A.S. Gnedenkov, S. L. Sinebryukhov, A.Y. Ustinov, A.V. Samokhin, S.V. Gnedenkov, J. Magnes. Alloys (2021), https://doi.org/10.1016/j.jma.2021.04.013. In press.
[27] Q. Li, J. Liang, B. Liu, Z. Peng, Q. Wang, Appl. Surf. Sci. 297 (2014) 176–181.
[28] Q. Luo, Q. Cai, X. Li, X. Chen, J. Alloys Compd. 597 (2014) 101–109.
[29] Q. Xia, D. Zhang, D. Li, Z. Jiang, Z. Yao, Surf. Coat. Technol. 369 (2019) 252–256.
[30] B. Mingo, R. Arrabal, M. Mohedano, A. Pardo, E. Matykina, Surf. Coat. Technol. 309 (2017) 1023–1032.
[31] R. Arrabal, E. Matykina, P. Skeldon, G.E. Thompson, Appl. Surf. Sci. 255 (2009) 5071–5078.
[32] Y. Chen, Y. Yang, W. Zhang, T. Zhang, F. Wang, J. Alloys Compd. 718 (2017) 92–103.
[33] J. Martin, A.V. Nominé, J. Stef, A. Nominé, J.X. Zou, G. Henrion, T. Grosdidier, Mater. Des. 178 (2019).
[34] C. Liu, T. Xu, Q. Shao, S. Huang, B. Jiang, J. Liang, H. Li, J. Alloys Compd. 784 (2019) 414–421.
[35] R.O. Hussein, X. Nie, D.O. Northwood, A. Yerokhin, A. Matthews, J. Phys. D. Appl. Phys. 43 (2010), 105203.
[36] R.O. Hussein, X. Nie, D.O. Northwood, Mater. Chem. Phys. 134 (2012) 484–492.
[37] A. Yerokhin, E.V. Parfenov, A. Matthews, Surf. Coat. Technol. 301 (2016) 54–62.
[38] X. Yang, L. Chen, Y. Qu, R. Liu, K. Wei, W. Xue, Surf. Coat. Technol. 324 (2017) 18–25.
[39] F. Gao, L. Hao, G. Li, Y. Xia, Appl. Surf. Sci. 431 (2018) 13–16.
[40] S.C. Troughton, A. Nominé, J. Dean, T.W. Clyne, Appl. Surf. Sci. 389 (2016) 260–269.
[41] Z.C. Oter, A.E. Gulec, Y. Gencer, M. Tarakci, Acta Phys. Pol. A 127 (2015) 1331–1335.
[42] Z.C. Oter, Y. Gencer, M. Tarakci, J. Alloys Compd. 650 (2015) 185–192.
[43] M. Tarakci, Mater. Charact. 62 (2011) 1214–1221.
[44] F. Xu, Y. Xia, G. Li, Appl. Surf. Sci. 255 (2009) 9531–9538.
[45] K.O. Gunduz, Z.C. Oter, M. Tarakci, Y. Gencer, Surf. Coat. Technol. 323 (2017) 72–81.
[46] X. Lu, C. Blawert, K.U. Kainer, M.L. Zheludkevich, Electrochim. Acta 196 (2016) 680–691.
[47] M. Niinomi, J. Mech. Behav. Biomed. Mater. 1 (2008) 30–42.
[48] C. Veiga, J.P. Davim, A.J.R. Loureiro, Rev. Adv. Mater. Sci. (2012) 133.
[49] S. Liu, Y.C. Shin, Mater. Des. 164 (2019).
[50] B. Song, S. Dong, B. Zhang, H. Liao, C. Coddet, Mater. Des. 35 (2012) 120–125.
[51] M. Fazel, H.R. Salimijazi, M.A. Golozar, M.R. Garsivaz Jazi, Appl. Surf. Sci. 324 (2015) 751–756.
[52] D. Dzhurinskiy, Y. Gao, W.K. Yeung, E. Strumban, V. Leshchinsky, P.J. Chu, A. Matthews, A. Yerokhin, R.G. Maev, Surf. Coat. Technol. 269 (2015) 258–265.
[53] S. Durdu, M. Usta, Ceram. Int. 40 (2014) 3627–3635.
[54] S.A. Adeleke, S. Ramesh, A.R. Bushroa, Y.C. Ching, I. Sopyan, M.A. Maleque, S. Krishnasamy, H. Chandran, H. Misran, U. Sutharsini, Ceram. Int. 44 (2018) 1802–1811.
[55] W.K. Yeung, G.C. Reilly, A. Matthews, A. Yerokhin, J Biomed Mater Res B Appl Biomater 101 (2013) 939–949.
[56] R.F. Zhang, L.P. Qiao, B. Qu, S.F. Zhang, W.H. Chang, J.H. Xiang, Mater. Lett. 153 (2015) 77–80.
[57] E. Matykina, R. Arrabal, B. Mingo, M. Mohedano, A. Pardo, M.C. Merino, Surf. Coat. Technol. 307 (2016) 1255–1264.
[58] J. Han, Y. Cheng, W. Tu, T. Zhan, Y. Cheng, Appl. Surf. Sci. 428 (2018) 684–697.
[59] Y. Cheng, Z. Peng, X. Wu, J. Cao, P. Skeldon, G.E. Thompson, Electrochim. Acta 165 (2015) 301–313.
[60] A. Baron-Wiecheć, M. Curioni, R. Arrabal, E. Matykina, P. Skeldon, G.E. Thompson, Trans. IMF 91 (2013) 107–112.
[61] C. Krywka, H. Neubauer, M. Priebe, T. Salditt, J. Keckes, A. Buffet, S.V. Roth, R. Doehrmann, M. Mueller, J. Appl. Crystallogr. 45 (2011) 85–92.
[62] J. Kieffer, D. Karkoulis, J. Phys. Conf. Ser. 425 (2013).
[63] V.S. de Viteri, R. Bayón, A. Igartua, G. Barandika, J.E. Moreno, C.P.-J. Peremarch, M.M. Pérez, Appl. Surf. Sci. 367 (2016) 1–10.
[64] J. Wang, J. Wang, Y. Lu, M. Du, F. Han, Appl. Surf. Sci. 324 (2015) 405–413.
[65] L.C. Campanelli, L.T. Duarte, P.S.C.P. da Silva, C. Bolfarini, Mater. Des. 64 (2014) 393–399.
[66] R.D. Shannon, J.A. Pask, J. Am. Ceram. Soc. 48 (1965) 8.
[67] J. Zhang, P. Zhou, J. Liu, J. Yu, Phys. Chem. Chem. Phys. 16 (2014) 20382–20386.
[68] M. Sowa, J. Worek, G. Dercz, D.M. Korotin, A.I. Kukharenko, E.Z. Kurmaev, S. O. Cholakh, M. Basiaga, W. Simka, Electrochim. Acta 198 (2016) 91–103.
[69] J. Baillieux, D. Poquillon, B. Malard, Philos. Mag. Lett. 95 (2015) 245–252.
[70] K.E. Wiedemann, R.N. Shenoy, J. Unnam, Metall. Trans. A. 18 (1987) 8.
[71] S. Andersson, B. Collén, U. Kuylenstierna, A. Magnéli, Acta Chem. Scand. 11 (1957) 12.
[72] J.L. Murray, H.A. Wriedt, J. Phase Equilib. 8 (1987) 18.
[73] Z.J. Liu, X. Zhong, H. Liu, I.L. Tsai, U. Donatus, G.E. Thompson, Electrochim. Acta 182 (2015) 482–492.
[74] T.A. Soares, H. Mozaffari, H. Reinecke, Surf. Coat. Technol. 278 (2015) 64–70.
[75] E. Matykina, J.M. Hernandez-López, A. Conde, C. Domingo, J.J. de Damborenea, M.A. Arenas, Electrochim. Acta 56 (2011) 2221–2229.

5.1.3. PEO of Ti6Al4V alloy in different electrolytes

Paper 3: Ting Wu, Carsten Blawert, Maria Serdechnova et al, Influence of electrolyte composition on PEO coatings of Ti6Al4V alloy, Applied Surface Science 595 (2022).https://doi.org/10.1016/j.apsusc.2022.153523

Graphical abstract

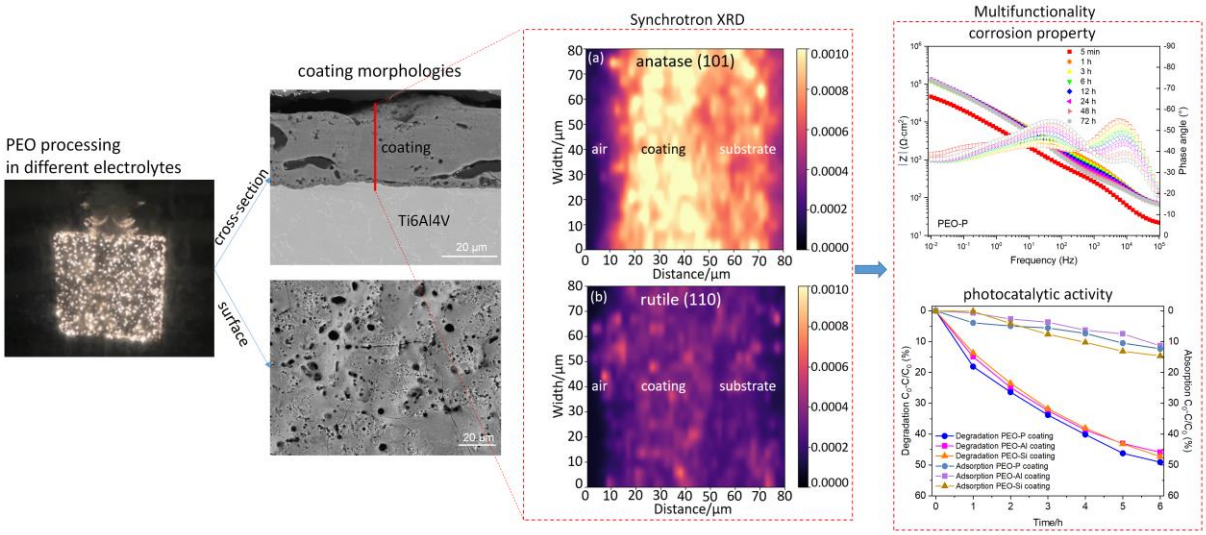

In paper *2*, the higher current density (10 A/dm^2 compared to 5 A/dm^2) produced a more uniform PEO coating on Ti6Al4V. Thus, a constant current density 10 A/dm^2 was used in paper *3*, to make a comparison of the coatings formation in different base electrolyte compositions. In addition, multifunctional coatings were produced, in combination with good corrosion resistance and photocatalytic activity. The most stable PEO process has been disclosed in the phosphate-containing electrolyte considering the ease of breakdown and the coating formation efficiency. Microstructure and elemental/phase composition of the different PEO coatings were evaluated. The PEO-P coating was mainly composed of anatase and rutile, however, there are Al_2O_3 and $TiAl_2O_5$ dominant in the PEO-Al coating and an amorphous silicate phase is detected in the PEO-Si coating. All coatings have shown noticeable corrosion resistance and semiconductive behavior. Moreover, in the photocatalytic measurements, MO degradation rates were higher than 45 % concerning all coatings, which indicates a good photocatalytic activities of the coatings.

Applied Surface Science 595 (2022) 153523

Contents lists available at ScienceDirect

Applied Surface Science

journal homepage: www.elsevier.com/locate/apsusc

Full Length Article

Role of phosphate, silicate and aluminate in the electrolytes on PEO coating formation and properties of coated Ti6Al4V alloy

Ting Wu [a,*], Carsten Blawert [a], Maria Serdechnova [a], Polina Karlova [a], Gleb Dovzhenko [b], D.C. Florian Wieland [c], Stevan Stojadinovic [d], Rastko Vasilic [d], Linqian Wang [a], Cheng Wang [a], Kristina Mojsilovic [d], Mikhail L. Zheludkevich [a,e]

[a] Institute of Surface Science, Helmholtz-Zentrum Hereon, Max-Planck Strasse 1, 21502 Geesthacht, Germany
[b] Institute of Materials Physics, Helmholtz-Zentrum Hereon, Max-Planck Strasse 1, 21502 Geesthacht, Germany
[c] Institute of Metallic Biomaterials, Helmholtz-Zentrum Hereon, Max-Planck Strasse 1, 21502 Geesthacht, Germany
[d] University of Belgrade, Faculty of Physics, Studentski trg 12-16, 11000 Belgrade, Serbia
[e] Institute for Materials Science, Faculty of Engineering, Kiel University, Kaiserstrasse 2, 24143 Kiel, Germany

ARTICLE INFO

Keywords:
Plasma electrolytic oxidation
Ti6Al4V
Corrosion resistance
Photocatalytic activity
Multifunctional coatings

ABSTRACT

A comparison of PEO layers on Ti6Al4V alloy formed in phosphate, aluminate and silicate-based electrolytes respectively, has been made to reveal the influence of the electrolyte composition on the formation process. The phosphate-based electrolyte has been identified as the most promising one as it has the best coating formation efficiency and the lowest breakdown voltage. On the bases of the microstructure and elemental/phase analysis of the different PEO coatings, it could be observed that the PEO coating formed in phosphate-based electrolyte is mainly composed of anatase and rutile. An amorphous phase is dominant in the coating produced in silicate-based electrolyte. Moreover, there are mainly γ-Al_2O_3, $Na_2Al_{2x}O_{3x+1}$ and $TiAl_2O_5$ present in the coating formed in the aluminate-based electrolyte. The coating formation process in silicate- and aluminate-based electrolytes is more dependent on the deposition originating from the electrolytes. All of the coatings have shown noticeable corrosion resistance and good performance in the photocatalytic test as the degradation rates of methyl orange higher than 45 %. Thus, multifunctional PEO coatings on Ti6Al4V alloy are obtained.

1. Introduction

Titanium alloys are currently in the focus of many applications. The interest for them arises due to the high specific strength and corrosion resistance, low elastic modulus and biocompatibility [1–4]. Various surface treatments have been widely used to introduce a thick and durable coating on the surface of titanium alloys, mainly to further improve their wear and corrosion protection [4–8]. In this respect, plasma electrolytic oxidation (PEO) as a surface modification process has a number of advantages, offering an attractive method for surface performance enhancement [9–11]. The relative high current densities necessary (especially for Al) processing resulting in high energy consumption and limited specimen sites are some drawbacks. Overall PEO is still an easy process to operate using nontoxic electrolyte. Thus, it can be considered a green alternative compared to many other treatments.

PEO coatings are produced to potentially extend the service life of titanium-based components under mechanical and tribological loads [12–15]. PEO coating formation process involves repeated dielectric breakdowns, in the form of discrete discharges commenced at the coating surface, once the applied voltage is higher than the threshold of breakdown [16–19]. This mechanism results in the production of thick, rough and adhesive coatings on titanium alloys [20–22]. In addition to the improvement of wear resistance and durability, the coatings are also attractive for photocatalysis and sensor applications [23–25] due to the presence of titanium oxides (TiO_2, gap bands around 3.05 eV) as a consequence of the substrate oxidation [23,26,27].

Recently, a wide range of studies have been conducted to prepare PEO coatings on titanium alloys in various electrolytes, in order to obtain multifunctional composite coatings for applications [28–31]. The addition of calcium acetate and calcium glycerophosphate resulted in the formation of hydroxyapatite-containing PEO coatings. It can not only improve the biocompatibility of titanium alloys [32–36], but also

* Corresponding author.
E-mail address: ting.wu@hereon.de (T. Wu).

https://doi.org/10.1016/j.apsusc.2022.153523
Received 7 February 2022; Received in revised form 14 April 2022; Accepted 27 April 2022
Available online 30 April 2022

avoid the release of harmful metal ions, eg. Al^{3+}, from the Ti based implant substrates into the body fluids [35,36]. The PEO coating on pure titanium doped with Eu^{3+} through the addition of Eu_2O_3 powder into phosphate-containing electrolyte was also studied [26]. It was found that Eu^{3+} ions are incorporated into TiO_2 lattice and, thus, Ti 2p spin–orbit components in the composite coatings were shifted towards higher binding energy compared to pure TiO_2-based coatings. Furthermore, these composite coatings showed much higher photocatalytic activity. In order to improve the wear resistance of PEO coatings on Ti6Al4V alloy, Al_2O_3 particles were added to a mixed silicate-aluminate electrolyte [37]. Al_2O_3 particles were reported to fill the micro-pores of the coating and reduce the friction coefficient of the layer. In addition, the formation of an Al_2TiO_5 phase was seen, which has a high thermal stability and improves the high-temperature wear resistance of the coating.

It is quite obvious that the electrolyte composition has a significant effect on the PEO process and the phase composition of the coatings; consequently, the properties of the coatings can be altered. Among different PEO electrolytes, phosphate, silicate and aluminate are typically the main composition, respectively [13,28,38]. The addition of aluminate resulted in the precipitation of aluminum hydroxide and further thermochemical processes occurred during the formation of PEO coatings, resulting in the formation of oxide mixture (Al_2TiO_5) [38]. Al_2TiO_5 in the PEO coatings is a good candidate for engineering ceramics characterized by prominent thermal expansion coefficient, high melting temperature and low thermal conductivity [39]. However, the phosphate/silicate in the electrolytes did not introduce any crystalline phosphorous/silicon containing phase in the coatings on Ti based materials [28,40]. Nevertheless, the amorphous phosphate/silica was identified and the incorporation of silicon and phosphorous in the coating is reported positive to the biocompatibility [10]. Moreover, the coatings formed in phosphate-based electrolyte showed larger micropores in comparison to the silicate-based electrolyte, due to the higher sparking voltage and thus the higher level of discharge energy [41]. In terms of the coating formation species, only amorphous phosphate and silicate/SiO_2 were identified in addition to anatase and rutile [20,41]. However, In order to produce multifunctional PEO coatings on titanium alloys, it is necessary to have a clear understanding in the influence of different electrolytes of the PEO process, and final properties of the coatings. Thus, the intention of the present study is to study the influence of electrolyte composition on PEO coatings, including the morphologies, microstructures and phase composition. For this, PEO coatings on Ti6Al4V alloys in different electrolytes containing phosphate, aluminate and silicate, respectively, are produced and systematically investigated. The corrosion degradation and the photocatalytic activity of the coatings are measured to understand the influence of electrolyte on the coating performance.

2. Experimental

Ti6Al4V alloy (7.564 wt% Al, 2.809 wt% V, 0.097 wt% Mn, 0.182 wt % Fe, 0.102 wt% Ge, 0.104 wt% Nb, 0.108 wt% Sn, 0.574 wt% Ta, Ti balance) with the size of 20 mm × 16 mm × 4 mm was selected as working anode subjected to the PEO processing. A DC power source with a pulsing unit was used to provide pulses with a duty cycle of 10 % and a frequency of 100 Hz. A constant current density of 10 A/dm^2 was applied. The stainless steel tube of the cooling system was used as a cathode. The temperature of the electrolyte was kept stable at 20 ± 2 °C. Three different electrolytes based on phosphate (containing Na_3PO_4 20 g/L and KOH 1 g/L, pH 12.72, conductivity 529 μS/cm), aluminate (containing $NaAlO_2$ 20 g/L and KOH 1 g/L, pH 12.49, conductivity 520 μS/cm) and silicate (containing Na_2SiO_3 20 g/L and KOH 1 g/L, pH 12.29, conductivity 496 μS/cm) were prepared. The treatments were carried out for 600 s. Magnetic stirring was used to agitate the electrolyte, to keep it homogeneous and avoid temperature gradients. The coatings produced in phosphate-, aluminate- and silicate-based electrolytes were labeled as PEO-P, PEO-Al and PEO-Si coatings, respectively. It should be noted that due to strong burning of the coating in silicate-base electrolyte, the voltage was set to 350 V maximum under this condition. A data acquisition system (SignaSoft 6000 software package, Gantner, Germany) was used to record the voltage response as a function of processing time.

The coating surface and cross-sectional morphology was analyzed using a scanning electron microscope (SEM, TESCAN Vega3 SB), equipped with an energy dispersive spectrometer system (EDS, eumeX IXRFsystems) to assess the elemental composition of the coatings. Further observation of surface morphology and evaluation of surface roughness (Ra, arithmetical mean roughness, ISO 4287, Sa, arithmetical mean height and Sdr, developed interfacial area ratio, ISO 25178) of the coatings was evaluated through a laser scanning confocal microscope (LSM 800, ZEISS) and analyzed by the surface imaging and analysis software ConfoMap® ST. The coating thickness was measured adopting a microprocessor coating thickness gauge (MiniTest 2100, ElektroPhysik), with an additional validation by SEM cross-section observations.

The crystalline phase composition of the substrate and the coatings were examined using X-ray diffraction (XRD, D8 Advance, Bruker AXS) with Cu K_α radiation at the diffraction angle 2θ range between 20° and 80°. The following settings were applied: a step size of 0.02° and an accumulation time of 1 s. A range of grazing angles from 0.5° to 13° were used to evaluate the depth of phase composition variation of the coatings.

To map the phase composition across the PEO coating thickness, scanning X-ray diffraction at the P03, PETRA III, Deutsches Elektronen-Synchrotron (DESY, Hamburg, Germany) was performed. The nano focus end station of the beamline P03, which is operated by Helmhotz Zentrum Hereon had a X-ray beam size of 1.5 by 1.5 μm, an energy of 19.7 KeV, an Eiger 9 M detector with a pixel size of 75 μm by 75 μm. The beam was stepwise scanned across a surface area of 80 × 80 μm, with a stepwise of 2 μm in vertical and 4 μm in horizontal direction respectively. The acquisition time for each XRD pattern was 0.5 s. The data was reduced through employing in-house developed Matlab® and Python code and the PyFAI [42] routine. The scattering angle 2θ of the diffraction patterns with the original wavelength of 0.9537 Å was converted to the wavelength of 1.5406 Å, equal to Cu K-alpha radiation used in lab XRD to simplify the comparison. The diffraction patterns were used to reveal the phase composition/distribution across the coating thickness.

Atomic emission spectroelectrochemistry (AESEC) measurements (coupled atomic emission spectroscopy measurements with electrochemical investigations) were used to provide a direct analysis of elemental dissolution rates of the PEO coated specimens and bare Ti6Al4V alloy during electrochemical testing [43–45]. The selected AESEC set-up is illustrated in Fig. 1.

A three-electrode electrochemical flow cell (Fig. 1(a)) was connected to an ICP-OES (Inductively Coupled Plasma-Optical Emission Spectrometry) machine from Spectro Ametek (Acros II FHX22), in radial plasma observation mode, with a flow rate of ca. 2 mL/min (Fig. 1(b)). The specimens were acting as a working electrode with an exposed surface area of 0.5 cm^2 to Ringer's solution (8.6 g/L NaCl, 0.3 g/L KCl and 0.56 g/L $CaCl_2{\cdot}6H_2O$) and connected to a computer controlled Gamry potentiostat Interface 1010E (Fig. 1 (c)). The counter and the reference electrode were a Pt wire and a saturated Ag/AgCl electrode, respectively. After 1000 s immersion at open circuit potential, potentiodynamic polarization (PDP) scans were started from −1.0 V vs reference electrode at a scan rate of 0.5 mV/s and terminated at 10 V.

The electrochemical impedance spectroscopy (EIS) experiments were also performed to evaluate corrosion behavior over time. Firstly, the EIS measurements versus open circuit potential (OCP) were carried out with an AC amplitude of 10 mV RMS over the frequency range of 100 kHz – 0.01 Hz in Ringer's solution after subsequent immersion durations of 5 min, 1 h, 3 h, 6 h, 12 h, 24 h, 48 h, and 72 h, respectively.

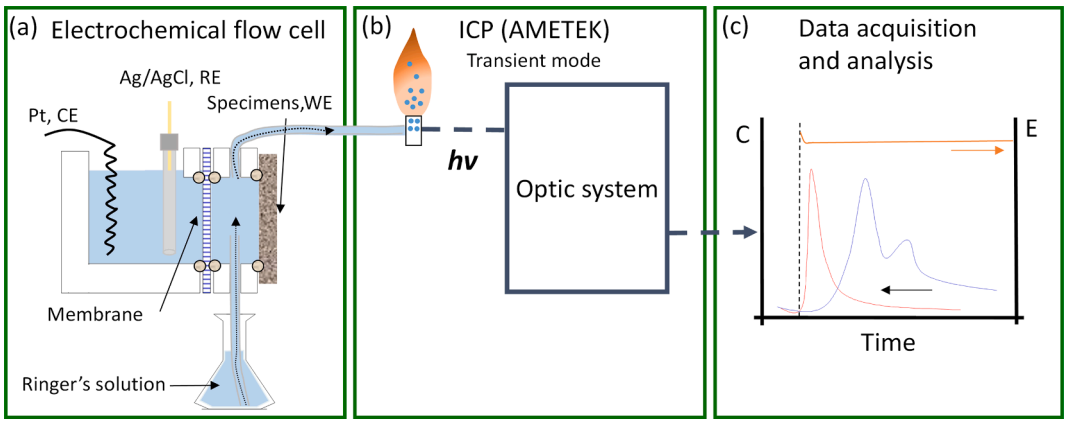

Fig. 1. Diagram of atomic emission spectroelectrochemistry (AESEC) set-up.

After that, in order to analyze the semiconductive property of TiO_2, additional EIS measurements were performed under the same condition, however, versus different potentials in the range from −0.4 V to 0.4 V versus open circuit potential in 0.1 V increments. Under the potential bias, the capacitance response is assumed to be modulated if the electrochemical response is influenced by the semiconductive behavior of the coating due to the formation of a space charge region at the layer/electrolyte interface [46]. The same three-electrode cell system was used and a specimen surface area of 0.5 cm^2 was exposed to the corrosive solution. The same measurement was reproduced on three specimens of each PEO treatment condition for repeatability.

The photocatalytic activity of bare and PEO coated Ti6Al4V alloy were evaluated via photodegradation measurements of methyl orange (MO). The temperature in the photoreactor was kept at room temperature by a water recirculation system. The specimen was placed on a perforated holder and then immersed in a 10 mL aqueous solution containing, 8 mg/L MO under constant stirring (300 rpm) and exposed to the irradiation source. Prior to the measurement, MO solution was firstly tested for photocatalysis in the absence of the PEO layers to confirm its stability. Then, the solutions were stirred in the darkness for 30 min with the presence of bare and coated Ti6Al4V alloy, respectively to achieve adsorption–desorption equilibrium before initiating the irradiation. A lamp (Osram Vitalux 300 W) was used to simulate the solar radiation providing 16,000 lx intensity, and it was fixed at 25 cm above the surface of the solution. In total, six hours of irradiation duration was selected. An Agilent Cary 60 UV–Vis spectrophotometer was applied to measure the MO concentration at the maximum of the absorption spectra ($\lambda = 464$ nm) for every hour by taking a fixed quantity of 1 mL MO solution from the photocatalytic reactor. Additional measurement of MO adsorption in darkness was also performed with the duration of six hours. The tested solution was returned to the photocatalytic reactor after each measurement. The absorption was converted to concentration based on a standard curve exhibiting a linear dependence between MO concentration and absorption at 464 nm wavelength. A change of MO concentration was absent after 6 h of irradiation without PEO treated specimen, indicating that MO stability and the observed degradation should result only from the presence of a photocatalyst under the applied condition. The degradation and adsorption rate of MO was given as $((C_0\text{-}C)/C_0)$, where C_0 was the initial MO concentration and C was the tested MO concentration after increasing exposure duration.

3. Results

3.1. PEO process

The voltage responses as a function of PEO processing time of Ti6Al4V alloy in different electrolytes are shown in Fig. 2. Due to a

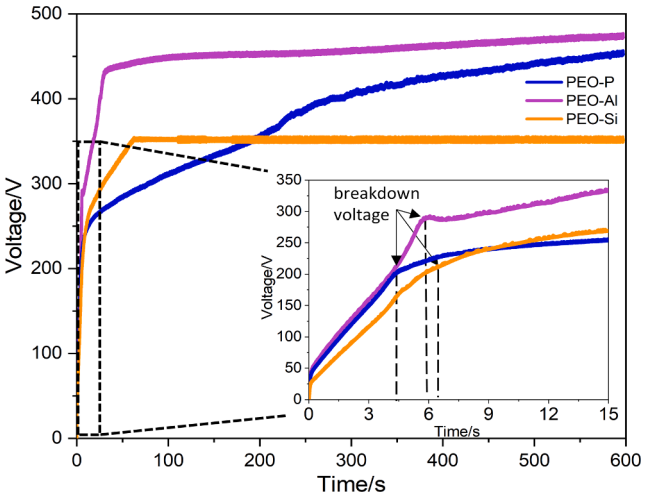

Fig. 2. Voltage response as a function of treatment time in phosphate- aluminate- and silicate-based electrolytes.

severe burning phenomenon at later stage of processing under a current density of 10 A/dm^2, the process in silicate-based electrolyte was operated under different current and voltage control condition. The process began with the pre-set current density of 10 A/dm^2, but with reaching 350 V, the voltage control was enabled and the voltage kept at 350 V while the current density was dropping until the end of processing.

In the first stage, the voltages are ramping linearly at a similar speed (ca. 45 V/s) in the phosphate- and aluminate-based electrolytes, while the increase rate is ca. 32 V/s in silicate-based electrolytes. The breakdown threshold of initial gas and/or conversion layer in the phosphate- and silicate-based electrolytes occurs at ca. 190 V, which is much lower than in the aluminate-based electrolyte, where the breakdown voltage is reached at ca. 290 V. There is around 1 s delay for the observation of tiny shining discharges on the specimens after the onset of breakdown. In the second stage, the surface of specimens was characterized by a growing size of discharges, also leaving an impression of more stationary discharges in comparison to the fast moving discharges on the surface of Mg and Al substrates observed previously [16,17]. The voltage increases further, though the voltage ramp is not as steep as it in the beginning. This stage only sustains until ca. 40 s in aluminate-based electrolyte, with a reduced voltage ramp rate of ca. 4.3 V/s. However, in the phosphate-based electrolyte, this period of the process continues to ca. 250 s with an average voltage increase of ca. 0.8 V/s. Since the voltage reaches the pre-set voltage limit of 350 V (ca. 2.6 V/s) in the silicate-based electrolyte at this stage, the next stage is not reached anymore.

Nevertheless, the third stage can be still distinguished in the other two conditions by even slower voltage ramps and an altered appearance of discharges with larger sizes. This stage remains relatively stable until the end of the processing time and reaches final voltages of 450 V (0.2 V/s) and 475 V (0.07 V/s) for the phosphate- and aluminate-based electrolytes, respectively.

3.2. Surface and cross-sectional morphology of PEO coatings

Figs. 3 and 4 shows the surface and cross-sectional morphologies of the coatings prepared in different electrolytes for 600 s. The highest thickness is revealed for PEO-P coating ca. 25 μm, and ca. 11 and 5.3 μm for PEO-Al and PEO-Si coatings in Fig. 4, respectively. The lowest coating thickness of the PEO-Si coating is most likely the consequence of the controlled energy input with reduced current density due to the voltage restriction to 350 V. As a consequence, the current dropped to 1.5 A/dm^2 at the end of the treatment in the silicate-based electrolyte. The surface and cross-sectional morphologies show that the coatings have a large amount of micro-pores, left behind from the discharges due to the fast solidification of melted coating materials and gas inclusion [47,48]. Nevertheless, distinguishable coating morphologies can be noticed for the different electrolyte composition. The PEO-P coating (Fig. 3(a)) contains more large-sized micro-pores of ca. 10 μm in diameter and some segregations of tiny nano-pores are distributed randomly, reaching a total porosity of 6.72%, based on the surface area covered by open micro-pores. In comparison, the coating surface of the PEO-Al coating (Fig. 3(b)) shows clusters of small particles surrounding the micro-pores (ca. 5 μm) on the coating surface, showing a total porosity of 12.59%. This can be a reason for the higher Sdr value (141.308%) for PEO-Al coating as compared to that of PEO-P coating (63.735%), indicating the more contribution of additional surface area of the measured area to the surface morphology. There is an exception for the surface roughness of PEO-Si coating due to the same reason as for the lowest coating thickness. Consequently, the PEO-Si coating shows the most compact morphology with the smallest micro-pores (ca. 2 μm) and lowest porosity of 2.31%, since the thickness is only a few micrometers. Blawert et al. [49] have suggested the healing effect of potentiostatic control mode when applied to a PEO treatment of zinc, which could obviously improve the quality of PEO coatings. Similarly, in the silicate-containing electrolyte, the current-control at the beginning of the processing stimulates the coating growth. Afterwards, when the voltage reaches the pre-set 350 V, the maintained voltage and dropping current moderates the intensity of discharges, which can heal the weaker locations of the coating and further prevent the formation of destructive higher intensity discharges.

The elemental composition of the coatings evaluated by EDS surface

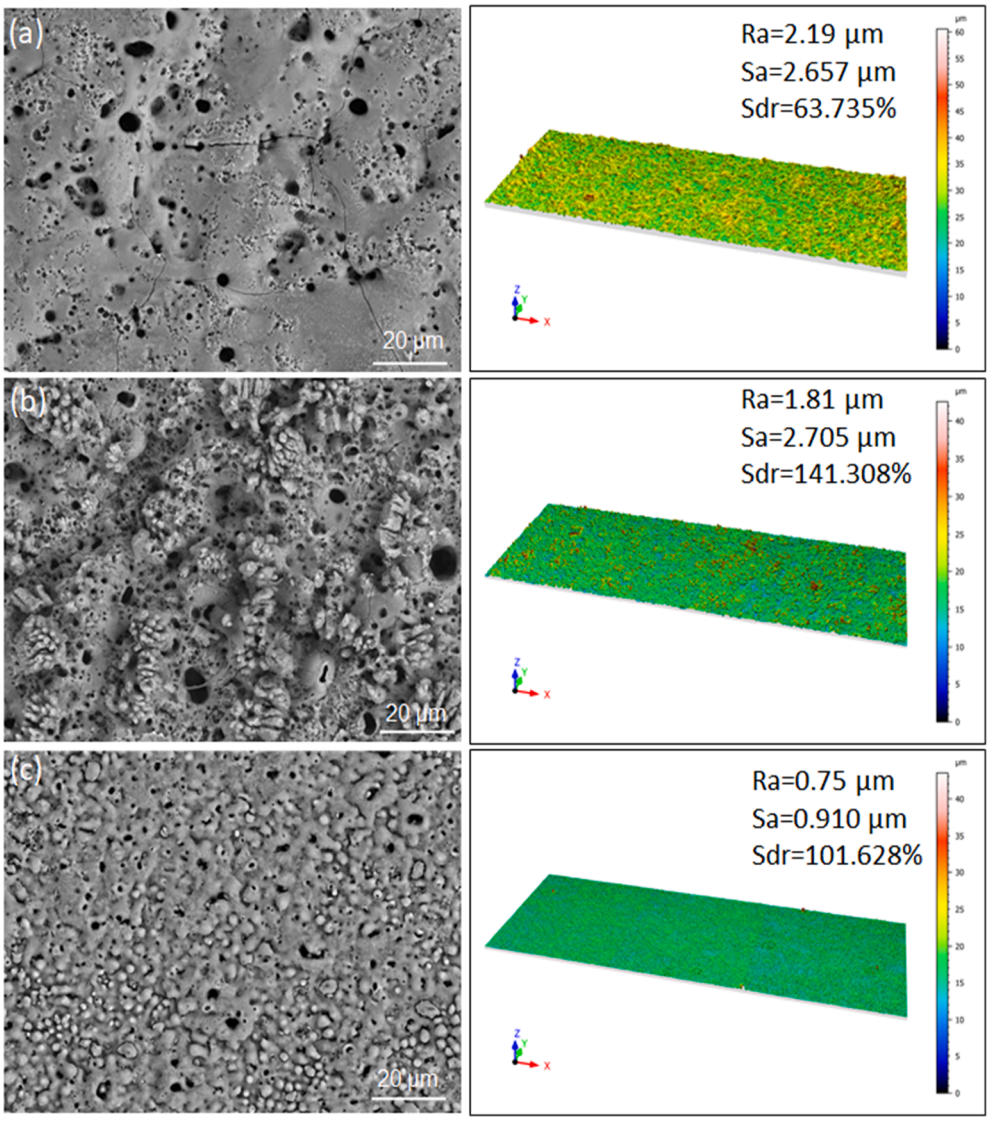

Fig. 3. Surface morphology of (a) PEO-P coating, (b) PEO-Al coating and (c) PEO-Si coating.

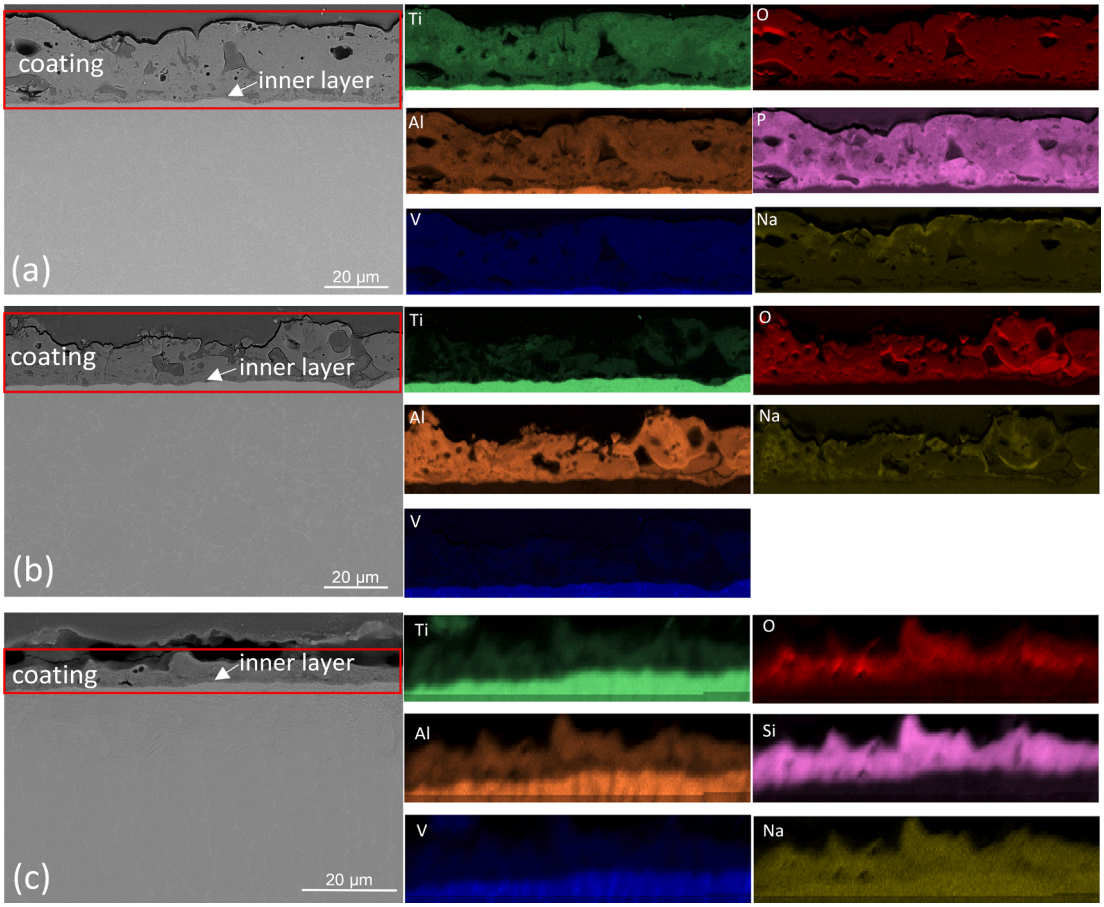

Fig. 4. Cross-sectional morphology and elemental mapping of (a) PEO-P coating, (b) PEO-Al coating and (c) PEO-Si coating.

mapping is displayed in Table 1. It is clear that the main coating formation elements are different due to the change of electrolyte composition. The PEO-P coating is composed of the highest levels of titanium and oxygen, however relatively lower contents of titanium for the PEO-Si coating and the PEO-Al coating were detected. The PEO-Al coating has a quite high level of aluminum with an average of 45 at.%, and only ca. 5 at.% of titanium. A higher content of Si (ca. 33 at.%) and ca. 11 at. % titanium were measured in the PEO-Si coating. It can be concluded that increased surface deposition of electrolyte phases from aluminate- and silicate-based electrolytes occur, while for the phosphate-based electrolyte, the deposition is less dominant and the primary phase is titanium oxide, generated from the substrate. The cross-sectional distribution of elements in Fig. 4 also confirms the significant deposition of Al and Si in the PEO-Al and PEO-Si coating s, respectively.

3.3. Phase composition and distribution of PEO coatings in different electrolytes

Fig. 5(a-c) presents a series of XRD patterns for each PEO coating using different grazing angles from 0.5 ° to 13 °. Near the coating surface (0.5 °), the intensity of all peaks is apparently low for all the coatings. It is correlated to the discharges and the resulting volcano-like morphology that are increasing the surface roughness, and thus the intensity of diffraction reduces. Fig. 5(a) illustrates that the phase composition (anatase and rutile) of the PEO-P coating does not show obvious change across the coating thickness. Nonetheless, one can find evident diffraction peaks of the substrate even at a grazing angle of 2° for PEO coated specimens in aluminate- and silicate-based electrolytes (Fig. 5(b) and (c)), indicating the penetration of X-rays through the coating into the substrate. The much stronger signal from the substrate compared to the PEO-P coating is explained by the lower thickness of PEO-Al and PEO-Si coating compared to the PEO-P coating since the α-Ti intensity decreases at the same incident angle with the coating thickening. In the two theta range of 20 – 30 °, a bump can be recognized and associated with an amorphous silicate phase since a high concentration of silicon in the PEO-Si coating was measured by EDS, but no crystalline Si containing phases are detected. Furthermore, the PEO-Si coating consists of similar crystalline phases as the PEO-P coating, anatase and rutile, however, the intensity of them is much lower compared to the substrate due to the lowest coating thickness (Fig. 4(c)). For the PEO-Al coating, the main phases are Al_2TiO_5 (a mixture of TiO_2 and Al_2O_3), γ-Al_2O_3 and $Na_2Al_{2x}O_{3x+1}$. No separate crystalline titanium oxide was observed in the coating, demonstrating the significant contribution of aluminate from electrolyte in the coating formation process, also in a good agreement with the EDS results.

Furthermore, two-dimensional scanning X-ray diffraction was

Table 1
Average content (at. %) of main coating formation elements on the surface of three different PEO coatings.

	Ti	Al	V	O	P	Si	Na	K
PEO-P	26.15 ± 1.25	2.05 ± 0.14	0.33 ± 0.03	54.52 ± 0.55	11.73 ± 1.11	–	4.87 ± 0.33	0.39 ± 0.05
PEO-Al	4.79 ± 0.04	45.38 ± 0.31	0.13 ± 0.02	47.06 ± 0.27	–	–	2.57 ± 0.08	0.35 ± 0.03
PEO-Si	11.38 ± 0.14	2.53 ± 0.07	0.12 ± 0.01	51.76 ± 0.65	–	33.35 ± 0.52	0.67 ± 0.06	0.19 ± 0.01

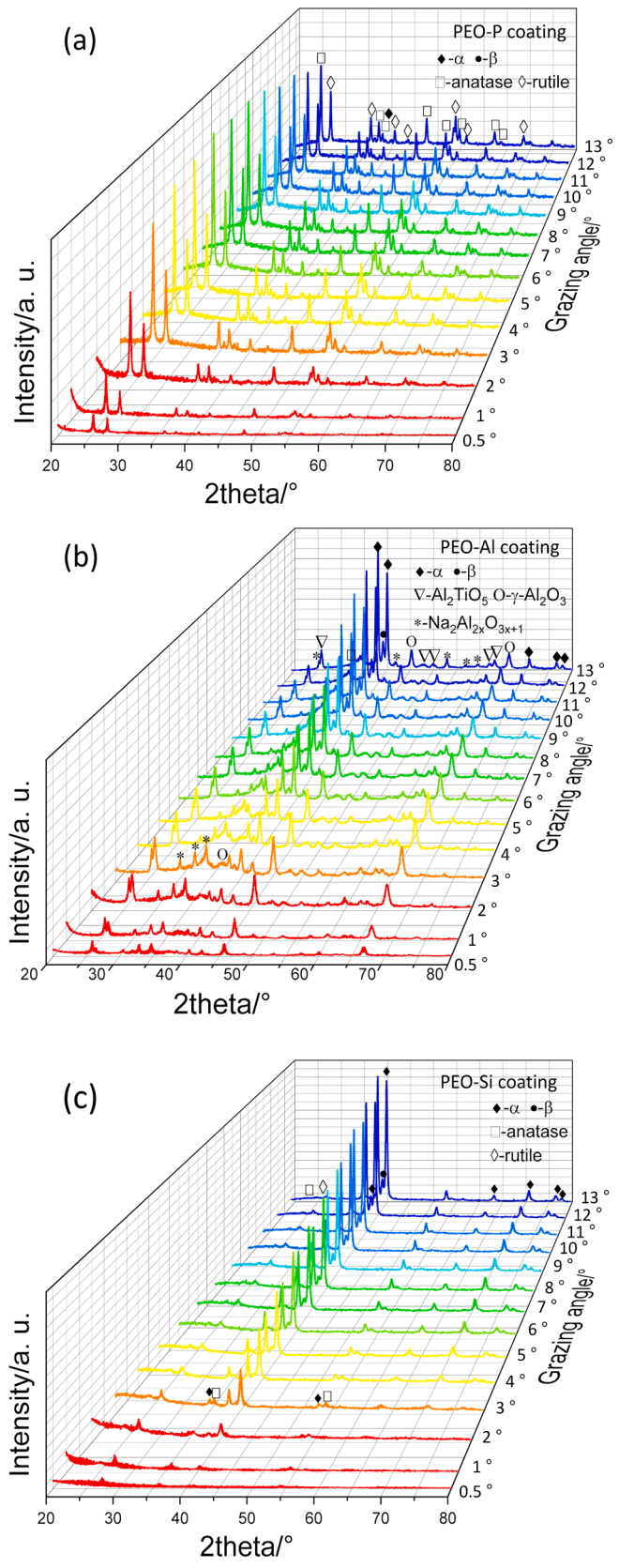

Fig. 5. XRD patterns of (a) PEO-P coating, (b) PEO-Al coating and (c) PEO-Si coating.

performed at P03 (DESY) to further analyze the spatial phase distribution across the coating thickness with a scan area of 80 × 80 μm. Fig. 6 displays two-dimensional maps of the intensity distribution of specific diffraction peaks across the coating thickness. The coating/substrate interface is well-defined by the different intensity of α-Ti (1 0 1) in the substrate and coating regions. Consistent with the lab XRD (Fig. 5), the results show that anatase and rutile are the main crystalline phases in the PEO-P and PEO-Si coatings. However, their intensity in the PEO-P coating is still much higher than in the PEO-Si coating. Moreover, in the thicker PEO-P coating, enrichment of anatase can be noticed in the outer layer (Fig. 6(b)), but such observation is not found for rutile (Fig. 6 (c)). The PEO-Si coating shows a similar thickness about 5 μm compared to the thickness measurements from thickness gauge and cross-section observation. However, the PEO-P coating (higher than 30 μm) appears to be thicker than measured from thickness gauge or SEM cross-sections, which can be caused by the higher roughness of coating surface and coating/substrate interface. Furthermore, a technical artifact, that specimen could not be perfectly placed horizontally thus being slightly tilted during DESY measurement, enlarged the beam penetrated coating area. For PEO-Al specimen, apart from a clear interface between coating/substrate, Fig. 6(d) shows that the interface appears extremely smooth and flat in comparison to the other two specimens (Fig. 6(a) and (h)). In correlation with the main phase/elemental compositions of PEO-Al coating (Table 1 and Fig. 5 (c)), it can be confirmed that the formation of the PEO-Al coating significantly happens via a deposition originated from the electrolyte rather than an oxidation of the substrate. The three main coating forming phases, Al_2TiO_5, γ-Al_2O_3 and $Na_2Al_{2x}O_{3x+1}$, are distributed mainly at the inner, intermediate and outer layers respectively (Fig. 6(e-g)). It reveals the enrichment of different phases at different depths of the coating, which is correlated with different dominant coating formation reactions across the coating thickness. At the outer and intermediate layers, the deposition from the electrolyte is essential (γ-Al_2O_3 and $Na_2Al_{2x}O_{3x+1}$); however, the sintering process between Al_2O_3 and TiO_2 is stronger at the inner layer and even penetrates into the substrate (Fig. 6(f)).

3.4. Dissolution measurement of bare and PEO coated Ti6A4V alloy

AESEC experiments are applied in order to verify whether any elemental dissolution either from PEO layer or from substrate during spontaneous corrosion can be detected. Firstly, the detection limits (DLs) of main involved elements were determined (Table 2). DLs are defined as 2 * (standard deviation) in the units of calibration standard (μg/L) at the respective wavelength.

Since titanium is a very corrosion resistant material, one can see in Fig. 7 that no dissolution of Ti from PEO-coated specimens is detectable. However, careful analysis of bare Ti6Al4V spontaneous corrosion shows a clear trend of titanium concentration increase in the electrolyte, but still staying within detection limit range. This can be related to the different surface microstructure of the bare alloy compared with the PEO coated ones. It is well known that the PEO coatings have a large amount of defects, especially micro-pores, flaws and micro-cracks. These defects could significantly trap the dissolved Ti and further impede the release of Ti into corrosion solution. However, there is only a semi-barrier layer on the bare alloy, which does not have such an amount of defects. As a result, the higher concentration of Ti was detected for bare alloy. Dissolution of all other analysed elements stays below the detection limit. Simultaneous measurements of corrosion potentials for all specimens were performed. Bare Ti6Al4V alloy has demonstrated a significantly different average OCP value of −0.4 V, compared to PEO-Al coating of 0.57 V, PEO-P coating of 0.61 V and PEO-Si coating of 0.3 V. In other words, one can expect more active surface of bare substrate in comparison with PEO treated specimens.

The analysis of elements was also carried out for both bare and PEO-treated systems during PDP measurements, as seen in Fig. 8. One should notice that there is potentially a strong IR drop effect since the presence

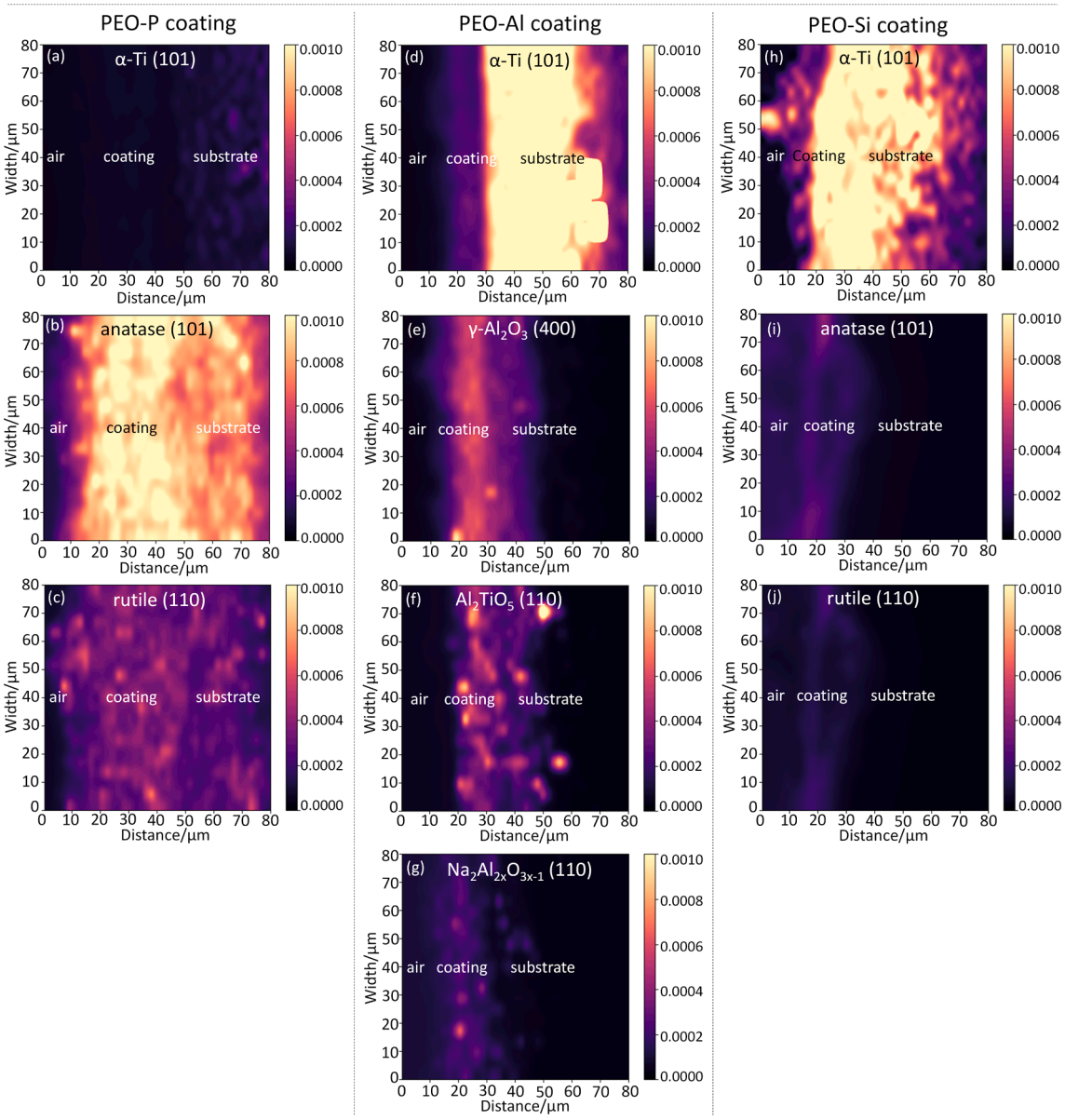

Fig. 6. Phase distribution across PEO coating thickness measured at P03 (DESY): (a) PEO-P coating, (b) PEO-Al coating and (c) PEO-Si coating.

Table 2
The detection limits of main coating formation elements.

Element	Titanium	Vanadium	Aluminium	Silicon	Phosphorus
Wavelength, nm	334.94	309.31	167.08	251.61	178.29
DL, μg/L	4.0	1.5	4.0	10.5	22

of a membrane with a certain resistance in the between of the reference and working electrodes. Clear passive behaviour of bare and PEO coated Ti6Al4V specimens in the potential range between 0 and ca. 8 V vs Ag/AgCl is visible. For bare Ti6Al4V the breakdown of the passive oxide layer takes place at 8.86 V. After that, a fast increase of anodic current happens. Using an in situ cell, connected to ICP, we have determined the main elements, titanium, aluminium and vanadium, released to the electrolyte at the moment of breakdown in Fig. 9(a) and their ratio is illustrated in Fig. 9(b). Unfortunately, only very narrow range of potential can be used for this analysis, since the significant dissolution of elements rapidly leads to a fast saturation of emission lines during measurements. From the calculated values, one can see that the average amount of aluminium and vanadium is higher in corrosive electrolyte than substrate material (Al: 8.4 wt% vs. 7.564 wt% in the substrate and V: 7.7 wt% vs. 2.809 wt% in the substrate). The high dissolution level of aluminium can be explained in the way of selective dissolution of α-Ti phase, in which aluminium dissolves more rapidly than titanium. The α-Ti phase contains a higher aluminium content of 8.1 ± 0.3 wt%, correlating to the detection of 8.4 wt% of aluminium dissolved during PDP test. Regarding the higher dissolution level of vanadium, it could be assigned to the preferential dissolution of β-Ti phase (11.4 ± 0.6 wt% vanadium) compared to α-Ti [50,51].

During PDP measurements, breakdown is also reached for the PEO-Si treated sample, but not for the PEO-Al and PEO-P systems. This can be explained in a way that the barrier property of PEO-Si coating is lower in comparison to the other layers, relating to the lower thickness as revealed from cross-sectional observations. Furthermore, during the PEO treatment silicates can participate in the formation of an amorphous barrier oxide-based layer, making it less resistant to corrosion due to the decreased dielectric property compared to pure TiO_2 film [52]. However, Si is not detected within the detection limitation using ICP

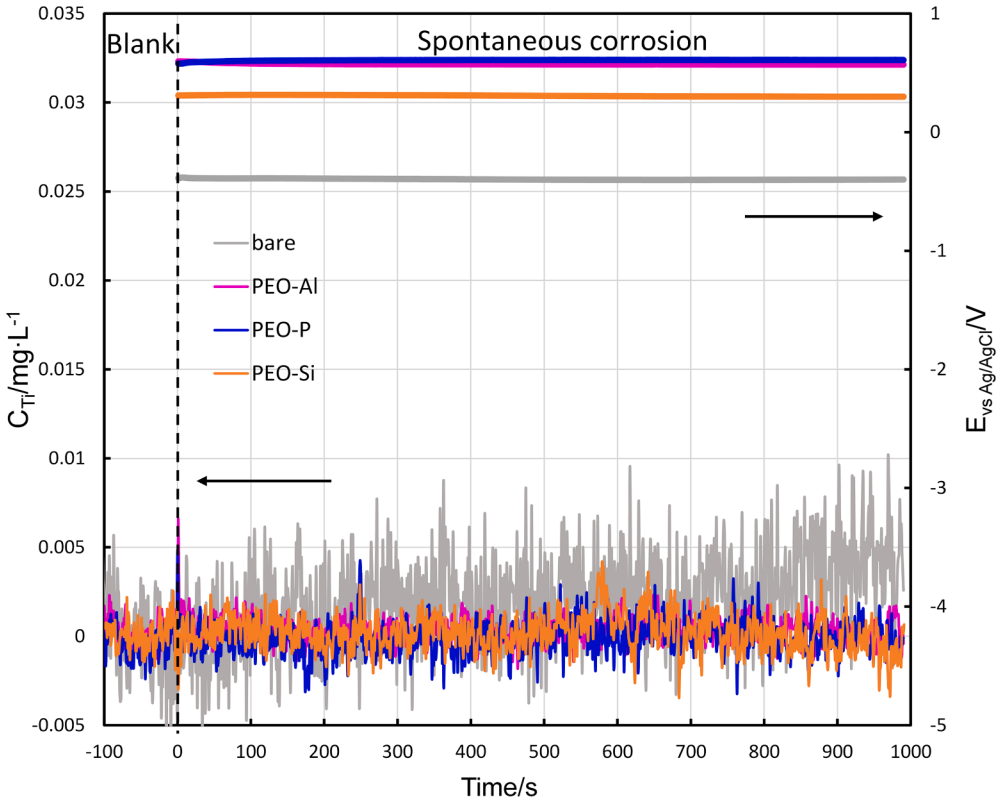

Fig. 7. Spontaneous corrosion of bare and PEO treated Ti6Al4V: OCP and titanium concentration in the electrolyte as a function of immersion time.

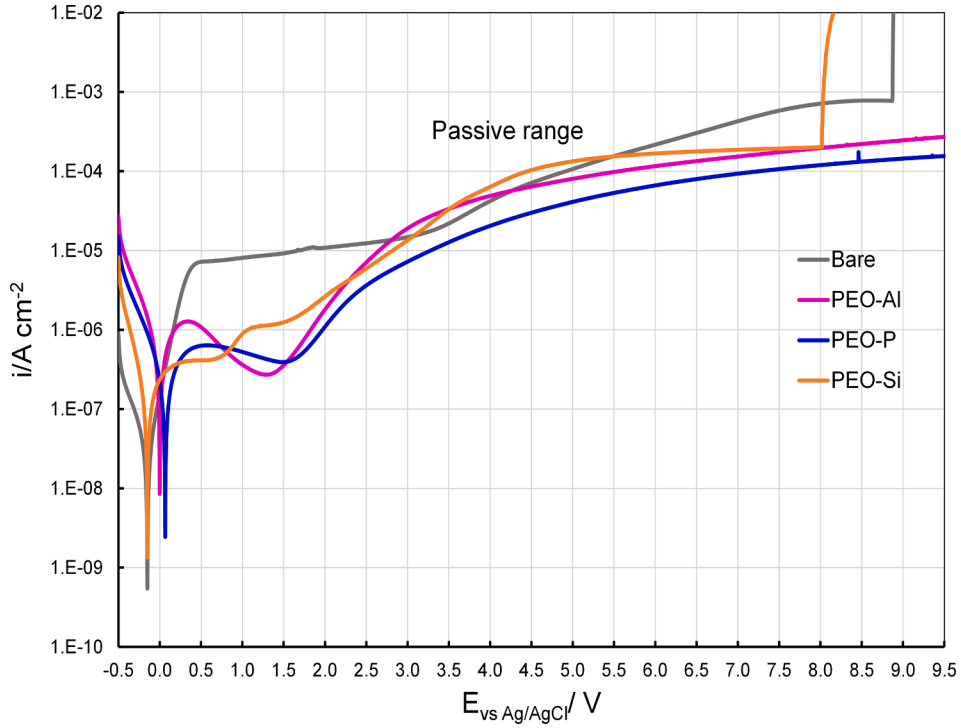

Fig. 8. PDP measurements of bare and PEO treated Ti6Al4V alloy.

after breakdown during polarization. For PEO-P and PEO-Al systems, the breakdown was not reached in the conditions of PDP experiment. However, for the PEO-Al coating, an interesting effect was observed (Fig. 10). As soon as voltage increase reaches ca. 3.5 V, slight dissolution of titanium and noticeable dissolution of aluminium can be observed during AESEC analysis.

3.5. Corrosion resistance and electrochemical response of PEO coatings

EIS measurements were applied to further evaluate the corrosion

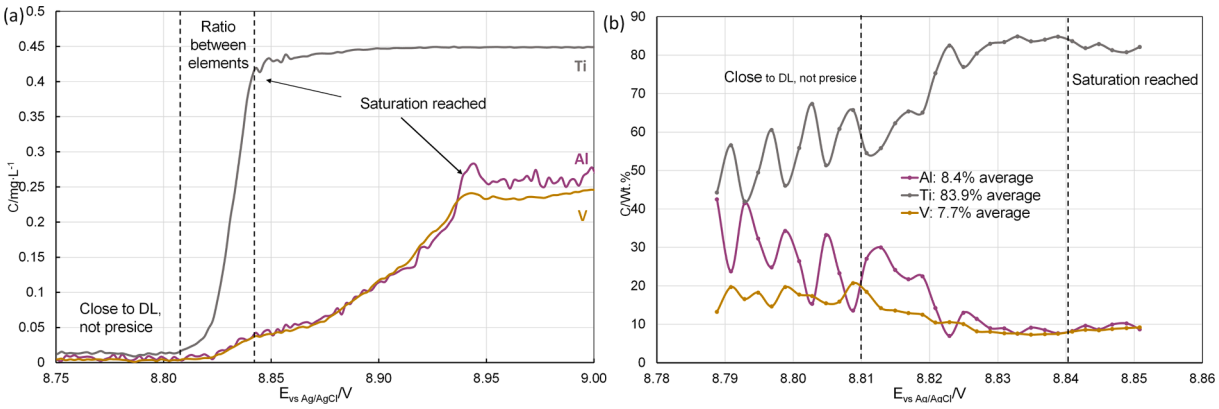

Fig. 9. Ratio of dissolved elements during breakdown of Ti6Al4V alloy during PDP.

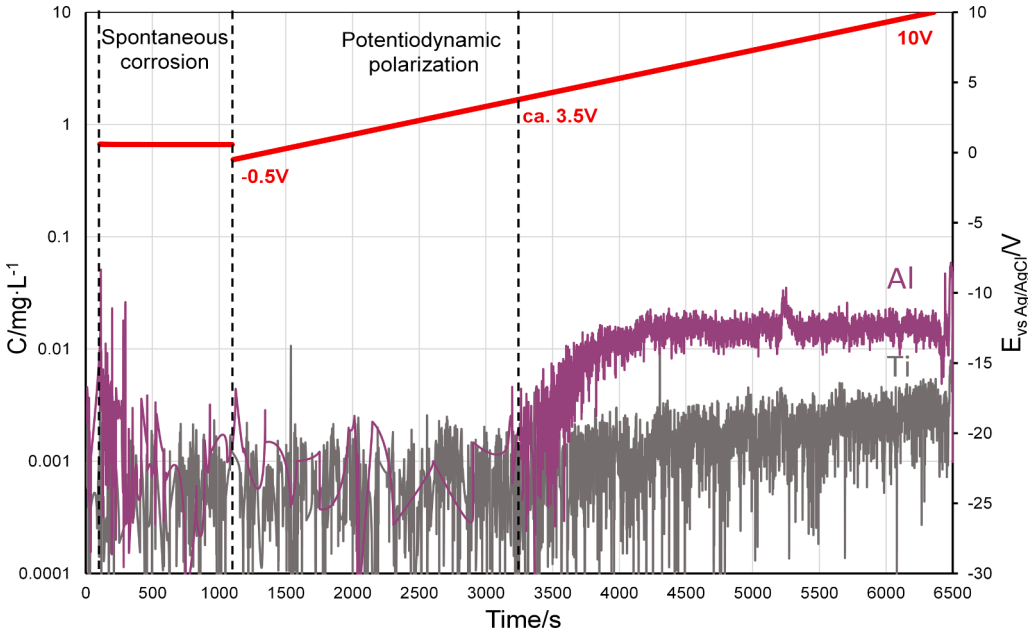

Fig. 10. Elemental dissolution during PDP of PEO-Al treated Ti6Al4V alloy.

performance of the specimens before and after PEO treatments. Fig. 11 illustrates the Nyquist and Bode plots of the bare and PEO coated Ti6Al4V alloy immersed in Ringer's solution for up to 72 h. For the bare alloy, one can see a well-defined time constant at the frequency of 10 Hz for all measurements (Fig. 11(a)), which is related to the response of the native oxide layer, possibly including the influence of a space charge region [46] at the oxide-electrolyte interface in regard to the semiconductive behavior of titanium oxide. During the first measurement after 5 min of immersion, it shows the narrowest capacitive loop, which is in agreement with the slightly higher dissolution rate of titanium during spontaneous corrosion detected in AESEC measurement. With increasing immersion time, the total impedance at lower frequency is increasing and an almost pure capacitive response is illustrated by a stable phase angle near −90° at a wider range of frequency from 10 Hz to 0.01 Hz. Meanwhile, the capacitive loop is expanding, suggesting an improvement of the barrier property of the native oxide layer. For the PEO-P coating, Bode plots in Fig. 11(b) clearly demonstrate two well-defined time constants at high (10^4 Hz) and medium frequencies (10^2 Hz) during the measurements, which are associated with the layered structure of the coating. The first time constant at high frequency is disappearing with prolonged immersion, suggesting the gradual degradation of the layer by the penetration of corrosive solution. The second time constant at medium frequency becomes more evident, which can be assigned to the response from the barrier layer at the interface. The low frequency response mainly comes from the space charge layer, which can be seen from Fig. 12(b). Fig. 11(c) shows the electrochemical response of PEO-Al coating in the measurements. One well-defined time constant observed at the frequency of 10^3 Hz is also attributed to the penetration of corrosive solution into the layer. However, the second time constant is forming but is not completely developed. Thus, the solution does not reach the interface between the coating and substrate yet. Similar electrochemical response is revealed for the PEO-Si coating, but the first time constant is present at a frequency of 10^4 Hz. Although the thinnest, the PEO-Si coating presents the highest total impedance value at the lowest frequency (0.01 Hz) in comparison to the other two coatings. This could be attributed to the most uniform surface morphology without large-sized micro-pores in the coating. For all conditions, the total impedance at the lowest frequency increases after the first measurement and the bare alloy presents the highest value after 72 h of immersion. However, it seems that the corrosive solution has not reached the interface between the substrate and the coating for all coated specimens, and there is no sign of corrosion reaction initiated.

An additional EIS experiment was performed to confirm further whether the semiconductive behavior of anatase (n-type) plays a role in

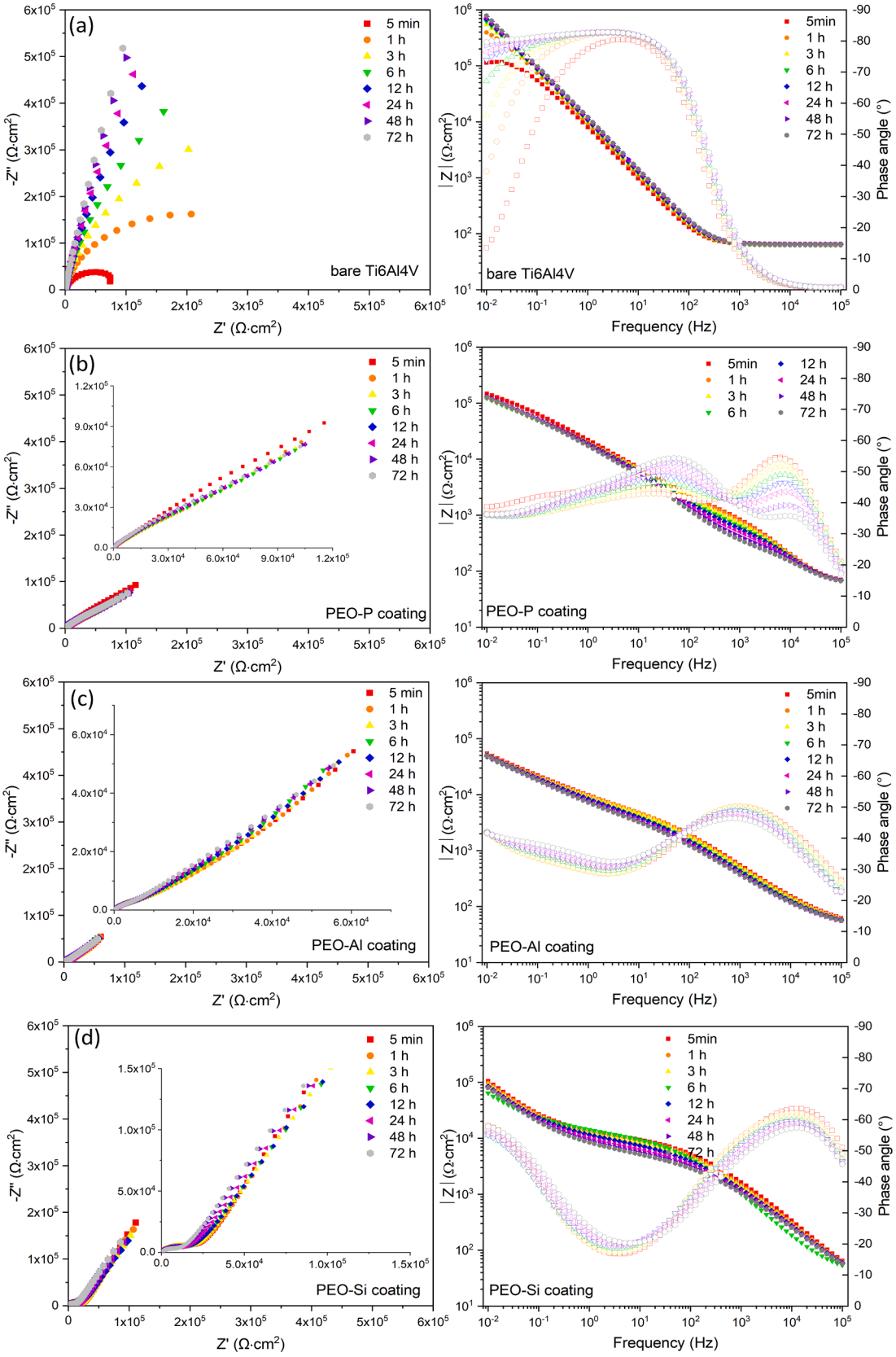

Fig. 11. Electrochemical impedance spectra of (a) bare Ti6Al4V alloy and PEO coated Ti6Al4V specimens: (b) PEO-P coating, (c) PEO-Al coating and (d) PEO-Si coating recorded versus open circuit potential in Ringer's solution.

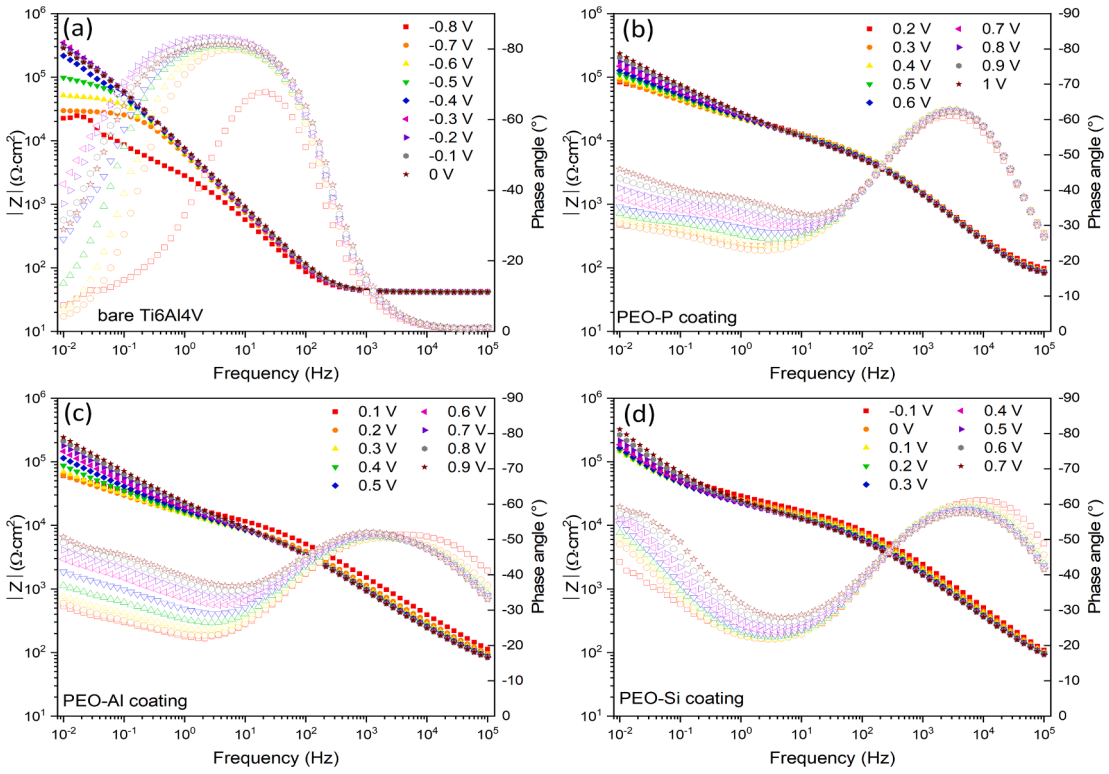

Fig. 12. Impedance spectra of (a) bare Ti6Al4V alloy and PEO coated Ti6Al4V specimens (b) PEO-P coating, (c) PEO-Al coating and (d) PEO-Si coating at different potential bias ± 0.4 V versus open circuit potential in Ringer's solution.

formation of the electrochemical response of formed coatings. The capacitance of semiconductive layer will change depending on the polarization conditions and thus can be tracked in impedance spectra [46,53–55]. Fig. 12 shows the Bode plots taken when the specimens are polarized at ± 0.4 V vs. open circuit potential on bare and PEO coated specimens. At the lowest frequency at 0.01 Hz, it is quite obvious that the total impedance increases with the increase of electrode potential, suggesting the response from space charge region. The impedance spectra of the bare Ti6Al4V (Fig. 12(a)) exhibit only one time constant as an almost pure capacitive response indicated by the phase angle close to −90° at the frequency range of 10^2 to 0.3 Hz. With the increase of polarization potential, it can be noticed that the time constant is gradually shifting to lower frequencies. Only at lower frequencies, there is a sign of resistive response originating from the native barrier layer. In terms of PEO-Si coated specimen (Fig. 12(d)), the first time constant at the frequency of 10^4 Hz is related to the inner layer. The additional time constant at lower frequency range originates from the space charge region. For PEO-P and PEO-Al coated specimens, three time constant can be recognized and possibly correlated with the higher thickness of the coatings. The first time constant can be assigned to the response of inner layer at the higher frequency range. However, the second and third time constants are very difficult to distinguish due to an overlapping, which can be attributed to the capacitive response from the barrier layer and space charge region, respectively.

Considering the structure of the PEO coatings, two different equivalent circuits are adopted for fitting the impedance spectra, as shown in Fig. 13, in order to meet the requirement to describe the impedance spectra with a minimum error and number of elements. In addition, taking into account the contribution of the space charge region, the equivalent circuits are also selected to evaluate correctly the change of

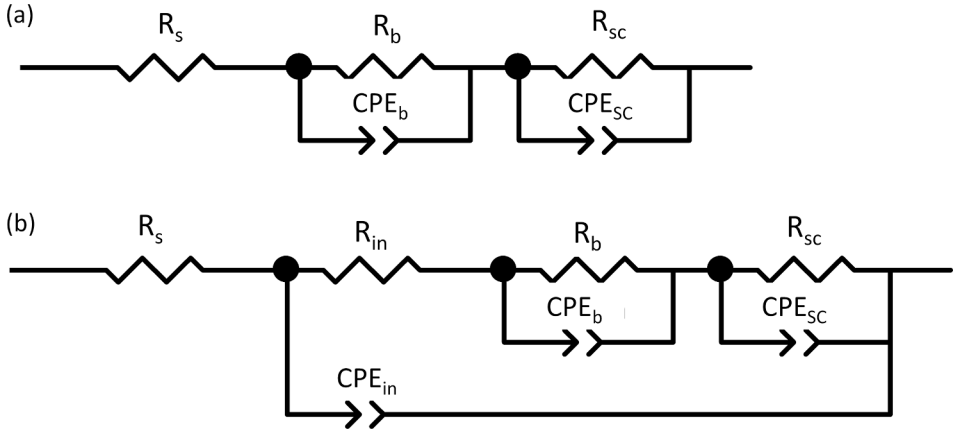

Fig. 13. Equivalent circuits used for fitting the impedance spectra of the (a) bare Ti6Al4V and PEO-Si coating, and (b) PEO-P and PEO-Al coatings under potential bias versus reference.

capacitance under the potential bias. Fig. 13(a) is suitable for fitting the impedance spectra of bare Ti6Al4V and PEO-Si coatings (thinner coating), where the constant phase elements of barrier layer and space charge layer are represented by CPE_b and CPE_{sc}, and the resistances of Ringer's solution, barrier layer and space charge layer are indicated as R_s, R_b and R_{sc} respectively. Fig. 13(b) is used for fitting the impedance spectra of PEO-P and PEO-Al coatings (thicker coatings), where CPE_{in} and R_{in} represent the capacitance and resistance of the inner layer. Further calculations are carried out to evaluate the influence of the space charge region at the interface of the PEO coatings and the substrate on the electrochemical behavior. Fig. 14 shows the calculation of C_{sc}^{-2} as a function of applied electrode potential for bare and PEO coated Ti6Al4V. From the analysis of the electrochemical response from the space charge region, the semiconductive property can be assessed using Mott-Schottky equation:

$$C_{sc}^{-2} = \left(\frac{2}{eN_d\varepsilon\varepsilon_0}\right)\left(E - E_{fb} - \frac{kT}{e}\right) \quad (1)$$

where C_{sc} is the capacitance of space charge layer in a semiconductive coating, N_d the donor concentration for n-type semiconductor, $\varepsilon = 57$ (dielectric constant of TiO_2 film) [46], $\varepsilon_0 = 8.85 \times 10^{-12}$F/m (vacuum permittivity) [54], E is the applied electrode potential, E_{fb} is the flat band potential, $k = 1.38 \times 10^{-23}$ J/K (Boltzmann's constant), $T = 298.15$ K (room temperature) and $e = 1.602 \times 10^{-19}$C (charge of an electron). A relatively linear portion of the plots in Fig. 14 was extracted, which determined the applied electrode potential E and the average flat band potential E_{fb} (-0.72 V for bare alloy, 0.08 V for PEO-P coating, 0.12 V for PEO-Al coating and −0.28 V for PEO-Si coating). As a result, the calculated donor concentration N_d was averaged for bare alloy and PEO coated specimens, respectively. Fig. 15 presents the calculated donor concentrations in average. One can notice that bare Ti6Al4V and PEO-Si coating have higher donor concentrations with a magnitude of 10^{19}, however, for PEO-P and PEO-Al coatings, the donor concentrations are two orders of magnitude lower and PEO-P coating shows the lowest donor concentration.

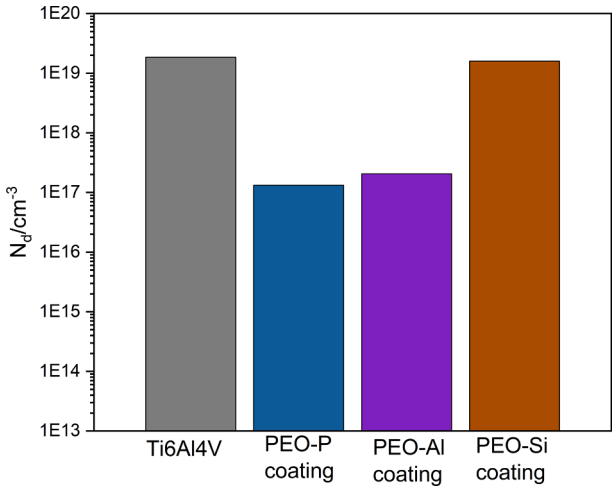

Fig. 15. Evolution of the donor concentration Nd calculated from Mott-Schottky plots on bare and PEO coated Ti6Al4V alloy.

3.6. Photocatalytic activity of PEO coatings

Fig. 16 shows the average efficiency of MO photodegradation and

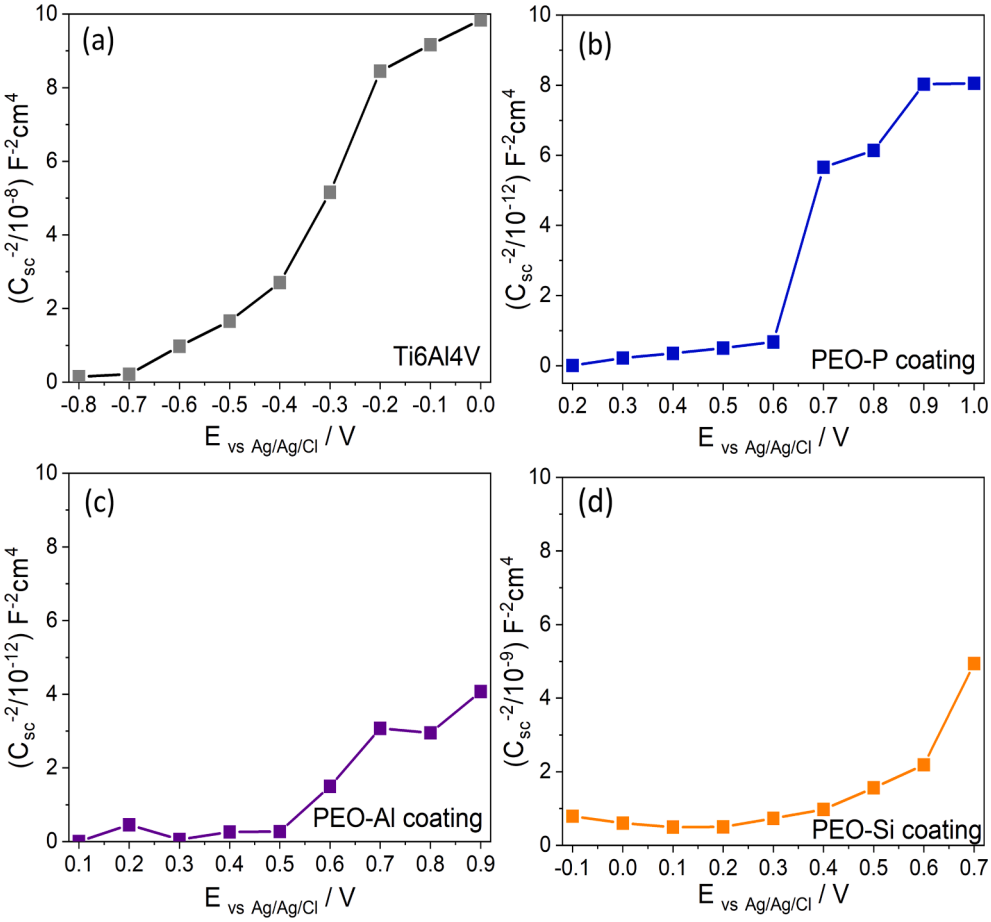

Fig. 14. Mott-Schottky plots constructed from the data in Fig. 12 for (a) bare Ti6Al4V, (b) PEO-P coating, (c) PEO-Al coating and (d) PEO-Si coating.

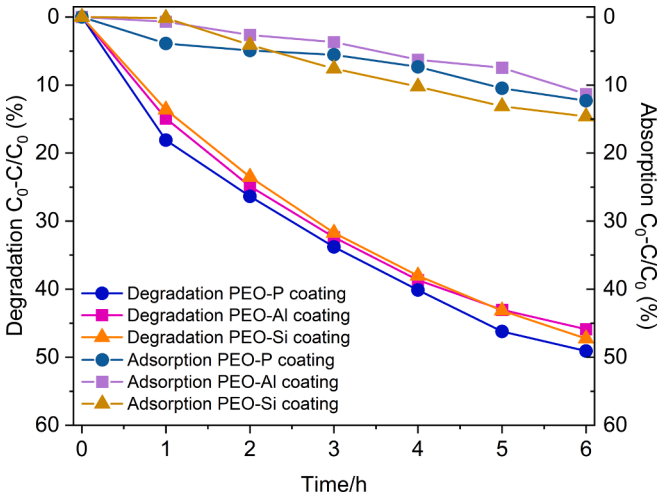

Fig. 16. MO degradation and absorption as a function of time in respect to PEO coatings formed in different electrolytes.

absorption in the presence of different PEO coatings on Ti6Al4V alloy, respectively. Please note that bare Ti6Al4V did not show noticeable photocatalytic activity during the experiment, moreover, natural titania is amorphous and no photoactivity is expected. The MO absorption of different coatings in darkness increases with exposure time, and the final absorption rates after 6 h are in the range of 10–15%, indicating a quite similar absorption behavior. The photocatalytic activity of the coatings can be evaluated by the degradation rate of MO and shows a positive correlation. It is obvious that the degradation efficiency of MO for the three coatings increases to a value higher than ca. 45 % after 6 h of exposure, suggesting a reasonable photocatalytic activity of these coatings. Meanwhile, the photocatalytic activity of different coatings almost does not depend on the composition of the coatings. The MO degradation rates are quite similar for the three different coatings during the measurements. However, the degradation efficiency for the PEO-P coating is slightly higher than that of the other two coatings. It could be correlated with the rougher coating surface and main phase composition of anatase in the coating, which has higher active surface area and possibly has higher concentration of charge carriers [56], in comparison with the other coatings. It is worth mentioning that PEO-Al coating shows comparable photocatalytic degradation rate even through there is almost no TiO_2. This can be assigned to the newly formed Al_2TiO_5 phase, which has a narrow band gap of 2.88 eV and has already been reported as an efficient photocatalyst in organic pollutant degradation process [57,58].

4. Discussion

Looking at the voltage responses during PEO processing, the higher breakdown voltage (ca. 290 V) for the PEO-Al coating suggests a higher electrical resistance of the initial barrier layer compared to the PEO-P and PEO-Si coatings (ca. 190 V). It does not seem to be influenced by the conductivity of the electrolytes, since the aluminate-based electrolyte has a comparable conductivity to the silicate-based electrolyte, which is higher than that of the phosphate-based electrolyte. However, the effect of a different composition of initial barrier layer or a different formation rate of the initial titanium oxide layer in different electrolytes could be more significant. Based on the phase composition of the coatings, one can notice that the PEO-Al coating contains a significant amount of non-conductive γ-Al_2O_3 and $Na_2Al_{2x}O_{3x+1}$, which can only originate from the electrolyte. Thus, the breakdown voltage is mainly controlled by the composition of the coating, which is determined by the electrolyte composition. The following main reactions (Eqs. (2)-(7)) are suggested for the formation of crystalline phase in the PEO-Al coating at different depth of the coating:

In the outer layer,

$$2Na^+ + 2xAlO_2^- + (x-1)H_2O \rightarrow Na_2Al_{2x}O_{3x+1} + 2(x-1)OH^- \quad (2)$$

In the intermediate layer,

$$AlO_2^- + 2H_2O \rightarrow Al(OH)_3 + OH^- \quad (3)$$

$$2Al(OH)_3 \rightarrow Al_2O_3 + 3H_2O \quad (4)$$

In the inner layer near the substrate,

$$Ti \rightarrow Ti^{4+} + 4e^- \quad (5)$$

$$Ti^{4+} + 4OH^- \rightarrow TiO_2 + 2H_2O \quad (6)$$

$$TiO_2 + Al_2O_3 \rightarrow Al_2TiO_5 \quad (7)$$

From Eqs. (2)-(7), it can be expected that the thickness difference between the PEO-Al and PEO-P coatings is probably related to the different coating formation processes, where the deposition from the electrolyte is dominating for PEO-Al systems. However, the reactive formation involving oxidation of the substrate is the primary reaction for the PEO-P system. The voltage is always higher for PEO-Al system than PEO-P system at the same current density. That is to say, the energy input for PEO-Al system is higher, but the lower thickness of PEO-Al coating elucidates a lower coating formation efficiency. One reason could be that, the formation of Al_2TiO_5 in PEO-Al coating through the interaction between Al_2O_3 and TiO_2 is accompanied by a volume shrinkage (11% molar volume) [59]. Hence, a lower thickness in comparison to the TiO_2 dominated PEO-P coating (Pilling-Bedworth ratio of 1.73) was revealed. Another explanation is also associated with the different composition and microstructure of the coatings in different electrolytes, which can result in different barrier property of the coating and further change the coating formation behavior, indicated by a different voltage response. An alternative explanation is associated with the higher oxygen diffusivity in TiO_2 compared to Al_2O_3, and SiO_2 [60–62]. Our previous study [63] has demonstrated that the expanded α-Ti peaks due to high solubility of oxygen in Ti lattice in the phosphate-based electrolyte. The faster oxygen diffusion in TiO_2 supported the continuous penetration of oxygen into the Ti substrate and thus the coating formation process could be accelerated. However, in the aluminate- and silicate-based electrolytes, the outer layers are Al_2O_3 and SiO_2 dominated, respectively. The lower oxygen diffusivity in Al_2O_3 and SiO_2 in comparison to TiO_2 could interrupt the fast diffusion of oxygen to the coating/substrate interface. As a result, the oxidation process of Ti substrate was impeded, and the coating growth was much dependent on the deposition from the electrolytes.

Considering the coating composition, we conclude that the reactions in Eq. (5) and (6) are the main process for the formation of PEO-P coating and the fabrication of crystalline phases in PEO-Si coatings. A closer observation reveals a slightly increased amount of rutile in the PEO-P coating towards the coating surface. It is clear that the high-temperature stable rutile is transformed from anatase due to the high temperature of the discharges. The increased intensity of rutile peaks suggests that the highest temperature in the coating is reached at the oxide/electrolyte interface where melted material is ejected through the discharge channels. For the PEO-Si coating, the main coating formation process is deposition-controlled similar to the PEO-Al coating, with significant deposition/formation of amorphous phase. The declined electrical power input in PEO-Si system is the reason for the lower coating thickness. However, the electrical controlled mode also prevents the generation of destructive discharges, attaining a less porous and compact coating.

It is well known that the morphology, microstructure and phase composition of the PEO coatings have an effect on their performance. During PDP measurement, the breakdown of the PEO-Al coating is not reached; however, a higher dissolution of Al is noticed after reaching

3.5 V. It might take place due to water decomposition process under anodic polarization condition, leading to the formation of oxygen. As a result, there could be a decreasing of pH value, and further accelerating the dissolution of aluminium oxides/hydroxides compounds. The second option can be that at ca. 3.5 V vs Ag/AgCl electrode, the so-called band-gap potential [64] was reached and resulted in a change of the layer conductivity. Thus, the layer is not that protective anymore because the electrons can pass through it causing further dissolution. The result is also in agreement with the EIS measurements, showing that the PEO-Al coating has lower impedance. However, at the lowest frequency of 0.01 Hz, the low frequency loop is still incomplete for all coatings and there is no sign for a well-defined time constant. Thus, the real corrosion resistance of the coatings cannot be evaluated through the impedance spectra. Nevertheless, in the EIS measurement, the semiconductive behaviour of the TiO_2-containing coating could not be ignored. The impedance spectra do not only demonstrate the physical structure of the coating formed in different electrolyte, which is in agreement with the observation of cross-sectional analysis, but can also reveal the response from the space charge layer originated from the coating-electrolyte interface [46]. The Mott-Schottky analysis from additional EIS measurements is adequate for elucidating the contribution of space charge region since the capacitance of space charge layer is shifting dependent on the applied potential. However it does not happen on inner and barrier layers. Although Mott-Schottky equation reveals a linear relationship between C_{sc}^{-2} and the applied electrode potential (E) as seen in Eq. (1), the C_{sc}^{-2} - E plots in Fig. 14 show a nonlinear increasing trend with the potential bias. The possible reason could be generally correlated with the complex coating composition and the heterogeneous microstructure of the coatings.

It should be noted that the semiconductivity of the coatings evaluated in present work is an assessment of the interface between the coatings and the substrate. However, the photocatalytic activity of the coating is focusing on the outer layer with numerous micro-pores formed during PEO. That is to say, the calculated donor density cannot be associated with the photocatalytic activity in this case. The photocatalytic activity of the coatings only shows small differences and a slight advantage of PEO-P coating is illustrated. The PEO-P coating contains higher amount of anatase, which would theoretically increase the amount of charge carriers since the indirect band gap shows a longer lifetime of photo-excited electrons and holes than the direct band gap of rutile [56]. Although lacking crystalline TiO_2, the PEO-Al and PEO-Si coatings still show considerable photocatalytic activity. The possible explanations are based on the total active surface area and the additional active species for photocatalysis [65,66]. For PEO-Al coating, it can be partly assigned to either amorphous TiO_2 or the satisfactory photodegradation capacity of Al_2TiO_5. Besides, the highest surface roughness (Sdr = 141.308%) can also expand the coating surface area and further increase the exposed active surface area for the MO photodegradation process. The recombination and trapping of photo-generated charge carriers [46,67] could be increased in the porous outer layer produced by the repeated discharges. In terms of PEO-Si coating, the composition the TiO_2/amorphous silica composite was already reported to exhibit better photocatalytic performance in comparison to pure TiO_2 [65]. Moreover, the higher additional surface area (Sdr = 101.628%) could explain such high photocatalytic performance.

5. Conclusions

The composition of the electrolyte influences the PEO process on Ti alloy. The PEO process in phosphate-based electrolyte was the most stable in comparison to the aluminate- and silicate-based electrolytes. The PEO-P coating is mainly composed of anatase and rutile due to the oxidation of substrate. However, for PEO-Al and PEO-Si systems, the major coating formation process is largely dependent on the deposition of the species from the electrolytes. Al_2O_3 and $Na_2Al_{2x}O_{3x+1}$, as well as Al_2TiO_5 oxide mixture are the main phases in the PEO-Al coating. An amorphous silicate phase in combination with anatase and rutile are dominant in the PEO-Si coating. The three formed coatings have also noticeably different morphology, of which the PEO-P coating showed the highest surface roughness, while the most uniform coating was formed in the silicate-containing electrolyte.

Regarding the corrosion properties, a breakdown during PDP was only observed for the PEO-Si coating due to the lowest coating thickness and amorphous phase fractions. Nonetheless, the dissolution of aluminum was detected for the PEO-Al coating without a sign of coating breakdown. The space charge region response was illustrated in the impedance spectra at potential bias because of the semi-conductive property of TiO_2-containing coatings. Furthermore, all the coatings have good photocatalytic activity with a MO photodegradation rate higher than 45 %.

CRediT authorship contribution statement

Ting Wu: Visualization, Formal analysis, Investigation, Writing – original draft, Writing – review & editing. **Carsten Blawert:** Conceptualization, Supervision, Writing – review & editing. **Maria Serdechnova:** Formal analysis, Visualization, Writing – review & editing. **Polina Karlova:** Investigation, Visualization, Writing – review & editing. **Gleb Dovzhenko:** Investigation, Visualization, Writing – review & editing. **D. C. Florian Wieland:** Investigation, Writing – review & editing. **Stevan Stojadinovic:** Investigation, Writing – review & editing. **Rastko Vasilic:** Investigation, Writing – review & editing. **Linqian Wang:** Investigation, Writing – review & editing. **Cheng Wang:** Investigation, Writing – review & editing. **Kristina Mojsilovic:** Investigation, Writing – review & editing. **Mikhail L. Zheludkevich:** Supervision, Writing – review & editing.

Declaration of Competing Interest

The authors declare that they have no known competing financial interests or personal relationships that could have appeared to influence the work reported in this paper.

Acknowledgement

Ting Wu, Linqian Wang and Cheng Wang thanks China Scholarship Council for the award of fellowship and funding (NO.201708510113, No. 201706370183, NO. 201806310128). The technical support of Mr. Volker Heitmann, Mr. Ulrich Burmester and Mr. Daniel Strerath during this work is gratefully acknowledged.

References

[1] R.R. Boyer, R.D. Briggs, The use of β titanium alloys in the aerospace industry, J. Mater. Eng. Perform. 14 (2005) 681–685.
[2] I.V. Gorynin, Titanium alloys for marine application, Mater. Sci. Eng., A 263 (1999) 5.
[3] H.J. Rack, J.I. Qazi, Titanium alloys for biomedical applications, Mater. Sci. Eng., C 26 (2006) 1269–1277.
[4] X. Liu, P. Chu, C. Ding, Surface modification of titanium, titanium alloys, and related materials for biomedical applications, Materials Science and Engineering: R: Reports 47 (2004) 49–121.
[5] G.W. Critchlow, D.M. Brewis, Review of surface pretreatments for titanium alloys, International Journal of Adhesion and Adhesives, 15 (1995) 12.
[6] Y.S. Tian, C.Z. Chen, S.T. Li, Q.H. Huo, Research progress on laser surface modification of titanium alloys, Appl. Surf. Sci. 242 (2005) 177–184.
[7] T.R. Rautray, R. Narayanan, T.Y. Kwon, K.H. Kim, Surface modification of titanium and titanium alloys by ion implantation, J Biomed Mater Res B Appl Biomater 93 (2010) 581–591.
[8] L. Zhang, L. Chen, L. Wang, Surface Modification of Titanium and Titanium Alloys: Technologies, Developments, and Future Interests, Adv. Eng. Mater. 22 (2020).
[9] Y. Wang, H. Yu, C. Chen, Z. Zhao, Review of the biocompatibility of micro-arc oxidation coated titanium alloys, Mater. Des. 85 (2015) 640–652.
[10] X. Lu, M. Mohedano, C. Blawert, E. Matykina, R. Arrabal, K.U. Kainer, M. L. Zheludkevich, Plasma electrolytic oxidation coatings with particle additions - A review, Surf. Coat. Technol. 307 (2016) 1165–1182.

[11] T.W. Clyne, S.C. Troughton, A review of recent work on discharge characteristics during plasma electrolytic oxidation of various metals, Int. Mater. Rev. 64 (2018) 127–162.
[12] S. Durdu, M. Usta, The tribological properties of bioceramic coatings produced on Ti6Al4V alloy by plasma electrolytic oxidation, Ceram. Int. 40 (2014) 3627–3635.
[13] S. Aliasghari, P. Skeldon, G.E. Thompson, Plasma electrolytic oxidation of titanium in a phosphate/silicate electrolyte and tribological performance of the coatings, Appl. Surf. Sci. 316 (2014) 463–476.
[14] K. Rokosz, T. Hryniewicz, S. Raaen, Development of plasma electrolytic oxidation for improved Ti6Al4V biomaterial surface properties, The International Journal of Advanced Manufacturing Technology 85 (2015) 2425–2437.
[15] H. Cimenoglu, M. Gunyuz, G.T. Kose, M. Baydogan, F. Uğurlu, C. Sener, Micro-arc oxidation of Ti6Al4V and Ti6Al7Nb alloys for biomedical applications, Mater. Charact. 62 (2011) 304–311.
[16] T. Wu, C. Blawert, M.L. Zheludkevich, Influence of secondary phases of AlSi9Cu3 alloy on the plasma electrolytic oxidation coating formation process, J. Mater. Sci. Technol. 50 (2020) 75–85.
[17] T. Wu, C. Blawert, X. Lu, M. Serdechnova, M.L. Zheludkevich, Difference in formation of plasma electrolytic oxidation coatings on MgLi alloy in comparison with pure Mg, J. Magnesium Alloys 9 (5) (2021) 1725–1740.
[18] A.L. Yerokhin, L.O. Snizhko, N.L. Gurevina, A. Leyland, A. Pilkington, A. Matthews, Spatial characteristics of discharge phenomena in plasma electrolytic oxidation of aluminium alloy, Surf. Coat. Technol. 177–178 (2004) 779–783.
[19] Y. Wu, H. Wu, L. Wu, Z.-H. Xie, L. Liu, X.u. Dai, G. Zhang, W. Yao, Y.u. Li, F. Pan, Influence of Electrolyte Temperature on Morphology and Properties of Composite Anodic Film on Titanium Alloy Ti-10V-2Fe-3Al, Coatings 10 (11) (2020) 1109.
[20] S. Stojadinović, R. Vasilić, M. Petković, B. Kasalica, I. Belča, A. Žekić, L. Zeković, Characterization of the plasma electrolytic oxidation of titanium in sodium metasilicate, Appl. Surf. Sci. 265 (2013) 226–233.
[21] H.-P. Teng, C.-J. Yang, J. Lin, Y. Huang, F. Lu, A Simple Method to Functionalize the Surface of Plasma Electrolytic Oxidation Produced TiO_2 Coatings for Growing Hydroxyapatite, Electrochim. Acta 193 (2016) 216–224.
[22] L.C. Campanelli, L.T. Duarte, P.S.C.P. da Silva, C. Bolfarini, Fatigue behavior of modified surface of Ti-6Al-7Nb and CP-Ti by micro-arc oxidation, Mater. Des. 64 (2014) 393–399.
[23] S. Franz, D. Perego, O. Marchese, A. Lucotti, M. Bestetti, Photoactive TiO_2 coatings obtained by Plasma Electrolytic Oxidation in refrigerated electrolytes, Appl. Surf. Sci. 385 (2016) 498–505.
[24] J.-H. Lee, J.-I. Youn, Y.-J. Kim, I.-K. Kim, K.-W. Jang, H.-J. Oh, Photocatalytic characteristics of boron and nitrogen doped titania film synthesized by micro-arc oxidation, Ceram. Int. 41 (2015) 11899–11907.
[25] S. Stojadinović, N. Tadić, N. Radić, B. Grbić, R. Vasilić, TiO_2/SnO_2 photocatalyst formed by plasma electrolytic oxidation, Mater. Lett. 196 (2017) 292–295.
[26] S. Stojadinović, N. Radić, B. Grbić, S. Maletić, P. Stefanov, A. Pačevski, R. Vasilić, Structural, photoluminescent and photocatalytic properties of TiO_2: Eu^{3+} coatings formed by plasma electrolytic oxidation, Appl. Surf. Sci. 370 (2016) 218–228.
[27] Y. Cheng, Z. Peng, X. Wu, J. Cao, P. Skeldon, G.E. Thompson, A comparison of plasma electrolytic oxidation of Ti-6Al-4V and Zircaloy-2 alloys in a silicate-hexametaphosphate electrolyte, Electrochim. Acta 165 (2015) 301–313.
[28] J. Han, Y. Cheng, W. Tu, T. Zhan, Y. Cheng, The black and white coatings on Ti-6Al-4V alloy or pure titanium by plasma electrolytic oxidation in concentrated silicate electrolyte, Appl. Surf. Sci. 428 (2018) 684–697.
[29] F. Muhaffel, G. Cempura, M. Menekse, A. Czyrska-Filemonowicz, N. Karaguler, H. Cimenoglu, Characteristics of multi-layer coatings synthesized on Ti6Al4V alloy by micro-arc oxidation in silver nitrate added electrolytes, Surf. Coat. Technol. 307 (2016) 308–315.
[30] H. Sharifi, M. Aliofkhazraei, G.B. Darband, A.S. Rouhaghdam, Characterization of PEO nanocomposite coatings on titanium formed in electrolyte containing atenolol, Surf. Coat. Technol. 304 (2016) 438–449.
[31] M. Babaei, C. Dehghanian, M. Vanaki, Effect of additive on electrochemical corrosion properties of plasma electrolytic oxidation coatings formed on CP Ti under different processing frequency, Appl. Surf. Sci. 357 (2015) 712–720.
[32] D. Dzhurinskiy, Y. Gao, W.K. Yeung, E. Strumban, V. Leshchinsky, P.J. Chu, A. Matthews, A. Yerokhin, R.G. Maev, Characterization and corrosion evaluation of TiO_2:n-HA coatings on titanium alloy formed by plasma electrolytic oxidation, Surf. Coat. Technol. 269 (2015) 258–265.
[33] S. Liu, B. Li, C. Liang, H. Wang, Z. Qiao, Formation mechanism and adhesive strength of a hydroxyapatite/TiO_2 composite coating on a titanium surface prepared by micro-arc oxidation, Appl. Surf. Sci. 362 (2016) 109–114.
[34] W. Simka, A. Krząkała, D.M. Korotin, I.S. Zhidkov, E.Z. Kurmaev, S.O. Cholakh, K. Kuna, G. Dercz, J. Michalska, K. Suchanek, T. Gorewoda, Modification of a Ti–Mo alloy surface via plasma electrolytic oxidation in a solution containing calcium and phosphorus, Electrochim. Acta 96 (2013) 180–190.
[35] S. Durdu, K. Korkmaz, S.L. Aktuğ, A. Çakır, Characterization and bioactivity of hydroxyapatite-based coatings formed on steel by electro-spark deposition and micro-arc oxidation, Surf. Coat. Technol. 326 (2017) 111–120.
[36] E. Matykina, R. Arrabal, B. Mingo, M. Mohedano, A. Pardo, M.C. Merino, In vitro corrosion performance of PEO coated Ti and Ti6Al4V used for dental and orthopaedic implants, Surf. Coat. Technol. 307 (2016) 1255–1264.
[37] S. Wang, Q. Zhao, D. Liu, N. Du, Microstructure and elevated temperature tribological behavior of TiO_2/Al_2O_3 composite ceramic coating formed by microarc oxidation of Ti6Al4V alloy, Surf. Coat. Technol. 272 (2015) 343–349.
[38] A.L. Yerokhin, A. Leyland, A. Matthews, Kinetic aspects of aluminium titanate layer formation on titanium alloys by plasma electrolytic oxidation, Appl. Surf. Sci. 200 (2002) 13.
[39] N. Sarkar, K.S. Lee, J.G. Park, S. Mazumder, C.G. Aneziris, I.J. Kim, Mechanical and thermal properties of highly porous Al_2TiO_5 –Mullite ceramics, Ceram. Int. 42 (2016) 3548–3555.
[40] O.A. Galvis, D. Quintero, J.G. Castaño, H. Liu, G.E. Thompson, P. Skeldon, F. Echeverría, Formation of grooved and porous coatings on titanium by plasma electrolytic oxidation in H_2SO_4/H_3PO_4 electrolytes and effects of coating morphology on adhesive bonding, Surf. Coat. Technol. 269 (2015) 238–249.
[41] M. Shokouhfar, C. Dehghanian, M. Montazeri, A. Baradaran, Preparation of ceramic coating on Ti substrate by plasma electrolytic oxidation in different electrolytes and evaluation of its corrosion resistance: Part II, Appl. Surf. Sci. 258 (7) (2012) 2416–2423.
[42] J. Kieffer, D. Karkoulis, PyFAI, a versatile library for azimuthal regrouping, J. Phys. Conf. Ser. 425 (20) (2013) 202012.
[43] V. Shkirskiy, P. Maciel, J. Deconinck, K. Ogle, On the time resolution of the atomic emission spectroelectrochemistry method, J. Electrochem. Soc. 163 (3) (2016) C37–C44.
[44] J. Światowska, P. Volovitch, K. Ogle, The anodic dissolution of Mg in NaCl and Na_2SO_4 electrolytes by atomic emission spectroelectrochemistry, Corros. Sci. 52 (2010) 2372–2378.
[45] K. Ogle, A. Tomandl, N. Meddahi, M. Wolpers, The alkaline stability of phosphate coatings I: ICP atomic emission spectroelectrochemistry, Corros. Sci. 46 (2004) 979–995.
[46] S.K. Poznyak, A.D. Lisenkov, M.G.S. Ferreira, A.I. Kulak, M.L. Zheludkevich, Impedance behaviour of anodic TiO_2 films prepared by galvanostatic anodisation and powerful pulsed discharge in electrolyte, Electrochim. Acta 76 (2012) 453–461.
[47] J.A. Curran, T.W. Clyne, Porosity in plasma electrolytic oxide coatings, Acta Mater. 54 (2006) 1985–1993.
[48] X. Yu, L. Chen, H. Qin, M. Wu, Z. Yan, Formation process of in situ oxide coatings with high porosity using one-step plasma electrolytic oxidation, Appl. Surf. Sci. 366 (2016) 432–438.
[49] C. Blawert, S.A. Karpushenkov, M. Serdechnova, L.S. Karpushenkava, M. L. Zheludkevich, Plasma electrolytic oxidation of zinc alloy in a phosphate-aluminate electrolyte, Appl. Surf. Sci. 505 (2020), 144552.
[50] J. Li, X. Lin, J. Wang, M. Zheng, P. Guo, Y. Zhang, Y. Ren, J. Liu, W. Huang, Effect of stress-relief annealing on anodic dissolution behaviour of additive manufactured Ti-6Al-4V via laser solid forming, Corros. Sci. 153 (2019) 314–326.
[51] H. Zhang, C. Man, L. Wang, C. Dong, L. Wang, D. Kong, X. Wang, Different corrosion behaviors between α and β phases of Ti6Al4V in fluoride-containing solutions: Influence of alloying element Al, Corros. Sci. 169 (2020).
[52] M. Vishwas, K.N. Rao, K.V. Gowda, R.P. Chakradhar, Optical, electrical and dielectric properties of TiO_2-SiO_2 films prepared by a cost effective sol-gel process, Spectrochim Acta A Mol Biomol Spectrosc 83 (2011) 614–617.
[53] S.V. Gnedenkov, S.L. Sinebryukhov, Electrochemical impedance spectroscopy of oxide layers on the titanium surface, Russ. J. Electrochem. 41 (2005) 8.
[54] P. Handzlik, K. Fitzner, Semiconducting properties of anodic oxide films grown on titanium in Ringer and PBS solutions, Arch. Metall. Mater. 55 (2010) 13.
[55] J. Liu, A. Alfantazi, E. Asselin, The anodic passivity of titanium in mixed sulfate-shloride solutions, J. Electrochem. Soc. 162 (2015) E289–E295.
[56] J. Zhang, P. Zhou, J. Liu, J. Yu, New understanding of the difference of photocatalytic activity among anatase, rutile and brookite TiO_2, Phys Chem Chem Phys 16 (2014) 20382–20386.
[57] A. Azarniya, M. Zekavat, M. Soltaninejad, F. Bakhshandeh, H. Reza Madaah Hosseini, S. Kashani, C. Amutha, S. Khatiboleslam Sadrnezhaad, S. Ramakrishna, Preparation of nitrogen-doped aluminium titanate (Al_2TiO_5) nanostructures: Application to removal of organic pollutants from aqueous media, Advanced Powder Technology, 31 (2020) 3328-3341.
[58] A. Azarniya, M. Soltaninejad, M. Zekavat, F. Bakhshandeh, H.R. Madaah Hosseini, C. Amutha, S. Ramakrishna, Application of nanostructured aluminium titanate (Al_2TiO_5) photocatalyst for removal of organic pollutants from water: Influencing factors and kinetic study, Materials Chemistry and Physics, 256 (2020).
[59] Z.-Y. Ding, Y.-H. Wang, J.-H. Ouyang, Z.-G. Liu, Y.-M. Wang, Y.-J. Wang, Influence of Al2O3 addition in $NaAlO_2$ electrolyte on microstructure and high-temperature properties of plasma electrolytic oxidation ceramic coatings on Ti2AlNb alloy, Surf. Coat. Technol. 370 (2019) 187–195.
[60] F. Ping, Q. Hu, A. Bakulin, S. Kulkova, R. Yang, Alloying effects on properties of Al_2O_3 and TiO_2 in connection with oxidation resistance of TiAl, Intermetallics 68 (2016) 57–62.
[61] S. Taniguchi, T. Shibata, Influence of additional elements on the oxidation behaviour of TiAl, Intermetallics 4 (1996) 9.
[62] G. Bomchil, G. Goeltz, J. Torres, Influence of oxygen on the formation of refractory metal silicides, Thin Solid Films 140 (1986) 12.
[63] T. Wu, C. Blawert, M. Serdechnova, P. Karlova, G. Dovzhenko, D.C.F. Wieland, M. L. Zheludkevich, Role of polymorph microstructure of Ti6Al4V alloy on PEO coating formation in phosphate electrolyte, Surf. Coat. Technol. 428 (2021) 127890.
[64] J. Kunze, A. Ghicov, H. Hildebrand, J.M. Macak, L. Traveira, P. Schmuki, Challenges in the Surface Analytical Characterisation of Anodic TiO_2 Films – a Review, Z. Phys. Chem. 219 (2005) 1561–1582.

[65] Z. Sun, C. Bai, S. Zheng, X. Yang, R.L. Frost, A comparative study of different porous amorphous silica minerals supported TiO_2 catalysts, Appl. Catal. A 458 (2013) 103–110.
[66] T. Wu, C. Blawert, M. Serdechnova, P. Karlova, G. Dovzhenko, D.C. Florian Wieland, S. Stojadinovic, R. Vasilic, K. Mojsilovic, M.L. Zheludkevich, Formation of plasma electrolytic oxidation coatings on pure niobium in different electrolytes, Appl. Surf. Sci. 573 (2022) 151629.
[67] Z. Yao, F. Jia, S. Tian, C. Li, Z. Jiang, X. Bai, Microporous Ni-doped TiO_2 film photocatalyst by plasma electrolytic oxidation, ACS Appl Mater Interfaces 2 (9) (2010) 2617–2622.

5.2 Influence of additional substrate phases

In addition to the phase transformation of substrate, the addition of alloying element can result in the precipitation of other second phases/intermetallics, which are significantly different from the matrix. Furthermore, the reinforcement process can introduce different reinforcement phases into the alloys that are not suitable for PEO treatment, such as Si phase and Al_2O_3 fibers. As a result of this different oxidation behavior, to obtain uniform PEO coatings on these micro-scaled material mixes is a challenge in comparison to the matrix. Finally, the study was progressed to micro-scaled material mix with more complex phases.

5.2.1 PEO of Al-Si material mix

Paper 4: Ting Wu, Carsten Blawert and Mikhail Zheludkevich. Influence of secondary phases of AlSi9Cu3 alloy on the plasma electrolytic oxidation coating formation process. Journal of Materials Science & Technology 50 (2020). https://doi.org/10.1016/j.jmst.2019.12.031

Graphical abstract

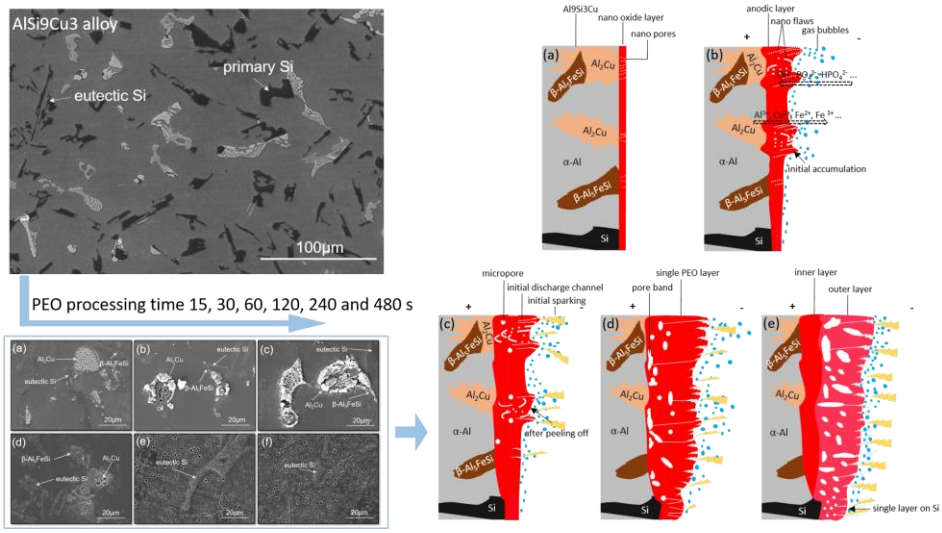

AlSi9Cu3 alloy is a good model alloy for PEO treatment of multi-material mix, revealing the problems of delayed sparking and different coating growth/phase composition if two different materials should be treated simultaneously. This work studied the oxidation behavior of α-Al matrix, intermetallics Al_2Cu, β-Al_5FeSi, and Si phases in Al9Si3Cu alloy, as a function of processing time during PEO treatment. From the local observation of the evolution of Al9Si3Cu substrate, different phases/intermetallics have shown distinguishable responses to the current and different oxidation behaviors with increasing processing time. Especially at the initial stage of the processing, an obvious sequential oxidation was demonstrated, starting on Al matrix, following with two intermetallics and finally extending to Si phases, due to a different chemical and electrochemical stability of the intermetallics. Moreover, Si phase is known to be not suitable for PEO and thus it was only oxidized slightly on the surface. The final coatings displayed distinct local morphology/microstructure on the surface due to the presence of intermetallics and Si, nevertheless, the surface heterogeneity can be erased gradually with prolonged treatment time.

Journal of Materials Science & Technology 50 (2020) 75–85

Contents lists available at ScienceDirect

Journal of Materials Science & Technology

journal homepage: www.jmst.org

Research Article

Influence of secondary phases of AlSi9Cu3 alloy on the plasma electrolytic oxidation coating formation process

Ting Wu [a,*], Carsten Blawert [a], Mikhail L. Zheludkevich [a,b]

[a] MagIC-Magnesium Innovation Centre, Helmholtz-Zentrum Geesthacht, 21502 Geesthacht, Germany
[b] Institute of Materials Science, Faculty of Engineering, Kiel University, Kaiserstrasse 2, 24143 Kiel, Germany

ARTICLE INFO

Article history:
Received 5 September 2019
Received in revised form
18 November 2019
Accepted 10 December 2019
Available online 7 March 2020

Keywords:
Plasma electrolytic oxidation
Aluminum alloy
Secondary phases

ABSTRACT

To understand the formation and growth of plasma electrolytic oxidation (PEO) coatings in presence of different secondary phases in a substrate, PEO treatment was carried out on AlSi9Cu3 alloy at different treatment times ranging from 15 s to 480 s. The coating formation and evolution process was traced by surface and cross-sectional observation of the layers on the different phases of the alloy. The results demonstrated a sequential involvement of the different phases in the plasma discharges: firstly, discharges start on the α-Al matrix, then on the intermetallic Al_2Cu and β-Al_5FeSi phases at the same time and finally on the eutectic Si. The presence of intermetallic Al_2Cu remarkably affects the initial dissolution, the deposition of conversion products and the ignition of discharges at the early stages of processing. Eutectic Si in the substrate exhibits the highest electrochemical stability at all stages and contributes in the beginning to a distinct coating morphology eventually. The resultant PEO coating tends to be uniform if processing times are longer and a double-layer structure appears in the coating.

1. Introduction

Plasma electrolytic oxidation (PEO) [1–6], as an eco-friendly surface modification technology based on plasma-assisted anodic oxidation for lightweight materials (aluminum, magnesium, titanium etc.), allows the creation of ceramic-like oxide coatings with firm adhesion to the substrate. Previous studies have demonstrated that PEO coatings, particularly alumina coatings, possess excellent resistances to environmental corrosion and abrasion damages, thus, this technique has been applied on aluminum alloys in a wide range of industrial applications for decades [7–11]. Many studies [12–14] focused on optimizing the combination of electrolytes and electric parameters in order to improve the performance of resultant PEO coatings. However, the quality of PEO coatings is often determined also by the chemical composition of the aluminum alloys, either by the alloying elements influencing PEO layer composition or via formation of secondary phases affecting the PEO process directly [15,16].

To investigate the effects of chemical composition of substrates, attempts have been made to study aluminum alloys, which contain different alloying elements. The major alloying element Cu generally exists in form of precipitates in aluminum alloys. An earlier study [17] explained the absence of Cu in PEO coatings of a commercial Al-Cu-Mg alloy (3.8–4.9 wt% Cu) by the dissolution of Cu-rich precipitates into the electrolyte during PEO processing and incapability of being absorbed and deposited into PEO coatings. However, a later research [18] reported the irregularity distribution of Cu in the outer layer of PEO coating on 2024 aluminum alloy, confirming Cu incorporation in the coatings. Afterwards, Oh et al. [19] identified approximately a Cu residual ratio of 0.1 in the PEO coating relative to that in the substrate of 2024 aluminum alloy and revealed an adverse role of Cu in α-Al_2O_3 transition. A brownish-red PEO coating on 2A97 aluminum alloy (3.8 wt% Cu) was obtained, which was attributed to the generation of dark red Cu_2O from oxidation of Cu in 2A97 aluminum alloy [20] by specific B-type discharges [21]. Furthermore, Veys-Renaux et al. [22] tracked the evolution of Cu-rich precipitates in AA2214 aluminum alloy during PEO processing and discovered the de-alloying of Cu-rich precipitates into Cu nanoparticles. Cu nanoparticles increased the electrical conductivity of the oxides, delaying the initiation of dielectric breakdown.

PEO coatings of binary Al-Mn alloys with increasing alloying content of Mn (1–8 at.%) exhibited increased surface roughness, coating thickness, amount and size of porosities [23]. Electrochemically active Mn, having a similar oxidation potential to Al, could easily substitute Al in Al_2O_3 crystal structure thus accelerating coat-

* Corresponding author.
E-mail address: ting.wu@hzg.de (T. Wu).

https://doi.org/10.1016/j.jmst.2019.12.031
1005-0302/

ing growth. The higher vapor pressure of Mn resulted in a higher porosity and hence higher surface roughness of PEO coatings during spark formation. In PEO studies of 2214-T6 and 7050-T74 aluminum alloys, the inhibition of α-Al_2O_3 growth in the coating of 7050-T74 aluminum alloy was ascribed to the abundant Zn in the substrate [24]. However, another study [19] identified a more significant contribution of Mg to suppress the formation of α-Al_2O_3 as compared with that of Cu and Zn. PEO coating formed on high Si containing aluminum alloys were mainly composed of γ-Al_2O_3, α-Al_2O_3, SiO_2 and a small amount of mullite phase ($Al_2O_3{\cdot}SiO_2$) [25]. The presence of Si in Al matrix led to lower efficiency in coating formation and lower porosity of the coating during PEO treatment due to the lower electrical conductivity of Si [26].

Although the influence of separate alloying elements in the substrate on the characteristics of resultant PEO coatings has been investigated, there is still a challenge to control the synthesis of PEO coating when there is lack of knowledge about coating formation and evolution on different materials and phases during PEO processing for multiphase aluminum alloys. AlSi9Cu3 alloy as an engineering material normally requires surface pretreatment before application [27–29]. Unfortunately, the large-sized secondary phases and high quantity of Si restrict the conventional anodization since the thinner and vulnerable anodic film is not able to fulfill the mechanical and tribological requirements [22,26]. As a potential solution, PEO treatment was performed on AlSi9Cu3 alloy in this work. It is noteworthy that AlSi9Cu3 alloy is a good model system of hybrid materials for the purpose of investigating PEO coating growth on different materials (α-Al, Si) and phases (Al_2Cu and β-Al_5FeSi) at the same time. Our studies disclosed the inhomogeneous growth and discontinuity of PEO coatings in presence of these different phases in AlSi9Cu3 alloy. The growth behavior of the coating from initial stage of PEO coating formation and further coating evolution was analyzed in detail and discussed.

2. Experimental

Rectangular specimens of as-cast AlSi9Cu3 alloy with dimensions of 15 mm × 15 mm × 4 mm were selected. The mass fraction of the substrate is 9.57 wt% Si, 2.56 wt% Cu, 0.93 wt% Sn, 0.83 wt% Mg, 0.38 wt% Zn, 0.35 wt% Fe, 0.14 wt% Mn and Al balance. Prior to PEO treatment, the surface of the specimens was ground using abrasive papers from 1200 grit to 4000 grit and polished with 3 μm polishing agent, then flushed by ethanol and distilled water respectively and dried in air at ambient temperature.

PEO process was carried out by using a unipolar-pulsed DC power source. In this work, a constant current regime was applied with a current density of 3 A/dm^2 and a duty cycle of 10 % (t_{on} : t_{off} =0.5 ms : 4.5 ms) in an alkaline electrolyte (pH = 12.4, conductivity 23.2 mS/cm) composed of 20 g/L Na_3PO_4 and 1 g/L KOH. The test specimens connected with a conductive holder worked as anode. The stainless steel tube being part of the heat-exchange system was adopted as cathode. The temperature of electrolyte was kept at 20 ± 1 °C. The PEO treatment was implemented at different treatment times ranging from 15 s to 480 s (15 s, 30 s, 60 s, 120 s, 240 s and 480 s, respectively).

The resulting voltage as a function of processing time was recorded with a data acquisition system (SignaSoft 6000 software package) provided by Gantner. The distribution of different phases of the substrate, surface and cross-sectional morphologies as well as chemical composition of the coatings were evaluated by means of scanning electron microscope (SEM, TESCAN Vega3 SB) equipped with an energy dispersive spectrometer system of eumeX (EDS, IXRFsystems). The phase composition of the substrate and coatings were analyzed using X-ray diffraction (XRD, D8 Advance, Bruker AXS) with CuK_α radiation (40 kV, 40 mA). Diffraction pattern were obtained at diffraction angle 2θ from 20° to 80° with a step size of 0.02°/s and grazing angle of 1°.

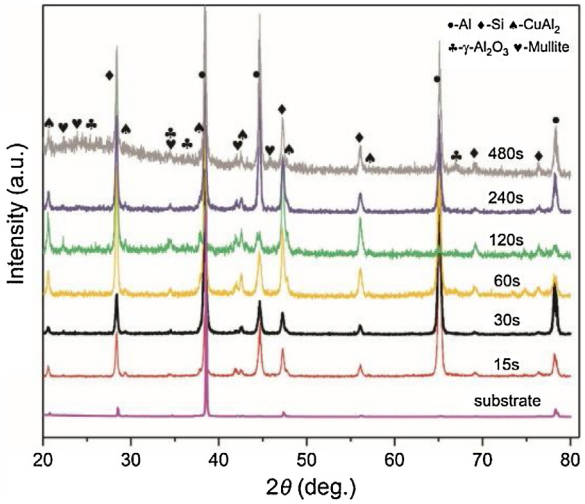

Fig. 1. X-ray diffraction patterns of the specimens before (substrate) and after PEO treatment for different times.

3. Results

3.1. Microstructure and composition of AlSi9Cu3 alloy

Fig. 1 reveals that AlSi9Cu3 alloy is mainly composed of α-Al and Si with additional intermetallic compounds Al_2Cu and β-Al_5FeSi respectively. The characteristic peaks of intermetallics can be hardly observed because of their lower intensity relative to the matrix. Simultaneously, Fig. 2 illustrates the microstructure of the bare AlSi9Cu3 alloy with the phases indexed, in accordance with the study of Puga et al. [30]. The microstructure is characterized as grey α-Al matrix with lath-liked eutectic Si, herringbone-structured intermetallic Al_2Cu and irregular intermetallic β-Al_5FeSi. At higher magnification (Fig. 2(c) and (d)), the overlapping distribution of intermetallic Al_2Cu and β-Al_5FeSi is revealed as another feature of the substrate microstructure. The observation of substrate microstructure provided visual information to differentiate the phases and further assisted in monitoring the coating evolution on these phases during PEO processing.

3.2. Characterization of PEO coating formation on AlSi9Cu3 alloy

3.2.1. Voltage evolution during PEO processing

Fig. 3 shows the change of voltage with increasing treatment time until 480 s. It is the typical form of voltage-time curve when a constant current density is applied in PEO processing of aluminum alloys [31,32]. The curve can be divided into two discernable stages: firstly, the stage of conventional anodic oxidation featured by a rapid and linear increase of oxidation voltage at a rate of 3.3 V/s, when the treatment time is shorter than 60 s. The first stage indicates the initial mostly electrochemical-driven dissolution of the substrate and the formation of thin passive barrier layer on the interface of substrate/electrolyte [33]. First tiny arcs were observed after 60 s at a voltage of 200 V. Afterwards, the process progresses into the second stage, characterized by the phenomenon of numerous visible micro arcs moving around on the surface of the specimen. However, at this point, the slope of the voltage-time curve decreases associated with the continuous thickening of the porous PEO coating. The PEO process remains at this stage until 480 s and the increase of voltage is slowing down further, reaching a final voltage of 350 V.

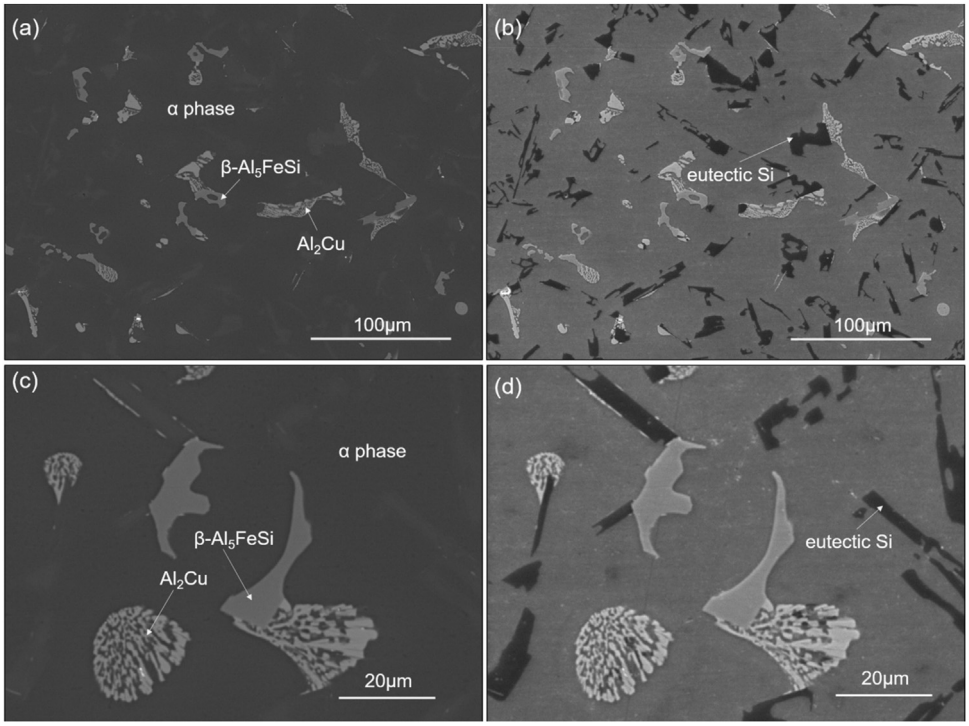

Fig. 2. Microstructures of AlSi9Cu3 alloy with four different phases: (a, c) BSE images; (b, d) SE images.

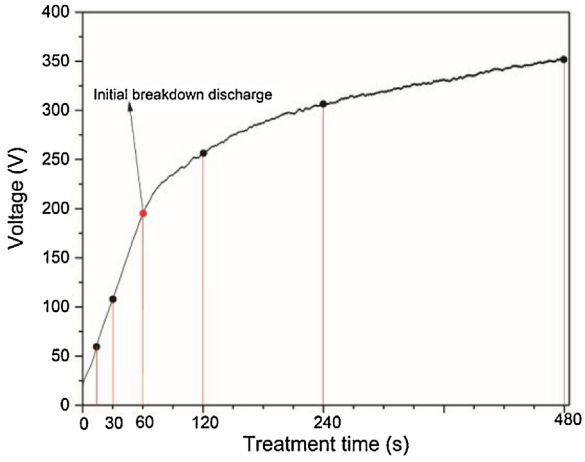

Fig. 3. Voltage-time response during 480 s of PEO processing.

3.2.2. *Phase composition*

The phase composition of the coatings after different treatment times is shown in the XRD patterns (Fig. 1). Besides the intensive peaks from the substrate (α-Al, Si and Al_2Cu) due to the X-ray penetrating through the coating into the substrate, some weak signals (mainly after 480 s treatment) demonstrate that the coatings consist of γ-Al_2O_3 and mullite ($3Al_2O_3{\cdot}2SiO_2$) respectively. Interestingly, although the phase composition of the coatings seems not to change with treatment time, some substrate signals appear to be stronger indicating that in spite of coating formation the Al matrix is preferentially etched with intermetallic Al_2Cu remaining. Only at 480 s, an additional amorphous phase appears as a broad bump at 2θ around 20° to 35°. The transformation from amorphous alumina to crystalline Al_2O_3 mostly depends on the temperature [34]. However, discharges providing enough energy for phase transformation and heating the specimen and electrolyte up, are still not occurring within the short treatment times and a final voltage of 350 V.

3.2.3. *Surface morphologies and element distribution*

Fig. 4 displays the surface morphologies on AlSi9Cu3 after different PEO treatment times and reveals the coating evolution on the four different phases (α-Al, eutectic Si, Al_2Cu and β-Al_5FeSi intermetallics). At the very beginning (the first 15 s), initial selective dissolution occurs in the interface to Al_2Cu, as the denuded net structure of Al_2Cu is clearly revealing in Fig. 4(a). In the meantime, the deposition of conversion products is observed preferentially surrounding the periphery of the intermetallic Al_2Cu, which is supported by O and P signals shown in the EDS analysis in Fig. 5(a).

After 30 s, the conversion products accumulate around Al_2Cu and β-Al_5FeSi intermetallics as revealed in (Fig. 4(b)). The signals of the characteristic elements Fe, O and P in these positions (Fig. 5(b)) confirm the involvement of β-Al_5FeSi in formation of the conversion products. However, the coverage of the surface in larger distance from these intermetallics by elements O and P originated from the electrolyte is limited and the boundaries of Si are still recognizable. The conversion products pile up further until 60 s treatment (Fig. 4(c)) and the elements O and P start to cover the entire surface (Fig. 5(c)), whereas, it seems that the conversion products peel off from the surface, leaving behind some voids around the Al_2Cu phases after 120 s (Fig. 4(d)). According to observation of the sparking, the first sparks appear already after 60 s and it is likely that they are involved in the removal of the conversion products around the intermetallics.

The topography of intermetallic Al_2Cu after 120 s features some lower areas (Fig. 6(a)), which are obviously a result of the preferential dissolution of Al_2Cu intermetallics. Micro-pores from initial discharges can be seen at 120 s as well. They are largely distributed on the junction of intermetallic Al_2Cu and surrounded α-Al matrix (Fig. 6(a)) and less on the surface of Al_2Cu and β-Al_5FeSi (Fig. 6(b)). It can be inferred that the initial discharges have started on certain regions of the barrier layer when the voltage reached 200 V after 60 s. These regions are apparently related to the fast growing conversion layer on the top of α-Al matrix around the intermetallics. When the voltage gradually ramps up to 250 V at 120 s, it also exceeds the breakdown potential of the barrier layer on all phases

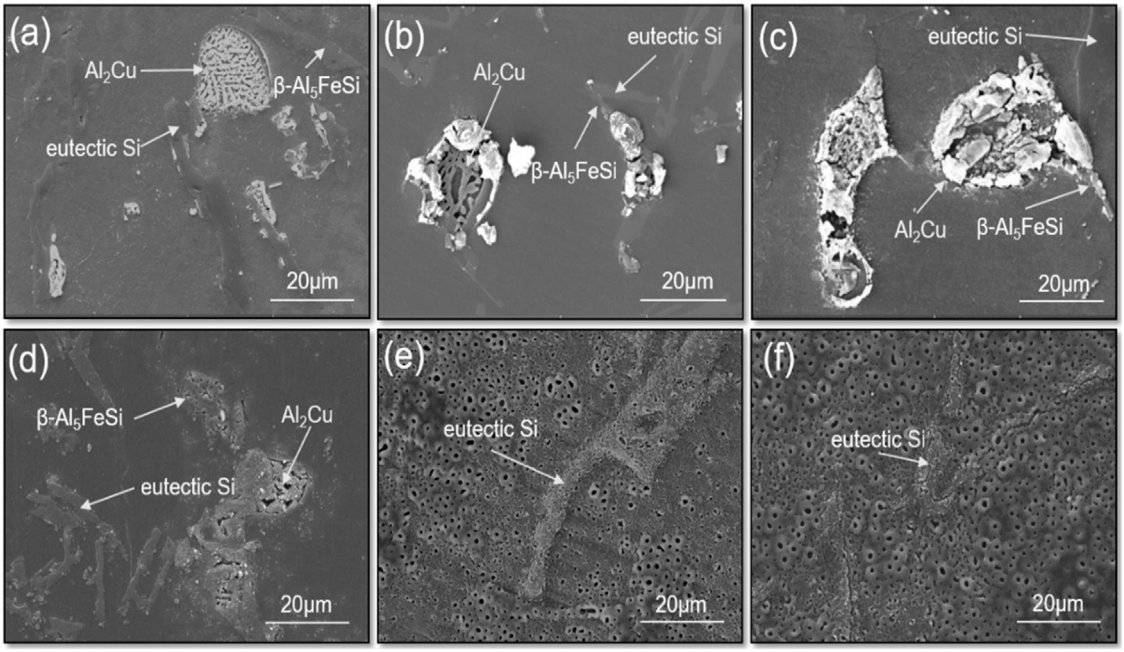

Fig. 4. Surface micro-morphologies on specimens after PEO treatment: (a) 15 s; (b) 30 s; (c) 60 s; (d) 120 s; (e) 240 s; (f) 480 s.

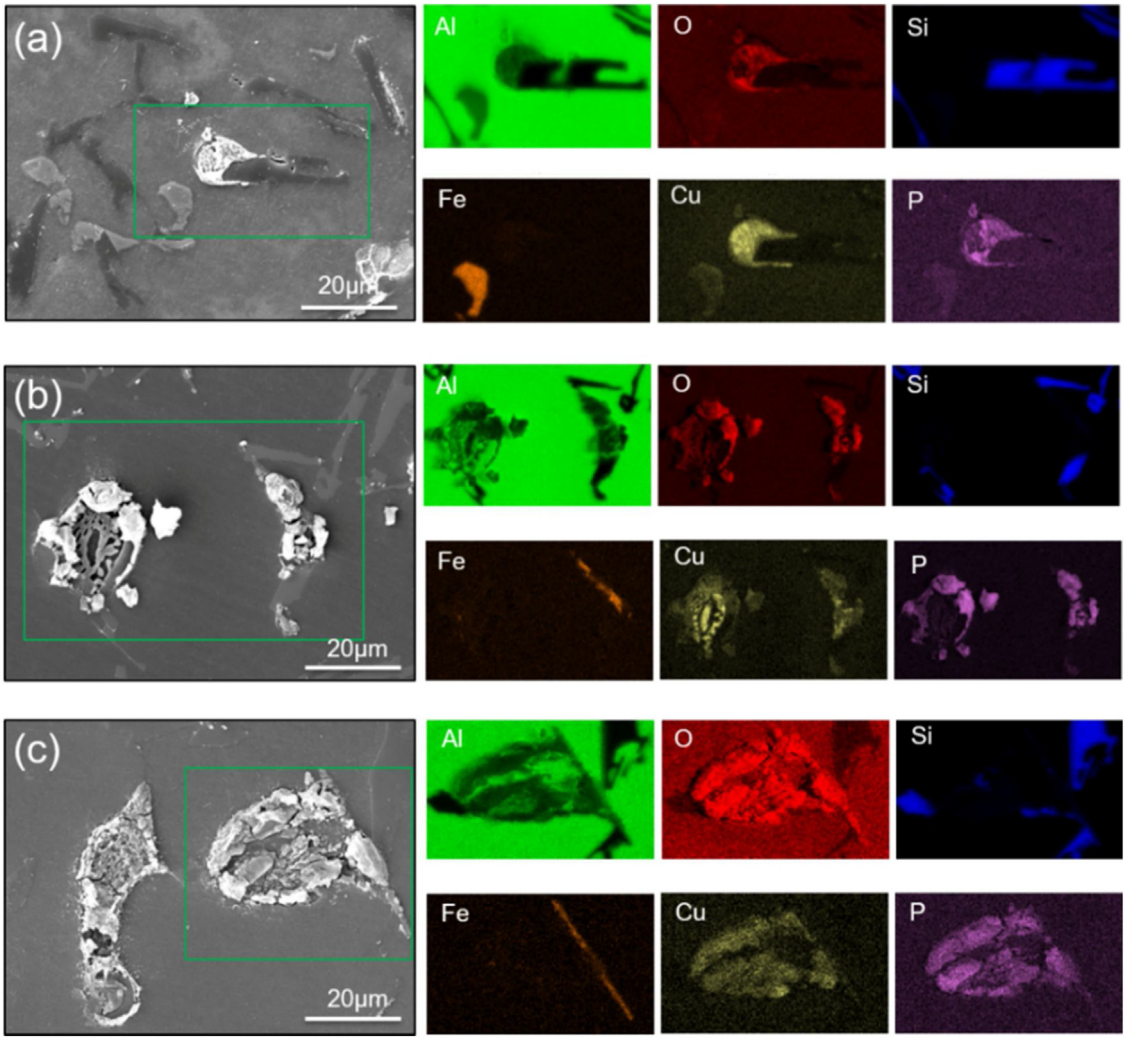

Fig. 5. EDS mapping results of local micro-areas on AlSi9Cu3 after different PEO treatment times: (a) 15 s; (b) 30 s; (c) 60 s.

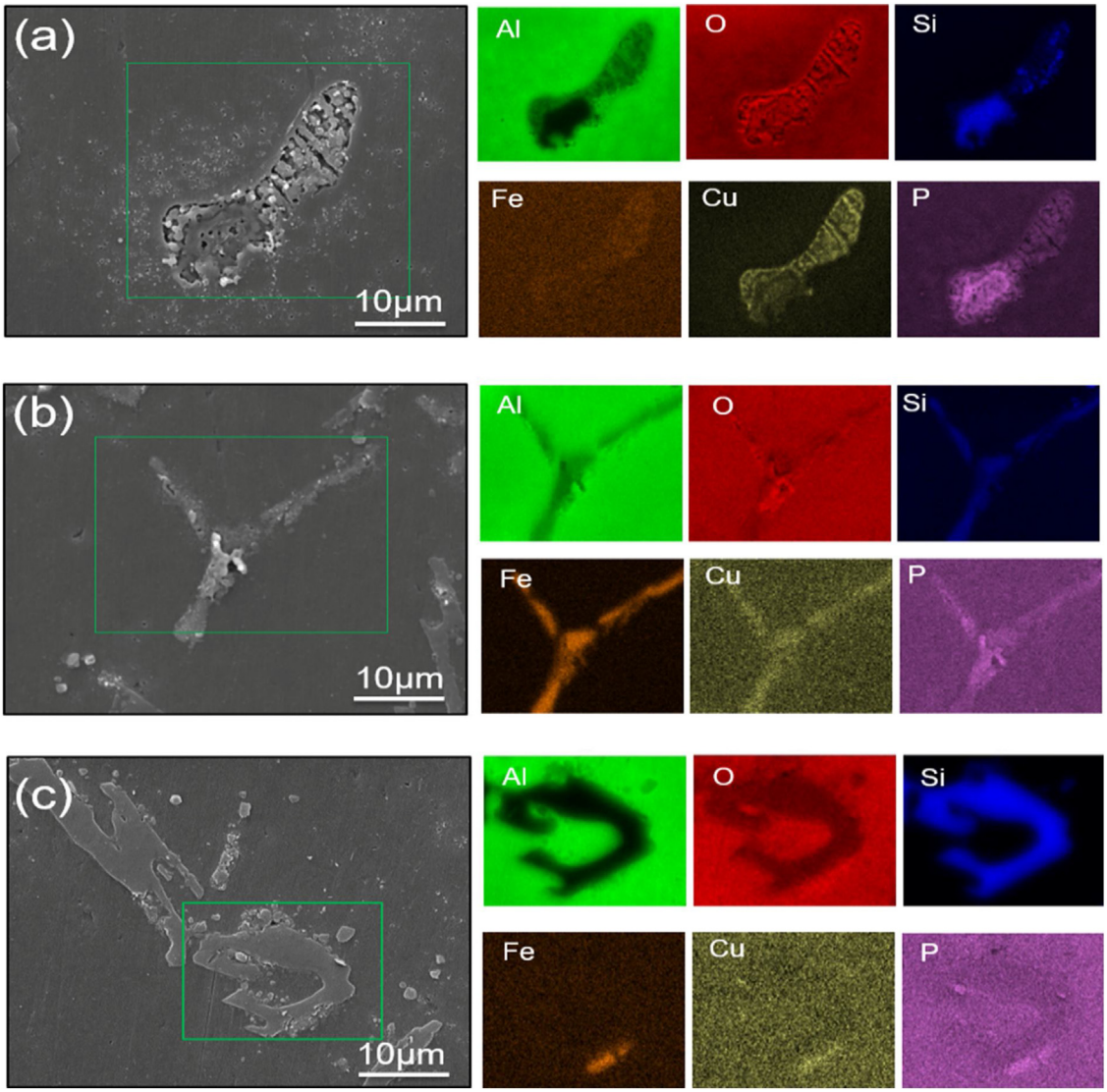

Fig. 6. Surface morphologies and local EDS mapping results on different secondary phases after 120 s PEO treatment: (a) Al_2Cu; (b) β-Al_5FeSi; (c) eutectic Si.

except of eutectic Si [35], because of its lowest rates in anodizing and formation of oxides illustrated by the weak coverage of O/P on it (Fig. 6(c)).

The surface is firstly fully covered with a typical PEO coating showing numerous micro-pores after 240 s treatment (Fig. 4(e)). The continuous coverage of O on eutectic Si (Fig. 7(a)) reveals that silicon surface is oxidized and an oxide layer is formed already. Interestingly, there are discernible surface micro-morphologies distinguishable by the distribution of micro-pores of different sizes. According to the distribution of the characteristic elements (Al, Si, Cu and Fe), the three distinct surface micro-morphologies are related to the phases present at the surface, indicating the substantial effect of secondary phases on the surface morphologies of the coating at this stage. At higher magnification, the coating on eutectic Si (Fig. 7(b)) shows a few small micro-pores and the boundaries of eutectic Si underneath are still visible because the layer is too thin to cover the morphology of eutectic Si completely. The mostly sintered coating with the largest micro-pores is certainly growing on the overlapping area of Al_2Cu and β-Al_5FeSi in Fig. 7(d).

After longer treatment (480 s), the surface morphologies of PEO coatings evolve significantly (Fig. 4(f)). Besides micro-pores spread on the entire surface, even some micro-cracks form already in particular regions at 480 s. An increase in micro-pore sizes is observed on the PEO coating surface compared with that of 240 s (Figs. 7(a) and 8 (a)) due to the higher energy (voltage and current) in the discharge as resistance of the coating is increasing with thickness of the coating. Three micro-morphologies characterized by divergent porosities as observed on the coating surface of 240 s are still discernible with extended treatment time, shown in Fig. 8(b)–(d)) (marked areas 1, 2 and 3). The inhomogeneity in the micro-morphology is mainly controlled by the intensity and density of discharges, which can be related to different resistance of the oxide film on the different phases. The main element composition and content of the coating in the three different micro-morphologies are determined in Fig. 8(e). The amount of characteristic elements (Al, Si, Cu and Fe) indicates the locations of the phases underneath the coatings and is beneficial to trace the evolution of coating formation and surface features on these phases respectively. Area 1 containing the highest amount of Si and lowest concentration of Al, Cu and Fe is corresponding to the coating formed on eutectic Si. Area 2 featured by the highest Al content among the three regions refers to the coating deposited on α-Al matrix. While the highest Cu and Fe quantities of area 3 indicate the coating on the typical overlapping region of Al_2Cu and β-Al_5FeSi intermetallics, which could hardly be distinguished after 480 s treatment.

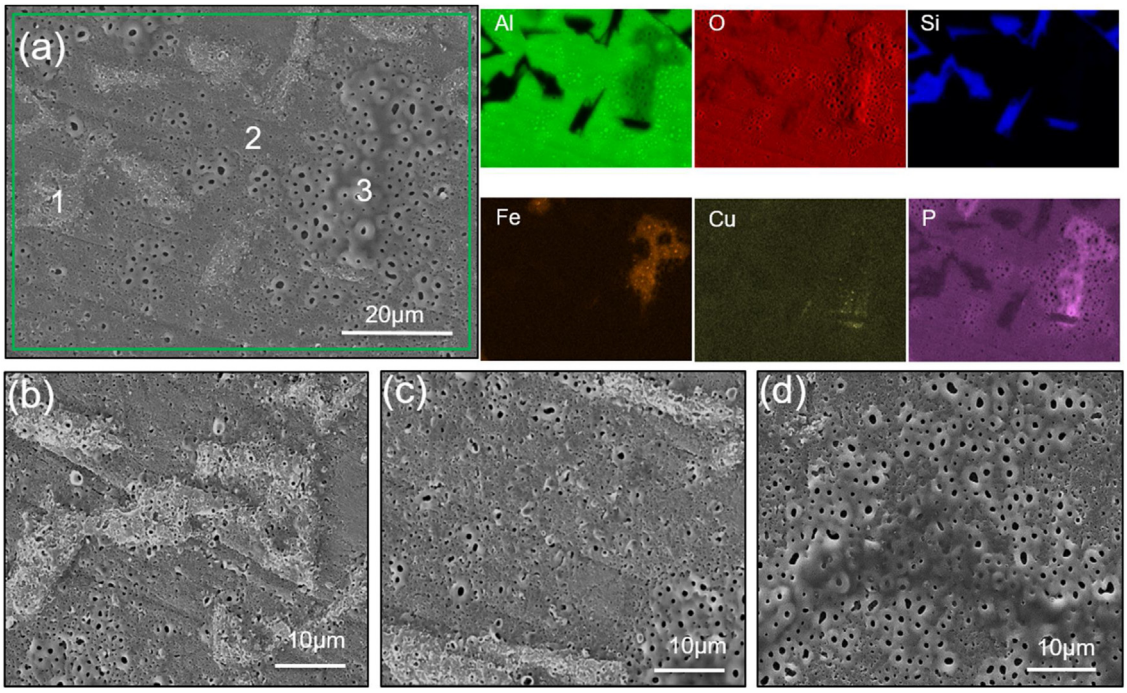

Fig. 7. Surface evolution of PEO coating after 240 s treatment: (a) overview of PEO coating on AlSi9Cu3 with EDS mapping results; surface morphologies on (b) eutectic Si, (c) α-Al matrix and (d) the overlapping location of Al_2Cu and β-Al_5FeSi.

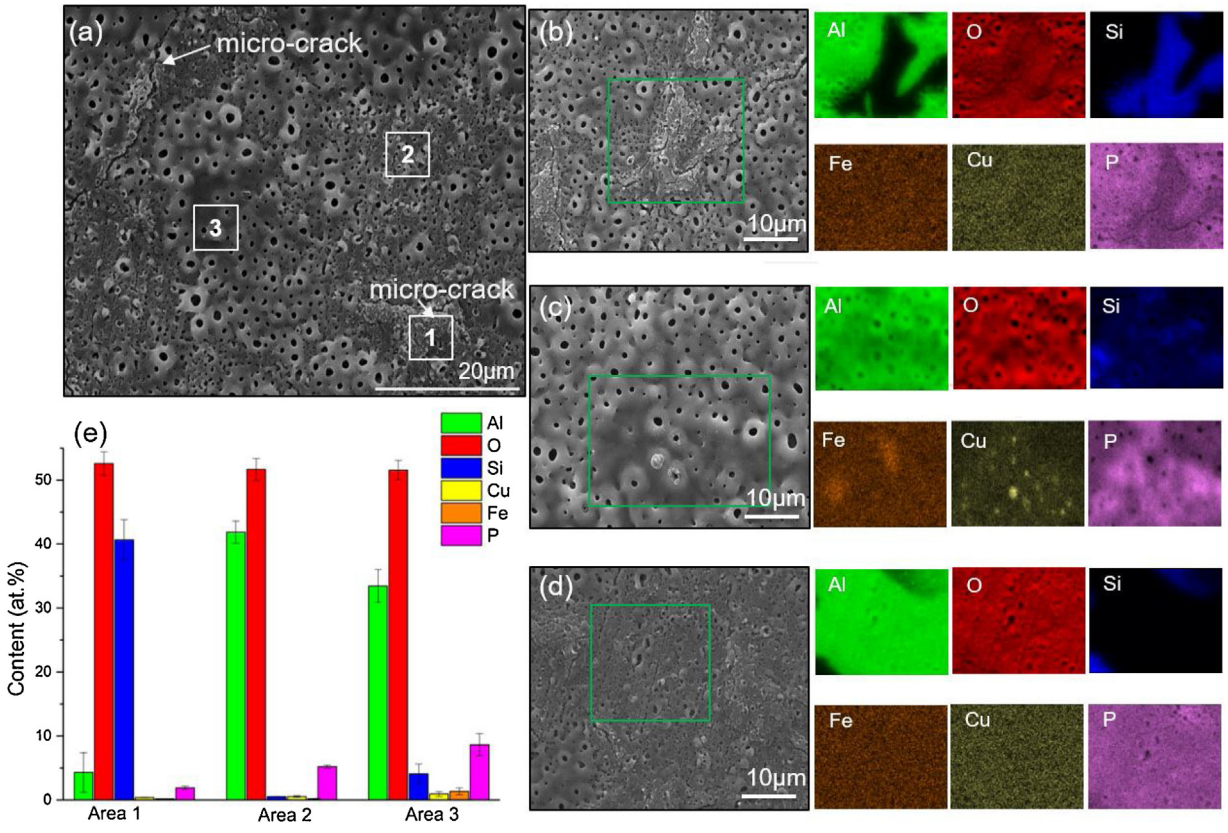

Fig. 8. Surface evolution of PEO coating after 480 s treatment: (a) overview of PEO coating on AlSi9Cu3. Surface morphologies on different phases with EDS mapping results: (b) on eutectic Si; (c) on α-Al matrix; (d) on the overlapping location of Al_2Cu and β-Al_5FeSi; (e) characteristic element contents at different selected areas in (a).

The micro-pore size of the resultant coating on the overlapping of Al_2Cu and β-Al_5FeSi is 0.078-0.95 μm, 0.32-0.75 μm on α-Al matrix and 0.05-0.26 μm on eutectic Si respectively. Micro-cracks appear mainly in the coating grown on eutectic Si (Fig. 8(a)), which is confirmed by the clustering of Si (Fig. 8(b) and (e)). A high PBR value of 2.22 for SiO_2 indicates higher internal stresses of oxide mixtures mainly containing SiO_2. With smallest micro-pores on eutectic Si, the inefficient release of internal stresses consequently

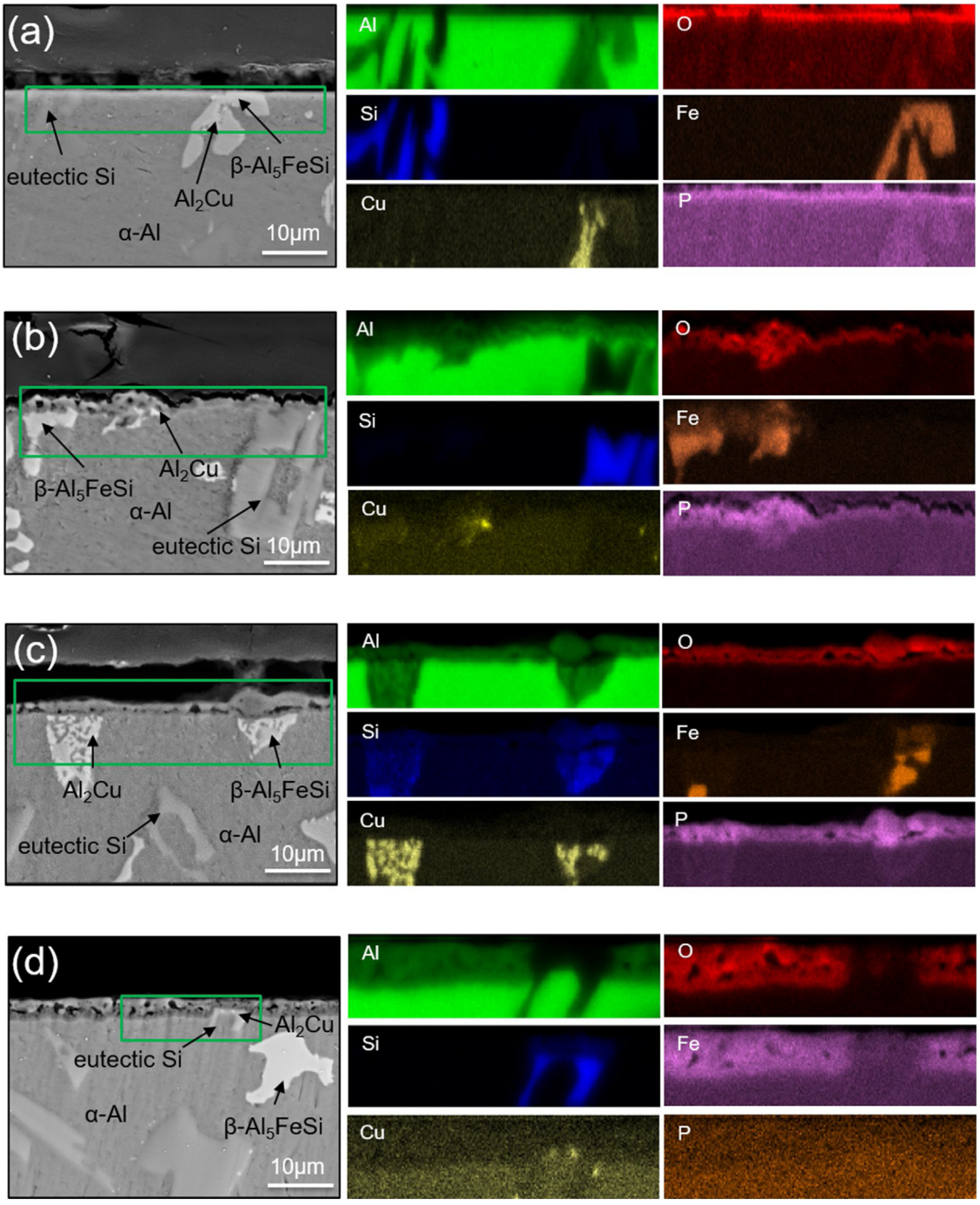

Fig. 9. Cross-sectional morphologies and EDS mapping results of PEO coating after different treatment time: (a) 60 s; (b) 120 s; (c) 240 s; (d) 480 s.

results in the generation of micro-cracks at these regions. Besides, the additional mismatch in an oxide mixture is prone to cause more micro-cracks in the coating as well.

3.2.4. Cross-sectional morphologies and element composition

With the goal of investigating the evolution of PEO coating, the cross-sectional morphologies in Fig. 9 demonstrates different growth stages of the coating (from 60 s to 480 s). It is obvious that the growth of coating on the different phases is dependent on the treatment time. Even after 60 s treatment, the oxide layer on the specimen is hard to recognize (Fig. 9(a)). However, the cross-sectional mapping result at 60 s (Fig. 9(a)) reveals a thin and discontinuous coverage of O on the surface of the specimen, chiefly associated with the disruption of the oxide layer by stable eutectic Si. It is worth noting that there is most likely an oxide layer already after 15 s and 30 s, but the metallographic preparation technique leads to rounding effects at the edges removing the thin film. Afterwards, protuberant porous oxides already start to deposit on the intermetallics of Al_2Cu and β-Al_5FeSi within 120 s, as shown by the distribution of Cu, Fe and O in Fig. 9(b), whereas only a thinner oxide layer covers the surface of eutectic Si.

A dense and continuous PEO coating coverage is firstly observed at 240 s (Fig. 9(c)). The coating on overlapping region of Al_2Cu and β-Al_5FeSi intermetallics is still thicker, mainly due to the lower melting temperature of the mixed oxides (Cu and Fe oxides) allowing faster sintering and coating growth. The gap between coating

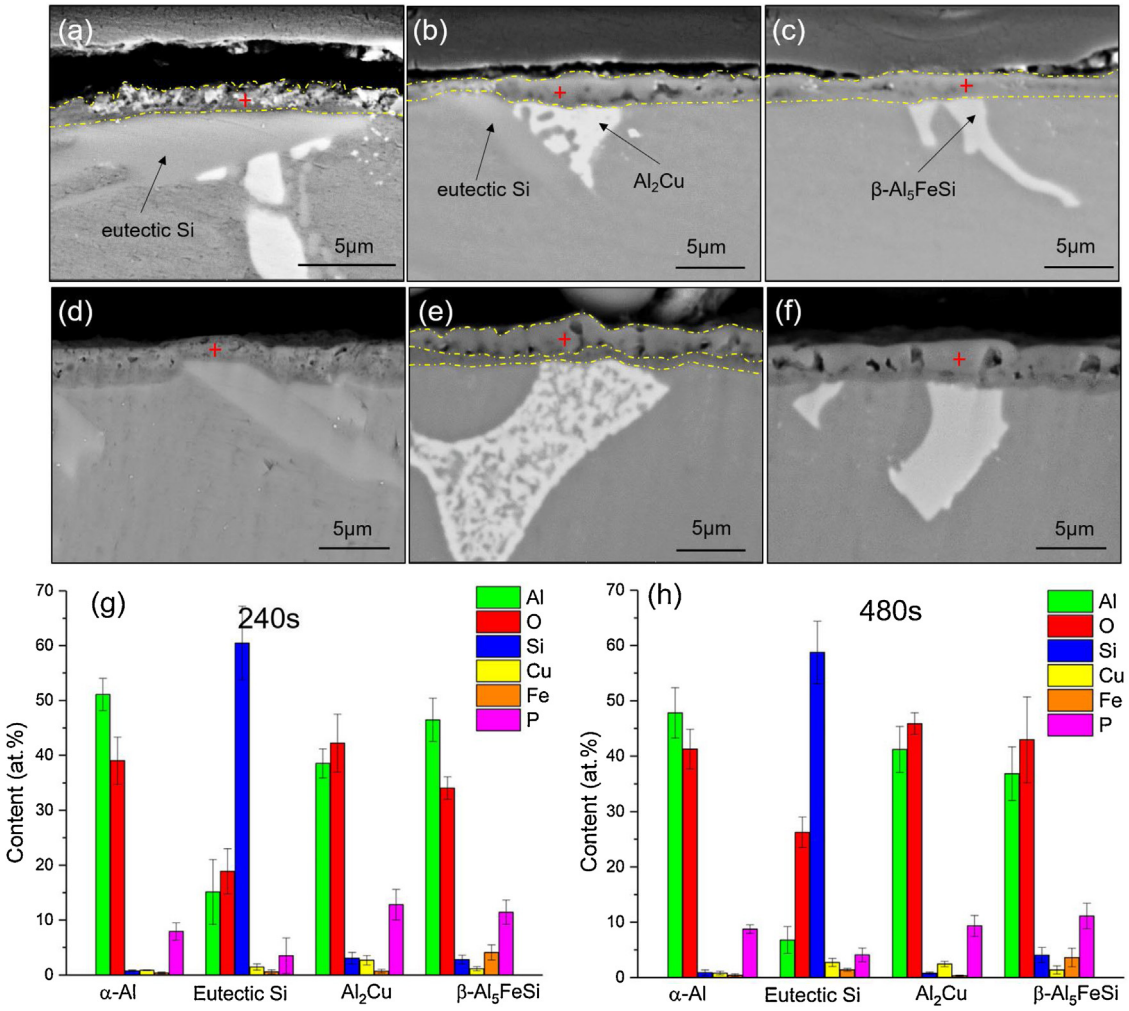

Fig. 10. Cross-sectional evolution of PEO coatings at 240 s and 480 s: (a, b, c) cross-sectional morphologies of PEO coatings on different secondary phases at 240 s; (d, e, f) cross-sectional morphologies of PEO coatings on different secondary phases at 480 s; (g, h) characteristic element contents on different phases at 240 s and 480 s, respectively.

and substrate discloses a pore band in the interface. After that, the coating develops further up to 480 s. The coating becomes denser and more uniform in both morphology and thickness on all phases as presented in Fig. 9(d). This is most likely the results of the successive discharge breakdown in the weakest areas of the coating and deposition of reinforced coatings in these regions. The higher position of the interface of eutectic Si/coating relative to surrounding α-Al matrix/coating (Fig. 9(d)) indicates a delay of dissolution and oxidation of Si and a thinner oxide layer on eutectic Si. Simultaneously, the distribution of O on eutectic Si also suggests the highest stability of Si among all phases in the substrate.

For PEO coatings after 240 s and 480 s treatments, Fig. 10 reveals the coating evolution on the different phases in more details. The coating appears as undulant single-layer morphology on all phases at 240 s. The layer on eutectic Si is thin and jagged (Fig. 10(a)), while the layers on Al_2Cu and β-Al_5FeSi (Fig. 10(b) and (c)) are quite thick and dense, in agreement with results in literature [36]. The most visible pore bands arise up in the coating on the α-Al, adjacent to Al_2Cu and β-Al_5FeSi intermetallics, primarily attributed to the severe plasma discharges in these regions [37]. According to the element composition of the coating on different phases at 240 s (Fig. 10(g)), there seems to be less mixing of coating above eutectic Si. Si (SiO_2) still dominates the coating on eutectic Si and only little phosphate is incorporated. However, some Al_2O_3 seems to be present as well.

The coating thickens evidently on all phases after 480 s treatment (Fig. 10(d)–(f)). The average thickness values of the coating on α-Al matrix, Al_2Cu, β-Al_5FeSi and eutectic Si, measured from the cross-sections, are 2.62 ± 0.28 μm, 3.01 ± 0.29 μm, 3.06 ± 0.29 μm and 1.96 ± 0.38 μm respectively. A dense layer with smooth and sealed surface is successfully deposited on eutectic Si, despite the coating thickness remains the thinnest with respect to the other phases. The smooth conversion of the coating surface demonstrates that sufficient molten oxide was involved in coating formation at the final voltage of 350 V, even for the formation of SiO_2 (T_m>1600 °C).

Fig. 10(h) shows the chemical composition of the coatings on the four different phases at 480 s and a general increase of O content on eutectic Si from 240 s (less than 20 at.%) to 480 s (more than 25 at.%) can be seen. However, this seems to be more an artefact since there is more volume of the matrix region analyzed when the layer is thinner. Interestingly, the structure of the coating converts from a single-layer morphology to double-layer morphology on the matrix, Al_2Cu and β-Al_5FeSi intermetallics as shown in Fig. 10(e) and (f) after 480 s. It may arise from a change of main growing direction of the coating at 240 s. The subsistent thick coating impedes the breakdown discharges, which further impairs the outwards growing of the coating while inwards growth rate of the coating increases [3]. With increase of treatment time, an outer layer with

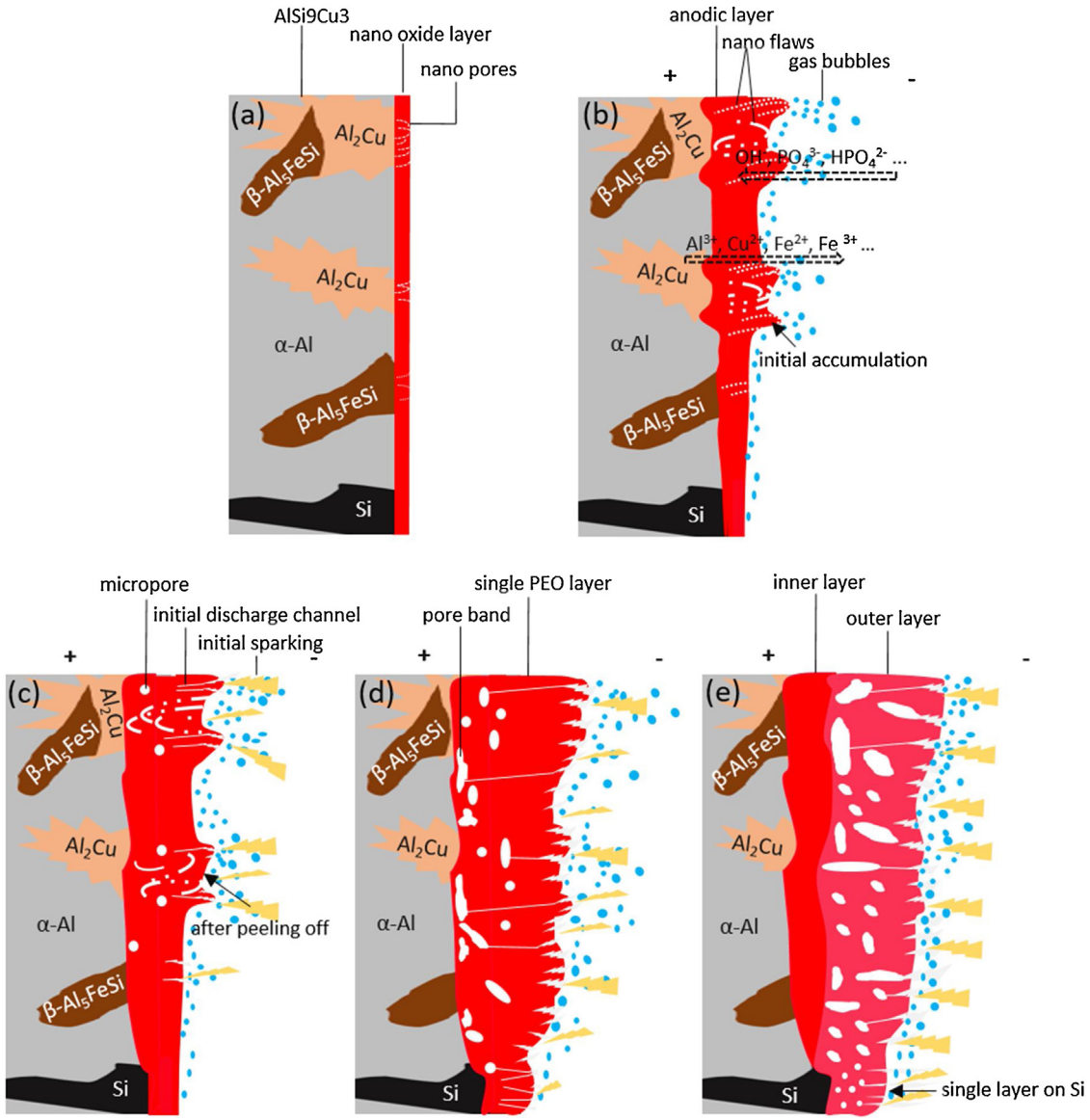

Fig. 11. Schematic diagram of coating formation before and during PEO process: (a) air-formed oxide layer prior PEO processing; (b) initial deposition and accumulation of conversion products around Al_2Cu intermetallics; (c) initial plasma breakdown discharges on all phases except eutectic Si; (d) non-uniform growth of PEO coating with single layer morphology; (e) uniform growth of PEO coating with inner layer and outer layer.

visible micro-pores and an inner compact layer free of micro-pores develop eventually.

4. Discussion

At the very beginning, the boundary of intermetallics Al_2Cu is initially dissolved (Fig. 4(a)) with the assistance of applied electrical field. Prior to anodizing, a native oxide layer formed in air already covers the alloy (Fig. 11(a)). The oxide layer on Al_2Cu intermetallics is not as protective as that on α-Al matrix as a result of the high content of Cu. Inevitably, the intermetallics underneath are exposed directly to the electrolyte and especially at the interface of Al_2Cu/α-Al the native oxide layer compromises even more defects [38]. Consequently, the electrical field-assisted dissolution is preferentially initiated and enhanced at the verge of Al_2Cu intermetallics. Afterwards, conversion products start to deposit in these specific regions by the combination of Al^{3+}/Cu^{2+} from dissolved matrix and PO_4^{3-}/OH- originating from the electrolyte. They form of low soluble Al/Cu-based oxides and phosphates (Figs. 5(a) and (b) and 11 (b)). The enrichment of Fe will produce residual defects in the native oxide layer on β-Al_5FeSi providing a path for the penetration of electrolyte. The presence of Si in β-Al_5FeSi tend to change the current flow into less resistive α-Al matrix around [39] and reduce the anodizing efficiency. Overall, β-Al_5FeSi presents a lower oxide growth rate relative to intermetallic Al_2Cu (Fig. 5). With the increased voltage, conversion products gradually spread to the surface of intermetallics and accumulate further (Fig. 11(b)).

The unexpected peeling-off (Fig. 4(d)) interrupts the collection of conversion products after the breakdown voltage is reached. It could be related to the thermal and mechanical stresses generated by the first discharges. Due to the excess of flaws within high Cu contained conversion products the poor adhesion to the substrate beneath is also a possible factor (Fig. 11(c)). The disappearance of protuberant conversion products potentially provides more weak regions for the plasma breakdown discharges and the coating growth will be enhanced by the intensive and frequent discharges [40].

Plasma discharges after their extinguishing, are responsible for the typical surface morphology with micro-pores on the coating surface. When the increased voltage reaches the critical breakdown voltage, the breakdown of dielectric layer takes place hence leaves behind the characteristic micro-pores near the coating surface and micro-channels within the coating [41].

The micro-pores from initial discharges are largely distributed on the top of α-Al matrix (Fig. 6), demonstrating the ease of breakdown discharge in corresponding barrier layers. Interestingly, these micro-pores are preferentially surrounding Al_2Cu intermetallics (Fig. 6(a)). A possible explanation is associated with the modified structure and composition of the preferential barrier layer on α-Al matrix next to the interface of Al_2Cu/α-Al.

Severe gas generation during anodizing at the layer/electrolyte interface prevents the penetration of electrolyte into the layer, insulating the substrate and creating numerous resembling capacitors in the interface barrier layer/electrolyte. Once the voltage exceeds the breakdown voltage, gas discharges take place accompanying with the breakdown of the barrier layer. Considering the layers having excess of defects, i.e. the layers on Al_2Cu containing high content of copper oxide [42], are more prone to pass through by the current flow and sustain dissolution and oxidation of the intermetallics underneath rather than to be a barrier element of the capacitors before reaching a specific thickness. In regards to layers of bare imperfection, i.e. the crystalline layer on α-Al, although served as a part of the capacitors, are hardly to be broken down due to the low dielectric permittivity of Al_2O_3 (7.5-15) relative to CuO (around 18) [43]. Nevertheless, layers around the interface of Al_2Cu/α-Al are modified either by morphology or composition (Fig. 5(b)) arising from diffusion of Al^{3+}/Cu^{2+} in these regions compared to layers strictly formed on Al_2Cu and α-Al. Subsequently, layers at the interface of Al_2Cu/α-Al mixed with Al_2O_3 offering good passivity and CuO with high dielectric permittivity is precisely subjected to the breakdown.

The continuous increase of voltage determines the growth of PEO coatings. The cycles of arcing, melting, sintering and quenching of the coating during pulsed PEO processing cause the sintered appearance of the coating on the overlapping regions of Al_2Cu and β-Al_5FeSi (Fig. 7(d)). Actually, lower melting points of FeO (1377 °C), Fe_2O_3 (1565 °C) and CuO (1450 °C) relative to higher melting points of Al_2O_3 (2072 °C) can be responsible for the more sintered morphologies with larger micro-pore size compared to the denser coatings on the surrounding α-Al matrix.

The continuous PEO coatings possess the smallest micro-pores on eutectic Si (Figs. 7, 8 and 11(d)), determined by less intensive breakdown discharges on eutectic Si. At this stage, all phases are on the same potential. In terms of the low conductivity of eutectic Si, less current can flow through the combination of Si/SiO_2 (semiconductor/oxide) than through the combination Al/Al_2O_3. The wider band gap of SiO_2 compared with other oxides also contributes to the lower current passing. Weaker current flow makes the ignition of energetic discharges on eutectic Si more difficult as well as being responsible for lower intensity of discharges. Besides this, the hardship in breaking down the SiO_2 barrier layers with low dielectric permittivity 3.8 on eutectic Si [43] further prevent the formation of large-sized micro-pores. Generally, every single discharge is a transient process to generate energetic species from the collisions between high-energy electrons with gas molecules and atoms in gasification. These energetic species then react with the barrier layers by breaking the chemical bonds in barrier layers, revealing a typical breakdown process [44]. Highest ionization energy of SiO_2 (11.43 eV) relative to Al_2O_3 (10.5 eV), CuO (9.41 eV) and FeO (8.56 eV) [45] eventually moderates strength of reactions on the barrier layer of eutectic Si.

With the thickening of the coating, the breakdown of the coating becomes more difficult and the outward growth of the coating reaches a limit soon. In this case, the bottom of some large-sized discharge channels turn into new reaction zones for the inward growth of the coating. The opposite directions in coating growth finally give rise to the double layer morphology in the coating as shown in Fig. 10(e) and (f) and depicted in Fig. 11(e). At this stage, gas discharges are prone to take place at the bottom of micro-pores [46], from which the pore bands generate. The high electric field forces the ionized gases inward from the electrolyte/coating interface to the substrate and drives the aluminum ions outward via the discharge channels. The inward ionized gases, filling the discharge channels at high pressure, consequently constrain the accesses of electrolyte into the discharge channels. A quenching effect of the electrolyte on the solidification of the newly formed molten oxides is hence prevented. As a result, a micro-pore free inner layer is deposited next to the substrate.

5. Conclusions

(1) Al_2Cu intermetallics, β-Al_5FeSi and eutectic Si in AlSi9Cu3 alloy exhibit significant influence on phase formation and coating growth during PEO processing mainly attributed to their different chemical-, electrochemical- and physical properties. The coatings formed in phosphate electrolyte are mainly composed of γ-Al_2O_3, mullite ($3Al_2O_3{\cdot}2SiO_2$) and an amorphous phase.

(2) The involvement of the phases in the PEO process (discharge formation) after initial conventional anodic oxidation is α-Al matrix, followed by Al_2Cu and β-Al_5FeSi and finally eutectic Si in sequential order. The majority of initial micro-pores (discharges) appear preferentially on the α-Al matrix surrounding Al_2Cu intermetallics, indicating more active sites for plasma discharges at these regions.

(3) Resultant PEO coatings show distinct surface morphologies on different phases. The coating on Al_2Cu and β-Al_5FeSi intermetallics reveals a sintered morphology with large micro-pores. The thinnest coating with smallest micro-pores and some microcracks is found on eutectic Si.

(4) A double-layer morphology in the resultant coating is observed on all phases except of eutectic Si, characterized by a porous outer layer and a compact inner layer, due to the reverse growing directions (outward firstly then inward) of the coating.

(5) The alloy AlSi9Cu3 is a good model alloy for PEO treatment of multi-material mix, revealing the problems of delayed sparking and different coating growth/phase composition if two different materials should be treated.

Acknowledgements

The author Ting Wu (CSC No. 201708510113) would like to thank the financial surpport from China Scholarship Council(CSC). The technical support of Mr. Volker Heitmann and Mr. Ulrich Burmester during this work is gratefully acknowledged.

References

[1] A.L. Yerokhina, A. Voevodinb, V.V. Lyubimova, M. Donleyb, Surf. Coat. Technol. 110 (1998) 140–146.
[2] A.L. Yerokhin, V.V. Lyubimov, R.V. Ashitkov, Ceram. Int. 24 (1998) 1–6.
[3] R.O. Hussein, X. Nie, D.O. Northwood, Electrochim. Acta 112 (2013) 111–119.
[4] X. Lu, C. Blawert, M.L. Zheludkevich, K.U. Kainer, Corros. Sci. 101 (2015) 201–207.
[5] Y. Cheng, Z. Peng, X. Wu, J. Cao, P. Skeldon, G.E. Thompson, Electrochim. Acta 165 (2015) 301–313.
[6] S. He, Y. Ma, H. Ye, X. Liu, Z. Dou, Q. Xu, H. Wang, Corros. Sci. 122 (2017) 108–117.
[7] A.L. Yerokhin, L.O. Snizhko, N.L. Gurevina, A. Leyland, A. Pilkington, A. Matthews, J. Phys. D 36 (2003) 2110–2120.
[8] D. Kong, H. Liu, J. Wang, J. Alloys. Compd. 650 (2015) 393–398.
[9] Z. Wu, Y. Xia, G. Li, F. Xu, Appl. Surf. Sci. 253 (2007) 8398–8403.

[10] N. Barati, A. Yerokhin, F. Golestanifard, S. Rastegari, E.I. Meletis, J. Alloys. Compd. 724 (2017) 435–442.
[11] V.S. Egorkin, S.V. Gnedenkov, S.L. Sinebryukhov, I.E. Vyaliy, A.S. Gnedenkov, R.G. Chizhikov, Surf. Coat. Technol. 334 (2018) 29–42.
[12] V. Dehnavi, B.L. Luan, D.W. Shoesmith, X.Y. Liu, S. Rohani, Surf. Coat. Technol. 226 (2013) 100–107.
[13] V. Dehnavi, X.Y. Liu, B.L. Luan, D.W. Shoesmith, S. Rohani, Surf. Coat. Technol. 251 (2014) 106–114.
[14] A.G. Rakoch, A.A. Gladkova, Z. Linn, D.M. Strekalina, Surf. Coat. Technol. 269 (2015) 138–144.
[15] T.W. Clyne, S.C. Troughton, Int. Mater. Rev. 64 (2019) 127–162.
[16] K. Li, W. Li, G. Zhang, W. Zhu, F. Zheng, D. Zhang, M. Wang, J. Alloys. Compd. 790 (2019) 650–656.
[17] C. Wang, D. Zhang, Y. Jiang, Appl. Surf. Sci. 253 (2006) 674–678.
[18] Y. Guan, X. Yuan, L. Guang, Surf. Coat. Technol. 202 (2008) 4602–4612.
[19] Y. Oh, J. Mun, J. Kim, Surf. Coat. Technol. 204 (2009) 141–148.
[20] Y. Cheng, Z. Xue, Q. Wang, X. Wu, E. Matykina, P. Skeldon, G.E. Thompson, Electrochim. Acta 107 (2013) 358–378.
[21] R.O. Hussein, X. Nie, D.O. Northwood, A. Yerkhin, A. Matthews, J. Phys. D 43 (2010) 1–13.
[22] D. Veys-Renaux, E. Rocca, J. Solid State Electrochem. 19 (2015) 3121–3129.
[23] Z.C. Oter, Y. Gencer, M. Tarakci, J. Alloys. Compd. 650 (2015) 185–192.
[24] K. Tillous, T. Toll-Duchanoy, E. Bauer-Grosse, L. Hericher, G. Geandier, Surf. Coat. Technol. 203 (2009) 2969–2973.
[25] J. He, Q.Z. Cai, H.H. Luo, B.K. Wei, J. Alloys. Compd. 47 (2009) 395–399.
[26] A.E. Gulec, Y. Gencer, M. Tarakci, Surf. Coat. Technol. 269 (2015) 100–107.
[27] H.O. Santos, M.M. Serna, N.B. Lima, I. Costa, J.L. Rossi, Mater. Res. 8 (2005) 181–186.
[28] K.L. Fan, G.Q. He, X.S. Liu, B. Liu, M. She, Y.L. Yuan, Y. Yang, Q. Lu, Mater. Sci. Eng. A 586 (2013) 78–85.
[29] K.L. Fan, X.S. Liu, G.Q. He, H. Chen, Mater. Sci. Eng. A 632 (2015) 127–136.
[30] H. Puga, S. Costa, J. Barbosa, S. Ribeiro, M. Prokic, J. Mater. Process. Technol. 211 (2011) 1729–1735.
[31] P. Wang, T. Wu, Y.T. Xiao, J. Pu, X.Y. Guo, Mater. Lett. 182 (2016) 27–31.
[32] P. Wang, T. Wu, H. Peng, X.Y. Guo, Mater. Lett. 170 (2016) 171–174.
[33] M.A. Páez, J.H. Zagal, O. Bustos, M.J. Aguirre, P. Skeldon, G.E. Thompson, Electrochim. Acta 42 (1997) 3453–3459.
[34] C.S. Nordahl, G.L. Messing, Thermochim. Acta 318 (1998) 187–199.
[35] Y. Wang, X. Wang, T. Zhang, K. Wu, F. Wang, J. Mater. Sci. Technol. 29 (2013) 1129–1133.
[36] J. He, Q.Z. Cai, H.H. Luo, L. Yu, B.K. Wei, J. Alloys. Compd. 471 (2009) 395–399.
[37] F. Xu, X. Yuan, L. Guang, Appl. Surf. Sci. 255 (2009) 9531–9538.
[38] Y. Ma, X. Zhou, G.E. Thompson, M. Curioni, X. Zhong, E. Koroleva, P. Skeldon, P. Thomson, M. Fowles, Corros. Sci. 53 (2011) 4141–4151.
[39] L. Efratila-Apachitei, H. Terryn, P. Skeldon, G.E. Thompson, J. Duszczyk, L. Katgerman, Electrochim. Acta 49 (2004) 1127–1140.
[40] X. Lu, C. Blawert, K.U. Kainer, M.L. Zheludkevich, Electrochim. Acta 196 (2016) 680–691.
[41] U. Kogelschatz, Plasma Chem. Plasma Process. 23 (2003) 1–46.
[42] M.S. de Miera, M. Curioni, P. Skeldon, G.E. Thompson, Corros. Sci. 52 (2010) 2489–2497.
[43] J.W. Schultze, M.M. Lohrengel, Electrochim. Acta 45 (2000) 2499–2513.
[44] C. Wang, G. Zhang, X. He, Appl. Surf. Sci. 256 (2010) 6047–6052.
[45] R.B. Metz, C. Nicolas, M. Ahmed, R.S. Leone,J. Chem. Phys. 123 (2005), 114313.
[46] L. Zhu, Z. Guo, Y. Zhang, Z. Li, M. Sui, Electrochim. Acta 208 (2016) 296–303.

5.2.2 PEO of AZ91Nd/Al_2O_3 Mg composite

Paper 5: Ting Wu, Carsten Blawert, Maria Serdechnova et al., PEO processing of AZ91Nd/Al_2O_3 MMC - The role of alumina fibers, Journal of Magnesium and Alloys 10(2022). https://doi.org/10.1016/j.jma.2021.09.017

Graphical abstract

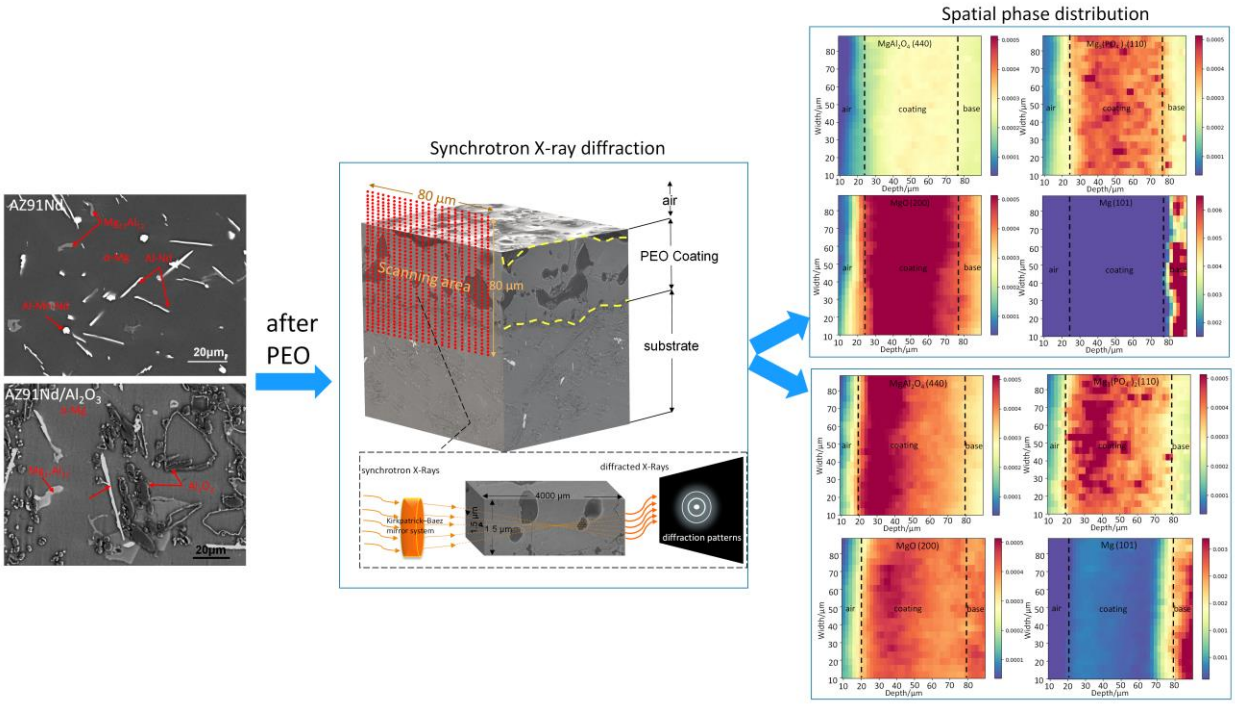

This work mainly investigated the influence of a ceramic reinforcement phase-alumina fibers in AZ91Nd alloy on the PEO processing. Al_2O_3 fibers are already in a stable oxidation state. This gives a fundamental understanding for the application of PEO processing with oxide particle additions in nano- and micro-scale. Pure AZ91Nd alloy (1.14 wt.% Nd) was used as a reference, which offers a relatively high amount of secondary phases, such as Al-Nd and Al-Mn-Nd intermetallics in the substrate. A lower voltage response of the MMC was observed compared to the pure alloy, indicating that the composite is less sensitive to the applied current and larger formation is disturbed. The coating thickness of the MMC was also lower than that of the pure alloy. The coatings on the MMC showed a different morphology due to the presence of alumina fibers, interrupting the continuity of the coatings especially at the layer near the substrate. Alumina fibers were firstly embedded inertly in the coating. Then under the effect of the discharges, the Al_2O_3 fibers were reactively incorporated in a thermal-stimulated reaction with MgO, and a new phase $MgAl_2O_4$ spinel was formed. As a result, the homogeneity of the coatings improved especially closer to the coating surface.

Available online at www.sciencedirect.com

ScienceDirect

Journal of Magnesium and Alloys 10 (2022) 423–439

www.elsevier.com/locate/jma

Full Length Article

PEO processing of AZ91Nd/Al_2O_3 MMC-the role of alumina fibers

Ting Wu[a,*], Carsten Blawert[a], Maria Serdechnova[a], Polina Karlova[a], Gleb Dovzhenko[b], D.C. Florian Wieland[c], Mikhail L Zheludkevich[a,d]

[a] *Institute of Surface Science, Helmholtz-Zentrum Hereon, Max-Planck Strasse. 1, Geesthacht 21502, Germany*
[b] *Institute of Materials Physics, Helmholtz-Zentrum Hereon, Max-Planck Strasse. 1, Geesthacht 21502, Germany*
[c] *Institute of Metallic Biomaterials, Helmholtz-Zentrum Hereon, Max-Planck Strasse. 1, Geesthacht 21502, Germany*
[d] *Faculty of Engineering, Institute of Materials Science, Kiel University, Kaiserstrasse 2, Kiel 24143, Germany*

Received 5 May 2021; received in revised form 18 August 2021; accepted 22 September 2021
Available online 5 December 2021

Abstract

This work reports the influence of alumina fiber reinforcement of an AZ91Nd MMC (metal matrix composite) on the PEO coating formation process in a sodium phosphate-based electrolyte. By comparison with the pure AZ91Nd, the evolution of alumina fiber during the processing and the characteristics of the resultant PEO coating were investigated. The voltage response as a function of processing time was changed. Lower voltage in the presence of alumina fiber is responsible for the lower coating thickness. The morphology and phase composition of the coatings are also influenced by the incorporation of the fiber. Firstly, the fiber is embedded in the coating and interrupts the continuity of the coating. With increasing processing time, the fiber is found to be reactively incorporated in the coating. The intention to produce a $MgAl_2O_4$ containing coating is achieved and it is mainly accumulated near the coating surface. However, due to the low number of fibers, the Al content is overall still low and only near to the fibers the $MgAl_2O_4$ spinel phase can form.

Keywords: Plasma electrolytic oxidation; Mg alloy; Metal matrix composite; Al_2O_3; $MgAl_2O_4$.

1. Introduction

Plasma electrolytic oxidation (PEO) is a promising surface engineering technology for Mg alloys to enhance the surface properties, renowned for the ease of operation and environmentally friendly process [1–8]. In the case of AZ91 Mg alloys, PEO processing allows the formation of a ceramic-like coating of generally tens of microns thick [3,6,9]. PEO coatings can eradicate the surface heterogeneity of AZ91 Mg alloys, which is caused by the dual-phase microstructure (α-Mg and more inert β-$Mg_{17}Al_{12}$ precipitates) [10,11]. In addition, the PEO coatings on AZ91 Mg alloys are typically layered [12,13] and the inner barrier layer towards the substrate of a few hundred nanometers thick enables the mitigation of the corrosion process from delaying the penetration of corrosive media [1,11,14,15].

The formation of PEO coatings on Mg alloys involves chemical, electrochemical, plasma, and thermal activated processes in combination with the transition among solid, liquid, gas and plasma states of the species, originated from substrate and electrolyte [16–18]. Thus, the process is strongly dependent on the applied voltage/current and the composition of substrate and electrolyte. Many combinations of electrical parameters and electrolytes have been studied extensively for the last decades, in order to improve the performance of PEO coating on Mg alloys [16,19–23]. Some effective ap-

* Corresponding author.
E-mail address: ting.wu@hereon.de (T. Wu).

https://doi.org/10.1016/j.jma.2021.09.017

proaches, such as adding ceramic particles [24,25], applying bipolar electrical pulses [26,27] and post-healing process [9,28] have been proposed. However, in the case of Mg substrates, the role of alloying additions and the effect of the presence of impurities, second phases and ceramic reinforcement in the alloy microstructure during PEO processing are scarcely discussed.

In fact, different anodic behavior of α-Mg and β-$Mg_{17}Al_{12}$ in AZ91 Mg alloys have been observed during PEO processing [6,29]. The discrepancy is stemming from the nature of the two phases as well as the corresponding conversion products formed during initial conventional anodizing [11,30,31]. At the very beginning, the oxidation and deposition starts on the α-Mg and then extends to the β-$Mg_{17}Al_{12}$ intermetallics due to the electrochemically more active α-Mg. The respective conversion products of α-Mg and β-$Mg_{17}Al_{12}$ present discernible local morphologies and have different dielectric properties. As a result, the discharge properties, e. g. intensity and number, which depend on the breakdown of the conversion film, change at different locations [11]. It was also observed that the intensity of discharges is stronger in the presence of Al in Mg alloys [3,12,32–34]. Furthermore, the $MgAl_2O_4$ spinel phase has been identified in the PEO coatings on AZ91 Mg alloys [6,34–36]. The contribution of $MgAl_2O_4$ to the corrosion resistance and the hardness of PEO coatings has been reported in some works [37–40]. Nevertheless, without additional Al supply, the nominal 9.0 wt.% Al of AZ91 Mg alloys is not sufficient to synthesize $MgAl_2O_4$ in a large amount during PEO processing [41].

AZ91Nd matrix reinforced with alumina fibers is a metal matrix composite (AZ91Nd/Al_2O_3 MMC), which significantly enhance the mechanical strength of the resulting materials [42,43]. Due to the introduction of alumina fibers, a large number of different material phases and thus interface combinations are introduced into the AZ91Nd/Al_2O_3 MMC. To the best of our knowledge, no published research has put emphasis on the PEO process on AZ91Nd/Al_2O_3 MMC and the role of ca. 20 vol.% alumina fibers on the coating formation. In the published studies of PEO treatment on Mg-based MMCs [5,44–48], reinforcement phases of SiC and Al_2O_3-SiO_2 were reactively incorporated in the coating as silicate and aluminate. Hence, whether or not the alumina fibers of AZ91Nd/Al_2O_3 MMC facilitates the formation of $MgAl_2O_4$ in the PEO coating is worthy of being studied.

This work focuses on PEO processing and coating evolution of AZ91Nd/Al_2O_3 MMC compared with pure AZ91Nd Mg alloy in a sodium phosphate-based electrolyte. The modification of oxidation behavior in the presence of alumina fibers and the stability of the alumina fiber during the processing was studied at different treatment times. The phase composition and distribution across the thickness of the coatings on AZ91Nd/Al_2O_3 MMC and on AZ91Nd Mg alloy were investigated via micro-focused X-ray diffraction experiments. In addition, the $MgAl_2O_4$ formation in the coatings was compared for the mentioned substrates in sodium phosphate and phosphate-aluminate electrolytes to understand the role of different Al sources on phase formation.

2. Experimental

As-received AZ91Nd Mg alloy was selected as the matrix. The composition was 7.16 wt.% Al, 0.57 wt.% Zn, 1.14 wt.% Nd, 0.21 wt.% Mn, 0.0049 wt.% Fe, 0.0044 wt.% Cu, 0.0006 wt.% Ni and Mg balance analyzed using Arc Spark OES (Spark analyze M9, Spectro Ametek, Germany). The samples of AZ91Nd/Al_2O_3 MMC (18.022 wt.% Al) were taken from as received squeeze cast blocks consisting of 50 vol.% Saffil alumina fiber reinforcement and 20 vol.% alloy. The short alumina fibers (95.0–97.0% δ-Al_2O_3, 3.0–5.0% silica binder and $<$ 0.5% trace elements) are approximately 3 μm in diameter and up to 100 μm in length.

Rectangular specimens (15 mm × 15 mm × 4 mm) of AZ91Nd/Al_2O_3 MMC and as-received AZ91Nd were used as the working anodes. PEO processing was performed using a pulsed DC power source under a constant current density of 6 A/dm^2 with a duty cycle of 10% (1 ms: 9 ms) and a frequency of 100 Hz. The basic alkaline electrolyte was prepared via dissolution of Na_3PO_4 (20 g/L) and KOH (1 g/L) in deionized water under continuously stirring in order to keep the solution homogeneous. A cooling system, using a stainless steel tube cathode, was employed to control the temperature (10 ± 2 °C) of the electrolyte. Before and after the PEO processing, the specimens were rinsed with deionized water and dried with compressed air. Processing times of 15, 30, 60, 300, 600, and 1200 s were selected, respectively. During the processing, the voltage as a function of processing time was recorded using the SignaSoft 6000 software package, Gantner, Germany. For understanding the role of different Al sources in the synthesis of $MgAl_2O_4$ based PEO coatings on pure AZ91Nd, PEO treatment was additionally employed in a phosphate-aluminate electrolyte (Na_3PO_4 10 g/L, $NaAlO_2$ 15 g/L and KOH 1 g/L) for 600 s and 1200 s, respectively under the same electrical PEO parameters.

The microstructure of the substrates with and without Saffil alumina fiber reinforcement were examined applying optical microscopy (OLYMPUS BX53M), scanning electron microscopy (SEM, TESCAN Vega3 SB) and X-ray diffractometry (XRD, D8 Advance, Bruker AXS), respectively. For the XRD measurement, the following parameters were selected: diffraction angle 2θ between 20° and 80°, step size of 0.02°, acquisition time of 1 s per point and grazing angle of 1°

For the characterization of PEO coatings, surface and cross-sectional morphologies, micro-pore size (at 500 × magnification) and elemental distribution for the MMC and the pure AZ91Nd alloy as a function of processing time were investigated using a SEM combined with an energy dispersive spectrometer system (EDS, eumeX IXRFsystems). The coating thickness measurements were performed with a coating thickness gage (MiniTest 2100, ElektroPhysik), which was validated from the cross-section observations of the SEM. The phase composition of the coatings was obtained from the aforementioned XRD measurement. Further investigation of the phase formation of the PEO coatings formed in the phosphate electrolyte after 600 s processing was carried out

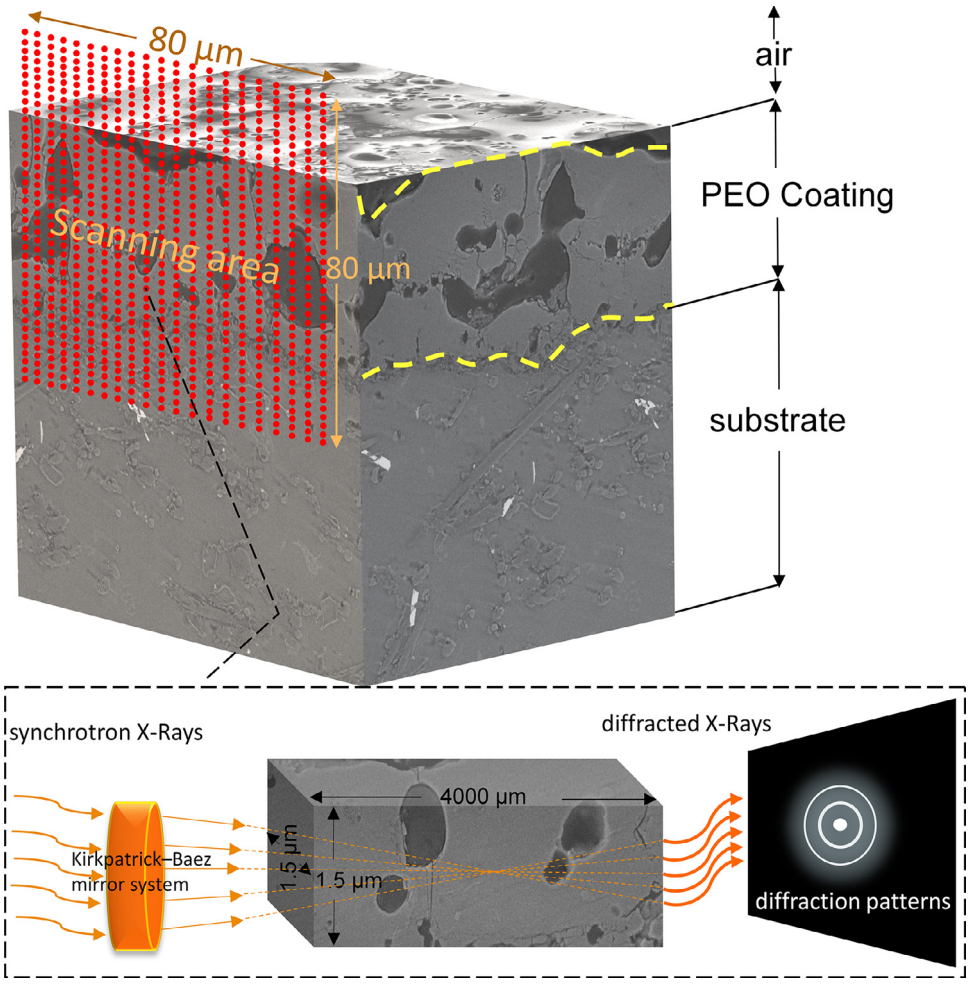

Fig. 1. Schematic scanning diagram of each point of analysis (1.5 × 1.5 µm, 0.5 s) via synchrotron X-ray diffraction giving a total scanning area of 80 × 80 µm across three-phase of air/PEO coating/substrate.

at Deutsches Elektronen-Synchrotron (DESY, Hamburg, Germany) using the nano-focus end station of the beamline P03 at PETRAIII storage ring [49]. The measurement set-up is illustrated in Fig. 1. An Eiger 9 M detector was used, which has a pixel size of 75 µm by 75 µm. The X-ray beam had an energy of 19.7 keV and was focused to a beam size of 1.5 µm by 1.5 µm. A mesh scan of the interface was performed with 40 steps in the direction perpendicular to the interface with 2 µm step size and 20 steps parallel to the interface with a step size of 4 µm. This resulted in a measured area of 80 × 80 µm. We have chosen this setting as a resolution parallel to the interface was not necessary and would have cost too much time. At each point, a diffraction pattern was acquired for 0.5 s. Data reduction was done by employing in-house developed MAtlab® code and the PyFAI [50] routine. The scattering angles of the diffraction patterns were transformed to Cu K-alpha radiation for simplicity. To access the phase distribution across the coating thickness, a lab-made script in Python programming language, operated in the "Spyder" package software environment included with Anaconda Navigator, was used for analyzing and generating the two-dimensional phase mapping graphics.

3. Results

3.1. Microstructure of substrates

Fig. 2 shows the XRD patterns of pure AZ91Nd and AZ91Nd/Al_2O_3 MMC. In addition to the phases of α, β, Al-Mn and Al-Mn-Nd, which are present in both materials, the additional diffraction peaks of δ-Al_2O_3 from the reinforcement fiber are found in the MMC. Al-Mn and Al-Mn-Nd intermetallics can hardly be differentiated due to the relatively similar values of their diffraction peak positions. In the MMC, Mg_2Si was recognized in LM and SEM studies and consistent with the atomic ratio of Mg/Si in EDS analysis (Fig. 3(b) and (d)). However, it is not detected during XRD measurement because of the relatively low content. The residual Mg_2Si is attributed to the interaction between Mg substrate and the silica binder in Saffil alumina fiber during

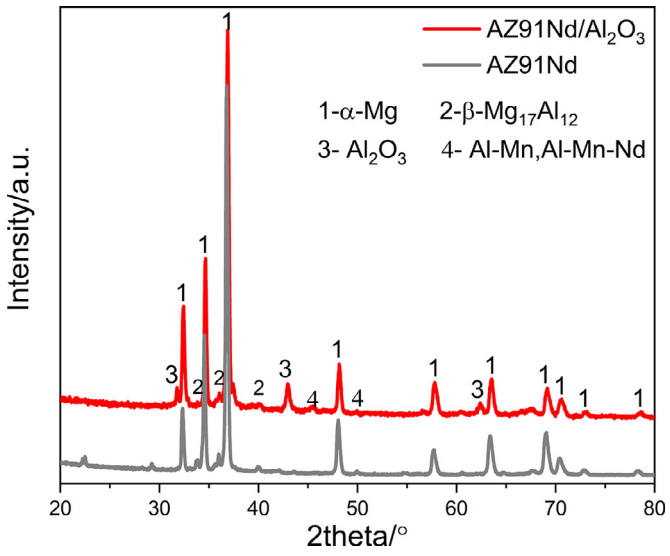

Fig. 2. XRD patterns of AZ91Nd and AZ91Nd/Al_2O_3 MMC.

the squeeze casting process. The metallographic images of the two substrates with and without the alumina fibers are given in Fig. 3, which are consistent with the phase analysis. Larger solid β precipitated at the grain boundaries of the α matrix are visible, surrounded by eutectic $\alpha+\beta$ morphology. Particulates of Al-Nd intermetallics and aciculae Al-Mn-Nd intermetallics are dispersed within the grains, respectively. Nevertheless, for the MMC, Al-Mn-Nd intermetallics are recognized less frequently, and the alumina fibers exhibit different orientations.

3.2. PEO process

The voltage responses as a function of processing time for AZ91Nd and AZ91Nd/Al_2O_3 MMC in phosphate electrolyte are displayed in Fig. 4(a), respectively. Four stages of the PEO process can be distinguished as listed in Table 1. For the pure AZ91Nd, the voltage at the first stage is ramping up linearly at the rate of ca. 30 $V{\cdot}s^{-1}$, indicating the rapid formation of a dielectric passive film on AZ91Nd. The voltage is increasing to maintain the pre-set current density. The second stage is established once reaching the breakdown voltage of ca. 150 V. The voltage ramp at this stage decreases to the average rate of ca. 2.5 $V{\cdot}s^{-1}$, accompanied by short-living discharges firstly appearing on the surface of AZ91Nd. At the third stage, the voltage rise is at a lower rate of ca. 0.4 $V{\cdot}s^{-1}$, also the size and color of the discharges are changing as the initial small white discharges become larger and orange. With further increase of treatment time, the ramp of the voltage reduces further (0.07 $V{\cdot}s^{-1}$) at the last stage and further evolution of the discharges is observed, as the orange-yellow sparks are getting more stationary and larger at local regions. The final voltage reaches a value of 530 V after 1200 s.

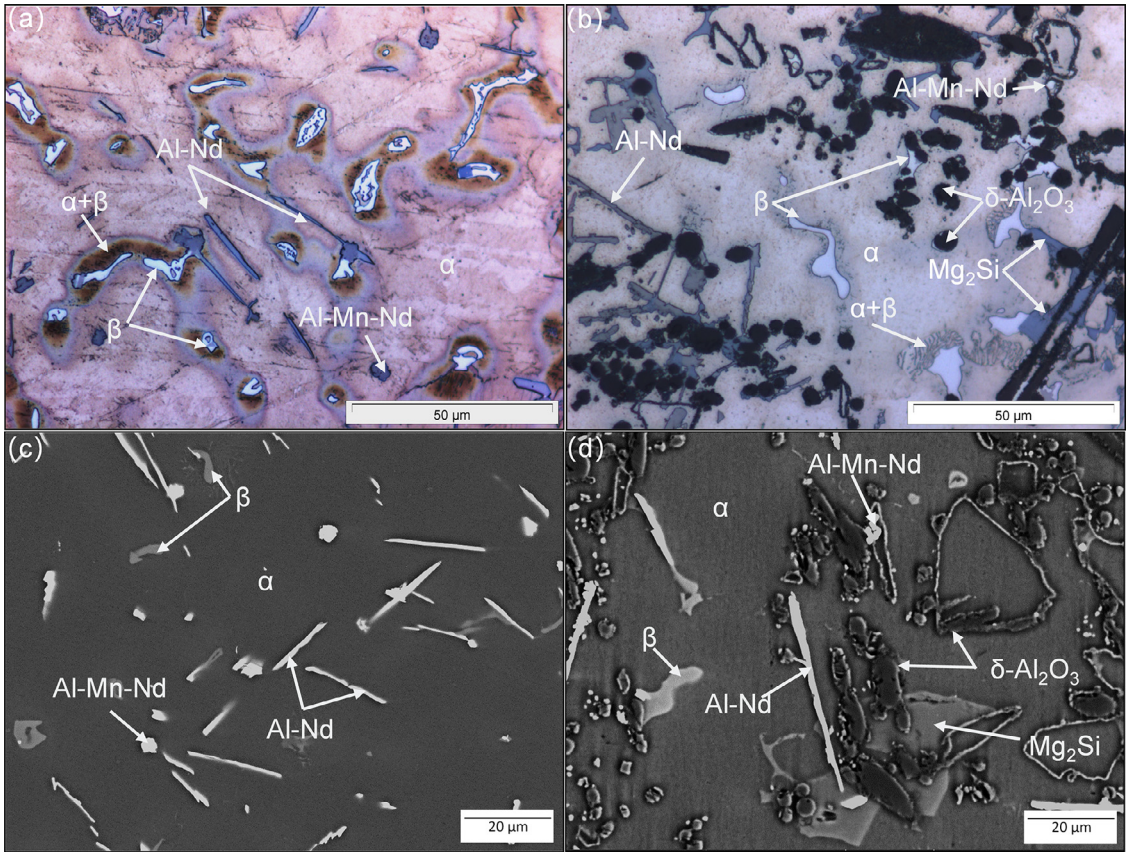

Fig. 3. Optical and SEM (BSE) micrographs of AZ91Nd: (a), (c) and AZ91Nd/Al_2O_3 MMC: (b), (d).

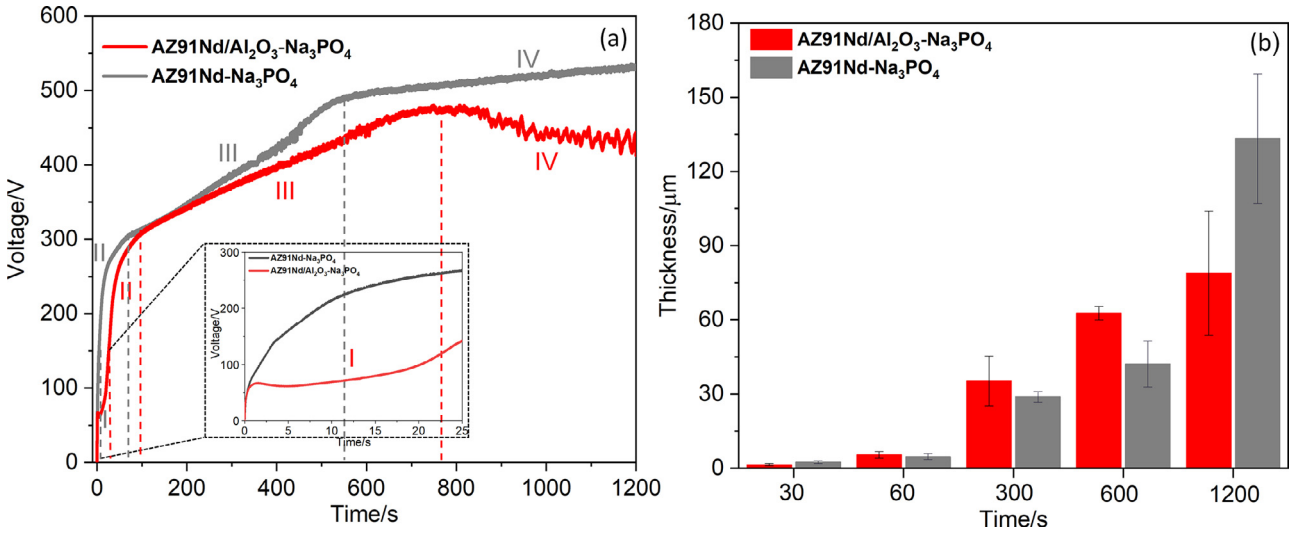

Fig. 4. Evolutions of voltage (a) inserted with detailed voltage change from 0 to 25 s and coating thickness (b) as a function of PEO processing time in sodium phosphate-based electrolyte.

Table 1
Voltage-time parameters at different stages of PEO treatment.

	AZ91Nd			$AZ91Nd/Al_2O_3$		
Stage	End time	Final voltage	Average rate	End time	Final voltage	Average rate
I	5 s	150 V	30 $V{\cdot}s^{-1}$	25 s	150 V	6 $V{\cdot}s^{-1}$
II	65 s	300 V	2.5 $V{\cdot}s^{-1}$	90 s	300 V	2.3 $V{\cdot}s^{-1}$
III	515 s	480 V	0.4 $V{\cdot}s^{-1}$	775 s	470 V	0.25 $V{\cdot}s^{-1}$
IV	1200 s	530 V	0.07 $V{\cdot}s^{-1}$	1200 s	425 V	−0.12 $V{\cdot}s^{-1}$

Obviously, the evolution of the voltage for $AZ91Nd/Al_2O_3$ MMC is different from the pure alloy. Following a surge to 60 V within the first 1 s of treatment, the voltage undergoes a short delay (ca. 10 s) as seen in the inset of Fig. 4(a) during the first stage. The delay is associated with the defects in the dielectric film due to the alumina fibers' presence. Afterward, the rapid voltage increase resumes, and the average rate of the voltage ramp for the first stage is ca. 6 $V{\cdot}s^{-1}$. It takes 20 s more to reach the breakdown voltage (150 V) compared with pure AZ91Nd. At the second stage, the average rate (2.3 $V{\cdot}s^{-1}$) for the voltage increase is similar to the pure AZ91Nd (2.5 $V{\cdot}s^{-1}$). Nevertheless, the distribution of the initial discharges is not as uniform as on the pure AZ91Nd. It can be speculated that this is attributed to the disturbance of the alumina fibers. With further processing (at the third stage), the combination of fast-moving tiny sparks and long-lasted large sparks dominates the surface of the MMC. The voltage increase of the MMC at this stage declines to ca. 0.25 $V{\cdot}s^{-1}$, which is lower than that of AZ91Nd. After reaching a maximum of 470 V (775 s), the process enters the last stage. The voltage is surprisingly dropping down with increasing fluctuations to a final value of ca. 425 V after 1200 s. It is possibly associated with the instability of the coating/electrolyte interface, such as the flaking-off of the coating.

The coating thickness of AZ91Nd and $AZ91Nd/Al_2O_3$ MMC in phosphate electrolyte increases with processing time, as indicated by Fig. 4(b). The coating on the MMC is growing faster than that of AZ91Nd for the first 600 s of processing after the occurrence of discharges. However, after 1200 s of treatment, the coating thickness of the MMC is lower than that of the pure AZ91Nd and even no further increase is observed for the last 600 s. It could be assigned to a local detachment of the outermost layer on the MMC due to thermal stress and/or poorer interface, larger pore bands, which also leads to the oscillation of the voltage at the last stage.

3.3. Surface morphologies

Fig. 5(a) reveals the micro-pores on the coating surface of AZ91Nd alloy, indicating the occurrence of discharges already after 15 s of processing, which is in agreement with the voltage exceeding the threshold for breakdown. In addition, discernible local morphologies of the coating surface are present correlating with the presence of the intermetallics. The boundaries of the intermetallics are still visible via different contrast of the elements from the substrate (Al, Mn, Zn and Nd), due to the penetration of electrons through the relatively thin coating. A more intense sintering morphology and larger micro-pores of the coating are found on the β phases, confirming the stronger discharges at the regions of abundant Al. Furthermore, the conversion products are preferentially accumulated around the Al-Mn-Nd particulates and seem to be rich in O and P. The strong cathodic effect of Al-Mn-Nd particulates relative to Mg matrix possibly accelerates

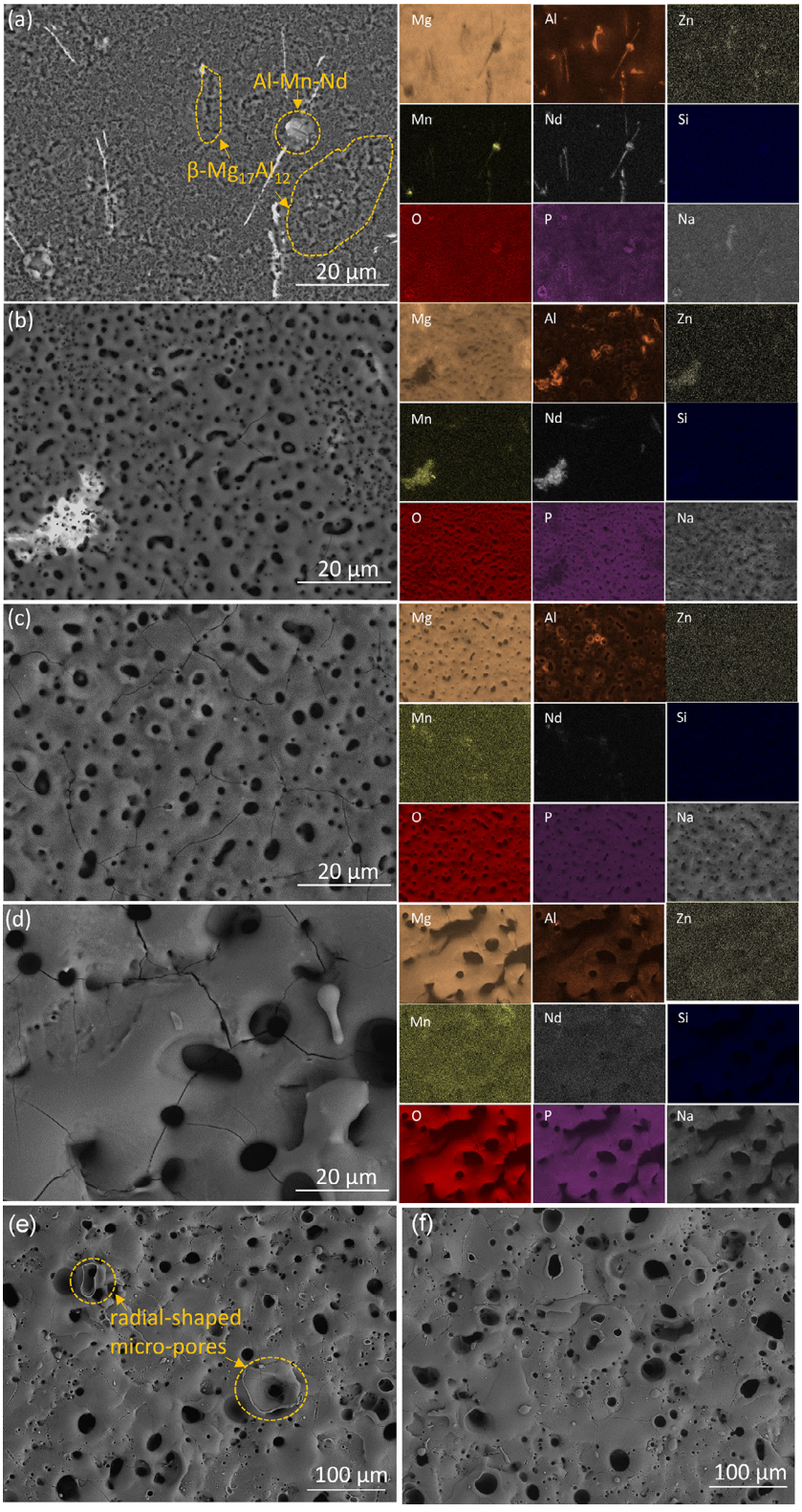

Fig. 5. Surface morphologies (BSE) and elemental distribution (EDS) of PEO coatings on AZ91Nd in sodium phosphate-based electrolyte after different processing time: (a) 15 s, (b) 30 s, (c) 60 s and (d) 300 s, (e) 600 s and (f) 1200 s.

the dissolution and oxidation of Mg during conventional anodization [11]. The heterogeneity of the local morphology is disappearing after 30 s of processing, and the size of micro-pores is in the range of ca. 0.5–3.6 μm (Fig. 5(b)). With the increasing treatment time (60 and 300 s), the elemental distribution on the coating surface also becomes uniform (Fig. 5(c) and (d)). The size of micro-pores on the coating surface increases further, in the range of ca. 0.6–6.1 μm for 60 s and ca. 0.7–24.5 μm for 300 s, respectively, and the number of micro-pores decreases correspondingly. After 600 and 1200 s of treatment, the size range of micro-pores on the coatings are of ca. 0.8–27.8 μm and ca. 0.8–34.5 μm, respectively. It should be noted that there are always two discernible types of micro-pores on the coating surface on different substrates due to the visible difference of their sizes. This is the reason for the wider range of the micro-pore size especially for the coatings processed for longer treatment. A few radial-shaped micro-pores appear on the coating surface highlighted in Fig. 5(e), which are possibly stemming from strong gas pressure release pushing out melted coating material.

As seen in Fig. 6(a), after 15 s, dissolution and deposition processes have started on the α matrix as well as on the intermetallics of the MMC. The elements from the electrolyte (P and Na) are indicators of deposition on the surface. However, different to the rapid development of the coating on pure AZ91Nd, the continuity of the coating on the MMC is interrupted by the presence of alumina fibers, and the discharge formation is retarded. This is consistent with the delayed voltage ramp during the initial conventional anodization. Micro-pores (ca. 0.3–2.3 μm) are firstly appearing on the surface of the MMC after 30 s of processing, as shown in Fig. 6(b). Different local morphology on the different intermetallics is also found, which is similar to that of AZ91Nd. Furthermore, the boundaries of alumina fibers are still visible, and the alumina fibers are embedded in the coating. The fibers are still more or less inert at this stage, and no continuous coating is forming.

After 60 s of treatment (Fig. 6(c)), micro-pores with an increased size in the range of ca. 0.3–6.9 μm dominate the coating surface on the MMC. Few micro-pores are firstly recognized on the alumina fiber, and only the accumulation of Al at some regions indicates traces of the fibers underneath the coating. As depicted in Fig. 6(d), a uniform coating is finally formed on the MMC after 300 s of processing, with homogeneous elemental distribution and a further increased micro-pores size of ca. 0.6–28.4 μm. Compared with the coatings on AZ91Nd after 600 s and 1200 s of processing (Fig. 5(e) and (f)), the coatings on the MMC are more porous (Fig. 6(e) and (f)), with the micro-pore sizes in wider ranges of ca. 0.6–30.7 μm and ca. 0.6–42.5 μm, respectively. Similarly, radial-shaped micro-pores are also discovered even more frequently on the coating of the MMC. This may indicate that the discharges generate more melt volume due to a change of the main coating composition by the reaction of the fibers with the coating phase.

3.4. Cross-sectional morphologies

Examinations of the cross-sections of the coatings on AZ91Nd following the processing of 60, 300, 600 and 1200 s in the phosphate electrolyte are displayed in Fig. 7. The increase of coating thickness with treatment time agrees with the observation of the coating thicknesses shown in Fig. 4(b). A horizontal pore band is already formed after 60 s of treatment, and the coating is somehow separated by it (Fig. 7(a)). The strong contrast of Al-Nd and Al-Mn-Nd intermetallics in BSE mode allow deducing their location in the coating regions. The inset in Fig. 7(a) illustrates that the chunks of the intermetallics are embedded in the coating near the interface of the coating/substrate. After 300 s of processing (Fig. 7(b)), it is found that the coating materials converted from the Al-Nd and Al-Mn-Nd intermetallics are preferentially distributed around micro-pores. As the micro-pores result from the discharges, the local regions of the coating with elemental heterogeneity probably ease the discharging. Furthermore, it seems as if the barrier layer in or close to the intermetallics are the locations for ignition of stronger discharges, which form the larger pores, as shown in Fig. 7(b). With further treatment (Fig. 7(c)), the size of pore bands is surprisingly diminishing, and the element distribution across the coating thickness is becoming uniform towards the electrolyte. The highest thickness coating after 1200 s of treatment (Fig. 7(d)) presents the most uniform cross-sectional morphology and elemental distribution.

The cross-sectional observations of the coatings on the MMC after different processing times (60, 300, 600 and 1200 s) are shown in Fig. 8. The evolution of intermetallics during the processing of the MMC resembles that of AZ91Nd. However, the coatings are more porous with considerable micro-cracks and, thus, more stressed compared with the coatings on AZ91Nd. An origin for this might be the more frequent and/or intense discharges in the presence of alumina fiber. After 60 s of processing, a discharge channel close to alumina fibers shown in Fig. 8(a) agrees with the observation of micro-pores in the coating surrounding an alumina fiber in Fig. 6(c). However, the alumina fibers remain stable in the coating visible by the clear boundary between alumina fibers and coating. With the coating growth (Fig. 8(b)), the distribution of Al, similar to Nd, is dispersing around the alumina fibers, demonstrating the local dissolution or reactive incorporation of alumina fibers after 300 s of processing. It can be concluded that a voltage in the approximate range of 280–370 V (60–300 s) is necessary to start the reactive incorporation via reaction of fiber with the surrounding melt. In the phosphate electrolyte, $MgAl_2O_4$ spinel is confirmed by X-ray diffraction in the coating on the MMC (Fig. 9(b)) and supports the reaction process stimulated by the assistance of intense discharges [17,51]. However, at the interface between the coating and substrate, the passive alumina fiber interrupts the continuity of the coating. After 600 s of processing (Fig. 8(c)), the elemental distribution of the coating is becoming uniform towards the coating surface, but hetero-

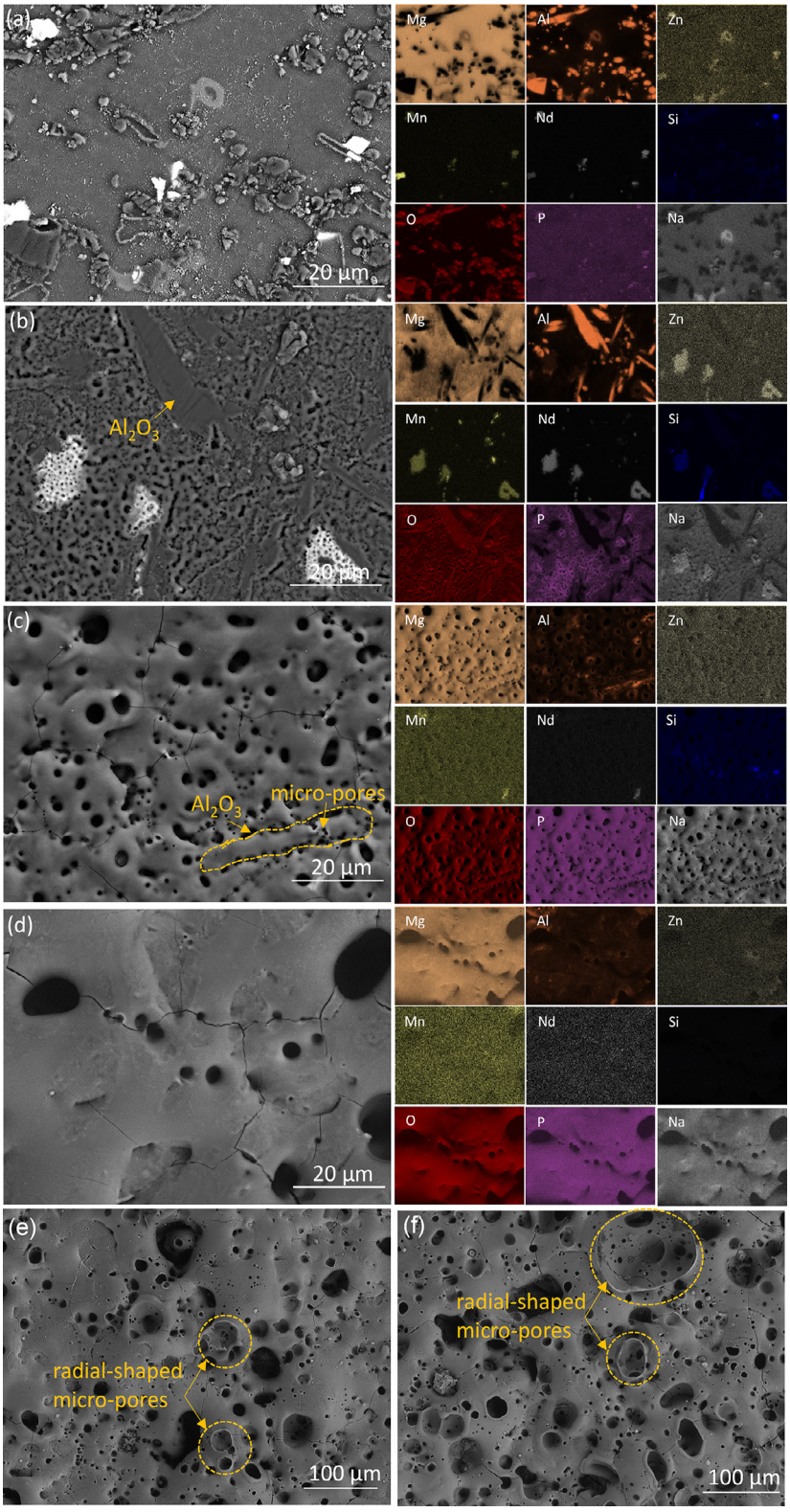

Fig. 6. Surface morphologies (BSE) and elemental distribution (EDS) of PEO coatings on AZ91Nd/Al_2O_3 MMC in sodium phosphate-based electrolyte after different processing time: (a) 15 s, (b) 30 s, (c) 60, (d) 300 s, (e) 600 s and (f) 1200 s.

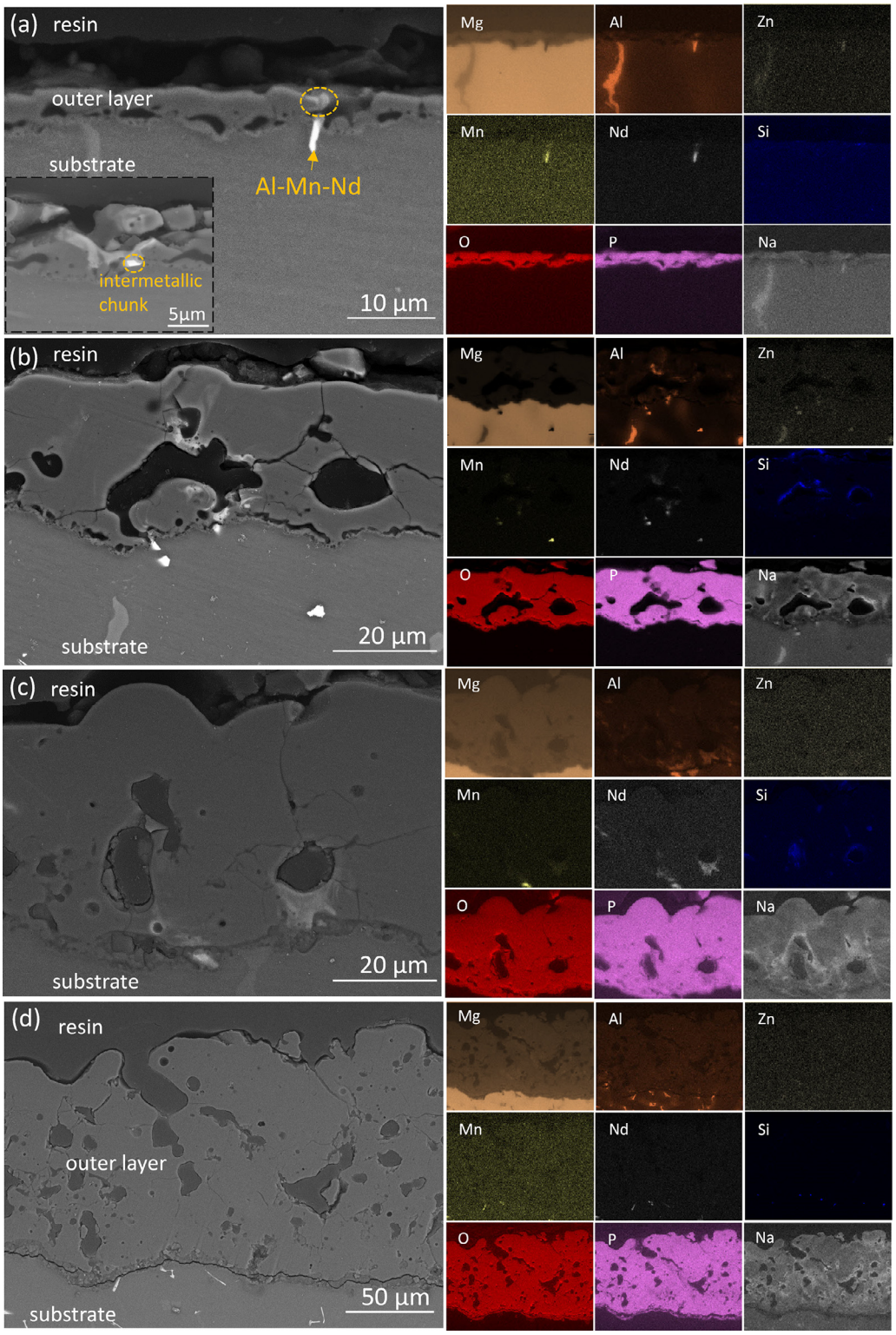

Fig. 7. Cross-section morphologies (BSE) and elemental distribution (EDS) of PEO coatings on AZ91Nd in sodium phosphate-based electrolyte after different processing time: (a) 60 s, (b) 300 s, (c) 600 s and (d) 1200 s.

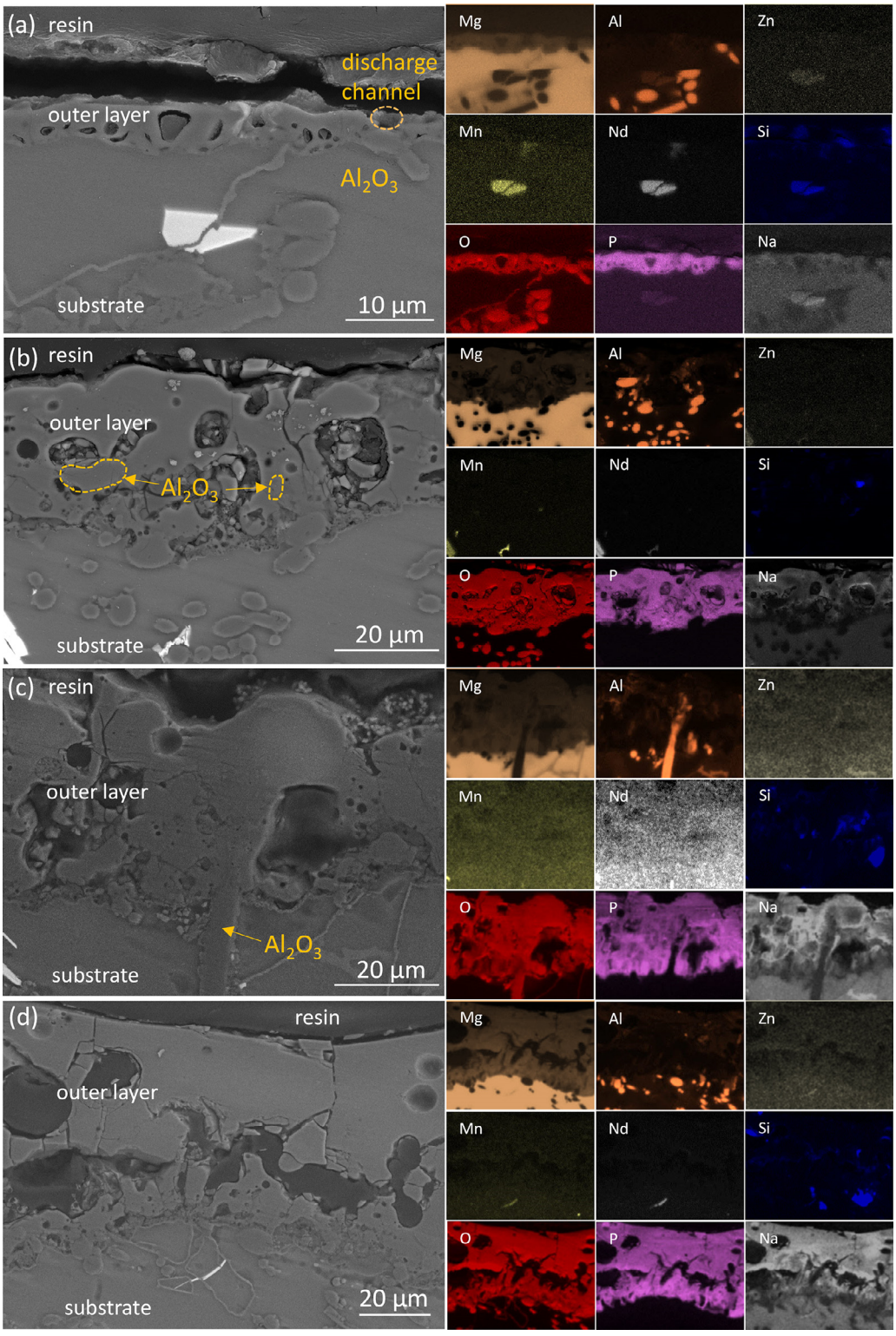

Fig. 8. Cross-section morphology (BSE) and elemental distribution (EDS) of PEO coatings on AZ91Nd/Al_2O_3 MMC in sodium phosphate-based electrolyte after different processing time: (a) 60 s, (b) 300 s, (c) 600 s and (d) 1200 s.

geneity remains at the interface of coating/substrates, where the alumina fibers and intermetallics are present. With further treatment (Fig. 8(d)), horizontal pore bands are formed in the coating, and the heterogeneous elemental distribution is disappearing. However, a large number of micro-cracks indicate that the coating neither have good cohesion nor adhesion to the substrate. A local peel-off caused by cohesion problems could be the reason for the lower thickness of the coating

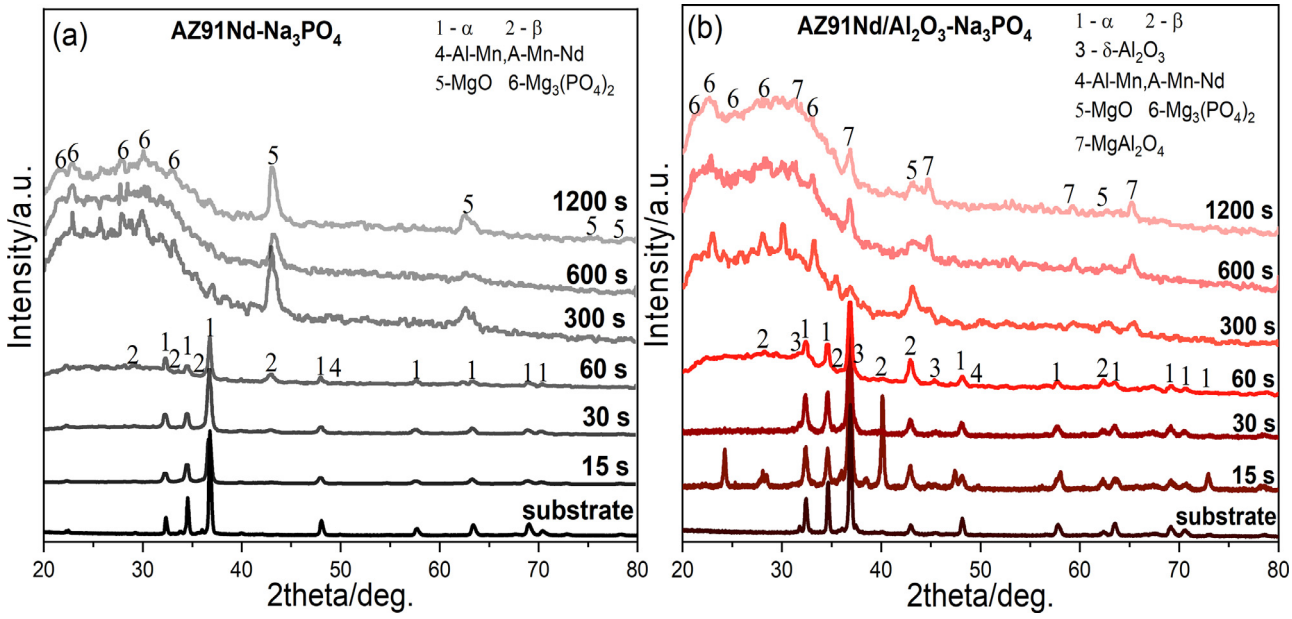

Fig. 9. XRD patterns of PEO coatings after different treatment times: (a) AZ91Nd and (b) AZ91Nd/Al_2O_3 MMC in phosphate electrolyte.

Table 2
Average composition (at.%) of PEO coatings by EDS analysis of the coating surface.

Substrate	Electrolyte	Time	Mg	Al	Zn	Mn	Nd	Si	O	P	Na
AZ91Nd/Al_2O_3	Na_3PO_4	15 s	63.05	15.52	0.36	0.05	0.11	0.69	17.98	1.09	1.15
		30 s	38.04	12.28	0.21	0.02	0.30	1.41	39.19	7.13	1.42
		60 s	25.82	1.70	0.21	0.01	0.01	0.27	51.12	15.99	4.87
		300 s	21.75	2.33	0.68	0.29	0.44	0.74	52.80	13.19	7.78
		600 s	21.88	3.48	0.67	0.25	0.39	1.14	50.72	13.38	8.09
		1200 s	21.91	3.49	0.61	0.28	0.45	1.03	49.82	13.96	8.45
AZ91Nd	Na_3PO_4	15 s	56.09	3.69	0.69	0.28	0.46	0.68	31.72	5.05	1.34
		30 s	29.23	2.29	0.68	0.26	0.52	0.71	51.27	11.77	3.27
		60 s	25.31	1.72	0.63	0.26	0.41	0.69	53.46	12.80	4.72
		300 s	23.39	1.55	0.72	0.31	0.45	0.69	52.83	13.15	6.91
		600 s	22.90	2.24	0.68	0.28	0.46	0.91	49.82	14.64	8.07
		1200 s	22.99	2.42	0.72	0.32	0.48	0.93	49.33	14.47	8.34
	Na_3PO_4	600 s	18.90	18.99	0.67	0.29	0.45	0.89	48.76	6.46	4.59
	+$NaAlO_2$	1200 s	20.16	18.67	0.68	0.31	0.46	0.88	48.49	5.92	4.43

compared to pure AZ91Nd after 1200 s of processing and almost no thickness increase compared to 600 s processing of the MMC.

3.5. Elemental and phase composition of PEO coatings

Table 2 provides the elemental composition of the coatings near the surface analyzed by EDS. In the case of the sodium phosphate-based electrolyte, the concentration of the coating forming elements Mg and Al are from the substrate decreasing with reaction time. However, the change of elements O, P and Na from the electrolyte shows a reverse trend with increasing treatment time to 60 s. Afterward, the concentration of all elements is constant. The highest Mg content after 15 s of processing is associated with the penetration of electrons into the substrates through the thin conversion layer. There is a significant discrepancy of the oxygen fraction between the coatings on the pure alloy (31.72 at.% and 51.27 at.%) and the MMC (17.98 at.% and 39.19 at.%) after 15 s and 30 s, respectively. The lower oxygen concentration observed in the coatings on the MMC confirms the delay of the oxidation process at the initial stage due to the presence of alumina fibers, which reduces the initial growth rate of the coating. After 60 s of treatment, the outward growth of the coating on the MMC leads to the sharp decreasing of Al content from 12.28 at.% to 1.70 at.%, without interacting with the fibers. For other treatment times, the constant Al level in coatings on the MMC is slightly higher compared to the pure alloy, suggesting the mixing with the coating materials and dilution due to coating formation of MgO and phosphate.

The phase composition of the PEO coatings on the MMC and the pure AZ91Nd in phosphate electrolyte is illustrated in Fig. 9, respectively. The diffraction signal of all the samples processed within 60 s is dominated by the scattering from the substrates since X-rays are easily penetrating the thin coatings and reach the substrate underneath. The broad bumps of amor-

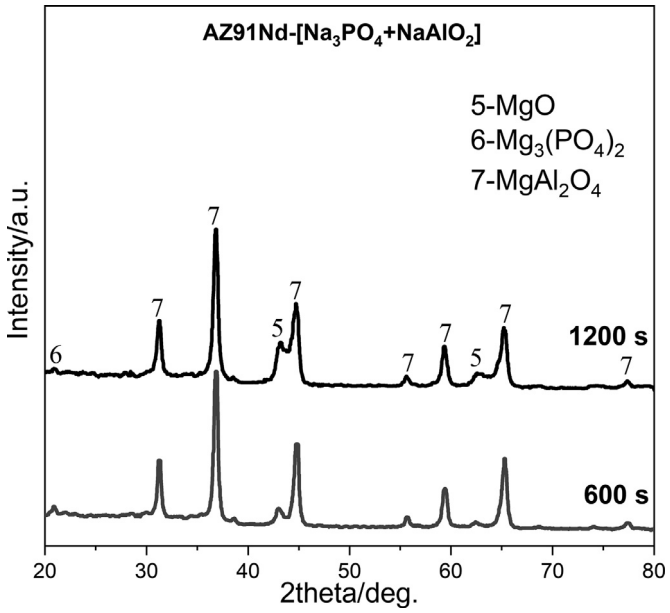

Fig. 10. XRD patterns of PEO coatings on AZ91Nd in phosphate-aluminate electrolyte after 600 s and 1200 s of processing.

phous phosphate [52] and crystalline MgO start to appear in the two theta range between 20° and 35° after 60 s of treatment. Afterwards, the coatings on AZ91Nd and MMC reveal the formation of an $Mg_3(PO_4)_2$ phase after 300 s, 600 s and 1200 s of processing. Furthermore, some diffraction peaks are recognized as $MgAl_2O_4$ in the coatings on the MMC, confirming the reactive incorporation of alumina fibers as the only additional source of Al. Overall SEM, EDS and XRD do suggest that the coatings are a mixture of nano-crystalline MgO, $Mg_3(PO_4)_2$ phases, where in the case of the MMC some of the MgO has reacted with the Al_2O_3 of the fibers forming $MgAl_2O_4$.

In contrast to the presence of alumina fibers in the AZ91Nd matrix, the phosphate-aluminate electrolyte can provide an alternative and more effective Al source for the formation of $MgAl_2O_4$ spinel phase in the PEO coating on pure AZ91Nd. The highest atomic concentrations of Al demonstrated in Table 2 are formed for the coatings on AZ91Nd in the phosphate-aluminate electrolyte after 600 s and 1200 s of treatments. Fig. 10 reveals that the coatings are crystalline and composed of primary $MgAl_2O_4$, MgO and a little amount of $Mg_3(PO_4)_2$, indicating that $MgAl_2O_4$-based PEO coatings are achieved with the addition of aluminate in the electrolyte much more efficiently. The cross sectional morphology and elemental distribution of the coatings are illustrated in Fig. S1. There are fewer micro-pores present within the coatings, compared to the coatings formed in sodium phosphate-based electrolyte. Additionally, the distribution of Al is uniform and shows a strong contrast in the coatings.

3.6. Synchrotron X-ray diffraction

The measurements utilizing a nano-focused X-ray beam at the P03 have been conducted to understand the phase distribution of the coatings. Fig. 11 presents the high-resolution localized XRD patterns of the coatings on AZ91Nd and the MMC after 600 s of processing in phosphate electrolyte. The XRD patterns are selected from one line of the scan across the coating from the surface to the substrate, as illustrated in Fig. 1. The phase composition of the coatings is consistent with the results in Fig. 9, and the diffraction peaks in the two theta range of 30–40° are more discernible in Fig. S2. From the diffraction patterns of the completely scanned areas (80 × 80 μm), the local intensity of the primary coating phases including $MgAl_2O_4$ (440), MgO (200) and $Mg_3(PO_4)_2$ (110) are extracted. The two-dimensional maps are plotted in Fig. 12 to shows the spatial intensity of the phases across the coating thickness. The distribution of Mg (101) from the substrates is also displayed to illustrate the location of the substrate. For the coating on AZ91Nd, it is evident that MgO is the primary phase and almost uniformly spreading through the entire thickness of the coating. The coating to substrate and coating to air interface can be clearly separated by the intensity change of MgO and Mg. The coating thickness is estimated to be 60 μm, which is higher compared to the cross-sectional observation. This difference could be attributed to the wavy interfaces of the coating/substrate (Fig. 7(c)). The distribution of $Mg_3(PO_4)_2$ is similar to that of MgO, however, with lower intensity. In addition, there is only background noise of $MgAl_2O_4$. For the coating on the MMC, a $MgAl_2O_4$ rich layer of ca. 25 μm is formed near the surface in Fig. 12(a), demonstrating the transformation of the fiber near the coating surface in Fig. 8(c). In contrast to the coating results on AZ91Nd substrate, the coating on MMC shows another phase distribution as the phases of MgO and $Mg_3(PO_4)_2$ appear to accumulated preferentially in the $MgAl_2O_4$ rich layer. Moreover, the intensity of MgO is lower than that of $Mg_3(PO_4)_2$. This confirms the reactive incorporation consuming MgO while forming $MgAl_2O_4$. The low intensity of the phases in the other region of the coating near the substrate could be ascribed to the presence of pore bands and the remaining fibers, as displayed in Fig. 8(d). The coating/substrate interface is quite rough since the intensity of Mg from the substrate loses its sharpness. The observation of the coating thickness, of ca. 50 μm, is lower than the aforementioned measurement, possibly due to the disturbance of alumina fiber at the coating/substrate interface.

4. Discussion

The main intention of the study was to clarify the effect of the alumina fiber reinforcement in AZ91Nd matrix on the formation of PEO coatings during PEO processing in a phosphate electrolyte. From the comparison with pure AZ91Nd, it was demonstrated that the presence of alumina fiber influences the growth of the coating by affecting the PEO process itself as well as the phase formation, as the fibers are reactively incorporated into the coating. The delay of voltage ramp at the initial period for the MMC is found to be the first influence on the process due to the alumina fiber interrupting the continuous formation of the dielectric film. The defects

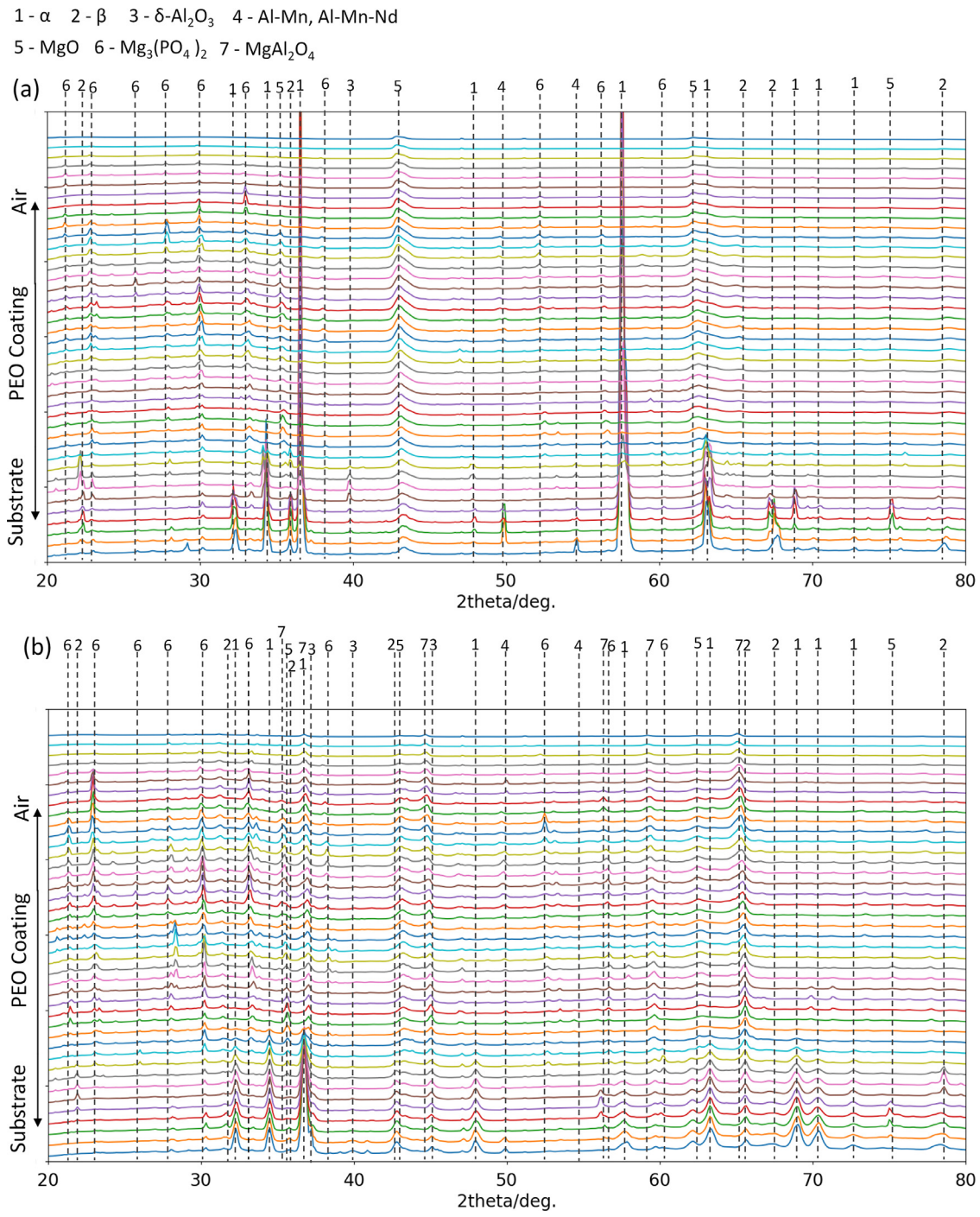

Fig. 11. High-resolution XRD patterns of a selected line perpendicular to the interface (air-coating-substrate) for the PEO coatings on AZ91Nd (a) and on AZ91Nd/Al_2O_3 MMC (b) in phosphate electrolyte after 600 s of processing.

at the interface between the alumina fibers and dielectric film serve as "shortcuts", through which the electrolyte is easily penetrating the gap between the alumina fibers and the matrix, allowing current to flow without voltage increase [43,53]. As a result, the formation of initial conversion coating on the surface of the MMC as well as the rapid voltage increase is suppressed at this stage. Subsequently, the layer thickness increase is driven by the polarization and, thus, the resistance of the forming film improves. The shortcuts are being closed, as the fibers are better integrated into the growing film. After the occurrence of discharges, the growth of the coating in terms of thickness is accelerated in the presence of alumina fiber within the first 600 s of processing. However, the decrease and fluctuation of the voltage at the last stage indicate further changes of coating development on the MMC. Lower coating thicknesses compared to pure AZ91Nd and actually no further increase in the last ten minutes of the treatment might be related to the high stresses and defects in the coat-

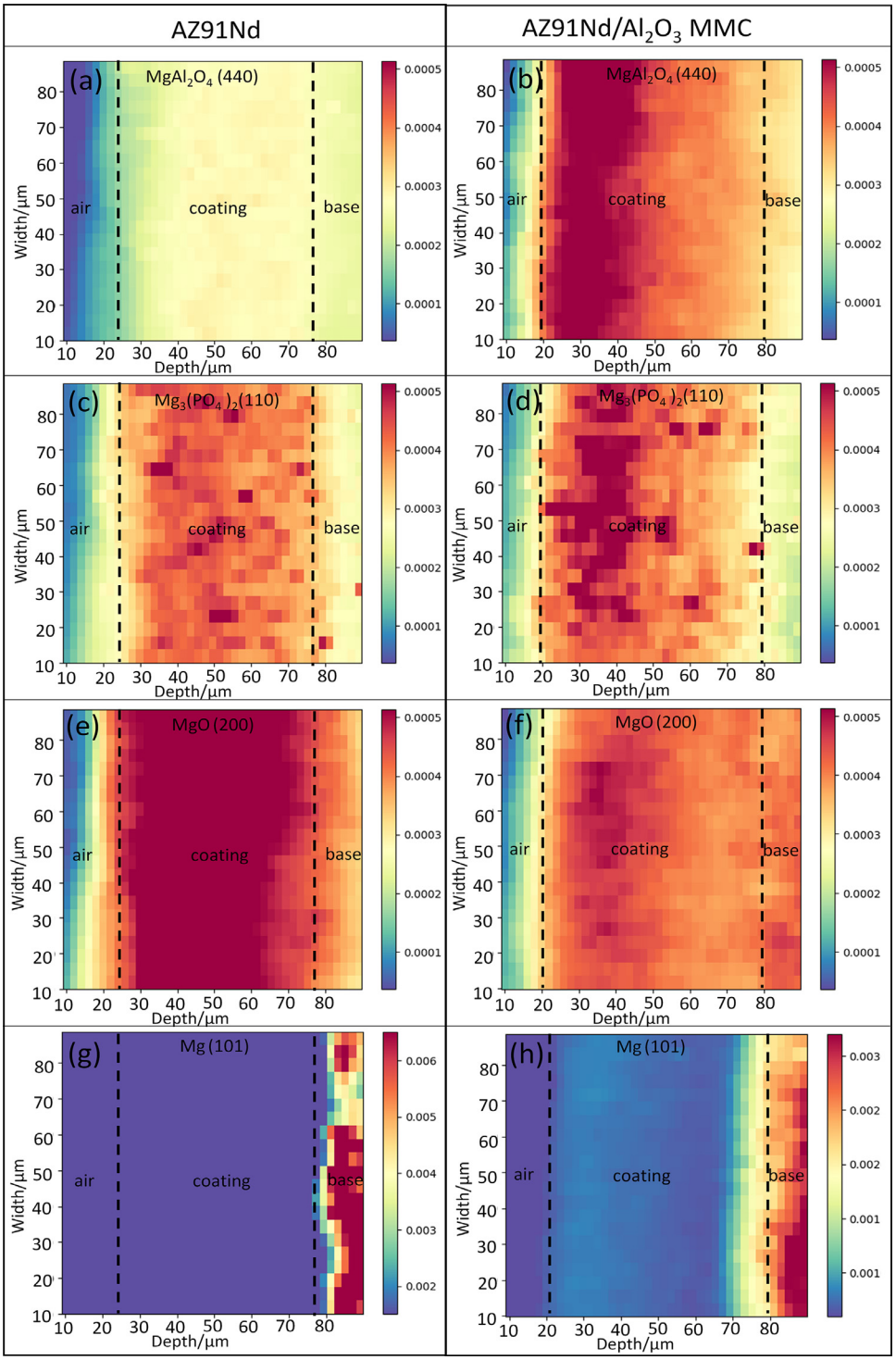

Fig. 12. 2D maps of phase distribution across coating thickness (600 s) on AZ91Nd: (a) $MgAl_2O_4$, (c) $Mg_3(PO_4)_2$ and (e) MgO and on AZ91Nd/Al_2O_3 MMC: (b) $MgAl_2O_4$, (d) $Mg_3(PO_4)_2$ and (f) MgO in phosphate electrolyte.

ing, which is consistent with the observation of the coating cross-sections of the MMC (Fig. 8) showing extensive porosity, extended pore band and micro-cracks. This could cause a local flaking off, and rebuild of the coating, which can further impedes the thickening of the coating. It should be noted that this is also consistent with the voltage drop and fluctuation at the end of the processing.

For the PEO processing of Mg alloys, the main steps of coating formation Eqs. (1)–((3)) [32] following are taking place near the substrate while the coating is growing inwards:

$$Mg \rightarrow Mg^{2+} + 2e \quad (1)$$

$$Mg^{2+} + 2OH^{-} \rightarrow Mg(OH)_2 \quad (2)$$

$$Mg(OH)_2 \rightarrow MgO + H_2O \quad (3)$$

$$3Mg^{2+} + 2PO_4^{3-} \rightarrow Mg_3(PO_4)_2 \quad (4)$$

Due to the high pressure in the discharges, the coating melt produced next to the substrate erupts outwards to the coating surface rapidly via the discharge channels. Directly at the interface also the reaction with phosphate occurs.

The findings of the present study suggest that the alumina fibers were involved in the coating formation at a voltage higher than 280 V. In the beginning, the fibers are stable enough that the coating can only grow around them even though the voltage was up to 280 V (breakdown voltage 150 V). Only when a higher voltage in the approximate range of 280–370 V (60–300 s) was reached, the reactive incorporation of the fiber into the coating started, as the alumina fibers close to the surface were disappearing and $MgAl_2O_4$ spinel was identified. The cross-sectional observation suggests the reactions initiated at the interface of fiber/coating and similar evolution of SiC fibers/particles were reported in [5,45–48]. The XRD peak intensity of $MgAl_2O_4$ was rising with processing time/voltage. From the intensity development of the XRD peaks of the MgO phase, we speculate that this phase is involved in the spinel formation. Its intensity increased during a processing time of 300 s with a subsequent decrease, indicating its consumption. The $MgAl_2O_4$ spinel formation was reported in the sintering process of MgO and Al_2O_3 at temperatures of 900–1200 °C [54,55]. This is much lower than the melting points of MgO (2827 °C), Al_2O_3 (2054 °C) as well as spinel (2105 °C) [56]. It can be inferred that the temperature in the discharges was sufficient for the formation of the spinel as the estimated temperature ranges from 4000–33,000 K in the PEO process [57]. Correlated to the applied voltage, the formation/sintering process only occurred at a voltage exceeding 280 V. Due to the short-living discharges and the rapid quenching effect of the electrolyte, the effective temperatures needed for sintering can be reached only when the external applied voltage exceeded 280 V. Therefore, we suggest the following $MgAl_2O_4$ formation reaction above 280 V:

$$MgO + Al_2O_3 \rightarrow MgAl_2O_4 \quad (5)$$

Further increase of the voltage accelerates the formation process. A single alumina fiber located across the coating thickness displayed in Fig. 8(c) indicates the continuous reconstruction of the coating via the discharges and step by step dissolution of the fiber. The reactive incorporation of the fiber commencing near the coating surface increases the composition/microstructure mismatches within the coating, which is visible by the non-uniform distribution of Al across the coating thickness. The discharges are preferred to occur at the locations of defects, which are weaker and have lower electrical resistance, like the coating interface around the fibers. Thus, discharges appear close to the fibers, but all Al oxides involved in the reaction and the spinel are quite temperature stable phases and concentration gradients remain much larger as melt volumes and/or diffusion in the solid is much more restricted. As a result, unlike the homogeneous coating on the alloy, the coating on the MMC consists of much more defects, eg. micro-pores, micro-cracks and wide pore bands, and concentration gradients which are disappearing much slower with processing time.

Regarding the large size and volume of alumina fibers, the accumulation of $MgAl_2O_4$, mainly at the outer layer, is related to the reaction of the fibers and melt towards the surface, where the largest number of discharges were occurring considering an inward growth of the coating. Additionally, the sintering of $MgAl_2O_4$ from the mixing oxides of MgO and Al_2O_3 was reported to cause a 5–7% volume expansion [58], which could be a reason for the highly stressed coatings.

The free energy changes for the formation of MgO, Al_2O_3 and Nd_2O_3 at 0 K are -1138.6 KJ·mol^{-1}, -1054.9 KJ·mol^{-1} and -1147.4 KJ·mol^{-1} per mole oxygen, respectively. With the increasing temperature, the rate of decrease of this energy change is still similar [59]. Therefore, the lateral dispersion of Nd surrounding the Nd-containing intermetallics at the coating/substrate interface indicates higher stability of the intermetallics with respect to the α-Mg. The oxidation process seems to take place at the interface between the coating and intermetallics in every single discharge event. However, not involving complete melting of the intermetallics since the melting point of Al-Nd intermetallics could be higher than 1400 °C [60].

It has been reported that the introduction of $MgAl_2O_4$ spinel into the PEO coatings through the addition of Al source in the electrolytes can significantly improve the corrosion performance [38,61–63]. One of the reasons is a lower porosity of $MgAl_2O_4$ based PEO coatings [62]. Furthermore, $MgAl_2O_4$ spinel also has many other attractive properties, including a high density (3.58 g/cm^3), high hardness (16 GPa), high mechanical strength, high melting point (2135 °C) and high chemical resistance [64,65]. The crystal structure of $MgAl_2O_4$ spinel is based on the structure of diamond, which can explain its good combination of properties and ensure the good stability in corrosion environments [64]. The introduction of Al_2O_3 to the matrix is a suitable way to increase the Al content in the alloy and stimulates the formation of spinel. A $MgAl_2O_4$ spinel-rich coating was achieved for the AZ91Nd/Al_2O_3 MMC. In the case of bare AZ91Nd alloy, it is possible to produce a spinel-based coating by introducing alternative Al source via using a phosphate-aluminate electrolyte. The presence of aluminate in the electrolyte is reported to moderate the discharges and, thus, gives rise to a low porosity of the coatings [66]. The formation process of $MgAl_2O_4$ in the coating of AZ91Nd alloy involving the alu-

minate originated from the electrolyte is different from the reinforcement alumina fiber, and the reactions are suggested as follows Eqs. (4)–((6)) [37]:

$$AlO_2^- + 2H_2O \rightarrow Al(OH)_3 + OH^- \quad (6)$$

$$2Al(OH)_3 \rightarrow Al_2O_3 + 3H_2O \quad (7)$$

$$MgO + Al_2O_3 \rightarrow MgAl_2O_4 \quad (8)$$

Without the disturbance of large size/volume alumina fibers, there is a more rapid mixing process of MgO and Al_2O_3 for the formation of $MgAl_2O_4$ in Eq. (4). Also, there is more Al_2O_3 available for the reaction which is also the more homogeneously distributed in the coating. All this results in the uniform distribution of $MgAl_2O_4$ as the main coating phase in case of AlO^{2-} addition from electrolyte. Summarizing, $MgAl_2O_4$ can be formed from Al source from the substrate, but from the practical point, the electrolyte is the more preferential approach.

5. Conclusion

(1) The presence of alumina fiber in the AZ91Nd matrix influenced the PEO process by firstly interrupting the continuous formation of the dielectric film, thus, leading to a short delay of the voltage increase at the conventional anodization stage. Secondly, the large size/volume of fibers led to a non-uniform distribution of the discharges on the surface of AZ91Nd/Al_2O_3 MMC after reaching the breakdown voltage. Finally, the voltage at the last stage declined with increasing fluctuations due to the reactive incorporation of the fibers disturbing the stability of the coating by causing high stresses.

(2) The coatings presented discernible local morphologies at the locations of intermetallics during the first two stages, and then the discrepancy was disappearing gradually. The coatings on the MMC were rougher than the coatings on the pure alloy in the phosphate electrolyte.

(3) The alumina fiber was embedded in the coating at first and then reactively incorporated in the coating. The large size and volume of the alumina fibers is responsible for the step by step dissolution of the fiber within the coatings preventing a fast and fully redistribution of Al in the coating.

(4) It is evident that the alumina fibers can be converted to the $MgAl_2O_4$ spinel phase by the interaction of the fiber and MgO. A $MgAl_2O_4$ rich layer of 25 μm at the outer layer of the coating was successfully formed on the MMC.

(5) Using an alternative Al source like a phosphate-aluminate electrolyte is the more practical approach and results in a $MgAl_2O_4$ based coating on the pure AZ91Nd alloy. This can be achieved due to higher Al_2O_3 concentrations and a more rapid mixing process of MgO and Al_2O_3.

Acknowledgement

Ting Wu thanks China Scholarship Council for the award of fellowship and funding (No. 201708510113). The authors would like to thank Dr. Anton Davydok for the experimental support during DESY beamline experiments. We also thank PETRA III (Hamburg, Germany) for accepting and granting the proposal I-20191340 (P.03 end-station) for localized phase composition analysis of PEO layers. The technical support of Mr. Volker Heitmann, Mr. Ulrich Burmester during this work is gratefully acknowledged.

Supplementary materials

Supplementary material associated with this article can be found, in the online version, at doi:10.1016/j.jma.2021.09.017.

References

[1] Y.L. Song, Y.H. Liu, S.R. Yu, X.Y. Zhu, Q. Wang, Appl. Surf. Sci. 10 (2008) 3014, doi:10.1016/j.apsusc.2007.10.043.
[2] K.M. Lee, K.R. Shin, S. Namgung, B. Yoo, D.H. Shin, Surf. Coat. Technol. 13-14 (2011) 3779, doi:10.1016/j.surfcoat.2011.01.033.
[3] D. Veys-Renaux, E. Rocca, J. Martin, G. Henrion, Electrochim. Acta (2014) 36, doi:10.1016/j.electacta.2013.08.023.
[4] R. Arrabal, A. Pardo, M.C. Merino, M. Mohedano, P. Casajús, K. Paucar, G. Garcés, Corros. Sci. (2012), doi:10.1016/j.corsci.2011.10.033.
[5] B. Mingo, R. Arrabal, M. Mohedano, A. Pardo, E. Matykina, Surf. Coat. Technol. (2017), doi:10.1016/j.surfcoat.2016.10.041.
[6] R. Arrabal, E. Matykina, F. Viejo, P. Skeldon, G.E. Thompson, Corros. Sci. 6 (2008) 1744, doi:10.1016/j.corsci.2008.03.002.
[7] T. Wu, C. Blawert, X. Lu, M. Serdechnova, M.L. Zheludkevich, J. Magnes. Alloy. (2021), doi:10.1016/j.jma.2021.03.017.
[8] B. Mingo, Y. Guo, R. Leiva-Garcia, B.J. Connolly, A. Matthews, A. Yerokhin, ACS Appl. Mater. Interfaces 27 (2020), doi:10.1021/acsami.0c07726.
[9] B. Mingo, R. Arrabal, M. Mohedano, Y. Llamazares, E. Matykina, A. Yerokhin, A. Pardo, Appl. Surf. Sci. (2018), doi:10.1016/j.apsusc.2017.10.083.
[10] G. Song, D. StJohn, Int. J. Cast Met. Res. 6 (2016) 327, doi:10.1080/13640461.2000.11819371.
[11] Y. Chen, Y. Yang, W. Zhang, T. Zhang, F. Wang, J. Alloy. Compd. (2017), doi:10.1016/j.jallcom.2017.05.010.
[12] K.M. Lee, B.U. Lee, S.I. Yoon, E.S. Lee, B. Yoo, D.H. Shin, Electrochim. Acta (2012) 6, doi:10.1016/j.electacta.2012.01.053.
[13] Z.U. Rehman, S.H. Shin, H.T. Lim, B.H. Koo, Surf. Coat. Technol. (2017), doi:10.1016/j.surfcoat.2016.12.112.
[14] X. Wang, X. Lu, P. Ju, Y. Chen, T. Zhang, F. Wang, Surf. Coat. Technol. (2020) 125709, doi:10.1016/j.surfcoat.2020.125709.
[15] L. Gawel, L. Nieuzyla, G. Nawrat, K. Darowicki, P. Slepski, J. Alloy. Compd. (2017), doi:10.1016/j.jallcom.2017.06.120.
[16] X. Lu, C. Blawert, M. Mohedano, N. Scharnagl, M.L. Zheludkevich, K.U. Kainer, Surf. Coat. Technol. (2016), doi:10.1016/j.surfcoat.2016.02.006.
[17] R.O. Hussein, X. Nie, D.O. Northwood, Electrochim. Acta (2013), doi:10.1016/j.electacta.2013.08.137.
[18] V. Dehnavi, W.J. Binns, J.J. Noël, D.W. Shoesmith, B.L. Luan, J. Magnes. Alloy. 3 (2018) 229, doi:10.1016/j.jma.2018.05.008.
[19] S. Farshid, M. Kharaziha, J. Magnes. Alloy. (2020), doi:10.1016/j.jma.2020.11.004.
[20] X. Lu, C. Blawert, K.U. Kainer, T. Zhang, F. Wang, M.L. Zheludkevich, Surf. Coat. Technol. (2018) 1, doi:10.1016/j.surfcoat.2018.08.003.
[21] G. Rapheal, S. Kumar, N. Scharnagl, C. Blawert, Surf. Coat. Technol. (2016), doi:10.1016/j.surfcoat.2016.01.033.

[22] H. Gao, M. Zhang, X. Yang, P. Huang, K. Xu, Appl. Surf. Sci. (2014), doi:10.1016/j.apsusc.2014.06.117.
[23] Z. Shahri, S.R. Allahkaram, R. Soltani, H. Jafari, J. Magnes. Alloy. 2 (2020) 431, doi:10.1016/j.jma.2018.10.001.
[24] X. Lu, C. Blawert, K.U. Kainer, M.L. Zheludkevich, Electrochim. Acta (2016), doi:10.1016/j.electacta.2016.03.042.
[25] X. Lu, C. Blawert, M.L. Zheludkevich, K.U. Kainer, Corros. Sci. (2015), doi:10.1016/j.corsci.2015.09.016.
[26] C. Liu, J. Liang, J. Zhou, Q. Li, L. Wang, Appl. Surf. Sci. (2016), doi:10.1016/j.apsusc.2016.04.047.
[27] A.S. Gnedenkov, S.L. Sinebryukhov, D.V. Mashtalyar, S.V. Gnedenkov, Corros. Sci. (2016), doi:10.1016/j.corsci.2015.10.026.
[28] A. Castellanos, A. Altube, J.M. Vega, E. García-Lecina, J.A. Díez, H.J. Grande, Surf. Coat. Technol. (2015), doi:10.1016/j.surfcoat.2015.07.017.
[29] B. Kazanski, A. Kossenko, M. Zinigrad, A. Lugovskoy, Appl. Surf. Sci. (2013), doi:10.1016/j.apsusc.2013.09.180.
[30] Y. Wang, X. Wang, T. Zhang, K. Wu, F. Wang, J. Mater. Sci. Technol. 12 (2013), doi:10.1016/j.jmst.2013.10.014.
[31] C. Liu, T. Xu, Q. Shao, S. Huang, B. Jiang, J. Liang, H. Li, J. Alloy. Compd. (2019), doi:10.1016/j.jallcom.2019.01.095.
[32] H. Duan, C. Yan, F. Wang, Electrochim. Acta 15 (2007) 5002, doi:10.1016/j.electacta.2007.02.021.
[33] A.G. Rakoch, E.P. Monakhova, Z.V. Khabibullina, M. Serdechnova, C. Blawert, M.L. Zheludkevich, A.A. Gladkova, J. Magnes. Alloy. (2020).
[34] Y.G. Ko, E.S. Lee, D.H. Shin, J. Alloy. Compd. (2014), doi:10.1016/j.jallcom.2013.03.015.
[35] Y. Wang, D. Wei, J. Yu, S. Di, J. Mater. Sci. Technol. 10 (2014), doi:10.1016/j.jmst.2014.03.006.
[36] D. Veys-Renaux, C.E. Barchiche, E. Rocca, Surf. Coat. Technol. (2014), doi:10.1016/j.surfcoat.2014.04.031.
[37] L.S. Wang, C.X. Pan, Surf. Eng. 5 (2013) 324, doi:10.1179/174329407x260519.
[38] M. Sieber, F. Simchen, I. Scharf, T. Lampke, J. Mater. Eng. Perform. 3 (2016) 1157, doi:10.1007/s11665-016-1917-7.
[39] R.O. Hussein, P. Zhang, X. Nie, Y. Xia, D.O. Northwood, Surf. Coat. Technol. 7 (2011) 1990, doi:10.1016/j.surfcoat.2011.08.060.
[40] E. Cakmak, K.C. Tekin, U. Malayoglu, S. Shrestha, Surf. Coat. Technol. 8 (2010) 1305, doi:10.1016/j.surfcoat.2009.10.012.
[41] X.J. Cui, C.H. Liu, R.S. Yang, M.T. Li, X.Z. Lin, Surf. Coat. Technol. (2015), doi:10.1016/j.surfcoat.2014.09.071.
[42] A. Nirala, S. Soren, N. Kumar, R. Garg, S.K. Sharma, A.K. Shrivastava, D.B. Singh, D. Yadav, J.K. Yadav, Mater. Today Proc. (2021), doi:10.1016/j.matpr.2021.04.062.
[43] Z. Trojanová, V. Gärtnerová, P. Lukáč, Z. Drozd, J. Alloy. Compd. 1-2 (2004) 19, doi:10.1016/j.jallcom.2003.12.047.
[44] W. Xue, Q. Jin, Q. Zhu, M. Hua, Y. Ma, J. Alloy. Compd. 1-2 (2009) 208, doi:10.1016/j.jallcom.2009.03.159.
[45] W. Xue, X. Wu, X. Li, H. Tian, J. Alloy. Compd. 1-2 (2006) 302, doi:10.1016/j.jallcom.2006.01.035.
[46] R. Liu, N. Weng, W. Xue, M. Hua, G. Liu, W. Li, Surf. Coat. Technol. (2015), doi:10.1016/j.surfcoat.2014.11.062.
[47] R. Arrabal, E. Matykina, P. Skeldon, G.E. Thompson, Appl. Surf. Sci. 9 (2009) 5071, doi:10.1016/j.apsusc.2008.12.070.
[48] R. Arrabal, A. Pardo, M.C. Merino, M. Mohedano, P. Casajús, E. Matykina, P. Skeldon, G.E. Thompson, Corros. Sci. 11 (2010) 3738, doi:10.1016/j.corsci.2010.07.024.
[49] C. Krywka, H. Neubauer, M. Priebe, T. Salditt, J. Keckes, A. Buffet, S.V. Roth, R. Doehrmann, M. Mueller, J. Appl. Crystallogr. 1 (2011) 85, doi:10.1107/s0021889811049132.
[50] J. Kieffer, D. Karkoulis, J. Phys. Conf. Ser. 20 (2013) 202012, doi:10.1088/1742-6596/425/20/202012.
[51] E.B. Watson, J.D. Price, Geochim. Cosmochim. Acta (2002) 2123.
[52] S. Ono, S. Moronuki, Y. Mori, A. Koshi, J. Liao, H. Asoh, Electrochim. Acta (2017), doi:10.1016/j.electacta.2017.04.110.
[53] C.Y.H. Lim, D.K. Leo, J.J.S. Ang, M. Gupta, Wear 1-6 (2005) 620, doi:10.1016/j.wear.2005.02.006.
[54] K.T. Jacob, K.P. Jayadevan, Y. Waseda, J. Am. Ceram. Soc. 1 (1998) 209.
[55] J. Meng, W. Chen, J. Zhao, L. Liu, High Temp. Mater. Process. 6 (2018) 581, doi:10.1515/htmp-2016-0254.
[56] T.E. Mitchell, J. Am. Ceram. Soc. 12 (2004) 3305, doi:10.1111/j.1151-2916.1999.tb02244.x.
[57] J. Jovović, S. Stojadinović, N.M. Šišović, N. Konjević, J. Quant. Spectrosc. Radiat. Transf. 15 (2012) 1928, doi:10.1016/j.jqsrt.2012.06.008.
[58] D. Mohapatra, D. Sarkar, J. Mater. Process. Technol. 1-3 (2007) 279, doi:10.1016/j.jmatprotec.2007.01.037.
[59] T.W. Clyne, S.C. Troughton, Int. Mater. Rev. 3 (2018) 127, doi:10.1080/09506608.2018.1466492.
[60] L. Jin, Y.B. Kang, P. Chartrand, C.D. Fuerst, Calphad 1 (2011) 30, doi:10.1016/j.calphad.2010.11.002.
[61] S.Y. Wang, Y.P. Xia, Trans. Nonferr. Met. Soc. China 2 (2013) 412, doi:10.1016/s1003-6326(13)62478-4.
[62] B.S. Lou, Y.Y. Lin, C.M. Tseng, Y.C. Lu, J.G. Duh, J.W. Lee, Surf. Coat. Technol. (2017), doi:10.1016/j.surfcoat.2017.05.094.
[63] B.V. Vladimirov, B.L. Krit, V.B. Lyudin, N.V. Morozova, A.D. Rossiiskaya, I.V. Suminov, A.V. Epel'feld, Surf. Eng. Appl. Electrochem. 3 (2014) 195, doi:10.3103/s1068375514030090.
[64] I. Ganesh, Int. Mater. Rev. 2 (2013) 63, doi:10.1179/1743280412y.0000000001.
[65] K. Shan, R. Li, J. Liu, Ceram. Int. 3 (2021) 4143, doi:10.1016/j.ceramint.2020.09.291.
[66] D. Sreekanth, N. Rameshbabu, K. Venkateswarlu, Ceram. Int. 6 (2012) 4607, doi:10.1016/j.ceramint.2012.02.040.

5.3 Influence of melting temperature of substrate

Paper 6: Ting Wu, Carsten Blawert, Maria Serdechnova et al., Formation of plasma electrolytic oxidation coatings on pure niobium in different electrolytes, Applied Surface Science 573(2022). https://doi.org/10.1016/j.apsusc.2021.151629

Graphical abstract

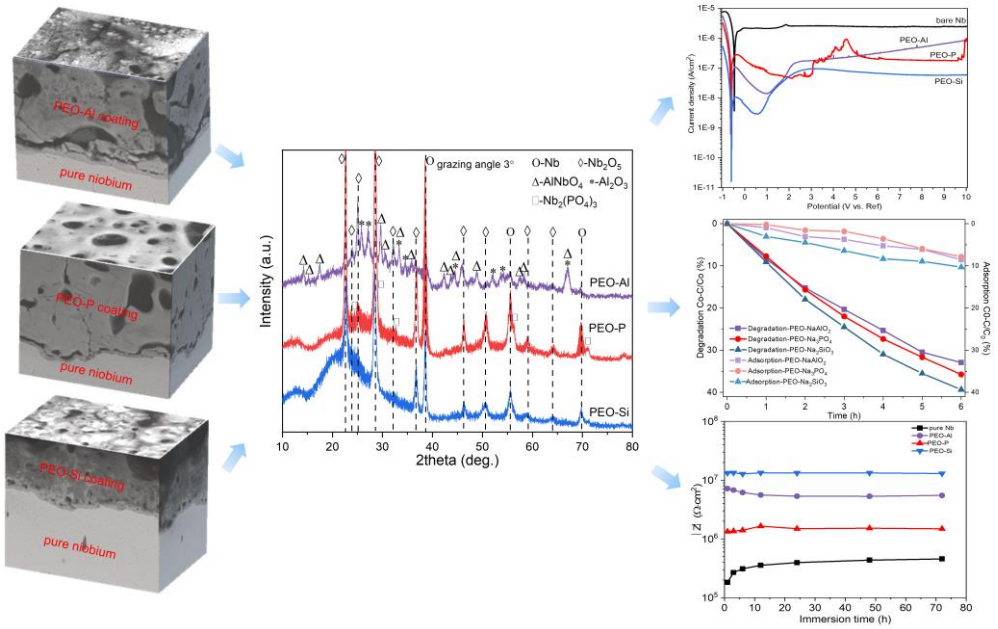

Nb is a transition metal that has many attractive properties, such as catalytic activity, biocompatibility, corrosion resistance and high specific strength. The oxides of Nb also show remarkable redox and acidic properties, as well as photosensitivity. This work was a preliminary investigation of PEO process on pure Nb, in order to study the coating formation process in terms of the high melting point of Nb, and produce functional coatings, i.e. anticorrosion and photocatalytic activity in different electrolytes. The monitoring of the optical discharges showed that Nb did not participate in the plasma reactions directly. Nb_2O_5 was the main phase in the coatings, in addition, a slight difference of phase composition was revealed in the coatings for three different processing conditions (aluminate-, phosphate-, silicate-base electrolytes, respectively). Multifunctional PEO coatings were finally obtained on pure Nb. All the coatings showed high corrosion resistance. A semiconductive behavior of the coating was also demonstrated in electrochemical tests due to Nb_2O_5, which is a typical n-type semiconductor. And the coatings displayed high photocatalytic activities (30 - 40 %) in degradation of methyl orange.

Applied Surface Science 573 (2022) 151629

Contents lists available at ScienceDirect

Applied Surface Science

journal homepage: www.elsevier.com/locate/apsusc

Full Length Article

Formation of plasma electrolytic oxidation coatings on pure niobium in different electrolytes

Ting Wu [a,*], Carsten Blawert [a], Maria Serdechnova [a], Polina Karlova [a], Gleb Dovzhenko [b], D. C. Florian Wieland [c], Stevan Stojadinovic [d], Rastko Vasilic [d], Kristina Mojsilovic [d], Mikhail L. Zheludkevich [a,e]

[a] Institute of Surface Science, Helmholtz-Zentrum Hereon, Max-Planck Strasse 1, 21502 Geesthacht, Germany
[b] Institute of Materials Physics, Helmholtz-Zentrum Hereon, Max-Planck Strasse 1, 21502 Geesthacht, Germany
[c] Institute of Metallic Biomaterials, Helmholtz-Zentrum Hereon, Max-Planck Strasse 1, 21502 Geesthacht, Germany
[d] University of Belgrade, Faculty of Physics, Studentski trg 12-16, 11000 Belgrade, Serbia
[e] Institute for Materials Science, Faculty of Engineering, Kiel University, Kaiserstrasse 2, 24143 Kiel, Germany

ARTICLE INFO

Keywords:
Plasma electrolytic oxidation
Niobium
Microstructure
Photocatalytic activity
Corrosion resistance

ABSTRACT

The development of PEO surface treatments for Nb (niobium) provides a possibility to produce functionalized coatings with a combination of new compositions and phases. In the frame of this work, PEO coatings on pure Nb are produced in three electrolytes containing aluminate, phosphate and silicate. Furthermore, the influence of the electrolyte composition on the PEO process and the microstructure, composition and properties of the coatings were studied. It was observed that most of the coating forming species did not participate in the plasma reactions directly, while the chemical-, electrochemical- and thermal stimulated reactions are dominating the coating formation. The results show that all the coatings are mainly composed of the Nb_2O_5 phase. An additional mixture of oxides (Al_2O_3 and $AlNbO_4$) is found in the coating formed in aluminate-containing electrolyte, and the coating formed in phosphate-containing electrolyte contains a small amount of $Nb_2(PO_4)_3$ and amorphous phosphate. No additional crystalline phase other than the amorphous silica phase is detected in the coating formed in silicate-containing electrolyte. Additionally, different morphology of the coatings is revealed and the most uniform coating is produced in silicate-containing electrolyte, which further improves its corrosion resistance. This coating also shows the highest photocatalytic activity due to the combination of Nb_2O_5 and silica. Since all PEO coatings on pure Nb show superior corrosion resistance and photocatalytic activity, they might be interesting for a wide range of applications ranging from transportation, biomedical implants to environmental protection.

1. Introduction

Niobium (Nb) based materials are of great interest in various applications, strikingly for the fields of catalysis [1–4] and biomedicine [5–9] relying upon their catalytic activity and bio functionality. Nb oxide's combination with redox property, acidic property and photosensitivity has been used especially in catalytic reactions where it can remarkably promote the processes [10–12]. As biomedical implants, the intriguing properties of biocompatibility, corrosion resistance and specific strength also render Nb materials practical to reconstruct the failed tissue in the body [13–16]. A thin oxide layer of Nb_2O_5 is deposited on the surface of pure Nb immediately through spontaneous oxidation, isolating it from the corrosive environment. Nevertheless, modification of the native oxide layer on pure Nb is necessary in terms of the microstructure and composition for further applications.

Plasma electrolytic oxidation (PEO) is an advanced surface modification process. It has been widely performed on light metals such as Al [17,18], Mg [19,20] and Ti [21,22] to form ceramic-like coatings. The PEO coatings are primarily composed of the metal oxides of the substrate metals [23–25], such as, Al_2O_3, MgO and TiO_2. PEO technology is also a promising candidate to produce functional coatings on pure Nb. The semiconducting Nb oxides in combination with the inherent porosity of PEO layer are potentially interesting for the catalytic efficiency as well as for the osseointegration of bio-implants.

* Corresponding author.
E-mail address: ting.wu@hereon.de (T. Wu).

https://doi.org/10.1016/j.apsusc.2021.151629
Received 2 July 2021; Received in revised form 7 October 2021; Accepted 14 October 2021
Available online 18 October 2021

According to the intensive studies of PEO processing on Al, Mg and Ti, the process is generally made up of few stages including the conventional anodization, discharging and sparking [26]. With the assistance of plasma, the electrochemical-driven process enables the formation of coatings with excellent corrosion and wear resistance. Most studies of plasma electrolytic oxidation involving Nb were focusing on metallic substrates alloyed with Nb, such as Ti-Nb, Zr-Nb and Ti-Nb-Zr alloys [27–29]. Only a limited number of studies are available for pure Nb substrates [30–38]. Stojadinovic et al. [30,32] studied the luminescence during PEO processing of pure Nb in acidic electrolyte before and after reaching the breakdown voltage. The sparking emissions were only composed of signals from oxygen and hydrogen atoms, originated from the electrolyte. The absent spectral line of Nb resulted from the high melting point of Nb (2447 °C) hindering its evaporation during the processing. PEO coatings on pure Nb were composed of Nb oxides and complex compounds deriving from the electrolytes. A study [34] has claimed hydroxyapatite formation in the coating on pure Nb during PEO processing after doping with calcium acetate in the phosphoric acid electrolyte. Furthermore, SiC particles, added to the electrolyte, were revealed partly buried in the coating on pure Nb [36].

With respect to the extensive reports of PEO processing on Mg, Al and Ti alloys [39–41], the insight of PEO process on pure Nb is also necessary considering the complexity of possible reaction mechanisms with the electrolytes. This work was focused on the formation of PEO coatings on pure Nb in three different types of PEO electrolytes, containing phosphate, silicate and aluminate, respectively. The evolution of the coating formation process in different electrolyte composition was studied during the treatment as a function of processing time. For comparison reasons, the microstructure and composition of the resultant PEO coatings were also characterized by a combination of analytical techniques, correlated with the evaluation of photocatalytic activity and degradation resistance.

2. Materials and methods

A pulsed DC power source was used to carry out the PEO processing on the pure Nb for 600 s under a constant current density of 10A/dm^2. A duty cycle of 10 % and a frequency of 100 Hz were selected. Rectangular specimens of pure Nb with dimensions of 15 × 15 × 4 mm were used as anode and processed in three different aqueous electrolytes, containing (1) $NaAlO_2$ 20 g/L and KOH 1 g/L (pH 12.49, conductivity 520 μS/cm), (2) Na_2SiO_3 20 g/L and KOH 1 g/L (pH 12.29, conductivity 496 μS/cm) and (3) Na_3PO_4 20 g/L and KOH 1 g/L (pH 12.72, conductivity 529 μS/cm), respectively. A stainless steel tube cathode was integrated in to the cooling system to keeping the temperature of the electrolyte at 20 ± 2 °C. A mechanical stirring system was used to agitate the electrolyte keeping it homogeneous and avoid temperature gradients. The specimens were labeled as PEO-Al, PEO-P and PEO-Si after treatment in aluminate-, phosphate- and silicate-based electrolyte, respectively. The voltage response as a function of processing time was recorded using a data acquisition system (SignaSoft 6000 software package, Gantner, Germany). The spectral emission of the plasma was monitored during PEO processing, using an Emicon OES system (PLASUS, Germany) with PLASUS SpecLine software (PLASUS, Germany).

The surface morphology of the coatings was measured by a laser scanning confocal microscope (LSM 800, ZEISS). Surface and cross-sectional morphology and elemental composition of the coatings were studied using a scanning electron microscope (SEM, TESCAN Vega3 SB) combined with an energy dispersive spectrometer system (EDS, eumeX IXRFsystems). The coating thickness was measured by a microprocessor coating thickness gauge (MiniTest 2100, ElektroPhysik) and further validated from the cross-section observations of the SEM.

The crystalline phase composition was measured by X-ray diffraction (XRD, D8 Advance, Bruker AXS) with Cu Kα radiation. The following diffraction settings were selected: diffraction angle 2θ between 20° and 80°, step size of 0.02°, dwell time of 1 s and grazing angle of 3°. Further study of phase composition and spatial distribution across the PEO-P and PEO-Al coatings were performed at Deutsches Elektronen-Synchrotron (DESY, Hamburg, Germany) using the nano focus end station of the beamline P03 at PETRAIII storage ring [42]. The X-ray beam energy was 19.7 keV with a beam size of 1.5 by 1.5 μm. An Eiger 9 M detector was employed with a pixel size of 75 μm by 75 μm. The beam was scanned across the surface in steps of 2 μm and 4 μm in vertical and horizontal direction respectively, covering a measured area of 80 μm × 80 μm. Each XRD pattern was recorded with an acquisition time of 0.5 s. Data reduction was done by employing in-house developed Matlab® code and the PyFAI [43] routine. The scattering angle 2θ of the diffraction patterns was converted to Cu K-alpha radiation with the wavelength of 1.5406 Å. The spatial distribution of the phases in the coating was reconstructed, in order to reveal the phase distribution across the coating thickness. A lab-made script in Python programming language was operated in the "Spyder" software package environment included with Anaconda Navigator, to analyze and generate two-dimensional phase map graphics.

The photocatalytic properties of the PEO coatings on pure Nb were investigated by measuring photodegradation of methyl orange (MO) at room temperature. The temperature in the photoreactor was kept constant by a water recirculation system. The specimen surface, placed on a perforated holder, was immersed in a 10 ml aqueous solution containing 8 mg/L of MO, under constant stirring conditions (300 rpm) and positioned under the irradiation source. Prior to irradiation, the catalyst and solution were stirred in the dark for 30 min to achieve adsorption–desorption equilibrium. Then, the solar radiation was simulated using a lamp (Osram Vitalux 300 W), fixed at 25 cm above the surface of the solution providing 16,000 lx intensity. The total irradiation duration was selected to be 6 h. A fixed quantity of 1 ml MO solution was taken every hour to measure the MO concentration at the maximum of the absorption spectra ($\lambda = 464$ nm) by Agilent Cary 60 UV–vis spectrophotometer. The absorption was converted to concentration according to a standard curve showing the linear dependence between MO concentration and absorption at 464 nm wavelength. Similarly, the MO adsorption in darkness with the presence of photocatalyst was also recorded every hour during 6 h. After each measurement, the solution was returned to the photocatalytic reactor. Prior to the measurement, MO solution was tested for photocatalysis in the absence of the photocatalyst to confirm its stability. The absence of change in MO concentration after 6 h of irradiation indicated its stability under the applied conditions and its degradation resulted only from the presence of a photocatalyst. The adsorption and degradation percentage of MO was given as $((C_0\text{-}C)/C_0)$, where C_0 was the initial MO concentration and C was the MO concentration before and after exposure.

The corrosion resistance of the PEO coated specimens and bare Nb was evaluated by performing potentiodynamic polarization and electrochemical impedance spectroscopy experiments, with a computer controlled Gamry potentiostat Interface 1010E. A classical three-electrode cell system was used and the specimens were acting as a working electrode. The counter and the reference electrode were a Pt wire and a saturated Ag/AgCl electrode, respectively. A specimen surface area of 0.5 cm^2 was exposed to Ringer's solution (8.6 g/L NaCl, 0.3 g/L KCl and 0.56 g/L $CaCl_2{\cdot}6H_2O$). After 1000 s immersion at open circuit potential, potentiodynamic polarization scan started from −1.0 V vs reference electrode at a scan rate of 0.5 mV/s and terminated at 10 V. EIS (electrochemical impedance) tests were carried out at open circuit potential with AC amplitude of 10 mV RMS over the frequency range of 100 kHz - 0.01 Hz. The measurements were performed after subsequent immersion durations of 5 min, 1 h, 3 h, 6 h, 12 h, 24 h, 48 h, and 72 h, respectively. The same measurement was reproduced on three specimens for each PEO coating for repeatability.

3. Results

3.1. Voltage evolution

The voltage as a function of processing time in three different electrolytes containing aluminate, phosphate and silicate is shown in Fig. 1, respectively. The voltage response is typical for the current-controlled PEO processing [44–46] and two stages are obviously revealed. At the initial conventional anodization, the primary oxide layer from air and electrolyte passivation facilitates the rising of the voltage. The continuous voltage increase, resulting from the coating formation and increasing electrical resistance, maintains the pre-set current density. The voltage ramp shows average growth rates of 27.8 V/s, 13.8 V/s and 27.1 V/s in aluminate-, phosphate- and silicate-based electrolytes, respectively. Subsequently, the voltage ramp experiences a transition due to the development of discharges on the specimen surface. The presence of discharges manifests the commencement of the second stage. It takes 20 s and by reaching ca. 350 V, the discharges become visible in the aluminate-based electrolyte. However, it only takes around 10 s in phosphate- and silicate-based electrolytes to reach the breakdown voltage of ca. 240 V and ca. 260 V, respectively. Afterwards, the voltage increase declines further, at average rates of 0.13 V/s, 0.30 V/s and of 0.29 V/s for PEO-Al, PEO-P and PEO-Si specimens, respectively. The final voltage of PEO-Al specimen is 489 V after 600 s of processing, much higher than that of PEO-P (402 V) and PEO-Si (418 V) specimens.

3.2. Optical emission

At the beginning of the process, anodic luminescence is observed with color evolution on the specimen surface. It is associated with the collision-radiative recombination of electrons and bremsstrahlung radiation at the conventional oxidation stage [20,30,47]. Once the discharges appear, they rapidly cover the entire specimen surface. The discharges are firstly tiny, short living and fast moving, and then their size and lifetime increase, accompanied by a color change. Their motion slows down with time. At the end of the process, the discharge number dwindles obviously and they become large-sized and long-lasting. It seems that the appearance of static large-sized discharges at certain regions is due to the rapid creating and extinguishing of a cluster of discharges [47]. Furthermore, the process is always accompanied by gas evolution on the surface due to the oxygen production and electrolyte evaporation under the high temperature of the discharges.

The characteristics of the discharges have a great influence on the PEO coatings, such as its growth, composition and morphology [26].

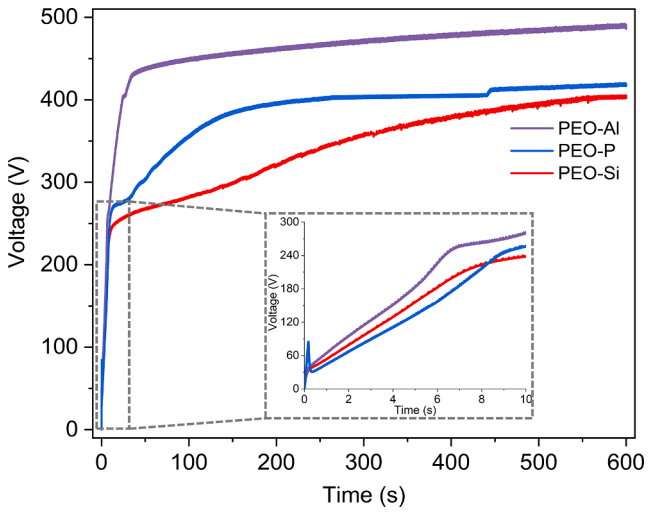

Fig. 1. Applied voltage as a function of PEO processing time on pure Nb in different electrolytes.

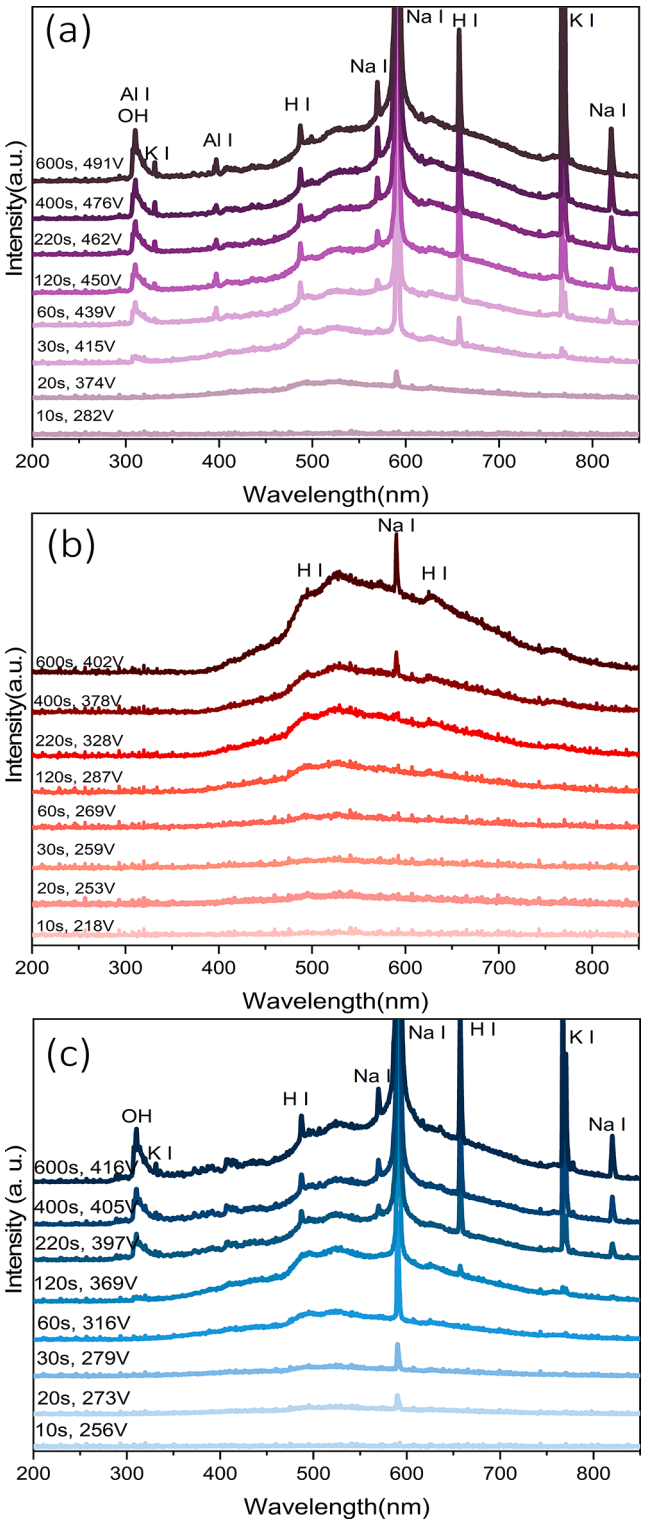

Fig. 2. Optical emission spectra of pure Nb during PEO processing in (a) aluminate-containing, (b) phosphate-containing and (c) silicate-containing electrolytes.

Fig. 2 illustrates the evolution of optical emission spectra from the discharges with treatment time in different electrolytes. All species that participate in the plasma discharges are originated from the electrolytes, including H, O, Na, K and Al (in aluminate containing electrolyte). The absence of Nb emission lines during the entire process is not surprising, since Nb has a pretty high melting point (2477 °C) and high chemical

stability. This was also observed in an investigation using phosphoric acid [30]. With increasing processing time, the emission intensity for all specimens rises. A broad halo was observed in the visible wavelength range between 450 nm and 650 nm at 374 V after 20 s of treatment in the aluminate-based electrolyte (Fig. 2(a)). It confirms the first observation of the white shining at the voltage up to 350 V. Subsequently, the color of the discharges changes immediately from white to orange-yellow. At that moment, a surge of discharging intensity at 598 nm (Na I) is found to reach the technical saturation limit of the detector under 415 V (30 s). Thus, the color change of the discharges is ascribed to the dominant Na species in the plasma discharges. In addition, it can be seen that the spectral lines of H I, K I, Al I and OH band are also present with further increasing voltage. In the silicate-based electrolyte, the discharge emission shows similar patterns under a lower voltage (Fig. 2(c)). The strong line of Na I appears already at 273 V (10 s). The spectral lines of other species, including H I, OH and K I, are starting to be seen under a voltage of 397 V (220 s). For the treatment in the phosphate-based electrolyte, the emission intensity is revealed to be the lowest (Fig. 2 (b)). Even at the end of the process, the spectrum still shows continuous emission and only the spectral lines of Na I at 598 nm, H_β at 486 nm and H_α at 656 nm are recognized at low intensity. It seems that the voltage influences the emission intensity. The final voltage (402 V) in phosphate electrolyte is lower compared to the other two electrolytes, possibly resulting in the lower energy of the discharges and thus the lowest emission intensity.

3.3. Surface characterization

The surface morphology of the coatings is visible in the three-dimensional view of the surfaces and the extracted profile curves (Fig. 3). Similar surface roughness Ra (arithmetical mean height, μm) values are revealed for PEO-Al and PEO-P coatings, which are 3.24 ± 0.30 μm and 3.04 ± 0.25 μm, respectively, while PEO-Si coating has a lower Ra of 2.53 ± 0.21 μm. The results also indicate the highest and the lowest RSm (mean width of the profile, mm) values (Gaussian filter, 0.8 mm) of PEO-Al and PEO-P coatings, 0.039 ± 0.011 mm and 0.018 ± 0.002 mm, respectively. Between them, RSm of PEO-Si coating is with a value equal 0.024 ± 0.003 mm. The higher Ra combined with lower RSm gives an impression of a larger coating surface area to a certain degree, demonstrating that PEO-P coating probably has the largest surface area. One should notice that the surface laser scanning measurement conducted at 20 × magnitude can not fully consider the contribution of the detailed surface morphology to the surface area at the micrometer or nanometer scales.

Fig. 4 illustrates surface morphologies of the coatings on the PEO-Al, PEO-P and PEO-Si specimens, respectively. Discernible local morphologies can be easily found on each coating surface. Typical regions are marked by rectangles in Fig. 4 and the composition was determined there as well (Table 1). It is clearly revealed in Fig. 4(a) that the coating surface of PEO-Al specimen appears as the network of crater-centered islands. The crater morphology is constructed from the discharge channels, where the discharges generate and extinguish (Fig. 4(c)). The yellow-circled (Fig. 4(a)) present as molten morphology near the crater mostly resulted from the fast solidification of melts, which are ejected from the discharge channel. Between the sintered islands, there are many tiny particles and micro-pores appearing within the transition regions (Fig. 4(b)). The main element content shows a mass of Al incorporated into the coating, of up to 32.4 at.% on the sintered islands and 27.4 at.% within the transition regions. Nb content rises from 5.5 to 11.2 at.% at different regions. The higher content of Nb is more likely involved at the locations closer to the centered pores (discharge channels), in which large and strong discharges are formed.

As shown in Fig. 4(d), open micro-pores of ca. 8 μm in diameter spread on the entire PEO-P coating surface. What is visible in Fig. 4(e) is that the micro-pores are connected from the coating surface ending up to the inner coating towards the substrate. The large number and size of

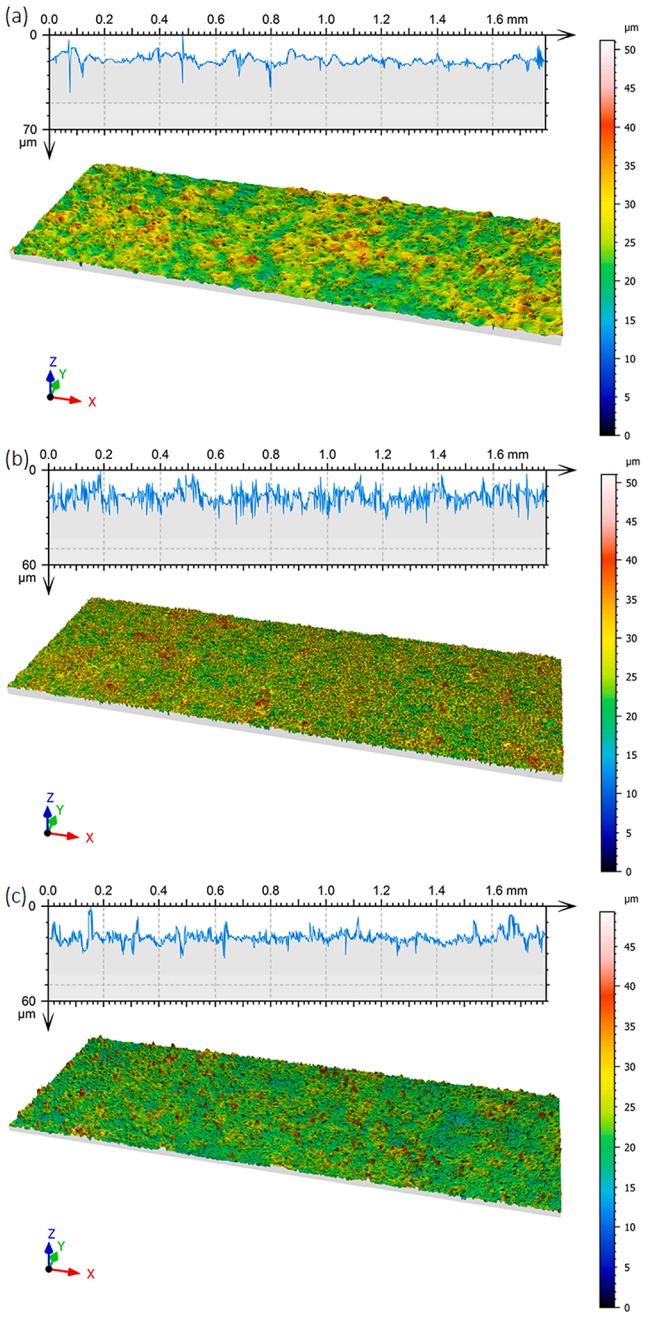

Fig. 3. Surface profiles of (a) PEO-Al, (b) PEO-P and (c) PEO-Si coatings.

micro-pores indicate the intensive gas release during the processing, thus confirming the melting of coating materials during coating formation process. In addition, some relatively large sintered-discs are appearing sporadically (Fig. 4(f)), which is speculated to correlate with the discharges that have the lowest emission intensity. The PEO-P coating has the highest Nb content with respect to PEO-Al and PEO-Si coatings, reaching 29.0 at.% at the more porous regions, as exhibited in Fig. 4(e). The coating seems mainly composed of Nb oxide. In spite of some discharges, it seems that the coating formation process is not typical with mixed oxides from substrate and electrolyte, however, is more a conventional anodization.

The PEO-Si specimen Fig. 4(g) has the most compact morphology, characterized by the highly sintered surface. Similar to PEO-Al coating, the coating surface consists of relatively low Nb content, but higher Si concentration originated from the electrolyte. The high brightness regions around the micro-pore shown at a higher magnitude in Fig. 4(i)

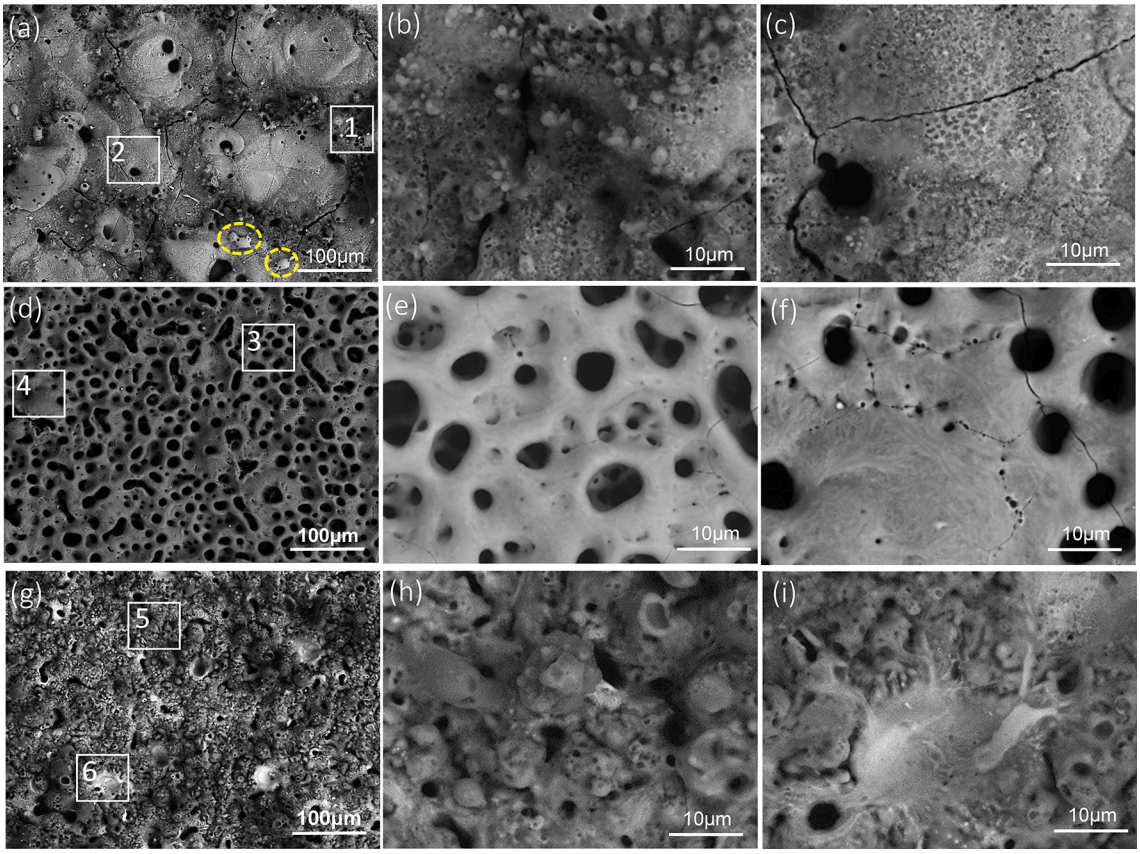

Fig. 4. Surface morphologies of PEO-Al coating (a), PEO-P coating (d) and PEO-Si coating (g), with local high magnitude (b) and (c) for region 1 and 2, (e) and (f) for region 3 and 4, (h) and (i) for region 5 and 6.

Table 1
Content of main elements (at. %) at different regions (Fig. 4) of coating surface in different electrolytes.

	Nb	O	Al	P	Si	Na	K
1	5.5	57.6	32.4	–	–	4.1	0.4
2	11.2	59.2	27.4	–	–	2.1	0.1
3	29.0	62.7	–	5.6	–	2.5	0.2
4	24.4	64.7	–	7.2	–	3.5	0.2
5	1.8	58.6	–	–	33.1	5.7	0.8
6	7.9	63.5	–	–	26.0	2.3	0.3

contains a relatively high Nb concentration of 7.9 at.% compared to the other regions (1.8 at.%). It shows that the melted material was ejected through the discharge channel and solidified on the surface. Thus, it should be rich in Nb as it originated from the interface region of coating/substrate. Furthermore, the different brightness might indicate a not complete mixing of the coating materials since the image is taken under the BSE (backscattered electron) mode.

3.4. Cross-sectional characterization

Fig. 5 displays the cross-sectional morphologies of different coatings, as well as the EDS line scan across coating thickness, respectively. The observations confirm that PEO-Al coating has the highest thickness of 24.9 ± 5.5 μm, similar to 22.9 ± 4.1 μm of PEO-P coating, and the lowest coating thickness, 16.6 ± 4.0 μm, is revealed for PEO-Si coating. All the coatings show porous cross-sectional morphology and a layered structure, with a thin barrier layer of a few hundred nanometers thickness at the interface of substrate/coating typically [48–50]. Pore bands parallel to the coating surface are found in the PEO-Al coating (Fig. 5(a)), between the more porous outer layer and the inner barrier layer. EDS line scan shows the uniform distribution of Na and K across the coating thickness, having a concentration lower than 10 wt%. As expected, fluctuations of Nb, O and Al signals were detected along the micro-pores. The concentration of Nb is higher than Al since Nb is 3.4 times the atomic mass of Al. Near the coating/substrate interface there is a small decrease of Al concentration while the O concentration increases slightly towards the substrate. For PEO-P coating, open micro-pores stretch from the coating surface to the inner layer (Fig. 5(b)), agreeing with the surface observation. The EDS line scan shows that almost all of the main coating composition elements are distributed uniformly across coating thickness. Nb is dominant reaching 70 wt% and the O concentration is about 20 wt%. One could observe a slight increase of P concentration to 10 wt% near the pore band, suggesting a preferred P accumulation at this region. As seen in Fig. 5(c), it is obvious that PEO-Si coating shows the most compact cross-sectional morphology and only relatively small-sized micro-pores are present near the coating/substrate interface. Nevertheless, the local morphology at a high magnitude should be responsible for the absence of large-sized micro-pores/pore bands, which could be seen in Fig. 6(c). The elemental distribution across the coating seems not uniform. The concentration of Nb initially decreases from 70 wt% to 40 wt%, starting at the coating surface to a distance of 6 μm towards the coating/substrate interface, in contrast, the concentration of O and Si show a reverse change. Before reaching stable value, there is a bump and a hollow for the concentration of Nb and Si, respectively, at the blue-marked area with high brightness in BSE image (Fig. 5(c)). Interestingly, a track with higher brightness (highlighted by red dash line) compared to the surrounding was found to extend across almost the entire coating thickness. According to the BSE result, this track contains a high accumulation of Nb, which indicates the outward transport of coating formation species from the substrate to the coating/electrolyte interface. These observations are also supported by the EDS

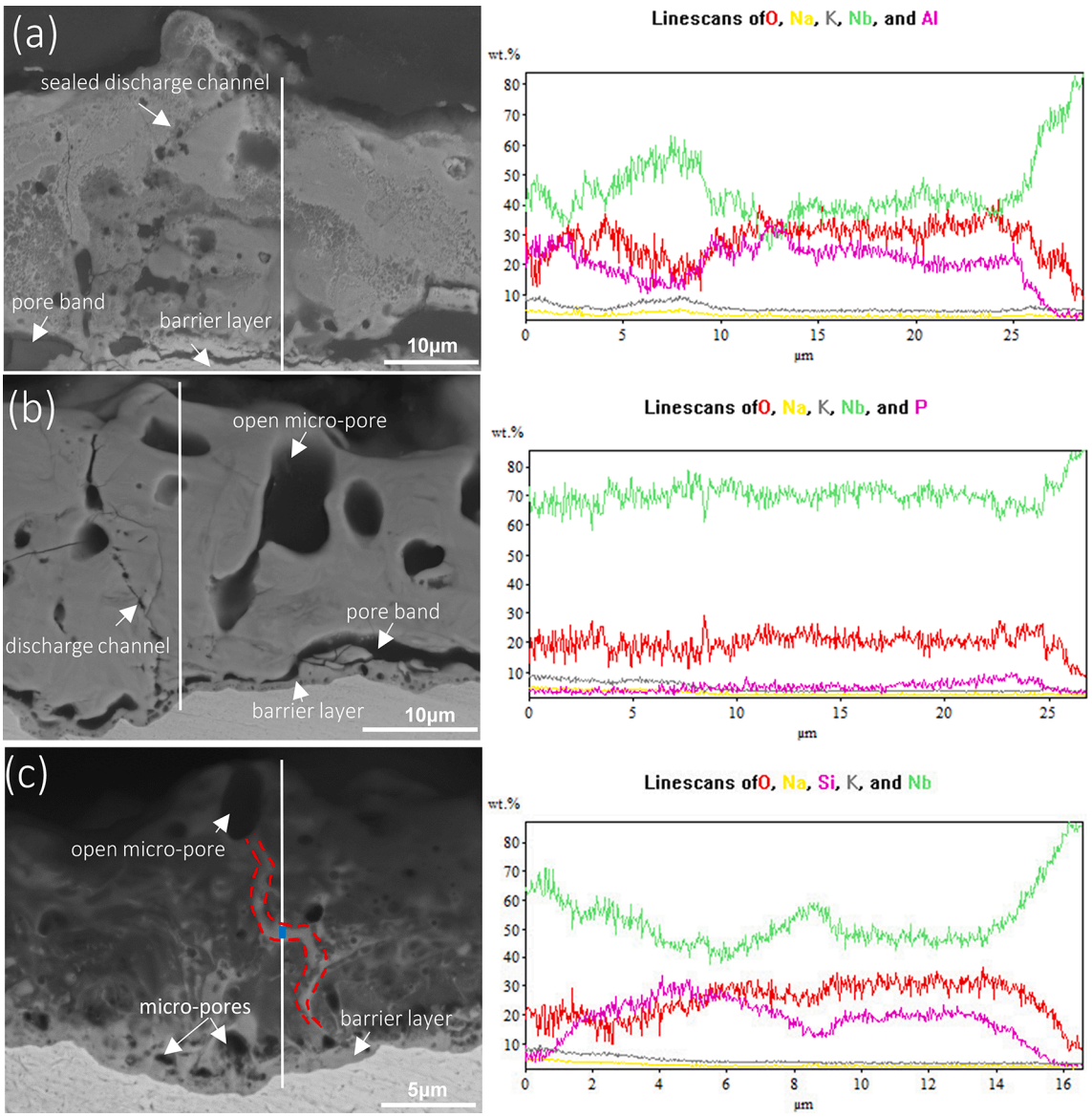

Fig. 5. Cross-sectional morphologies of (a) PEO-Al, (b) PEO-P and (c) PEO-Si coatings with EDS line scan across coating thickness.

mapping results in Fig. 6. Al and Si have slightly stronger signals in PEO-Al (Fig. 6(a)) and PEO-Si coatings (Fig. 6(c)), respectively. As a result, Nb signals are diluted in the coatings. Especially at the region of micro-pores and pore bands, PEO-Al coating shows a more intensive signal, indicating that these regions are enriched with the species from the electrolyte. The open porosity of the coating is obviously the preferential place for the penetration of electrolytes. Similar observations are found for P in PEO-P coating although the overall signal is quite low compared to Nb and O (Fig. 6(b)).

3.5. Phase composition

The XRD patterns in Fig. 7 show a large, broad bump at the two theta range between 15° - 35° for all the coatings, suggesting the presence of amorphous phases. The crystalline Nb_2O_5 phase is visible in all the coatings, especially for the PEO-Si coating it looks like the main phase. It can be inferred that the large amount of Si in the PEO-Si coating is responsible for the large halo since Si can form a glassy phase [51]. Additionally, Nb peaks are shown in all the coatings due to the X-rays penetrating the coating and reaching the Nb substrate. The PEO-Al coating contains additional crystalline phases of Al_2O_3, and a mixed oxide $AlNbO_4$ formed between Nb_2O_5 and Al_2O_3. Thus, the formation of $Al_2O_3/AlNbO_4$ can also explain the high Al concentration in the coating. It has been previously reported that Al_2O_3 can be produced in PEO coatings in aluminate-containing electrolytes [52]. Besides amorphous phosphate and Nb_2O_5, additional crystalline $Nb_2(PO_4)_3$ is also observed in PEO-P coating, however, at a lower intensity with respect to Nb_2O_5, in accordance with the much lower P concentration in the coating.

High-resolved localized XRD measurement was conducted in order to unveil the spatial phase distribution in the PEO coatings. Fig. 8 and Fig. 10 display the XRD patterns across the coating moving from the air above the surface via the coating towards the substrate for the PEO-P and PEO-Al specimens, respectively. It shows the identical phase composition of the coatings as depicted in Fig. 7. It is evident that Nb_2O_5 is dominant in the PEO-P coating (Fig. 8). The spatial Nb_2O_5 distribution (Fig. 9(a)) separated from the high contrast of Nb substrate (Fig. 9(b)) can be easily distinguished, crossing the entire coating thickness. The well-defined region of Nb_2O_5 appears to be thicker in comparison to the thickness measurements and cross-sectional observation. This could have resulted from the rough coating surface and interface of coating/substrate. Additionally, the spatial distribution of $Nb_2(PO_4)_3$ phase in Fig. 9(c)) suggests a thickness of ca. 15 μm near the coating/air

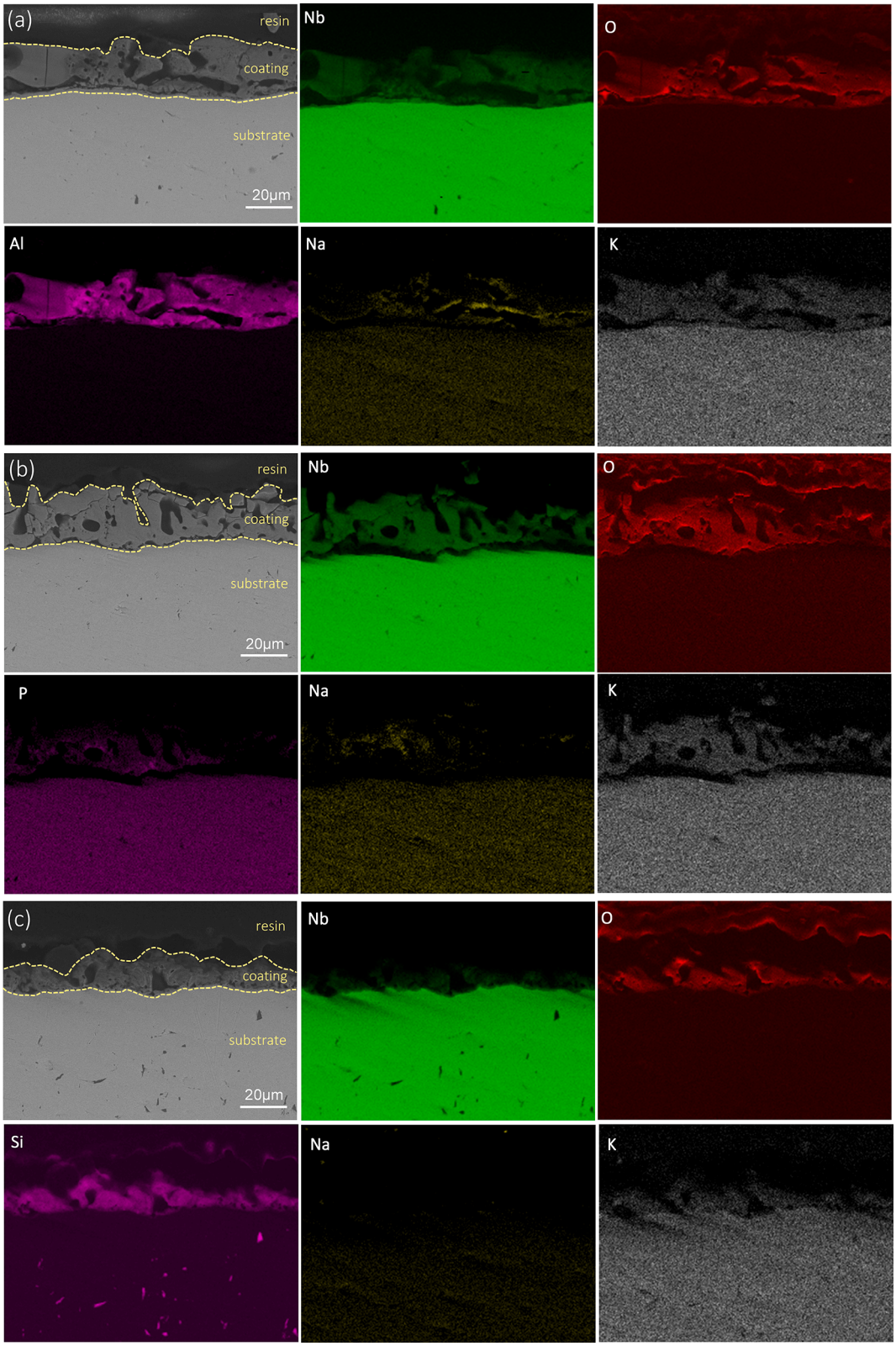

Fig. 6. Cross-sectional morphologies and elemental distributions of (a) PEO-Al, (b) PEO-P and (c) PEO-Si coatings.

interface.

A well-defined interface of coating/substrate for PEO-Al specimen is visible in Fig. 11. At the substrate side (Fig. 11(b)), the intensity of Nb shows an intensity reduction towards the inner substrate. The limited transmission of the synchrotron X-ray beam due to the strong absorption of photons through the Nb substrate [53] is responsible for this absence. The coating thickness is estimated to be at 30 μm, also slightly higher than the observation from the cross-section. The spatial intensity shows the highest concentration of $AlNbO_4$ in the center of the coating, perpendicular to the coating/substrate interface. Compared with the

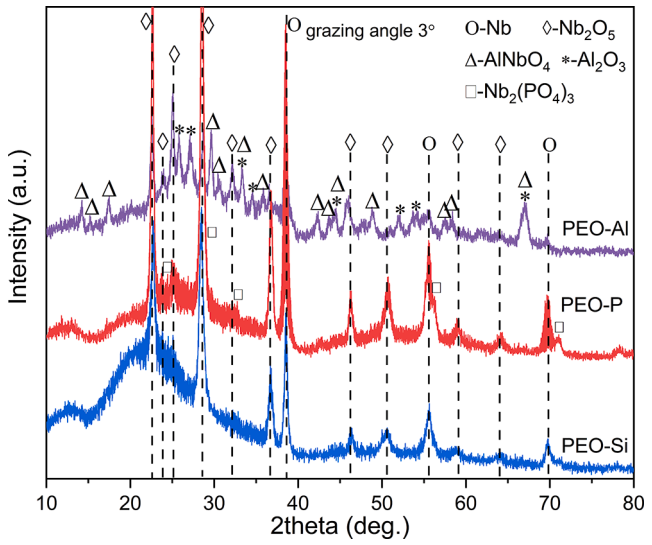

Fig. 7. XRD patterns of PEO-Al, PEO-P and PEO-Si coatings at grazing angle of 3°.

distribution of $AlNbO_4$, the spatial distribution of the Al_2O_3 and Nb_2O_5 across the coating thickness is less uniform. It could be assigned to the inhomogeneous accumulation of Al near the micro-pores/pore bands similar to the elemental mapping in Fig. 6(a). The large amount of Al at these regions may promote the deposition of Al_2O_3.

3.6. Photocatalytic activity

Fig. 12 shows the efficiency of MO photodegradation for the different coatings in a photocatalytic activity tests a function of time. While the bare substrate does not show photocatalytic activity, thus there are only comparisons between different coatings. All coatings have shown considerable photocatalytic activity, with MO degradation increasing gradually with time. The best photocatalytic activity has demonstrated for the PEO-Si specimens showing a MO degradation of ca. 39.3 % within 6 h. The MO degradation of the PEO-P specimens is ca. 35.7 % and the lowest MO degradation rate of ca. 32.9 % is revealed for the PEO-Al specimens. Additionally, all coatings also show obvious MO adsorption in the dark. This could be related to the surface morphology of the coatings, where the excess of micro-pores increases the surface area for the adsorption of MO to the internal surface area.

3.7. Corrosion performance

3.7.1. Potentiodynamic polarization

Fig. 13 (a) reveals an obvious increase of open circuit potential of specimens after PEO processing and the most significant enhancement is found for PEO-Al coating, stabilizing at a value of 0.015 V. The potentiodynamic polarization profiles of PEO coatings and bare Nb are presented in Fig. 13(b). It can be seen that the corrosion potentials for PEO coated specimens are similar and show negative shift, which could be attributed to the decreased cathodic current [54]. While no visible change for that of bare Nb is found, which is slightly nobler than the cases after PEO processing. During anodic polarization, bare Nb shows a stable corrosion current density about 2.62×10^{-6} A/cm^2, indicating the passive behavior. Nevertheless, the corrosion current densities for all PEO coated specimens are lower compared to bare Nb, especially for PEO-Si coating having the lowest corrosion current density of 5.695×10^{-8} A/cm^2 , while for PEO-Al coating showing a higher current density of 8.578×10^{-7} A/cm^2. For PEO-P coated specimen, the corrosion current density experiences a remarkable scattering at the potential range of 2-5 V and then remains at 1.876×10^{-7} A/cm^2 before an obvious breakdown of the passive film. It can be expected that PEO-P coating is less stable than the other two coatings during the polarization.

3.7.2. EIS measurement

The long-term degradation of PEO coated specimens and bare Nb in Ringer's solution after different immersion duration up to 72 h is evaluated by EIS technique and the results are presented in Fig. 14. It can be seen that one well-defined time constant is detected on the Bode plots of bare Nb for all measurements (Fig. 14(a)). This time constant is the electrochemical response of the native oxide layer, indicating the capacitance of the barrier passive film. With immersion time, the resistive response at the low frequency (0.01 Hz) is disappearing and a near pure capacitive response is illustrated by the phase angle close to -90°. Meanwhile, the impedance loop expands, indicating that the native oxide layer is becoming more protective.

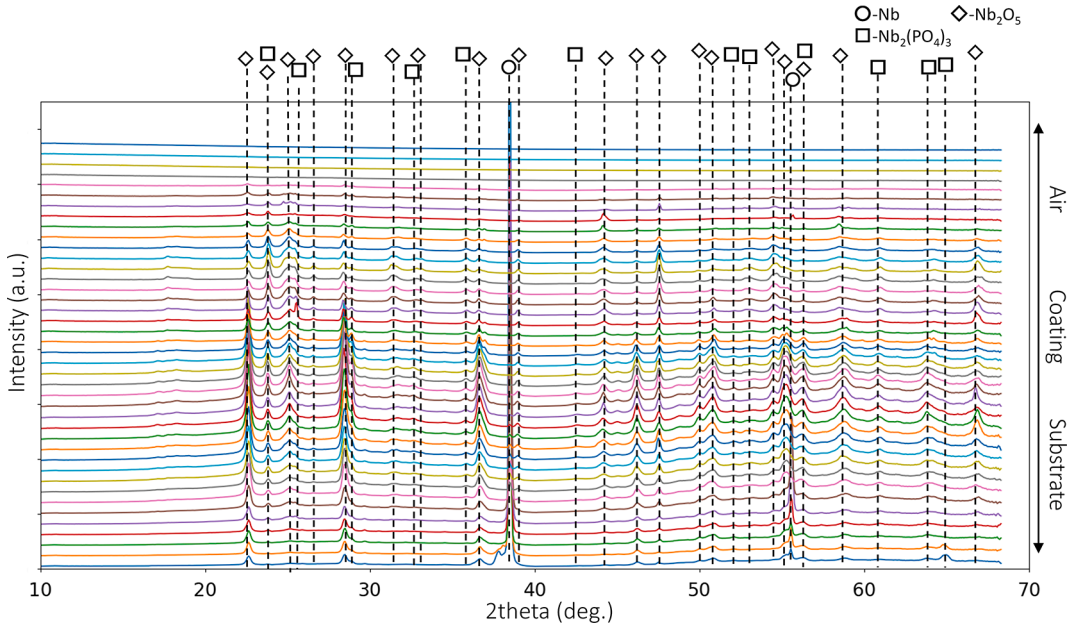

Fig. 8. XRD patterns crossing the thickness of PEO-P coating on Ti6Al4V.

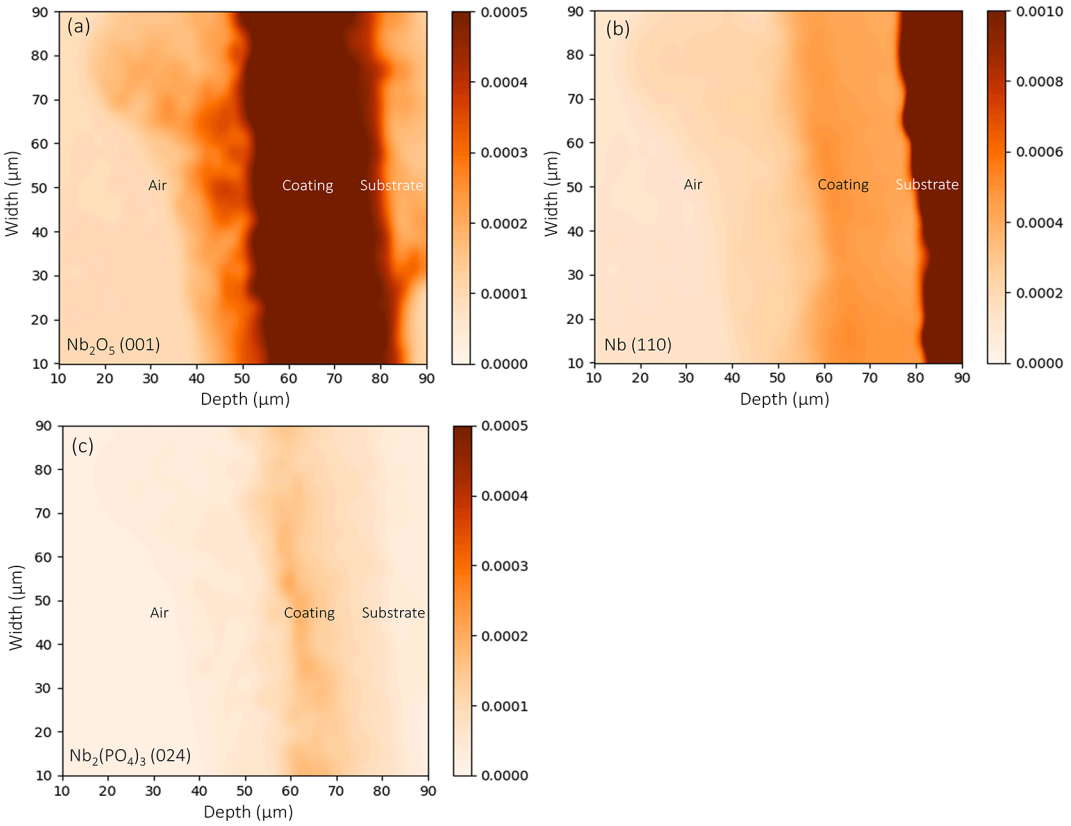

Fig. 9. Two-dimensional distribution of (a) Nb_2O_5, (b) Nb and (c) $Nb_2(PO_4)_3$ crossing the thickness of PEO-P coating on Ti6Al4V.

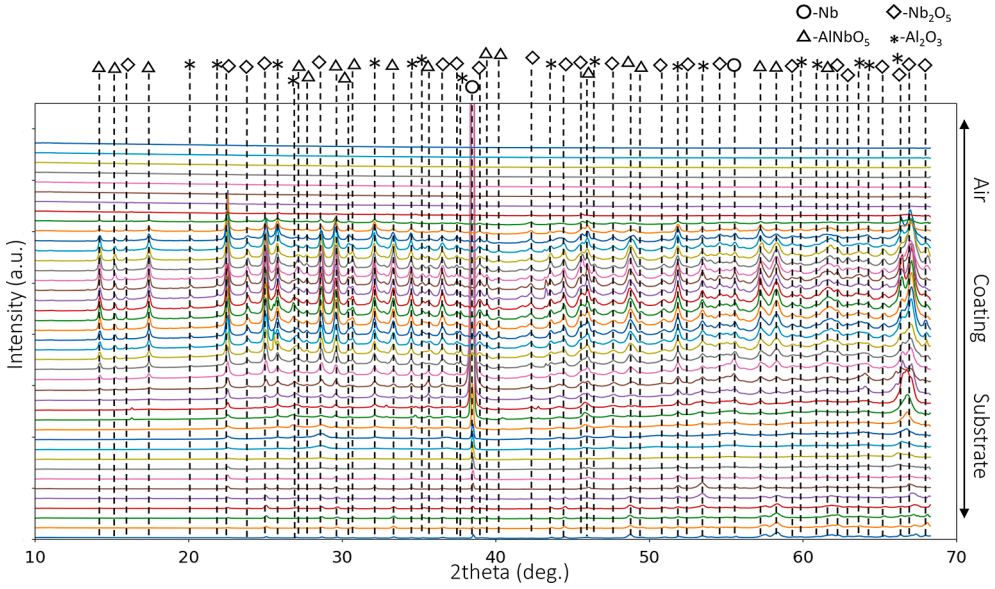

Fig. 10. XRD patterns crossing the thickness of PEO-Al coating on Ti6Al4V.

It has been know that anodic niobium oxide is a *n*-type semiconductor [55], therefore, the influence of the space charge layer due to the well defined semiconductive behavior could be noticed on the electrochemical impedance spectra [54,56]. Fig. 14(b)-(d) shows the respective impedance spectra of the three PEO coated specimens. For the measurement of PEO-Al specimen (Fig. 14(b)), two time constants can be recognized. Although the porous outer layer is observed from cross-section, however, the fast infiltration of corrosive solution makes it not possible to show any clear electrochemical response from it. As a result, the first time constant at the high frequency (10^3 –10^4 Hz) is assigned to the capacitance of inner barrier layer, combined with the subtle influence of the outer layer that is disappearing with immersion time. At the low frequency around 0.1 Hz, a second time constant appears, related to the space charge region formed at the layer-electrolyte interface. Similar for PEO-P specimen (Fig. 14(c)), two time constants can be also observed at high and medium frequencies of 10^4 Hz and 10^2 Hz, attributed to the capacitance of the inner layer and the space charge region respectively. As for the PEO-Si coating (Fig. 14(d)), the first time

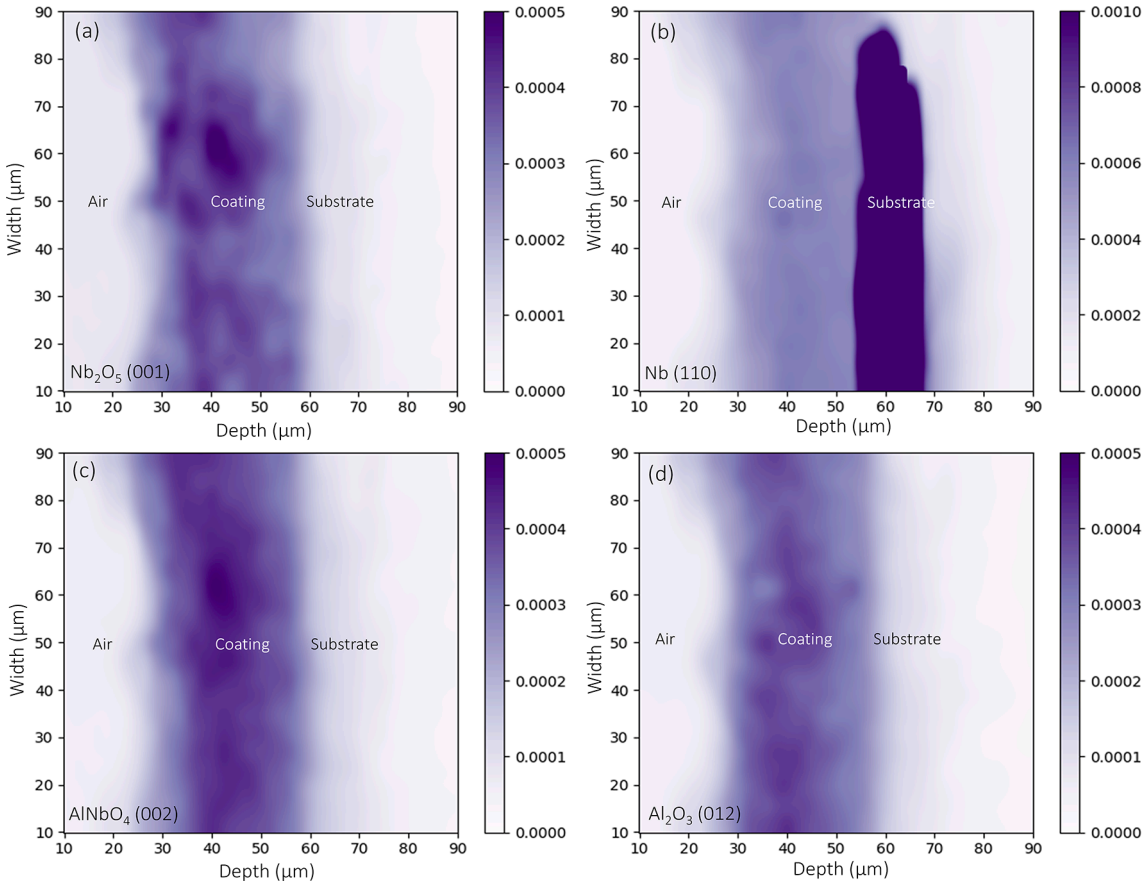

Fig. 11. Two-dimensional distribution of (a) Nb_2O_5, (b) Nb, (c) $AlNbO_4$ and (d) Al_2O_3 crossing the thickness of PEO-Al coating on Ti6Al4V.

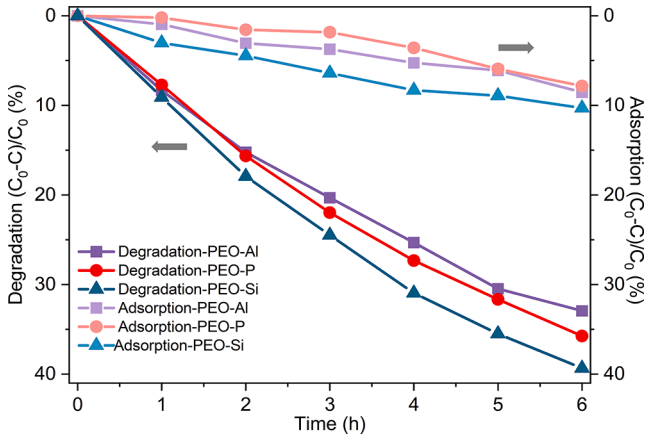

Fig. 12. MO degradation and adsorption as a function of time.

constant related to inner layer at 10^4 Hz is well-defined and always present for all measurements during the immersion. Nevertheless, it can be seen that the second time constant at low frequencies is shifting to lower frequencies with immersion time, indicating the relaxation process regulated by the space charge layer response. The impedance value at the lowest frequency of 0.01 Hz is shown in Fig. 15 used to evaluate the total impedance of the pure Nb and PEO coatings. All cases show a slight fluctuation for the first 24 h immersion and then reaches a stable value for the remaining immersion time. It is obvious that the total impedance for PEO coated specimens is better than bare Nb and especially the PEO-Si coating shows the highest total impedance value.

4. Discussion

It is obvious that the different electrolyte composition influences the PEO processing, the coating formation, chemical and phase composition and morphology, as well as the coating performance. In previous studies, the PEO coatings on pure Nb were composed of Nb_2O_5 oxide phase [30,31,57], which we also find in the present work. It is known that the coating phase composition during PEO process is greatly connected to the change of discharges [26,58]. According to the OES results, the coating forming element Nb is absent in the discharging emission, which indicates that the formation of Nb_2O_5 is not produced directly from the plasma interactions. This is easy to understand in terms of the high melting temperature (2477 °C) and chemical stability. In the aluminate-based electrolyte, the coating forming element Al is found to be involved in the discharging emission. However, it does not mean that the formation of crystalline Al_2O_3 and mixed oxide $AlNbO_4$ in the coating happens directly in the plasma of the discharges. One can expect that the coating formation and deposition are not favored in the plasmas, estimated of an electron temperature up to 10^4 K [59]. The possibilities are the interactions of plasma and liquid/solid states [47] and the thermally assisted combination of the species at the end of discharges and the cooling of plasmas [26]. For PEO-Si coating, neither the production of a solid solution or the presence of silica phases is found. Only a wide halo associated with an amorphous phase could be attributed to a large amount of Si. It can be expected that the energy released from discharges enables to sinter an amorphous silica phase. For the coating of Nb, one could notice that this sintering process is similar to the calcination of the SiO_2/Nb_2O_5 binary oxides, which were used to modify the catalytic activity for environment protection [60,61]. There is only 5-7 at.% of P in PEO-P coating, some is incorporated in $Nb_2(PO_4)_3$ and the rest is assigned to the amorphous phosphate. It is

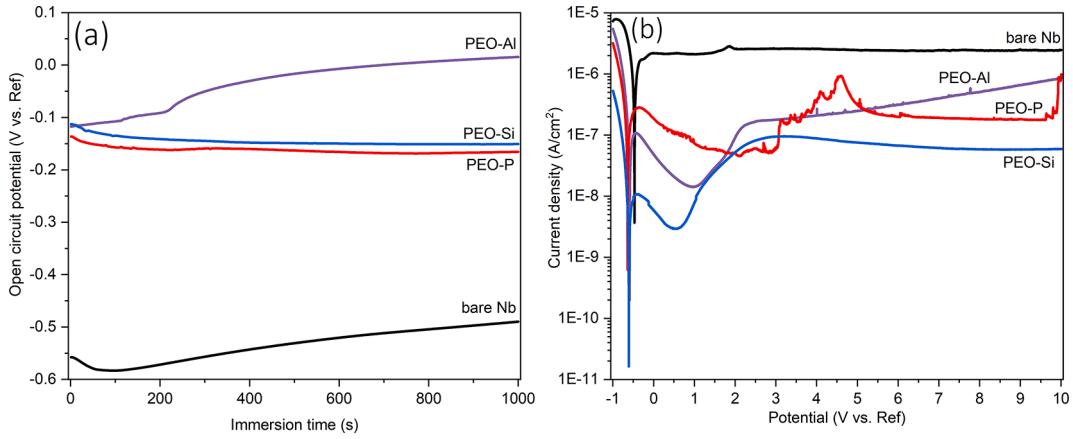

Fig. 13. Open circuit potential (a) and potentiodynamic polarization behavior (b) of PEO-Al, PEO-P and PEO-Si specimens and Nb substrate.

known that P also has the ability to form the amorphous phase during PEO processing [33,62]. However, the lowest emission intensity of the discharges and the more porous coating morphology are responsible for the low P content in the PEO-P coating [59]. The continuous emission is present in the entire processing duration in the phosphate-based electrolyte. Only moderate Na I and H I emission lines derived from the species of the electrolyte are visible. Since the emission intensity shows a dependence on the voltage, it can be speculated that the efficient temperature of discharges could not stimulate the formation of more $Nb_2(PO_4)_3$ or amorphous phosphate under such a low voltage. Additionally, widespread open micro-pores on the coating surface, in favor to fast electrolyte penetration, may cause strong quenching effect to prevent the thermal-stimulated formation of crystalline or amorphous phosphates.

Under a constant current density mode, the high electric field is maintained at the interface of specimen/electrolyte, which provides the energy for the discharges and further initiates thermal and chemical reactions, in combination with the electrochemical processes at the interface. The formation of Nb_2O_5 is suggested as following steps:

$$Nb \rightarrow Nb^{5+} + 5e^- \quad (1)$$

$$2Nb^{5+} + 10OH^- \rightarrow Nb_2O_5 + 5H_2O \quad (2)$$

Nb is firstly dissolving (Eq. (1)) under the high anodic voltage. Closely, the dissolved Nb reacts with OH^- under the effect of high voltage and the thermodynamic stimulation, resulting in the formation of Nb_2O_5 on the substrate (Eq. (2)).

In regard to the coating formed in aluminate-based electrolyte, the formation of Al_2O_3 is relying on electrochemical and plasma assisted thermal decomposition interactions [63]. The steps of the Al_2O_3 formation processes are simplified as follows:

$$AlO_2^- + 2H_2O \rightarrow Al(OH)_3 + OH^- \quad (3)$$

$$2Al(OH)_3 \rightarrow Al_2O_3 + 3H_2O \quad (4)$$

Further, due to the presence of Al_2O_3 in the coating, it is easy to deduce that the mixing oxide $AlNbO_4$ can form between the oxides Nb_2O_5 and Al_2O_3 through thermodynamic reactive sintering process:

$$Nb_2O_5 + Al_2O_3 \rightarrow 2AlNbO_4 \quad (5)$$

In fact, it was reported that at the Nb_2O_5 rich zone, the sintering process could happen around 1390 °C [64]. The melting point of the mixing oxide $AlNbO_4$ (Tm = 1530 °C [65]) is in the between of melting temperature of the single oxides Nb_2O_5 (Tm = 1512 °C) and Al_2O_3 (Tm = 2072 °C), possibly eases the formation process.

It is interesting to note that PEO-P coating, containing the highest amount of active Nb_2O_5 phase (the highest Nb concentration) and the largest surface area estimated, does not show the most efficient MO degradation. However, PEO-Si coating, revealing the lowest Nb content, represents the best photocatalytic activity. The photocatalytic activity of the coating is greatly dependent on the photogenerated hole/electron pairs and the recombination rate of photo-excited electrons and holes [30]. It was reported that higher catalytic activity of silica-supported/Nb_2O_5-supported catalysts was demonstrated by the addition of Nb_2O_5/silica [61]. The PEO-Si coating with the combined composition of Nb_2O_5 and silica could be the case containing higher concentration of charge carriers. Furthermore, the significantly distinct coating surface morphology, resulting from the different discharge behavior appears to influence the photocatalytic activity. The distribution of tiny sintered particles on the entire PEO-Si coating surface may effectively increase the active surface area for MO degradation. The open micro-pores extending into the inner layer on the PEO-P coating can additionally expand the surface area, however, does not make visible contribution to the active surface area for the degradation process.

All of the PEO coatings present a significant improvement of corrosion resistance, around one or two magnitudes of total impedance value higher than that of the bare substrate. PEO-Si coating shows the best corrosion performance compared to the other two coatings due to the most uniform and compact morphology. The space charge layer originated from the semi-conductive property of Nb_2O_5 is disclosed, which is similar to the anodic TiO_2 film [66]. The lowest corrosion resistance of PEO-P coatings is attributed to the large amount of open micro-pores on the coating surface and their connection to the inner layer. Nevertheless, even after 72 h immersion duration, the stable total impedance values can be seen for all coatings, indicating the slow degradation of the coatings. Therefore, the PEO coatings provide evidently additional protective properties and functionality to pure Nb.

5. Conclusions

Different PEO coatings were produced on pure Nb successfully. The coating formation process on Nb involves a combination of various interactions, including electrochemical/chemical conversions, and the thermal assisted sintering process. The Nb substrate and the electrolyte composition are highly effective in controlling the morphology and composition (elements and phases) of the coatings, by influencing the characteristics of the discharges during PEO processing. Nb_2O_5 and $Nb_2(PO_4)_3$ are formed in the phosphate-based electrolyte with additional amorphous phosphate. Amorphous silicon phase can be produced in the coating in the silicate-based electrolyte. Furthermore, the electrolyte containing aluminate tends to form a composite coating with a mixture of oxides (Nb_2O_5, Al_2O_3 and $AlNbO_4$).

The photocatalytic activity is determined by the coating composition and active surface area of the coatings. The large active surface area of

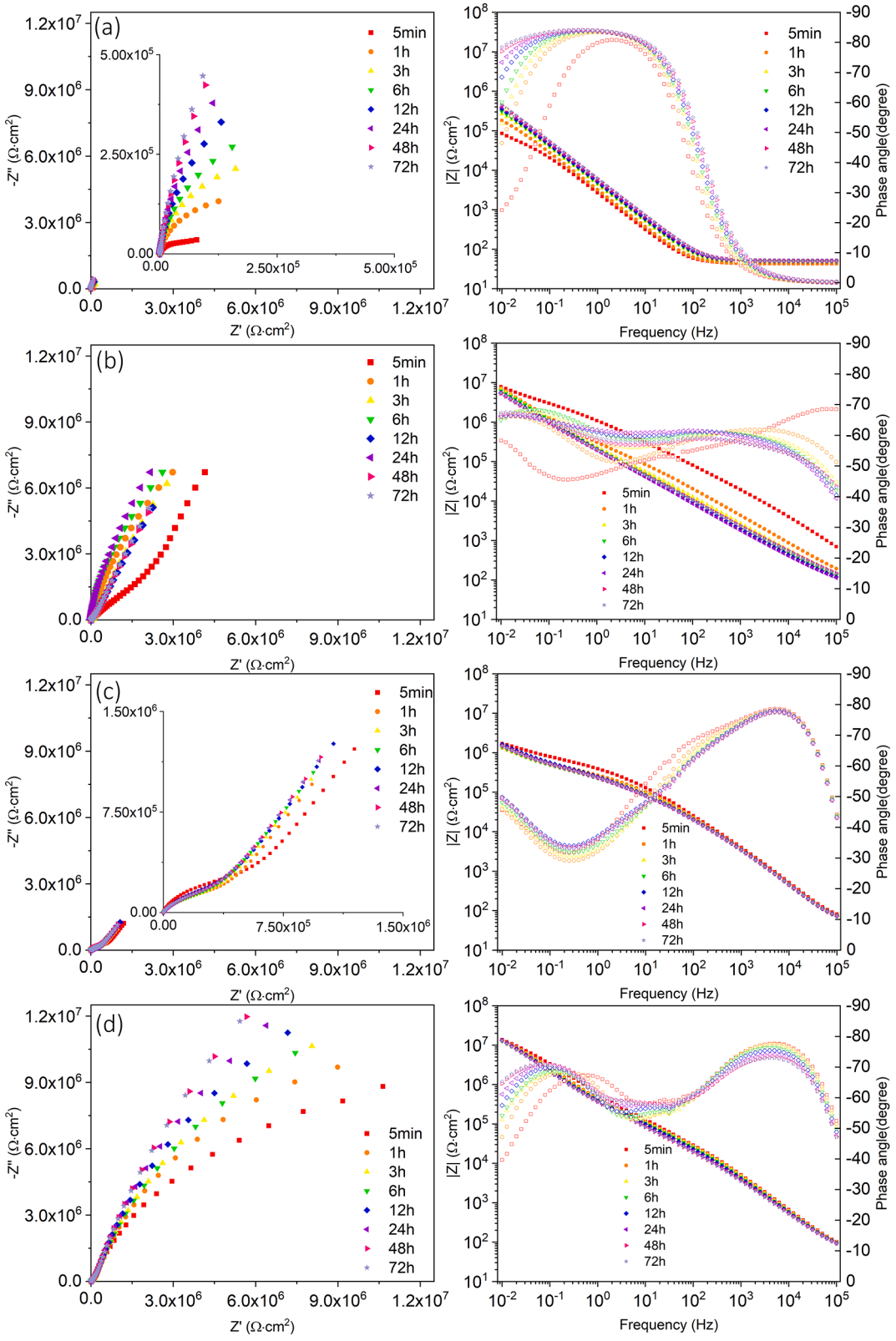

Fig. 14. EIS spectra of pure Nb (a), PEO-Al specimen (b), PEO-P specimen (c) and PEO-Si specimen (d) in Ringer's solution.

the coating can obviously increases the degradation rate of methyl orange. PEO-Si coating, containing an amorphous silica phase that also improves the photocatalytic activity. The order of the photocatalytic activity of the three coatings is PEO-Al < PEO-P < PEO-Si.

The coating morphology also has an evident influence on the degradation of the coating in Ringer's solution, by influencing the paths of infiltration of the corrosive solution. The corrosion resistance of the coatings and bare substrate follows the order Nb < PEO-P < PEO-Al < PEO-Si.

Due to the respectable photocatalytic activity and the high corrosion

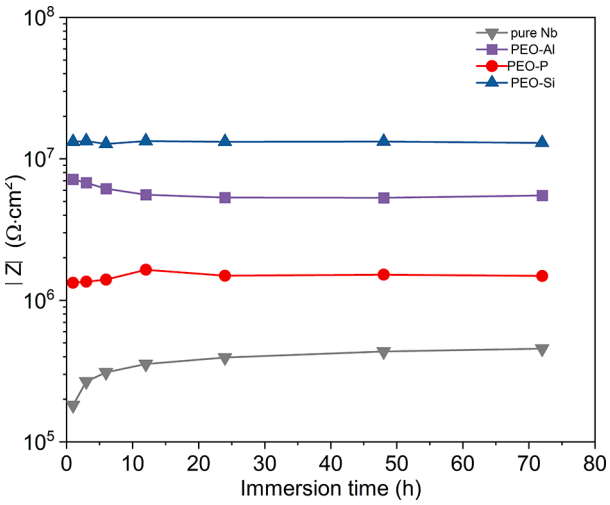

Fig. 15. Total impedance values of three different coatings after different immersion time.

resistance, the environmentally friendly PEO coatings on Nb, could potentially attract great interests for the environmental protection of photocatalysis and biomedical degradation of implants.

CRediT authorship contribution statement

Ting Wu: Visualization, Formal analysis, Investigation, Writing – original draft, Writing – review & editing. **Carsten Blawert:** Conceptualization, Supervision, Writing – review & editing. **Maria Serdechnova:** Formal analysis, Visualization, Writing – review & editing. **Polina Karlova:** Investigation, Visualization, Writing – review & editing. **Gleb Dovzhenko:** Investigation, Visualization, Writing – review & editing. **D. C. Florian Wieland:** Investigation, Writing – review & editing. **Stevan Stojadinovic:** Investigation, Writing – review & editing. **Rastko Vasilic:** Investigation, Writing – review & editing. **Kristina Mojsilovic:** Investigation, Writing – review & editing. **Mikhail L. Zheludkevich:** Supervision, Writing – review & editing.

Declaration of Competing Interest

The authors declare that they have no known competing financial interests or personal relationships that could have appeared to influence the work reported in this paper.

Acknowledgement

Ting Wu thanks China Scholarship Council for the award of fellowship and funding (NO.201708510113). The technical support of Mr. Volker Heitmann, Mr. Ulrich Burmester during this work is gratefully acknowledged. We also thank PETRA III (Hamburg, Germany) for accepting and granting the proposal I-20191340 (P.03 end-station) and Dr. Anton Davydok for technical support at the beamline for localized phase composition analysis of PEO layers.

References

[1] P. Carniti, A. Gervasini, S. Biella, A. Auroux, Niobic acid and niobium phosphate as highly acidic viable catalysts in aqueous medium: Fructose dehydration reaction, Catal. Today 118 (3-4) (2006) 373–378.
[2] M. Ziolek, Niobium-containing catalysts—the state of the art, Catal. Today 78 (1-4) (2003) 47–64.
[3] A. Monassier, V. D'Elia, M. Cokoja, H. Dong, J.D.A. Pelletier, J.-M. Basset, F. E. Kühn, Synthesis of cyclic carbonates from epoxides and CO_2 under mild conditions using a simple, highly efficient niobium-based catalyst, ChemCatChem 5 (6) (2013) 1321–1324.
[4] C. Nico, T. Monteiro, M.P.F. Graça, Niobium oxides and niobates physical properties: Review and prospects, Prog. Mater Sci. 80 (2016) 1–37.
[5] M. Niinomi, M. Nakai, J. Hieda, Development of new metallic alloys for biomedical applications, Acta Biomater 8 (11) (2012) 3888–3903.
[6] H.Y. Kim, Y. Ikehara, J.I. Kim, H. Hosoda, S. Miyazaki, Martensitic transformation, shape memory effect and superelasticity of Ti–Nb binary alloys, Acta Mater. 54 (9) (2006) 2419–2429.
[7] R. Olivares-Navarrete, J.J. Olaya, C. Ramírez, S.E. Rodil, Biocompatibility of Niobium Coatings, Coatings 1 (1) (2011) 72–87.
[8] F. Rubitschek, T. Niendorf, I. Karaman, H.J. Maier, Corrosion fatigue behavior of a biocompatible ultrafine-grained niobium alloy in simulated body fluid, J Mech Behav Biomed Mater 5 (1) (2012) 181–192.
[9] P. Amaravathy, S. Sowndarya, S. Sathyanarayanan, N. Rajendran, Novel sol gel coating of Nb_2O_5 on magnesium alloy for biomedical applications, Surf. Coat. Technol. 244 (2014) 131–141.
[10] T. Murayama, J. Chen, J. Hirata, K. Matsumoto, W. Ueda, Hydrothermal synthesis of octahedra-based layered niobium oxide and its catalytic activity as a solid acid, Catal, Sci. Technol. 4 (12) (2014) 4250–4257.
[11] C. García-Sancho, I. Sádaba, R. Moreno-Tost, J. Mérida-Robles, J. Santamaría-González, M. López-Granados, P. Maireles-Torres, Dehydration of xylose to furfural over MCM-41-supported niobium-oxide catalysts, ChemSusChem 6 (4) (2013) 635–642.
[12] B. Li, M. Gu, Z. Nie, X. Wei, C. Wang, V. Sprenkle, W. Wang, Nanorod niobium oxide as powerful catalysts for an all vanadium redox flow battery, Nano Lett 14 (1) (2014) 158–165.
[13] S.A. Pauline, N. Rajendran, Biomimetic novel nanoporous niobium oxide coating for orthopaedic applications, Appl. Surf. Sci. 290 (2014) 448–457.
[14] G. Ramírez, S.E. Rodil, H. Arzate, S. Muhl, J.J. Olaya, Niobium based coatings for dental implants, Appl. Surf. Sci. 257 (7) (2011) 2555–2559.
[15] E. Eisenbarth, D. Velten, M. Müller, R. Thull, J. Breme, Nanostructured niobium oxide coatings influence osteoblast adhesion, J Biomed Mater Res A 79A (1) (2006) 166–175.
[16] D. Pradhan, A.W. Wren, S.T. Misture, N.P. Mellott, Investigating the structure and biocompatibility of niobium and titanium oxides as coatings for orthopedic metallic implants, Mater Sci Eng C Mater Biol Appl 58 (2016) 918–926.
[17] L. Zhu, Z. Guo, Y. Zhang, Z. Li, M. Sui, A mechanism for the growth of a plasma electrolytic oxide coating on Al, Electrochim. Acta 208 (2016) 296–303.
[18] E. Matykina, R. Arrabal, D.J. Scurr, A. Baron, P. Skeldon, G.E. Thompson, Investigation of the mechanism of plasma electrolytic oxidation of aluminium using ^{18}O tracer, Corros. Sci. 52 (2010) 1070–1076.
[19] D. Veys-Renaux, E. Rocca, J. Martin, G. Henrion, Initial stages of AZ91 Mg alloy micro-arc anodizing: Growth mechanisms and effect on the corrosion resistance, Electrochim. Acta 124 (2014) 36–45.
[20] S. Stojadinović, R. Vasilić, M. Petković, I. Belča, B. Kasalica, M. Perić, L. Zeković, Luminescence during anodization of magnesium alloy AZ31, Electrochim. Acta 59 (2012) 354–359.
[21] W. Simka, A. Krząkała, D.M. Korotin, I.S. Zhidkov, E.Z. Kurmaev, S.O. Cholakh, K. Kuna, G. Dercz, J. Michalska, K. Suchanek, T. Gorewoda, Modification of a Ti–Mo alloy surface via plasma electrolytic oxidation in a solution containing calcium and phosphorus, Electrochim. Acta 96 (2013) 180–190.
[22] H. Zhang, J. Geng, X. Li, Z. Chen, M. Wang, N. Ma, H. Wang, The micro-arc oxidation (MAO) behaviors of in-situ TiB_2/A201 composite, Appl. Surf. Sci. 422 (2017) 359–371.
[23] P. Wang, T. Wu, Y.T. Xiao, J. Pu, X.Y. Guo, Effects of $Ce(SO_4)_2$ concentration on the properties of micro-arc oxidation coatings on ZL108 aluminum alloys, Mater. Lett. 182 (2016) 27–31.
[24] B. Mingo, Y. Guo, R. Leiva-Garcia, B.J. Connolly, A. Matthews, A. Yerokhin, Smart functionalization of ceramic-coated AZ31 magnesium alloy, ACS Appl Mater Interfaces 12 (2020) 30833–30846.
[25] R. Arrabal, M. Mohedano, E. Matykina, A. Pardo, B. Mingo, M.C. Merino, Characterization and wear behaviour of PEO coatings on 6082–T6 aluminium alloy with incorporated α-Al_2O_3 particles, Surf. Coat. Technol. 269 (2015) 64–73.
[26] T.W. Clyne, S.C. Troughton, A review of recent work on discharge characteristics during plasma electrolytic oxidation of various metals, Int. Mater. Rev. 64 (2018) 127–162.
[27] M. Sowa, M. Piotrowska, M. Widziolek, G. Dercz, G. Tylko, T. Gorewoda, A. M. Osyczka, W. Simka, Bioactivity of coatings formed on Ti-13Nb-13Zr alloy using plasma electrolytic oxidation, Mater Sci Eng C Mater Biol Appl 49 (2015) 159–173.
[28] O. Oleshko, V. Deineka V, Y. Husak, V. Korniienko, O. Mishchenko, V. Holubnycha, M. Pisarek, J. Michalska, A. Kazek-Kęsik, A. Jakóbik-Kolon, W. Simka, M. Pogorielov, Ag nanoparticle-decorated oxide coatings formed via plasma electrolytic oxidation on ZrNb alloy, Materials (Basel) 12 (22) (2019) 3742.
[29] M. Kaseem, H.-C. Choe, Electrochemical and bioactive characteristics of the porous surface formed on Ti-xNb alloys via plasma electrolytic oxidation, Surf. Coat. Technol. 378 (2019) 125027.
[30] S. Stojadinović, N. Tadić, N. Radić, P. Stefanov, B. Grbić, R. Vasilić, Anodic luminescence, structural, photoluminescent, and photocatalytic properties of anodic oxide films grown on niobium in phosphoric acid, Appl. Surf. Sci. 355 (2015) 912–920.
[31] M. Sowa, J. Worek, G. Dercz, D.M. Korotin, A.I. Kukharenko, E.Z. Kurmaev, S. O. Cholakh, M. Basiaga, W. Simka, Surface characterisation and corrosion behaviour of niobium treated in a Ca- and P-containing solution under sparking conditions, Electrochim. Acta 198 (2016) 91–103.
[32] S. Stojadinović, R. Vasilić, Orange–red photoluminescence of Nb_2O_5: Eu^{3+}, Sm^{3+} coatings formed by plasma electrolytic oxidation of niobium, J. Alloy. Compd. 685 (2016) 881–889.

[33] M. Sowa, A. Kazek-Kęsik, A. Krząkała, R.P. Socha, G. Dercz, J. Michalska, W. Simka, Modification of niobium surfaces using plasma electrolytic oxidation in silicate solutions, J. Solid State Electrochem. 18 (2013) 3129–3142.
[34] B.L. Pereira, C.M. Lepienski, I. Mazzaro, N.K. Kuromoto, Apatite grown in niobium by two-step plasma electrolytic oxidation, Mater Sci Eng C Mater Biol Appl 77 (2017) 1235–1241.
[35] M. Sowa, K. Gren, A.I. Kukharenko, D.M. Korotin, J. Michalska, L. Szyk-Warszynska, M. Mosialek, J. Zak, E. Pamula, E.Z. Kurmaev, S.O. Cholakh, W. Simka, Influence of electropolishing and anodic oxidation on morphology, chemical composition and corrosion resistance of niobium, Mater Sci Eng C Mater Biol Appl 42 (2014) 529–537.
[36] Y.L. Ge, Y.M. Wang, Y.F. Zhang, L.X. Guo, D.C. Jia, J.H. Ouyang, Y. Zhou, The improved thermal radiation property of SiC doped microarc oxidation ceramic coating formed on niobium metal for metal thermal protective system, Surf. Coat. Technol. 309 (2017) 880–886.
[37] D. Quintero, M.A. Gómez, W.S. Araujo, F. Echeverría, J.A. Calderón, Influence of the electrical parameters of the anodizing PEO process on wear and corrosion resistance of niobium, Surf. Coat. Technol. 380 (2019), 125067.
[38] M. Sowa, W. Simka, Electrochemical behavior of plasma electrolytically oxidized niobium in simulated physiological environment, Surf. Coat. Technol. 344 (2018) 121–131.
[39] X. Lu, M. Mohedano, C. Blawert, E. Matykina, R. Arrabal, K.U. Kainer, M. L. Zheludkevich, Plasma electrolytic oxidation coatings with particle additions - A review, Surf. Coat. Technol. 307 (2016) 1165–1182.
[40] Y. Wang, H. Yu, C. Chen, Z. Zhao, Review of the biocompatibility of micro-arc oxidation coated titanium alloys, Mater. Des. 85 (2015) 640–652.
[41] A.L. Yerokhin, X. Nie, A. Leyland, A. Matthews, S.J. Dowey, Plasma electrolysis for surface engineering, Surf. Coat. Technol. 122 (1999) 73–93.
[42] C. Krywka, H. Neubauer, M. Priebe, T. Salditt, J. Keckes, A. Buffet, S.V. Roth, R. Doehrmann, M. Mueller, A two-dimensional waveguide beam for X-ray nanodiffraction, J. Appl. Crystallogr. 45 (2011) 85–92.
[43] J. Kieffer, D. Karkoulis, PyFAI, a versatile library for azimuthal regrouping, J. Phys. Conf. Ser. 425 (20) (2013) 202012.
[44] T. Wu, C. Blawert, M.L. Zheludkevich, Influence of secondary phases of AlSi9Cu3 alloy on the plasma electrolytic oxidation coating formation process, J. Mater. Sci. Technol. 50 (2020) 75–85.
[45] X. Lu, C. Blawert, K.U. Kainer, M.L. Zheludkevich, Investigation of the formation mechanisms of plasma electrolytic oxidation coatings on Mg alloy AM50 using particles, Electrochim. Acta 196 (2016) 680–691.
[46] E. Matykina, R. Arrabal, B. Mingo, M. Mohedano, A. Pardo, M.C. Merino, In vitro corrosion performance of PEO coated Ti and Ti6Al4V used for dental and orthopaedic implants, Surf. Coat. Technol. 307 (2016) 1255–1264.
[47] C. Blawert, S.A. Karpushenkov, M. Serdechnova, L.S. Karpushenkava, M. L. Zheludkevich, Plasma electrolytic oxidation of zinc alloy in a phosphate-aluminate electrolyte, Appl. Surf. Sci. 505 (2020), 144552.
[48] A. Lugovskoy, M. Zinigrad, A. Kossenko, B. Kazanski, Production of ceramic layers on aluminum alloys by plasma electrolytic oxidation in alkaline silicate electrolytes, Appl. Surf. Sci. 264 (2013) 743–747.
[49] X. Ma, C. Blawert, D. Höche, M.L. Zheludkevich, K.U. Kainer, Investigation of electrode distance impact on PEO coating formation assisted by simulation, Appl. Surf. Sci. 388 (2016) 304–312.
[50] H. Sharifi, M. Aliofkhazraei, G.B. Darband, A.S. Rouhaghdam, Characterization of PEO nanocomposite coatings on titanium formed in electrolyte containing atenolol, Surf. Coat. Technol. 304 (2016) 438–449.
[51] X. Lu, S.P. Sah, N. Scharnagl, M. Störmer, M. Starykevich, M. Mohedano, C. Blawert, M.L. Zheludkevich, K.U. Kainer, Degradation behavior of PEO coating on AM50 magnesium alloy produced from electrolytes with clay particle addition, Surf. Coat. Technol. 269 (2015) 155–169.
[52] Y. Cheng, J. Cao, Z. Peng, Q. Wang, E. Matykina, P. Skeldon, G.E. Thompson, Wear-resistant coatings formed on Zircaloy-2 by plasma electrolytic oxidation in sodium aluminate electrolytes, Electrochim. Acta 116 (2014) 453–466.
[53] H.A. Liebhafsky, E.H. Winslow, H.G. Pfeiffe, X-ray absorption and emission, Anal. Chem. 34 (1962) 13.
[54] F.D. Quarto, S. Piazza, C. Sunseri, Amorphous semiconductor-electrolyte junction. Impedance study on the a-Nb_2O_5 - electrolyte junction, Electrochim. Acta 35 (1990) 9.
[55] K.E. Heusler, M. Schulze, Electron-transfer reactions at semiconducting anodic niobium oxide films, Electrochim. Acta 20 (1975) 8.
[56] F.D. Quarto, S. Piazza, R. Agostino, C. Sunseri, Amorphous semiconductor-electrolyte junction Influence of the wavelength and oxide thickness on the photocharacteristics of a-Nb_2O_5 anodic films, J. Electroanal. Chem. Interfacial Electrochem. 228 (1987) 16.
[57] Y. Ge, Y. Wang, Y. Cui, Y. Zou, L. Guo, J. Ouyang, D. Jia, Y. Zhou, Growth of plasma electrolytic oxidation coatings on Nb and corresponding corrosion resistance, Appl. Surf. Sci. 491 (2019) 526–534.
[58] R.O. Hussein, P. Zhang, X. Nie, Y. Xia, D.O. Northwood, The effect of current mode and discharge type on the corrosion resistance of plasma electrolytic oxidation (PEO) coated magnesium alloy AJ62, Surf. Coat. Technol. 206 (2011) 1990–1997.
[59] R.O. Hussein, X. Nie, D.O. Northwood, A. Yerokhin, A. Matthews, Spectroscopic study of electrolytic plasma and discharging behaviour during the plasma electrolytic oxidation (PEO) process, J. Phys. D Appl. Phys. 43 (2010), 105203.
[60] M.S.P. Francisco, Y. Gushikem, Synthesis and characterization of SiO_2–Nb_2O_5 systems prepared by the sol–gel method: structural stability studies, J. Mater. Chem. 12 (2002) 2552–2558.
[61] S. Damyanova, L. Dimitrov, L. Petrov, P. Grange, Effect of niobium on the surface properties of Nb_2O_5-SiO_2-supported Mo catalysts, Appl. Surf. Sci. 214 (1–4) (2003) 68–74.
[62] Z. Yao, Q. Xia, L. Chang, C. Li, Z. Jiang, Structure and properties of compound coatings on Mg alloys by micro-arc oxidation/hydrothermal treatment, J. Alloy. Compd. 633 (2015) 435–442.
[63] L.S. Wang, C.X. Pan, Characterisation of microdischarge evolution and coating morphology transition in plasma electrolytic oxidation of magnesium alloy, Surf. Eng. 23 (5) (2007) 324–328.
[64] X.Z. Zhang, J.E. Zhou, Y.H. Jiang, C.R. Wu, C.Y. Lin, Preparation and Characterization of Nb_2O_5-Al_2O_3 System Ceramics with Different Al_2O_3 Additions, Key Eng. Mater. 544 (2013) 60–63.
[65] R. Serrazina, J.S. Dean, I.M. Reaney, L. Pereira, P.M. Vilarinho, A.M.O.R. Senos, Mechanism of densification in low-temperature FLASH sintered lead free potassium sodium niobate (KNN) piezoelectrics, J. Mater. Chem. C 7 (45) (2019) 14334–14341.
[66] S.K. Poznyak, A.D. Lisenkov, M.G.S. Ferreira, A.I. Kulak, M.L. Zheludkevich, Impedance behaviour of anodic TiO_2 films prepared by galvanostatic anodisation and powerful pulsed discharge in electrolyte, Electrochim. Acta 76 (2012) 453–461.

6. Discussion

6.1 Influence of base metal on PEO process

All PEO processes performed in present work were under galvanostatic control. Once switching on the pulse, the voltage ramps up promptly as a response to the current due to the presence of native oxide layer already [30, 33, 42]. Afterwards, with the continuous growing of the barrier films, the improved barrier properties of the films result in the further increase of the voltage in order to maintain the pre-selected current, similar to the conventional anodizing process [43-45]. When the voltage is adequate to stimulate the breakdown of the films, the discharges are generated. The discharges evolve and prompt the growth and re-structuring of the coating further, following which the voltage changes further. From this point, the varied ramp rate of the voltage and the transition of discharges could be good indicators for the development of the coating as a function of processing time. As a consequence, the process has been generally divided into several stages according to the voltage ramp and the appearance of discharges [31, 46-50]:

Stage I: the conventional anodizing stage at the beginning of the processing is distinguished by the most rapid increase of the voltage, manifesting the barrier property of the initial conversion layer/dielectric film. This stage could continue for few seconds to minutes depending on the specific conditions of the PEO system.

Stage II: the stage is mainly characterized by the start of sparking at the surface of specimens, with a reduced ramp rate of voltage for the first time. At this stage, it is accompanied by tiny discharges fast moving on the coating surface, with an increasing population.

Stage III: this stage is sometimes the final stage; nevertheless, it depends mainly on the operating parameters such as treatment time and current density. Further decreasing of the ramp rate of the voltage is typical for this stage. Also, the development of the discharges could be observed visually, generally, the number of discharges reduces; however, the size of the discharges increases. This stage could remain for few minutes to tens of minutes that is still determined by the operating conditions.

Stage IV: if the processing time was long enough, a fourth stage could be noticed from the voltage curve, which is almost flat with only slow changes. The number of the discharges decreases further, but the size increases, appearing as long lasting sparks on the surface of specimens.

6.1.1 Breakdown voltage

It is well known that the oxidation of the substrate is the main process for PEO coating formation. Regarding different substrates, eg,. Mg, Al, Ti and Nb included in present work, the composition and microstructure of initial barrier layers and of following PEO coatings are different due to the different nature of base metals even using the same parameters for the PEO processing. Thus, the properties and microstructure of the layer/coating, eg. the electrical resistance, the electrochemical and chemical stability, and the compactness are different from each other, as seen in Tab. 6-1. For respective base

metals, as a result, different PEO process can be distinguished due to the different oxidation behavior of substrates at the interface of coating /electrolyte.

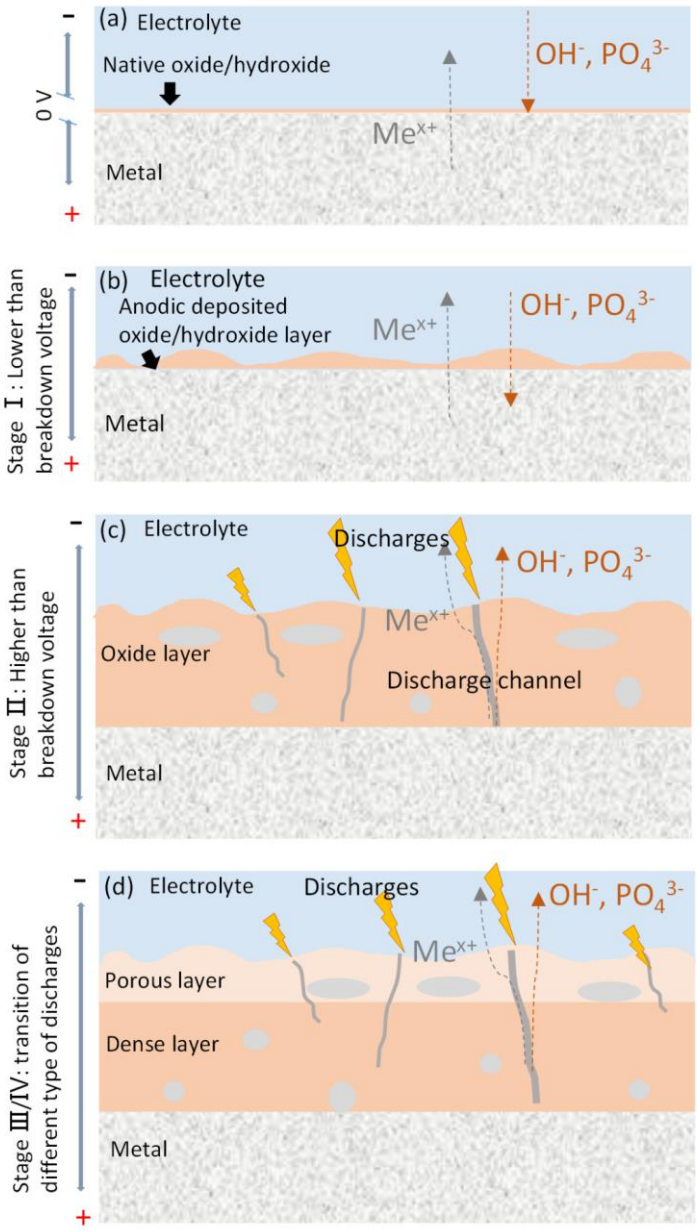

Figure 6-1 Diagram of PEO coating growth process in phosphate-based electrolyte

Table 6-1 Properties of oxides for different substrate

	PBR	Melting temperature	Gibbs free energy	Solubility
MgO	0.81	2852 ℃	-1138.6 kJ/mol	soluble in acid, ammonia
Al_2O_3	1.28	2072 ℃	-1054.8 kJ/mol	insoluble in all solvents
TiO_2	1.73	1843 ℃	-888.8 kJ/mol	soluble in concentrated sulfuric, chlorhydric and nitric acid
Nb_2O_5	2.69	1512 ℃	-706.3 kJ/mol	soluble in HF

The voltage response to constant current input is a good reflection of the process for different PEO systems [32, 50-52]. Since the identical parameters (the same phosphate-based electrolyte and electrical

parameters) were used in present study, the breakdown voltage of the barrier layers was mainly dependent on the barrier property of different oxides/phosphate from the oxidation of substrates and decomposition of electrolyte. The oxides of the four types of substrates are all quite stable, where the MgO and Al_2O_3 are both good electrical insulators [53, 54], and TiO_2 and Nb_2O_5 have high electrochemical stability [55, 56]. Nevertheless, these oxides have different structure, such as atom packing and lattice size that changes the microstructure of the oxide layer spontaneously (eg. microdefects and Pilling-Bedworth ratios 0.81 for MgO, 1.28 for Al_2O_3, 1.73 for TiO_2 and 2.69 for Nb_2O_5 respectively). It can be seen in Tab. 6-2 that the breakdown voltage changes with an increasing order from Mg to Ti and Al, and to Nb in phosphate electrolyte.

The lowest breakdown voltage for Mg substrates could be related to the PBR ratio of MgO (0.804), which is lower than 1. It can result in an incomplete coverage of the surface on Mg substrate during the oxidation. Hence, there are probably some microdefects in the initial layer, which deteriorates the barrier property of the film. As a result, the breakdown voltage required is decreased in comparison to a compact MgO layer. Moreover, for MgLi alloy in paper *1*, the active Li further reduced the dielectric property of the layer, and the discharges were initially observed even at ca. 110 V.

Table 6-2 Breakdown and final voltage for different substrates during PEO processing in phosphate-based electrolyte (20 g/L Na_3PO_4 and 1 g/L KOH) at 6 A/dm^2 for 10 min, and the thickness of resultant coating

Substrate	Breakdown voltage/V	Final voltage/V	Thickness/ μm
MgLi	110 (4 s)	372	37.7
pure Mg	150 (10 s)	486	28.3
AZ91Nd	150 (5 s)	493	62.6
AZ91Nd/Al_2O_3	150 (25 s)	447	42.1
Ti6Al4V	180 (6 s)	358	28.7
AlSi9Cu3	200 (50 s)	384	10.3
Nb	220 (11 s)	373	22.6

The breakdown voltage for Ti6Al4V is in between of Mg and Al substrates. Since TiO_2 is quite stable, it could be assigned to a different oxidation manner of Ti substrate. In paper *2*, the in-situ PEO treatment with time-resolved high energy XRD diffraction has demonstrated high solubility of oxygen in Ti lattices, so that oxygen could penetrate into the Ti substrate more rapidly. The fast up-take and diffusion of oxygen in the lattice caused the expansion of the lattice, and speeded up the oxidation process, which potentially provided more preferred locations for discharges. However, the Ti oxide layer is still denser relative to MgO regarding the PBR ratio. Compared to Al alloy, the higher breakdown voltage elucidates that the Si phases are not the defects for the dense Al_2O_3 layer. Alternatively, the presence of Si phase could be a reason for the higher breakdown voltage since Si is not ideal for current passing. As a result, the breakdown voltage for Ti6Al4V was around 180 V, higher than that of Mg-based materials but lower than Al alloy.

As a transition metal, the oxide layer/coating of Nb is quite stable. That is to say, the initial layer

possibly had a better barrier property in comparison to other base metals. As a result, the highest breakdown voltage for pure Nb was determined.

6.1.2 Coating growth

Obviously, the PEO coating commonly contains many species originating from substrate and electrolyte, as seen in Fig. 6-1. At the similar processing conditions, the coating formation is much more dominated by the oxidation of substrate in comparison to decomposition of electrolyte. The oxides of the four base metals have respective Gibbs free energy of formation, which favor the oxidation of the metals. With higher driving force, it is likely that the plasmas are created easily during PEO. In a decreasing order, that is -1138.6 kJ/mol of MgO, -1054.8 kJ/mol of Al_2O_3, -888.8 kJ/mol of TiO_2 and -706.3 kJ/mol of Nb_2O_5 for per mole of oxygen molecule, respectively. From the comparison of final voltage and coating thickness for different substrates in Tab. 6-1, the most rapid coating growth is on Mg based materials. Furthermore, the coating growth on Mg based materials can be stimulated at a relatively low voltage, such as MgLi alloy. It should be noted for AZ91Nd/Al_2O_3 containing additional Al_2O_3 fibers that is already in oxidized state. Al_2O_3 could be reactively incorporated into the coating formation resulting in the mixed oxides formation ($MgAl_2O_4$) as demonstrated in paper *5*.

However, the coating thickness is only ca. 10.3 µm after 10 min treatment on Al9SiCu3, indicating the lowest coating growth efficiency. It can be concluded that the coating growth on AlSi9Cu3 requires the highest voltage (energy input) in comparison to other substrates. The presence of Si phase can impede the coating formation efficiency since Si is not very easy to be oxidized with lower Gibbs free energy of SiO_2 formation (-910.7 kJ/mol per mole oxygen molecule) in comparison to Al_2O_3. Hence, the coating formation process is much dependent on the melted coating materials converted from Al for short treatment time (paper *4*).

Although Ti6Al4V shows high electrochemical/chemical stability, the growing of PEO coating remains much easier than that of AlSi9Cu3, which can be still associated with the high solubility and rapid penetration of oxygen in the lattices, which is not found in Al or Mg substrates.

6.1.3 Influence of high melting temperature (pure Nb)

As reported already [6, 7, 9, 27], the spectral emission of Al, Mg and Ti originating from the substrates were detected during PEO processing, identified the incorporation in plasma reactions. However, as seen in Fig. 6-2, it is apparent that PEO processing on Nb is different, since Nb did not participate in the plasma reactions as demonstrated in paper *6*. Regarding the selected base metals in present study, they have a wide range of melting temperature from ca. 650 to ca. 2500 °C (650 °C of Mg, 660 °C of Al, 1668 °C of Ti and 2447 °C of Nb). Whether the base metals participate in the plasma reactions could be related to the melting temperature of the metals. With such high melting point (2447 °C) and thermal stability, the effective discharge temperature is not adequate to stimulate the ionization of Nb [15, 57] and only electrochemical-driven oxidation can happen. As a result, the coating on Nb is not formed

directly through plasma reactions.

However, the PEO coating formation on Nb substrate with high melting temperature is probably based on the following processes. At first, the electrochemical-driven oxidation of Nb substrate accelerated the formation of Nb oxide. At the same time, an electrophoretic deposition of the species from the electrolytes could occur under the high voltage, such as the deposition of amorphous phosphate, silica and Al_2O_3 in phosphate-, silicate- and aluminate-based electrolytes respectively. Afterwards, due to the formation of the discharges (only containing species originating from the electrolytes, Fig. 6-2), the high temperature can further stimulated the thermal process, resulting in the crystalline transformation from amorphous phase and/or the sintering process. For example, the formation of $AlNbO_4$ is due to the sintering between Nb_2O_5 and Al_2O_3 in aluminate-based electrolyte. Finally, different phases were present in the coatings regarding the electrolytes. In the phosphate-based electrolyte, it mainly contained Nb_2O_5 and amorphous phosphate. However, in the silicate-based electrolytes, the deposition from electrolyte was dominant, and the coating was mainly composed of amorphous silica. In the aluminate-based electrolyte, Al_2O_3, Nb_2O_5 and oxide mixture $AlNbO_4$ were produced. The formation of Nb_2O_5, Al_2O_3 and $AlNbO_4$ in aluminate electrolyte are suggested as following steps:

$$\mathrm{Nb} \rightarrow Nb^{5+} + 5e^- \quad (6\text{-}1)$$

$$2Nb^{5+} + 10OH^- \rightarrow Nb_2O_5 + 5H_2O \quad (6\text{-}2)$$

$$AlO_2^- + 2H_2O \rightarrow Al(OH)_3 + OH^- \quad (6\text{-}3)$$

$$2Al(OH)_3 \rightarrow Al_2O_3 + 3H_2O \quad (6\text{-}4)$$

$$Nb_2O_5 + Al_2O_3 \rightarrow 2AlNbO_4 \quad (6\text{-}5)$$

As a consequence, different electrolytes have shown obvious influences on the PEO coating formation. The distinct PEO processes, and distinguishable coating morphologies and composition are revealed in the different electrolytes. Nevertheless, all coatings present a significant improvement of corrosion resistance around one or two magnitudes of total impedance value higher than that of the bare substrate, and noticeable photocatalytic activity with the MO degradation rate of 30 - 40 %.

6.2 Influence of lattice structure in substrate

In comparison to pure metals, alloys are more widely used in industrial applications because their comprehensive performance is more satisfactory in general, especially the mechanical properties. It is well known that the alloying can influence lattice transformations and/or modify properties of alloys. For Mg alloy, with the excess Li content (11.5 wt%), the original hexagonal structure is completely transformed into cubic. For Ti alloy, V is an alloying element that stabilizes the cubic β phase, thus stimulates the lattice transformation from α-Ti (hcp) to β-Ti (bcc), which is distributed at the grain boundaries. During PEO treatment, also the coating formation process could be influenced. Thus, the PEO coating formation process on alloys with different lattice structures might be different from the pure metals (paper *1* and *2*).

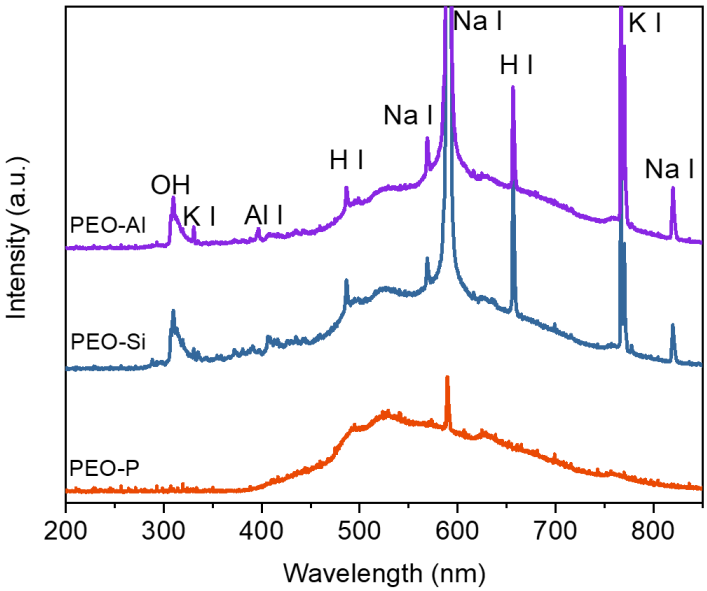

Figure 6-2 Optical emission spectra recorded at 10 min during PEO processing on pure Nb at 10 A/dm^2 in different electrolytes

6.2.1 Lattice transformation (α-Mg→β-Mg)

In paper *1*, the development of PEO process on MgLi alloy (cubic lattice) was faster in comparison to pure Mg with original hexagonal microstructure, considering the voltage response and the start of breakdown at lower voltage and shorter treatment time. However, compared with the lattice structure, the alloying element Li played a more relevant role in the coating formation. There are three reasons: Firstly, due to the high activity of Li in comparison to Mg, the alloy was less stable than pure Mg, as a result, it can be oxidized faster under the polarization at the first conventional anodizing stage. Secondly, Li participated in plasma reactions after the initiation of discharges, which means that Li was actively involved in the coating formation process. Finally, at the interface of coating and substrate, the Li was detected, which could deteriorate the stability of the coating. In addition, the high solubility of Li-containing species in alkaline electrolyte might reduce the compactness of the resultant coating. As a result, the faster degradation of the coating was revealed during EIS measurement.

The poor coating quality can be also confirmed from the voltage response. The voltage for pure Mg is always higher than that of MgLi alloy, indicating a poorer barrier property of the coating on MgLi alloy, compared with the coating on pure Mg. The characteristics (morphology, structure, composition) of the coatings was different between MgLi alloy and pure Mg, and the electrochemical resistance of the coatings was discernible.

As a consequence, it is probably more important that the formation of MgO (via $Mg(OH)_2$ formation) is the step that controls the coating growth rate and it does not matter whether Mg comes/dissolves from a cubic or hexagonal lattice. The presence of alloying element that results in the lattice transformation in MgLi alloy also has more obvious effect on the coating formation process, compared to the lattice structure.

6.2.2 Polymorph structure (α-Ti + β-Ti)

In paper *2*, the in-situ PEO result (Fig. 15) of Ti6Al4V has revealed that, the α-Ti lattice at the beginning of the processing was expanded. As seen in Fig. 6-3, the broadening of the α-Ti peaks can be observed at three different current density within 5 s of processing. The calculation stated that the lattice parameters of α-Ti were expanded near the surface region of the specimens (Fig. 17 in paper *2*), due to the continuous incorporation of oxygen in solid solution. Nevertheless, the lattice expansion was disappearing with treatment time. Besides, the diffraction peaks for anatase and rutile became visible gradually. At first, both crystalline Ti oxides formed and disappeared during the processing under higher current densities (5 and 10 A/dm^2). Then, the peaks of crystalline Ti oxides reappeared after switching off the high voltage (Fig. 18 in paper *2*). The amorphous phase was present for the entire PEO process, but disappeared after a week of the in-situ experiments. This observation is associated with a temperature and discharge energy controlled process, where the preferred formation of amorphous phase at higher temperature and energy. However, the crystalline TiO_2 phases form mainly from the precipitation of amorphous phase after the PEO processing.

Nonetheless, the signal of β-Ti phase is always absent, probably due to the low content of β-Ti phases. Additionally, the possible fast up-take of oxygen could stimulate the transformation of β-Ti to α-Ti with oxygen saturation since oxygen is stabilizing the α-phase. In this sense, the lattice structure does not have significant influence on the coating formation.

In the ex-situ experiment, the initial micro-pores firstly appeared on the layer on β-Ti and then extends to α-Ti, indicating the initial discharges occurred on β-Ti phase due to a less resistant barrier layer. One possibility is that the oxygen driven transformation of β-Ti to α-Ti can cause more preferred locations (defects) on β-Ti for the discharges. Alternatively, the composition heterogeneity of α-Ti and β-Ti could be the reason for the different discharge behavior. Because the β-Ti phase is enriched with vanadium, and the vanadium oxides are not stable in alkaline electrolyte.

A model experiment (paper *2*) adopting the separate α-Ti (pure Ti, hcp) and β-Ti (Ti-35Nb-6Ta, bcc) substrate couples in the phosphate-based electrolyte was performed to confirm this order of breakdown and reveal that under the same applied voltage the current through α-Ti and β-Ti phases is different. Fig. 6 and Fig. 7 in paper *2* evidence that the different oxidation behavior we found on the micro-scaled coupled materials (polymorph structured Ti6Al4V alloy) during PEO processing also happens to the coupled materials in large-size: The discharges were firstly observed on β-Ti and then they are developed on α-Ti rapidly. The change of current densities also confirms the higher current pass through β-Ti substrate at the initial stage stimulating the first discharges. Then the current density is higher for α-Ti, which is correlated with the more rapid development of discharges on the entire surface of the substrate. Fig. 6-4 illustrates that the surface morphology of the coatings on the two substrates are quite different. The coating on α-Ti has tiny micro-pores in the surface, with the randomly distribution of sintered islands. However, the coating surface on β-Ti shows larger micro-pores with irregular shape.

Nevertheless, the surface difference is more likely influenced by the alloying elements in β-Ti considering the nominal 35 wt.% of Nb.

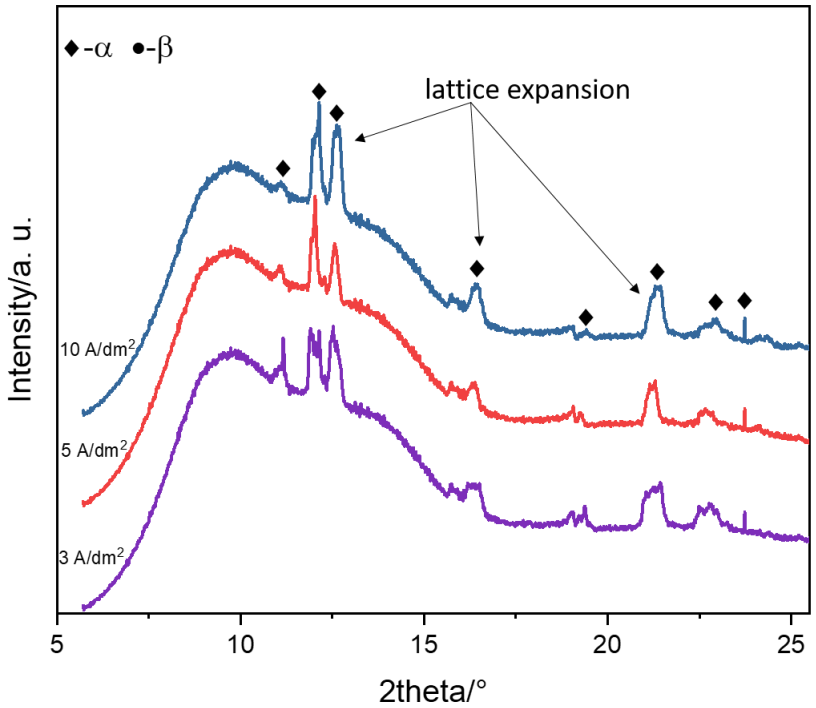

Figure 6-3 XRD patterns of the Ti6Al4V surface at the very beginning of in-situ PEO treatment (within 5 s) under different current density

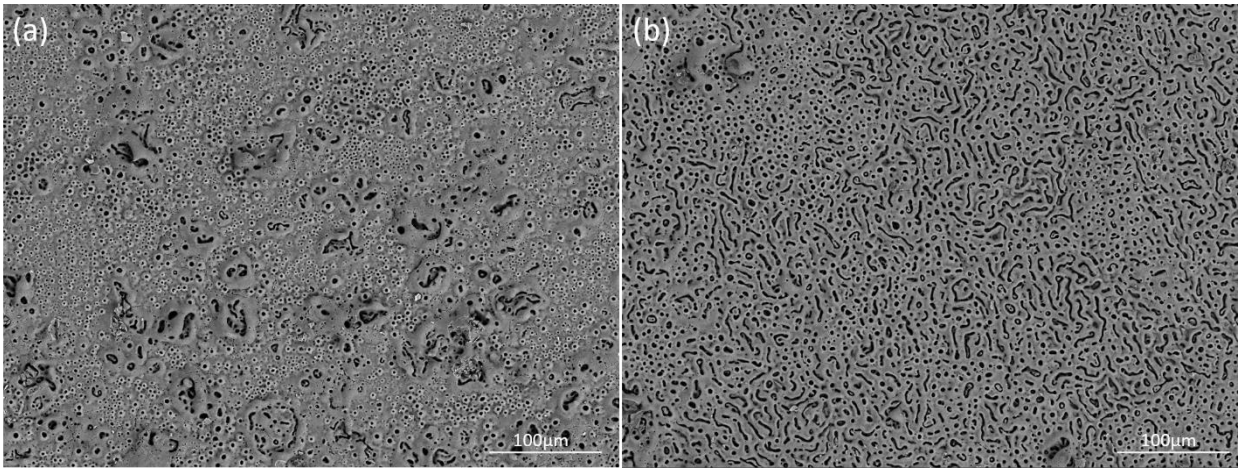

Figure 6-4 Surface morphology of PEO coating on (a) α-Ti and (b) β-Ti

For Ti6Al4V alloy, the influence of two Ti phases on the coating formation is very limited, especially the coating is quite uniform processed under higher current density. Nevertheless, this model experiment also identifies the possibility of PEO treatment on real galvanically coupled materials. However, obtaining uniform coatings on the coupled materials is more difficult in comparison to the alloys. The reason is that the differences in the coatings could be magnified in macro scale. Thus, further investigation to achieve the uniformity/enhancement of the coatings on gavanically-coupled materials is more urgent and the optimization of the parameters is still necessary. By adjusting the electrolyte, it can be possible to reach comparable coating growth rate, porosity and/or composition (which can, for

instance, reduce the electrochemical potential difference and enhance the general corrosion resistance) on different materials. The optimization of the electrical parameters can control the progress of PEO stages and further control the growing of the coating. From this point, the PEO treatment on coupled materials is one of the promising applications for future studies.

6.3 Influence of additional phases on coating formation

In addition to the transformation of lattice structure, alloys often consist of secondary phases due to the segregation of alloying elements, which can be considered as the material mixes in micro-scale. Furthermore, metal matrix composites reinforced with ceramic phases could be also treated as the micro-scaled material mixes showing higher strength, such as the ceramic Al_2O_3 fibers and Si phase for Mg and Al alloys in present study. Inevitably, the presence of additional phases in the material mix can alter the coating formation process during PEO due to the heterogeneous composition, which is much complicated compared to pure metals.

6.3.1 Secondary phases

The presence of secondary phases in the alloys have an influence on the coating formation. Especially at the initial conventional anodizing and the beginning of discharges stages, the different morphologies of conversion layer could be recognized on the intermetallics. At the conventional anodizing stage, it is dominated by the electrochemical-driven dissolution and deposition processes, depending significantly on the electrochemical stability of the intermetallics relative to the matrix. Different conversion products on the intermetallics regarding the local composition and morphology can be noticed. Afterwards, at the beginning of discharges, due to the altered local composition/microstructure, the local conversion layer is effective to change the local discharging behavior.

In paper *1*, the initial $MgLi_2Al$ particles conversion products were found to be accumulated on the $MgLi_2Al$ particles in MgLi alloy, indicating the faster oxidation of $MgLi_2Al$ particles compared to the surrounding β-Mg matrix. However, Li was not detected in the resultant coating, possibly due to the high solubility of Li-containing species in alkaline phosphate-based electrolyte.

In paper *4*, Al9Si3Cu alloy was composed of Al_2Cu and β-Al_5FeSi intermetallics. It has shown different coating growing behavior on different metallic phases, as illustrated in Fig. 11 in paper *4*. Before applying the polarization voltage, there is already an oxide layer on the surface of the alloy in an alkaline electrolyte. When the voltage applied, a dielectric conversion layer is firstly formed on the surface and the conversion products deposit more rapidly at the verge of Al_2Cu and Al_5FeSi intermetallics, indicating the electrochemical-driven dissolution and deposition are more intensive at the interfaces of Al_2Cu/α-Al and Al_5FeSi/α-Al. It is probably ascribed to the higher electrochemical potential relative to the matrix during polarization [58, 59]. After reaching the breakdown voltage, the discharges start on the layer of α-Al near Al_2Cu and Al_5FeSi intermetallics, possibly due to the layer formed adjacent to the intermetallics has more defects. Because the mixed oxides can be formed due to the incorporation

of alloying elements, and thus the presence of potential mismatches in microstructure. Then the discharges extend to the layer on the intermetallics, and finally spread on the entire surface. Since the coating growth on Al alloy requires higher voltage, in paper *4*, the relatively low current density of 3 A/dm^2 resulted in a long period (8 min) to produce a layered coating with only 3 μm thickness.

In paper *5*, due to the presence of $Mg_{17}Al_{12}$, Al-Mn-Nd and Al-Nd intermetallics, the similar sequential oxidation of the local areas on the surface of AZ91Nd alloy and AZ91Nd/Al_2O_3 MMC could be observed in the first stage of PEO processing. This is also assigned to the higher electrochemical stability of the intermetallics in comparison to α-Mg matrix. The strong cathodic effect of Al-Mn-Nd intermetallics even stimulated stronger oxidation of adjacent α-Mg and deposition. After the occurrence of discharges, it was found that the large micro-pores and intensively sintered morphology appeared on the layer converted from $Mg_{17}Al_{12}$ intermetallics, probably related to the intensive discharges with the participation of Al [60, 61].

6.3.2 Reinforcement phases

There are two ways for the reinforcement phases to participate in the coating growth. The first inert participation is depending on the embedding of reinforcement phases by the melted coating materials; however, the reinforcement phase remained stable. This occurred for Si phase in AlSi9Cu3 alloy in paper *4*. However, the reactive participation is via the reactions between the reinforcement phase and coating formation species, such as the formation of $MgAl_2O_4$ from the reaction between Al_2O_3 reinforcement fiber and MgO for AZ91Nd/Al_2O_3 MMC in paper *5*.

For Al9Si3Cu alloy, the Si phases was almost stable during the entire processing, and was only covered gradually by the melted coating materials from the oxidation of other phases in local areas. The lower current density/voltage (lower than 400 V) only drove less efficient coating growth in present study. As illustrated in Fig. 6-5(b), Si phases are embedded in the coating and no further interaction happened after PEO treatment. It has been evidenced that the discharges can reach a high electron temperature up to 2000-3500 K [6, 62]. However, the efficient discharge temperature cannot reach such high value, and the primary Si has a higher melting temperature (Tm = 1410 ℃) in comparison with Al (660 ℃) and Cu (1085 ℃) in Al9Si3Cu alloy. Thus, the reactive incorporation of Si was barely detected in paper *4*.

However, it should be noted that the inert incorporation of Si phase could be evolved to reactive incorporation, but the influence of the electrical parameters used during PEO are more significant. Some studies [64, 65] have reported the reactive incorporation of Si phase in PEO coating formation using extended processing time up to 45 min. The mixture of oxides, mullite ($Al_2O_3{\cdot}SiO_2$), was produced from the sintering of SiO_2 and Al_2O_3 in Al-Si alloys, as Si source was only originated from the Al-Si substrates. As a consequence, the fast PEO coating formation process, such as flash PEO, can not easily produce high quality PEO coatings on Al-Si alloys because of the presence of stable Si phase.

As an alternative, increasing the energy input, such as using higher current density/voltage [66] and/or extending the treatment time [64, 65] could be good choices to obtain uniform coatings on Al-Si alloys. For Mg MMC, the incorporation of Al_2O_3 fibers in PEO coating during the processing is different. The Al_2O_3 fibers are already in a stable oxidation state, however, additional reactive incorporation occurred with longer treatment time:

$$Mg \rightarrow Mg^{2+} + 2e \quad (6\text{-}6)$$

$$Mg^{2+} + 2OH^- \rightarrow Mg(OH)_2 \quad (6\text{-}7)$$

$$Mg(OH)_2 \rightarrow MgO + H_2O \quad (6\text{-}8)$$

$$MgO + Al_2O_3 \rightarrow MgAl_2O_4 \quad (6\text{-}9)$$

The melting point of reinforcement alumina fibers is ca. 2054 ℃, lower than MgO (2827 ℃). As the efficient discharge temperature reaches the value for the formation of $MgAl_2O_4$ spinel (ca. 2105 ℃), the reaction Eq. 6-9 can be stimulated. However, the large size of the fibers (ca. 3 μm in diameter, ca. 100 μm in length) in AZ91Nd substrate could also delay the reactive incorporation in the coating. Note that near the interface of coating and substrate, fibers still could be found, which interrupt the continuity of the coating due to the step by step dissolution of the fiber and deposition of coating materials. As illustrated in Fig. 6-5 (c), the Al_2O_3 fibers were finally dissolved and incorporated in the coating completely during PEO treatment.

Given the mechanism of PEO processing involving chemical-, plasma-chemical, electrochemical-, pressure and thermal activated processes, the incorporation mode of the reinforcement phases is largely dependent on the properties of these phases, such as their melting point and thermal stability. Furthermore, the size and distribution of the reinforcement phases in the substrate are important to influence the rapid incorporation. In addition, the electrical parameters are also primary factors determined the incorporation process of the reinforcement phases during PEO.

It can be summarized that the most important influence comes from the base metals (Mg, Al, Ti and Nb) since the oxidation of substrate is the main process for PEO coating formation. Primarily, the different Gibbs free energy of formation for the oxides converted from the metals determine whether the oxidation process is more favored or not. The favored oxidation process is beneficial for the coating growth; nevertheless, the coating formation are altered with the presence of additional phases. In addition, the melting temperature of the substrate is a factor that influences the discharging behavior, such as, Nb with high melting temperature is difficult to participate in the discharges. However, the lattice structure of the substrate does not have obvious influence on the coating formation as expected. Alternatively, the oxygen solubility is high in the hexagonal Ti lattice, which can speed up the oxidation process by fast penetration.

Besides, at the identical PEO conditions, the corresponding oxides of different substrate, to a large extent, have significantly influenced the PEO process, eg. the period of each stage, the breakdown voltage, the coating formation efficiency. Before the start of breakdown, the microstructure and the

dielectric property of the corresponding barrier layer formed via the electrochemical-driving process determine the initiation of the discharges. At the same time, the additional phases in the substrate participated in the oxidation influence the start of the discharges, due to the local composition/microstructure heterogeneity of the layer. Moreover, the additional phases can also change the microstructure of the resultant coatings.

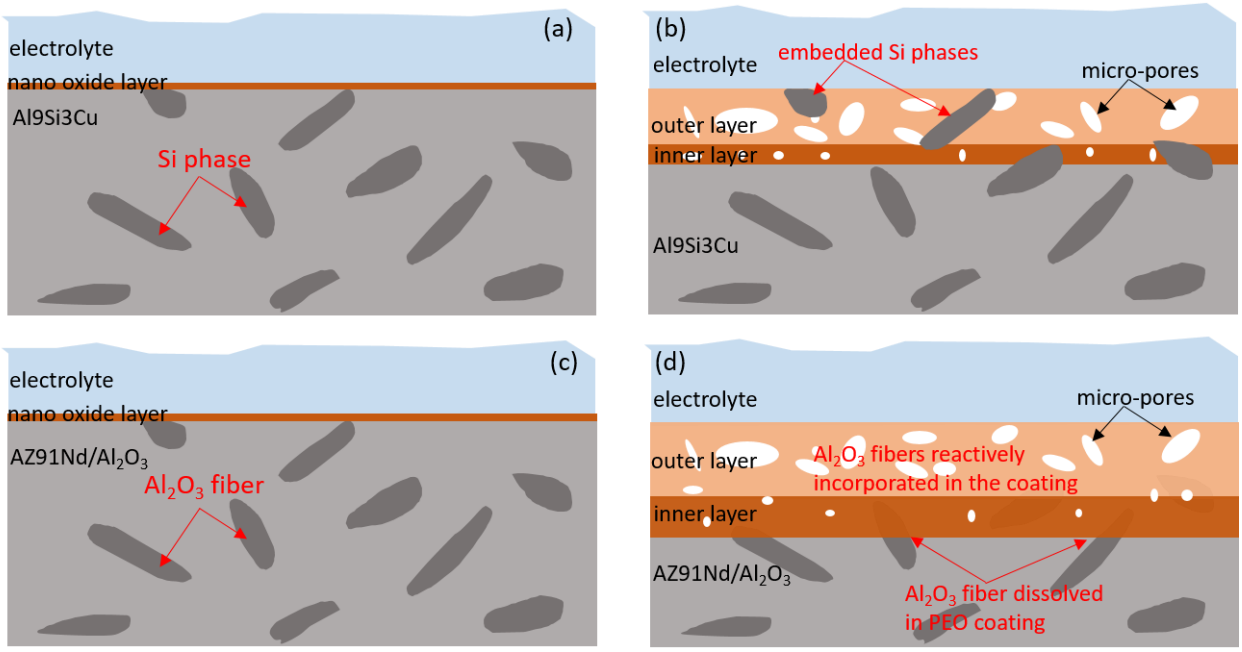

Figure 6-5 Evolution of reinforcement phases before and after PEO treatment: (a) before and (b) after PEO processing on Al9Si3Cu alloy, and (c) before and (d) after PEO processing on AZ91Nd/Al_2O_3 MMC.

7. Conclusions

The influence of microstructure and properties of different Mg, Al, Ti and Nb based metals, alloys and composites has been studied to reveal the role of the lattice structures, additional phases and intermetallics of the substrate in the formation process of PEO coatings. At the same time, the evolution behavior of the substrate during the processing were investigated. In addition, the influence of properties of hydroxides and other phases (phosphate, silicate and aluminate) due to the oxidation of substrate and decomposition of electrolyte should not be neglected concerning the anodic deposition stage. Finally, the morphology, microstructure, composition and properties of the PEO coatings were also studied. The studies in present thesis have demonstrated that the substrate is a very important and underestimated parameter in PEO processing. Accordingly, the main findings and conclusions are listed as follows:

1. In general, the barrier layers of different metal matrixes have different breakdown voltage, and it is Mg, Ti, Al and Nb in an increasing sequence from ca. 110 V to ca. 220 V under the same processing conditions. The addition of alloying elements and reinforcement phases can increase or reduce the breakdown voltage through the modification of the coating composition and microstructure.

2. The lattice transformation of MgLi alloy is less effective to influence the PEO process in comparison with the chemically and electrochemically active Li. The voltage response and discharging behavior are modified as the voltage increases slower than that of pure Mg. Additionally, Li participates in the plasma reactions and the intensity the discharges are also changed. The high solubility of Li containing species in alkaline electrolyte determines that the coating only composes of Li at the interface near the substrate.

3. However, the polymorph microstructure of Ti alloy shows the influence on the initial oxidation and generation of discharges during PEO. The lattice expansion of α-Ti is revealed at the initial stage of PEO processing, due to the high solubility of oxygen in the lattices at the surface of the substrate. The fast penetration of oxygen can accelerate the oxidation process and thus the coating growth. Nevertheless, the lattice expansion gradually disappears due to the precipitation of TiO_2 and the thickening of the coating. Afterwards, the initial discharges start on the layer of β-Ti and then develop to α-Ti. Moreover, the micro-pore on the β-Ti is larger in comparison to α-Ti.

4. In addition, the electrolyte composition also plays an important role in coating formation phases on Ti alloy. The coating are mainly composed of anatase and rutile in phosphate-based electrolyte. Nevertheless, in the aluminate- and silicate-based electrolytes, the deposition becomes more dominant. The coating formation species are mainly originated from the electrolytes, presenting as Al_2O_3 and $TiAl_2O_5$, and amorphous silicate, respectively.

5. The intermetallics in AlSi9Cu3 (Al_2Cu and Al_5FeSi) and AZ91Nd ($Mg_{17}Al_{12}$, Al-Nd, and Al-Mn-Nd) interrupt the coating continuity, and the discernible coating microstructure at local areas can be noticed. The oxidation process develops more slowly for the intermetallics in comparison to the Al and Mg matrix, due to the higher electrochemical stability of the intermetallics. The surface

heterogeneity can be erased with prolonged processing time, but the discontinuity can be also notice in cross-sections. The accumulation of alloying elements in local areas of the coatings can be detected. Nevertheless, the coatings are not composed of crystalline phases that contain the alloying elements, due to the dilution of alloying elements with the incorporation of electrolyte species.

6. Moreover, the reinforcement phases (Si phases in AlSi9Cu3 and Al_2O_3 fibers in AZ91Nd/Al_2O_3) can still incorporate in the coating formation though they have higher melting temperature and thermal stability. At first, the Si phases and Al_2O_3 fibers are just inertly embedded in the coating. Afterwards, the gradual degradation of Si phase for AlSi9Cu3 can be detected with time, and the sintering process between SiO_2 and Al_2O_3 can be activated as reported if the processing time further extended and/or current density (applied voltage) increased. That is to say, the fast coating formation on Al-Si alloys is not easy to achieve. Similarly, the more severe PEO conditions (high voltage, high temperature and pressure) stimulate the sintering between the Al_2O_3 fiber and MgO for Mg composite, in the form of oxide mixture $MgAl_2O_4$ spinel. $MgAl_2O_4$ spinel is mainly distributed at the outer layer. Nevertheless, the Al_2O_3 fiber can be observed embedded in the inner layer, which interrupt the continuity of the coating near the substrate.

7. Nb does not participate in the plasma reaction directly due to the high melting temperature. However, similar to Mg, Al and Ti substrates, the coating formation is also dependent on the composition of electrolyte, such as the formation of amorphous phosphate and silicate, and Al_2O_3. Therefore, the coating morphology and composition are also determined by the electrolyte composition.

8. The multifunctional PEO coatings have been produced on Ti alloy and pure Nb. In addition to good corrosion resistance of PEO coatings, attractive photocatalytic activity is also demonstrated for the coatings on Ti alloy with MO degradation rate higher than 40 % and on pure Nb with MO degradation rate in the range of 30 - 40 %. This is due to the semiconductive property of the coatings (mainly TiO_2 and Nb_2O_5).

From the micro-scale, this work studied the PEO coating formation on material mixes including alloys and composites, having phases with different composition and microstructure. The results obtained in this work demonstrate that the substrate influences the PEO coating formation process through changing the voltage evolution and the characteristics of the discharges. In addition, each phase and/or intermetallic react differently on the applied current density and voltage, and the discharges. As a consequence, the coating growth rate, composition, morphology, microstructure, and properties are all different. The local differences can be noticed on the resultant coatings, which means the fast formation of more uniform coatings on material mixes, eg. flash PEO, is not applicable. Alternatively, the optimized parameters such as prolonged processing time combined increased current density/voltage can be adopted to remove the heterogeneity and obtain the uniform coatings.

Extending to the macro-scale, joint materials are more widely applied in industry and surface protection are sometimes necessary and required. The separate constituents of joint materials are predictable to have different response to the PEO processing. It may lead to different development of PEO process

such as different start of discharges and further cause the different coating thickness on separate material parts, and even result in the failure of the process. The reason is similar to the difficulty to form uniform PEO coatings on the micro-scaled material mixes, related to the different coating formation behavior on the different materials. It means the influence of the substrate microstructure on coating formation process also apply to the joint materials in macro-scale. With the foundation of present study, it is worthy for further investigation and application of PEO process on joint materials.

Appendix

1. List of symbols and abbreviations

AESEC	Atomic emission spectroelectrochemistry
Al	Aluminum
Al9Si3Cu	Al-9 wt.% Si-3 wt.% Cu
AZ91Nd	Mg-9 wt.%Al-1 wt.% Zn-1 wt.% Nd
AZ91Nd/Al_2O_3	Mg-9 wt.%Al-1 wt.% Zn-1 wt.% Nd-20 vol.% Al_2O_3
BSE	Backscattered electron
Cu	Copper
CPE	Constant phase angle element
DC	Direct current
EDS	Energy dispersive spectrometer
EIS	Electrochemical impedance spectroscopy
H	Hydrogen
ICP-OES	Inductively coupled plasma-optical emission spectrometry
K	Potassium
Li	Lithium
Mg	Magnesium
MgLi	Mg-11.36 wt.% Li-2.39 wt.% Al
MMC	Metal matrix composite
MO	Methyl orange
Na	Sodium
Nb	Niobium
OCP	Open circuit potential
OH	Hydroxyl
OES	Optical emission spectroscopy
P	Phosphorous
PEO	Plasma electrolytic oxidation
PDP	Potentiodynamic polarization
R	Resistance
Ra	Arithmetical mean roughness
Rin	Resistance of inner layer
Rout	Resistance of outer layer
Rp	Polarization resistance
Rs	Solution resistance
Rsc	Resistance of space charge layer

RSm	Mean width of profile elements
SE	Secondary electron
SEM	Scanning electron microscope
Ti	Titanium
Ti6Al4V	Ti-6 wt.% Al-4 wt.% V
V	Vanadium
Zr	Zirconium

2. Table (Cited reference number refer to the review paper in Chapter 2)

Table 1 Summary of secondary phases of Mg alloys studied in PEO process

Mg alloys	Secondary phases	Size	Stability	PEO process	Coating thickness	Coating morphology	Coating micro-hardness	Corrosion resistance	Ref.
AZ91D	$Mg_{17}Al_{12}$	-	Higher electrochemical potential vs. α-Mg	-	Lower growth rate on $Mg_{17}Al_{12}$	More large-sized micro-pores on $Mg_{17}Al_{12}$	-	-	[6]
AZ91D	$Mg_{17}Al_{12}$	-	160 mV higher vs. α-Mg	5.7 $V \cdot s^{-1}$ within 250 s, then diminished to 1.38 × 10^{-2} $V \cdot s^{-1}$, final voltage in the range of 500 - 515 V	20 μm	4 - 40 μm micro-pores	-	50 times higher than bare substrate (3.5 wt.% NaCl)	[28]
	Al_8Mn_5		-						
WE43-T6	$Mg_{14}Nd_2Y$		-	7.5 $V \cdot s^{-1}$ within 250 s, then diminished to 1.79 × 10^{-2} $V \cdot s^{-1}$, final voltage in the range of 500 - 515 V	30 μm	4 - 40 μm micro-pores		215 times higher than bare substrate (3.5 wt.% NaCl)	
	$Mg_{12}Nd$		220 mV higher vs. α-Mg						
	Nd-rich phase		-						
	Y-rich phase		-						
AZ91	$Mg_{17}Al_{12}$	50 - 80 μm	-	-	-	5 μm micro-pores, unclosed holes	-	2.75 mA/cm^2 (5.0 wt.% NaCl)	[63]
AZ91NdA	$Mg_{17}Al_{12}$	5 - 10 μm	-		-	Even and smooth		1.75 mA/cm^2 (5.0 wt.% NaCl)	
	Al_2Nd	Fine particles	Higher vs. α-Mg		Thinner vs. α-Mg and $Mg_{17}Al_{12}$				
AZ92	$Mg_{17}Al_{12}$	-	50 mV higher vs. α-Mg	-	70 μm	More uniform vs. PEO coated AZ92/SiC	510 ± 25 HV	15 kΩ (3.5 wt.% NaCl) after 1 h immersion	[38]
	Al_8Mn_5	-	200 mV higher vs. α-Mg			Lateral oxidation/dispersion of Al and Mn			

AZ91/SiC/5p	$Mg_{17}Al_{12}$	-	50 mV higher vs. α-Mg		65 µm	Rougher interfaces vs. PEO coated AZ92	589 ± 30 HV	12 kΩ (3.5 wt.% NaCl) after 1 h immersion	
	Al_8Mn_5	-	200 mV higher vs. α-Mg						
	SiC	5 µm	-						
AZ91/SiC/10p	$Mg_{17}Al_{12}$	-	50 mV higher vs. α-Mg		62 µm	Rougher interfaces vs. PEO coated AZ92	644 ± 60 HV	67 kΩ (3.5 wt.% NaCl) after 1 h immersion	
	Al_8Mn_5	-	200 mV higher vs. α-Mg						
	SiC	5 µm	-						
AZ91D	$Mg_{17}Al_{12}$	-	-	Influenced by different solutions	4.4 - 6.6 µm	Anodic coating formed on α-Mg preferentially	-	E_{corr} of -1.513 to -1.14 V vs. SCE, I_{corr} of 1.226E-4 to 1.385E-7 A/cm^2 (3.5 wt.% NaCl)	[64]
AM60B	$Mg_{17}Al_{12}$	-	-	-	12 - 33 µm	1 - 10 µm micro-pores, 2-4 %porosity	-	Coated AJ62 < coated AM60B < coated AZ91D (3.5 wt.% NaCl)	[30]
	Al-Mn intermetallic								
AJ62	Al_4Sr				7 - 32 µm	10 µm micro-pores, higher porosity			
	Mg-Al-Sr intermetallic								
AZ91D	$Mg_{17}Al_{12}$				14 - 35 µm	Higher porosity			
AZ91D	$Mg_{17}Al_{12}$	Lamellar	-	-	Similar thickness	Open holes	-	PEO coated ECAPed AZ91D is more corrosion resistant (3.5 wt.% NaCl)	[65]
ECAPed AZ91D	$Mg_{17}Al_{12}$	Fine particles				Uniform and compact with few small open holes			
AZ61	$Mg_{17}Al_{12}$	-	-	A sharp drop from 280 V to 190 V occurred in KF free electrolyte	-	-	6 - 7 GPa of outer layer	-	[4]
	Al_8Mn_5	15 µm				Deposition near Al-Mn particles			
	Mg_2Si					Oxidized without causing significant corrosion			
E21	Nb-rich	Precipitates	-		12.3 ± 2.7 µm	Similar	-		[66]

	Zr-rich			In the second and third stages, the voltage of AZ31B are lower than RE containing alloys				0.39 mg/cm^2 per year (3.5 wt.% NaCl)	
WE43	Nb-rich Zr-rich Y-rich				13.2 ± 1.9 μm			0.53 mg/cm^2 per year (3.5 wt.% NaCl)	
AZ31B	-	-			8 ± 1.6 μm			0.11 mg/cm^2 per year (3.5 wt.% NaCl)	
AZ91D	$Mg_{17}Al_{12}$	Eutectic/particles	-	Sparking discharge occurred mainly on α phase at early stage of micro-arc oxidation	Similar to α-Mg	More porous on α-Mg initially	-	5.4E6 Ω·cm^2 of coated AZ91D compared to 1.1E3 Ω·cm^3 of bare alloy (3.5 wt.% NaCl)	[67]
FSW AZ31B	SZ zone ($Mg_{17}Al_{12}$ particle)	11 μm grain size	-	-	50 μm	Similar	-	Best corrosion resistance (3.5 wt.% NaCl)	[68]
	HAZ zone ($Mg_{17}Al_{12}$ particle)	26 μm grain size						severe corrosion attacks (3.5 wt.% NaCl)	
	BM zone ($Mg_{17}Al_{12}$ particle)	22 μm average						-	
AZ61	$Mg_{17}Al_{12}$	-	-	-	5.4 ± 0.7 μm	5 μm micro-pores, surface roughness of 2.4 ± 0.5 μm	-	-	[69]
	Al-Mn intermetallic	1 - 15 μm							
AZ31/SiC_p	SiC	10 μm	-	-	60 μm	-	-	-	[57]
AZ91/Al_2O_3-SiO_{2sf}	Al_2O_3-SiO_2	D 1 - 3 μm, L 50 - 100 μm			65 μm				
AM50	$Mg_{17}Al_{12}$	-	-	Current for pure AM50 was higher in constant voltage mode, indicating the	25 ± 5 μm	Similar to that with Ce addition	-	$Al_{11}Ce_3$ reduce pitting corrosion (0.5 wt.% NaCl)	[70]
AM50Ce0.5	$Mg_{17}Al_{12}$				20 ± 2 μm	Increased number of pimples with Ce			
	$Al_{11}Ce_3$								
AM50Ce1	$Mg_{17}Al_{12}$				20 ± 2 μm				

	$Al_{11}Ce_3$			smaller coating resistance					
AZ91	$Mg_{17}Al_{12}$	10 - 100 μm	-	-	-	Similar surface morphology	-	1.29E6 Ω·cm^2 (3.5 wt.% NaCl)	[71]
AZ91-T6	$Mg_{17}Al_{12}$	1.2 μm lamellar, 0.5 μm precipitates				fewer micro-pores on cross-section		1.62E7 Ω·cm^2 (3.5 wt.% NaCl)	
AZ91D	$Mg_{17}Al_{12}$	Grain size decrease from 200 to 1 - 2 μm, final $Mg_{17}Al_{12}$ particle of 7 μm	-	-	Increase firstly and then decrease with ECAP passes	Smallest micro-pores	-	Highest mass loss (3.5 wt.% NaCl)	[72]
UFG AZ91D 4P						More compact and good adhesion to matrix		-	
UFG AZ91D 8P									
UFG AZ91D 12P									
UFG AZ91D 16P									
AM50	$Mg_{17}Al_{12}$	-	-	Microdischarges commence at 190 V and constant slope on voltage-time curve	75 μm	5 μm micro-pores	700 ± 200 HV0.01	0.18 mm/y (SBF)	[73]
	Al-Mn intermetallic								
AZ31B	Al_6Mn	Particles	-	-	10 μm	Similar	-	Higher corrosion resistance (5 wt.% NaCl)	[74]
	Al_8Mn_5								
AMX602	Al_6Mn					Less but larger micro-pores, Al_2Ca may be included in PEO layer		Lower corrosion resistance (5 wt.% NaCl)	
	Al_8Mn_5 (Tm 1321 k)								
	Al_2Ca (Tm 1352 k)		Nobler vs. α-Mg						
AZ91D	$Mg_{17}Al_{12}$	-	-0.9 V	Similar voltage-time patterns, initial conversion products are	1.6 ± 0.3 μm, 0.1 - 0.2 μm thinner than on matrix	Small micro-pores with coarse boundaries	-	138550 Ω·cm^2 (3.5 wt.% NaCl)	[54]
	AlMn phase (high T_m)	-	-0.42 V			-			

SS-AZ91	$Mg_{17}Al_{12}$	Dissolved in matrix	-0.9 V	observed around intermetallics and sparking on α matrix firstly, and later on β phase	Inhomogeneous with uncoated region	-		67702 Ω·cm² (3.5 wt.% NaCl)	
	AlMn phase (high T_m)	-	-0.42 V			Larger cluster of pores			
SA-AZ91	$Mg_{17}Al_{12}$	200 nm	-0.9 V		1.8 ± 0.2 μm	Uniform		291766 Ω·cm² (3.5 wt.% NaCl)	
	AlMn phase (high T_m)	-	-0.42 V						
Mg-2Al	-	-	-	-	140 ± 30 μm (Mg-8Al), decreased with Al	Rougher with Al	Max. 931 ± 71 HV (Mg-8Al), increased with Al	-	[75]
Mg-4Al	$Mg_{17}Al_{12}$	Increased with Al							
Mg-8Al									
Mg-2Zn	-	-			Decreased with Zn	Smoother with Zn	Max. 832 ± 31 HV (Mg-2Zn), insignificant change with Zn		
Mg-4Zn	Mg_7Zn_3	Increased with Zn							
Mg-8Zn									
AZ91	$Mg_{17}Al_{12}$	-	130 - 240 mV higher vs. α-Mg	Two different tendencies between unreinforced and reinforced materials. Voltage is slightly lower for reinforced materials and AZ91/0-2p-PEO shows a current drop after 200s and 240 s respectively	55 μm	Ra 2.1 ± 1.8 μm, Rz 18.3 ± 0.8 μm	300 HV0.025	-	[40]
	Al_8Mn_5	14 μm	160 - 300 mV higher vs. α-Mg						
AZ91/SiC/2p	$Mg_{17}Al_{12}$	-	130 - 240 mV higher vs. α-Mg		55 - 80 μm	Ra 3.6 ± 0.1 μm, Rz 21.5 ± 1.0 μm	At the cluster of SiC 80 HV0.025	Corrosion resistance decreased with SiC content (3.5 wt.% NaCl)	
	Al_8Mn_5	14 μm	160 - 300 mV higher vs. α-Mg						
	SiC	15-25 μm	130 - 240 mV higher vs. α-Mg						
AZ91/SiC/5p	$Mg_{17}Al_{12}$	-	130 - 240 mV higher vs. α-Mg			Ra 6.8 ± 0.2 μm, Rz 41.3 ± 1.0 μm			

	Al_8Mn_5	14 µm	160 - 300 mV higher vs. α-Mg						
	SiC	15 - 25 µm	130 - 240 mV higher vs. α-Mg						
AZ91/SiC/10p	$Mg_{17}Al_{12}$	-	130 - 240 mV higher vs. α-Mg			Ra of 7.4 ± 1.5 µm, Rz of 39.0 ± 1.5 µm			
	Al_8Mn_5	14 µm	160 - 300 mV higher vs. α-Mg						
	SiC	15 - 25 µm	130 - 240 mV higher vs. α-Mg						
Mg-0.8wt.%Ca	Mg_2Ca	Small globules	Slight difference, no coupling phenomenon	-	70 ± 5 µm	Depends on electrolytes	-	Depends on electrolytes	[76]
	Mg-Si-Ca	Impurities	120 - 330 mV higher vs. α-Mg						
	Mg-Si-Ca-Fe								
AZ31	$Mg_{17}Al_{12}$	-	-	-	-	-	-	Increased firstly then decreased with Al content (3.5 wt.% NaCl)	[77]
AZ91									
AZ111									
AZ141						Some sunken area			
AZ91	$Mg_{17}Al_{12}$	-	-	WE43 showed higher voltage. For AZ91, formation of conversion film started on α phase and then extended to β phase, however, WE43 showed	17.1 ± 2.3 µm	Initial conversion film formed on matrix	-	-	[78]
WE43	$Mg_{14}Nd_2Y$				21.6 ± 3.2 µm	Initial conversion film start on $Mg_{14}Nd_2Y$			

				the opposite trend.					
As extruded Mg-Gd-Y	-	Grain size 15 μm	-	-	26 μm	-	572 HV	-	[29]
Mg-Gd-Y T4	$Mg_5(GdY)$	Grain size 55 - 65 μm, nano meter precipitate			53 μm	Less porous	641 HV		
Mg-Gd-Y T6					20 μm	Largest pores	541 HV		

Table 2 Summary of secondary phases of Al alloys studied in PEO process

Al alloys	Secondary phases	Size	Stability	PEO process	Coating thickness	Coating morphology	Coating micro-hardness	Corrosion resistance	Ref.
Al	AlmFe	Particles along grain boundary	Inert/oxidation at a lower rate	-	Block further coating formation	Some occulated in coating, larger fluctuations a substrate/coating interface	-	-	[47]
	α-AlFeSi	2 - 5 μm in grains							
AlSi10	eutectic Si	< 5 μm particles							
	primary Si	5 - 20 μm flakes/needles							
	α-AlFeSi	Particles							
AlSi10Cu3	eutectic Si	< 5 μm particles							
	primary Si	5 - 20 μm flakes/needles							
	α-AlFeSi	Particles							
	Al_2Cu	3 - 20 μm particles	Al_2Cu oxidized/dissolved more rapidly		Advances more rapid to Al_2Cu	Large voids left due to oxidation and dissolution			
AA2024-T351	Cu-rich intermetallic	10 μm precipitates	-	-	20 - 25 μm (5 - 10 μm porous layer)	-	-	-	[79]
Peened AA2024	Cu-rich intermetallic	Changed distribution				More porous	Higher hardness		
319 Al-Si	eutectic Si	Fine	-		-	Initial oxide around Si particles, voids	-	-	[80], [81]

Appendix

				More rapid increase of voltage with lower Si content		and cavities in Si region			
390 Al-Si	primary Si	Needles				Similar, higher surface roughness			
2024/15SiC	SiC	12.8 μm particles	SiC hindered film growth	Film thickness increases with time: firstly grows linearly and then growth rate reduces	180 μm	Irregular composite/film interface	Max. 2000 HV (50g)	R_p is 4 orders of magnitude lower than composite (3.5 wt.% NaCl)	[39]
Al-12wt%Si	eutectic Si	-	Deposited on α-Al more rapid	The surface remained uncoated after 250 s of processing and a non-uniform oxide layer on eutectic Si	-	Different local morphology	-	-	[82]
AA2099-T8	Cu-rich intermetallic	Particles	-	Initial non-uniform film formation with voltage increasing and detachment of initial film due to the formation of fine voids at alloy/film interface	-	Preferential oxidation of intermetallic and voids at the region	-	-	[42]
2A97 Al-Cu-Li	Al_2Cu	Particles	Cathodic to α-Al	Galvanoluminescence brightness is largely increased by the addition of Mn, suppressed by Zn, and unaffected by Cr, Cu, Fr or Mg	32 μm	Pancake structure	-	-	[83]
	Al_2CuLi	Particles	Anodic to α-Al, Li dissovled firstly to Al_2Cu						
	$MgZn_2$	Particles	Anodic to α-Al, dissovled firstly						
Al-1Si	Si	Increase with Si content	Lower affinity of Si towards O and lower electrical conductivity and oxidation kinetics	-	Decrease in an exponential manner with Si content	Firstly increased spherical droplet feature with Si content and then become smoother and more porous.	600 - 2000 HV	-	[84]
Al-2Si									
Al-4Si									
Al-8Si									
Al-12Si									

Al-16Si						Surface roughness decreased			
Al-32Si									
A356-GC	eutectic Si	-	Lower electrical conductivity and lower oxidation rates vs. α-Al	-	20.1 ± 0.6 μm	Some irregularities	850 HV	I_{corr} of 5.2E-5 mA/cm^2 (3.5 wt.% NaCl)	[85], [86]
	primary Si	Flakes							
	β-AlFeSi	-							
A356-RC	eutectic Si	1.8 ± 0.6 μm			20.7 ± 1.8 μm	Some irregularities, 8 μm on eutectic Si	1000 HV	icorr 4.2E-5 mA/cm^2 (3.5 wt.% NaCl)	
	π-AlFeSiMg	-							
Al-1Mn	$Al_{17}Mn_{22}$	Amount and size increased with Mn content	Electrochemical active Mn has a similar oxidation potential to Al	-	116 μm	Surface roughness increased, 6.6 - 8.4 μm.	Decreased with Mn content, max. 1500-2000HV	-	[87]
Al-2Mn					119 μm				
Al-4Mn					127 μm				
Al-8Mn					162 μm				
AA1050	-	-	-	The presence of Cu nanoparticles in oxide layer increase the electrical conductivity and lead to the delay of breakdown	-	-	-	-	[88]
AA2214	Al_2Cu					Dealloyed Cu-rich particles incorporated in coating and large holes formed on surface			
	AlCuFeMnSi intermetallic								
6061	Al-Fe-Si intermetallic	Large Al-Fe-Si particles, grain size 150 μm in width	-	-	-	Average 1.01 μm micro-pores	-	3.4E4 Ω·cm^2 (3.5 wt.% NaCl)	[89]
	Mg/Si rich intermetallic								
NZ-6061	Al-Fe-Si intermetallic	Fine Al-Fe-Si particles, grain size 20 μm in width				Lowest amount of micro-pores with average 0.91 μm		2.1E4 Ω·cm^2 (3.5 wt.% NaCl)	
	Mg/Si rich intermetallic								
TM-HAZ-6061	Al-Fe-Si intermetallic	Large Al-Fe-Si particles, grain size 3 mm in width				Average 1.06 μm micro-pores		2.5E5 Ω·cm^2 (3.5 wt.% NaCl)	
	Mg/Si rich intermetallic								

cast AlSi12	Eutectic Si	1 - 5 μm	-	-	102 ± 6 μm	-	300 - 560 $HV_{0.2}$	-	[34]
3D printed AlSi12	Eutectic Si	300 nm			109 ± 7 μm		430 - 610 $HV_{0.2}$		
AlSi9Cu3	Eutectic Si	Lath-liked	-	A sequential involvement of different phases in plasma discharges: start on α-Al , then on Al_2Cu and β-Al_5FeSi and finally on eutectic Si	1.96 ± 0.38 μm	0.05-0.26 μm of micro-pores	-	-	[49]
	Al_2Cu	Herringbone-structured			3.01 ± 0.29 μm	Preferential deposition around Al_2Cu, sintered morphology, with micro-pores of 0.078-0.95 μm			
	β-Al_5FeSi	Irregular			3.06 ± 0.29 μm				

Table 3 Summary of secondary phases of Ti alloys studied in PEO process

Ti alloys	Secondary phases	Size	Stability	PEO process	Coating thickness	Coating morphology	Coating micro-hardness	Corrosion resistance	Ref.
Ti6Al4V	α	-	Dissolution of β-Ti was greater than in α-Ti	The coating grows faster on β-Ti than on α-Ti	-	The oxide layer was not uniform at first, then a uniform porous structure was produced	-	-	[35]
	β								
Ti-6Al-7Nb	α	Fine dispersion	-	-	280 - 420 nm	Many micro-protrusions containing uniformly pores	-	-	[90]
	β								
cp Ti	-	grain size 30 μm			400 - 600 nm				
Ti6Al4V	α	Equiaxed	-	Breakdown voltage of ~200 V_{rms} at ~50 s	10 μm	Micro-pore of 0.4 - 3.6 μm, pore density of 20 × 10^3 mm^{-2}	205 $HV_{0.025}$	-	[51]
	β	Integranular							
cp Ti	-	Fine grain			-	Micro-pore of 0.4 - 2.0 μm, pore density of 36 × 10^3 mm^{-2}	-	10 times more passive than PEO coated alloy (3 M KCl)	

Ti-35Ta	α″	Needle-like	-	-	-	-	-	-	[91]
Ti-35Ta-10Nb	α″	Needle-like				Larger micropores			
	β	Equiaxed							
Ti-10Nb	α′	Needle-like	-	Higher current density levels with increasing of Nb content at potentio-static condition	1.82 ± 0.1 μm	10.13 ± 1.3 % porosity, micro-pores of 1.05 ± 0.9 μm	-	$6.1\times10^4\ \Omega\cdot cm^2$ (SBF)	[92]
Ti-30Nb	α′	Needle-like			1.85 ± 0.3 μm	12.53 ± 1.2 % porosity, micro-pores of 1.13 ± 0.8 μm		$8.5\times10^4\ \Omega\cdot cm^2$ (SBF)	
	α″	Needle-like							
	β	Equiaxed							
Ti-50Nb	β	Equiaxed			1.86 ± 0.6 μm	40.83 ± 1.5 % porosity, micro-pores of 6.43 ± 1.1 μm		$5.0\times10^4\ \Omega\cdot cm^2$ (SBF)	

Table 4 Effect of alloying elements of Mg alloys on PEO coatings

Alloying element	Substrate	PEO process	coating composition	coating thickness	coating morphology	Ref.
Al	AZ31, AZ91, AZ111, AZ141	With the increasing of Al in Mg alloys, the oxidation slope firstly increased and then decreased	With increasing of Al content, the peak intensity of MgO weakened and the peak intensity of $MgAl_2O_4$ became stronger (higher than 9 % Al)	-	The formation of some sunken area and changed porosity. Relatively compact coating on AZ91 alloy	[77]
	Mg- 2 at.% Al Mg- 4 at.% Al Mg- 8 at.% Al	Breakdown voltage increased with Al content	Mg_2SiO_4 and MgO, no extra aluminum containing phase were observed	Decrease with increasing of Al content	The coating got relatively rougher, and the size distribution and the arrangement of discharge channels became inhomogeneous	[75]

Zn	Mg-2 at.%Zn, Mg-4 at.% Zn Mg-8 at.% Zn	Delay oxidation due to the presence of Mg_7Zn_3 intermetallic compound	Mg_2SiO_4 and MgO, no extra aluminum containing phase were observed	Decrease with increasing of Zn content	Smaller discharge channels and less accumulated around discharge channels with Zn content	[75]
Li	MgLiAl	Decrease the breakdown voltage and slow down the increase of voltage	The formation of MgO and $Mg_2(PO_4)_2$, and the accumulation of Li in the initial conversion layer at the coating/substrate interface	Lower coating thickness compared with pure Mg	Rougher surface morphology with treatment time	[50]
Ca	AZCa612	-	The formation of Mg-Al-Mn oxide and MgO	Approximately 30 μm	Rough and porous surface appearance with the pore size ranged from submicron scale to several micrometers	[93]
Nd	WE43-T6	Depend on the electrolyte composition, initial short-lived sparks distributed uniformly and long-lasting sparks occurred at high voltage	In silicate electrolyte, MgO, $MgSiO_3$ and Mg_2SiO_4 phases were formed. In phosphate electrolyte, MgO and $Mg_3(PO_4)_2$ were formed	Increased with treatment time, up to 30 μm	There were Nd-enriched regions with cellular-like sodification structure	[94]

Table 5 Effect of alloying elements of Al alloys on PEO coatings

Alloying element	Substrate	Coating composition	Coating thickness	Coating morphology	Ref.
Cu	AA2099-T8	The formation of α-Al_2O_3 and γ-Al_2O_3	~25 - 50 μm	Single-layer structure and pancake structures	[42]

Mg	pure Al, Al-0.5 wt.% Mg Al-1 wt.% Mg Al-2 wt.% Mg Al-4 wt.% Mg Al-7 wt.% Mg Al-15 wt.% Mg	Peak intensity of α-Al_2O_3 decreases and formation of $Mg_{0.388}Al_{2.408}O_4$ with Mg content	Increase with Mg content, from 85 to 150 µm	Porosity increased and dominant by spherical particles with Mg content	[95]
Mn	Al-1 at.% Mn Al-2 at.% Mn Al-4 at.% Mn Al-8 at.% Mn	Peak intensity of γ-Al_2O_3 decreased with Mn content	Increase with Mn content, from 116 to 162 µm	The number and size of spongy features as well as surface roughness increased with Mn content, from 6.6 to 8.4 µm	[87]
Si	Al-1 at.% Si Al-2 at.% Si Al-4 at.% Si Al-8 at.% Si Al-12 at.% Si Al-16 at.% Si Al-32 at.% Si	Peak intensity of mullite and γ-Al_2O_3 decreased with Si content	Decreased In an exponential manner with Si content	The number and size of droplet feature decreased (smoother) but the porosity increased with Si content	[84]
Zn	Al-1 wt.% Zn Al-4 wt.% Zn Al-8 wt.% Zn Al-10 wt.% Zn Al-15 wt.% Zn Al-33 wt.% Zn	Peak intensity mullite decreased with Si content and the formation of α-Al_2O_3 was suppressed	Increased to 120 µm with Zn content	The number and size of porosity increased with Zn content	[96]
Sn	Al-1 at.% Sn Al-2 at.% Sn Al-4 at.% Sn Al-6 at.% Sn Al-8 at.% Sn	α-Al_2O_3 only observed at lowest Sn content and the peak intensity of mullite increased with Sn content, SnO_2 also detected	Increased from 91 to 95 µm , then decreased to 73 µm (the coating was not formed at 8 at% Sn)	The glassy appearance dominated at 6 at% Sn with decreasing sponge feature	[97]
Ce	Al-18 wt.% Ce alloy	γ-Al_2O_3, $Al_6Si_2O_{13}$, α-Al_2O_3 and CeO_2 phases were formed	64 ± 7.1 µm, the coating thickness of oxide layer increased with addition of Ce	Outer porous and inner dense regions of the coating	[98]

Appendix

Table 6 Effect of alloying elements of Ti alloys on PEO coatings

Alloying element	Substrate	PEO process	Coating composition	Coating thickness	Coating morphology	Ref.
Mo	Ti-15Mo	-	The layer is composed of anatase and rutile and silicon species	-	With increasing voltage, the surface roughness increased from 0.33 to 3.17 μm	[99]
Nb	Ti-10 wt.% Nb Ti-30 wt.% Nb Ti-50 wt.% Nb	At potentio-static condition, the increasing of Nb content caused a higher current density	With increasing Nb content, brookite disappeared, however, rutile and Nb_2O_5 were formed	Insignificant effect on coating thickness, around 1.8 μm	For higher than 30 wt% Nb, large sized crater with grooved structure are observed	[92]
V/Al	pure Ti Ti6Al4V	Breakdown voltage is 90 V for pure Ti, 80 - 83 V for Ti6Al4V	-	Higher layer on β-Ti than on α-Ti	Higher porosity (8.9%) on alloy, with distribution of irregular vermiform slots on surface	[100]

Table 7 Effects of reinforcement phases of MMCs on PEO process

Matrix	Reinforcement phase	Size	Melting point	PEO process	Incorporation mode	Morphology	Coating composition	Ref.
AZ31	6 vol.% SiC	10 μm in average (particles)	3003 K	Take part in discharges detected by OES, molten firstly and then reacted with oxygen and MgO	Partially reactive incorporation	Appear in the substrate near the composite/coating interface, reduced number in the coating	Mainly contains MgO, minor content of Mg_2SiO_4 (produced from SiC),MgF_2 and $Mg_3(PO_4)_2$	[57, 101]
AZ91	Al_2O_3-SiO_2	1 - 3 μm in diameter, 50 - 100 μm in length (fiber)	2123 K	Take part in discharges detected by OES, molten firstly and then reacted with oxygen and MgO	Partially reactive incorporation	Appear in the substrate near the composite/coating interface, reduced number in the coating	Mainly contains MgO, and mullite ($3Al_2O_3 \cdot 2SiO_2$), $MgAl_2O_4$ and $MgSiO_3$ also observed, formed from Al_2O_3 and SiO_2	[57]
AZ91Nd	50 vol.% Al_2O_3	ca. 3 μm in diameter, ca.	2054 ℃	Delay of voltage ramp at initial stage, and	Partially reactive incorporation	Visible on the surface at first, then the surface	MgO, $MgAl_2O_4$ and $Mg_3(PO_4)_2$	[102]

		100 μm in length (fiber)		fluctuation of voltage at the last stage		become uniform however, the cross-sections shows the continuity interrupted by the fiber		
AZ91	2 vol.% SiC 5 vol.% SiC 10 vol.% SiC 15 vol.% SiC	ca. 5 μm (particles)	-	Voltage increment became lower than pure alloy, at lower current density, even the voltage cannot increase with increasing SiC content	Partially reactive incorporation	At lower voltage, SiC particles can be still observed, then the uniform porous coating is formed	SiO_2 was produced, and SiC is still detected in the coating	[25]
AZ92	5 vol.% SiC 10 vol.% SiC	ca. 5 μm (particles)	-	Average growth rate of 1 - 1.2 μm/min, slightly decrease for higher SiC content	Partially reactive incorporation	A rougher interface of substrate/coating than pure alloy, a Si-rich interface around SiC particles	SiO_2 was produced	[38]
AZ91	2 vol.% SiC 5 vol.% SiC 10 vol.% SiC	ca. 15 - 25 μm (particles)	-	Voltage is slightly lower for reinforced alloy than pure alloy, no voltage drop observed for higher SiC contents (5-10 vol.%)	Partially reactive incorporation	Increased surface roughness with increasing SiC content	MgO, Al_2O_3, MgF_2 and CeO_2	[40]
LA142	5 wt.% YAl_2	ca. 0.5 - 3 μm (particles)	-	-	-	-	MgO, Mg_2SiO_4, $Mg_9(SiO_4)_4(OH,F)_2$	[103]
AZ91	20 vol.% SiC	0.1 - 1.0 μm in diameter, 30-100 μm in length (fiber)	-	-	Inert incorporation	Some micro-cracks were observed	MgO, minor $MgAl_2O_4$, MgF_2, and magnesium silicate	[52]
ZC71	12 vol.% SiC	ca. 0.5 - 3 μm (particles)	2730 ℃	-	Inert incorporation	Numerous pores with an average size in the range of 1-4 μm, SiC particles are largely unchanged in the coating	MgO, Mg_2SiO_4,$Mg(OH)_2$	[104]
AZ31B	0.5 wt.% MWCNT,	Nano tubes	-	-	-	Crater-like holes with small size and low	MgO and Mg_2SiO_4	[105]

						amount of porosity and micro-cracks		
AZ31B	0.25 wt.% MWCNT, 0.5 wt.% MWCNT, 1.0 wt.% MWCNT	Outer diameter 10 - 40 nm, inner diameter 10 - 20 nm, length 30 - 50 nm (fiber)	-	-	-	More inhomogeneities in coating with higher content	MgO and Mg_2SiO_4 and Al_2SiO_5	[106]
Pure Mg	10 wt.% HA 20 wt.% HA	-	-	-	-	-	HA and MgO	[107]
2024	15 vol.% SiC	ca. 12.8 µm	-	-	Mostly incorporated reactively	Composite/coating interface is irregular and a few SiC appear at the interface	α- and γ-Al_2O_3, and mullite	[39]
A201	8 wt.% TiB_2	-	-	Four stages of voltage response, characterized by evolution of sparks and buzzing sounds	Reactive incorporation	Highly porous layer on TiB_2, the porosity decreased with PEO processing	α- and γ-Al_2O_3	[108]
A356	20 vol.% SiC	particles	-	-	-	Mainly composed of two layers, a 60 µm dense layer and a 30 µm porous layer	α-Al_2O_3 and mullite are the main phases, γ-Al_2O_3 is formed.	[109]
pure Al	15 wt.% CuO	ca. 40 µm	-	-	-	Very rough and porous coating surface. The coarse pores at the outermost section of the coating about 7 µm.	Al_2O_3	[110]
Al-1.2Mg-0.6Si-0.3Cu	55 vol.% SiC	40 and 60 µm particles	-	Four stages for current evolution. SiC hindered the formation of the coating	Reactive incorporation	Rough and uneven pores at variable size	Mullite as main phase, in addition to α-Al_2O_3, γ-Al_2O_3 and amorphous phase	[111]

3. Publications during candidate

Peer-reviewed papers

1) **T. Wu**, C. Blawert and M. L. Zheludkevich, Influence of secondary phases of AlSi9Cu3 alloy on the plasma electrolytic oxidation coating formation process, Journal of Materials Science & Technology, (2020) 75. 10.1016/j.jmst.2019.12.031.

2) **T. Wu**, C. Blawert, X. Lu, M. Serdechnova and M. L. Zheludkevich, Difference in formation of plasma electrolytic oxidation coatings on MgLi alloy in comparison with pure Mg, Journal of Magnesium and Alloys, (2021) 10.1016/j.jma.2021.03.017.

3) **T. Wu**, C. Blawert, M. Serdechnova, P. Karlova, G. Dovzhenko, D. C. F. Weiland and M. L. Zheludkevich, PEO processing of AZ91Nd/Al_2O_3 MMC – The role of alumina fibers, Journal of Magnesium and Alloys, (2022) 10.1016/j.jma.2021.09.017.

4) **T. Wu**, C. Blawert, M. Serdechnova, P. Karlova, G. Dovzhenko, D. C. F. Weiland, S. Stojadinovic, R. Vasilic, K. Mojsilovic and M. L. Zheludkevich, Formation of Plasma Electrolytic Oxidation Coatings on Pure Niobium in Different Electrolytes, Applied Surface Science, (2022) 573. 10.1016/j.apsusc.2021.151629.

5) **T. Wu**, C. Blawert, M. Serdechnova, P. Karlova, G. Dovzhenko, D. C. F. Weiland and M. L. Zheludkevich, Role of polymorph microstructure of Ti6Al4V alloy on PEO coating formation in phosphate electrolyte, Surface & Coating Technology, (2021)428. 10.1016/j.surfcoat.2021.127890.

6) **T. Wu**, C. Blawert, M. Serdechnova, P. Karlova, G. Dovzhenko, D. C. F. Weiland, S. Stojadinovic, R. Vasilic, L. Wang, C. Wang, K. Mojsilovic and M. L. Zheludkevich, Role of phosphate, silicate and aluminate in the electrolytes on PEO coating formation and properties on Ti6Al4V alloy, Applied Surface Science, (2022) 595. 10.1016/j.apsusc.2022.153523.

7) **T. Wu**, C. Blawert, M. Serdechnova and M. L. Zheludkevich, Influence of micro- and macro scale material mix on plasma electrolytic oxidation processing, submitted for publication.

4. Publications included in this dissertation

1) **T. Wu**, C. Blawert and M. L. Zheludkevich, Influence of secondary phases of AlSi9Cu3 alloy on the plasma electrolytic oxidation coating formation process, Journal of Materials Science & Technology, (2020) 75. 10.1016/j.jmst.2019.12.031.

T. Wu conceived and designed the study in discussion with C. Blawert. T. Wu carried out the experimental work. C. Blawert and M. L. Zheludkevich gave constructive comments on data analysis. All the authors contributed to the interpretation of the results and to writing of the paper.

2) **T. Wu**, C. Blawert, X. Lu, M. Serdechnova and M. L. Zheludkevich, Difference in formation of plasma electrolytic oxidation coatings on MgLi alloy in comparison with pure Mg, Journal of Magnesium and Alloys, (2021) 10.1016/j.jma.2021.03.017.

T. Wu conceived and designed the study in discussion with C. Blawert. T. Wu carried out the experimental work. C. Blawert, X. Lu, M. Serdechnova and M. L. Zheludkevich gave constructive comments on data analysis. All the authors contributed to the interpretation of the results and to writing of the paper.

3) **T. Wu**, C. Blawert, M. Serdechnova, P. Karlova, G. Dovzhenko, D. C. F. Weiland and M. L. Zheludkevich, PEO processing of AZ91Nd/Al_2O_3 MMC – The role of alumina fibers, Journal of Magnesium and Alloys, (2022) 10.1016/j.jma.2021.09.017.

T. Wu conceived and designed the study in discussion with C. Blawert and M. Serdechnova. T. Wu carried out the main experimental work. P. Karlova, G. Dovzhenko and D. C. F. Weiland helped with DESY measurement. M. L. Zheludkevich gave constructive comments on data analysis. All the authors contributed to the interpretation of the results and to writing of the paper.

4) **T. Wu**, C. Blawert, M. Serdechnova, P. Karlova, G. Dovzhenko, D. C. F. Weiland, S. Stojadinovic, R. Vasilic, K. Mojsilovic and M. L. Zheludkevich, Formation of Plasma Electrolytic Oxidation Coatings on Pure Niobium in Different Electrolytes, Applied Surface Science, (2022) 573. 10.1016/j.apsusc.2021.151629.

T. Wu conceived and designed the study in discussion with C. Blawert and M. Serdechnova. T. Wu carried out the main experimental work. P. Karlova, G. Dovzhenko and D. C. F. Weiland helped with DESY measurement. S. Stojadinovic, R. Vasilic and K. Mojsilovic helped with photocatalytic measurement. M. L. Zheludkevich gave constructive comments on data analysis. All the authors contributed to the interpretation of the results and to writing of the paper.

5) **T. Wu**, C. Blawert, M. Serdechnova, P. Karlova, G. Dovzhenko, D. C. F. Weiland and M. L. Zheludkevich, Role of polymorph microstructure of Ti6Al4V alloy on PEO coating formation in phosphate electrolyte, Surface & Coating Technology, (2021)428. 10.1016/j.surfcoat.2021.127890.

T. Wu conceived and designed the study in discussion with C. Blawert and M. Serdechnova. T. Wu carried out the main experimental work. P. Karlova, G. Dovzhenko and D. C. F. Weiland helped with DESY measurement. M. L. Zheludkevich gave constructive comments on data analysis. All the authors

contributed to the interpretation of the results and to writing of the paper.

6) **T. Wu**, C. Blawert, M. Serdechnova, P. Karlova, G. Dovzhenko, D. C. F. Weiland, S. Stojadinovic, R. Vasilic, L. Wang, C. Wang, K. Mojsilovic and M. L. Zheludkevich, Role of phosphate, silicate and aluminate in the electrolytes on PEO coating formation and properties on Ti6Al4V alloy, Applied Surface Science, (2022) 595. 10.1016/j.apsusc.2022.153523.

T. Wu conceived and designed the study in discussion with C. Blawert and M. Serdechnova. T. Wu carried out the main experimental work. P. Karlova, G. Dovzhenko and D. C. F. Weiland helped with DESY measurement. S. Stojadinovic, R. Vasilic and K. Mojsilovic helped with photocatalytic measurement. L. Wang and C. Wang helped with EIS analysis. M. L. Zheludkevich gave constructive comments on data analysis. All the authors contributed to the interpretation of the results and to writing of the paper.

7) **T. Wu**, C. Blawert, M. Serdechnova and M. L. Zheludkevich, Influence of micro- and macro scale material mix on plasma electrolytic oxidation processing, submitted for publication

T. Wu conceived and designed the study in discussion with C. Blawert. C. Blawert, M. Serdechnova and M. L. Zheludkevich gave constructive comments on data analysis. All the authors contributed to the interpretation of the results and to writing of the paper.

Bibliography

[1] A. L. Yerokhin, X. Nie, A. Leyland, A. Matthews and S. J. Dowey, Plasma electrolysis for surface engineering, Surface and Coatings Technology, 122 (1999) 73.

[2] X. Nie, A. Leyland, H. W. Song, A. L. Yerokhin, S. J. Dowey and A. Matthews, Thickness effects on the mechanical properties of micro-arc discharge oxide coatings on aluminium alloys, Surface and Coatings Technology, (1999) 1055.

[3] R. Arrabal, E. Matykina, F. Viejo, P. Skeldon, G. E. Thompson and M. C. Merino, AC plasma electrolytic oxidation of magnesium with zirconia nanoparticles, Applied Surface Science, 21 (2008) 6937. 10.1016/j.apsusc.2008.04.100

[4] X. Lu, M. Mohedano, C. Blawert, E. Matykina, R. Arrabal, K. U. Kainer and M. L. Zheludkevich, Plasma electrolytic oxidation coatings with particle additions - A review, Surface and Coatings Technology, (2016) 1165. 10.1016/j.surfcoat.2016.08.055

[5] C. Blawert, W. Dietzel, E. Ghali and G. Song, Anodizing treatments for magnesium alloys and their effect on corrosion resistance in various environments, Advanced Engineering Materials, 6 (2006) 511. 10.1002/adem.200500257

[6] R. O. Hussein, X. Nie, D. O. Northwood, A. Yerokhin and A. Matthews, Spectroscopic study of electrolytic plasma and discharging behaviour during the plasma electrolytic oxidation (PEO) process, Journal of Physics D: Applied Physics, (2010) 105203. 10.1088/0022-3727/43/10/105203

[7] R. O. Hussein, X. Nie and D. O. Northwood, A spectroscopic and microstructural study of oxide coatings produced on a Ti-6Al-4V alloy by plasma electrolytic oxidation, Materials Chemistry and Physics, 1 (2012) 484. 10.1016/j.matchemphys.2012.03.020

[8] R. O. Hussein, D. O. Northwood and X. Nie, Coating growth behavior during the plasma electrolytic oxidation process, Journal of Vacuum Science & Technology A: Vacuum, Surfaces, and Films, 4 (2010) 766. 10.1116/1.3429583

[9] T. W. Clyne and S. C. Troughton, A review of recent work on discharge characteristics during plasma electrolytic oxidation of various metals, International Materials Reviews, 3 (2018) 127. 10.1080/09506608.2018.1466492

[10] K. Babaei, A. Fattah-alhosseini and R. Chaharmahali, A review on plasma electrolytic oxidation (PEO) of niobium: Mechanism, properties and applications, Surfaces and Interfaces, (2020) 100719. 10.1016/j.surfin.2020.100719

[11] Z. Li, Q. Kuang, X. Dong, T. Yuan, Q. Ren, X. Wang, J. Wang and X. Jing, Characteristics of high-performance anti-corrosion/anti-wear ceramic coatings on magnesium-lithium alloy by plasma electrolytic oxidation surface engineering, Surface and Coatings Technology, (2019) 600. 10.1016/j.surfcoat.2019.07.066

[12] B. Mingo, R. Arrabal, M. Mohedano, A. Pardo and E. Matykina, Corrosion and wear of PEO coated AZ91/SiC composites, Surface and Coatings Technology, (2017)

10.1016/j.surfcoat.2016.10.041

[13] M. Mohedano, B. J. C. Luthringer, B. Mingo, F. Feyerabend, R. Arrabal, P. J. Sanchez-Egido, C. Blawert, R. Willumeit-Römer, M. L. Zheludkevich and E. Matykina, Bioactive plasma electrolytic oxidation coatings on Mg-Ca alloy to control degradation behaviour, Surface and Coatings Technology, (2017) 454. 10.1016/j.surfcoat.2017.02.050

[14] M. Kaseem and H. C. Choe, Electrochemical and bioactive characteristics of the porous surface formed on Ti-xNb alloys via plasma electrolytic oxidation, Surface and Coatings Technology, (2019) 125027. 10.1016/j.surfcoat.2019.125027

[15] S. Stojadinović, N. Tadić, N. Radić, P. Stefanov, B. Grbić and R. Vasilić, Anodic luminescence, structural, photoluminescent, and photocatalytic properties of anodic oxide films grown on niobium in phosphoric acid, Applied Surface Science, (2015) 912. 10.1016/j.apsusc.2015.07.174

[16] S. Stojadinović, N. Tadić, N. Radić, B. Grbić and R. Vasilić, MgO/ZnO coatings formed on magnesium alloy AZ31 by plasma electrolytic oxidation: Structural, photoluminescence and photocatalytic investigation, Surface and Coatings Technology, (2017) 10.1016/j.surfcoat.2016.12.073

[17] L. Yu, J. Cao and Y. Cheng, An improvement of the wear and corrosion resistances of AZ31 magnesium alloy by plasma electrolytic oxidation in a silicate–hexametaphosphate electrolyte with the suspension of SiC nanoparticles, Surface and Coatings Technology, (2015) 10.1016/j.surfcoat.2015.07.014

[18] D. Jiang, H. Zhou, S. Wan, G.-Y. Cai and Z.-H. Dong, Fabrication of superhydrophobic coating on magnesium alloy with improved corrosion resistance by combining micro-arc oxidation and cyclic assembly, Surface and Coatings Technology, (2018) 10.1016/j.surfcoat.2018.02.001

[19] S. Farshid and M. Kharaziha, Micro and nano-enabled approaches to improve the performance of plasma electrolytic oxidation coated magnesium alloys, Journal of Magnesium and Alloys, (2020) 10.1016/j.jma.2020.11.004

[20] G. Rapheal, S. Kumar, N. Scharnagl and C. Blawert, Effect of current density on the microstructure and corrosion properties of plasma electrolytic oxidation (PEO) coatings on AM50 Mg alloy produced in an electrolyte containing clay additives, Surface and Coatings Technology, (2016) 10.1016/j.surfcoat.2016.01.033

[21] Z. Shahri, S. R. Allahkaram, R. Soltani and H. Jafari, Optimization of plasma electrolyte oxidation process parameters for corrosion resistance of Mg alloy, Journal of Magnesium and Alloys, 2 (2020) 431. 10.1016/j.jma.2018.10.001

[22] G. Zhang, L. Wu, A. Tang, Y. Ma, G. L. Song, D. Zheng, B. Jiang, A. Atrens and F. Pan, Active corrosion protection by a smart coating based on a MgAl-layered double hydroxide on a cerium-modified plasma electrolytic oxidation coating on Mg alloy AZ31, Corrosion Science, (2018) 10.1016/j.corsci.2018.05.010

[23] X. Lu, C. Blawert, K. U. Kainer, T. Zhang, F. Wang and M. L. Zheludkevich, Influence of particle additions on corrosion and wear resistance of plasma electrolytic oxidation coatings on Mg alloy,

Surface and Coatings Technology, (2018) 1. 10.1016/j.surfcoat.2018.08.003

[24] B. Mingo, R. Arrabal, M. Mohedano, Y. Llamazares, E. Matykina, A. Yerokhin and A. Pardo, Influence of sealing post-treatments on the corrosion resistance of PEO coated AZ91 magnesium alloy, Applied Surface Science, (2018) 10.1016/j.apsusc.2017.10.083

[25] Y. Guan, Y. Xia and G. Li, Growth mechanism and corrosion behavior of ceramic coatings on aluminum produced by autocontrol AC pulse PEO, Surface and Coatings Technology, 19 (2008) 4602. 10.1016/j.surfcoat.2008.03.031

[26] E. Matykina, R. Arrabal, D. J. Scurr, A. Baron, P. Skeldon and G. E. Thompson, Investigation of the mechanism of plasma electrolytic oxidation of aluminium using ^{18}O tracer, Corrosion Science, 3 (2010) 1070. 10.1016/j.corsci.2009.11.038

[27] R. O. Hussein, X. Nie and D. O. Northwood, An investigation of ceramic coating growth mechanisms in plasma electrolytic oxidation (PEO) processing, Electrochimica Acta, (2013) 10.1016/j.electacta.2013.08.137

[28] X. Lu, C. Blawert, M. Mohedano, N. Scharnagl, M. L. Zheludkevich and K. U. Kainer, Influence of electrical parameters on particle uptake during plasma electrolytic oxidation processing of AM50 Mg alloy, Surface and Coatings Technology, (2016) 10.1016/j.surfcoat.2016.02.006

[29] D. Quintero, M. A. Gómez, W. S. Araujo, F. Echeverría and J. A. Calderón, Influence of the electrical parameters of the anodizing PEO process on wear and corrosion resistance of niobium, Surface and Coatings Technology, (2019) 125067. 10.1016/j.surfcoat.2019.125067

[30] R. Arrabal, E. Matykina, T. Hashimoto, P. Skeldon and G. E. Thompson, Characterization of AC PEO coatings on magnesium alloys, Surface and Coatings Technology, 16 (2009) 2207. 10.1016/j.surfcoat.2009.02.011

[31] D. Veys-Renaux, E. Rocca, J. Martin and G. Henrion, Initial stages of AZ91 Mg alloy micro-arc anodizing: Growth mechanisms and effect on the corrosion resistance, Electrochimica Acta, (2014) 36. 10.1016/j.electacta.2013.08.023

[32] Y. Q. Wang, X. J. Wang, W. X. Gong, K. Wu and F. H. Wang, Effect of SiC particles on microarc oxidation process of magnesium matrix composites, Applied Surface Science, (2013) 10.1016/j.apsusc.2013.07.041

[33] A. V. Apelfeld, A. M. Borisov, B. L. Krit, V. B. Ludin, M. N. Polyansky, E. A. Romanovsky, S. V. Savushkina, I. V. Suminov, N. V. Tkachenko, A. V. Vinogradov and V. G. Vostrikov, The study of plasma electrolytic oxidation coatings on Zr and Zr-1% Nb alloy at thermal cycling, Surface and Coatings Technology, (2015) 10.1016/j.surfcoat.2015.02.039

[34] R. Arrabal, E. Matykina, P. Skeldon and G. E. Thompson, Coating formation by plasma electrolytic oxidation on ZC71/SiC/12p-T6 magnesium metal matrix composite, Applied Surface Science, 9 (2009) 5071. 10.1016/j.apsusc.2008.12.070

[35] K. O. Gunduz, Z. C. Oter, M. Tarakci and Y. Gencer, Plasma electrolytic oxidation of binary Mg-

Al and Mg-Zn alloys, Surface and Coatings Technology, (2017) 10.1016/j.surfcoat.2016.08.040

[36] T. R. Thomas, Characterization of surface roughness, Precision Engineering, (1981) 97.

[37] C. Krywka, H. Neubauer, M. Priebe, T. Salditt, J. Keckes, A. Buffet, S. V. Roth, R. Doehrmann and M. Mueller, A two-dimensional waveguide beam for X-ray nanodiffraction, Journal of Applied Crystallography, 1 (2011) 85. 10.1107/s0021889811049132

[38] J. Kieffer and D. Karkoulis, PyFAI, a versatile library for azimuthal regrouping, Journal of Physics: Conference Series, 20 (2013) 202012. 10.1088/1742-6596/425/20/202012

[39] V. Shkirskiy, P. Maciel, J. Deconinck and K. Ogle, On the time resolution of the atomic emission spectroelectrochemistry method, Journal of The Electrochemical Society, 3 (2015) C37. 10.1149/2.0991602jes

[40] J. Światowska, P. Volovitch and K. Ogle, The anodic dissolution of Mg in NaCl and Na_2SO_4 electrolytes by atomic emission spectroelectrochemistry, Corrosion Science, 7 (2010) 2372. 10.1016/j.corsci.2010.02.038

[41] K. Ogle, A. Tomandl, N. Meddahi and M. Wolpers, The alkaline stability of phosphate coatings I: ICP atomic emission spectroelectrochemistry, Corrosion Science, 4 (2004) 979. 10.1016/s0010-938x(03)00182-3

[42] T. Arunnellaiappan, N. Kishore Babu, L. Rama Krishna and N. Rameshbabu, Influence of frequency and duty cycle on microstructure of plasma electrolytic oxidized AA7075 and the correlation to its corrosion behavior, Surface and Coatings Technology, (2015) 10.1016/j.surfcoat.2015.08.043

[43] A. L. Yerokhin, L. O. Snizhko, N. L. Gurevina, A. Leyland, A. Pilkington and A. Matthews, Discharge characterization in plasma electrolytic oxidation of aluminium, Journal of Physics D: Applied Physics, (2003) 2110.

[44] A. L. Yerokhin, X. Nie, A. Leyland, A. Matthews and S. J. Dowey, Plasma electrolysis for surface engineering, Surface and Coatings Technology, (1999) 73.

[45] R. Arrabal, E. Matykina, P. Skeldon, G. E. Thompson and A. Pardob, Transport of species during plasma electrolytic oxidation of WE43-T6 magnesium alloy, 10.1149/1.2823374

[46] C. Blawert, S. A. Karpushenkov, M. Serdechnova, L. S. Karpushenkava and M. L. Zheludkevich, Plasma electrolytic oxidation of zinc alloy in a phosphate-aluminate electrolyte, Applied Surface Science, (2020) 144552. 10.1016/j.apsusc.2019.144552

[47] B. Mingo, Y. Guo, A. Němcová, A. Gholinia, M. Mohedano, M. Sun, A. Matthews and A. Yerokhin, Incorporation of halloysite nanotubes into forsterite surface layer during plasma electrolytic oxidation of AM50 Mg alloy, Electrochimica Acta, (2019) 772. 10.1016/j.electacta.2019.01.047

[48] T. Wu, C. Blawert and M. L. Zheludkevich, Influence of secondary phases of AlSi9Cu3 alloy on the plasma electrolytic oxidation coating formation process, Journal of Materials Science & Technology, (2020) 75. 10.1016/j.jmst.2019.12.031

[49] T. Wu, C. Blawert, X. Lu, M. Serdechnova and M. L. Zheludkevich, Difference in formation of plasma electrolytic oxidation coatings on MgLi alloy in comparison with pure Mg, Journal of

Magnesium and Alloys, (2021) 10.1016/j.jma.2021.03.017

[50] D. Veys-Renaux and E. Rocca, Initial stages of multi-phased aluminium alloys anodizing by MAO: micro-arc conditions and electrochemical behaviour, Journal of Solid State Electrochemistry, 10 (2015) 10.1007/s10008-015-2935-3

[51] L. E. Fratila-Apachitei, H. Terryn, P. Skeldon, G. E. Thompson, J. Duszczyk and L. Katgerman, Influence of substrate microstructure on the growth of anodic oxide layers, Electrochimica Acta, 7 (2004) 1127. 10.1016/j.electacta.2003.10.024

[52] K. Li, W. Li, G. Zhang, W. Zhu, F. Zheng, D. Zhang and M. Wang, Effects of Si phase refinement on the plasma electrolytic oxidation of eutectic Al-Si alloy, Journal of Alloys and Compounds, (2019) 650. 10.1016/j.jallcom.2019.03.217

[53] H. Liu, X. Mao, J. Cui, S. Jiang and W. Zhang, Investigation of high temperature electrical insulation property of MgO ceramic films and the influence of annealing process, Ceramics International, 18 (2019) 24343. 10.1016/j.ceramint.2019.08.151

[54] L. Zhang, H. C. Jiang, C. Liu, J. W. Dong and P. Chow, Annealing of Al_2O_3 thin films prepared by atomic layer deposition, Journal of Physics D: Applied Physics, 12 (2007) 3707. 10.1088/0022-3727/40/12/025

[55] A. A. Levchenko, G. Li, J. Boerio-Goates, B. F. Woodfield and A. Navrotsky, TiO_2 stability landscape: polymorphism, surface energy, and bound water energetics, Chemistry of Materials, 26 (2006) 6324.

[56] M. Abood, E. T. Salim and J. A. Saimon, Optical investigations of Nb_2O_5 at different teamperatures for optoelectronic devices, Journal of Ovonic Research, 2 (2019) 109.

[57] S. Stojadinović and R. Vasilić, Orange–red photoluminescence of Nb_2O_5 :Eu^{3+} , Sm^{3+} coatings formed by plasma electrolytic oxidation of niobium, Journal of Alloys and Compounds, (2016) 10.1016/j.jallcom.2016.06.192

[58] L. E. Fratila-Apachitei, I. Apachitei and J. Duszczyk, Characterization of cast AlSi(Cu) alloys by scanning Kelvin probe force microscopy, Electrochimica Acta, 26 (2006) 5892. 10.1016/j.electacta.2006.03.027

[59] R. Arrabal, B. Mingo, A. Pardo, M. Mohedano, E. Matykina and I. Rodríguez, Pitting corrosion of rheocast A356 aluminium alloy in 3.5 wt.% NaCl solution, Corrosion Science, (2013) 342. 10.1016/j.corsci.2013.04.023

[60] H. Duan, C. Yan and F. Wang, Growth process of plasma electrolytic oxidation films formed on magnesium alloy AZ91D in silicate solution, Electrochimica Acta, 15 (2007) 5002. 10.1016/j.electacta.2007.02.021

[61] A. G. Rakoch, E. P. Monakhova, Z. V. Khabibullina, M. Serdechnova, C. Blawert, M. L. Zheludkevich and A. A. Gladkova, Plasma electrolytic oxidation of AZ31 and AZ91 magnesium alloys: Comparison of coatings formation mechanism, Journal of Magnesium and Alloys, 3 (2020) 587.

10.1016/j.jma.2020.06.002

[62] K. M. Lee, B. U. Lee, S. I. Yoon, E. S. Lee, B. Yoo and D. H. Shin, Evaluation of plasma temperature during plasma oxidation processing of AZ91 Mg alloy through analysis of the melting behavior of incorporated particles, Electrochimica Acta, (2012) 6. 10.1016/j.electacta.2012.01.053

[63] J. G. Speight, Lange's handbook of chemistry, (2017)

[64] L. Wang and X. Nie, Silicon effects on formation of EPO oxide coatings on aluminum alloys, Thin Solid Films, 1-2 (2006) 211. 10.1016/j.tsf.2005.07.184

[65] H. Yu, Q. Dong, Y. Chen and C. Chen, Influence of silicon on growth mechanism of micro-arc oxidation coating on cast Al-Si alloy, R Soc Open Sci, 7 (2018) 10.1098/rsos.172428

[66] F. Xu, Y. Xia and G. Li, The mechanism of PEO process on Al–Si alloys with the bulk primary silicon, Applied Surface Science, 23 (2009) 9531. 10.1016/j.apsusc.2009.07.090

Acknowledgement

It is my pleasure to express sincere gratitude to all the people who have contributed to this dissertation by their kind support, assistance and encouragement. The dissertation would not be accomplished successfully without their contributions.

Firstly, I would particularly express my appreciation in earnest to Prof. Mikhail Zheludkevich for giving me this great opportunity to conduct my PhD work in the institute of Surface Science at Helmholtz Zentrum Hereon and the chances to communicate with peer scientists worldwide. His guidance and willingness to share his views and knowledge to all group members inspire me to keep moving in academic. All of my work was companied with his constructive comments and advices.

Many thanks to my daily supervisor, Dr. Carsten Blawert, a senior scientist in the field of PEO research. Based on his expertise and experience, he is always willing to share valuable opinions and suggestions on my work, which is significant for me to address the problems I meet. I have truly learnt much about PEO technique in our daily discussions. Special thanks are given to Dr. Maria Serdechnova, a senior scientist in our Functional Surface Department, who participated in the most of my work and encouraged me for innovative ideas. Our discussions are always important for me to modify the experimental design and to better address the issues relevant to my topic. I will never forget the evening we two sat on the floor and listen to Carsten about the suggestions for my thesis at DESY.

I also want to show my acknowledgement to Mr. Volker Heitman, Mr. Ulrich Burmester, Mr. Gert Wiese, Ms. Petra Fischer, Mr. Daniel Strerath, and Ms. Sabine Schubert regarding all the assistance on materials preparation, characterization and chemical analysis. Besides, I would like to thank all the colleagues from MO, especially Ms. Polina Karlova and the colleagues Dr. Gleb. Dovzhenko, Dr. Florian Weiland from WPD and MBS. My research work would not go well without their kind collaboration and support at DESY. Many thanks to all my Chinese friends in Geesthacht enabling me to have cheerful leisure time after exhausted work. I really enjoy all the time travelling and hanging out with them.

Sincerely I appreciate the fellowship from China Scholarship Council (CSC) for supporting the whole work described in this thesis.

Most importantly, I would like to express my deepest gratitude to my family, particularly my parents and my husband Mr. Jiashun Luo. I am grateful to my family for supporting every of my career plans, including studying aboard to achieve higher educational degree. The lovely harmonious family atmosphere built by parents is certainly the cornerstone of the completion of my PhD and my growing in good health. They set a good example for me to learn how to build a long-term and stable relationship.